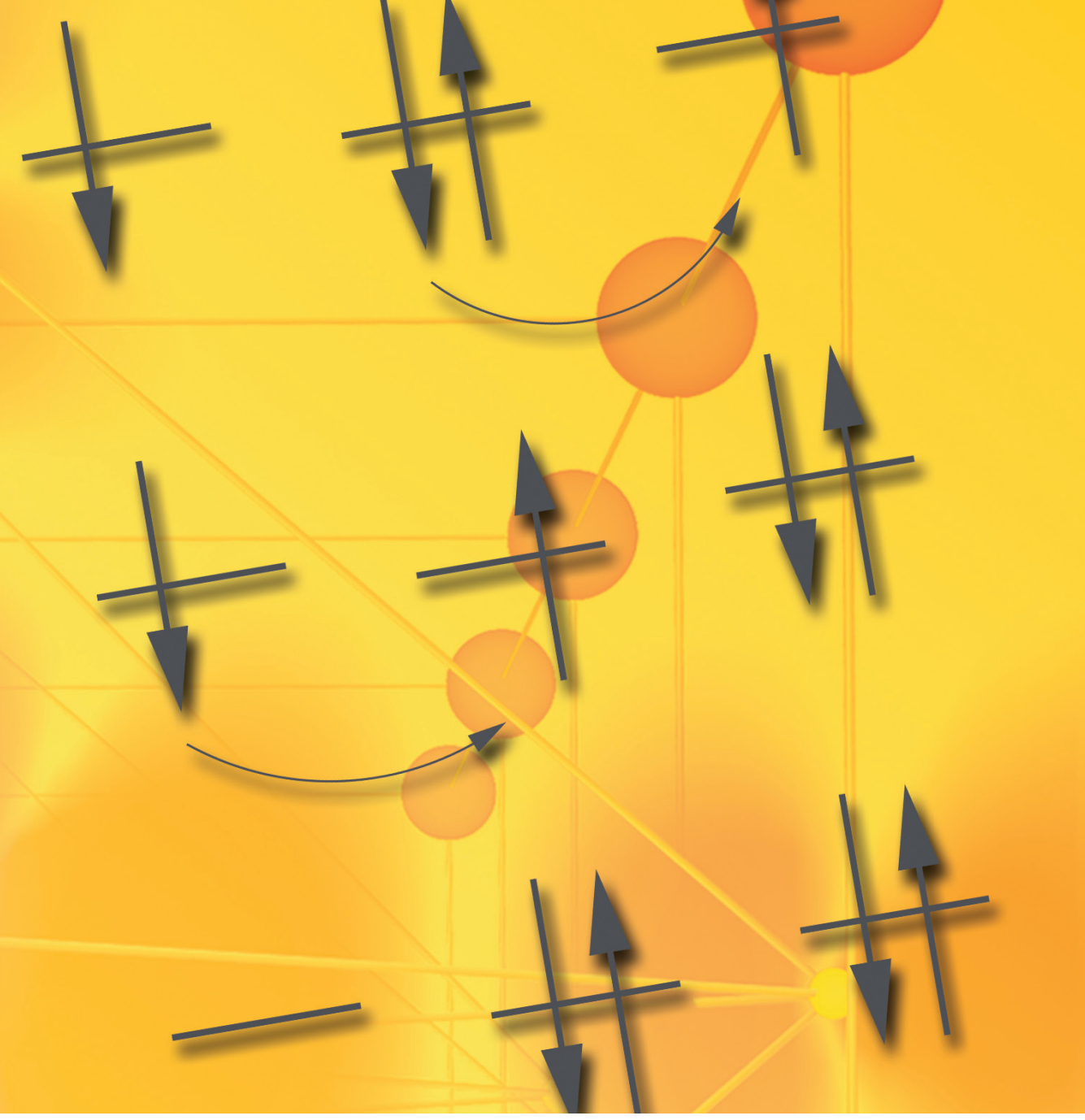

Correlated Electrons: From Models to Materials

Eva Pavarini, Erik Koch, Frithjof Anders, and Mark Jarrell (Eds.)

German Research School
for Simulation Sciences

JÜLICH
FORSCHUNGSZENTRUM

Schriften des Forschungszentrums Jülich
Reihe Modeling and Simulation Band / Volume 2

Forschungszentrum Jülich GmbH
Institute for Advanced Simulation

German Research School for
Simulation Sciences GmbH

Lecture Notes of the Autumn School
Correlated Electrons 2012

Eva Pavarini, Erik Koch, Frithjof Anders, and Mark Jarrell (Eds.)

Correlated Electrons: From Models to Materials

Autumn School organized by
the Forschungszentrum Jülich
and the German Research School
for Simulation Sciences

at Forschungszentrum Jülich
3 – 7 September 2012

Schriften des Forschungszentrums Jülich
Reihe Modeling and Simulation

Band / Volume 2

ISSN 2192-8525

ISBN 978-3-89336-796-2

Bibliographic information published by the Deutsche Nationalbibliothek.
The Deutsche Nationalbibliothek lists this publication in the Deutsche Nationalbibliografie; detailed bibliographic data are available in the Internet at http://dnb.d-nb.de.

Publisher:	Forschungszentrum Jülich GmbH Institute for Advanced Simulation
Cover Design:	Grafische Medien, Forschungszentrum Jülich GmbH
Printer:	Druckerei Schloemer, Düren
Copyright:	Forschungszentrum Jülich 2012
Distributor:	Forschungszentrum Jülich Zentralbibliothek, Verlag D-52425 Jülich Phone +49 (0)2461 61-5368 · Fax +49 (0)2461 61-6103 e-mail: zb-publikation@fz-juelich.de Internet: http://www.fz-juelich.de

Schriften des Forschungszentrums Jülich
Reihe Modeling and Simulation Band / Volume 2

ISSN 2192-8525
ISBN 978-3-89336-796-2

The complete volume ist freely available on the Internet on the Jülicher Open Access Server (JUWEL) at http://www.fz-juelich.de/zb/juwel

Contents

Preface

Density-functional theory (DFT) is considered the Standard Model of solid-state physics. The state-of-the-art approximations to DFT, the local-density approximation (LDA) or its simple extensions, fail, however, even qualitatively, for strongly-correlated systems. When correlations are strong, electrons become entangled and novel properties emerge. Mott-transitions, Kondo- and heavy-fermion behavior, non-conventional superconductivity and orbital-order are just some examples of this emergent behavior.

The realistic description of emergent properties is one of the grand-challenges of modern condensed-matter physics. To understand this physics beyond the Standard Model, non-perturbative many-body techniques are essential. Still, DFT-based methods are needed to devise materials-specific Hamiltonians for strong correlations. Mastering these novel techniques requires a vast background, ranging from DFT to model building and many-body physics.

The aim of this school is to introduce advanced graduate students and up to the modern methods for modeling emergent properties of correlated electrons and to explore the relation of electron correlations with quantum entanglement and concepts from quantum information.

A school of this size and scope requires support and help from many sources. We are very grateful for all the financial and practical support we have received. The Institute for Advanced Simulation and the German Research School for Simulation Sciences at the Forschungszentrum Jülich provided the funding and were vital for the organization of the school and the production of this book. The DFG Forschergruppe FOR1346 offered travel grants for students and the Institute for Complex Adaptive Matter (ICAM) travel support for international speakers and participants.

The nature of a school makes it desirable to have the lecture-notes available already during the lectures. In this way the participants get the chance to work through the lectures thoroughly while they are given. We are therefore extremely grateful to the lecturers that, despite a tight schedule, provided their manuscripts in time for the production of this book. We are confident that the lecture notes collected here will not only serve the participants of the school but will also be useful for other students entering the exciting field of strongly correlated materials.

We thank Mrs. H. Lexis of the Forschungszentrum Jülich Verlag and Mr. D. Laufenberg of the Graphische Betriebe for providing their expert support in producing the present volume on a tight schedule and for making even seemingly impossible requests possible. We heartily thank our students and postdocs that helped in proofreading the manuscripts, often on short notice: Carmine Autieri, Fabio Baruffa, Michael Baumgärtel, Monica Bugeanu, Andreas Flesch, Evgeny Gorelov, Amin Kiani Sheikhabadi, Joaquin Miranda, German Ulm, and Guoren Zhang.

Finally, our special thanks go to Dipl.-Ing. R. Hölzle for his invaluable advice on all questions concerning the organization of such a school and to Mrs. L. Snyders and Mrs. E. George for expertly handling all practical issues.

Eva Pavarini, Erik Koch, Frithjof Anders, and Mark Jarrell

August 2012

1 Correlated Electrons: Why we need Models to Understand Real Materials?

Alexander Lichtenstein
I. Institut für Theoretische Physik
Universität Hamburg, 20355 Hamburg, Germany

Contents

E. Pavarini, E. Koch, F. Anders, and M. Jarrell
Correlated Electrons: From Models to Materials
Modeling and Simulation Vol. 2
Forschungszentrum Jülich, 2012, ISBN 978-3-89336-796-2
http://www.cond-mat.de/events/correl12

1 Introduction

The technical inventions of the last century are closely related with the design of silicon based materials for the semiconductor industry. The theoretical development of the last fifty years and the associated success in describing electronic properties of such weakly correlated materials started with the conception of the density functional theory (DFT), which was initiated by seminal works of Walter Kohn, Pierre Hohenberg, and Lu Sham [1, 2]. This is the first-principles scheme based on the exact theorem, stating that the ground state of interacting electron systems can be found by minimizing an universal functional of the density in some additional external field. The main problem of DFT is related with the fact, that this functional is not known in general and can be calculated numerically with a reasonable accuracy only for the simple case of the homogeneous electron gas. These calculations, which have been proven to be very useful for the DFT scheme, have been done by David Ceperley and Berni Alder [3] using the two-step quantum Monte Carlo procedure starting from the "fixed-node" approximation followed by a "released-node" calculation. Nevertheless the accuracy of such scheme is still limited and is very sensitive to the computational details [4]. The main restriction of the density functional scheme is the fact that it only gives ground state properties, while spectral information can be found only in the time-dependent DFT scheme [5]. While the structural relaxation of complex materials can be carried out very efficiently in the generalized gradient approximation of the DFT, due to almost spherical properties of the exchange-correlation hole [6], the quality of spectral properties crucially depends on systems in question. The TDFT scheme has more problems than the static DFT approach, since there are no suitable time-dependent reference systems to find an exchange correlation kernel.

The enormous progress of the last three decades in designing completely new materials for high-T_c superconductivity, giant and colossal magnetoresistance, or artificially created two-dimensional lattices brings new importance to the theory of transition-metal systems. It turns out that even the ground state properties of antiferromagnetic oxides or orbitally ordered com-

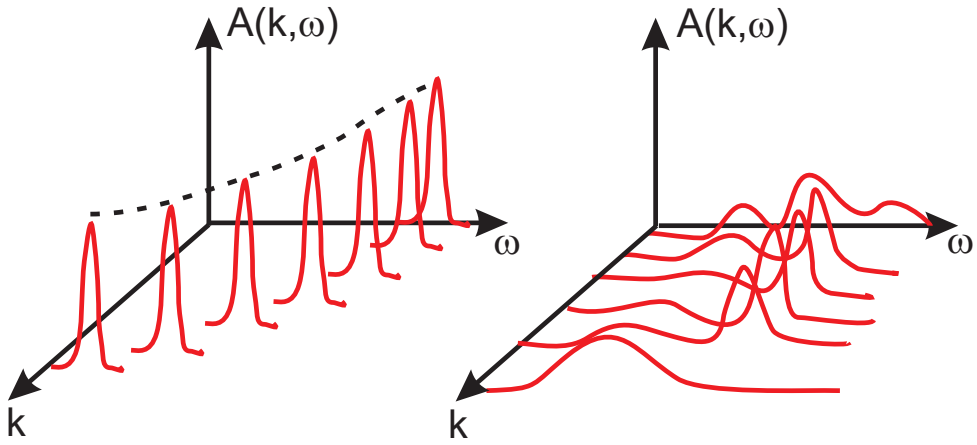

Fig. 1: *Schematic view of angular-resolved photoemission spectra (ARPES) for normal (left) and correlated electron materials (right).*

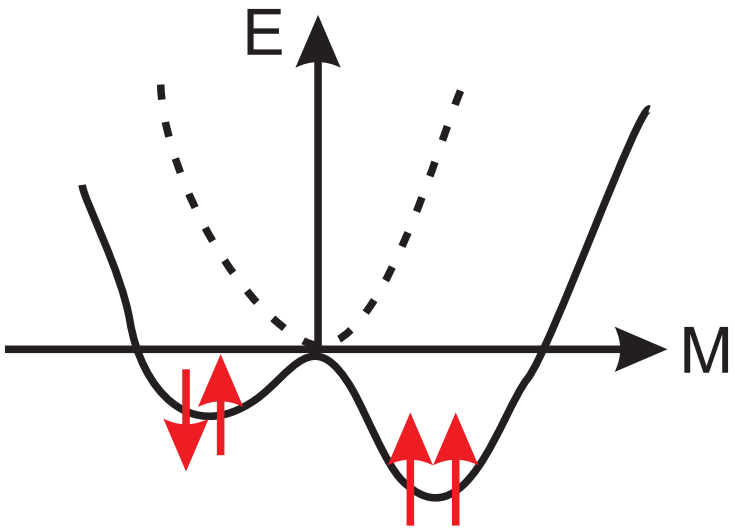

Fig. 2: *Schematic representation of spin (as well as charge or orbital) fluctuations in correlated electron systems.*

pounds are not described well in the DFT scheme [7]. The accurate angle-resolved photoemission study of the cuprate superconductors clearly shows, that the spectral properties of such systems, with strong electron-electron interactions in the $3d$-shell of transition metals has well pronounced incoherent features [8]. We present in Fig. 1 the qualitative difference between the spectral function of normal metals with well-defined quasiparticle peaks at all momenta $\mathbf{k}$ and the strongly correlated case with an incoherent part and a non-quasiparticle spectrum in the Brillouin zone.

The main source of complex correlated behavior of electronic systems, related with strong fluctuations between different low-energy fermionic configurations, is shown schematically in Fig. 2. For example, if the free energy of an electronic system has only one well defined minimum at zero local moment (the dashed curve) then one can expect small electron fluctuations and normal paramagnetic quasiparticle behavior. In the case of two low-lying minima corresponding to singlet and triplet excitations (solid curve) one can expect strong many-body fluctuations and possibly non-quasiparticle behavior related with local so-called Hund's rule physics [9]. In order to treat the system with such effective energy profiles, we need to use the path-integral approach and calculate the corresponding correlation functions using complicated quantum Monte Carlo schemes, which can handle many local minima in the free-energy functional on an equal footing.

In this lecture we review the general functional approach to strongly correlated electron systems, discuss an elegant way to separate the local and non-local correlations, and show how one can solve the local correlation problem using the recently developed continuous time Monte Carlo (CT-QMC) scheme. Finally we show an efficient way to go from the simple model investigations of strongly correlated systems to realistic investigation of complex electronic materials.

2 Functional approach: Route to fluctuations

We introduce a general functional approach which will cover Density Functional (DFT), Dynamical Mean-Field (DMFT), and Baym-Kadanoff (BK) Theory [10]. Let us start from the full many–body Hamiltonian describing electrons moving in the periodic external potential of ions $V(\mathbf{r})$, with chemical potential μ, and interacting via Coulomb law: $U(\mathbf{r}-\mathbf{r}') = 1/|\mathbf{r}-\mathbf{r}'|$. We use atomic units $\hbar = m = e = 1$. In the field-operator representation the Hamiltonian takes the form

$$\begin{aligned} H &= \sum_{\sigma} \int d\mathbf{r}\, \hat{\psi}^{\dagger}_{\sigma}(\mathbf{r}) \left(-\frac{1}{2}\nabla^2 + V(\mathbf{r}) - \mu \right) \hat{\psi}_{\sigma}(\mathbf{r}) \\ &+ \frac{1}{2} \sum_{\sigma\sigma'} \int d\mathbf{r} \int d\mathbf{r}'\, \hat{\psi}^{\dagger}_{\sigma}(\mathbf{r}) \hat{\psi}^{\dagger}_{\sigma'}(\mathbf{r}')\, U(\mathbf{r}-\mathbf{r}')\, \hat{\psi}_{\sigma'}(\mathbf{r}') \hat{\psi}_{\sigma}(\mathbf{r}). \end{aligned} \tag{1}$$

We can always use a single-particle orthonormal basis set $\phi_n(\mathbf{r})$, for example Wannier orbitals, with a full set of quantum numbers, e.g., site, orbital and spin index: $n = (im\sigma)$ and expand the fields in creation and annihilation operators

$$\begin{aligned} \hat{\psi}(\mathbf{r}) &= \sum_{n} \phi_n(\mathbf{r}) \hat{c}_n \\ \hat{\psi}^{\dagger}(\mathbf{r}) &= \sum_{n} \phi^*_n(\mathbf{r}) \hat{c}^{\dagger}_n \end{aligned} \tag{2}$$

Going from fermionic operators to the Grassmann variables $\{c^*_n,\, c_n\}$, we can write the functional integral representation of the partition function of the many-body Hamiltonian in the imaginary time domain using the Euclidean action S

$$Z = \int \mathcal{D}[c^*, c] e^{-S} \tag{3}$$

$$S = \sum_{12} c^*_1\, (\partial_\tau + t_{12})\, c_2 + \frac{1}{4} \sum_{1234} c^*_1 c^*_2\, U_{1234}\, c_4 c_3\,, \tag{4}$$

where the one- and two-electron matrix elements are defined as

$$\begin{aligned} t_{12} &= \int d\mathbf{r}\, \phi^*_1(\mathbf{r}) \left(-\frac{1}{2}\bigtriangledown^2 + V(\mathbf{r}) - \mu \right) \phi_2(\mathbf{r}) \\ U_{1234} &= \int d\mathbf{r} \int d\mathbf{r}'\, \phi^*_1(\mathbf{r}) \phi^*_2(\mathbf{r}')\, U(\mathbf{r}-\mathbf{r}')\, \phi_3(\mathbf{r}) \phi_4(\mathbf{r}'). \end{aligned} \tag{5}$$

and we use the following short definition of the sum:

$$\sum_{1} ... \equiv \sum_{im} \int d\tau ... \tag{6}$$

The one-electron Green function is defined via a simplest non-zero correlation function

$$G_{12} = -\langle c_1 c^*_2 \rangle_S = -\frac{1}{Z} \int \mathcal{D}[c^*, c]\, c_1 c^*_2\, e^{-S} \tag{7}$$

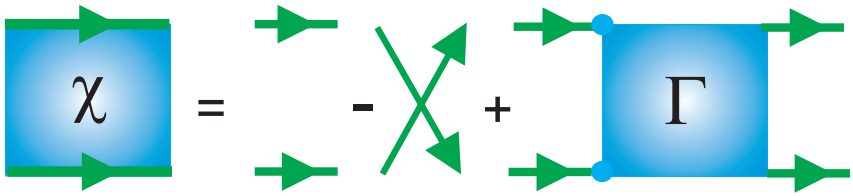

Fig. 3: *Representation of the full two-particle Green function in terms single-particle Green functions and the full vertex function Γ.*

The main problems of strongly interacting electronic systems are related to the fact that the higher order correlation functions do not separate into a product of lower order correlation functions. For example the two-particle Green function or generalized susceptibilities, χ, are defined in the following form [11]

$$\chi_{1234} = \langle c_1 c_2 c_3^* c_4^* \rangle_S = \frac{1}{Z} \int \mathcal{D}[c^*, c]\, c_1 c_2 c_3^* c_4^*\, e^{-S}\,, \tag{8}$$

and can be expressed graphically through Green functions and the full vertex function Γ_{1234} [12] as shown in Fig. 3

$$X_{1234} = G_{14}G_{23} - G_{13}G_{24} + \sum_{1'2'3'4'} G_{11'}G_{22'}\Gamma_{1'2'3'4'}G_{3'3}G_{4'4} \tag{9}$$

In the case of non-interacting electron systems, the high-order correlations χ are reduced to the antisymmetrized products of lower-order correlations G, which would correspond to the first two terms (Hartree and Fock like) with the vertex function Γ in Eq. (9) equal to zero. In strongly correlated electron systems the last part with the vertex is dominant and even diverges close to an electronic phase transition.

The Baym-Kadanoff functional [13] gives the one-particle Green function and the total free energy at its stationary point. In order to construct the exact functional of the Green function (Baym-Kadanoff), we modify the action by introducing the source term J

$$S[J] = S + \sum_{ij} c_i^* J_{ij} c_j\,. \tag{10}$$

The partition function Z, or equivalently the free energy of the system F, becomes a functional of the auxiliary source field

$$Z[J] = e^{-F[J]} = \int \mathcal{D}[c^*, c]\, e^{-S[J]}\,. \tag{11}$$

Variation of this source function gives all correlation functions, for example the Green function

$$G_{12} = \frac{1}{Z[J]} \frac{\delta Z[J]}{\delta J_{12}}\bigg|_{J=0} = \frac{\delta F[J]}{\delta J_{12}}\bigg|_{J=0}\,. \tag{12}$$

Likewise, the generalized susceptibility χ is obtained as a second variation of the partition function $Z[J]$. The second variation of the free energy functiontional $F[J]$ gives the connected part of the χ-function, which is the last term of Eq. (9).

The Baym–Kadanoff functional can be obtained by Legendre transforming from J to G

$$F[G] = F[J] - \mathrm{Tr}(JG), \tag{13}$$

We can use the standard decomposition of the free energy F into the single particle part and the correlated part

$$F[G] = \mathrm{Tr}\ln G - \mathrm{Tr}\,(\Sigma G) + \Phi[G], \tag{14}$$

were Σ_{12} is single particle self-energy and $\Phi[G]$ is a correlated part of the Baym–Kadanoff functional and is equal to the sum of all two-particle irreducible diagrams. At its stationary point this functional gives the free energy of the system. One can use a different Legendre transform and obtain functionals of the self-energy Σ [14], or complicated functionals of two variables G and Γ [15], or a more simple functional of G and screened Coulomb interactions W [10] which is useful in GW theory.

In practice, $\Phi[G]$ is not known for interacting electron systems, which is similar to the problem of the unknown universal functional in density functional theory. Moreover, this general functional approach reduces to the DFT theory, if one only uses the diagonal part in the space-time representation of the Green function, which corresponds to the one-electron density

$$n_1 = G_{12}\delta_{12} = \langle c_1^* c_1 \rangle_S, \tag{15}$$

with the Kohn-Sham potential $V_{KS} = V_{ext} + V_H + V_{xc}$ playing the role of the"constrained field" J. In this case we lose information about the non equal-time Green's function, which gives the single-particle excitation spectrum as well as the k-dependence of the spectral function, and we restrict ourselves to only the ground state energy of the many-electron system. Moreover, we also lose information about all collective excitations in solids, such as plasmons or magnons, which can be obtained from a generalized susceptibility or from the second variation of the free energy.

One can probably find the Baym-Kadanoff interacting potential $\Phi[G]$ for simple lattice models using quantum Monte Carlo (QMC). Unfortunately, due to the sign problem in lattice simulations, this numerically exact solution of electronic correlation problem is not possible. On the other hand, one can obtain the solution of local interacting quantum problem in a general fermionic bath, using a QMC scheme, which has no sign problem if it is diagonal in spin and orbital space. Therefore, a reasonable approach to strongly correlated systems is to keep only a local part of the many-body fluctuations. In such a Dynamical Mean-Field Theory (DMFT) one can obtain numerically the correlated part of the local functional. In this scheme we only use the local part of the many-electron vertex and obtain, in a self-consistent way, an effective functional of the local Green function. In the following section we discuss the general dual-fermion (DF) transformations [16] which will help us to separate the local fluctuations in many-body system and show a perturbative way to go beyond the DMFT approximations.

3 Local correlations and beyond

We will only consider the local, but multiobital, interaction vertex $U^i_{mm'm''m'''}$. Sometimes we will omit all orbital indices for simplicity. All equations will be written in matrix form, giving the idea of how to generalize a dual-fermion (DF) scheme to the multi-orbital case [17,18]. The general strategy to separate the local and non-local correlations effects is associated with the introduction of auxiliary fermionic fields which will couple separated local correlated impurities models back to the lattice [16]. In order to include the smaller non-local part of the Coulomb interactions one can use a more general approach using auxiliary fermionic and bosonic fields [19].

We rewrite corresponding original action, Eq. (3), in Matsubara space as a sum of the non-local one-electron contribution with t_{12} and the local interaction part U

$$S[c^*,c] = -\sum_{\omega\mathbf{k}\sigma\, mm'} c^*_{\omega\mathbf{k}\sigma m}\left[(i\omega+\mu)\mathbf{1} - t^{mm'}_{\mathbf{k}\sigma}\right] c_{\omega\mathbf{k}\sigma m'} + \sum_i S_{\mathrm{U}}[c^*_i, c_i]. \tag{16}$$

The index i labels the lattice sites, m refers to different orbitals, σ is the spin projection and the $\mathbf{k}$-vectors are quasi-momenta. In order to keep the notation simple, it is useful to introduce the combined index $\alpha \equiv \{m,\sigma\}$. Translational invariance is assumed for simplicity in the following, although a real space formulation is straightforward. The local part of the action, S_{U}, may contain any type of local multi-orbital interaction.

In order to formulate an expansion around the best possible auxiliary local action, a quantum impurity problem is introduced

$$S_{\mathrm{loc}}[c^*,c] = -\sum_{\omega\,\alpha\beta} c^*_{\omega\alpha}\left[(i\omega+\mu)\mathbf{1} - \Delta^{\alpha\beta}_{\omega}\right] c_{\omega\beta} + S_{\mathrm{U}}[c^*,c], \tag{17}$$

where Δ_ω is the effective hybridization matrix describing the coupling of the impurity to an auxiliary fermionic bath. The main motivation for rewriting the lattice action in terms of a quantum impurity model is that such a reference system can be solved numerically exactly for an arbitrary hybridization function using the CT-QMC methods [20]. Using the locality of the hybridization function Δ_ω, the lattice action (16) can be rewritten exactly in terms of individual impurity models and the effective one-electron coupling $(t_{ij} - \Delta_\omega)$ between different impurities

$$S[c^*,c] = \sum_i S_{\mathrm{loc}}[c^*_i, c_i] + \sum_{\omega\mathbf{k}\,\alpha\beta} c^*_{\omega\mathbf{k}\alpha}\left(t^{\alpha\beta}_{\mathbf{k}} - \Delta^{\alpha\beta}_{\omega}\right) c_{\omega\mathbf{k}\beta}. \tag{18}$$

We will find the condition for the optimal choice of the hybridization function later. Although we can solve the individual impurity model exactly, the effect of spatial correlations due to the second term in Eq. (18) is very hard to treat, even perturbatively, since the impurity action is non-Gaussian and one cannot use the Wick theorem. The main idea of a dual-fermion transformation is the change of variables from (c^*, c) to weakly correlated Grassmann fields (f^*, f) in the path integral representation of the partition function, Eq. (3), followed by a simple perturbative treatment. The new variables are introduced through the Hubbard-Stratonovich

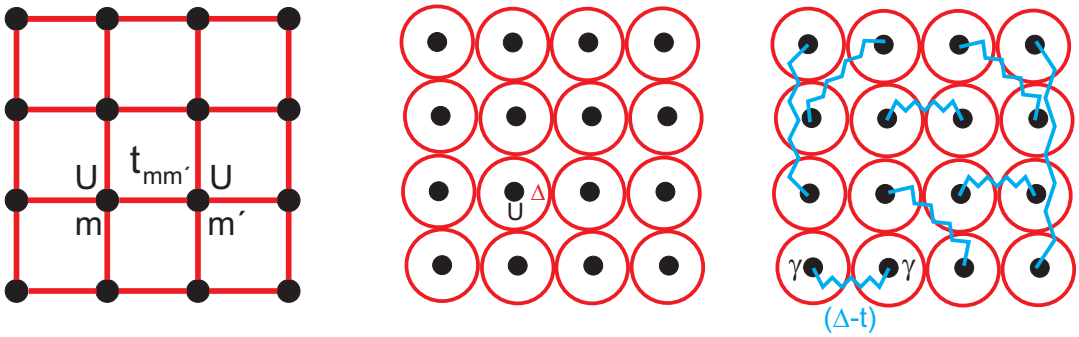

Fig. 4: *From the lattice model (left) via real-space DMFT (middle) to the non-local dual-fermion perturbation (right).*

transformation

$$\exp\left(c^*_\alpha b_\alpha (M^{-1})_{\alpha\beta} b_\beta c_\beta\right) = \frac{1}{\det M} \int \mathcal{D}[f^*, f] \exp\left(-f^*_\alpha M_{\alpha\beta} f_\beta - c^*_\alpha b_\alpha f_\alpha - f^*_\beta b_\beta c_\beta\right). \quad (19)$$

In order to transform the exponential of the bilinear term in (18), we choose the matrices $M_{\alpha\beta}$, and scaling function b_α (if we assume for simplicity that the local Green's function is diagonal in orbital and spin space) in accordance with Refs. [16] as

$$M = g_\omega^{-1} \left(\Delta_\omega - t_{\mathbf{k}}\right)^{-1} g_\omega^{-1}, \qquad b = g_\omega^{-1}, \quad (20)$$

where g_ω is the local, interacting Green function of the impurity problem

$$g_{12} = -\langle c_1 c_2^* \rangle_{\text{loc}} = -\frac{1}{\mathcal{Z}_{\text{loc}}} \int \mathcal{D}[c^*, c] c_1 c_2^* \exp\Big(- S_{\text{loc}}[c^*, c]\Big). \quad (21)$$

With this choice, the lattice action transforms to

$$S[c^*, c, f^*, f] = \sum_i S^i_{\text{site}} + \sum_{\omega \mathbf{k}\, \alpha\beta} f^*_{\omega \mathbf{k}\alpha} [g_\omega^{-1} \left(\Delta_\omega - t_{\mathbf{k}}\right)^{-1} g_\omega^{-1}]_{\alpha\beta} f_{\omega \mathbf{k}\beta}. \quad (22)$$

Hence the coupling between sites is transferred to a local coupling to the auxiliary fermions

$$S^i_{\text{site}}[c^*_i, c_i, f^*_i, f_i] = S_{\text{loc}}[c^*_i, c_i] + \sum_{\alpha\beta} f^*_{\omega i\alpha}\, g^{-1}_{\omega\,\alpha\beta} c_{\omega i\beta} + c^*_{\omega i\alpha}\, g^{-1}_{\omega\,\alpha\beta} f_{\omega i\beta}. \quad (23)$$

Since g_ω is local, the sum over all states labeled by $\mathbf{k}$ can be replaced by a summation over all sites by a change of basis in the second term. The crucial point is that the coupling to the auxiliary fermions is purely local and S_{site} decomposes into a sum of local terms. The lattice fermions can therefore be integrated-out from S_{site} for each site i separately. This completes the change of variables

$$\int \mathcal{D}[c^*, c] \exp\left(-S_{\text{site}}[c^*_i, c_i, f^*_i, f_i]\right) = \mathcal{Z}_{\text{loc}} \exp\Big(- \sum_{\omega\, \alpha\beta} f^*_{\omega i\alpha}\, g^{-1}_{\omega\,\alpha\beta} f_{\omega i\beta} - V_i[f^*_i, f_i]\Big). \quad (24)$$

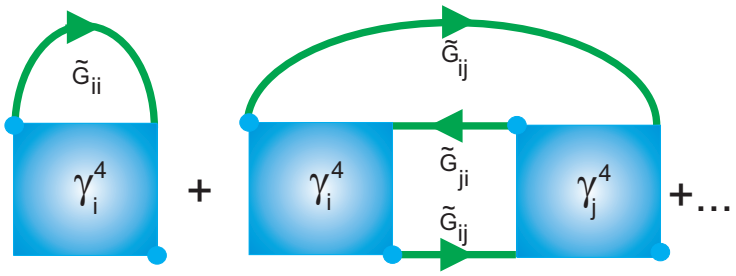

Fig. 5: *Diagrams contributing to the dual self-energy $\tilde{\Sigma}$.*

The above equation may be viewed as the defining equation for the dual potential $V[f^*, f]$. The choice of matrices (20) ensures a particularly simple form of this potential. An explicit expression is found by expanding both sides of Eq. (24) and equating the resulting expressions order by order. Formally this can be done to all orders and in this sense the transformation to the dual-fermions is exact. For most applications, the dual potential is approximated by the first non-trivial interaction vertex

$$V[f^*, f] = \frac{1}{4}\,\gamma_{1234}\, f_1^* f_2^* f_4 f_3, \tag{25}$$

where the combined index $1 \equiv \{\omega\alpha\}$ comprises frequency, spin and orbital degrees of freedom. γ is the exact, fully antisymmetric, reducible two-particle vertex of the local quantum impurity problem. It is given by

$$\gamma_{1234} = g^{-1}_{11'} g^{-1}_{22'} \left[\chi_{1'2'3'4'} - \chi^0_{1'2'3'4'}\right] g^{-1}_{3'3} g^{-1}_{4'4}, \tag{26}$$

with the two-particle Green function of the impurity being defined as

$$\chi_{1234} = \langle c_1 c_2 c_3^* c_4^* \rangle_{\text{loc}} = \frac{1}{Z_{\text{loc}}} \int \mathcal{D}[c^*, c]\; c_1 c_2 c_3^* c_4^*\; e^{-S_{\text{loc}}[c^*, c]}\;. \tag{27}$$

The disconnected part reads

$$\chi^0_{1234} = g_{14} g_{23} - g_{13} g_{24}\;. \tag{28}$$

The single- and two-particle Green functions can be calculated using the CT-QMC [20]. After integrating-out the lattice fermions, the dual action depends only on the new variables

$$\tilde{S}[f^*, f] = -\sum_{\omega \mathbf{k}\, \alpha\beta} f^*_{\omega\mathbf{k}\alpha} [\tilde{G}^0_\omega(\mathbf{k})]^{-1}_{\alpha\beta} f_{\omega\mathbf{k}\beta} + \sum_i V_i[f_i^*, f_i]. \tag{29}$$

and the bare dual Green function involves the local Green function g_ω of the impurity model

$$\tilde{G}^0_\omega(\mathbf{k}) = \left[g_\omega^{-1} + \Delta_\omega - t_{\mathbf{k}}\right]^{-1} - g_\omega\;. \tag{30}$$

Up to now, Eqs. (29) and (30) are mere reformulations of the original problem. In practice, approximate solutions are constructed by treating the dual problem perturbatively. Several diagrams contributing to the dual self-energy are shown in Fig. 5. These are constructed from the impurity vertices and dual Green functions. The first diagram is purely local, while higher

orders contain nonlocal contributions, e.g., the second diagram in Fig. 5. In practice, approximations to the self-energy are constructed in terms of skeleton diagrams. The lines shown in Fig. 5 are therefore understood to be fully dressed propagators. The use of skeleton diagrams is necessary to ensure that the resulting theory is conserving in the Baym-Kadanoff sense [13], i.e., it fulfills the basic conservation laws for energy, momentum, spin, and particle number. The most useful property of such dual perturbation theory is good convergence both in the weak-coupling limit, when the local vertex is small and in the strong-coupling limit, when the dual Green's function is small [21].

The hybridization function Δ, which so far has not been specified, allows to optimize the starting point of the perturbation theory and should be chosen in an optimal way. The condition of the first diagram (Fig. 5) as well as all local diagrams with higher-order correlation functions in the expansion of the dual self-energy to be equal to zero at all frequencies, fixes the hybridization. This eliminates the leading-order diagrammatic correction to the self-energy and establishes a connection to DMFT, which can be seen as follows: Since the γ vertex is local, this condition amounts to demanding that the local part of the dual Green function be zero

$$\sum_{\mathbf{k}} \tilde{G}_{\omega}(\mathbf{k}) = 0. \tag{31}$$

The simplest nontrivial approximation is obtained by taking the leading-order correction, the first diagram in Fig. 5, evaluated with the bare dual propagator (30). Using the expression for the DMFT Green function [22]

$$G^{\mathrm{DMFT}}_{\omega}(\mathbf{k}) = \left[g^{-1}_{\omega} + \Delta_{\omega} - t_{\mathbf{k}}\right]^{-1}, \tag{32}$$

it immediately follows that (31) evaluated with the bare dual Green function is exactly equivalent to the DMFT self-consistency condition for Δ_{ω}

$$\frac{1}{N_k}\sum_{\mathbf{k}} G^{\mathrm{DMFT}}_{\omega}(\mathbf{k}) = g_{\omega}\,. \tag{33}$$

In the limit of infinitely large lattice connectivity the DMFT scheme becomes exact with the local self-energy [23]. The DMFT approximation for real lattice models appears to be one of the most successful many body schemes for realistic multi orbital systems [10]. Since it involves the exact solution of the many-body multi-orbital impurity model Eq. (21) all local quantum fluctuations of different orbitals, spins, and charges (Fig. 6) are included in this scheme.

In the DMFT approach one can study paramagnetic correlated phases of complex crystals with strong spin and orbital fluctuations above transition temperatures of the spin- and orbital-ordered states [24].

Hence DMFT appears as the zero-order approximation in this approach and corrections to DMFT are included perturbatively. A formal relation to DMFT can be established using the Feynman variational functional approach. In this context, DMFT appears as the optimal approximation to a Gaussian ensemble of dual fermions [25].

When diagrammatic corrections are taken into account and the first diagram is evaluated with the dressed propagator $\tilde{G}$, the condition (31) will in general be violated. It can be reinforced

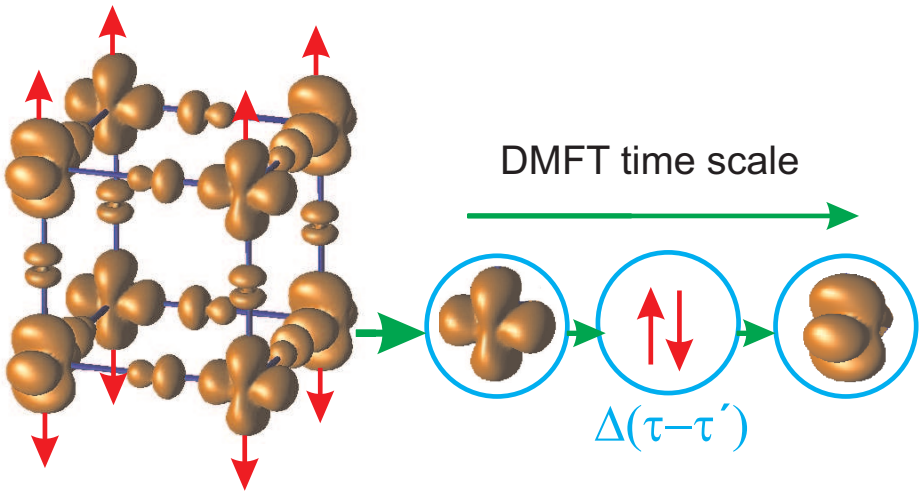

Fig. 6: *Schematic representations of initial lattice model (left) and the local DMFT approach with orbital and spin fluctuations (right).*

by adjusting the hybridization function iteratively. This corresponds to eliminating an infinite partial series of all local diagrams, starting from the first term in Fig. 5. These contributions are effectively absorbed into the impurity problem. Note that such an expansion is not one around DMFT, but rather around an optimized impurity problem.

The only difference between a DMFT and a DF calculation are the diagrammatic corrections which are included into the dual Green function. To this end, the local impurity vertex γ has to be calculated in addition to the Green function in the impurity solver step.

It is an important consequence of the exact transformation (19) that for a theory, which is conserving in terms of dual fermions, the result is also conserving in terms of lattice fermions [25]. This allows to construct general conserving approximations within the dual fermion approach. Numerically, the self-energy is obtained in terms of skeleton diagrams by performing a self-consistent renormalization as described below. Once an approximate dual self-energy is found, the result may be transformed back to a physical result in terms of lattice fermions using exact relations.

The action (29) allows for a Feynman-type diagrammatic expansion in powers of the dual potential V. The rules are similar to those of the antisymmetrized diagrammatic technique [26]. Extension of these rules to include generic n-particle interaction vertices is straightforward. Due to the use of an antisymmetrized interaction, the diagrams acquire a combinatorial prefactor. For a tuple of n equivalent lines, the expression has to be multiplied by a factor $1/n!$. As simplest example we can write schematically the first self-energy correction of the diagram in Fig. 5, which contains a single closed loop

$$\tilde{\Sigma}^{(1)}_{12} = -T \sum_{34} \gamma_{1324}\, \tilde{G}^{\mathrm{loc}}_{43} \tag{34}$$

where $\tilde{G}^{\mathrm{loc}} = (1/N_k) \sum_{\mathbf{k}} \tilde{G}(\mathbf{k})$ denotes the local part of the dual Green function. The second-order contribution represented in Fig. 5 contains two equivalent lines and one closed loop, and

hence is k-dependent

$$\tilde{\Sigma}_{12}^{(2)}(\mathbf{k}) = -\frac{1}{2}\left(\frac{T}{N_k}\right)^2 \sum_{\mathbf{k}_1\mathbf{k}_2}\sum_{345678} \gamma_{1345}\, \tilde{G}_{57}(\mathbf{k}_1)\, \tilde{G}_{83}(\mathbf{k}_2)\, \tilde{G}_{46}(\mathbf{k}+\mathbf{k}_2-\mathbf{k}_1)\, \gamma_{6728}\ . \qquad (35)$$

In practice, it is more efficient to evaluate the lowest-order diagrams in real space and transform back to reciprocal space using the fast Fourier transform. After calculating the best possible series for the self-energy $\tilde{\Sigma}$ in the dual space one can calculate the renormalized Green function matrix for the original fermions using the following simple transformations [19]

$$G_\omega(\mathbf{k}) = \left[\left(g_\omega + g_\omega \tilde{\Sigma}_\omega(\mathbf{k}) g_\omega\right)^{-1} + \Delta_\omega - t_k\right]^{-1} \qquad (36)$$

which is a useful generalization of the DMFT Green's function (see Eq. (32)) to include non-local correlation effects.

The progress of the DMFT approach strongly depends on the development of efficient numerical solvers for an effective quantum impurity model.

4 Solving multiorbital quantum impurity problems

Even though DMFT reduces the extended lattice problem to a single-site problem, the solution of the underlying Anderson impurity model remains a formidable quantum many-body problem, which requires accurate solvers. Recently a new class of solvers has emerged, the continuous-time quantum impurity solvers. These are based on stochastic Monte-Carlo methods and mainly come in two different flavors: The weak and strong-coupling approach.

The weak-coupling or interaction expansion continuous-time (CT-INT) quantum Monte Carlo algorithm for fermions was originally introduced by Aleksei Rubtsov [27]. There are two main previous attempts: the first work by Nikolay Prokof'ev *et. al* [29], who devised a continuous-time scheme to sample the infinite series of Feynman diagrams for bosons, and a second work by Natalie Jachowicz and co-workers [30], who developed a continous-time lattice Monte Carlo algorithm using the Hubbard-Stratonovich decomposition. The power of new CT-QMC scheme is that it represents just the integration of the complex path integral without any transformation to effective non-interacting models and can be used for any compacted electron-electron vertex. We introduce the algorithm in the path integral formulation for the single-orbital Anderson impurity problem with a Hubbard-type interaction $Un_\uparrow n_\downarrow$. The generalization to the multiorbital case can be found in Ref. [20]. First, the action of the Anderson impurity model is divided into a Gaussian part S_0 and an interaction part S_U as follows:

$$S_0 = \sum_\sigma \int_0^\beta d\tau \int_0^\beta d\tau' c_\sigma^*(\tau)\, \left[\partial_\tau - \mu + \Delta(\tau-\tau') + U\alpha_{-\sigma}(\tau)\delta(\tau-\tau')\right]\, c_\sigma(\tau')\ , \qquad (37)$$

$$S_U = U\int_0^\beta d\tau \left[c_\uparrow^*(\tau)c_\uparrow(\tau) - \alpha_\uparrow(\tau)\right]\left[c_\downarrow^*(\tau)c_\downarrow(\tau) - \alpha_\downarrow(\tau)\right]\ . \qquad (38)$$

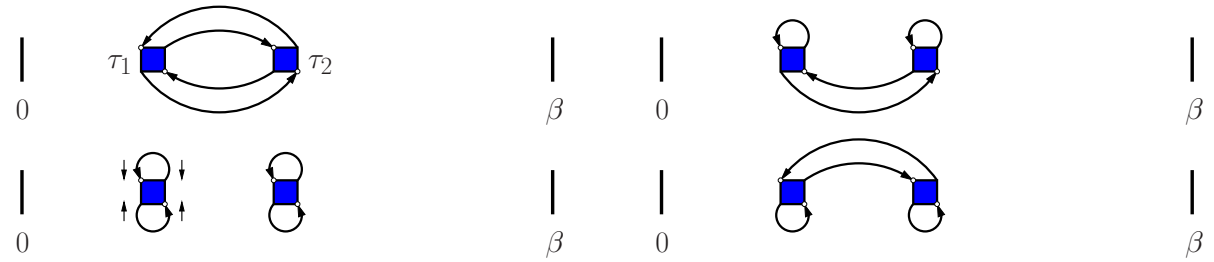

Fig. 7: *The four contributions to the partition function for $k = 2$. The interaction vertices are depicted by squares, bare Green functions as lines.*

The parameters α are introduced to control the sign problem. A formal series expansion for the partition function is obtained by expanding the exponential in the interaction term,

$$\mathcal{Z} = \int \mathcal{D}[c^*, c]\, e^{-S_0[c^*,c]} \sum_{k=0}^{\infty} \frac{(-1)^k}{k!} U^k \int_0^\beta d\tau_1 \ldots \int_0^\beta d\tau_k \, [c^*_\uparrow(\tau_1)c_\uparrow(\tau_1) - \alpha_\uparrow(\tau_1)] \tag{39}$$
$$\times [c^*_\downarrow(\tau_1)c_\downarrow(\tau_1) - -\alpha_\downarrow(\tau_1)] \ldots [c^*_\uparrow(\tau_k)c_\uparrow(\tau_k) - \alpha_\uparrow(\tau_k)][c^*_\downarrow(\tau_k)c_\downarrow(\tau_k) - \alpha_\downarrow(\tau_k)] \, .$$

Using the definition of the average over the noninteracting action

$$\langle ... \rangle_0 = \frac{1}{\mathcal{Z}_0} \int \mathcal{D}[c^*, c] ... \exp(-S_0), \tag{40}$$

the partition function can be expressed in the following form

$$\mathcal{Z} = \mathcal{Z}_0 \sum_{k=0}^{\infty} \int_0^\beta d\tau_1 \ldots \int_{\tau_{k-1}}^\beta d\tau_k \, \mathrm{sgn}(\Omega_k) \, |\Omega_k| \, , \tag{41}$$

where the integrand is given by

$$\Omega_k = (-1)^k U^k \langle [c^*_\uparrow(\tau_1)c_\uparrow(\tau_1) - \alpha_\uparrow(\tau_1)][c^*_\downarrow(\tau_1)c_\downarrow(\tau_1) - \alpha_\downarrow(\tau_1)] \ldots$$
$$\ldots [c^*_\uparrow(\tau_k)c_\uparrow(\tau_k) - \alpha_\uparrow(\tau_k)][c^*_\downarrow(\tau_k)c_\downarrow(\tau_k) - \alpha_\downarrow(\tau_k)] \rangle_0 \, . \tag{42}$$

Note that here the range of time integration has been changed such that time ordering is explicit: $\tau_1 < \ldots < \tau_{k-1} < \tau_k$. For a given set of times all $k!$ permutations of this sequence contribute to Eq. (39). These can be brought into the standard sequence by permuting quadruples of Grassmann numbers, and hence without gaining an additional sign. Since all terms are subject to time-ordering, their contribution to the integral is identical, so that the factor $1/k!$ in Eq. (39) cancels. A configuration can be fully characterized by specifying a perturbation-order k and a set of k times: $C_k = \{\tau_1, \ldots, \tau_k\}$.

The Monte Carlo algorithm performs importance sampling over this configuration space. The weight of a configuration is thereby taken to be equal to the modulus of the integrand, Eq. (42). Since S_0 is Gaussian, the average over the noninteracting system can be evaluated using Wick's theorem. Hence the weight of a configuration is essentially given by a fermionic determinant of a matrix containing the bare Green functions

$$\Omega_k = (-1)^k U^k \prod_\sigma \det \hat{g}^\sigma, \tag{43}$$

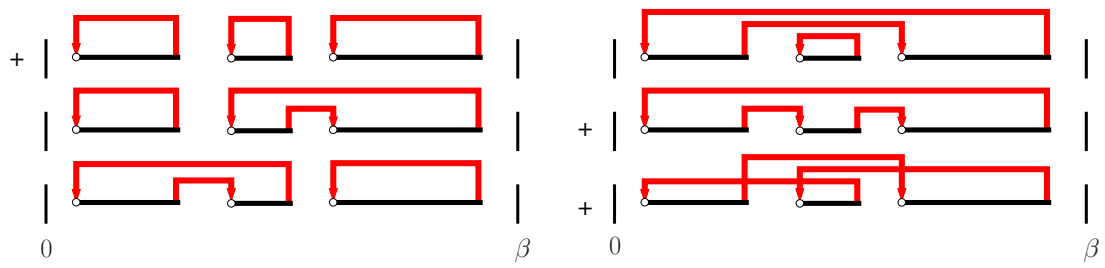

Fig. 8: *Diagrammatic representation of the six contributions to the partition function for spinless fermions at $k = 3$. An electron is inserted at the start of a segment (marked by an open circle) and removed at the segment endpoint. The hybridization function lines $\Delta(\tau_i - \tau'_j)$ (shown in red) are connected to the segments in all possible ways. The sign of each diagram is given on the left. (Reproduced from Ref. [28].)*

where the local Green function in the α fields is equal to

$$(\hat{g}^{\sigma})_{ij} = g_0^{\sigma}(\tau_i - \tau_j) - \alpha_{\sigma}(\tau_i)\delta_{ij} \; . \tag{44}$$

Note that determinants for different spin-orientations factorize, since the Green function is diagonal in spin-space.

The hybridization expansion (CT-HYB) or strong-coupling algorithm was initially introduced by Philipp Werner *et al.* [28] and has been generalized to multiorbital systems with general interactions [31, 32]. Here the algorithm is discussed in the segment representation, which exploits the possibility of a very fast computation of the trace for a density-density type of interaction. The action is regrouped into the atomic part

$$S_{\text{at}} = \int_0^{\beta} d\tau \sum_{\sigma} c^*_{\sigma}(\tau) \left[\partial_{\tau} - \mu\right] c_{\sigma}(\tau) + U \int_0^{\beta} d\tau \, c^*_{\uparrow}(\tau) c_{\uparrow}(\tau) c^*_{\downarrow}(\tau) c_{\downarrow}(\tau) \tag{45}$$

and the part of the action S_{Δ} which contains the hybridization term

$$S_{\Delta} = -\int_0^{\beta} d\tau' \int_0^{\beta} d\tau \sum_{\sigma} c_{\sigma}(\tau) \Delta(\tau - \tau') \, c^*_{\sigma}(\tau') \, . \tag{46}$$

Here the sign is taken out by reversing the original order of c and c^* to avoid an alternating sign in the expansion. To simplify the notation, consider first the spinless-fermion model, which is obtained by disregarding the spin sums and interaction in Eqs. (45) and (46). The series expansion for the partition function is generated by expanding in the hybridization term:

$$\begin{aligned} \mathcal{Z} = \int \mathcal{D}[c^*, c] \, e^{-S_{\text{at}}} \sum_k \frac{1}{k!} \int_0^{\beta} d\tau'_1 \int_0^{\beta} d\tau_1 \ldots \int_0^{\beta} d\tau'_k \int_0^{\beta} d\tau_k \times \\ \times \, c(\tau_k) c^*(\tau'_k) \ldots c(\tau_1) c^*(\tau'_1) \Delta(\tau_1 - \tau'_1) \ldots \Delta(\tau_k - \tau'_k). \end{aligned} \tag{47}$$

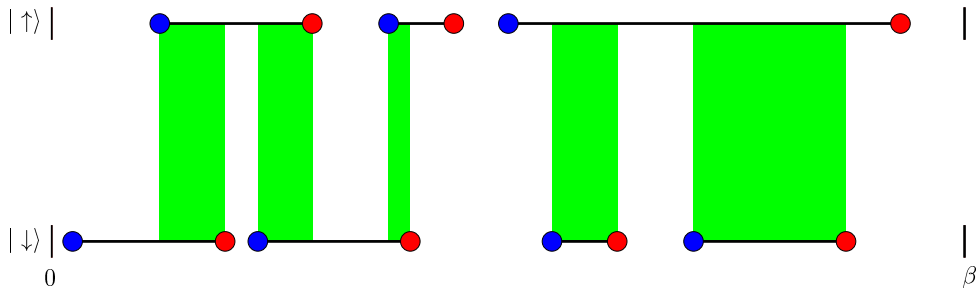

Fig. 9: *Example single-band CT-HYB in a segment picture: blue dots illustrate a creation operator, red ones annichilation operators and the black line represents the hybridization function $\Delta(\tau_i - \tau'_j)$. The green regions represent the time interval at which two electrons are present on the impurity with the total time l_d and the price U has to be paid.*

The important observation now is that, at any order, the diagrams can be collected into a determinant of hybridization functions. The partition function then takes the form

$$\mathcal{Z} = \mathcal{Z}_{\text{at}} \sum_k \int_0^\beta d\tau'_1 \int_{\tau'_1}^\beta d\tau_1 \ldots \int_{\tau_{k-1}}^\beta d\tau'_k \int_{\tau'_k}^{\circ\tau'_k} d\tau_k \, \langle c(\tau_k) c^*(\tau'_k) \ldots c(\tau_1) c^*(\tau'_1) \rangle_{\text{at}} \, \det \hat{\Delta}^{(k)}, \quad (48)$$

where the average is over the states of the atomic problem described by S_{at}. Here $\det \hat{\Delta}^{(k)}$ denotes the determinant of the matrix of hybridizations $\hat{\Delta}_{ij} = \Delta(\tau_i - \tau'_j)$. The diagrams contributing to the partition function for $k = 3$ are shown in Fig. 8. A diagram is depicted by a collection of segments, where a segment is symbolic for the time interval where the impurity is occupied. The collection of diagrams obtained by connecting the hybridization lines in all possible ways corresponds to the determinant. Collecting the diagrams into a determinant is essential to alleviate, or completely suppress the sign problem. Note that the imaginary-time interval in Eq. (48) is viewed as a circle denoted by $\circ\tau'_k$. The trajectories in the path integral are subject to antiperiodic boundary conditions which is accommodated by an additional sign if a segment winds around the circle.

For the single-orbital Anderson impurity model with Hubbard interaction the segment picture still holds and gives a very intuitive picture of the imaginary time dynamics. A configuration is visualized by two separate timelines, one for each spin. The additional sum over spins, $\sum_{\sigma_1 \ldots \sigma_k}$, which enters in the first line of Eq. (48), generates contributions such as the one shown in Fig. 9. The only difference to the spinless-fermion model is, that when the impurity is doubly occupied, the energy U has to be paid and the trace is $e^{\mu(l_\uparrow + l_\downarrow) - U l_d}$, where l_σ is the time spent on the impurity for an electron with spin σ and l_d is the time the impurity is doubly occupied.

In the Fig. 10 shows the comparison of CT-INT and CT-HYB for the strong-coupling case $U \geq W$ of single-band model. The perfect agreement of these two complementary CT-QMC schemes gives evidence for the possibility of a numerically exact solution of the quantum impurity problem.

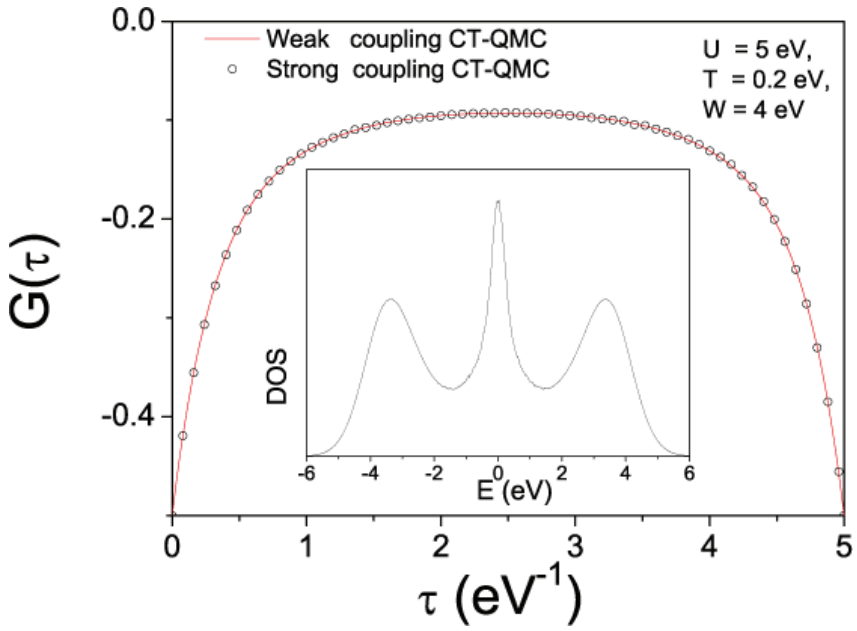

Fig. 10: *Comparison of the weak- (CT-INT) and strong-coupling (CT-HYB) CT-QMC impurity solvers for a one-band, semicircular model with $U \geq W$. The insert shows the density of states obtained with maximum entropy scheme.*

5 From models to real materials

In order to investigate real correlated systems with the local DMFT scheme, we need to have an efficient way of partitioning the spacial and orbital degrees of freedom. For example in the high-temperature superconducting oxide $YBa_2Cu_3O_7$, the strongly correlated electrons are Cu-$3d$, and, moreover, there is only one per non-equivalent copper $d_{x^2-y^2}$ band which crosses the Fermi level with strong many-body fluctuations. Just a few percent of the total number of electronic states need to be included in the DMFT calculations. Therefore the simplest realistic correlated scheme would be a DFT+DMFT approach [33, 34] with partitioning of the orbital space into normal band electrons $|K\rangle$ described by the DFT Bloch basis and correlated local orbitals $|L\rangle$ described by some optimal Wannier basis (see Fig. 11 for illustration).

The treatment of correlated electron systems requires the calculation of Green functions and hybridization functions in terms of local orbitals. This is readily achieved when using a basis set, which is localized in real space, such as linear (or N-th order) muffin-tin orbitals (NMTO) [35] or Gaussian basis sets [37]. However, many implementations of the density functional theory use a delocalized plane-wave basis set. This has the advantage, that the basis set is simple, universal, and its convergence is controlled in principle by a single parameter, the energy cutoff. The projector augmented wave method (PAW) [38], being a representative of a plane-wave based methods, can be used as a simple example of the general projection scheme from the Bloch to the local basis: $\langle K|L\rangle$.

Following the general projection scheme of Ref. [36,37], the desired quantity for an implementation of a DFT+DMFT method is a projection $\mathcal{P}^{\mathcal{C}} = \sum_L |L\rangle\langle L|$ of the full DFT Kohn-Sham

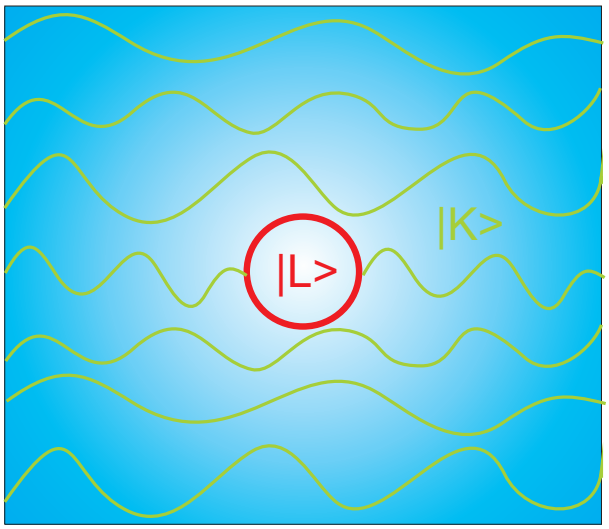

Fig. 11: *Schematic representation of the projection from a Bloch basis to a local Wannier correlated subset.*

Green function $G_{\mathrm{KS}}(\omega)$ on a set of localized orbitals $\{|L\rangle\}$

$$G^{\mathcal{C}}(\omega) = \mathcal{P}^{\mathcal{C}} G^{\mathrm{KS}}(\omega) \mathcal{P}^{\mathcal{C}}. \tag{49}$$

The subspace $\mathcal{C} = \mathrm{span}(\{|L\rangle\})$ is usually called correlated subspace. It is the subspace of orbitals in which many-body fluctuations play a major role and where the DMFT corrections to the DFT will be considered. In plane-wave based calculations, $G^{\mathrm{KS}}(\omega)$ in Matsubara space is available in terms of an almost complete set of Bloch states $|K\rangle$ that are eigenstates of the Kohn-Sham Hamiltonian $H_{\mathrm{KS}}|K\rangle = \varepsilon_K|K\rangle$:

$$G_{\mathrm{KS}}(\omega) = \sum_K \frac{|K\rangle\langle K|}{i\omega + \mu - \varepsilon_K}\,. \tag{50}$$

Inserting equation (50) into equation (49) shows that one needs to evaluate projections of the type $\langle L|K\rangle$ in order to access the matrix elements $G^{\mathcal{C}}_{LL'}(\omega)$ of the local Green function. In most cases the correlated orbitals are d- or f-orbitals, which are localized inside the PAW augmentation spheres to a good approximation. For $|L\rangle$ within these spheres and given the PAW decomposition [38] of a Bloch state $|K\rangle$ one obtains

$$\langle L|K\rangle = \sum_i \langle L|\phi_i\rangle\langle\tilde{p}_i|\tilde{K}\rangle.$$

The index i of the augmentation functions $|\phi_i\rangle$ includes site s, angular momentum l, and m as well as an index ν labeling the radial function: $i = (s, l, m, \nu)$. $|\tilde{p}_i\rangle$ are the PAW projectors.
In the described projection scheme the $|L\rangle\langle L|$ matrices are not properly normalized for two reasons: (1) the Bloch basis is incomplete since only a limited number of Bloch bands is included and (2) the PAW augmentation functions are, in general, not orthonormal. The simplest way is to orthonormalize the projection matrices by the following Wannier-type construction: By definition, the localized states $|L\rangle$ are labeled by site and angular-momentum indices: $L = (s, l, m)$.

We split the site index $s = \mathbf{R} + \mathbf{T}$ such that $\mathbf{R}$ labels the position within the unit cell and $\mathbf{T}$ is the Bravais lattice vector of the unit cell in which s is located. This allows us to construct the Bloch transform of the localized states

$$|L_{\mathbf{k}}\rangle = \sum_{T} e^{i\mathbf{k}\mathbf{T}} |L_{\mathbf{T}}\rangle, \tag{51}$$

where $\mathbf{k}$ is from the first Brillouin zone and $|L_{\mathbf{T}}\rangle \equiv |L\rangle = |s, l, m\rangle$. The sum in equation (51) runs over the Bravais lattice. Labeling the Bloch states $|K\rangle = |\mathbf{k}, n\rangle$ by their crystal momentum, $\mathbf{k}$, and band index, n, we normalize our projection matrices $\mathcal{P}^{\mathcal{C}}_{Ln}(\mathbf{k}) = \langle L_{\mathbf{k}}|\mathbf{k}, n\rangle$ using the overlap operator

$$O_{LL'}(\mathbf{k}) = \sum_{n} \mathcal{P}^{\mathcal{C}}_{Ln}(\mathbf{k}) \mathcal{P}^{*\mathcal{C}}_{L'n}(\mathbf{k}) \tag{52}$$

in

$$\bar{\mathcal{P}}^{\mathcal{C}}_{Ln}(\mathbf{k}) = \sum_{L'} O^{-1/2}_{LL'}(\mathbf{k}) P^{\mathcal{C}}_{L'n}(\mathbf{k}). \tag{53}$$

These orthonormalized projection matrices are calculated once at the beginning of any calculation and can then be used to obtain the local Green function of the correlated orbitals from the full Bloch Green function $G^{B}_{nn'}$

$$G^{\mathcal{C}}_{LL'}(\omega) = \sum_{\mathbf{k}, nn'} \bar{\mathcal{P}}^{\mathcal{C}}_{Ln}(\mathbf{k}) G^{B}_{nn'}(\mathbf{k}, \omega) \bar{\mathcal{P}}^{*\mathcal{C}}_{L'n'}(\mathbf{k}).$$

Similarly the hybridization function, $\Delta(\omega)$, is available. It is related to the local Green function by

$$G^{-1}(\omega) = i\omega - \epsilon_d - \Delta(\omega), \tag{54}$$

where ϵ_d is the static crystal field. Equation (54) is a matrix equation with G, Δ, and ϵ_d being $\dim \mathcal{C} \times \dim \mathcal{C}$ matrices, in general. To separate the hybridization from the static DFT crystal field, we numerically evaluate the limit $\omega \to \infty$, where $\omega - G^{-1}(\omega) \to \epsilon_d$.

In a DFT+DMFT calculation the projection matrices $\bar{\mathcal{P}}^{\mathcal{C}}_{Ln}(k)$ are used for up- and down-folding quantities like the Green function and the self-energy in the course of the iterative DMFT procedure in exactly the same way as shown for the local Green function above. For example, the self-energy obtained by an impurity solver for the effective impurity model $\Sigma^{\mathcal{C}}_{LL'}(\omega)$ can be upfolded to the Bloch basis as follows

$$\Sigma^{B}_{nn'}(\mathbf{k}, \omega) = \sum_{LL'} \overline{P}^{*\mathcal{C}}_{Ln}(\mathbf{k}) \; \Sigma^{\mathcal{C}}_{LL'}(\omega) \; \overline{P}^{\mathcal{C}}_{L'n'}(\mathbf{k}) \, .$$

Since the self-energy in DMFT is a purely local quantity, the index $\mathbf{k}$ on $\Sigma^{B}_{nn'}(\mathbf{k}, \omega)$ reflects the momentum dependence brought about by the projection matrices. The presented projection scheme allows for the inclusion of both correlated and uncorrelated states in the procedure. Therefore, information about the interplay of correlated orbitals with their uncorrelated ligands can be obtained. As example, we show a realistic DFT+DMFT calculation of the $SrVO_3$ spectral function in the Fig. 12, were one can see the renormalisation of the valence correlated V-t_{2g} states as well as broadening of the Bloch O-$2p$ states [39].

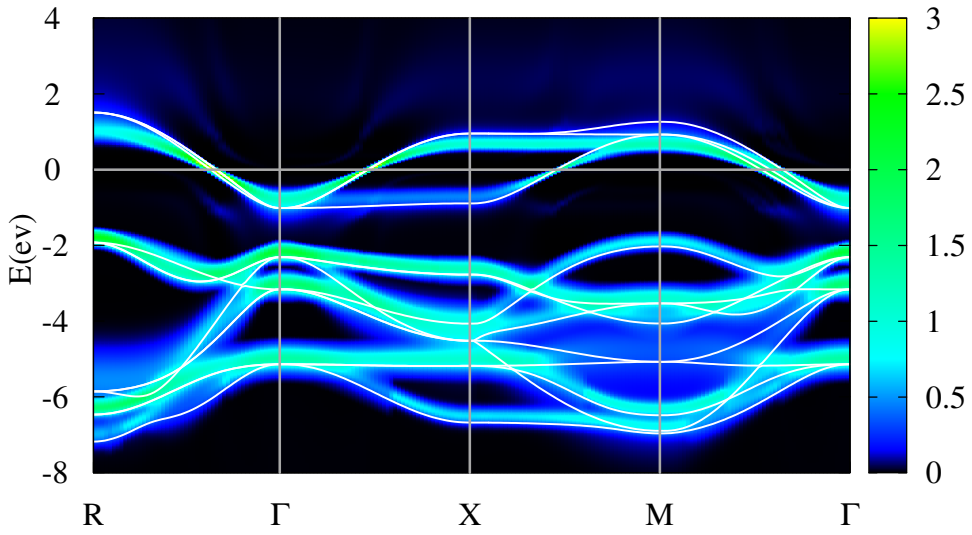

Fig. 12: *Momentum resolved impurity spectral function of $SrVO_3$ obtained by DFT+DMFT. The LDA band-structure of the V-t_{2g} and O-$2p$ Bloch states is shown for comparison.*

6 Summary and outlook

We have learnt from simple model investigations how to treat electronic correlations within the local DMFT scheme. This knowledge can be used in realistic DFT+DMFT calculations for strongly correlated transition metals and rare earth systems, where the spin, orbital and charge fluctuations in the d- of f-shell play the crucial role for the photoemission spectrum as well as magnetic and optical excitations. The numerically exact solution of the quantum impurity problem gives us an effective local exchange-correlation functional for a given correlation material in a specific external field. Moreover, we have shown a direct way to include effects of non-local fluctuations in terms of a renormalized, locally screened dual perturbation scheme. The combination with first-principle approaches still offers many challenging problems.

Acknowledgment

Support of the Deutsche Forschungsgemeinschaft through FOR1346 is gratefully acknowledged.

References

[1] P. Hohenberg and W. Kohn, Phys. Rev. **136**, B864 (1964)

[2] W. Kohn and L.J. Sham, Phys. Rev. **140**, A1133 (1965)

[3] D.M. Ceperley and B.J. Alder, Phys. Rev. Lett. **45**, 566 (1980)

[4] G. Ortiz and P. Ballone, Phys. Rev. B **50**, 1391 (1994)

[5] E.K.U. Gross and W. Kohn, Adv. Quantum Chem. **21**, 255 (1990)

[6] R. O. Jones and O. Gunnarsson, Rev. Mod. Phys. **61**, 689 (1989)

[7] V.I. Anisimov, F. Aryasetiawan, and A.I. Lichtenstein, J. Phys.: Condens. Matter **9**, 767 (1997)

[8] A. Damascelli, Z. Hussain, and Z.-X. Shen, Rev. Mod. Phys. **75**, 473 (2003), G. Kotliar and D. Vollhardt, Physics Today **57**, 53 (2004)

[9] L. de Medici, J. Mravlje, and A. Georges, Phys. Rev. Lett. **107**, 256401 (2011)

[10] G. Kotliar, S.Y. Savrasov, K. Haule, V.S. Oudovenko, O. Parcollet, and C.A. Marianetti, Rev. Mod. Phys. **78**, 865 (2006)

[11] A.B. Migdal: *Theory of finite Fermi Systems and applications to atomic nuclei* (Interscience Publishers, New York, 1967)

[12] P. Nozières: *Theory of interacting Fermi systems* (Benjamin, New York, 1964)

[13] G. Baym and L.P. Kadanoff, Phys. Rev. **124**, 287 (1961)

[14] M. Potthoff, Eur. Phys. J. B **32**, 429 (2003)

[15] R. van Leeuwen, N.E. Dahlen, and A. Stan Phys. Rev. B **74**, 195105 (2006)

[16] A.N. Rubtsov, M.I. Katsnelson, and A.I. Lichtenstein, Phys. Rev. B **77**, 033101 (2008)

[17] H. Hafermann, F. Lechermann, A.N. Rubtsov, M.I. Katsnelson, A. Georges, and A.I. Lichtenstein, Lecture Notes in Physics **843**, 145 (2012), D.C. Cabra, A. Honecker, and P. Pujol (eds.): *Modern Theories of Many-Particle Systems in Condensed Matter Physics* (Springer, Berlin 2012)

[18] H. Hafermann, S. Brener, A.N. Rubtsov, M.I. Katsnelson, A.I. Lichtenstein, JETP Lett. **86**, 677 (2007)

[19] A.N. Rubtsov, M.I. Katsnelson, and A.I. Lichtenstein, Annals Phys. **327**, 1320 (2012)

[20] E. Gull, A.J. Millis, A.I. Lichtenstein, A.N. Rubtsov, M. Troyer, and P. Werner, Rev. Mod. Phys. **83**, 349 (2011)

[21] H. Hafermann, G. Li, A.N. Rubtsov, M.I. Katsnelson, A.I. Lichtenstein, and H. Monien, Phys. Rev. Lett. **102**, 206401 (2009)

[22] A. Georges, G. Kotliar, W. Krauth, and M.J. Rozenberg, Rev. Mod. Phys. **68** , 13 (1996)

[23] W. Metzner and D. Vollhardt, Phys. Rev. Lett. **62**, 324 (1989)

[24] E. Pavarini, E. Koch, and A.I. Lichtenstein, Phys. Rev. Lett. **101**, 266405 (2008)

[25] A.N. Rubtsov, M.I. Katsnelson, A.I. Lichtenstein, and A. Georges, Phys. Rev. B **79**, 045133 (2009)

[26] A.A. Abrikosov, L.P. Gorkov, and I.E. Dzyaloshinskii: *Methods of Quantum Field Theory in Statistical Physics* (Pergamon Press, New York, 1965)

[27] A.N. Rubtsov and A.I. Lichtenstein, JETP Lett. **80**, 61 (2004)

[28] P. Werner, A. Comanac, L. deMedici, M. Troyer, and A.J. Millis, Phys. Rev. Lett. **97**, 076405 (2006)

[29] N.V. Prokofev, B.V. Svistunov, and I.S. Tupitsyn, JETP Sov. Phys. **87**, 310 (1998)

[30] S.M.A. Rombouts, K. Heyde, and N. Jachowicz Phys. Rev. Lett. **82**, 4155 (1999)

[31] P. Werner and A.J. Millis, Phys. Rev. B **74**, 155107 (2006)

[32] K. Haule, Phys. Rev. B **75**, 155113 (2007)

[33] V.I. Anisimov, A.I. Poteryaev, M.A. Korotin, A.O. Anokhin, and G. Kotliar, J. Phys.: Condensed Matter **9**, 7359 (1997)

[34] A.I. Lichtenstein and M.I. Katsnelson, Phys. Rev. B **57**, 6884 (1998)

[35] O.K. Andersen and T. Saha-Dasgupta, Phys. Rev. B **62**, R16219 (2000)

[36] V.I. Anisimov, D.E. Kondakov, A.V. Kozhevnikov, I.A. Nekrasov, Z.V. Pchelkina, J.W. Allen, S.-K. Mo, H.-D. Kim, P. Metcalf, S. Suga, A. Sekiyama, G. Keller, I. Leonov, X. Ren and D. Vollhardt, Phys. Rev. B **71**, 125119 (2005)

[37] F. Lechermann, A. Georges, A. Poteryaev, S. Biermann, M. Posternak, A. Yamasaki and O.K. Andersen, Phys. Rev. B **74**, 125120 (2005)

[38] P. E. Blöchl, Phys. Rev. B **50**, 17953 (1994)

[39] M. Karolak, T.O. Wehling, F. Lechermann and A.I. Lichtenstein, J. Phys.: Condens. Matter **23**, 085601 (2011)

2 Density Functional Theory and Applications to Transition Metal Oxides

David J. Singh
Oak Ridge National Laboratory
Oak Ridge, TN 37831-6056, USA

Contents

E. Pavarini, E. Koch, F. Anders, and M. Jarrell
Correlated Electrons: From Models to Materials
Modeling and Simulation Vol. 2
Forschungszentrum Jülich, 2012, ISBN 978-3-89336-796-2
http://www.cond-mat.de/events/correl12

1 Introduction

These are the lecture notes for a talk in a Course on Correlated Electrons: From Models to Materials held in Juelich in September, 2012. This lecture is intended to provide an introductory description of standard density functional calculations, with emphasis on oxides. In the context of the course it is a starting point for the advanced correlated methods that will be discussed in the following lectures.

This chapter consists of two main parts. The first part is a very basic introduction to density functional theory (DFT). The second part focuses on a particular aspect of transition metal oxide physics, that is magnetism and the formation of magnetic moments illustrated by the example of three rather different perovskite compounds, $SrMnO_3$, $SrTcO_3$ and $SrRuO_3$.

2 Density functional theory in condensed matter physics

It is fair to say that DFT calculations play a central role in condensed matter theory and have revolutionized the way we understand the physical properties of solids today. This chapter discusses aspects of DFT in relation to correlated materials and its use in providing microscopic understanding in diverse systems.

DFT, and the widely used local density approximation (LDA) to it, were formulated in the 1960's in two seminal papers by Kohn, Hohenberg and Sham [1, 2] and started to be applied to real solids in the 1970's. Normally, when one uses approximations, one imagines that the availability of better computers would mean that one could do better and use more exact theories. Computer speeds have followed Moore's law from that time to the present, increasing by approximately three orders of magnitude per decade, or by $\sim 10^9$ from the $\sim$10 MFlop computers of the late 1970's to the present state of the art of $\sim$10 PFlops as realized on the Fujitsu K computer in 2011.

10^9 is a big number. A person with a dollar (or Euro) standing outside a McDonald's can eat at the most famous restaurant in the world. A billionaire has more options, and one should take note if he chooses the dine at the same place. Today, DFT calculations based on the LDA and the computationally similar generalized gradient approximations (GGAs) remain the standard workhorse in condensed matter. This can perhaps be appreciated by noting some citation statistics. As of this writing, the paper of Perdew, Burke and Ernzerhof [3], which lays out one of the more commonly used generalized gradient approximations for solids has been cited 21,557 times, including 4,056 times in 2011 alone, while that of Perdew and co-workers laying out the so-called "PW91" functional [4], which is another common functional was cited 9,084 times, including 845 times in 2011. This reflects just how useful these approximations are.

There are many reasons for the popularity and successes of DFT calculations. Two particularly important ones are (1) the fact DFT calculations are based on the chemical compositions and structures of materials without the use of intervening models and (2) the fact that such calculations, while approximate, are predictive.

Condensed matter physics increasingly focuses on materials that are structurally and chemically complex. This trend started with the 1986 discovery of cuprate superconductivity in $(La,Ba)_2CuO_4$, which is a layered perovskite material. This was closely followed by discoveries in increasingly complex materials, $YBa_2Cu_3O_{7-\delta}$, $Bi_2SrCu_2O_8$, and $HgBa_2Ca_2Cu_3O_{8+\delta}$. Approximate DFT calculations were helpful in establishing the large scale features of the electronic structure of these cuprates [5, 6]. In complex materials it is particularly difficult to sort out the key structural features and how they relate to the physical properties. One may guess the shape of the Fermi surface of Na metal without recourse to detailed calculations but it is unlikely that one would correctly guess the complex multisheet Fermi surfaces of materials like $YBa_2Cu_3O_7$. A more recent example comes from the iron-pnictide superconductors, where DFT calculations revealed a very non-oxide-like electronic structure and the presence of relatively small disconnected multisheet Fermi surfaces that are of importance for understanding the superconductivity [7, 8].

There have been many excellent reviews of DFT and DFT calculations, and so we do not attempt to provide another one here. We simply mention a few relevant points and refer the reader to the extensive literature on this subject for detailed discussions. Some excellent resources are the books, *Density Functional Theory of Atoms and Molecules*, by Parr and Yang [9], *Density Functional Methods in Physics*, by Dreizler and da Provincia [10], *Density Functionals: Where do the come from, why do they work?*, by Ernzerhof, Burke and Perdew [11], *Theory of the Inhomogeneous Electron Gas*, by Lundqvist and March [12], and the review article by Callaway and March [13].

Finally, we note that while DFT is an exact theory, practical applications require tractable approximations to the DFT functional. The success of DFT really rests on the fact that relatively simple and general approximate forms such as the LDA and GGAs yield very good descriptions of the properties of diverse solid state and molecular systems. The remarkable success of simple approximations, such as the local density approximation, in accurately describing the properties of condensed matter was hardly anticipated before detailed calculations were performed starting in the 1970's. There has been theoretical discussion of the reasons for the successes of simple approximations like the LDA since then. However, it remains the case that approximate DFT calculations are used to predict many properties of materials based mainly on the fact that previous calculations have shown these properties to be in good agreement with experiment on other materials. Put another way, the local density approximation is built around the many body physics of the uniform electron gas. Nonetheless it is able to describe materials that have highly inhomogeneous electron distributions that at first sight have nothing to do with the electron gas. The success of these simple approximations in describing diverse properties of materials without experimental input provides an explanation for the conundrum, posed above, i.e. the long lived popularity of DFT methods.

A simple example is bcc Fe, which is a commonly known ferromagnet. Like Fe, the uniform electron gas shows magnetism. However, the magnetism of the uniform electron gas only occurs at densities of $\sim 10^{20}$ cm^{-3} and below [14]. In contrast the average electron density of bcc Fe is 2.2x10^{24} cm^{-3} including all electrons and 6.8x10^{23} cm^{-3} if only the valence electrons are

included. Thus Fe shows ferromagnetism at densities four orders of magnitude above where the uniform electron gas does. So the non-uniform electron gas constituting Fe has very different properties than the uniform electron gas. Nonetheless, this non-uniform electron gas is extremely well described by the local density approximation, with a moment that agrees within $\sim$3% of the experimental value, and a lattice parameter also in good agreement.

The point is that even though the LDA and GGAs are seemingly rather simple approximations they have certain advantages. These are (1) that they are truly ab-initio, in the sense of not requiring any input from experiment specific to the material being studied – this is key to making predictions – and (2) they are often rather precise for properties of materials, including non-trivial but important properties such as Fermi surfaces. In fact, the predictions made by simple LDA and GGA calculations have been transformational in many areas of condensed matter, e.g. the prediction of high pressure phases and their properties, complex Fermi surfaces of materials such as the high T_c cuprate superconductors, and many other areas.

Clearly, as will be shown in subsequent lectures of this school, these simple approximations have important deficiencies, especially in treating so-called strongly correlated systems. The simplest example is the failure of these approximations to describe the insulating ground states of Mott insulators, such NiO and the physics associated with the electron correlations that produce such ground states. In devising needed improvements to these approximations for treating correlated materials it is perhaps helpful to keep in mind the features of the LDA that make it so successful – absence of empirical or material specific parameters or tunable heuristics (i.e. making choices based on knowledge of the material in question) and its ability to make predictions based on the chemical composition and structure of a material and not much else.

2.1 Basics

Density functional theory itself is, as the name implies, an exact theorem. It states that the ground state energy, E of an interacting system subject to an external potential, $V_{ext}(\mathbf{r})$ is a functional of the density, E=$E[\rho(\mathbf{r})]$, and furthermore that the actual density, $\rho(\mathbf{r})$ is the density that minimizes this total energy functional. This means that the density $\rho(\mathbf{r})$, which is a non-negative function of the three spatial variables, can be used as the fundamental variable in quantum mechanical descriptions of the correlated system, as opposed to the many-body wavefunction, which is a function of $3N$ spatial variables for an N particle system.

As mentioned, while DFT is an exact theorem, the important aspect is that there are practical approximations based on it that can be applied to a wide variety of materials with frequently useful results. The first practical approximation to DFT was the local density approximation (LDA), which was proposed by Kohn and Sham in the paper where they derived the so-called Kohn-Sham equations [2]. They proceeded by observing that any density corresponding to an interacting N electron density can be written as the density corresponding to some N electron non-interacting wavefunction. Thus,

$$\rho(\mathbf{r}) = \sum_i \varphi_i^*(\mathbf{r})\varphi_i(\mathbf{r}); i = 1, 2, ..., N, \quad (1)$$

where the φ_i are the so-called Kohn-Sham orbitals and are orthonormalized functions. While the density can be exactly written in this way, it is to be emphasized that a determinant of the Kohn-Sham orbitals would typically be a very poor approximation to the true wavefunction, and so in general the Kohn-Sham orbitals are quite distinct from the actual wavefunction of a system.

Kohn and Sham then separated from the functional, $E[\rho]$, some large terms that are readily evaluated, leaving a presumably smaller remainder $E_{xc}[\rho]$ to be approximated.

$$E[\rho] = T_s[\rho] + E_{ext}[\rho] + U_{Hartree}[\rho] + E_{xc}[\rho], \tag{2}$$

where E_{ext} is the interaction with the external potential, $U_{Hartree}$ is the Hartree energy,

$$U_{Hartree}[\rho] = \frac{e^2}{2} \int \mathrm{d}^3\mathbf{r}\mathrm{d}^3\mathbf{r}' \, \frac{\rho(\mathbf{r})\rho(\mathbf{r}')}{|\mathbf{r} - \mathbf{r}'|}. \tag{3}$$

and T_s is the non-interacting kinetic energy of the Kohn-Sham orbitals (which is not the true kinetic energy of the many-body system).

The Kohn-Sham equations can then be derived using the fact that the true density is the density that minimizes $E[\rho]$,

$$\left(T_s + V_{ext} + V_{Hartree} + V_{xc}\right) \varphi_i = \varepsilon_i \varphi_i, \tag{4}$$

where the ε_i are the Kohn-Sham eigenvalues, which are not equal to true excitation energies of the system, T_s is the single particle kinetic energy operator and the various potential terms V are functional derivatives of the corresponding energy terms with respect to $\rho(\mathbf{r})$.

The local density approximation is obtained by writing,

$$E_{xc}[\rho] = \int \mathrm{d}^3\mathbf{r} \;\; \rho(\mathbf{r}) \epsilon_{xc}(\rho(\mathbf{r})), \tag{5}$$

where $\epsilon_{xc}(\rho)$ is approximated by a local function of the density, usually that which reproduces the known energy of the uniform electron gas.

To treat spin-polarized systems, a generalization to so-called spin-density functional theory is needed to produce useful approximations. The generalization is straight-forward. For a collinear magnetic system one replaces ρ by the two spin-densities, $\rho^{\uparrow}$ and $\rho^{\downarrow}$, so that the energy becomes a functional of these two spin-densities, $E[\rho^{\uparrow}, \rho^{\downarrow}]$, $E_{xc}[\rho^{\uparrow}, \rho^{\downarrow}]$, and $V_{xc}[\rho^{\uparrow}, \rho^{\downarrow}]$ [15]. Replacing E_{xc} by the exchange-correlation energy of the partially spin polarized electron gas using the local spin densities yields the so-called local spin density approximation (LSDA), which is a very popular and effective method at least as a starting point. In the more general non-collinear case, the magnetization has both a magnitude and direction that vary with position, and so the density takes four components, instead of two as in the collinear case. In this case, the LSDA is formulated in terms of 2x2 density and potential matrices, $\boldsymbol{\rho}$ and $\mathbf{V}$, which can be expanded in terms of Pauli spin matrices, e.g. $\boldsymbol{\rho} = \rho\mathbf{1} + \mathbf{m} \cdot \boldsymbol{\sigma}$ [15]. This formalism, with a local approximation in which the exchange correlation term is again taken from the uniform electron gas with the same local polarization magnitude and a direction for $\mathbf{V}_{xc}$ parallel to the

local magnetization direction, yields a useful non-collinear version of the LSDA that has been widely applied to non-collinear systems [16].

The generalized gradient approximations (GGAs) are the other commonly used class of density functionals in solids. They use the local gradient as well as the density in order to incorporate more information about the electron gas in question, i.e. $\epsilon_{xc}(\rho)$ is replaced by $\epsilon_{xc}(\rho, |\nabla\rho|)$. These generalized gradient approximations, which originated in the work of Langreth and Mehl [17] and Perdew and co-workers [4] are very different from gradient expansions, which lead to greatly degraded results from the LDA.

Actually, considering how different the electron gas in solids is from the uniform electron gas, it is perhaps not surprising that a Taylor expansion, which treats solids as a minor perturbation of the homogeneous gas, would not work. The modern GGA's are instead rather sophisticated functionals build around sum rules and scaling relations for the exchange-correlation hole in the general non-uniform electron gas.

The central relation is the adiabatic connection formula, which in Rydberg units is

$$E_{xc}[n] = \int d^3\mathbf{r} \int d^3\mathbf{r}' \, \frac{n(\mathbf{r})n(\mathbf{r}')}{|\mathbf{r}-\mathbf{r}'|}(\bar{g}[n,\mathbf{r},\mathbf{r}'] - 1) = \int d^3\mathbf{r} \int d^3\mathbf{r}' \, \frac{n(\mathbf{r})\bar{n}_{xc}(\mathbf{r},\mathbf{r}')}{|\mathbf{r}-\mathbf{r}'|}\,, \quad (6)$$

where $\bar{g}$ is the coupling-constant average (from the non-interacting $e^2 = 0$ value to the physical value of e^2) of the pair distribution function, n is the density as usual and $\bar{n}_{xc}$ is defined by the equation. This may be understood as the interaction energy of each electron with its exchange correlation hole less the energy needed to "dig out" the hole. The latter includes contributions to the kinetic energy beyond the single-particle level. The LDA then consists of the replacement of $n(\mathbf{r}')\bar{g}[n,\mathbf{r},\mathbf{r}']$ by $n(\mathbf{r})\bar{g}^h(n(\mathbf{r}), |\mathbf{r}-\mathbf{r}'|)$, where $\bar{g}^h$ is the coupling constant averaged pair distribution function of the homogeneous electron gas.

Modern GGA functionals are built using the adiabatic connection formula based on knowledge of exact sum rules, scaling relations and limits for the exchange correlation hole in the general non-uniform case. The simplest such sum rule is that the exchange correlation hole contains a charge of exactly unity. This rule, which is satisfied by the LDA, and the spherical Coulombic average in Eqn. 6 have been used to explain why such a simple approximation works as well as it does (see especially, Ref. [12] for clear discussions of this).

2.2 DFT, Jellium and Hartree-Fock

In thinking about DFT and approximations, it is helpful to remember what it is not, particularly when considering what one might do to improve such approximations to DFT. Sometimes it is said that LDA or GGA calculations represent either a jellium or a Hartree-Fock approximation to the many-body system. One purpose of this section is to emphasize that this is not really correct.

Hartree-Fock, unlike approximate DFT methods, is a variational method based on the exact Hamiltonian. The Hartree-Fock energy is always higher than the true energy. Hartree-Fock consists of restricting the wavefunctions to Slater determinants. This gives an exact exchange

description with no correlation. Hartree-Fock generally overestimates the band gaps of semiconductors and insulators, opposite to standard approximate DFT methods, such as the LDA. Furthermore, importantly, unlike DFT, Hartree-Fock cannot describe metals, since all metals are unstable in this approximation. Thus it is incorrect to consider a starting description of a metal within e.g. the LSDA as representing a Hartree-Fock description to which one may add correlations as if none were present in this starting point. Also, it should be noted that approximate DFT because of its uncontrolled approximations is not self-interaction free. Specifically, while the exact exchange correlation hole has a charge of exactly unity, this is not the case for e.g. the LDA in a non-uniform electron gas. Hartree-Fock on the other hand has an exchange hole that does contain a charge of exactly unity and therefore is self-interaction free.

The distinction between Hartree Fock and approximate DFT is also important from a historical point of view. Several approximations similar to the LSDA had been proposed and widely used prior to the development of Kohn-Sham DFT. The $X\alpha$ method of Slater and co-workers is the most widely known such method [18]. However, while the formalism of the $X\alpha$ method is very similar in appearance to that of the LSDA, from a conceptual point of view it is very different. In particular, the $X\alpha$ method was viewed as a simplification of the Hartree-Fock method, i.e. an approach for fast approximate Hartree-Fock calculations. As such, it was typically parametrized to reproduce Hartree-Fock as well as possible, often taking the band gap as a quantity that should be fit. When used in this way it gave many interesting and useful results, e.g. the body of work produced by J.C. Slater and his group, but did not approach the predictive capabilities of modern approximate DFT methods. The key point is that approximate DFT methods, like the modern LDA, are approximations to an exact theory that has density and energy as fundamental quantities, and which does not reproduce band gaps. This new view led to the use of the energy of the uniform electron gas in the LDA, rather than a functional form that comes from the high density exchange, and is what underlies the much better predictive power of the modern approximate DFT methods.

We now turn to jellium. Jellium is the uniform electron gas that forms the basis of the LDA. It is a metal that at densities appropriate to solids is far from magnetism. It is also a gas and as such has no shear strength. In solid state physics, perhaps the simple materials closest to jellium are the alkali metals, e.g. K or Cs, which are indeed very soft metals that are far from magnetism. Also, like jellium, they have nearly spherical Fermi surfaces. In any case, the implication of regarding the LDA as a jellium model is that one adopts a view in which solids that are well described by the LDA are essentially well described as a uniform electron gas with weak perturbation by pseudopotentials representing the atomic cores. However, while LDA and GGA calculations do provide a reasonable description of K and Cs, they provide an equally good description of materials like diamond and Al_2O_3, which are insulators and not only support shear modes, but in fact are among the stiffest known materials.

The point is that solids are not like blueberry muffins (a kind of small cake with embedded berries that is popular in the United States). The characteristic of blueberry muffins is that they taste roughly the same independent of the exact number or distribution of the blueberries inside them. Solids are not at all like that. Instead they show a tremendous diversity of properties

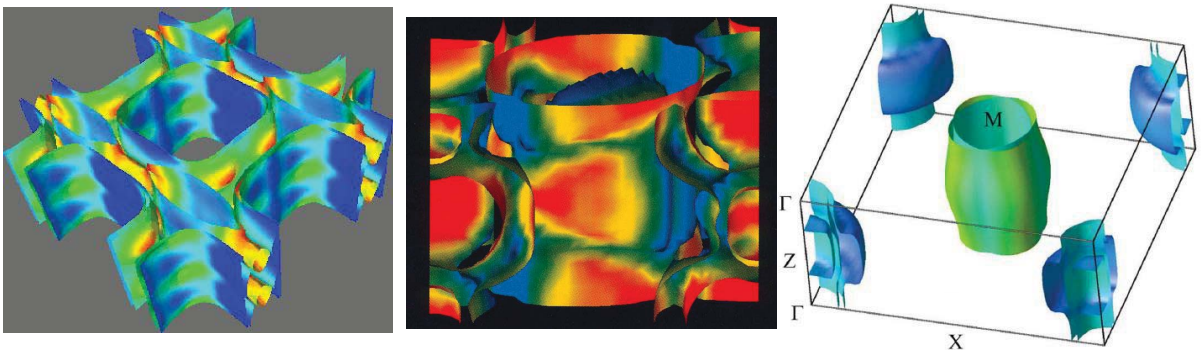

Fig. 1: *The Fermi surfaces of three superconductors, $YBa_2Cu_3O_7$ (left, following Ref. [6]), YNi_2B_2C (middle, following Ref. [19]) and LaFeAsO (right, following Ref. [7]).*

depending on the exact type and arrangement of the atoms making them up. Many of the diverse observed behaviors of materials are in fact rather well described by approximate DFT calculations. The fact that the properties of Cs appear to be like those of jellium, while those of diamond appear to be very different does not imply that diamond is a more strongly correlated material than Cs but is simply a reflection of the fact that the properties of non-uniform electron gasses, are different from those of the uniform electron gas. This emphasizes the fact that LDA and GGA approximations do not represent some kind of slowly varying approximation for the electron gas and so they are often well able to describe the highly non-uniform electron gasses that comprise condensed matter.

Related to this, in solid state physics it is very useful to start with simple models in order to understand phenomena. For metals, jellium is a very useful pedagogical starting point, and because of this many common formulas for metals are written in text books for the case of a spherical Fermi surface. On the other hand the Fermi surfaces of real metals are often very complex, as shown for three superconductors in Fig. 1.

All three of these superconductors show multiple sheets, with no obvious relationship to a simple sphere. However, these Fermi surfaces from LDA calculations agree remarkably well with experiment. This was perhaps particularly surprising in the case of the high T_c cuprate, $YBa_2Cu_3O_7$, since like the other cuprates it is in close proximity to undoped phases ($YBa_2Cu_3O_6$ in this case) that are Mott insulators and are not even qualitatively described by standard LSDA calculations.

In any case, the Fermi surface plays the central role in setting the low energy properties of a metal. Also, superconductivity is fundamentally an instability of the Fermi surface, and so knowledge of the Fermi surface can reveal a lot about the nature of the superconductivity in a given compound. For example, all three materials shown in Fig. 1 have crystal structures that may be described as layered. However, as shown, the Fermi surfaces of the boro-carbides and boro-nitrides ($LuNi_2B_2C$, YNi_2B_2C, etc.) are clearly three dimensional and in particular do not

take the form of cylinders. This was one of the first indications following their discovery that the superconductivity of these materials is unrelated to that of the high T_c cuprates [20]. It is also an illustration of why approximate DFT has become so widely used – DFT calculations predicted the three dimensionality of the Fermi surfaces and some other important aspects well in advance of experimental measurements.

Returning to the jellium model, in characterizing the nature of correlations in a material, the fact that experiment may show that a certain metal cannot be described by spherical Fermi surface formulas, does not in itself mean that it cannot be described by detailed DFT calculations, nor does it in itself imply that a material is strongly correlated (although it may be). In other words, unconventional behavior in relation to simple jellium based models could be a consequence of strong correlations, or it could alternatively be a consequence of a non-trivial electronic structure that is, however, still well described by approximate DFT calculations. It is important to sort this out in each case. Also, there is sometimes confusion that arises from the simplifications in spherical Fermi surface models. For example, in a metal the bands and their dispersions at the Fermi energy E_F play a central role in the low energy physics.

The band velocity, $\mathbf{v_k} = \nabla_{\mathbf{k}}\varepsilon(\mathbf{k})$, where $\varepsilon(\mathbf{k})$ are the band energies, is an important quantity both for transport and thermodynamic properties. Within Boltzmann theory the conductivity is essentially related to the velocity, $\sigma_{xx} \sim N(E_F)\langle v_x^2\rangle\tau$, where τ is an inverse scattering rate, $\langle\ \rangle$ denotes the Fermi surface average, and $N(E_F)$ is the density of states at E_F. The square of the Drude plasma frequency, which can be measured from infrared optics, is given by a similar factor, $N(E_F)\langle v_x^2\rangle$. However, for a parabolic band (spherical Fermi surface) system this can also be written as n/m, where m is the effective mass, and n is the carrier density (volume of the Fermi surface), and similarly one can also eliminate n in favor of the Fermi energy, E_F relative to the band edge. However, it is to be emphasized that infrared optics does not measure E_F nor does it measure n or m (and obviously considering the excitation energy it cannot be sensitive to such high energy properties), but only a certain integral over the actual Fermi surface.

The bottom line is that extraction of high energy quantities such as Fermi energy and band filling from experiments such as transport, infrared optics, superconducting properties etc., is generally model dependent and simple conclusions about high energy properties based on such measurements should be carefully considered. One exception is the extraction of the Fermi surface volume in layered materials from Hall data, which has been shown to be exact, independent of the detailed band dispersions and Fermi surface shape provided that the Fermi surfaces are all open (e.g. cylinders) in the third dimension [21].

3 Aspects of magnetism in oxides

In this section we illustrate some aspects of magnetism in oxides using three compounds, cubic perovskite $SrMnO_3$, perovskite $SrTcO_3$ and the ferromagnetic perovskite metal $SrRuO_3$.

3.1 $SrMnO_3$

Manganites attracted much attention because of the colossal magnetoresistance effect (CMR) and novel exchange couplings in materials like (La,Ca)MnO_3 and (La,Sr)MnO_3. starting in the 1950's [22–25] and then again following the rediscovery and enhancement of the CMR effect the 1990's [26, 27]. The basic features of the electronic structure from point of view of band theory have been extensively elucidated by many authors. (see e.g. [28]). Here we focus on the end-point compound $SrMnO_3$.

$SrMnO_3$ has both hexagonal and cubic polytypes, with hexagonal being the ground state. Here we consider the cubic polytype, which is an antiferromagnet with Neel temperature, T_N=240 K [29]. The related, and more studied compound, $CaMnO_3$ has an orthorhombic structure, characterized by tilts of the MnO_6 octahedra, up to $T_s \sim 720$ K, above which it takes a different rhombohedral structure. The ground state is a G-type antiferromagnet (nearest neighbor antiferromagnetism) with a Neel temperature T_N=124 K. Importantly, the resistivity is insulating both above and below T_N, which is a characteristic of a correlated (i.e. Mott type) insulator [30,31]. Interestingly, there is a metal-insulator transition at the structural transition, T_s, and in the rhombohedral phase $CaMnO_3$ is metallic.

Standard DFT calculations for $CaMnO_3$ predict a G-type antiferromagnetic insulator with a small band gap [28]. Like $CaMnO_3$, standard DFT calculations (without U) yield a small band gap insulator for $SrMnO_3$ (see Fig. 2) with G-type AFM order. In contrast, if ferromagnetic order is imposed, $SrMnO_3$ is predicted to be a metal. Here we discuss some calculations, which were done with the LAPW method using the standard PBE GGA functional at the experimental cubic lattice parameter (a=3.808 Å), and are basically the same as previously reported results. Integration of the spin density within the Mn LAPW spheres, radius 1.9 Bohr, yields moments within the spheres of 2.52 μ_B for the ferromagnetic (corresponding to 3 μ_B per formula unit for the whole cell), and a similar value of 2.41 μ_B for the ground state antiferromagnetic structure. This weak dependence of the moment on the ordering means that even at the level of standard band calculations, $SrMnO_3$ behaves like a local moment magnet.

From an experimental point of view $SrMnO_3$ is a borderline material. It is clearly insulating both above and below T_N, although very small perturbations make it metallic [30]. In any case, it illustrates some important features of the band description of correlated oxides.

First of all, there can be some ambiguity, because band calculations can yield an insulating state and so it can in some cases be difficult to decide if a material is a band insulator or a true Mott-Hubbard system. In a Mott system, one expects insulating behavior independent of magnetic order, one manifestation is that the resistivity shows similar insulating behavior both above and below T_N. In contrast the band picture in a material like $SrMnO_3$ implies that the conductivity should increase when the AFM order is destroyed above T_N since it relates to the specific magnetic order. Also, in strongly correlated transition metal oxides, the gaps predicted by standard DFT calculations are often very small in comparison with experiment, for example tenths of an eV in materials that have several eV band gaps, such as NiO. Essentially, while there can be a band gap for such materials in standard band calculations, the description of the

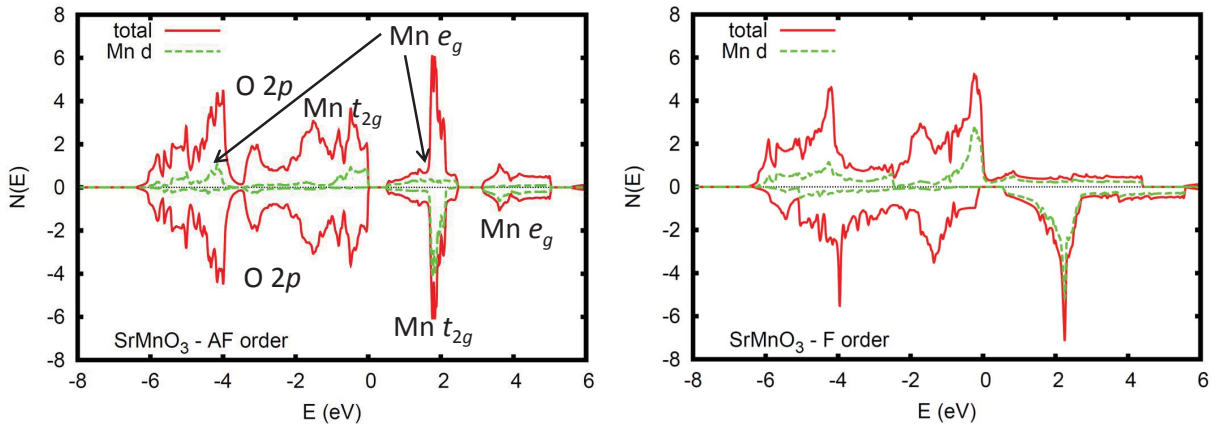

Fig. 2: *Electronic density of states of cubic perovskite $SrMnO_3$ as obtained with the PBE GGA. The calculations were done using the LAPW method and the projections are onto the Mn LAPW spheres of radius 1.9 Bohr. Majority spin is shown above the horizontal axis, and minority below. The left panel shows the result for the G-type antiferromagnetic ground state, while the right panel is for ferromagnetic order.*

electronic structure and the true nature of the gap is qualitatively incorrect. Cases like $SrMnO_3$ are less clear. This is because there is not a clear experiment showing the magnitude of the gap in the paramagnetic phase for this material, and because very tiny dopings produce metallic conduction about T_N suggesting that the material is almost metallic [30]. In general, care is needed in deciding the extent and nature of correlations in materials.

The second point is the connection between structure and correlations. $CaMnO_3$ is a much more clear case of a Mott insulator that $SrMnO_3$, which from an experimental point of view is more borderline. The principal difference between the two materials is structural, i.e. that in $CaMnO_3$ the MnO_6 octahedra are rotated yielding an orthorhombic structure. Such a structural distortion will generally narrow the bands (especially the e_g band) in a perovskite, favoring a correlated state. The Mott transition is typically first order and is frequently strongly coupled to structure. Thus properties of a metal near a Mott transition, as in the cuprate superconductors, can be very different from those of the nearby Mott insulator. The presence of the Mott phase in materials like cuprates shows the importance of the interactions that give rise to it on both sides of the metal-insulator transition, but the manifestation of these interactions in the physical properties can be very different in these different phases. An interesting note is that, even though standard band calculations yield completely wrong descriptions of the Mott phases, many aspects of the nearby conducting phases, such as the Fermi surfaces of $YBa_2Cu_3O_7$, can be well described. While, as will be discussed in other chapters in this volume, there has been significant recent progress, it remains challenging to add the essential effect of the missing correlations to DFT calculations, without destroying the good features of those calculations, or changing from a first principles approach to an approach based on model parameters.

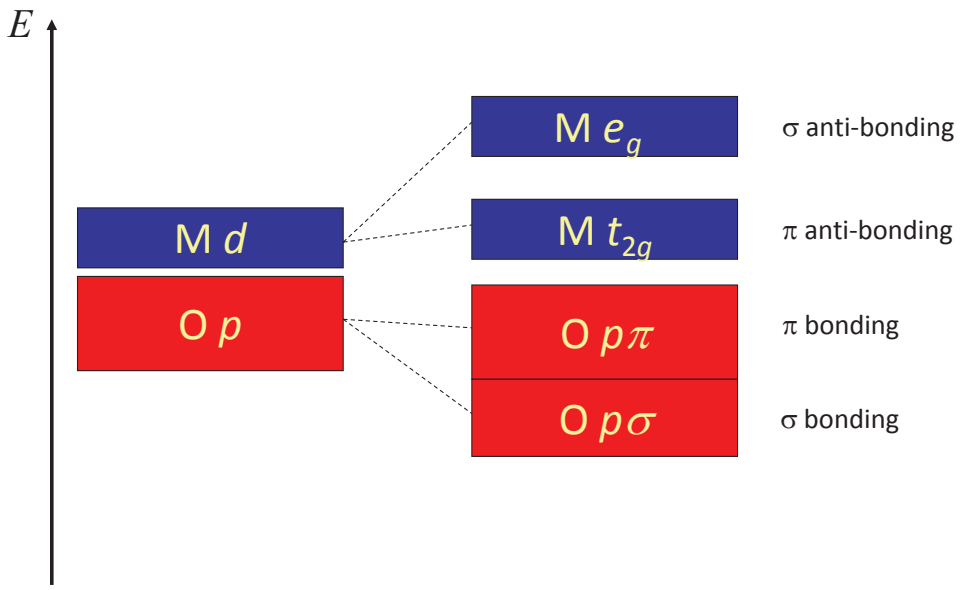

Fig. 3: *The octahedral crystal field splitting in transition metal oxides such as $SrMnO_3$.*

3.2 Crystal fields, moment formation and ordering

In order to continue with our discussion of $SrMnO_3$, it is useful to first overview some aspects of magnetism in perovskite oxides. In the cubic perovskite ABO_3 structure the B-site ions are separated by the lattice parameter a, typically $\sim$4 Å in oxides, while the bond lengths along B-site – O – B-site paths are $a/2$. Thus the main interactions both for forming the electronic structure and for magnetism are through the oxygen ions, specifically the O $2p$ orbitals. These orbitals are p_x, p_y and p_z.

These orbitals mix with the transition metal d orbitals. The Pauling electronegativity of O is 3.44, which is higher than that of any transition element. Therefore the center of the transition metal d bands lies above the center of the O p bands in almost any such material (for this purpose ZnO, CdO and HgO with their full d shells are not regarded as transition metal oxides). In a cubic environment, the five d orbitals are separated by symmetry into a two-fold degenerate (per spin) e_g and a three-fold degenerate t_{2g} set.

The e_g orbitals, labeled $x^2 - y^2$ and z^2, have lobes that point towards the O ions in an octahedral environment, while the t_{2g} orbitals, xy, xz and zy point in between the O ions. If one adopts a local frame in which the p_z orbital points to the B-site ion and the p_x and p_y are oriented perpendicular to this bond, one sees that there is a strong σ bonding interaction between the p_z the e_g d orbitals on the B-site and a weaker π bonding between the O p_x, p_y orbitals and the t_{2g} d B-site orbitals. This explains the crystal field scheme in perovskites. The metal bands are formally metal d – O p antibonding combinations. The t_{2g} bands are more weakly antibonding than the e_g bands, and therefore occur lower in energy. This is shown in Fig. 3. Also it follows that in perovskites absent structure distortions, the t_{2g} bands are generally narrower than the corresponding e_g bands and also that the e_g bands have a more mixed metal d – O p character than the t_{2g} bands. Importantly, the crystal field splittings in the d bands of transition metal

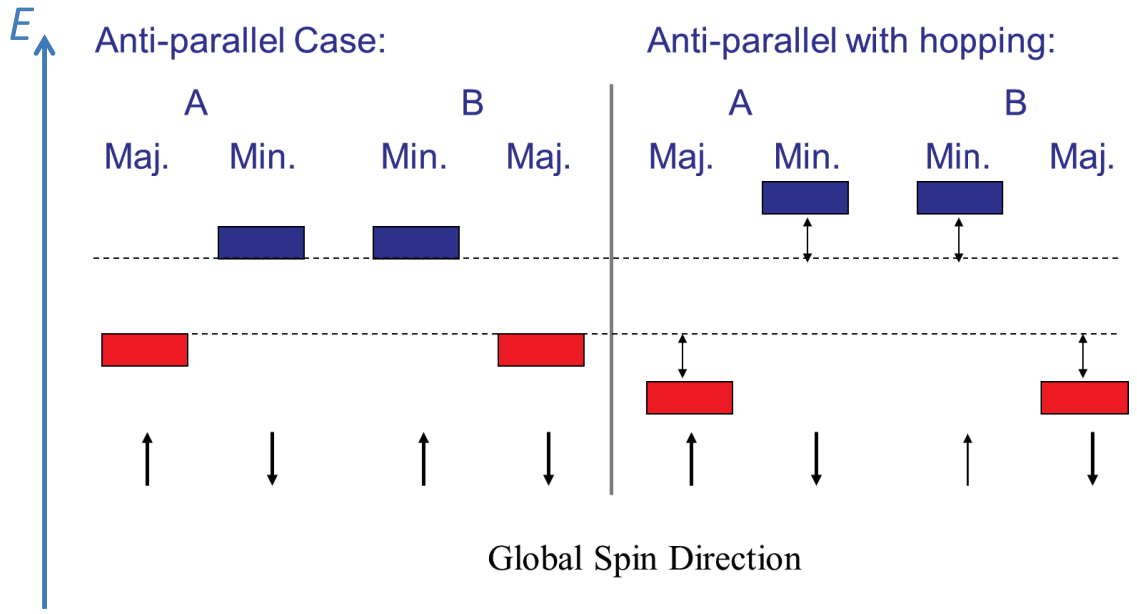

Fig. 4: *Band structure depiction of the superexchange mechanism for interaction between two transition metal ions.*

oxides are primarily due to hybridization and covalency with the p states of the neighboring O as opposed to non-spherical electrostatic potentials. As such, large crystal field splittings are an indicator of strong hybridization.

Within a local moment picture, which as mentioned is a good starting point for $SrMnO_3$, magnetism generally has two aspects: (1) Moment formation and (2) coupling of the moments at different sites to produce ordering. In most materials these two processes can be considered separately. The moment formation is driven by the on-site Hund's coupling in open shell ions, while the magnetic interactions are through the band formation, i.e. hopping between sites, which for the reasons discussed above in perovskites is expected to involve O.

For magnetic ordering, large inter-site interactions, i.e. large effective Heisenberg parameters J, or more generally large hopping integrals, should lead to high ordering temperatures. On the other hand, strong hopping implies both covalency between the B-site and O orbitals, which will reduce the on-site Hund's coupling through mixing of the orbitals and also large band width. If the band width becomes comparable to the Hund's coupling, one may expect the moments (and therefore magnetism) to be lost.

Superexchange is by far the most commonly discussed exchange mechanism in oxides. The theory for this interaction was formulated by P.W. Anderson [32] and further elucidated by Goodenough [33] and Kanamori [34]. Here we describe it within a band structure framework.

The left panel of Fig. 4 shows an energy level scheme for two ions with their spins aligned anti-parallel (i.e. anti-ferromagnetically, so that the majority spin is in the global spin-up direction on one site and in the opposite spin-down global direction on the other site). Allowing hopping through O mixes orbitals on different atoms within the same global spin direction. For anti-parallel alignment this means that the majority spin on one atom mixes with the minority spin

on the next, and vice versa. The result is that the lower lying majority states will be pushed down in energy and the minority spin states pushed up. If the Fermi level is placed so that the majority levels are occupied, while the minority are unoccupied, the result will be a net energy lowering. On the other hand, if the spins are aligned ferromagnetically, then the majority spin on one atom mixes with the majority spin on the neighboring atom, and if this level is completely occupied there will be no gain from this and similarly for the fully unoccupied minority spin channel. Thus one has an energy gain for antiferromagnetic alignment but not for ferromagnetic. This constitutes the superexchange interaction.

So, what favors strong superexchange from a chemical point of view? Superexchange arises due to hopping between sites via O. This means that strong hopping favors strong superexchange. Cases where this can be expected are (1) transition metal atoms in high valence states such as in the cuprate superconductors (because in that case the d levels will be low in energy, i.e. close to the O $2p$ levels); (2) cases involving e_g orbitals, i.e. systems with an empty e_g in the minority spin and a full e_g in the majority spin (since e_g orbitals participate in strong σ bonds with O $2p$ orbitals); (3) straight bonds for the e_g case, since the hopping will be strongest in that case; (4) structures with short metal – O distances; and (5) heavier $4d$ and $5d$ elements to the extent that they can have moments as in $SrTcO_3$, which we discuss below (these have larger d orbitals with more covalency than $3d$ elements) [35]. With the exception of straight bonds, these are the same factors that lead to large crystal field splittings.

3.3 $SrMnO_3$ revisited

Returning to $SrMnO_3$ (Fig. 2), one has both substantial crystal field and exchange splittings of the d bands. From electron counting, there are three d electrons in Mn^{4+}, and so this should normally lead to a fully occupied majority spin t_{2g} manifold, with the other d bands empty, and a spin moment of 3 μ_B/Mn, consistent with the calculated and experimental results. The main O $2p$ bands occur in the energy range from 0 eV (top of the valence band) to $\sim$ 6 eV binding energy (-6 eV), with the $p\sigma$ in the bottom 3 eV. Focusing on the G-AFM (left panel) the minority spin shows a crystal field splitting of $\sim$ 2 eV between well defined t_{2g} and e_g manifolds. In the majority spin the occupied t_{2g} manifold overlaps the top of the O $2p$ bands due to the exchange splitting, which is a little smaller than 3 eV.

A closer examination shows Mn e_g character at the bottom of the valence bands (i.e. the bonding O $p\sigma$ - Mn e_g combination) in both spin channels but much more strongly in the majority spin. The reason for the spin dependence is that the d bands are lower in energy in the majority channel, which favors covalency through a smaller energy denominator. Thus the hybridization in $SrMnO_3$ is very spin dependent, with clearly stronger hybridization for the majority spin e_g than for the minority spin. This is important for the metallicity of the ferromagnetic ordering, and also as it is generic to perovskite manganites, it is important for the band formation of those compounds in general.

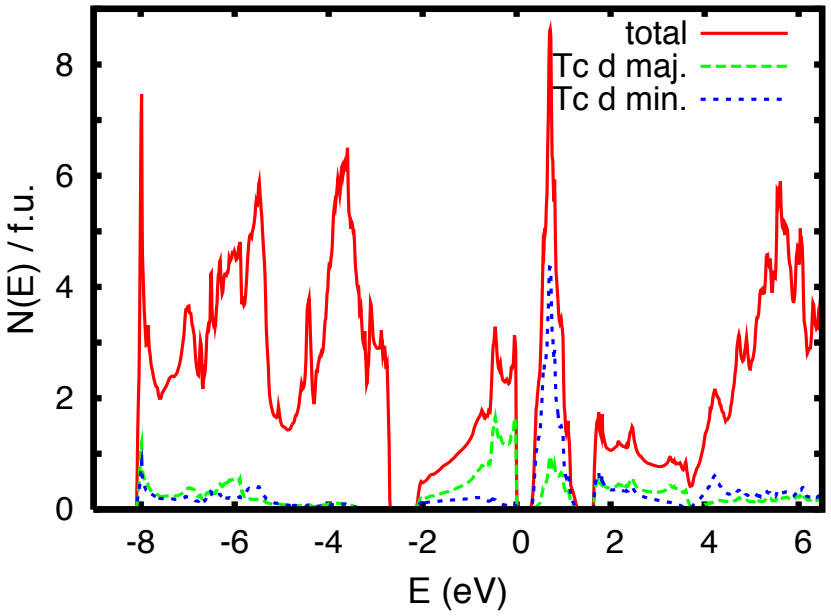

Fig. 5: *Electronic density of states of $SrTcO_3$ as obtained within the LSDA following Ref. [35]. The Tc d projections are onto the LAPW spheres of radii 2.1 Bohr.*

3.4 $SrTcO_3$

Tc is the element directly below Mn in the periodic table, i.e. it is the $4d$ analogue of the $3d$ element Mn. Tc is in general chemically similar to Mn, but as is generally the case in going from the $3d$ element to a $4d$ element, it has a lower Hund's coupling and more extended d orbitals, with the result that Tc has less tendency to form high spin compounds and has a tendency to be more covalent in compounds. Finally, Tc is larger than Mn in the sense that its Shannon ionic radii are larger than those of Mn. Structural distortions in ABO_3 perovskites are often understood in terms of a tolerance factor, $t = (r_A + r_O)/(\sqrt{2}(r_B + r_O))$, where r_A, r_B and r_O are the ionic radii of the A, B and O ions. Thus the tolerance factor of $SrTcO_3$ is smaller than that of $SrMnO_3$, which from a structural point of view makes it more analogous to $CaMnO_3$, and in accord with this $SrTcO_3$ forms in an orthorhombic distorted perovskite structure characterized by tilts of the TcO_6 octahedra.

As mentioned, the Neel temperature of $CaMnO_3$ is lower by approximately a factor of two than that of $SrMnO_3$. In contrast, $SrTcO_3$ has received recent attention because of its extremely high $T_N > 1000$ K [35]. Similar to $CaMnO_3$ and $SrMnO_3$, the ground state of $SrTcO_3$ is a G-type antiferromagnet.

The density of states for the ground state magnetic structure as obtained within the LSDA is shown in Fig. 5. As may be seen, again similar to $SrMnO_3$, a small band gap insulator is predicted. However, the electronic density of states (DOS) is qualitatively different. The projections show very strong covalency between O and Tc even for the nominal t_{2g} manifold (Tc t_{2g} – O p π antibonding combinations; recall that for $SrMnO_3$ the t_{2g} hybridization was weak and it was only the direct σ bonding e_g states that showed large hybridization). Because

of this strong covalency, the Tc d character as measured by the weight inside the 2.1 Bohr LAPW sphere amounts to only $\sim$60% of the total $N(E_F)$. Furthermore, the Hund's coupling on the $4d$ Tc atoms is smaller than that on $3d$ atoms because of the more extended orbitals in this case. One can see this in the smaller exchange splitting in the Tc compound, as compared to the Mn analogue (note the exchange splitting of the t_{2g} states, $\sim$ 1 eV).

As in $SrMnO_3$, the G-type ground state state can be understood in a simple chemical bonding picture. Hybridization occurs between states of the same global spin direction and yields the best energy lowering when occupied states mix with unoccupied states to leave bonding combinations occupied and antibonding combinations unoccupied. With G-type order, the occupied majority spin states on a given site hybridize with unoccupied minority states on each of the six neighboring sites, which is most favorable. However, unlike $SrMnO_3$, $SrTcO_3$ does not show local moment behavior at the DFT level. For example, it was found that the moments collapse to zero for ferromagnetic ordering. Rodriguez and co-workers also considered other orderings [35]. These were a so-called A-type ordering, consisting of ferromagnetic sheets of Tc stacked antiferromagnetically, a C-type arrangement with sheets of nearest neighbor antiferromagnetic Tc stacked to give ferromagnetic chains along the stacking direction, and a G-type nearest neighbor antiferromagnetic arrangement. They found that the A-type arrangement had no stable moments, similar to the ferromagnetic, while the C-type showed a very weak magnetic solution, with moments in the Tc LAPW spheres of 0.44 μ_B and an energy lower than the NSP state by only 0.4 meV / Tc. In contrast a very robust solution was found for the G-type ordering. Therefore, at the LSDA level, $SrTcO_3$ should be described not as a local moment system, but as being closer to the itinerant limit.

In standard oxide magnets there are two energy scales. The first is a scale set by intra-atomic Coulomb repulsions, particularly the Hund's coupling, which drive moment formation. This is typically a high energy scale and leads to stable moments at all solid state temperatures. The second scale controls the ordering temperature, and is that associated with the relative orientation of moments on neighboring sites. This is determined by inter-atomic hopping, as for example in the superexchange mechanism. In perovskites it arises from the hybridization between transition metal d orbitals and oxygen p orbitals. Importantly, the ordering temperature is set by the energy differences between different configurations of the moments, and these differences in turn are related to metal oxygen covalency and details of the bonding topology.

In $SrTcO_3$ the larger extent of the Tc $4d$ orbitals relative to e.g. the $3d$ orbitals of Mn lowers the on-site interactions that underlie moment formation, but strongly increases the amount of covalency as seen in the DOS projections. The result is that the two energy scales become comparable and moment formation and ordering are intertwined. This type of situation is often described as itinerant magnetism. This term should however be used with caution, since the moments are not small, and as a result there is a rearrangement of the DOS not only near E_F but over most of the $\sim$3 eV wide t_{2g} manifold.

There are two important differences between $SrMnO_3$ and $SrTcO_3$ that imply high ordering temperature in the Tc compound. First of all, the energy scale is increased because of the greater hybridization and the smaller energy splitting between minority and minority spin orbitals (this

enters in the denominator). Secondly, because the moment formation is intimately connected to the magnetic order, competing states, as exemplified by the C-type pattern are suppressed: with two of the six neighboring Tc flipped the moment is strongly reduced, so that even though four neighbors are oppositely aligned for a net favorable alignment of two neighbors, the energy that might have been gained is lost because the moment collapses. This is related to the physics that leads to high ordering temperatures in low moment itinerant magnets such as Cr and Ni. In any case, these two facts provide a qualitative explanation for the high observed Neel temperature.

Turning to the connection of approximate DFT results with experiment, we note that in the Mott case the insulating state is incorrectly described. The band prediction for $SrTcO_3$ would be that it has a metal-insulator transition associated with magnetic order, i.e. that it becomes conducting above T_N. It is not known at present what happens in $SrTcO_3$ from an experimental point of view. However, the $5d$ analogue, $NaOsO_3$, which shows many features in common with $SrTcO_3$, except that T_N=410 K is lower, is reported to have a metal-insulator transition associated with magnetic ordering [36].

3.5 $SrRuO_3$ and itinerant ferromagnetism

As mentioned, the half-filled t_{2g} band is important for the G-type antiferromagnetism in $SrTcO_3$; with G-type order, one has a majority spin band of bonding character that is filled, and a corresponding minority spin band of antibonding character that is empty. Thus one may expect interesting behavior with doping.

Ru is the element next to Tc in the periodic table. Thus $SrRuO_3$ can be roughly viewed as an electron doped $SrTcO_3$. Like $SrTcO_3$, $SrRuO_3$ has an orthorhombic distorted perovskite structure characterized by octahedral tilts. The ground state is metallic and ferromagnetic, with a total spin moment of $\sim$1.6 μ_B on a per Ru basis (this is distributed between Ru and O, however) and a Curie temperature, T_c=160 K [37–39, 41]. The material is of interest in its own right as a rare example of a $4d$ ferromagnet, and also because many of the related ruthenate phases show very unusual physical behavior, much of it related to magnetism and electron correlations. Notably, the layered perovskite, Sr_2RuO_4, which has the same Ru valence and coordination as ferromagnetic $SrRuO_3$, is an apparently triplet superconductor [42, 43], while Ca_2RuO_4 is a Mott insulator [44]. The bilayer perovskite $Ca_3Ru_2O_7$ is a metamagnetic metal and is ferromagnetic within its bilayers, but with very slight alloying by Ti, becomes a G-type antiferromagnetic Mott insulator [45], again showing borderline behavior in ruthenates.

DFT calculations for $SrRuO_3$ show a clear ferromagnetic instability, with parameters (such as moments) that are in accord with experimental measurements. Also, like $SrTcO_3$, but in contrast to $SrMnO_3$, the moments are highly dependent on the magnetic order; in $SrRuO_3$ the moments are suppressed for G-type order. Also, there is a strong dependence on structure. Without the octahedral tilting, i.e. with the cubic perovskite structure the moment is reduced from 1.59 μ_B per formula unit to 1.17 μ_B in the LSDA [40]. $CaRuO_3$, which differs structurally from the Sr compound in having larger tilts due to the smaller ionic radius of Ca, is paramagnetic although highly enhanced (i.e. very near ferromagnetism) according to experiment. This is in accord with

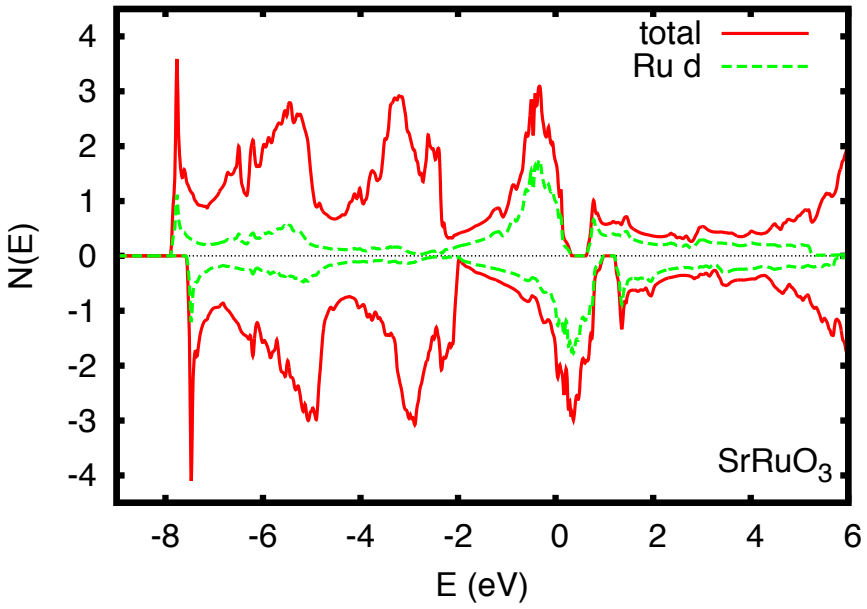

Fig. 6: *Electronic density of states of $SrRuO_3$ as obtained within the LSDA (see Ref. [40]) on a per formula unit basis. The Ru d projections are onto the LAPW spheres of radii 2.0 Bohr.*

LSDA calculations [46], although within the LSDA $CaRuO_3$ is closer to ferromagnetism than in experiment. This may be a sign of renormalization due to quantum spin fluctuations associated with the proximity to the ferromagnetic state. Such renormalizations are not described by standard approximate DFT calculations, because the electron gas upon which these approximations are based is at densities that place the uniform electron gas far from magnetism [47–49]. In any case, the strong dependence of the moments on the ordering as well as on the structure indicate an itinerant aspect to the magnetism.

The interplay between moment formation and magnetic order discussed above for $SrTcO_3$ and $SrRuO_3$ is a characteristic common to many $4d$ and $5d$ magnetic oxides. Essentially, compared to $3d$ magnets, (1) the Coulomb interactions, including the exchange interactions are relatively weaker since they depend on Slater integrals, which are smaller for more extended orbitals and (2) the hopping and covalency involving the d orbitals is stronger, as these larger orbitals overlap more strongly with orbitals on neighboring O atoms. These two characteristics are generic to such materials.

Another aspect that is important is that because of the heavier atoms involved, spin orbit can play a more important role. Although we do not discuss this in detail here, we note that it has received recent attention both in terms of correlation effects in materials such as iridates [50], and in providing mechanisms for high magnetocrystalline anisotropies and magneto-optical coefficients. This may be important from a practical point of view especially in ferromagnetic (or ferrimagnetic) materials with heavy element moments and Curie temperatures above room temperature, such as double perovskites (e.g. Sr_2CrReO_6 [51]).

Fig. 6 shows the calculated density of states of orthorhombic $SrRuO_3$ in its ferromagnetic

ground state as obtained within the LSDA (this is a new calculation, done similarly to that reported in Ref. [40] but with a better converged zone sampling; the moment of 1.55 μ_B in this calculation is slightly lower than in the reference, 1.59 μ_B). The electronic structure shows exchange split bands that are otherwise similar between the majority and minority spin. The region near the Fermi energy is derived primarily from Ru t_{2g} states as expected. However, even in the π bonding t_{2g} manifold strong hybridization with O is evident. This can be seen clearly in the DOS via the Ru d bonding contributions to the nominal O $2p$ bands.

$SrRuO_3$ provides an example of itinerant magnetism. In its simplest form it arises from an instability of the Fermi surface, but in general the moments are finite and states away from the Fermi surface are important as well. In any case, in the simplest picture, if the density of states at the Fermi energy, $N(E_F)$ is high then a system may lower its energy by an exchange splitting where the majority spin states move to higher binding energy (lower absolute energy) relative to the minority spin and accordingly charge is transferred from the minority to the majority channel as seen in the DOS. This instability is described by Stoner theory [52], and was generalized to the case of finite moments in the so-called extended Stoner theory [53] (ref. [46] discusses ruthenates from this point of view).

Within Stoner theory, the bare Pauli susceptibility ($\chi_0 = N(E_F)$, with suitable units) is enhanced by a factor (1-$N(E_F)I)^{-1}$, where $N(E_F)$ is expressed on a per spin basis. An instability towards ferromagnetism occurs when the Stoner parameter, $N(E_F)I$ exceeds unity. The physical origin of I is in the exchange interaction, i.e. through the Coulomb repulsion, and therefore more compact orbitals lead to larger I, while covalency reduces I. The Stoner criterion amounts to a criterion that the gain in exchange energy from polarizing the bands exceeds the loss in kinetic energy due to the unequal occupation. Typical values of I for $3d$ transition elements are in the range 0.7-0.8 eV, and so a Stoner instability can be anticipated if $N(E_F)$ for a $3d$ transition atom exceeds $\sim$1.3 eV^{-1} on a per spin per atom basis. Values for various elements can be found in Ref. [54]. However, it should be noted that while these values are useful for understanding the type of magnetic behavior that is expected in a given material, in practice the precise value of I varies from material to material and one would not use the tabulated values of I, but would directly obtain the susceptibility and magnetic behavior from self-consistent calculations.

Actually, the Stoner enhancement, above, is a special case of the RPA enhancement, which can be written,

$$\chi(\mathbf{q}) = \chi_0(\mathbf{q})/(1 - I(\mathbf{q})\chi_0(\mathbf{q})), \tag{7}$$

where χ_0 is the bare Lindhard susceptibility, and $I(\mathbf{q})$ is an interaction term that is now $\mathbf{q}$-dependent. As in the case of ferromagnetism, an instability occurs when the product $I(\mathbf{q})\chi_0(\mathbf{q})$ reaches unity, in this case towards a spin density wave at the nesting vector, $\mathbf{q}$. Details and interesting discussion about itinerant magnetism from a band structure point of view can be found in the book of Kubler [55].

Returning to $SrRuO_3$, one sees a substantial peak in the DOS, which is what drives the magnetic instability. Because this peak is derived from hybridized bands rather than pure d bands a rigid splitting will result in a magnetization density that reflects this character, i.e. the character of the band states near the Fermi energy. In the case of $SrRuO_3$ this is approximately 2/3 from

Ru t_{2g} states and 1/3 from O $2p$ states (note that there is always ambiguity in defining where contributions to states come from as there is no unique physical decomposition of the charge density into atomic contributions). In $SrRuO_3$ the t_{2g} bands do in fact exchange split rather rigidly as can be seen by comparing the majority and minority DOS, and similarly for the Ru d projection of the DOS. The reason why the bands exchange-split rigidly in this way is that the energy cost associated with breaking the Ru - O hybridization is high in this material. In any case, the consequence is the prediction of substantial moments on the O sites amounting in aggregate to $\sim$1/3 of the total magnetization. This has been confirmed by neutron diffraction measurements.

Another consequence of the induced spin-polarization on O is that not only the $p\pi$ states of O that are hybridized with the polarized Ru t_{2g} orbitals are exchange-split, but as seen in the DOS, the entire O $2p$ manifold is exchange-split. This includes the lower part that comes from the $p\sigma$ orbitals.

As was discussed in Ref. [46], the ferromagnetic ground state of $SrRuO_3$ can be analyzed using extended Stoner theory. Extended Stoner analysis helps shed some additional light on the general features of the magnetic instabilities in ruthenates. The key parameter in this theory is $N(E_F)I$, where the Stoner I is a normally atomic-like quantity giving the local exchange enhancement. Generally, I is determined by the density distribution on an ion, and is larger for more compact orbitals, as in $3d$ ions relative to $4d$ ions. In compounds, I is replaced by a material dependent average I. The appropriate averaging for calculating the energetics is with the decomposed DOS, $I = I_A n_A^2 + I_B n_B^2$, for two components, A and B, where I_A and I_B are the Stoner I for atoms A and B, and n_A and n_B are the fractional weights of A and B in $N(E_F)$ (normalized to $n_A + n_B = 1$). The O^{2-} ion is highly polarizable (it does not exist outside crystals) and because of this the value of I_O may be expected to be material dependent. Nonetheless, O^{2-} is a small ion and so I_O may also be large. Mazin and Singh got I_{Ru}=0.7 eV and I_O = 1.6 eV for $SrRuO_3$, yielding I = 0.38 eV including O and I = 0.31 eV without the O contribution. The O contribution to I is generic to perovskite derived ruthenates, as it simply reflects the hybridization of the t_{2g} orbitals of nominally tetravalent octahedrally coordinated Ru with O. This provides a ferromagnetic interaction between Ru ions connected by a common O. The interaction comes about because for a ferromagnetic arrangement the O polarizes, and this contributes to the energy, while for a strictly antiferromagnetic arrangement, O does not polarize by symmetry, and so in this case there is no O contribution to the magnetic energy. This is local physics and so this contribution to the paramagnetic susceptibility, while peaked at the zone center, is smooth in reciprocal space.

This ferromagnetic tendency, which is generic to all the ruthenates, competes with an antiferromagnetic nesting related tendency in the layered perovskite Sr_2RuO_4, which is a superconductor. In that compound, spin-fluctuation theory predicts that the ferromagnetic tendency provides an interaction that can stabilize the triplet state [56, 57]. It is not clear what the role of the antiferromagnetic tendency is in the superconductivity, but one possibility is that it competes with the ferromagnetic tendency, moving the system away from magnetic ordering and thus allowing triplet superconductivity to appear as the ground state.

3.6 Summary

There are a wide variety of oxide magnets, including many useful materials. In spite of many decades of productive research on these, entirely new systems and new physics continue to be discovered in oxides. The above represents a narrow selection of three materials that illustrate some concepts (and leaves out other very important topics, e.g. orbital ordering). Nonetheless, I hope that it is useful.

4 Concluding remarks

Life would be much less interesting (and perhaps not existent at all) in a universe where all substances had roughly the same properties, e.g. a world where all solids had the mechanical properties of Jello. Fortunately for us this is not the case, and instead condensed matter displays a richly varied diversity of properties. According to density functional theory, all of this variety is fundamentally associated with the different charge-density distributions in materials. If one considers that the valence charge-density is most important, it is remarkable to observe that the average valence-density in a material like diamond is not so much different from that in iron or $BaTiO_3$ even though the properties of those substances are very different. As mentioned, solids are not like blueberry muffins. From this point of view it is most remarkable that approximate DFT methods, such as the LDA, effectively describe many of these differences even though it would seem at least superficially to be based on a description adapted from the uniform electron gas. This success, which is reflected in the widespread use of approximate DFT in condensed matter physics, chemistry and materials science, often provides a very useful starting point for understanding correlated materials and their properties.

Acknowledgements

This work was supported by the Department of Energy, Basic Energy Sciences, Materials Sciences and Engineering Division.

References

[1] H. Hohenberg and W. Kohn, Phys. Rev. **136**, B864 (1964)

[2] W. Kohn and L.J. Sham, Phys. Rev. **140**, A1133 (1965)

[3] J.P. Perdew, K. Burke and M. Ernzerhof, Phys. Rev. Lett. **77**, 3865 (1996)

[4] J.P. Perdew, J.A. Chevary, S.H. Vosko, K.A. Jackson, M.R. Pederson, D.J. Singh and C. Fiolhais, Phys. Rev. B **46**, 6671 (1992)

[5] W.E. Pickett, Rev. Mod. Phys. **61**, 433 (1989)

[6] W.E. Pickett, H. Krakauer, R.E. Cohen and D.J. Singh, Science **255**, 54 (1992)

[7] D.J. Singh and M.H. Du, Phys. Rev. Lett. **100**, 237003 (2008)

[8] I.I. Mazin, D.J. Singh, M.D. Johannes and M.H. Du, Phys. Rev. Lett. **101**, 057003 (2008)

[9] R.G. Parr and W. Yang, *Density Functional Theory of Atoms and Molecules* (Oxford Press, New York, 1994)

[10] R.M. Dreizler and J. da Provincia, *Density Functional Methods in Physics* (Plenum, New York, 1985)

[11] M. Ernzerhof, J.P. Perdew and K. Burke, *Density Functionals: Where Do They Come From, Why Do They Work?*, in *Topics in Current Chemistry*, vol. 180, R.F. Nalewajski (ed.) (Springer, Berlin, 1996)

[12] S. Lundqvist and N.H. March, *Theory of the Inhomogeneous Electron Gas* (Plenum, New York, 1983)

[13] J. Callaway and N.H. March, in *Solid State Physics*, H. Ehrenreich and D. Turnbull (eds.), vol. 38, pp. 135 (1984)

[14] D. Ceperley, Nature (London) **397**, 386 (1999)

[15] U. von Barth and L. Hedin, J. Phys. C **5**, 1629 (1972)

[16] L. Nordstrom and D.J. Singh, Phys. Rev. Lett. **76**, 4420 (1996)

[17] D.C. Langreth and M.J. Mehl, Phys. Rev. Lett. **47**, 446 (1981)

[18] J.C. Slater, Phys. Rev. **81**, 385 (1951)

[19] D.J. Singh, Solid State Commun. **98**, 899 (1996)

[20] W.E. Pickett and D.J. Singh, Phys. Rev. Lett. **72**, 3702 (1994)

[21] N.P. Ong, Phys. Rev. B **43**, 193 (1991)

[22] G.H. Jonker and J.H. van Santen, Physica (Amsterdam) **16**, 337 (1950);
G.H. Jonker and J.H. van Santen, Physica (Amsterdam) **16**, 559 (1950)

[23] C. Zener, Phys. Rev. **82**, 403 (1951)

[24] J.B. Goodenough, Phys. Rev. **100**, 564 (1955)

[25] C.W. Searle and S.T. Wang, Can. J. Phys. **48**, 2023 (1970)

[26] R. von Helmolt, J. Wecker, B. Holzapfel, L. Schultz and K. Samwer,
Phys. Rev. Lett. **71**, 2331 (1993)

[27] S. Jin, T.H. Tiefel, M. McCormack, R.A. Fastnacht, R. Ramesh and L.H. Chen,
Science **264**, 413 (1994)

[28] W.E. Pickett and D.J. Singh, Phys. Rev. B **53**, 1146 (1996)

[29] A.A. Belik, Y. Matsushita, T. Katsuya, M. Tanaka, T. Kolodiazhnyi, M. Isobe and E. Takayama-Muromachi, Phys. Rev B **84**, 094438 (2011)

[30] H. Sakai, S. Ishiwata, D. Okuyama, A. Nakao, H. Nakao, Y. Murakami, Y. Taguchi and Y. Tokura, Phys. Rev. B **82**, 180409 (2010)

[31] J.A. Souza, J.J. Neumeier, R.K. Bollinger, B. McGuire, C.A.M. dos Santos, and H. Terashita, Phys. Rev. B **76**, 024407 (2007)

[32] P.W. Anderson, Phys. Rev. **115**, 2 (1959)

[33] J.B. Goodenough, *Magnetism and the Chemical Bond* (Wiley, New York, 1963)

[34] J. Kanamori, J. Phys. Chem. Solids, **10**, 87 (1959)

[35] E.E. Rodriguez, F. Poineau, A. Llobet, B.J. Kennedy, M. Avdeev, G.J. Thorogood, M.L. Carter, R. Seshadri, D.J. Singh and A.K. Cheetham,
Phys. Rev. Lett. **106**, 067201 (2011)

[36] Y.G. Shi, Y.F. Gao, S. Yu, M. Arai, A.A. Belik, A. Sato, K. Yamaura, E. Takayama-Muromachi, H.F. Tian, H.X. Yang, J.Q. Li, T. Varga, J.F. Mitchell and S. Okamoto,
Phys. Rev. B **80**, 161104 (2009)

[37] J.J. Randall and R. Ward, J. Am. Chem. Soc. **81**, 2629 (1959)

[38] J.M. Longo, P.M. Raccah and J.B. Goodenough, J. Appl. Phys. **39**, 1327 (1968)

[39] A. Kanbayashi, J. Phys. Soc. Jpn. **44**, 108 (1978)

[40] D.J. Singh, J. Appl. Phys. **79**, 4818 (1996)

[41] G. Cao, S. McCall, M. Shepard, J.E. Crow and R.P. Guertin, Phys. Rev. B **56**, 321 (1997)

[42] Y. Maeno, H. Hashimoto, K. Yoshida, S. Nishizaki, T. Fujita, J.G. Bednorz and F. Lichtenberg, Nature (London) **372**, 532 (1994)

[43] A.P. MacKenzie and Y. Maeno, Rev. Mod. Phys. **75**, 657 (2003)

[44] S. Nakatsuji and Y. Maeno, Phys. Rev. Lett. **84**, 2666 (2000)

[45] X. Ke, J. Peng, D.J. Singh, T. Hong, W. Tian, C.R. Dela Cruz and Z.Q. Mao, Phys. Rev. B **84**, 201102 (2011)

[46] I.I. Mazin and D.J. Singh, Phys. Rev. B **56**, 2556 (1997)

[47] T. Moriya and A. Kawabata, J. Phys. Soc. Jpn. **34**, 639 (1973)

[48] M. Shimizu, Rep. Prog. Phys. **44**, 329 (1981)

[49] A. Aguayo, I.I. Mazin and D.J. Singh, Phys. Rev. Lett. **92**, 147201 (2004)

[50] B.J. Kim, H. Ohsumi, T. Komesu, S. Sakai, T. Morita, H. Takagi and T. Arima, Science **323**, 1329 (2009)

[51] F.D. Czeschka, S. Geprags, M. Opel, S.T.B. Goennenwein and R. Gross, Appl. Phys. Lett. **95**, 062508 (2009)

[52] E.C. Stoner, Proc. Roy. Soc. London Ser. A **169**, 339 (1939)

[53] G.L. Krasko, Phys. Rev. B **36**, 8565 (1987)

[54] J.F. Janak, Phys. Rev. B **16**, 255 (1977)

[55] J. Kubler, *Theory of Itinerant Electron Magnetism* (Clarendon, Oxford, 2000)

[56] I.I. Mazin and D.J. Singh, Phys. Rev. Lett. **79**, 733 (1997)

[57] I.I. Mazin and D.J. Singh, Phys. Rev. Lett. **82**, 4324 (1999)

3 NMTOs and their Wannier Functions

Ole K. Andersen
Max Planck Institute for Solid State Research
Heisenbergstrasse 1, D-70569 Stuttgart

Contents

E. Pavarini, E. Koch, F. Anders, and M. Jarrell
Correlated Electrons: From Models to Materials
Modeling and Simulation Vol. 2
Forschungszentrum Jülich, 2012, ISBN 978-3-89336-796-2
http://www.cond-mat.de/events/correl12

1 Introduction

The electronic structure of condensed matter is usually described in terms of one-electron *basis sets*. Basis functions used for computation, or rather, their envelopes are usually mathematically simple functions, plane waves or Gaussians, in particular. A plane wave is a solution of Schrödinger's equation for a flat potential, and products of plane waves are plane waves; as a result, the charge density and its Hartree potential are plane-waves as well. Similarly, a Gaussian is a solution of Schrödinger's equation for a parabolically increasing potential, products of Gaussians are Gaussians, and the Hartree potential for a Gaussian charge density is $1/r$ times the error function. However, in order for such sets to give accurate results, the number of basis functions must be orders of magnitude larger than the number of valence electrons to be described. This is so, because as illustrated at the top of Fig. 1, the potential $V(\mathbf{r})$ in the effective one-electron Schrödinger (Kohn-Sham) equation is neither flat inside the atoms nor parabolically increasing between them. Therefore, a plane-waves basis must include plane waves with energies spread over a region much larger than the one of the one-electron energies ε of interest, and a Gaussian basis must include Gaussians not only with many widths, but also at many positions displaced from those of the atoms. For a discussion of plane-wave basis sets, we refer to the last year's lecture notes [1] by Blöchl [2].

By virtue of solving Schrödinger's equation for a muffin-tin well, the classical linear muffin-tin orbitals (LMTOs) [3, 4] form a comparatively small basis set. But only in the atomic-spheres approximation (ASA) where the MTOs are expanded in partial waves inside atomic spheres, assumed to fill space, do the products $\varphi_l(\varepsilon, r)\, Y_{lm}(\hat{\mathbf{r}}) \times \varphi_{\bar{l}}(\bar{\varepsilon}, r)\, Y^*_{\bar{l}\bar{m}}(\hat{\mathbf{r}})$ have the same form, $f_{L'}(r)\, Y_{l'm'}(\hat{\mathbf{r}})$, as each factor, and this is what makes the LMTO-ASA method exceedingly fast. However, the ASA is only accurate when the atoms are at high-symmetry positions.

For many purposes it is therefore desirable to extract a *small set of intelligible, localized orbitals* spanning merely selected conduction and/or valence states. For instance, if we want to describe the bonding, we need a localized basis set which spans the occupied states only (bond orbitals). If we want to construct models which add interactions to the one-electron Hamiltonian, e.g. electron-electron repulsions, we need a basis set of localized, atomic-like orbitals which describes the one-electron energies and wave functions in a suitable region around the Fermi level.

For an isolated set of energy bands in a *crystal*, $\varepsilon_i(\mathbf{k})$ $(i = 1, ., A)$, this can be done by projecting from their delocalized Bloch eigenstates, $\Psi_i(\mathbf{k}; \mathbf{r})$ $(i = 1, ., A)$ computed with the large basis set, a suitable set of generalized *Wannier functions,* $w_a(\mathbf{r} - \mathbf{t})$. These are enumerated by a $(= 1, ., A)$ and the lattice translations, $\mathbf{t}$, of which there are $\mathrm{N} \to \infty$, and they form a set of orthonormal functions related to the orthonormal Bloch eigenstates by a unitary transformation:

$$\Psi_i(\mathbf{k}; \mathbf{r}) = \mathrm{N}^{-\frac{1}{2}} \sum\nolimits_{\mathbf{t}} \sum\nolimits_{a=1}^{A} u_{ia} \exp(i\mathbf{k} \cdot \mathbf{t})\; w_a(\mathbf{r} - \mathbf{t}), \tag{1}$$

The inverse transformation:

$$w_a(\mathbf{r} - \mathbf{t}) = \mathrm{N}^{-\frac{1}{2}} \sum\nolimits_{\mathbf{k}} \sum\nolimits_{i=1}^{A} u^*_{ai} \exp(-i\mathbf{k} \cdot \mathbf{t})\; \Psi_i(\mathbf{k}; \mathbf{r}), \tag{2}$$

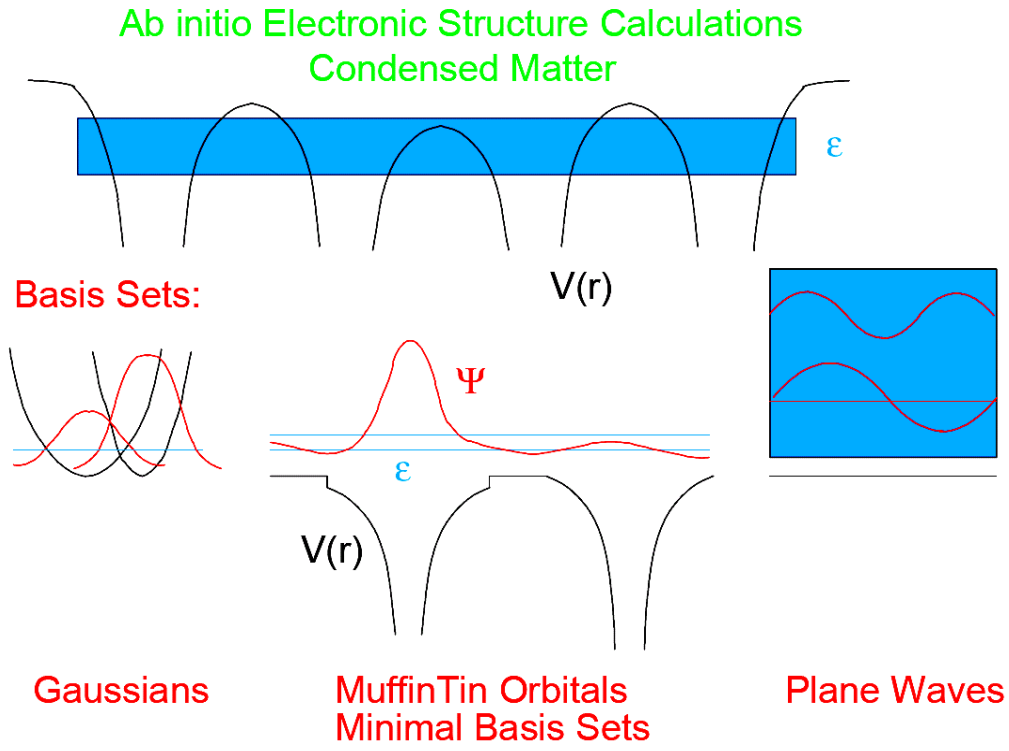

Fig. 1: *Top: Effective one-electron potential in condensed matter (black) and the energy region of interest (blue). Bottom: Basis functions (red), their generating potentials (black), and energies (blue).*

is the Wannier projection. Wannier functions are not unique, because performing a unitary transformation, $W_{a\bar{a};\mathbf{t}-\mathbf{t}'}$, of one set of Wannier functions produces another set which also satisfies Eq. (1), merely with different i and $\mathbf{k}$-dependent phases of the Bloch functions. So the art of Wannier projection from the Bloch states (2) is to choose the i and $\mathbf{k}$-dependent phases of the latter in such a way that the Wannier functions attain desired properties, in particular optimal localization – in some sense. Mazari and Vanderbilt chose to minimize the spread $\langle w \left|\left|\mathbf{r} - \langle w \left|\mathbf{r}\right| w\rangle\right|^2 \right| w \rangle$ and developed an – otherwise general – numerical procedure for projecting such "maximally localized" Wannier functions from Bloch states expanded in plane waves [5].

We shall only be interested in generating localized Wannier functions which resemble atomic orbitals, so-called *Wannier orbitals,* or simple linear combinations hereof such as bond orbitals. In this case, it is obvious that the phases in the projection (2) should be chosen such that when summing the Bloch states over i and $\mathbf{k}$, the atomic-orbital characters chosen for the Wannier functions should add up constructively. How localized the resulting Wannier orbitals are, then depends on how well the set of A bands are described by the characters chosen. This procedure was applied –presumably for the first time– by Satpathy and Pawlowska [6] to compute the sp^3 bond orbital in Si. They used the TB-LMTO basis [4] which makes the procedure quite obvious because the LMTO expansion has the same form as the expansion (2) in terms of Wannier functions, except that the unitary $A \times A$ matrix u_{ia} is replaced by the rectangular $A \times (A + P)$

matrix of LMTO eigenvectors. The projection is thus seen to be a *downfolding* in which each Wannier orbital becomes an *active* LMTO dressed by a tail of all the *passive* (P) LMTOs not in the set of active (A) ones. With other local-orbital basis sets, somewhat similar techniques can be used, but unless all basis functions are well localized, the Wannier orbitals obtained may not be sufficiently localized. For a further discussion we refer to last year's lecture notes by Kunes [7].

For molecules, Boys [8] had a long time ago recognized that chemical bonds should be associated with those linear combinations of the occupied molecular orbitals which are most localized, because those linear combinations are most invariant to the surroundings.

The present notes deal with a different kind of basis set, specifically with minimal bases of Nth-order muffin-tin orbitals (NMTOs), also known as 3rd generation MTOs [9–13]. We shall demonstrate that with *N*MTOs it is possible to generate Wannier functions *directly*, instead of via projection from the delocalized Bloch states. *N*MTOs are constructed from the partial-wave solutions of Schrödingers equation for a superposition of *overlapping* spherical potential wells (muffin tins, MTs) [14, 15] and *N*MTO sets are therefore selective in energy. As a consequence, one can construct an *N*MTO set which picks a specific set of isolated energy bands. Since *N*MTOs are atom-centered and localized by construction, they do –after symmetric orthonormalization– form a set of localized Wannier functions which, if needed, can be recombined locally to have maximal localization. The *N*MTO technique is primarily for generating a *localized, minimal basis set* with *specific orbital characters,* and it can therefore be used also to pick a set of bands which overlap other bands outside the energy region of interest [16]. The corresponding *N*MTOs –orthonormalized or not– we refer to as Wannier-like. Once a computationally efficient representation is implemented for products of NMTOs [17], they should be suitable for full-potential, real-space calculations with a computational effort increasing merely linearly with the size (N) of the system, so-called order-N calculations [18, 19].

We start by explaining the LMTO idea of how to construct small basis sets of orbitals, $\chi_{Rlm}(\mathbf{r})$, from partial waves, $\varphi_{Rl}(\varepsilon, r)\, Y_{lm}(\hat{\mathbf{r}})$, and spherical waves, $h_l(\kappa r)\, Y_{lm}(\hat{\mathbf{r}})$. Then we define the set of exact, energy-*de*pendent MTOs (EMTOs) [20, 21], also called kinked partial waves (KPWs), which includes *downfolding* and employs *overlapping* MT spheres for their definition. The KPWs are used to derive, first the screened KKR equations, and then the NMTO basis sets. NMTOs with N=1 turn out to have the same form as classical TB-LMTOs in their atomic-spheres approximation (ASA), but without invoking this approximation. Examples of Wannier functions which are orthonormalized NMTOs are given along the way.

2 Classical LMTOs

The idea [22,3,23,24] of how to generate small basis sets of accurate orbitals can be understood by considering first the way in which Wigner and Seitz [25] thought about solving the one-electron eigenvalue problem for a close-packed solid; in case of a crystal, that is the band-structure problem. They divided space into WS cells and assumed the potential to be spherically

symmetric inside each cell,

$$V(\mathbf{r}) = \sum\nolimits_R v_R(r_R). \tag{3}$$

Here and in the following, $r_R \equiv |\mathbf{r} - \mathbf{R}|$, and R labels the sites, $\mathbf{R}$. With this approximation, Schrödinger's equation (in atomic Rydberg units),

$$[\mathcal{H} - \varepsilon]\Psi(\varepsilon, \mathbf{r}) = \left[-\bigtriangledown^2 + V(\mathbf{r}) - \varepsilon\right]\Psi(\varepsilon, \mathbf{r}) = 0, \tag{4}$$

can be treated as a *separable differential equation*: The eigenfunctions must have a *partial-wave expansion* inside each cell,

$$\Psi(\varepsilon, \mathbf{r}) = \sum\nolimits_{lm} \varphi_{Rl}(\varepsilon, r_R) Y_{lm}(\hat{\mathbf{r}}_R)\ c_{Rlm}, \tag{5}$$

and one may therefore proceed by first solving the *radial* Schrödinger equations,

$$-[r\varphi_{Rl}(\varepsilon, r)]'' = \left[\varepsilon - v_R(r) - l(l+1)/r^2\right] r\varphi_{Rl}(\varepsilon, r), \tag{6}$$

for all R and l and a given energy, ε, and then seek coefficients, c_{Rlm}, for which the partial-wave expansions join together continuously and differentiably at the cell boundaries. The energies for which this is possible are the eigenvalues, ε=ε_i, and $\Psi_i(\varepsilon_i, \mathbf{r})$ the eigenfunctions.

This point of view for instance leads to the *approximate* Wigner-Seitz rules stating that for an elemental, close-packed crystal, where the cell can be substituted by an atomic sphere of the same volume (Ω=$4\pi s^3/3$), a band of l-character exists between the energies ε_{lB} and ε_{lA} for which respectively the slope and the value of $\varphi_l(\varepsilon, r)$ vanishes at the atomic sphere. These band edges correspond to the bonding and antibonding states of a homonuclear diatomic molecule. In this atomic-spheres approximation (ASA), the input to the band structure from the potential enters exclusively via the dimensionless, *radial logarithmic derivative functions,*

$$D\{\varphi_l(\varepsilon, s)\} \equiv \partial \ln|\varphi_l(\varepsilon, r)|/\partial \ln r|_s = s\varphi_l(\varepsilon, s)'/\varphi_l(\varepsilon, s), \tag{7}$$

evaluated at the WS sphere, s. These are ever decreasing functions of energy and the bonding/antibonding boundary condition is: $D\{\varphi_l(\varepsilon, s)\} = 0/\infty$. The shape of the l-partial wave thus changes significantly across a band of predominant l-character (Fig. 2) and, as we shall see in Sect. 3.4, even more across the hybridized sp^3 valence band of Si.

To set up this matching problem correctly, however, it is necessary to deal with cells rather than spheres *and* with all the partial waves required to make the one-center expansion (5) converged at the cell-boundary. This takes $l \lesssim 15$ and is *not* practical.

Next, consider the customary and more general way of solving Schrödinger's equation, namely by use of the Raleigh-Ritz variational principle for the Hamiltonian with a trial function expressed as a superposition of basis functions, $\chi_j(\mathbf{r})$,

$$\Psi(\mathbf{r}) \approx \sum\nolimits_j \chi_j(\mathbf{r})\ b_j. \tag{8}$$

Variation of the coefficients b_j leads to the algebraic, generalized eigenvalue problem:

$$\sum\nolimits_j \left(\langle\chi_{\bar{j}}|\mathcal{H}|\chi_j\rangle - \varepsilon\langle\chi_{\bar{j}}|\chi_j\rangle\right)\ b_j = 0, \tag{9}$$

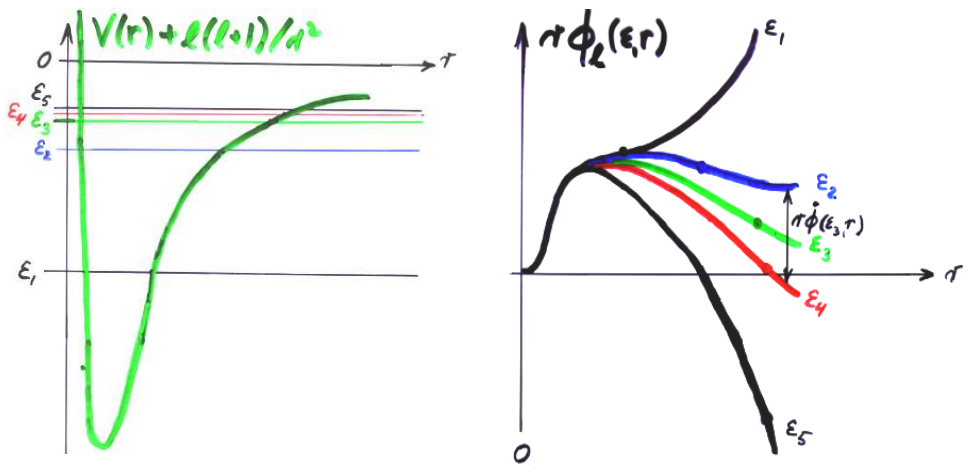

Fig. 2: *Radial potential (green) and energies (colored) together with the corresponding radial wave functions. The latter curve towards the r-axis in the classically allowed r-regions and away from the axis in the classically forbidden regions (schematic).*

for all $\bar{j}$, in terms of Hamiltonian and overlap matrices, $H = \langle\chi\,|\mathcal{H}|\,\chi\rangle$ and $O = \langle\chi|\chi\rangle$. The eigenvalues, ε_i, are variational estimates of the one-electron energies, and the eigenvectors, $b_{j,i}$, give the wave functions $\Psi_i(\mathbf{r})$.
The idea is now to construct the basis set in such a way that for the approximate model potential (3), the set solves Schrödinger's equation exactly to linear order in the deviation of the eigenvalue from an energy, ϵ_ν, chosen at the center of interest, i.e. such that the error is

$$\Psi_i(\mathbf{r}) - \Psi_i(\varepsilon_i, \mathbf{r}) \propto (\varepsilon_i - \epsilon_\nu)^2 .$$

By virtue of the variational principle, the errors of the eigenvalues will then be of order $(\varepsilon_i - \epsilon_\nu)^4$.
Imagine what such linear basis functions must look like if we choose them as atom-centered orbitals, $\chi_{Rlm}(\mathbf{r}_R)$: In order that the linear combination (8) be able to provide the correct eigenfunctions (5) for a spectrum of eigenvalues, ε_i, near ϵ_ν, the *tails* of the orbitals entering a particular cell (R) must, when expanded in spherical harmonics around $\mathbf{R}$, have radial parts which are *energy-derivative functions*, $\dot{\varphi}_{Rl}(\epsilon_\nu, r_R) \equiv \partial\varphi_{Rl}(\varepsilon, r_R)/\partial\varepsilon|_{\epsilon_\nu}$, because then, the sum of the tails added to the head of the orbital will be able to yield the result

$$\varphi_{Rl}(\epsilon_\nu, r_R) + (\varepsilon_i - \epsilon_\nu)\,\dot{\varphi}_{Rl}(\epsilon_\nu, r_R) = \varphi_{Rl}(\varepsilon_i, r_R) + O\left((\varepsilon_i - \epsilon_\nu)^2\right). \tag{10}$$

Hence, the radial shape of a *head* must be $\varphi_{Rl}(\epsilon_\nu, r_R)$, plus maybe a bit of $\dot{\varphi}_{Rl}(\epsilon_\nu, r_R)$.
The condition that the spherical-harmonics expansion of the tail around site R have the radial behavior $\dot{\varphi}_{Rl}(\epsilon_\nu, r_R)$ for all lm and all R, might seem to determine the shape of the orbital completely and not even allow it to be smooth, but merely continuous. However, adding φ to $\dot{\varphi}$

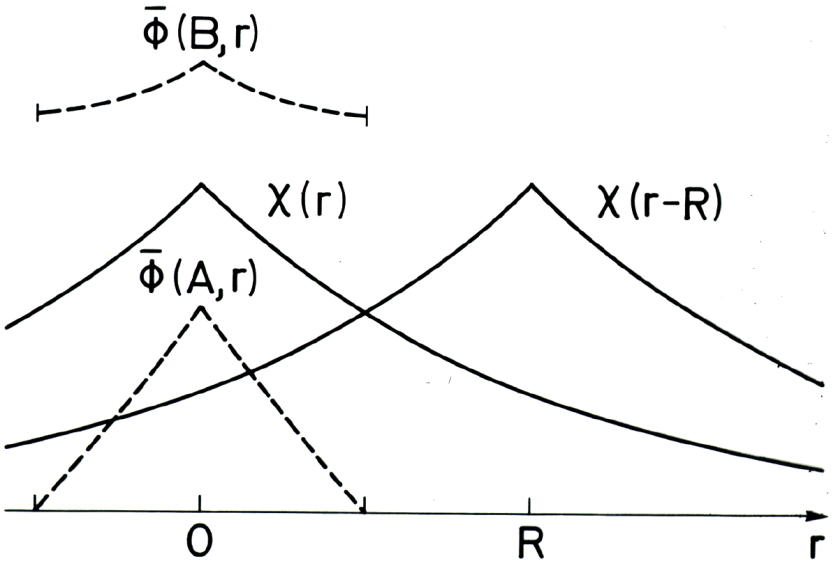

Fig. 3: *Partial waves for the bonding and antibonding states on the central site of a diatomic molecule and the LMTOs on the two sites (schematic). From Ref. [26].*

yields another $\dot{\varphi}$, corresponding to a different energy-dependent normalization, e.g.

$$\partial\left[1+\left(\varepsilon-\epsilon_\nu\right)o\right]\varphi\left(\varepsilon,r\right)/\partial\varepsilon\big|_{\epsilon_\nu}=\dot{\varphi}\left(\epsilon_\nu,r\right)+o\varphi\left(\epsilon_\nu,r\right).$$

Hence, $\dot{\varphi}_{Rl}\left(\epsilon_\nu,r\right)$ can be adjusted to have, say, a required value and slope at some radius, a_R, where a linear combination of $\dot{\varphi}_{Rl}\left(\epsilon_\nu,r_R\right)Y_{lm}\left(\hat{\mathbf{r}}_R\right)$ functions can then be matched smoothly onto any given orbital shape.

Fig. 3 illustrates that in order to describe the bonding $\varphi\left(\varepsilon_B,r\right)$ and antibonding $\varphi\left(\varepsilon_A,r\right)$ states for a diatomic molecule with energy-independent orbitals (LMTOs), those orbitals must have heads proportional to $\varphi_l\left(\varepsilon_B,r\right)+\varphi_l\left(\varepsilon_A,r\right)$ and tails proportional to $\varphi_l\left(\varepsilon_B,r\right)-\varphi_l\left(\varepsilon_A,r\right)$. Now, the overbars on the partial waves in the figure indicate that particular normalizations have been chosen. Had we renormalized say $\varphi_l\left(\varepsilon_A,r\right)$ to $o\varphi_l\left(\varepsilon_A,r\right)$, the shapes of the heads and tails of the orbitals would have changed.

More practical than matching the partial waves at the cell boundaries, is therefore to embed the partial waves in a set of *envelope functions* or, from the point of view of the latter, to *augment* the envelope functions with partial waves. In order that the one-center expansions (5) converge in l, the envelope functions must be such that they match $\varphi_{Rl}\left(\varepsilon,r_R\right)$ for high l, whereby augmentation of the high-l waves becomes unnecessary, as long as they are taken into account as the high-l part of the envelopes. As l increases, the centrifugal term of the radial Schrödinger equation (6) drives $\varphi_{Rl}\left(\varepsilon,r\right)$ outwards such that eventually only the outermost, flat part of the potential is being felt. At that point,

$$\varphi_{Rl}\left(\varepsilon,r\right)\rightarrow j_l\left(r\kappa_R\right)\rightarrow const.\times r^l,\quad\text{where}\quad\kappa_R^2\equiv\varepsilon-v_R\left(s_R\right). \tag{11}$$

Acceptable envelope functions are therefore decaying solutions of the wave equation:

$$\left[\bigtriangledown^2+\kappa^2\right]h_l\left(\kappa r\right)Y_{lm}\left(\hat{\mathbf{r}}\right)=0,\quad\text{with energies}\quad\kappa^2\sim\varepsilon, \tag{12}$$

and potential zero taken as the average between the atoms. These spherical waves may be linear combined into short-ranged, so-called *screened spherical waves* (SSWs). What makes the orbitals spread out are thus the requirements (*a*) that the orbitals be smooth in all space (hermeticity), (*b*) that partial waves with high l should be treated as tails from low-l orbitals at neighboring sites, and (*c*) that the basis set should span a range of energies. The two latter requirements are to some extent flexible: (*b*) is a choice of how many partial waves to *downfold*, the rest having to be kept as (active) orbitals, and (*c*) is a choice of linearization or N*-ization* of the energy dependence of the partial waves. Finally, it should be noted that any delocalization is enhanced by orthogonalization. But all of this should become clear in the following sections.
For all kinds of augmented basis sets, the model potential (3) defining the basis functions is a *superposition* of *spherically symmetric potential wells,* but their range, s_R, varies. LAPWs and LMTOs used in full-potential calculations employ muffin-tin potentials with non-overlapping spheres. Empty spheres –i.e. without nuclei– are included at interstitial sites for open structures. Owing to the sizeable interstitial region ($\sim 0.3\Omega$) and strong discontinuities of the potential at the spheres, such a MT-potential remains a bad approximation to the full potential, whose matrix elements must therefore be included in the Hamiltonian. Nevertheless, such a basis is not optimal and –whenever possible– one uses space-filling potential spheres with a positive radial overlap,

$$\omega^s_{R\bar{R}} \equiv \frac{s_R + s_{\bar{R}}}{\left|\mathbf{R} - \bar{\mathbf{R}}\right|} - 1, \tag{13}$$

not exceeding 20%, and usually neglects the associated errors. For comparison, the overlaps of the WS spheres in face-centered and body-centered cubic packings are respectively 11 and 14%. Nevertheless, if as in the LMTO-ASA method only the ASA potential is included in the one-electron Hamiltonian, the results are too dependent on the choice of sphere radii.
Since distances between close-packed spheres are small compared with the shortest wavelength $2\pi/\kappa_F$ of the valence electrons, the κ^2 dependence of the spherical waves (12) is of far less importance [27] than that of the ε dependence of the logarithmic derivatives (7). For that reason LMTOs of the 1st [22, 3] and 2nd [4] generations used $\kappa^2{\equiv}0$, thus simplifying the decaying Hankel functions to multipole potentials $\propto r^{-l-1}$, which got screened in the 2nd generation. With $\kappa{\equiv}0$ and the ASA, the WS rules for the energies of the band edges in an elementary close-packed solid could be generalized to the unhybridized band structures, $\varepsilon_{li}(\mathbf{k}) = fct(D_l)$, the so-called canonical bands [22, 3, 23, 24, 26, 28].
For the exact, energy-dependent MTOs (EMTOs) [20] with $\kappa^2{=}\varepsilon$, which we shall consider in the following section, the *overlap errors* turn out to be merely of 2nd order in the potential overlap [14] and, as a consequence, EMTOs can handle up to 50% overlap. The overlapping MT approximation (OMTA) is a least-squares fit to the full potential [14, 15] so that the MT discontinuities decrease with increasing overlap.
With EMTOs, also *downfolding* works perfectly [20], which was not the case with the old LMTOs [29]. However, with increasing downfolding, the range of the EMTOs and herewith their energy dependence increases. So it became necessary to construct not only energy-independent linear basis sets, but also basis sets of *arbitrary order* without increasing the size of the set.

Specifically, for a mesh of $N+1$ energies, $\epsilon_0, ..., \epsilon_N$, a basis set of Nth order will span the solutions of Schrödinger's equation for the model potential with the error

$$\Psi_i(\mathbf{r}) - \Psi_i(\varepsilon_i, \mathbf{r}) \propto (\varepsilon_i - \epsilon_0)(\varepsilon_i - \epsilon_1)...(\varepsilon_i - \epsilon_N). \tag{14}$$

These are the so-called NMTO and NAPW basis sets, of which we shall consider the former.

2.1 Crystals

In the above, R runs over all spheres in the system. If it is a crystal with translations $\mathbf{t}$, the wave functions and the basis functions can be chosen to translate according to: $\Psi(\mathbf{r}+\mathbf{t}) = \Psi(\mathbf{r})\exp(i\mathbf{k}\cdot\mathbf{t})$.
Orbitals can then be Bloch-summed:

$$\chi_{Rlm}(\mathbf{k};\mathbf{r}) \equiv \sum\nolimits_{\mathbf{t}} \chi_{Rlm}(\mathbf{r}_R - \mathbf{t})\exp(i\mathbf{k}\cdot\mathbf{t}),$$

where R now labels the atoms in the primitive cell. Rather than normalizing the Bloch sums over the entire crystal, we have normalized them in the primitive cell. Accordingly, $\sum_{\mathbf{k}}$ must be taken as the average, rather than the sum, over the Brillouin zone. Matrices like the Hamiltonian are translationally invariant, $\langle\chi_{\bar{R}\bar{l}\bar{m}}(\mathbf{r}_{\bar{R}})|\mathcal{H}|\chi_{Rlm}(\mathbf{r}_R-\mathbf{t})\rangle = \langle\chi_{\bar{R}\bar{l}\bar{m}}(\mathbf{r}_{\bar{R}}+\mathbf{t})|\mathcal{H}|\chi_{Rlm}(\mathbf{r}_R)\rangle$, and as a consequence,

$$\langle\chi_{\bar{R}\bar{l}\bar{m}}(\mathbf{k};\mathbf{r})|\mathcal{H}|\chi_{Rlm}(\mathbf{k};\mathbf{r})\rangle \equiv \sum\nolimits_{\mathbf{t}} \langle\chi_{\bar{R}\bar{l}\bar{m}}(\mathbf{r}_{\bar{R}})|\mathcal{H}|\chi_{Rlm}(\mathbf{r}_R-\mathbf{t})\rangle\exp(i\mathbf{k}\cdot\mathbf{t}).$$

Numerical calculations are often carried out in the $\mathbf{k}$-representation, but since it is trivial to add $\mathbf{k}$ and limit R to the sites in the primitive cell, in formalisms for orbitals it is simpler and more general to use the real-space representation.

3 EMTOs

In this section we define the set of EMTOs (KPWs) [20,21] and use them to derive the screened KKR equations (21). We first explain what the EMTOs are, starting with their envelope functions, and only thereafter, in Sect. 3.3, how to construct them.
Since EMTOs use *overlapping* MT-potentials for their definition, allow arbitrary downfoldings, enabling the construction of *truly* minimal sets [16], and are usually *localized*, their definition is tricky:

3.1 SSWs

The members, $h^{\alpha}_{\bar{R}\bar{l}\bar{m}}(\varepsilon, \mathbf{r}_R)$, of the set of envelope functions, $|h^{\alpha}(\varepsilon)\rangle$, are superpositions of the decaying spherical waves in Eq. (12), at all active sites R and with all active lm, but with the same energy, $\kappa^2{=}\varepsilon$. The *set* of SSW envelopes are thus:

$$|h^{\alpha}(\varepsilon)\rangle = |h(\varepsilon)\rangle M^{\alpha}(\varepsilon), \tag{15}$$

with a notation in which a set of functions is considered a row-vector: $|h(\varepsilon)\rangle$, for instance, has the elements $h_l(\kappa r_R)\,Y_{lm}(\hat{\mathbf{r}}_R) \equiv h_{Rlm}(\varepsilon,\mathbf{r})$ and $M^\alpha(\varepsilon)$ is a matrix with elements $M^\alpha_{Rlm,\bar{R}\bar{l}\bar{m}}(\varepsilon)$. The set of SSWs (15) is characterized by (*a*) the set of $\bar{R}\bar{l}\bar{m}$ values to be included in the set, the *active* values, (*b*) a set of non-overlapping screening spheres, so-called *hard-spheres,* with radii a_R for the active sites, and (*c*) the *phase shifts* $\eta_{Rl}(\varepsilon)$ of the MT potential for the remaining –the *passive*– Rlm values. With such a partition into active and passive channels, a choice of hard spheres for the former, and the phase shifts for the latter, we can state the *boundary condition* to be satisfied for a member, $h^\alpha_{\bar{R}\bar{l}\bar{m}}(\varepsilon,\mathbf{r}_R)$, of the set:
Its spherical-harmonics projections,

$$\mathcal{P}^a_{Rlm} \equiv \int d^3r\,\delta(a_R - r_R)\,Y^*_{lm}(\hat{\mathbf{r}}_R)\,, \tag{16}$$

onto the hard spheres must *vanish* for all active Rlm values, except for the *own* value, $\bar{R}\bar{l}\bar{m}$, for which we choose to normalize the hard-sphere projection to 1. For the the passive Rlm values, the projection $\mathcal{P}^r_{Rlm}h^\alpha_{\bar{R}\bar{l}\bar{m}}(\varepsilon,\mathbf{r}_{\bar{R}})$ should be a spherical wave phase shifted by $\eta_{Rl}(\varepsilon)$. As discussed in connection with Eq. (12), this holds automatically for all partial waves with $l > 1-3$ because their phase shifts vanish.
With this boundary condition satisfied, the passive channels can be *augmented smoothly* with the appropriate Schrödinger solutions, $\varphi_{Rl}(\varepsilon,r_R)$, and the active channels, which usually diverge at the origin of r_R, can be *truncated* inside the hard spheres, i.e. for $r_R < a_R$. This truncation of the active channels of $h^\alpha_{\bar{R}\bar{l}\bar{m}}(\varepsilon,\mathbf{r}_{\bar{R}})$ is continuous for $Rlm \neq \bar{R}\bar{l}\bar{m}$, but jumps by 1 in the own channel. In all active channels there is a discontinuity of outwards *slope,*

$$\frac{\partial}{\partial r}\mathcal{P}^r_{Rlm}h^a_{\bar{R}\bar{l}\bar{m}}(\varepsilon,\mathbf{r}_{\bar{R}})\bigg|_{a_R} \equiv S^a_{Rlm,\bar{R}\bar{l}\bar{m}}(\varepsilon)\,, \tag{17}$$

(for the own channel, the derivative should be taken slightly *outside* the sphere), specified by a *slope matrix* whose calculation we shall explain in the section 3.3.

3.2 KPWs

The resulting augmented, truncated, and renormalized SSW, usually denoted $\psi^a_{\bar{R}\bar{l}\bar{m}}(\varepsilon,\mathbf{r}_{\bar{R}})$, is now ready to have the hole in its own channel (head) filled: The radial filling function is obtained by integrating the radial $\bar{R}\bar{l}$ equation (6) outwards from 0 to $s_{\bar{R}}$ with the proper potential, and from there, smoothly inwards to $a_{\bar{R}}$ with the flat (zero) potential. The solution, $\bar{\varphi}_{\bar{R}\bar{l}}(\varepsilon,r)$, for the flat potential, and of course the one, $\varphi_{\bar{R}\bar{l}}(\varepsilon,r)$, for the proper potential, are subsequently normalized such that the value of the former is 1 at $a_{\bar{R}}$. This, we indicate by a superscript a :

$$\varphi^a_{\bar{R}\bar{l}}(\varepsilon,r) \equiv \varphi_{\bar{R}\bar{l}}(\varepsilon,r)\,/\bar{\varphi}_{\bar{R}\bar{l}}(\varepsilon,a_{\bar{R}})\,,\quad \bar{\varphi}^a_{\bar{R}\bar{l}}(\varepsilon,r) \equiv \bar{\varphi}_{\bar{R}\bar{l}}(\varepsilon,r)\,/\bar{\varphi}_{\bar{R}\bar{l}}(\varepsilon,a_{\bar{R}})\,. \tag{18}$$

Finally, $\bar{\varphi}^a_{\bar{R}\bar{l}}(\varepsilon,r)$ is matched continuously, but with a kink to $\psi^a_{\bar{R}\bar{l}\bar{m}}(\varepsilon,\mathbf{r}_{\bar{R}})$, and it is truncated outside the interval $a_{\bar{R}} \le r \le s_{\bar{R}}$. The Schrödinger solution, $\varphi_{\bar{R}\bar{l}}(\varepsilon,r)$, is truncated outside the interval $0 \le r \le s_{\bar{R}}$. Hence, the resulting radial function has been constructed like an

accordion: It starts from the origin as the regular Schrödinger solution which extends all the way out to the radius, $s_{\bar{R}}$, of the potential well. Here, it is matched smoothly to a phase-shifted wave, which then runs inwards to the radius, $a_{\bar{R}}$, of the hard sphere where it matches the SSW wave with a kink. Finally, the SSW continues outwards. The active channels of the SSW are truncated inside all hard spheres with kinks, and the passive channels are substituted smoothly inside all hard spheres with regular Schrödinger solutions. This is illustrated in Fig. 4.
The EMTO, also called the *kinked partial wave* (KPW) is now:

$$\phi^a_{\bar{R}\bar{l}\bar{m}}(\varepsilon, r_{\bar{R}}) = \left[\varphi^a_{\bar{R}\bar{l}}(\varepsilon, r_{\bar{R}}) - \bar{\varphi}^a_{\bar{R}\bar{l}}(\varepsilon, r_R)\right] Y_{\bar{l}\bar{m}}(\hat{\mathbf{r}}_{\bar{R}}) + \psi^a_{\bar{R}\bar{l}\bar{m}}(\varepsilon, \mathbf{r}_{\bar{R}}). \quad \blacktriangleleft \tag{19}$$

Here, the first term is the product of a spherical harmonic times a radial function, which vanishes smoothly at, and outside the own potential-sphere $(s_{\bar{R}})$. The second term is the augmented and truncated SSW, which matches onto the first, pure-angular-momentum term at the central hard sphere with a kink of size $S^a_{\bar{R}\bar{l}\bar{m},\bar{R}\bar{l}\bar{m}}(\varepsilon) - \bar{\varphi}^a_{\bar{R}\bar{l}}(\varepsilon, a_{\bar{R}})'$. Although the KPW is everywhere continuous, it has kinks at the hard spheres in all active channels, but is smooth in the passive channels.
We can now try to make a *linear combination*,

$$\sum\nolimits^A_{Rlm} \phi^a_{Rlm}(\varepsilon_i, r_R)\, c^a_{Rlm,i}, \tag{20}$$

of active (A) KPWs which is *smooth.* This requires that its coefficients satisfy the *kink-cancellation condition,*

$$\sum\nolimits^A_{\bar{R}\bar{l}\bar{m}} K^a_{Rlm,\bar{R}\bar{l}\bar{m}}(\varepsilon)\, c^a_{\bar{R}\bar{l}\bar{m}} = 0, \tag{21}$$

for each Rlm. Here we have multiplied each Rlm-equation by a_R^2 such that

$$K^a_{Rlm,\bar{R}\bar{l}\bar{m}}(\varepsilon) \equiv a_R^2 S^a_{Rlm,\bar{R}\bar{l}\bar{m}}(\varepsilon) - a_R D\left\{\bar{\varphi}^a_{Rl}(\varepsilon, a_R)\right\} \delta_{R\bar{R}}\delta_{l\bar{l}}\delta_{m\bar{m}}. \quad \blacktriangleleft \tag{22}$$

becomes a *Hermitian* matrix. Since the passive channels are smooth by construction, Eqs. (21) must be solved only for the active channels and therefore constitute a set of homogeneous, linear equations. These have a proper solution for those energies, ε_i, which make the determinant of the matrix vanish. Most importantly, the corresponding linear combination is a *solution of Schrödinger's equation* at energy ε_i for the overlapping MT potential to 1st order in the overlap. That this is true, can be seen from the following arguments: The kinks of a KPW are always between two solutions of the same radial wave equation, either partial-wave projections of SSWs, zero, or inwards integrated phase-shifted waves. Since only two linearly independent radial solutions exist, e.g. Bessel and Neumann functions, it follows that if they match without a kink at a_R, as they are required to do for the smooth linear combination of KPWs, then they must be *identical in the entire range* $a_R \le r \le s_R$. This means that throughout the MT-sphere at $\bar{R}$,

$$\sum_{Rlm}^{A} \psi^a_{Rlm}(\varepsilon_i, \mathbf{r}_{\bar{R}})\, c^a_{Rlm,i} = \sum_{\bar{l}\bar{m}}^{A} \bar{\varphi}^a_{\bar{R}\bar{l}}(\varepsilon_i, r_R)\, Y_{\bar{l}\bar{m}}(\hat{\mathbf{r}}_{\bar{R}})\, c^a_{\bar{R}\bar{l}\bar{m},i} + \sum_{\bar{l}\bar{m}}^{P} \varphi^a_{\bar{R}\bar{l}}(\varepsilon_i, r_R)\, Y_{\bar{l}\bar{m}}(\hat{\mathbf{r}}_{\bar{R}})\, c^a_{\bar{R}\bar{l}\bar{m},i}.$$

Here, the last term comes from the passive (P) channels and the corresponding coefficients, $c^a_{P,i}$ are given by the solutions, $c^a_{A,i}$, of (21), times PA expansion coefficients. If site $\bar{R}$ is passive

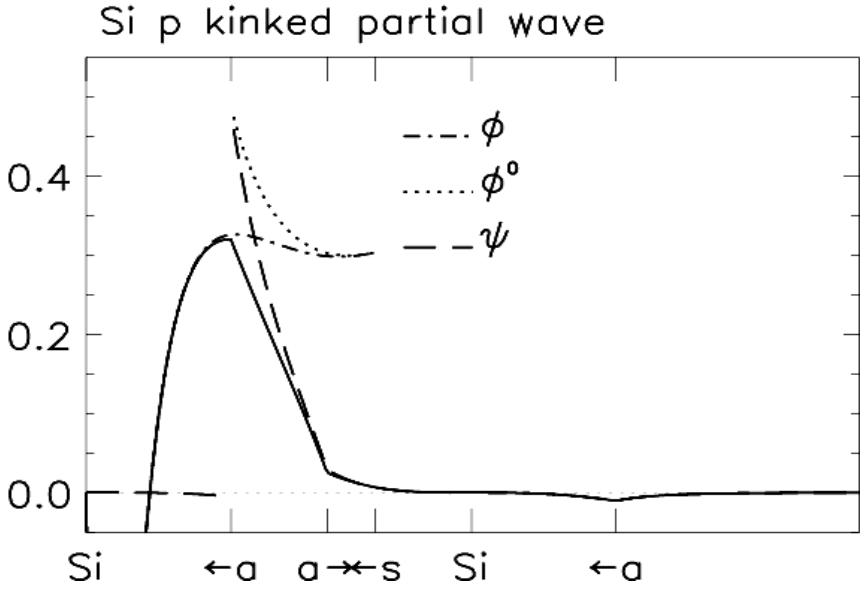

Fig. 4: *Si p_{111} KPW (full) and its constituents: the SSW $\psi_{p_{111}}(\epsilon_0, \mathbf{r})$ (dashed), the partial wave $\varphi^a_p(\epsilon_0, r)\, Y_{p_{111}}(111)$ labelled ϕ (dot-dashed) for the MT potential, and $\bar{\varphi}^a_p(\epsilon_0, r)\, Y_{p_{111}}(111)$ labelled ϕ^0 (dotted) for the flat potential. The plot is along the [111]-line from the central Si atom to its nearest neighbor, and from here into the large voids in the diamond structure. The latter were not described by empty-sphere potentials and, as a consequence, the MT overlap ω^s was as large as 50%; see definition (13). The overlap, ω^a, of the hard screening spheres was -25%. Kink are seen at the central and nearest-neighbor a-spheres. This KPW is the member of the 9 orbital/atom set of Si s, p, and d KPWs, so that the partial waves with $l > 2$ were downfolded into the SSWs. This is the reason why ψ does not exactly vanish inside the a-spheres. The value of ψ just outside the own a-sphere is $1 \times Y_{p_{111}}(111) < 1$. The energy of this KPW was chosen slightly above the bottom of the valence band. A 2D plot of this KPW in the $(1\bar{1}0)$-plane may be found in Fig. 5. From Ref. [12].*

(downfolded), only that term is present on the right-hand side. As a result, the smooth linear combination of KPWs reduces to:

$$\sum\nolimits_{Rlm}^{A} \phi^a_{Rlm}(\varepsilon_i, r_R)\, c^a_{Rlm,i} = \sum\nolimits_{\bar{l}\bar{m}}^{A+P} \varphi^a_{\bar{R}\bar{l}}(\varepsilon_i, r_{\bar{R}})\, Y_{\bar{l}\bar{m}}(\hat{\mathbf{r}}_{\bar{R}})\, c^a_{\bar{R}\bar{l}\bar{m},i} + \sum\nolimits_{R\neq\bar{R}}^{A} \sum\nolimits_{lm}^{A} \left[\varphi^a_{Rl}(\varepsilon_i, r_R) - \bar{\varphi}^a_{Rl}(\varepsilon_i, r_R)\right] Y_{lm}(\hat{\mathbf{r}}_R)\, c^a_{Rlm,i}, \tag{23}$$

near site $\bar{R}$. This is a solution of Schrödinger's equation, $\Psi_i(\varepsilon_i, \mathbf{r})$, plus an error consisting of *tongues* from the overlap of the neighboring muffin tins.
Now, the radial part of such a tongue is

$$\frac{1}{2}(s_R - r_R)^2\, v_R(s_R)\, \varphi^a_{Rl}(\varepsilon, s_R),$$

to lowest order in $s_R - r_R$, as may be seen from the radial equation (6). Here, $v_R(s_R)$ is the MT-discontinuity. Operating finally with $\mathcal{H} - \varepsilon_i$ on the smooth linear combination (20), of

which (23) is the expansion around site $\bar{R}$, yields the error:

$$\sum\nolimits_{\bar{R}} v_{\bar{R}}\left(r_{\bar{R}}\right) \sum\nolimits_{R\neq\bar{R}}^{A} \sum\nolimits_{lm}^{A} \left[\varphi_{Rl}^{a}\left(\varepsilon_i, r_R\right) - \bar{\varphi}_{Rl}^{a}\left(\varepsilon_i, r_R\right)\right] Y_{lm}\left(\hat{\mathbf{r}}_R\right) c_{Rlm,i}^{a}$$
$$\sim \frac{1}{2} \sum\nolimits_{R\bar{R}}^{\text{pairs}} v_{\bar{R}}\left(r_{\bar{R}}\right) \left[\left(s_{\bar{R}} - r_{\bar{R}}\right)^2 + \left(s_R - r_R\right)^2\right] v_R\left(s_R\right) \Psi_i\left(\mathbf{r}\right),$$

which is obviously of 2nd order in the potential overlap. Q.E.D.
The set of homogeneous linear equations (21) are the *screened KKR equations,* albeit in radial-derivative gauge (denoted by a Latin superscript, e.g. a) rather than in phase-shift gauge (denoted by the corresponding greek superscript, α). For other uses of screened KKR –or multiple scattering– theory see e.g. Refs. [31] and [32].
Before we use this to derive NMTOs, let us explain how the slope-matrix is computed.

3.3 Structure matrix

The bare Hankel function to be used in the construction (15) of the SSW envelopes, is a spherical harmonics times the radial function,

$$\begin{aligned} \kappa^{l+1}\left[n_l\left(\kappa r\right) - i j_l\left(\kappa r\right)\right] &= \left[\kappa^{l+1} n_l\left(\kappa r\right)\right] - i\kappa^{2l+1}\left[\kappa^{-l} j_l\left(\kappa r\right)\right] \\ &\to - \frac{(2l-1)!!}{r^{l+1}}\left[1 + \frac{\varepsilon r^2}{2(2l-1)}...\right] - i\kappa \frac{\left(\varepsilon r\right)^l}{(2l+1)!!}\left[1 - \frac{\varepsilon r^2}{2(2l+3)}...\right], \end{aligned} \tag{24}$$

for $\varepsilon \to 0$. Here, $(2l+1)!! \equiv (2l+1)(2l-1)\cdot..\cdot 3\cdot 1$ and $(-1)!! \equiv 1$. For $\varepsilon{=}\kappa^2 \leq 0$, this Hankel function is real and decays asymptotically as $e^{-r|\kappa|}/r$. The spherical Neumann and Bessel functions, normalized as respectively $\kappa^{l+1} n_l\left(\kappa r\right)$ and $\kappa^{-l} j_l\left(\kappa r\right)$, are real for all real energies and they are respectively irregular and regular at the origin. For $\varepsilon > 0$, the Hankel function therefore has an imaginary part, which is the solution for the homogeneous problem. The energy region of interest for the valence and low-lying conductions bands is $\varepsilon \sim 0$, and the advantage of using *screened* Hankel functions (15), is that in this region there are no solutions to the homogeneous hard-sphere problem; they start at higher energies. The screened Hankel functions are therefore localized and real.
In order to obtain explicit expressions for the transformation and slope matrices, $M^a\left(\varepsilon\right)$ and $S^a\left(\varepsilon\right)$, we first need to expand a bare spherical wave centered at $\bar{R}$ in spherical harmonics around $R \neq \bar{R}$. Since the wave is regular around R, its expansion is in terms of Bessel functions and is:

$$\begin{aligned} n_{\bar{l}}\left(\kappa r_{\bar{R}}\right) Y_{\bar{l}\bar{m}}\left(\hat{\mathbf{r}}_{\bar{R}}\right) &= \sum_{lm} j_l\left(\kappa r_R\right) Y_{lm}\left(\hat{\mathbf{r}}_R\right) \times \\ &\sum_{l'} 4\pi i^{-\bar{l}+l-l'} C_{\bar{l}\bar{m},lm,l'} \, n_{l'}\left(\kappa\left|\bar{\mathbf{R}} - \mathbf{R}\right|\right) Y_{l'\,m-\bar{m}}^{*}\left(\widehat{\bar{\mathbf{R}} - \mathbf{R}}\right). \end{aligned}$$

Here, $n_{\bar{l}}$ and $n_{l'}$ can be any l-independent linear combination of a Neumann and a Bessel function. For a pure Bessel function, the expansion holds for all r_R, while for an irregular function, it holds for $r_R < \left|\bar{\mathbf{R}} - \mathbf{R}\right| \neq 0$. The l'-summation runs over $\left|l-\bar{l}\right|,\ \left|l-\bar{l}\right|+2,\ ...,\ l+\bar{l}$ whereby

$i^{-\bar{l}+l-l'}$ is real, and $C_{\bar{l}\bar{m},lm,l'} \equiv \int Y_{\bar{l}\bar{m}}(\hat{r}) Y^*_{lm}(\hat{r}) Y_{l'\,m-\bar{m}}(\hat{r}) d\hat{r}$. Now, since we shall renormalize the Bessel and Neumann functions when changing to radial-derivative gauge, we can start out in phase-shift gauge and use these functions without prefactors which make them real, and for the Hankel function use:

$$\kappa \left[n_l (\kappa r) - i j_l (\kappa r) \right] \equiv h_l^{\alpha=0} (\kappa r) .$$

The conventional bare structure matrix is then

$$B^{\alpha=0}_{Rlm,\bar{R}\bar{l}\bar{m}} (\varepsilon) \equiv \sum_{l'} (-)^{\frac{-\bar{l}+l-l'}{2}} 4\pi C_{\bar{l}\bar{m},lm,l'} h^0_{l'} \left(\kappa \left| \bar{\mathbf{R}} - \mathbf{R} \right| \right) Y^*_{l'\,m-\bar{m}} \left(\widehat{\bar{\mathbf{R}} - \mathbf{R}} \right) \quad \blacktriangleleft \tag{25}$$

and if we define the on-site part of the structure matrix as $B^0_{\bar{R}lm,\bar{R}\bar{l}\bar{m}} (\varepsilon) = -i\kappa \delta_{l\bar{l}} \delta_{m\bar{m}}$, the one-center expansions may be written as:

$$\left| h^0 \right\rangle = |\kappa n\rangle + |j\rangle \, B^0 . \tag{26}$$

Here and in the following we drop the common energy argument.
This screening transformation (15) is now defined by the requirement that the set of screened Hankel functions have one-center expansions formally similar to (26):

$$|h^\alpha\rangle = \left| h^0 \right\rangle M^\alpha = |\kappa n\rangle + |j^\alpha\rangle \, B^\alpha , \tag{27}$$

but with modified radial tail-functions:

$$j^\alpha_{Rlm} (\varepsilon, r) \equiv j_l (\kappa r) - n_l (\kappa r) \tan \alpha_{Rlm} (\varepsilon) . \tag{28}$$

For the active channels, these should vanish at the hard sphere and for the passive channels, they should join onto the proper Schrödinger solutions. Hence, $\alpha_{Rlm} (\varepsilon)$ is the *hard-sphere phase shift* when Rlm is *active* and the *proper phase shift* when Rlm is *passive*, i.e.:

$$\tan \alpha_{Rlm} (\varepsilon) = \frac{j_l (\kappa a_R)}{n_l (\kappa a_R)} \frac{D \left\{ j^\alpha_{Rlm} (\varepsilon, a) \right\} - D \left\{ j_l (\kappa a_R) \right\}}{D \left\{ j^\alpha_{Rlm} (\varepsilon, a) \right\} - D \left\{ n_l (\kappa a_R) \right\}} \tag{29}$$

with

$$D \left\{ j^\alpha_{Rlm} (\varepsilon, a) \right\} \equiv \begin{cases} \infty & Rlm \in A \\ D \left\{ \bar{\varphi}_{Rl} (\varepsilon, a_R) \right\} & Rlm \in P \end{cases} .$$

$\alpha (\varepsilon)$ depends on m, only if the division into active and passive channels is m-dependent. This is the case, say, if one wants to select the Cu $d_{x^2-y^2}$ conduction band in a high-temperature superconducting cuprate [9, 12].
If we now insert Eqs. (28) and (26) in (27) and compare the coefficients of $|\kappa n\rangle$ and $|j\rangle$, we obtain the following expressions for the screening transformation and the screened structure matrix:

$$\begin{aligned} M^\alpha &= 1 - \frac{\tan \alpha}{\kappa} B^\alpha , \\ B^\alpha &= \kappa \cot \alpha - \kappa \cot \alpha \left[B^0 + \kappa \cot \alpha \right]^{-1} \kappa \cot \alpha . \end{aligned} \tag{30}$$

Here, all matrices are square with the high-l blocks neglected (see Eq. (11)) and $\kappa \cot \alpha$ is a diagonal matrix. We see that the amount of lm-multipole charge at site R which screens the $\bar{l}\bar{m}$-multipole at site $\bar{R}$, is $(\tan \alpha_{Rl}/\kappa)\, B^{\alpha}_{Rlm,\bar{R}\bar{l}\bar{m}}$. By taking the radial derivatives at the hard spheres, we can find the desired expression for the slope matrix:

$$a^2 S^a(\varepsilon) = aD\{j(\kappa a)\} + \frac{1}{j(\kappa a)}\left[B^0(\varepsilon) + \kappa \cot \alpha(\varepsilon)\right]^{-1} \frac{1}{j(\kappa a)}. \quad \blacktriangleleft \tag{31}$$

Note that $\kappa \cot \alpha(\varepsilon)$ is real for all real energies and that

$$j(\kappa a)\, \kappa \cot \alpha(\varepsilon)\, j(\kappa a) \rightarrow -\frac{1}{(2l+1)\, a} \frac{D\{j^{\alpha}(\varepsilon, a)\} + l + 1}{D\{j^{\alpha}(\varepsilon, a)\} - l}, \quad \text{for } \varepsilon \rightarrow 0.$$

For most purposes, the hard screening spheres can be taken to depend only on the type of atom, and it turns out that for respectively $spdf$-, spd-, sp-, and s-sets, the shortest range of the spherical waves is obtained for radial overlaps (13) of $\omega^a_{R\bar{R}} =$ –15, –23, –36, and –52%. In the first two cases, the range of the structure matrix is so short that it can be generated by inversion of $B^0(\varepsilon) + \kappa \cot \alpha(\varepsilon)$ in real space, using clusters of 20-100 sites, depending on the hard-sphere packing. Whereas a bare Hankel function has *pure* $\bar{l}\bar{m}$ character, and the bare structure matrix therefore transforms according to the Slater-Koster scheme, the screened structure matrix does *not,* because a screened Hankel function merely has *dominant* $\bar{l}\bar{m}$-character and tends to avoid the surrounding hard spheres.

Downfolding of channels with attractive potentials increases the range and energy dependence of the structure matrix (31). Downfolding is therefore usually performed as a second, **k**-space step, after the strongly screened structure matrix has been generated in real space and subsequently Bloch-summed to **k**-space.

3.4 Example: sp^3 bonded Si

As an example, let us now consider the effects of downfolding on the Si p_{111} member of the spd set of KPWs shown in Fig. 4. This KPW set was for an energy ϵ_0 near the bottom of the valence band. Using also the KPW set for an energy ϵ_1 at the middle of the valence band, plus the one for ϵ_3 near the top of the valence band, an spd NMTO set with $N = 2$ can be formed. How, will be explained in the following section. The p_{111} KPWs at the three energies, the NMTO, and the band structure obtained with the set of nine spd NMTOs per atom are all shown in the left-hand double column of Fig. 5. The middle column shows the same for the sp set, that is the one where also the Si d partial waves are downfolded, and therefore only contains four NMTOs per atom. With 2 atoms per cell, the first set yields 18 bands and the latter 8. Those bands are seen to be identical. In order to describe merely the filled bands, the 4 valence bands, we have to construct a set with merely 4 orbitals per cell and this we do by starting from the symmetry-breaking, completely ionic description $Si^{4-}Si^{4+}$ and put the s and p orbitals on Si^{4-} and *none* on Si^{4+}. That is, all partial waves are downfolded on every second Si atom. The corresponding KPW and NMTO sets are shown in the last column. We see that this NMTO set does give the

valence band only, and that it does so very well. Such a set which picks merely the occupied bands, we call truly minimal [16].
The pictures KPW(E0) show how for the spd set the p_{111} KPW has a kink at its own hard sphere and vanishes inside the neighboring sphere, except for the f and higher partial waves which are allowed to penetrate. Allowing also the d partial waves inside the neighbor has fairly little effect, but allowing all partial waves makes the KPW spill smoothly onto the site. Going now to higher energies, the KPW(E1) and KPW(E2) pictures show how the central kink vanishes as the p radial function bends increasingly toward the axis and how the KPW spreads increasingly around the neighboring hard sphere. Without any confinement in that sphere, the delocalization increases dramatically near the top of the valence band. Nevertheless, the NMTO valence band Wannier orbitals are correct and their sp^3 hybrid shown in Fig. 6 is the well-known bond orbital, which is as localized as can be. Examples for graphite sp^2 σ-bonds, as well as for p_z π-bonds and anti-bonds, may be found in Ref. [16].

4 NMTOs

Finally, we have come to construct energy-*in*dependent orbitals [10]. Specifically, we want to make a superposition of the set of KPWs (19), evaluated at a mesh of energies, $\epsilon_0, .., \epsilon_N$, such that the resulting set of NMTOs,

$$\left|\chi^{(0..N)}\right\rangle = \sum\nolimits_{n=0}^{N} \left|\phi\left(\epsilon_n\right)\right\rangle L_n^{(0..N)} = \tag{32}$$
$$\left|\phi\left[0\right]\right\rangle + \left|\phi\left[01\right]\right\rangle \left(E^{(0..N)} - \epsilon_0\right) + \ . \ + \left|\phi\left[0..N\right]\right\rangle \left(E^{(N-1,N)} - \epsilon_{N-1}\right) . \left(E^{(0..N)} - \epsilon_0\right), \ \blacktriangleleft$$

spans the solutions of Schrödinger's equation for the model potential to within an error given by Eq. (14). This is *discrete polynomial approximation* for a *Hilbert space,* and $L_n^{(0..N)}$ are Lagrangian matrices, whose sum is the unit matrix. For $N = 0$, the NMTO set is the set of EMTOs evaluated at the energy $\epsilon_0 \equiv \epsilon_\nu$. The second, rearranged series is the ascending Newton interpolation formula in terms of divided differences, e.g. $\phi\left[0\right] \equiv \phi\left(\epsilon_0\right)$ and $\phi\left[01\right] \equiv \frac{\phi(\epsilon_0)-\phi(\epsilon_1)}{\epsilon_0-\epsilon_1}$. In general, they are defined by:

$$\phi\left[0..N\right] \equiv \sum_{n=0}^{N} \frac{\phi\left(\epsilon_n\right)}{\prod_{m=0,\neq n}^{N}\left(\epsilon_n - \epsilon_m\right)}. \tag{33}$$

Moreover, $\left(E^{(N-1,N)} - \epsilon_{N-1}\right) . \left(E^{(0..N)} - \epsilon_0\right)$ is a product of N energy *matrices,* which are generally not Hermitian and do not commute. The NMTO is independent of the order of the energy points, but the individual terms in the Newton series are not, and only when the energies are ordered according to size does this series have a clear interpretation. If the energy mesh condenses onto ϵ_ν, then $\phi\left[0..N\right] \rightarrow \overset{(N)}{\phi}\left(\epsilon_\nu\right)/N!$ and the Newton series becomes a truncated Taylor series. In order to be able to pick bands which overlap other bands, it is necessary to put the energies where only active bands are present. With only one energy point at disposal, there is little flexibility, so the Taylor series is not practical.

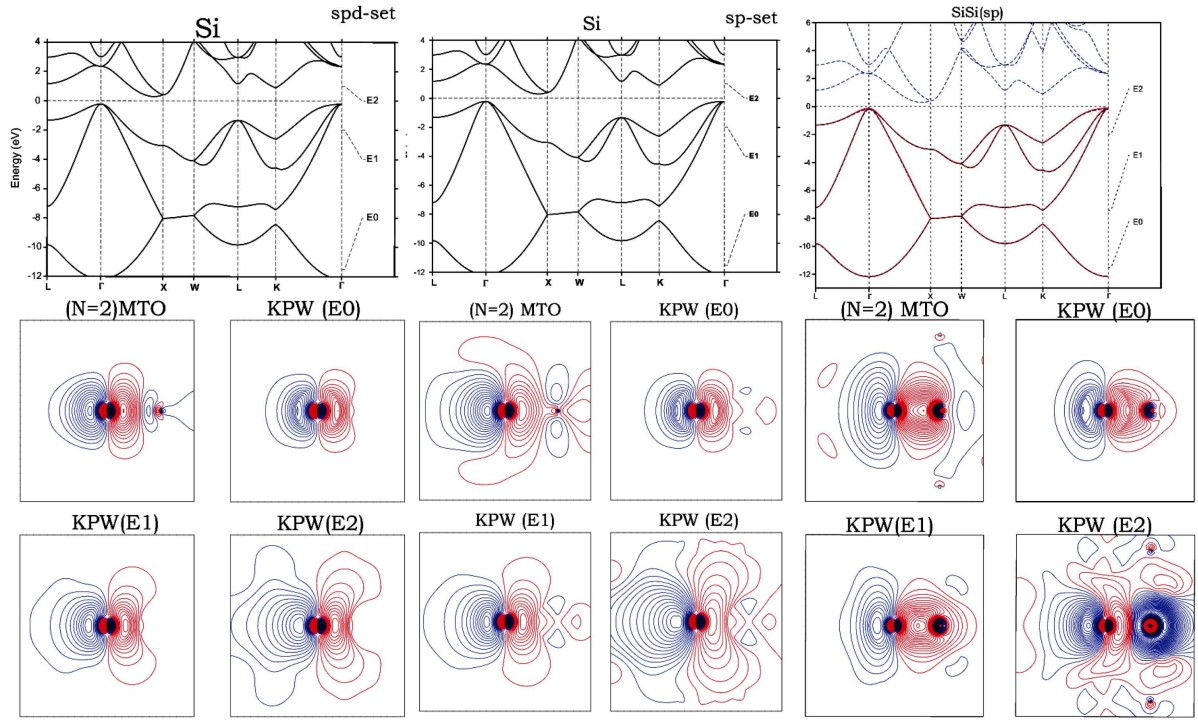

Fig. 5: *Band structure of Si obtained with* $(N{=}2)$*MTO sets of increasing downfolding. The first set contains the 9* s, p, *and* d N*MTOs per atom, the second the 4* s *and* p N*MTOs per atom, and the last merely the* s *and* p N*MTOs on every second atom. The Si* p_{111} *members of the corresponding* N*MTO sets, as well as of the constituting KPW sets at the three energies,* ϵ_0, ϵ_1, *and* ϵ_2, *indicated to the right of the band structures, are shown in the* $(1\bar{1}0)$ *plane containing a Si and its nearest neighbor along* $[111]$. *The* N*MTO bands are red and the exact ones blue. For the first two sets, no difference can be seen. The last set is seen to give merely the valence bands, and that very well. After orthonormalization, this* N*MTO set is thus a set of Wannier functions for the valence band. By being placed only on every second atom, this* N*MTO set breaks the symmetry, but does spills onto the other atoms correctly because the* sp^3 *hybrid of the orthonormalized* N*MTOs yields the well-known, symmetric bond orbital shown in Fig. 6. Hence, by starting from the ionic* $Si^{4-}Si^{4+}$ *picture, which gets the electron count right, the* N*MTO method creates the correct covalency. From Ref. [12]*

We have dropped all superscripts a because, from now on they do not change; screening and downfolding is done at the level of forming the EMTOs. Note that, in contrast to LMTO sets of the 2nd generation [4], NMTO sets for different screenings span different Hilbert spaces; the factor in front of the error term (14) depends on $s - a$ [10]. It is obvious that for N given, the error must increase with the degree of downfolding, because downfolding decreases the size of the basis set. This, on the other hand, makes it necessary to go beyond *linear* basis sets if one wants to generate truly minimal basis sets picking merely the *occupied* bands (see Fig. 6).

NMTOs can be used to generate Wannier functions directly, because with an appropriate choice of active channels, one can generate an NMTO set for the isolated set of bands in question. Upon making the mesh finer, the NMTO set will converge to the proper Hilbert space spanned by any set of Wannier functions. After orthonormalization, the NMTO set will therefore *be* a set

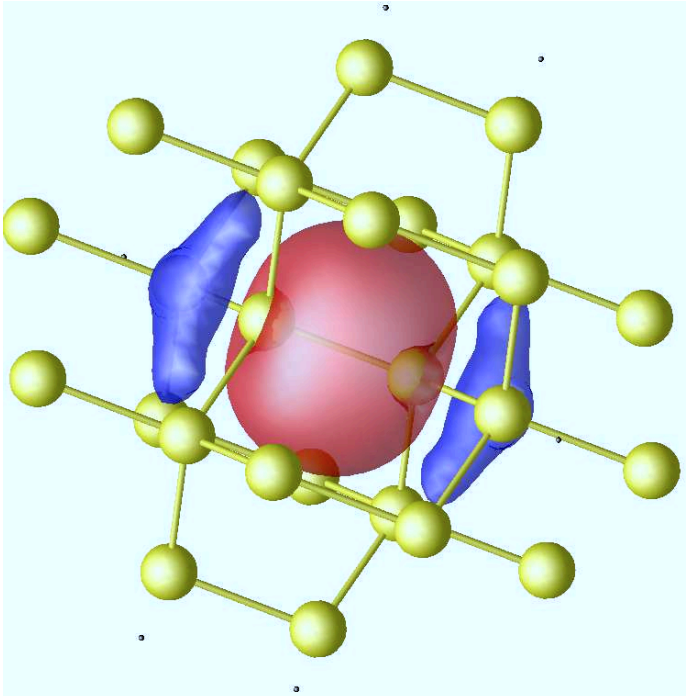

Fig. 6: *Si sp^3 bond orbital computed as the sp^3 directed orbital from the set of s and p NMTOs on every second atom. See Fig. 5. In order that no asymmetry of the bond orbital could be seen, it was necessary to use $N = 6$. (Courtesy A. Alam).*

of Wannier functions. NMTOs are localized *a priory* by virtue of the hard-sphere confinement of the constituent EMTOs, and since NMTOs are not orthonormal, they can –but must not– be more localized than maximally localized Wannier functions.

We shall now see that the Lagrangian matrices as well as the Hamiltonian and overlap matrices for the model potential, are all expressed solely in terms of the kink- or KKR matrix (22) and its first energy derivative matrix evaluated at points of the energy mesh. In fact, the NMTO formalism is much simpler if expressed in terms of the Green matrix,

$$G\left(\varepsilon\right) \equiv K\left(\varepsilon\right)^{-1}, \qquad \blacktriangleleft \tag{34}$$

also called the resolvent or scattering path operator [31, 32].

Since a single KPW (19) solves Schrödinger's differential equation for the model potential, except at the kinks, operation with the Hamiltonian gives a series of delta-functions at the hard spheres in the active channels:

$$\left(\varepsilon - \mathcal{H}\right) \phi_{\bar{R}\bar{l}\bar{m}}\left(\varepsilon, \mathbf{r}\right) = \sum_{Rlm}^{A} \delta\left(r_R - a_R\right) Y_{lm}\left(\hat{\mathbf{r}}_R\right) K_{Rlm,\bar{R}\bar{l}\bar{m}}\left(\varepsilon\right). \tag{35}$$

Solving for $\delta\left(r_R - a_R\right) Y_{lm}\left(\hat{\mathbf{r}}_R\right)$, leads to:

$$\delta\left(r_R - a_R\right) Y_{lm}\left(\hat{\mathbf{r}}_R\right) = \left(\varepsilon - \mathcal{H}\right) \sum\nolimits_{\bar{R}\bar{l}\bar{m}}^{A} \phi_{\bar{R}\bar{l}\bar{m}}\left(\varepsilon, \mathbf{r}\right) G_{\bar{R}\bar{l}\bar{m},Rlm}\left(\varepsilon\right) \tag{36}$$

which shows that the linear combinations,

$$\gamma_{Rlm}(\varepsilon,\mathbf{r}) = \sum_{\bar{R}\bar{l}\bar{m}}^{A} \phi_{\bar{R}\bar{l}\bar{m}}(\varepsilon,\mathbf{r})\, G_{\bar{R}\bar{l}\bar{m},Rlm}(\varepsilon)\,, \tag{37}$$

of KPWs –all with the same energy and screening– may be considered a Green function, $G(\varepsilon,\bar{\mathbf{r}},\mathbf{r})$, which has $\bar{\mathbf{r}}$ *confined* to the hard spheres, i.e. $\bar{\mathbf{r}} \to Rlm$. Considered a function of $\mathbf{r}$, this Green function is a solution with energy ε of the Schrödinger equation, except at its own sphere and for its own angular momentum, where it has a kink of size unity. This kink becomes negligible when ε is close to a one-electron energy, because the Green function has a pole there. In Eq. (37), the confined Green function is factorized into a vector of KPWs, $|\phi(\varepsilon)\rangle$, which has the full spatial dependence and a weak energy dependence, and a Green matrix, $G(\varepsilon)$, which has the full energy dependence. Now, we want to factorize the $\mathbf{r}$ and ε-dependences *completely* and, hence, to approximate the confined Green function, $|\phi(\varepsilon)\rangle\, G(\varepsilon)$, by $\left|\chi^{(0..N)}\right\rangle G(\varepsilon)$.
Note that subtracting from the Green function a function which is analytical in energy and remains in the Hilbert space spanned by the set $|\phi(\epsilon_n)\rangle$ produces an equally good Green function, in the sense that both yield the same solutions of Schrödinger's equation. We therefore first define a set $\left|\chi^{(0..N)}(\varepsilon)\right\rangle$ by:

$$|\gamma(\varepsilon)\rangle = |\phi(\varepsilon)\rangle\, G(\varepsilon) \equiv \left|\chi^{(0..N)}(\varepsilon)\right\rangle G(\varepsilon) + \sum_{n=0}^{N} |\phi(\epsilon_n)\rangle\, G(\epsilon_n)\, F_n^{(0..N)}(\varepsilon)\,, \tag{38}$$

and then determine the analytical functions, $F_n^{(0..N)}(\varepsilon)$, in such a way that $\left|\chi^{(0..N)}(\varepsilon)\right\rangle$ takes the *same* value, $\left|\chi^{(0..N)}\right\rangle$, at all mesh points. If that can be done, then

$$\left|\chi^{(0..N)}(\varepsilon)\right\rangle = \left|\chi^{(N)}\right\rangle + O\left((\varepsilon-\epsilon_0)\,..\,(\varepsilon-\epsilon_N)\right),$$

and $\left|\chi^{(0..N)}\right\rangle$ is the set of NMTOs. Now, since

$$\left|\chi^{(0..N)}(\epsilon_0)\right\rangle = .. = \chi^{(0..N)}(\epsilon_N)\,,$$

the Nth divided difference of $\left|\chi^{(0..N)}(\varepsilon)\right\rangle G(\varepsilon)$ equals $\left|\chi^{(0..N)}\right\rangle$ times the Nth divided difference of $G(\varepsilon)$. Moreover, if we let $F_n^{(0..N)}(\varepsilon)$ be a polynomium of (N-1)st degree (Nth degree yields zero-solutions for the NMTOs), their Nth divided difference on the mesh will vanish. As a result

$$|\gamma[0..N]\rangle = (|\phi\rangle\, G)[0..N] = \left|\chi^{(0..N)}\right\rangle G[0..N]\,,$$

and we have therefore found the solution:

$$\left|\chi^{(0..N)}\right\rangle = (|\phi\rangle\, G)[0..N]\; G[0..N]^{-1} \tag{39}$$

for the NMTO set. The divided difference of the product is easily evaluated using (33):

$$(|\phi\rangle\, G)[0..N] = \sum_{n=0}^{N} \frac{|\phi(\epsilon_n)\rangle\, G(\epsilon_n)}{\prod_{m=0,\neq n}^{N}(\epsilon_n-\epsilon_m)},$$

in terms of the values of the KPWs and the Green matrix on the energy mesh. This expression, together with the similar one for $G[0..N]$, are those needed to determine the Lagrange matrices in Eq. (32).

4.1 Smoothness and products of NMTOs

$(N{=}0)$MTOs are of course the *kinked* partial waves at ϵ_0, but $(N{>}0)$MTOs are *smooth* because according to (36), the kinks of $|\gamma(\varepsilon)\rangle$ are independent of ε. This does however not imply that for a single NMTO, the KPW accordion is completely compressed, like for a smooth linear combination of KPWs (20) with the same energy. The linear combinations making up an NMTO have *different* energies and, as a consequence, discontinuities remain in $(2N{+}1)$st radial derivatives at the hard spheres. Projecting an NMTO onto an active channel, leads to a radial function of the type $\varphi(r) - \bar{\varphi}(r) + \mathcal{P}^r\psi(\mathbf{r})$, where $\varphi(r) - \bar{\varphi}(r) \propto (s-r)^2$ near s and

$$\mathcal{P}^r\psi(\mathbf{r}) - \bar{\varphi}(r) \propto (r-a)^{2N+1}(\varepsilon-\epsilon_0)..(\varepsilon-\epsilon_N)$$

near a. Since the latter error is of the same order as (14), it should be included there. This means that *cross-terms* between φ, $\bar{\varphi}$, and $\mathcal{P}^r\psi$ can be *neglected*, and that leads to the following simple prescription for evaluating the *product* of two KPWs with different energies:

$$|\phi\rangle\langle\phi| \;=\; |\varphi Y\rangle\langle Y\varphi| \;-\; |\bar{\varphi}Y\rangle\langle Y\bar{\varphi}| \;+\; |\psi\rangle\langle\psi|\,, \tag{40}$$

occurring in the expression for the product $\left|\chi^{(N)}\right\rangle\left\langle\chi^{(N)}\right|$ of two NMTOs as needed for evaluation of matrix elements and the *charge density.* The sum of the first two terms in (40) is simply a finite sum of spherical harmonics times radial functions which vanish smoothly outside the MT spheres. The third term is more complicated because the SSWs do not have pure lm-character but merely short range. What we know about the SSWs is the structure matrix which specifies the spherical-harmonics expansions of the radial derivatives at the hard spheres. It is therefore practical to *interpolate* a *product* of *strongly* screened spherical waves across the hard-sphere interstitial by a *sum* of SSWs. Specifically, we fit –at all spheres and for all spherical-harmonics with $l \lesssim 6-$ the radial values plus first 3 derivatives of the product (e.g. the charge-density) to those of a sum of SSWs with 4 different energies. The so-called *value-and-derivative functions,* each one vanishing in all channels except its own, are purely structural and exceedingly well localized because the value and first 3 derivatives vanish at all *other* spheres. We are currently writing an efficient self-consistent, full-potential NMTO code using this interpolation technique [17].

In order to figure out how the Hamiltonian operates on an NMTO, we use Eq (35) for $N{=}0$ and obtain: $(\mathcal{H}-\varepsilon_0)\left|\chi^{(0)}\right\rangle = -|\delta\rangle K(\epsilon_0)$. For the smooth NMTOs with $N{>}0$ we can neglect the kink terms when operating on (38), and then take the Nth divided difference to get rid of the polynomials:

$$\mathcal{H}\,|\gamma[0..N]\rangle = |(\varepsilon\gamma(\varepsilon))[0..N]\rangle = |\gamma[0.N-1]\rangle + \epsilon_N\,|\gamma[0..N]\rangle\,. \tag{41}$$

Using the definition (39) of the NMTO we multiply by $G[0..N]^{-1}$ from the right and obtain:

$$(\mathcal{H}-\epsilon_N)\left|\chi^{(0..N)}\right\rangle = |\gamma[0.N-1]\rangle\; G[0..N]^{-1} = \left|\chi^{(0.N-1)}\right\rangle\left(E^{(0..N)}-\epsilon_N\right), \tag{42}$$

where $\left|\chi^{(0.N-1)}\right\rangle$ is the set obtained by omitting the last point on the mesh and

$$E^{(0..N)} - \epsilon_N \equiv G[0..N-1]\,G[0...N]^{-1}$$

is the coefficient of all but the first term of the descending Newton series analogous to the ascending one in (32). The energy matrices are in general given by:

$$E^{(0..M)} = (\varepsilon G)\,[0..M]\; G\,[0..M]^{-1} \tag{43}$$

Expression (42) shows that increasing N increases the smoothness of the NMTOs and also their range, unless $E^{(0..N)}$ converges as is the case for a set of isolated bands. If $E^{(0..N)}$ is converged, so is the NMTO basis, and so is the Newton series. This series expresses the NMTO as a kinked partial wave at the same site and with the same angular momentum, plus a smoothing cloud of energy-derivative functions centered at all sites and with all angular momenta.

4.2 Hamiltonian and overlap matrices

With the aim of obtaining the expressions for the overlap and Hamiltonian matrices needed in a variational calculation (9), we first find expressions involving $|\phi(\varepsilon)\rangle$ and $|\gamma(\varepsilon)\rangle$.
Multiplication of (35) from the left by $\langle\phi(\varepsilon)|$ and using (40), together with the facts that $\bar{\varphi}(\varepsilon, a)$=1, that $\mathcal{P}^a\psi(\varepsilon, \mathbf{r})$=1 in the own channel, 0 in the other active channels, and solves the radial Schrödinger equation in the passive channels, leads to the result:

$$\langle\phi(\varepsilon)\,|\mathcal{H}-\varepsilon|\,\phi(\varepsilon)\rangle = -K(\varepsilon). \qquad \blacktriangleleft \tag{44}$$

Here again we have resorted to matrix notation. The Hamiltonian matrix for the N=0 set is thus

$$\left\langle\chi^{(0)}\,|\mathcal{H}-\epsilon_0|\,\chi^{(0)}\right\rangle = -K(\epsilon_0). \tag{45}$$

In a similar way, and with the use of Green's second theorem, one finds that the overlap matrix between two EMTOs with different energies is:

$$\langle\phi(\bar{\varepsilon})\,|\phi(\varepsilon)\rangle = \frac{K(\bar{\varepsilon})-K(\varepsilon)}{\bar{\varepsilon}-\varepsilon} \to \dot{K}(\varepsilon), \quad \text{for } \bar{\varepsilon}\to\varepsilon. \tag{46}$$

Note that by virtue of the definition of $|\psi\rangle$, there are no 3-center terms here. Hence, the overlap matrix for the N=0 set is simply:

$$\left\langle\chi^{(0)}|\chi^{(0)}\right\rangle = \langle\phi(\epsilon_0)\,|\phi(\epsilon_0)\rangle = \dot{K}(\epsilon_0). \tag{47}$$

From Eqs. (44), (46), and (37) one finds:

$$\langle\gamma(\bar{\varepsilon})\,|\gamma(\varepsilon)\rangle = -\frac{G(\bar{\varepsilon})-G(\varepsilon)}{\bar{\varepsilon}-\varepsilon} \to \dot{G}(\varepsilon) = G(\varepsilon)\,\dot{K}(\varepsilon)\,G(\varepsilon), \text{ for } \bar{\varepsilon}\to\varepsilon. \tag{48}$$

If we now take the Mth divided difference with respect to $\bar{\varepsilon}$ and the Nth with respect to ε, both on the mesh, then use (33) and order such that $M \le N$, we find a double sum. If reordered to a single sum, with due care taken for the terms where $\bar{\varepsilon}$=ε, it reduces to the expression

$$\langle\gamma\,[0..M]\,|\gamma\,[0...N]\rangle = -G\,[[0..M]\,..N], \tag{49}$$

where the right-hand side is minus the highest derivative of that polynomium of degree $M+N+1$ which coincides with $G(\varepsilon)$ at the points $\epsilon_0, ..., \epsilon_N$ *and* has the same first derivatives $\dot{G}(\varepsilon)$ at the points $\epsilon_0, .., \epsilon_M$ (Hermit interpolation) [10]. For the matrix element of the Hamiltonian, expressions (41) and (49) yield:

$$\langle \gamma[0..N] | \mathcal{H} - \epsilon_N | \gamma[0..N] \rangle = \langle \gamma[0..N] | \gamma[0.N-1] \rangle = -G[[0.N-1]N].$$

The NMTO Hamiltonian and overlap matrices are thus given by the following, most elegant expression which involves nothing but the values and first derivatives of the KKR Green matrix, $G(\varepsilon)$, on the energy mesh:

$$G[0..N] \left\langle \chi^{(0..N)} | \mathcal{H} - \varepsilon | \chi^{(0..N)} \right\rangle G[0..N] = -G[[0.N-1]N] + (\varepsilon - \epsilon_N) G[[0..N]], \quad (50)$$

i.e.

$$\left\langle \chi^{(0..N)} | \mathcal{H} - \epsilon_N | \chi^{(0..N)} \right\rangle = -G[0..N]^{-1} \; G[[0.N-1]N] \; G[0..N]^{-1} \; \blacktriangleleft \quad (51)$$

and

$$O^{(0..N)} \equiv \left\langle \chi^{(0..N)} \mid \chi^{(0..N)} \right\rangle = G[0..N]^{-1} \; G[[0..N]] \; G[0..N]^{-1}. \; \blacktriangleleft \quad (52)$$

The variational calculation will give eigenvalues, which for the model potential have errors proportional to $(\varepsilon_i - \epsilon_0)^2 (\varepsilon_i - \epsilon_1)^2 .. (\varepsilon_i - \epsilon_N)^2$.

4.3 Orthonormal NMTOs (Wannier orbitals)

In many cases one would like to work with a set of *orthonormal* NMTOs, e.g. Wannier orbitals, and preserve the Rlm-character of each NMTO. In order to arrive at this, we should – in the language of Löwdin – perform a *symmetrical orthonormalization* of the NMTO set. According to (52), such a representation is obtained by the following transformation:

$$\left| \check{\chi}^{(0..N)} \right\rangle = \left| \chi^{(0..N)} \right\rangle G[0..N] \sqrt{-G[[0..N]]}^{-1} = \left| \chi^{(0..N)} \right\rangle \sqrt{O^{(0..N)}}^{-1}, \; \blacktriangleleft \quad (53)$$

because it yields:

$$\left\langle \check{\chi}^{(0..N)} \mid \check{\chi}^{(0..N)} \right\rangle = -\sqrt{-G[[0..N]]}^{-1\dagger} G[[0...N]] \sqrt{-G[[0..N]]}^{-1} = 1.$$

Note that this means: $-G[[0..N]] = \sqrt{-G[[0..N]]}^{\dagger} \sqrt{-G[[0..N]]}$. In this orthonormal representation, the Hamiltonian matrix becomes:

$$\left\langle \check{\chi}^{(0..N)} | \mathcal{H} - \epsilon_N | \check{\chi}^{(0..N)} \right\rangle = -\sqrt{-G[[0..N]]}^{-1\,\dagger} G[[0.N-1]N] \; \sqrt{-G[[0..N]]}^{-1}. \; \blacktriangleleft \quad (54)$$

To find an efficient way to *compute* the *square root* of the Hermitian, positive definite matrix $-G[[0...N]]$ may be a problem. Of course one may diagonalize the matrix, take the square root of the eigenvalues, and then back-transform, but this is time consuming. Cholesky decomposition is a better alternative, but that usually amounts to staying in the original representation. Löwdin orthogonalization works if the set is nearly orthogonal, because then the overlap matrix is nearly diagonal, and Löwdin's solution was to normalize the matrix such that it becomes 1 along the diagonal and then expand in the off-diagonal part, Δ :

$$\sqrt{1+\Delta}^{-1} \; = \; 1 - \frac{1}{2}\Delta + \frac{3}{8}\Delta^2 - ... \quad (55)$$

This should work for the NMTO overlap matrix (52) when the NMTOs are nearly orthogonal.

4.4 LMTOs

For N=0, we have the results: $\left|\chi^{(0)}\right\rangle = \left|\phi\left(\epsilon_0\right)\right\rangle$, (45), and (47).
For comparison with classical TB-LMTOs [4, 26, 33, 34], now consider the case N=1 with the two-point mesh condensed onto ϵ_ν. From Eq. (43) we find the following energy matrix:

$$E^{(1)} = \epsilon_\nu + G\dot{G}^{-1} = \epsilon_\nu - \dot{K}^{-1}K = \epsilon_\nu + \langle\phi|\phi\rangle^{-1}\left\langle\phi\left|\mathcal{H}-\epsilon_\nu\right|\phi\right\rangle,$$

Here and in the following an omitted energy argument means that ε=ϵ_ν. Insertion in the Taylor series (32), yields:

$$\left|\chi^{(1)}\right\rangle = |\phi\rangle - \left|\dot{\phi}\right\rangle \dot{K}^{-1}K, \tag{56}$$

which shows that the LMTO is smooth and has the form anticipated in Sect. 2. The Hamiltonian and overlap matrices are from Eq. (50):

$$\left\langle\chi^{(1)}\left|\mathcal{H}-\epsilon_\nu\right|\chi^{(1)}\right\rangle = -\dot{G}^{-1}\frac{\ddot{G}}{2!}\dot{G}^{-1} = -K + K\dot{K}^{-1}\frac{\ddot{K}}{2!}\dot{K}^{-1}K,$$

$$\left\langle\chi^{(1)}\mid\chi^{(1)}\right\rangle = -\dot{G}^{-1}\frac{\dddot{G}}{3!}\dot{G}^{-1} = \dot{K} - K\dot{K}^{-1}\frac{\ddot{K}}{2!} - \frac{\ddot{K}}{2!}\dot{K}^{-1}K + K\dot{K}^{-1}\frac{\dddot{K}}{3!}\dot{K}^{-1}K.$$

Had we instead used the Taylor series (56) to compute the overlap matrix, we would of course have obtained the same result and as consequences, $\ddot{K}$=2! $\left\langle\phi|\dot{\phi}\right\rangle$ and $\dddot{K}$=3! $\left\langle\dot{\phi}|\dot{\phi}\right\rangle$. This may also be obtained from the general relation (49). Had we used the Taylor series to compute the Hamiltonian matrix, we would have used Eq. (42) with N=1, to obtain the same result.
In order to make $E^{(1)}$ Hermitian and, hence, to transform it into a 1st-order *Hamiltonian:*

$$\dot{K}^{\frac{1}{2}}E^{(1)}\dot{K}^{-\frac{1}{2}} = \epsilon_\nu - \dot{K}^{-\frac{1}{2}}K\dot{K}^{-\frac{1}{2}} \equiv H^\alpha,$$

one must symmetrically orthonormalize the 0th-order set, which now becomes:

$$\left|\check{\chi}^{(0)}\right\rangle = |\phi\rangle\,\dot{K}^{-\frac{1}{2}} = |\phi\rangle\,\langle\phi|\phi\rangle^{-\frac{1}{2}} \equiv |\phi^\alpha\rangle\,.$$

Here and in the following, the superscript α is the one used in the classical LMTO [4] –not the new NMTO– formalism. After applying the same transformation to the LMTO set (56), it becomes:

$$\left|\chi^{(1)}\right\rangle\dot{K}^{-\frac{1}{2}} = |\phi^\alpha\rangle + \left|\dot{\phi}^\alpha\right\rangle\left(H^\alpha-\epsilon_\nu\right) = |\chi^\alpha\rangle\,, \quad \blacktriangleleft$$

where $\left|\dot{\phi}^\alpha\right\rangle = \left|\dot{\phi}\right\rangle\dot{K}^{-\frac{1}{2}}$. This expression for the LMTO is the one envisaged in expression (10) of Sect. 2: The tail-functions are $\dot{\phi}^\alpha\left(\mathbf{r}\right)$ and the head of the $\bar{R}\bar{l}\bar{m}$-orbital is

$$\phi^\alpha_{\bar{R}\bar{l}\bar{m}}\left(\mathbf{r}_{\bar{R}}\right) + \sum\nolimits_{lm}\dot{\phi}^\alpha_{\bar{R}lm}\left(\mathbf{r}_{\bar{R}}\right)\left(H^\alpha-\epsilon_\nu\right)_{\bar{R}lm,\bar{R}\bar{l}\bar{m}}.$$

In order to show explicitly how the solutions of Schrödinger's equation for the solid can be described through overlap of orbitals, we may simply diagonalize H^α. Naming its eigenvectors and eigenvalues respectively $u_{Rlm,i}$ and ε_i, the linear combination of orbitals given by an eigenvector is:

$$\begin{aligned}|\chi^\alpha\rangle\,u_i &= |\phi^\alpha\rangle\,u_i + \left|\dot{\phi}^\alpha\right\rangle H^\alpha u_i = \left[|\phi^\alpha\rangle + \left|\dot{\phi}^\alpha\right\rangle\left(\varepsilon_i-\epsilon_\nu\right)\right]u_i \\ &= |\phi^\alpha\left(\varepsilon_i\right)\rangle\,u_i + O\left(\left(\varepsilon_i-\epsilon_\nu\right)^2\right),\end{aligned}$$

as anticipated. LMTOs thus naturally describe the way in which the overlap of orbitals leads to broadening of levels into bands. It is however worth pointing out that although this $(N{=}1)$MTO formalism has been brought to the same form as the classical TB-LMTO formalism in the ASA, the $(N{=}1)$MTO formalism employs *no* ASA.

4.5 Example: NiO

The Mott insulator NiO has the NaCl structure so that each Ni is surrounded by an O octahedron and vice versa. In the ionic picture, the configuration is Ni $3d^8$ with the 2 electrons of highest energy in the e_g orbitals. LDA band structures are shown on the left-hand side of Fig. 7 with the corresponding sets of $(N{=}1)$MTO Wannier orbitals on the right-hand side.

Starting from the bottom, we see the 3 O p bands and the 3 congruent Wannier orbitals which span those green bands. No discrepancy can be seen between the green and the highly accurate LAPW bands (black). We remember that, except for the effects of linearization and orthogonalization, which are small in this case of a rather narrow band, this O p_z orbital can have *no* O p character on any other O site. However, it has all other characters downfolded and we see, in particular, $pd\sigma$ bonds to two Ni e_g d_{3z^2-1} orbitals and $pd\pi$ bonds to the four Ni t_{2g} orbitals.

Going now to the 5 Ni d bands seen in the middle panel, we see the corresponding $pd\sigma$ anti-bonds for the Ni e_g orbitals to the appropriate O p orbitals and the corresponding $pd\pi$ anti-bonds for the Ni t_{2g} orbitals. Since $pd\sigma$ hopping is stronger than $pd\pi$, the reddish e_g-like band lies above the blueish t_{2g}-like band, which is full in the LDA. Like for a member of the O p set, the d_{3z^2-1} member of the Ni d set can have *no* d character on any other Ni atom, and this is seen to localize the orbitals quite well. The electronic configuration with respect to this set is $p^6d^8 = t_{2g}^6\, e_g^2$.

The members of the 8-orbital O p Ni d set describing the 10 eV wide pd band structure are shown at the top of the figure, to the right. By virtue of having neither O p nor Ni d character in their tails, these orbitals are more localized and atomic-like. Merely the O p orbitals have a bit of bonding Ni sp character due to covalency with the band seen above 2 eV. Due to the O p character in the empty part of the e_g the configuration and the concomitant e_g character in the full O p band, the configuration with respect to this set is $p^{5.4}d^{8.6}$, i.e. with holes in the p orbitals and more than 8 d electrons!

As is evident from the figure, NiO is a metal in the LDA, which is completely wrong. Nevertheless, LDA Wannier orbitals form very reasonable one-electron basis sets for many-electron calculations such as LDA+DMFT and multiplet ligand-field theory (MLFT) cluster calculations for x-ray spectroscopies [35]. Due to the complexities of many-electron calculations, one is tempted to use a small basis set, e.g. for NiO, the set of 5 Ni d orbitals, or even a set of merely 2 Ni e_g orbitals. This is however inaccurate, because the Coulomb repulsion is strong between two d electrons on the same site and one cannot neglect the d character in the p band. A small computational bonus for using the larger pd set, is that the d orbitals have simpler shapes so that the dd Coulomb repulsion with good approximation can be described by the 3 Slater integrals [35]. On the other hand, the pictures of the pd set tell little, whereas those of the smaller sets bring

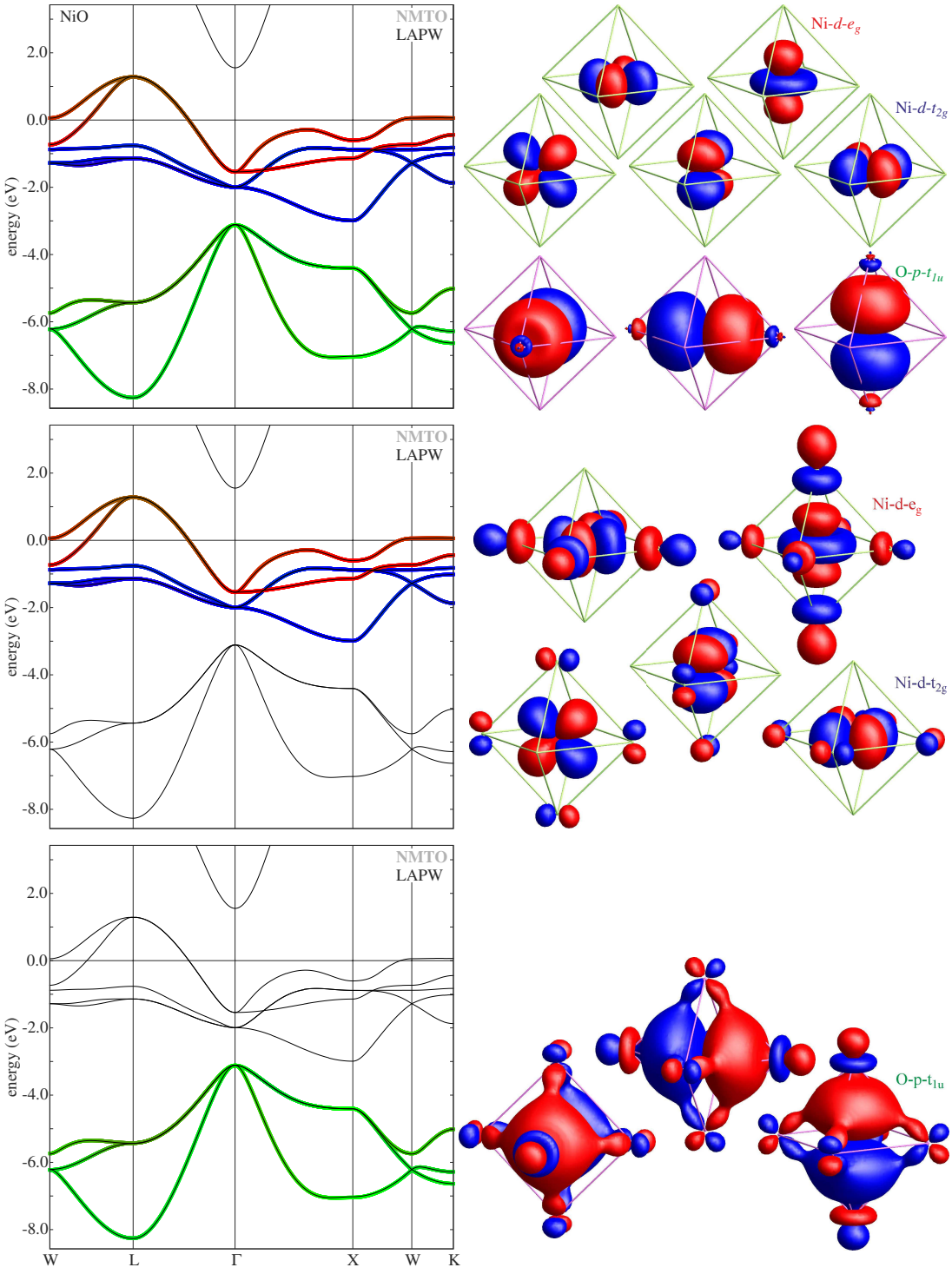

Fig. 7: *LDA band structures of NiO calculated with a large set of LAPWs (black) and three different* $(N{=}1)$*MTO basis sets (colored) whose Wannier orbitals are shown to the right of the bands. From the bottom and up: The 3 O* p *bands (green), the 5 Ni* d *bands with* t_{2g} *character blue and* e_g *character red, and the 8 O* p *Ni* d *bands. The Wannier orbitals are shown as* $w\left(\mathbf{r}\right) = \pm const$ *surfaces with the* $\pm$ *sign indicated by red/blue and* $const$ *determined by the condition that 90% of the probability density is inside the surface. From Ref. [35].*

out covalency effects very clearly. This becomes particularly relevant when symmetry-lowering lattice distortions take place. Examples may be found in Refs. [36], [37], [38, 39], and [40].

5 Standard Löwdin downfolding and N-ization

In the NMTO method we first construct the set of energy-dependent, downfolded KPWs (EMTOs) from multiple scattering theory, i.e. we compute the structure matrix (31) in a strongly screened (e.g. spd) representation and then downfold this matrix to the desired degree for each energy. *Thereafter* we N-ize the EMTOs to form the energy-independent NMTO basis set. This is different from standard Löwdin downfolding which partitions a given, large set of energy-independent, strongly localized orbitals into active and passive subsets, $|\chi\rangle = |\chi_A\rangle + |\chi_B\rangle$, and then eliminates the latter. Had one chosen this large basis set to be one of strongly screened NMTOs, N-ization would have come *before* downfolding, and this is also the sequence in which LMTO downfolding was first done [29]. Below, we shall first review Löwdin downfolding because it is similar to, but much more familiar than screened multiple scattering theory, and then indicate that *subsequent* use of the N-ization technique might be useful.
Partitioning the generalized eigenvalue equations (9) yields:

$$\begin{aligned}(H-\varepsilon O)_{AA}\, b_A + (H-\varepsilon O)_{AP}\, b_P = 0\\ (H-\varepsilon O)_{PA}\, b_A + (H-\varepsilon O)_{PP}\, b_P = 0\end{aligned}$$

in block notation. Solving the bottom equations for b_P,

$$b_P = -\left[(H-\varepsilon O)_{PP}\right]^{-1}(H-\varepsilon O)_{PA}\, b_A, \tag{57}$$

and inserting in the upper equations, yields the well-known set of Löwdin-downfolded secular equations:

$$\left\{(H-\varepsilon O)_{AA} - (H-\varepsilon O)_{AP}\left[(H-\varepsilon O)_{PP}\right]^{-1}(H-\varepsilon O)_{PA}\right\} b_A = 0. \tag{58}$$

These, together with the "upfolding" (57) give the exact eigenfunction coefficients $b_I = (b_A, b_P)$, as long as the proper energy dependences are kept. But in order for the secular matrix to have the desirable $H - \varepsilon O$ form, the energy dependence of the complicated matrix

$$(H-\varepsilon O)_{AP}\ \left[(H-\varepsilon O)_{PP}\right]^{-1}\ (H-\varepsilon O)_{PA}$$

is either neglected or linearized.
We are interested in the set of downfolded *orbitals* giving rise to this secular matrix. This is the energy-dependent set:

$$|\phi_A(\varepsilon)\rangle \equiv |\chi_A\rangle - |\chi_P\rangle\left[(H-\varepsilon O)_{PP}\right]^{-1}(H-\varepsilon O)_{PA} \equiv |\chi_A\rangle + |\chi_P\rangle\ D_{PA}(\varepsilon)\,, \quad \blacktriangleleft \tag{59}$$

with each member $|\phi_a(\varepsilon)\rangle$ being the active orbital $|\chi_a\rangle$, *dressed* by an *energy-dependent* linear combination of passive orbitals. How well localized $|\phi_a(\varepsilon)\rangle$ is, depends on how well the chosen set $|\chi_A\rangle$ reproduces the eigenstates at ε.

That $\mathcal{H}-\varepsilon$ represented in this set is the matrix in (58), is seen by first operating on (59) with $\mathcal{H}-\varepsilon$, and then projecting onto the active and passive subsets:

$$\langle\chi_A\left|\mathcal{H}-\varepsilon\right|\phi_A\left(\varepsilon\right)\rangle = \left(H-\varepsilon O\right)_{AA} - \left(H-\varepsilon O\right)_{AP}\left[\left(H-\varepsilon O\right)_{PP}\right]^{-1}\left(H-\varepsilon O\right)_{PA}$$
$$\langle\chi_P\left|\mathcal{H}-\varepsilon\right|\phi_A\left(\varepsilon\right)\rangle = 0.$$

Forming finally the linear combination (59) yields the desired result:

$$\left\langle\phi_A\left(\varepsilon\right)\left|\hat{H}-\varepsilon\right|\phi_A\left(\varepsilon\right)\right\rangle = \left(H-\varepsilon O\right)_{AA} - \left(H-\varepsilon O\right)_{AP}\left[\left(H-\varepsilon O\right)_{PP}\right]^{-1}\left(H-\varepsilon O\right)_{PA}. \quad \blacktriangleleft$$

One can show that this equals $-G_{AA}\left(\varepsilon\right)^{-1}$, exactly as equations (44) and (34) in MTO theory. In fact, the entire N-ization procedure could be used to remove the energy dependence of the Löwdin-downfolded set (59). The result for the dress is:

$$D_{PA}^{(0..N)} = G_{PA}\left[0..N\right]\, G_{AA}\left[0..N\right]^{-1} \approx G_{PA}\left(\varepsilon\right) G_{AA}\left(\varepsilon\right)^{-1} = D_{PA}\left(\varepsilon\right),$$

and therefore the major cause for delocalization seems to be the Löwdin downfolding (59).
This procedure is computationally more demanding than the one we have described, and yields less localized downfolded obitals. It certainly only works for orbital basis sets with merely one radial function per Rlm [41].

6 Localization

It seems to me, that the NMTO construction in which one first generates a set of most localized solutions (KPWs) of Schrödinger's equation at a each energy, and then interpolates both the local (from the radial functions) and the global (from the downfolding) energy dependencies in one, common N-ization step, leads to a set of Wannier orbitals which are at least as localized as those obtained by Löwdin downfolding of the set of classical LMTOs as explained above, and have a spread close to the minimal one [5]. Computed rms values, $\left\langle w\left|\left|\mathbf{r}-\langle w\left|\mathbf{r}\right|w\rangle\right|^2\right|w\right\rangle^{1/2}$, of the spread support this:
For the vanadium t_{2g} Wannier orbitals in V_2O_3, we [38] find 1.30 Å for the a_{1g} and 1.40 Å for the e_g^π orbitals. These values are significantly smaller than those, 1.35 Å and 1.57 Å obtained from TB-LMTOs [42]. This is consistent with results for the t_{2g} Wannier orbitals in the cubic perovskite $SrVO_3$ where the rms spread, 1.38 Å, of the NMTO Wannier orbital [43] is significantly smaller than the one, 1.54 Å, obtained by downfolding plus $(N{=}0)$-ization of the classical, nearly-orthonormal LMTO set [44]. The 1.38 Å rms spread of this NMTO Wannier orbital is, in fact, only marginally above the minimum value found to be 1.36̇ Å or 1.37 Å, depending on whether a mixed-basis-pseudopotential scheme or the FP-LAPW scheme was used for the LDA calculation of the Bloch functions in (2) [43]. Hence, at least for these t_{2g} systems, the NMTO Wannier functions seem to be close to those maximally localized in the sense of Marzari and Vanderbilt [5].

References

[1] E. Pavarini, E. Koch, A. Lichtenstein, D. Vollhardt (eds.)
The LDA+DMFT approach to strongly correlated materials,
Reihe Modeling and Simulation, Vol. 1 (Forschungszentrum Jülich, 2011)
`http://www.cond-mat.de/events/correl11`

[2] P. Blöchl: *Theory and Practice of Density-Functional Theory*, in [1]

[3] O.K. Andersen, Phys.Rev. B **12**, 3060 (1975)

[4] O.K. Andersen and O. Jepsen, Phys. Rev. Lett **53**, 2571 (1984)

[5] N. Marzari and D. Vanderbilt, Phys. Rev **B 56** 12847 (1997)

[6] S. Satpathy and Z. Pawlowska, Phys. Stat. Solidi (B), **145**, 555 (1988)

[7] J. Kunes: *Wannier functions and construction of model Hamiltonians*, in [1]

[8] S.F. Boys, Rev. Mod. Phys. **32**, 296 (1960)

[9] O.K. Andersen and T. Saha-Dasgupta, Phys. Rev. B **62**, R16219 (2000)

[10] O.K. Andersen, T. Saha-Dasgupta, R.W. Tank, C. Arcangeli, O. Jepsen, G. Krier in: *Electronic Structure and Physical Properties of Solids. The Uses of the LMTO Method*, ed. H. Dreyssé. Springer Berlin/Heidelberg (2000) [Springer Lecture notes in Physics, vol. 535]

[11] R.W. Tank and C. Arcangeli, phys. stat. sol. **217**, 89 (2000)

[12] O.K. Andersen, T. Saha-Dasgupta, S. Ezhov, L. Tsetseris, O. Jepsen, R.W. Tank, C. Arcangeli, G. Krier, Psi-k Newsletter **45** (June 2001), 86-119
`ftp://psi-k.dl.ac.uk./newsletters/news_45/Highlight_45.pdf`

[13] O.K. Andersen, T. Saha-Dasgupta, S. Ezhov, Bull. Mater. Sci. **26**, 19 (2003).

[14] O.K. Andersen, C. Arcangeli, R.W. Tank, T. Saha-Dasgupta, G. Krier, O. Jepsen, I. Dasgupta in: *Tight-Binding Approach to Computational Materials Science*, eds. L. Colombo, A. Gonis, P. Turchi. MRS Symposium Proceedings Series, vol 491 (1998)

[15] M. Zwierzycki and O.K. Andersen, Acta Physica Polonica A **115**, 64 (2009)

[16] E. Zurek, O. Jepsen, O.K. Andersen, ChemPhysChem **6**, 1934 (2005)

[17] Y. Nohara and O.K. Andersen, unpublished

[18] A. J. Williamson, R. Q. Hood, J. C. Grossman, Phys. Rev. Lett. **87** ,246406 (2001)

[19] A. J. Williamson, J. C. Grossman, R. Q. Hood, A. Puzder, G. Galli,
Phys.Rev. Lett. **89**, 196803 (2002)

[20] O.K. Andersen, O. Jepsen, and G. Krier in: *Lectures in Methods of Electronic Structure Calculations,* Eds.: V. Kumar, O.K. Andersen, A. Mookerjee, World Sci. Publ.Co., Singapore (1994)

[21] L. Vitos: *Computational Quantum Mechanics for Materials Engineers; The EMTO Method and Applications (*Springer, London, 2007)

[22] O.K. Andersen, Solid State Commun. **13**, 133 (1973)

[23] O.K. Andersen and O. Jepsen, Physica B+C **91**, 317 (1977)

[24] A.R. Mackintosh and O.K. Andersen in *Electrons at the Fermi Surface,* Ed. M. Springford, (Cambridge University Press, 1980)

[25] E. Wigner and F. Seitz, Phys. Rev. **43**, 804 (1933); *ibid* **46**, 509 (1934)

[26] O.K. Andersen, O. Jepsen, D. Glötzel in *Highlights of Condensed-Matter Theory*, Course LXXXIX, Eds. F. Bassani, F. Fumi and M.P. Tosi, "International School of Physics "Enrico Fermi", Varenna, Italy, (North-Holland, 1985)

[27] O.K. Andersen, Phys. Rev. Lett. **27**, 1211 (1971)

[28] H.L. Skriver: *The LMTO Method* (Springer, Berlin, Heidelberg, NewYork, Tokyo 1984)

[29] W.R.L. Lambrecht and O.K. Andersen, Phys. Rev. B **34**, 2439 (1986)

[30] W. Kohn and J. Rostoker, Phys. Rev., **94** 111, (1954)

[31] H. Ebert: *Multiple-Scattering Formalism for Correlated Systems: a KKR-DMFT Approach*, in [1]

[32] See lecture of R. Zeller

[33] O.K. Andersen, Z. Pawlowska, and O. Jepsen, Phys.Rev. B **34**, 5253 (1986)

[34] O.K. Andersen, O. Jepsen, and M. Sob in *The Electronic Band Structure and its Application*, Lecture Note Series, Vol. **283**, Ed. M.Yussouff (Springer-Verlag, 1987)

[35] M.W. Haverkort, M. Zwierzycki, and O.K. Andersen, Phys. Rev. B **85**, 165113 (2012)

[36] E. Pavarini, S. Biermann, A.P. Poteryaev, A.I. Lichtenstein, A. Georges, O.K. Andersen, Phys. Rev. Lett. **92**, 176403 (2004)

[37] E. Pavarini, A. Yamasaki, J. Nuss, O.K. Andersen, New Journal of Physics **7**, 188 (2005)

[38] T. Saha-Dasgupta, O. K. Andersen, J. Nuss, A. I. Poteryaev, A. Georges, A. I. Lichtenstein, arXiv: 0907.2841 v1

[39] A.I. Poteryaev, J.M. Tomczak, S. Biermann, A. Georges, A.I. Lichtenstein, A.N. Rubtsov, T. Saha-Dasgupta, O.K. Andersen, Phys. Rev. B **76**, 085127 (2007)

[40] E. Pavarini: *The LDA+DMFT Approach*, in [1]

[41] E. Zurek, J. Autschbach, O.K. Andersen, AIP Conf. Proc. **963**, 1421 (2007)

[42] I.V. Solovyev, Z.V. Pchelkina and V.I. Anisimov, Phys. Rev. B **75**, 0145110 (2007)

[43] F. Lechermann, A. Georges, A. Poteryaev, S. Biermann, M. Posternak, A. Yamasaki, and O.K. Andersen, Phys. Rev. B **74**, 125120 (2006)

[44] I. V. Solovyev, Phys. Rev. B **73**, 155177 (2006)

4 The LDA+U Approach: A Simple Hubbard Correction for Correlated Ground States

Matteo Cococcioni
Dept. of Chemical Engineering and Materials Science
University of Minnesota

Contents

E. Pavarini, E. Koch, F. Anders, and M. Jarrell
Correlated Electrons: From Models to Materials
Modeling and Simulation Vol. 2
Forschungszentrum Jülich, 2012, ISBN 978-3-89336-796-2
http://www.cond-mat.de/events/correl12

One of the most well known and well documented failures of Density Functional Theory (DFT) [1, 2] is certainly represented by Mott insulators . In these systems the insulating character of the ground state stems from the strong Coulomb repulsion between electrons that, prevailing on their kinetic energy (minimized by delocalization), forces them to localize on atomic-like orbitals (Mott localization) [3]. The precise description of this behavior requires the full account of the multi-determinant nature of the N-electron wave function and of the many-body terms of the electronic interactions. In molecular dissociation processes, for example, the localization of electrons on the resulting fragments can only be properly described if the so-called *ionic terms* (describing multiple valence electrons on the same site) of the ground state wave function are allowed to decrease their weight (e.g., in a variational calculation) while the distance between the fragments increases. This is only possible if the N-electron wave function is constructed as a linear combination of multiple Slater determinants. In other words, when electrons are strongly localized their motion becomes "correlated" and their wave function acquires a marked many-body character. Thus, the Hartree-Fock (HF) method, that describes the electronic ground state with a variationally optimized single determinant, cannot capture the physics of Mott insulators. The insulating character of these materials is also beyond reach for band theory.For these reasons they are generally classified as "strongly-correlated" materials (in fact, the formal definition of correlation energy is $E_c = E_{exact} - E_{HF}$ where E_{HF} represents the HF approximation to the exact quantity). Describing the behavior of these systems within (approximate) DFT is a formidable task (although the unknown exact exchange-correlation energy functional would be able to predict their ground state properties) due to the expression of the electron-electron interaction as a functional of the electronic charge density, and to the use of an effective single particle (Kohn-Sham) representation of this quantity [2]. In fact, most commonly used approximate exchange-correlation (xc) functionals such as, the Local Density Approximation (LDA) [4–6], or the Generalized Gradient Approximation (GGA), fail quite dramatically in predicting the insulating character of these materials and also provide a quite poor representation of other physical properties, including their equilibrium crystal structure, their magnetic moments, their vibrational spectrum, etc. In general, these problems can be traced back to the tendency of most approximate xc functionals to over-delocalize valence electrons and to over-stabilize metallic ground states. Other inaccuracies of approximate xc functionals such as, the imprecise account of the exchange interaction and the consequent incomplete cancellation of the electronic self-interaction contained in classical (density-density) Coulomb integrals may sometimes concur to the over-delocalization of electronic states.

One of the simplest models that have been formulated to rationalize (albeit in a semi-quantitative way) the physics of correlated materials, is the Hubbard model [7–12] whose real-space second-quantization formalism is ideally suited to describe systems with electrons localized on atomic orbitals. In its simplest, one-band incarnation, the Hubbard Hamiltonian can be written as follows:

$$H_{Hub} = t \sum_{\langle i,j\rangle,\sigma} (c^{\dagger}_{i,\sigma} c_{j,\sigma} + h.c.) + U \sum_{i} n_{i,\uparrow} n_{i,\downarrow} \tag{1}$$

where $\langle i, j\rangle$ denotes nearest-neighbor atomic sites, $c^{\dagger}_{i,\sigma}, c_{j,\sigma}$, and $n_{i,\sigma}$ are electronic creation,

annihilation and number operators for electrons of spin σ on site i. When electrons are strongly localized, their motion is described by a "hopping" process from one atomic site to its neighbors (first term of Eq. (1)) whose amplitude t is proportional to the dispersion (the bandwidth) of the valence electronic states and represents the single-particle term of the total energy. In virtue of the strong localization, the Coulomb repulsion is only accounted for between electrons on the same atom through a term proportional to the product of the occupation numbers of atomic states on the same site, whose strength is U (the "Hubbard U"). The hopping amplitude and the on-site Coulomb repulsion represent the minimal set of parameters necessary to capture the physics of Mott insulators. In fact, in these systems, the insulating character of the ground state emerges when single-particle terms of the energy (generally minimized by electronic delocalization on more extended states) [3] are overcome by short-range Coulomb interactions (the energy cost of double occupancy of the same site): $t << U$. In other words, the system becomes insulator (even at half-filling conditions, when band theory would predict a metal) when electrons cannot hop around because they don't have sufficient energy to overcome the repulsion from other electrons on neighbor sites. Therefore, the balance between U and t controls the behavior of these systems and the character of their electronic ground state. While the regime dominated by single-particle terms of the energy ($t >> U$) is generally well described by approximate DFT, the opposite one ($t << U$) is far more problematic.
The LDA+U (by this name I indicate a "+U" correction applied to a generic approximate DFT functionals, not necessarily LDA) is one of the simplest corrective approaches that were formulated to improve the accuracy of DFT functionals in describing the ground state of correlated systems [13–17]. The idea it is based on is quite simple and consists in using the the Hubbard Hamiltonian to describe "strongly correlated" electronic states (typically, localized d or f orbitals), while the rest of valence electrons are treated at the "standard" level of approximation. Within LDA+U the total energy of a system can be written as follows:

$$E_{LDA+U}[\rho(\mathrm{r})] = E_{LDA}[\rho(\mathrm{r})] + E_{Hub}[\{n^{I\sigma}_{mm'}\}] - E_{dc}[\{n^{I\sigma}\}]. \tag{2}$$

In this equation E_{Hub} is the term that contains electron-electron interactions as modeled in the Hubbard Hamiltonian. Because of the additive nature of this correction it is necessary to eliminate from the (approximate) DFT energy functional E_{LDA} the part of the interaction energy already contained in E_{Hub} to avoid double-counting problems. This task is accomplished by the subtraction of the so-called "double-counting" (dc) term E_{dc} that models the contribution to the DFT energy from correlated electrons as a mean-field approximation to E_{Hub}. Due to the lack of a precise diagrammatic expansion of the DFT total energy, the dc term is not uniquely defined, and different possible formulations and implementations will be discussed in section 2.1 It is important to stress that the Hubbard correction is only applied to the localized states of the system (typically the ones most affected by correlation effects). In fact, it is a functional of occupation numbers that are often defined as projections of occupied Kohn-Sham orbitals (ψ^{σ}_{kv}) on the states of a localized basis set (ϕ^{I}_{m}):

$$n^{I\sigma}_{m,m'} = \sum_{k,v} f^{\sigma}_{kv} \langle \psi^{\sigma}_{kv} | \phi^{I}_{m'} \rangle \langle \phi^{I}_{m} | \psi^{\sigma}_{kv} \rangle \tag{3}$$

where f_{kv}^{σ} are the Fermi-Dirac occupations of the Kohn-Sham (KS) states (k and v being, respectively, the k-point and band indexes). Using the occupations defined in Eq. (3) in the functional of Eq. (2) corresponds to substituting the number operators appearing in Eq. (1) with their (mean-field) average on the occupied manifold of the system. While this operation is necessary to use the Hubbard model in current implementations of DFT, the choice of the localized basis set is not unique. Some of the most popular choices, as atomic orbitals or maximally localized Wannier functions, are briefly discussed in section 2.3.
The reminder of this chapter is organized as follows. In section 1 I will review the historical formulation of LDA+U and the most widely used implementations, discussing the theoretical background of the method in the framework of DFT. In section 2 I will compare different flavors of LDA+U obtained from different choices of the corrective functional, of the set of interactions, of the localized basis set to define atomic occupations. In section 3 I will review different methods to compute the necessary interaction parameters, particularly focusing on one based on linear-response. Section 4 will illustrate the calculation of energy derivatives (forces, stress, dynamical matrix) in LDA+U. In section 5 I will present a recently introduced extension to the LDA+U that contains both on-site and inter-site effective interactions. Finally, in section 6 I will offer some conclusions and an outlook on the future of this method.

1 Basic formulations and approximations

1.1 General formulation

In Eq. (2) the general structure of the LDA+U energy functional was introduced. I will now discuss the most common implementations of this corrective approach starting from the simplest and most general one. The LDA+U approach was first introduced in Refs. [14–16] and consisted of an energy functional that, when specialized to on-site interactions, can be written as follows:

$$E = E_{LDA} + \sum_I \left[\frac{U^I}{2} \sum_{m,\sigma \neq m',\sigma'} n_m^{I\sigma} n_{m'}^{I\sigma'} - \frac{U^I}{2} n^I (n^I - 1) \right]. \tag{4}$$

In Eq. (4) $n_m^{I\sigma} = n_{mm}^{I\sigma}$, and $n^I = \sum_{m,\sigma} n_m^{I\sigma}$, and the index m labels the localized states of the same atomic site I. The second and the third terms of the right-hand side of this equation represent, respectively, the Hubbard and the double-counting terms of Eq. (2). Using the definition of atomic orbital occupations given in Eq. (3), one can easily define the action of the Hubbard corrective potential on the Kohn-Sham wave functions needed for the minimization process:

$$V|\psi_{k,v}^{\sigma}\rangle = V_{LDA}|\psi_{k,v}^{\sigma}\rangle + \sum_{I,m} U^I \left(\frac{1}{2} - n_m^{I\sigma} \right) |\phi_m^I\rangle\langle\phi_m^I|\psi_{k,v}^{\sigma}\rangle. \tag{5}$$

It is important to notice that, because the definition of the atomic occupations (Eq. (3)), the Hubbard potential is non-local. Therefore, the LDA+U energy functional (Eq. (4)) is out of the validity domain of the Hohenberg-Kohn theorem [1]. It respects, however, the conditions of the Gilbert theorem [18]; the Kohn-Sham equations obtained from Eq. (4) will thus yield

the ground state one-body density matrix of the system. As evident from Eq. (5), the Hubbard potential is repulsive for less than half-filled orbitals ($n_m^{I\sigma} < 1/2$), attractive for the others. This is the mechanism through which the Hubbard correction discourages fractional occupations of localized orbitals (often indicating significant hybridization with neighbor atoms) and favors the Mott localization of electrons ($n_m^{I\sigma} \to 1$). The difference between the potential acting on occupied and unoccupied states (whose size is of the order of U) also gives a measure of the energy gap opening between their eigenvalues. Thus, consistently with the predictions of the Hubbard model, the explicit account of on-site electron-electron interactions favors electronic localization and may lead to a band gap in the KS spectrum of the system, provided the on-site Coulomb repulsion prevails on the kinetic term of the energy, minimized through delocalization. Although this appears as a significant improvement over the result of approximate DFT, it is important to remark that a gap only appears in the band structure if possible degeneracies between the (localized) states around the Fermi level are lifted. To achieve this result it is sometimes necessary to artificially impose the symmetry of the electronic system to be lower than the point group of the crystal as, for example, in the case of FeO [19] and CuO [20]. This operation corresponds to "preparing" the system in one of the possibly degenerate insulating states (having electrons localized on different subsets of orbitals), characterized by a finite gap in the band structure of the corresponding KS spectrum. As will be discussed in sections 1.4 and 3.3, this result highlights that the LDA+U is out of the realm of DFT, as the Kohn-Sham spectrum of the exact functional is not constrained to reflect any physical property (while the charge density should maintain the whole symmetry of the crystal).

1.2 Rotationally-invariant formulation

While able to capture the main essence of the LDA+U approach, the formulation presented in Eq. (4) is not invariant under rotation of the atomic orbital basis set used to define the occupation of d states $n_{m\sigma}^I$, which produces an undesirable dependence of the results on the specific choice of the localized basis set. To solve these problems, A. Liechtenstein and coworkers [21] introduced a basis set independent formulation of LDA+U in which E_{Hub} and E_{dc} are given a more general expression borrowed from the HF method:

$$E_{Hub}[\{n_{mm'}^I\}] = \frac{1}{2}\sum_{\{m\},\sigma,I}\big\{\langle m,m''|V_{ee}|m',m'''\rangle n_{mm'}^{I\sigma}n_{m''m'''}^{I-\sigma} + (\langle m,m''|V_{ee}|m',m'''\rangle - \langle m,m''|V_{ee}|m''',m'\rangle)n_{mm'}^{I\sigma}n_{m''m'''}^{I\sigma}\big\} \quad (6)$$

$$E_{dc}[\{n_{mm'}^I\}] = \sum_I\{\frac{U^I}{2}n^I(n^I-1) - \frac{J^I}{2}[n^{I\uparrow}(n^{I\uparrow}-1) + n^{I\downarrow}(n^{I\downarrow}-1)]\}. \quad (7)$$

The invariance of the "Hubbard" term (Eq. (6)) stems from the fact that the interaction parameters transform as quadruplets of localized wavefunctions, thus compensating the variation of the (product of) occupations associated with them. In Eq. (7), instead, the invariance stems from the dependence of the functional on the trace of the occupation matrices. In Eq. (6) the V_{ee} integrals represents the electron-electron interactions computed on the wave functions of

the localized basis set (e.g., d atomic states) that are labeled by the index m. Assuming that atomic (e.g., d or f) states are chosen as the localized basis, these quantities can be computed from the expansion of the $e^2/|r-r'|$ Coulomb kernel in terms of spherical harmonics (see [21] and references quoted therein):

$$\langle m, m''|V_{ee}|m', m'''\rangle = \sum_k a_k(m, m', m'', m''')F^k \tag{8}$$

where $0 \leq k \leq 2l$ (l is the angular moment of the localized manifold; $-l \leq m \leq l$) and the a_k factors can be obtained as products of Clebsh-Gordan coefficients:

$$a_k(m, m', m'', m''') = \frac{4\pi}{2k+1} \sum_{q=-k}^{k} \langle lm|Y_{kq}|lm'\rangle\langle lm''|Y^*_{kq}|lm'''\rangle. \tag{9}$$

In Eq. (8) the F^k coefficients are the radial Slater integrals computed on the Coulomb kernel [21]. For d electrons only F^0, F^2, and F^4 are needed to compute the V_{ee} matrix elements (for higher k values the corresponding a_k would vanish) while f electrons also require F^6. Consistently with the definition of the dc term (Eq. (7)) as the mean-field approximation of the Hubbard correction (Eq. (6)), the effective Coulomb and exchange interactions, U and J, can be computed as atomic averages of the corresponding Coulomb integrals over the states of the localized manifold (in this example, atomic orbitals of fixed l):

$$U = \frac{1}{(2l+1)^2} \sum_{m,m'} \langle m, m'|V_{ee}|m, m'\rangle = F^0, \tag{10}$$

$$J = \frac{1}{2l(2l+1)} \sum_{m\neq m',m'} \langle m, m'|V_{ee}|m', m\rangle = \frac{F^2+F^4}{14}. \tag{11}$$

These equations have often been used (assuming that F^2/F^4 has the same value as in isolated atoms) to evaluate *screened* Slater integrals F^k from the values of U and J, computed from the ground state of the system of interest (some methods to calculate these quantities will be illustrated in section 3). The *screened* V_{ee} integrals, to be used in the corrective functional of Eq. (6), can then be easily obtained from the computed F^k using Eqs. (8) and (9). Although Eqs. (8)-(11) are strictly valid for atomic states and *unscreened* Coulomb kernels, this procedure can be assumed quite accurate for solids if the localized orbitals retain their atomic character.

1.3 A simpler formulation

The one presented in section 1.2 is the most complete formulation of the LDA+U, based on a multi-band Hubbard model. However, in many occasions, a much simpler expression of the Hubbard correction (E_{Hub}), introduced in Ref. [22], is actually adopted and implemented. This simplified functional can be obtained from the full formulation discussed in section 1.2 by retaining only the lower order Slater integrals F^0 and throwing away the others: $F^2 = F^4 = J = 0$. This simplification corresponds to neglecting the non-sphericity of

the electronic interactions ($a_0(m,m',m'',m''') = \delta_{m,m'}\delta_{m'',m'''}$) and the differences among the couplings between parallel spin and anti-parallel spin electrons (i.e., the exchange interaction J). The energy functional can be recalculated from Eqs. (6) and (7) and one easily obtains:

$$\begin{aligned} E_U[\{n^{I\sigma}_{mm'}\}] &= E_{Hub}[\{n^I_{mm'}\}] - E_{dc}[\{n^I\}] \\ &= \sum_I \frac{U^I}{2}\left[\left(n^I\right)^2 - \sum_\sigma \mathrm{Tr}\left[(\mathbf{n}^{I\sigma})^2\right]\right] - \sum_I \frac{U^I}{2} n^I(n^I-1) \\ &= \sum_{I,\sigma} \frac{U^I}{2} \mathrm{Tr}\left[\mathbf{n}^{I\sigma}(1-\mathbf{n}^{I\sigma})\right]. \end{aligned} \tag{12}$$

It is important to stress that the simplified functional in Eq. (12) still preserves the rotational invariance of the one in Eqs. (6) and (7), that is guaranteed by the dependence of the "+U" functional on the trace of occupation matrices and of their products. On the other hand, the formal resemblance to the HF energy functional is lost and only one interaction parameter (U^I) is needed to specify the corrective functional. This simplified version of the Hubbard correction has been successfully used in several studies and for most materials it shows similar results as the fully rotationally invariant one (Eqs. (6) and (7)). Some recent literature has shown, however, that the Hund's rule coupling J is crucial to describe the ground state of systems characterized by non-collinear magnetism [23, 24], to capture correlation effects in multiband metals [25, 26], or to study heavy-fermion systems, typically characterized by f valence electrons and subject to strong spin-orbit couplings [23, 24, 27]. A recent study [28] also showed that in some Fe-based superconductors a sizeable J (actually exceeding the value of U and resulting in negative $U_{eff} = U - J$) is needed to reproduce (with LDA+U) the magnetic moment of Fe atoms measured experimentally. Several different flavors of corrective functionals with exchange interactions were also discussed in Ref. [29]. Due to the spin-diagonal form of the simplified LDA+U approach in Eq. (12), it is customary to attribute the Coulomb interaction U an effective value that accounts for the exchange correction: $U_{eff} = U - J$. As discussed in section 2.2, this assumption is actually not completely justifiable as the resulting functional is missing other terms of the same order in J as the one included.

1.4 Conceptual and practical remarks

After introducing the general formulation of the LDA+U approach I think it is appropriate to clarify in a more detailed way its theoretical foundation (possibly in comparison with other corrective methods) and to discuss the range of systems it can be applied to, its strengths and its limitations.

The formal resemblance of the full rotationally invariant Hubbard functional (Eqs. (6)) with the HF interaction energy could be misleading: how can a corrective approach provide a better description of electronic correlation if it is based on a functional that, by definition, can not capture correlation? Some differences are, of course, to be stressed: i) the effective interactions in the LDA+U functional are *screened* rather than based on the *bare* Coulomb kernel (as in HF); ii) the LDA+U functional only acts on a subset of states (e.g., localized atomic orbitals of d or

f kind) rather than on all the states in the system; $iii)$ the effective interactions have an orbital-independent value and correspond to atomically averaged quantities. These differences between LDA+U and HF, while making the first approach more computationally efficient than the latter (and related ones as exact-exchange - EXX - and hybrid functionals), do not dissolve the doubts raised above, and actually make HF appear more accurate and general. In order to clarify this point one needs to keep in mind that LDA+U is designed to capture the *effects* of electronic correlation (more precisely, of the *static* correlation, descending from the multi-determinant nature of the electronic wave function) into an effective one-electron (KS) description of the ground state. From this point of view significant improvements in the description of a correlated system may result from the application of an HF-like correction to KS states. In other words, the main difference between LDA+U and HF is that the first approach applies a corrective functional (resembling a *screened* HF) to a sub-group of single-particle (KS) wave functions that do not have any physical meaning (except being constrained to produce the ground state density), in the assumption that this correction can help a better description of the properties of the correlated system they represent through the effects it has on the exchange-correlation functional. In real HF calculations, instead, no xc energy exist and the optimized single particle wave functions are associated with a physical meaning. In Mott insulators, for example, a more precise evaluation of the structural and the vibrational properties can be obtained using the LDA+U approach through improving the size of the fundamental gap (possibly after lowering the symmetry of their electronic system) that can be computed from total energy finite differences when varying the number of electrons in the system around a reference value (in a molecule this quantity corresponds to the difference between the first ionization potential and the electron affinity).

An equivalent way to look at this problem is to study the dependence of the total energy of a system on the number of electrons in its orbitals. As explained in Ref. [30], for example, the energy of a system exchanging electrons with a "bath" (a reservoir of charge), should be linear with the number of electrons (in either part) and the finite discontinuity in its derivative at integer values of this number, represents the fundamental gap. Approximate DFT functionals do not satisfy this condition and result in upward convex energy profiles (this flaw can be seen as caused by a residual self-interaction). The linearization of the total energy imposed by the Hubbard correction is more transparent from its simpler formulation (Eq. (12)) where it is evident that the corrective functional subtracts from the DFT energy the spurious quadratic term and substitutes it with a linear one. This topic will be discussed with more details in section 3 that describes a linear-response approach to the calculation of the Hubbard U. Self-interaction corrected (SIC) functionals [4] are specifically designed to eliminate the residual self-interaction that manifests itself with the lack of linearity of the energy profile. In HF, the exchange functional exactly cancels the self-Coulomb interaction contained in the Hartree term, but usually produces a downward convex energy profile. Therefore, in HF-related methods as hybrid functionals, the strength of the exchange interaction must be properly tuned by a scaling factor (see, for example, [31]). However, the value of the scaling factor (generally in the 0.2 - 0.3 range) is usually determined semi-empirically and has no immediate physical meaning. LDA+U performs a linearization of the energy only with respect to the electronic degrees of

freedom for which self-interaction is expected to be stronger (localized atomic states) and with an effective coupling that, although orbital-independent (indeed corresponding to an atomically averaged quantity), can be evaluated ab-initio. Thus it results, at the same time, more computationally efficient and (arguably) more physically transparent than EXX and hybrid functionals as a corrective scheme to DFT. The formal similarity with SIC and EXX approaches suggests that LDA+U should be also effective in correcting the underestimated band gap of covalent insulators (e.g., Si, Ge, or GaAs), for which a more precise account of the exchange interaction proves to be useful. Indeed, while the "standard" "+U" functional is not effective on these systems, this result is actually achievable through a generalized formulation of the "+U" functional (with inter-site couplings) that will be discussed in section 5.

It is important to notice that the orbital independence of the effective electronic interaction, makes the simpler version of the "+U" correction, Eq. (12), effectively equivalent to a penalty functional that forces the on-site occupation matrix to be idempotent. This action corresponds to enforcing a ground state described by a set of KS states with integer occupations (either 0 or 1) and thus with a gap in its band structure. While this is another way to see how the "+U" correction helps improving the description of insulators, it should be kept in mind that the linearization of the energy as a function of (localized) orbital occupations is a more general and important effect to be obtained. In fact, in case of degenerate ground states, charge densities with fractional occupations (corresponding to a metallic Kohn-Sham system) can, in principle, represent linear combinations of insulating states (with different subgroups of occupied single particle states), as long as the total energy is equal to the corresponding linear combination of the energies of the single configurations. Thus, the insulating character of the KS system should not be expected/pursued unless the symmetry of the electronic state is broken. An example of a degenerate ground state is provided by FeO. In fact, the energy of this system is minimized when the minority-spin d electron of Fe is described by a combination of states on the (111) plane of the crystal (lower left panel of Fig. 1) rather than by the z^2 state along the [111] (upper left panel of Fig. 1). This combination can only be obtained through lowering the symmetry of the lattice and breaking the equivalence between d states on the same (111) plane as explained in Ref. [19]. The right panel in Fig. 1 shows that the orbital-ordered broken symmetry phase not only gives a good estimate of the band gap but also reproduces the rhombohedral distortion of the crystal under pressure. The real material has to be understood as resulting from the superposition of equivalent orbital-ordered phases that re-establish the symmetry of the crystal.

In spite of the appealing characteristics described above, LDA+U provides a quite approximate description of correlated ground states. Being a correction for atomically localized states, their possible dispersion is totally ignored and so is the k-point dependence of the effective interaction (the Hubbard U). This limit can be alleviated, in part, by taking into account inter-site electronic interactions as explained in Ref. [34]. LDA+U also completely neglects the frequency dependence of the electronic interaction and, in fact, it has been shown [17] to correspond to the static limit of GW [35–44]. This particular aspect implies that LDA+U completely misses the role of fluctuations around the ground state which also corresponds to neglecting its pos-

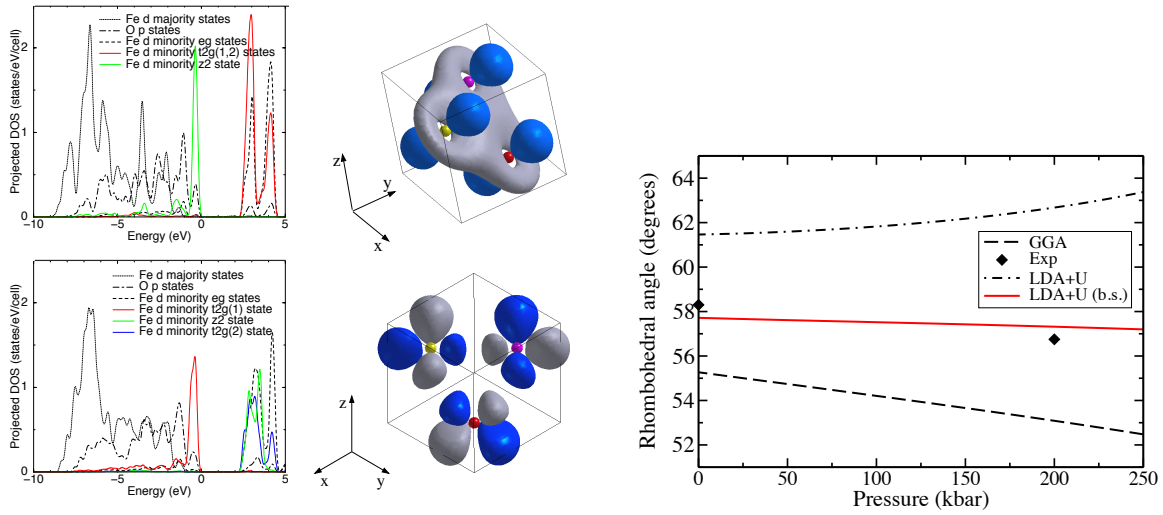

Fig. 1: *(From [19]). Projected density of states (left) and highest energy occupied orbital of FeO (center) in the unbroken symmetry (upper panels) and broken symmetry states (lower panels). In the graph on the right the rhombohedral angle is plotted as a function of pressure. The solid line describes DFT+U results in the broken-symmetry phase (from [19]). Diamonds represent the experimental data from [32, 33].*

sible multi-configurational character. In order to account for these dynamical effects higher order corrections are needed as, for example, the one provided by DMFT [45–50]. However, DFT+DMFT also solves a Hubbard model on each atom (treated as an impurity in contact with a "bath" represented by the rest of the crystal) and the final result depends quite strongly on the choice of the interaction parameter U. Recently, LDA+U has also been successfully used in conjunction with GW [51] and TDDFT [52] to compute the photo-emission spectra and quasi-particle energies of systems from their correlated ground states. Thus, in spite of its limits, LDA+U still plays an important role in the description of these materials (besides being one of the most inexpensive approaches to provide their ground state, at least) and improving its accuracy and its descriptive and predictive capabilities is very important.

2 Functionals and implementations

In this section I will discuss some particular aspects of the formulation and the implementation of LDA+U that can influence its effectiveness and accuracy.

2.1 Which double counting?

The lack of a diagrammatic expansion of the DFT total energy makes it quite difficult to model the electronic correlation already contained in semilocal xc functionals through simple dc terms (Eqs. (7) and (12)) that are general and flexible enough to work for many different classes of systems. As a result, the choice of E_{dc} is not univocal and different formulations have been proposed in literature for different kinds of materials.

The first one to be introduced was the one given in Eq. (7). that was obtained as a mean-field approximation to the Hubbard correction (Eq. 6) in the so-called "fully-localized" limit (FLL), in which each localized (e.g., atomic) orbital is either full or completely empty. This formulation of the dc term is consistent with the idea behind the Hubbard model as an expansion of the electronic energy around the strongly localized limit and thus tends to work quite well for strongly correlated materials with very localized orbitals. For other systems such as, for example, metals or "weakly correlated" materials in general, the excessive stabilization of occupied states due to the "+U" corrective potential (see Eq. 5) can lead to a description of the ground state inconsistent with experimental data and to quite unphysical results (such as, e.g., the enhancement of the Stoner factor [53]) that seriously question its applicability in these cases. In order to alleviate these difficulties a different Hubbard corrective functional, called "around mean-field" (AMF), was introduced in Ref. [54] and further developed in Ref. [53]. This functional can be expressed as follows:

$$E_{DFT+U} = E_{DFT} - \sum_I \frac{U^I}{2} \text{ Tr } \left(\mathbf{n}^I - \langle n^I \rangle\right)^2 \tag{13}$$

where $n^I = \text{Tr } \mathbf{n}^I$ and $\langle n^I \rangle$ is the average diagonal element of the occupation matrix $\mathbf{n}^I$ (multiplied by the unit matrix). As evident from Eq. (13), this functional encourages deviations from a state with uniform occupations (i.e., with all the localized states equally occupied) representing the approximate DFT ground state. Its expression can be obtained from the combination of the E_{Hub} term of Eq. (12) and a modified dc that reads:

$$E_{dc}^{AMF} = \sum_I \frac{U^I}{2} n^I (n^I - \langle n^I \rangle) \qquad . \tag{14}$$

In Ref. [53] a linear combination of the AMF and the FLL flavors of LDA+U is proposed, also used in [27]. The mixing parameter has to be determined for each material and is a function of various quantities related to its electronic structure. In spite of this connection between the two schemes, the AMF one has had limited success and diffusion, except for relatively few works [27, 29]. Because of its derivation from the Hubbard model, the LDA+U approach is generally viewed as a corrective scheme for systems with localized orbitals and the FLL limit is usually adopted. In cases where these are embedded in a "background" of more delocalized or hybridized states the use of the FLL flavor is still justifiable with a corrective functional that selectively correct only the most localized orbitals. This approach has recently shown promising results (to be published elsewhere) for bulk Fe with a FLL LDA+U applied on e_g states only.

2.2 Which corrective functional?

Another source of uncertainty when using LDA+U derives from the level of approximation in the corrective Hamiltonian. While rotational invariance is widely recognized as a necessary feature of the functional, whether to use the full rotationally invariant correction, Eqs. (6) and (7), or the simpler version of it, Eq. (12), seems more a question of taste or of availability in

current implementations. In fact, the two corrective schemes give very similar results for a large number of systems in which electronic localization is not critically dependent on Hund's rule magnetism. However, as mentioned in section 1.3, in some materials that have recently attracted considerable interest, this equivalence does not hold anymore and the explicit inclusion of the exchange interaction (J) in the corrective functional appears to be necessary. Examples of systems in this group include recently discovered Fe-pnictides superconductors [28], heavy-fermion [27, 24], non-collinear spin materials [23], or multiband metals for which the Hund's rule coupling, promotes, depending on the filling, metallic or insulating behavior [25, 26]. In our recent work on CuO [20] the necessity to explicitly include the Hund's coupling J in the corrective functional was determined by a competition (likely to exist in other Cu compounds as well, such as high T_c superconductors), between the tendency to complete the external $3d$ shell and the one towards a magnetic ground state (dictated by Hund's rule) with 9 electrons on the d manifold. The precise account of exchange interactions between localized d electrons beyond the simple approach of Eq. (12) (with $U_{eff} = U - J$) turned out to be crucial to predict the electronic and structural properties of this material. In this work we used a simpler J-dependent corrective functional than the full rotationally invariant one to reach this aim. The expression of the functional was obtained from the full second-quantization formulation of the electronic interaction potential,

$$\hat{V}_{\rm int} = \frac{1}{2} \sum_{I,J,K,L} \sum_{i,j,k,l} \sum_{\sigma,\sigma'} \langle \phi_i^I \phi_j^J | V_{ee} | \phi_k^K \phi_l^L \rangle \, \hat{c}^\dagger_{I\,i\,\sigma} \, \hat{c}^\dagger_{J\,j\,\sigma'} \, \hat{c}_{K\,k\,\sigma'} \, \hat{c}_{L\,l\,\sigma} \tag{15}$$

(where V_{ee} represent the kernel of the effective interaction, upper- and lower-case indexes label atomic sites and orbitals respectively) keeping only on-site terms describing the interaction between up to two orbitals. Approximating on-site effective interactions with the (orbital-independent) atomic averages of Coulomb and exchange terms,

$$U^I = \frac{1}{(2l+1)^2} \sum_{i,j} \langle \phi_i^I \phi_j^I | V_{ee} | \phi_j^I \phi_i^I \rangle,$$

and

$$J^I = \frac{1}{(2l+1)^2} \sum_{i,j} \langle \phi_i^I \phi_j^I | V_{ee} | \phi_i^I \phi_j^I \rangle,$$

and substituting the product of creation and destruction operators with their averages, associated to the occupation matrices defined in Eq. 3, $n^{I\,\sigma}_{i\,j} = \langle \hat{c}^\dagger_{I\,i\,\sigma} \hat{c}_{I\,j\,\sigma} \rangle$, one arrives at the following expression:

$$E_{\rm Hub} - E_{\rm dc} = \sum_{I,\sigma} \frac{U^I - J^I}{2} \, {\rm Tr}[\mathbf{n}^{I\,\sigma} \, (\mathbf{1} - \mathbf{n}^{I\,\sigma})] + \sum_{I,\sigma} \frac{J^I}{2} \, {\rm Tr}[\mathbf{n}^{I\,\sigma} \, \mathbf{n}^{I\,-\sigma}]. \tag{16}$$

Comparing Eqs. (12) and (16), one can see that the on-site Coulomb repulsion parameter (U^I) is effectively reduced by J^I for interactions between electrons of parallel spin and a positive J term further discourages anti-aligned spins on the same site stabilizing magnetic ground states. The second term on the right-hand side of equation (16) can be explicated as

$\sum_{I,\sigma} (J^I/2)\, n^{I\,\sigma}_{m\,m'}\, n^{I\,-\sigma}_{m'\,m}$ which shows how it corresponds to an "orbital exchange" between electrons of opposite spins (e.g. up spin electron from m' to m and down spin electron from m to m'). It is important to notice that this term is genuinely beyond Hartree-Fock. In fact, a single Slater determinant containing the four states $m\uparrow$, $m\downarrow$, $m'\uparrow$, $m'\downarrow$ would produce no interaction term like the one above. Thus, the expression of the J term given in equation (16), based on a product of $\mathbf{n}^{I\,\sigma}$ and $\mathbf{n}^{I\,-\sigma}$ is an approximation of a functional that would require the calculation of the 2-body density matrix to be properly included. However, in the spirit of the elimination of the spurious quadratic behavior of the total energy, one can assume that the J term in Eq. (16) is a fair representation of the exchange energy contained in the approximate DFT functionals. Therefore its formulation and use in corrective functionals are legitimate. Similar terms in the corrective functional have already been proposed in literature [25, 26, 55–57] although with slightly different formulation than in Eq. (16) when used in model Hamiltonians.

Eq. (16) represents a significant simplification with respect to Eqs. (6) and (7) and proved effective to predict the insulating character of the cubic phase of CuO and to describe its tetragonal distortion [20]. The simplicity of its formulation greatly facilitates its use and the implementation of other algorithms (such as, for example, the calculation of forces, stresses or phonons that will be discussed below). It is also important to report that the LDA+U scheme has recently been implemented with a non-collinear formalism (see, e.g., Ref. [23]). to study correlated systems characterized by canted magnetic moments, magnetic anisotropy or strong spin-orbit interactions (as common in rare earth compounds) [24]. This extension will not be further discussed in this chapter.

2.3 Which localized basis set?

The formulation of the corrective LDA+U functional discussed so far is valid independently from the particular choice of the localized set used to define the occupation matrices that enter the expression of the same functional. Many different choices are indeed possible. The first formulations of LDA+U [14–16] were based on a linear muffin-tin orbital (LMTO) implementation and thus had muffin-tin-orbitals (MTOs - constructed using Bessel, Neumann and Henkel spherical functions and spherical harmonics) as a natural choice to define on-site occupations. In plane-wave - pseudo-potential implementations of DFT, the atomic wave functions used to construct the pseudopotentials probably represent the easiest basis to use. In this case, it is useful to keep in mind that, since the valence electrons wave functions are defined at every point in the unit cell and are expanded on a plane-wave basis set, the definition of the occupation of atomic orbitals requires a projection of valence states on the atomic one. This is reflected in the expression in Eq. (3) and obviously determines the way the Hubbard potential acts on the Kohn-Sham states (Eq. (5)). Other choices are also possible as, for example, atomically centered gaussians or maximally localized Wannier functions [58].

In principles, the final result (the description of the properties of a system obtained from the LDA+U) should not depend on the choice of the localized basis set, provided the effective interaction parameters appearing in the functional (U and possibly J) are computed consistently,

as described in section 3. However, the approximations operated in the Hubbard functional (and the consequent lack of flexibility) may introduce some basis set dependence. Another source of (undesirable) dependence on the basis set is represented by the lack of invariance of the corrective functional with respect to possible rotations of its wave function. In sections 1.2 and 1.3 I highlighted the rotational invariance of the LDA+U formulated in Eqs. (6) and (7). However, it is important to stress that this formulation is only invariant for rotations of localized wave functions belonging to the *same atomic site*. In other words, if one mixes orbitals centered on different atoms the corrective energy changes. In these conditions different basis sets may show different ability to capture the localization of electrons and yield results somewhat different from each other. A particularly good choice in this context seems to be represented by Wannier functions [59, 60]. This choice may lead, however, to some additional computational cost related to the necessity to optimize the localized basis set and to adapt it to the system for optimal performance [60]. An alternative solution to the problem is represented by the extension of the corrective functional to include inter-site interactions (and, ideally higher order terms) that will be discussed in section 5.

3 Computing U (and J?)

3.1 The necessity to compute U

As evident from the expression of the Hubbard functionals discussed in previous sections, the "strength" of the correction to approximate DFT total energy functionals is controlled by the effective on-site electronic interaction - the Hubbard U - whose value is not known a-priori. Consistently with a wide-spread use of this approach as a means to roughly assess the role of electronic correlation, it has become common practice to tune the Hubbard U in a semiempirical way, through seeking agreement with available experimental measurements of certain properties and using the so determined value to make predictions on other aspects of the system behavior. Besides being not satisfactory from a conceptual point of view, this practice does not allow to appreciate the variations of the on-site electronic interaction U, e.g., during chemical reactions, structural transitions or under changing physical conditions. Therefore, in order to obtain quantitatively predictive results, it is crucial to have a method to compute the Hubbard U (and possibly J) in a consistent and reliable way. The interaction parameters should be calculated, in particular, for every atom the Hubbard correction is to be used on, for the crystal structural and the magnetic phase of interest. The obtained value depends not only on the atom, its crystallographic position in the lattice, the structural and magnetic properties of the crystal, but also on the localized basis set used to define the on-site occupation (the same as in the LDA+U calculation). Therefore, contrary to another practice quite common in literature, these values have limited portability, from one crystal to another, or from one implementation of LDA+U to another.

3.2 Other approaches: a quick overview

In the first implementations of LDA+U, based on the use of localized basis sets (e.g., in the LMTO approximation), the Hubbard U was calculated (consistently with its definition as the energy cost of the reaction $2d^n \rightarrow d^{n+1} + d^{n-1}$) from finite differences between Kohn-Sham energy eigenvalues computed (within the atomic sphere approximation) with one more or one less electron on the d states. [13]. This approach allows to obtain a value that is automatically screened by electrons of other kinds on the same atom (e.g., on $4s$ and $4p$ orbitals for a $3d$ transition metal). The use of the LMTO basis set also makes it possible to change the occupation of $3d$ states and to eliminate hopping terms between these atomic orbitals (for which U is calculated) and the rest of the crystal so that single-particle terms of the energy, accounted for explicitly in the Hubbard model, are not included in the calculation. These latter features are quite specific to implementations that use localized basis sets (e.g., LMTO); other implementations (based, e.g., on plane waves) require different procedures to compute the effective interaction parameters [61].
One of the latest methods to compute the effective (screened) Hubbard U is based on constrained RPA (cRPA) calculations and yields a screened, fully frequency dependent interaction parameter that can be used, e.g., in DFT+DMFT calculations [62]. This approach has been extensively described in one of the chapter of the 2011 volume of this same series [57] and will not be discussed here.

3.3 Computing *U* from linear-response

In the following I will describe a linear response approach to the calculation of the effective Hubbard U [19] that allows to use atomic occupations defined as projections of Kohn-Sham states on a generic localized basis set, as shown in Eq. (3). The one described below is the method implemented in the plane-wave pseudopotential total-energy code of the Quantum-ESPRESSO package [63]. The basic idea of this approach is the observation that the (approximate) DFT total energy is a quadratic function of on-site occupations (as also suggested in Ref. [64]). This is consistent with the definition of the dc term (Eq. (7)). In fact, if one considers a system able to exchange electrons with a reservoir (e.g., an atom exchanging electrons with a metallic surface or another atom) the approximate DFT energy is an analytic function of the number of electrons on the orbitals of the system. As demonstrated by quite abundant literature [65, 30, 66], it should consist, instead, of a series of straight segments joining the energies corresponding to integer occupations. Examining Fig. 2, that compares the DFT total energy with the piece-wise linear behavior of the exact energy (it should be noted that they represent cartoons as the energy of the system does not increase for larger N), it is easy to understand that, if the DFT energy profile is represented by a parabola (actually a very good approximation within single intervals between integer occupations [67]), the correction needed to recover the physical piece-wise linear behavior (blue curve) has the expression of the Hubbard functional of Eq. (12), provided that U represents the (spurious) curvature of the approximate total energy profile one aims to eliminate. It is important to notice that recovering the linear behav-

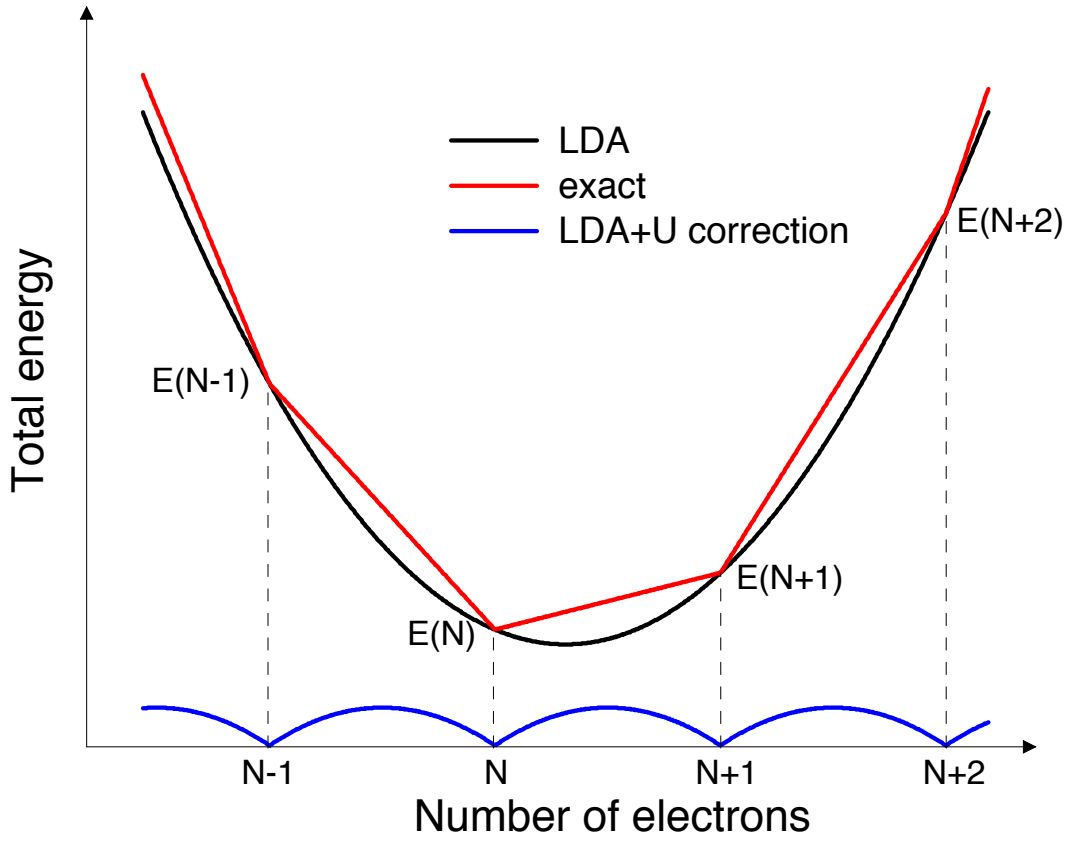

Fig. 2: *(From [19]) Sketch of the total energy profile as a function of the number of electrons in a generic atomic system in contact with a reservoir. The black line represents the DFT energy, the red the exact limit, the blue the difference between the two. The discontinuity in the slope of the red line for integer occupations, corresponds to the difference between ionization potential and electron affinity and thus measures the fundamental gap of the system.*

ior corresponds to reintroducing the discontinuity in the first derivative of the energy (i.e., the single-particle eigenvalue) when the number of electrons increases by one, from N to $N+1$. This discontinuity, also proportional to U, represents the fundamental gap of the system (i.e., the difference between ionization potential and electron affinity in molecules). Thus, the Hubbard U is associated to important physical quantities if calculated as the second derivative of the (approximate) DFT energy.

Unfortunately, when using plane waves (and, typically, pseudopotentials) the on-site occupations cannot be controlled or changed "by hand" because they are obtained as an outcome from the calculation after projecting Kohn-Sham states on the wave function of the localized basis set (Eq. (3)). Therefore, to obtain the second derivative of the total energy with respect to occupations we adopted a different approach that is based on a Legendre transform [19]. In practice, we add a perturbation to the Kohn-Sham potential that is proportional to the projector on the localized states ϕ^I_m of a certain atom I,

$$V_{tot}|\psi^\sigma_{kv}\rangle = V_{KS}|\psi^\sigma_{kv}\rangle + \alpha^I \sum_m |\phi^I_m\rangle\langle\phi^I_m|\psi^\sigma_{kv}\cdot\rangle \tag{17}$$

In this equation α^I represents the "strength" of the perturbation (usually chosen small enough to maintain a linear response regime). The potential in Eq. 17 is the one entering the Kohn-Sham equations of a modified energy functional that yields a α-dependent ground state:

$$E(\alpha^I) = \min_{\gamma} \left\{ E_{DFT}[\gamma] + \alpha^I n^I \right\} \tag{18}$$

where γ is the one-body density matrix. If one defines $E[\{n^I\}] = E(\alpha^I) - \alpha^I n^I$ (where n^I indicates the value of the on-site occupation computed when the minimum in Eq. (18) is achieved), the second derivative $d^2E/d(n^I)^2$ can be computed as $-d\alpha^I/d(n^I)$. In actual calculations, we change α^I on each "Hubbard" atom and, solving the minimization problem of Eq. (18) through modified Kohn-Sham equations, we collect the response of the system in terms of variation in all the n^J. Thus, the quantity that we can directly measure is the response function $\chi_{IJ} = d(n^I)/d\alpha^J$, where I and J are site indexes that label all the Hubbard atoms. The Hubbard U is obtained from the inverse of the response matrix: $U^I = -\chi^{-1}$. This definition is actually not complete. In fact, a term to the energy second derivative, coming from the reorganization (rehybridization) of the electronic wave functions in response to the perturbation of the potential, Eq. (17), would be present even for independent electron systems and is not related to electron-electron interactions. Thus, it must be subtracted out. The final expression of the Hubbard U then results:

$$U^I = (\chi_0^{-1} - \chi^{-1})_{II} \tag{19}$$

where χ_0 measures the response of the system that accounts for the rehybridization of the electronic states upon perturbation. Subtracting this term corresponds to eliminate the hopping between the localized "Hubbard" states and the rest of the system, or to kill the kinetic contribution to the second derivative of the energy as suggested in Ref. [61]. The necessity to compute χ_0 (besides χ) actually dictates the the way these calculations are performed. The first step is a well converged self-consistent calculation of the system of interest with the approximate xc functional of choice. Starting from the ground-state potential and wave functions we then switch the perturbation on and run separate DFT calculations (solving the problem in Eq. (18)) for each Hubbard atom and for each alpha in an interval of values typically centered around 0. The variation of on-site occupation at the *first iteration of the perturbed run* defines χ_0. In fact, at this stage electron-electron interactions have not yet come into play to screen the perturbation, and the response one obtains is that of a system that has the same electronic density of the ground state but the potential frozen to its self-consistent value. Thus it is entirely due to the re-hybridization of the orbitals. The response measured at self-consistency will give, instead, χ. More details about the theoretical aspects of this calculation can be found in Ref [19], and a useful hands-on tutorial with examples on these calculations is linked from the web-page of the Quantum-ESPRESSO package (http://wwww.quantumespresso.org).

The Hubbard U, calculated as in Eq. (19), is screened by other orbitals and atoms: in fact, when perturbing the system the "non-Hubbard" degrees of freedom silently participate to the redistribution of electrons and to the response of "Hubbard" orbitals. To account for this contribution more explicitly an extra row and column are added to the response matrices χ and χ_0 to con-

tain the collective response (computed with a simultaneous perturbation) of these "background" states.

The calculation of J could, in principles, be performed along similar lines, adding a perturbation that effectively couples with the on-site magnetization $m^I = n^{I\uparrow} - n^{I\downarrow}$. However, the energy of a magnetic ground state is not generally quadratic in the magnetization as it is minimized on the domain-border. In other words, the magnetization is often the maximum it could be compatibly with the number of electronic localized states. In these circumstances n^I and m^I are not independent variables and one can only obtain linear combinations of U and J but not solve them separately. A possible way around this problem could be to perturb a state corresponding to a magnetization slightly decreased with respect to its ground state value (e.g., with a penalty functional) in order to allow for the independent variation of n^I and m^I. However, this calculation has not been actually attempted yet and it is impossible to comment on its reliability.

The approach described above renders the LDA+U ab-initio, eliminating any need of semi-empirical evaluations of the interaction parameters in the corrective functional. It also introduces the possibility to re-compute the values of these interactions in dependence of the crystal structure, the magnetic phase, the crystallographic position of atoms, etc. This ability proved critical to improve the predictive capability of LDA+U and the agreement of its results with available experimental data for a broad range of different materials and different conditions. The ability to consistently recompute the interaction parameters significantly improved the description of the structural, electronic and magnetic properties of a variety of transition-metal-containing crystals and was particularly useful in presence of structural [19, 68], magnetic [69] and chemical transformations [70, 71]. In Ref. [69] the use of the "self-consistent" Hubbard U (recomputed for different spin configurations) allowed to predict a ground state for the (Mg,Fe)(Si,Fe)O_3 perovskite with high-spin Fe atoms on both A and B sites, and a pressure-induced spin-state crossover of Fe atoms on the B sites that couples with a noticeable volume reduction, an increase in the quadrupole splitting (consistent with recent x-ray diffraction and Mössbauer spectroscopy measurements) and a marked anomaly in the bulk modulus of the material. These results have far-reaching consequences for understanding the physical behavior of the Earth's lower mantle where this mineral is particularly abundant. The calculation of the Hubbard U also improved the energetics of chemical reactions [72, 73], and electron-transfer processes [74]. Thanks to this calculation, LDA+U has become significantly more versatile, flexible and accurate. A recent extension to the linear response approach has further improved its reliability through the self-consistent calculation of the U from an LDA+U ground state [34, 72]. This improved method, that is mostly useful for systems where the LDA and LDA+U ground states are qualitatively different, is based on a similar calculation to the one described above with a perturbed run performed on a LDA+U ground state for which the "+U" corrective *potential* is frozen to its self-consistent unperturbed value. This guarantees that the +U part does not contribute to the response and, consistently to its definition, the Hubbard U is measured as the curvature of the LDA energy in correspondence of the LDA+U ground state charge density.

4 Energy derivatives

One of the most important advantages brought about by the simple formulation of the LDA+U corrective functional consists in the possibility to easily compute energy derivatives, as forces, stresses, dynamical matrices, etc. These are crucial quantities to identify and characterize the equilibrium structure of materials in different conditions, and to compute various other properties (as, e.g., vibrational spectra) or to account for finite temperature effects in insulators. In this section I will review the calculation of LDA+U forces, stresses, and second derivatives (see Refs. [75,76] for details), that are contained in the total energy, Car-Parrinello MD, and phonon codes of the QUANTUM-ESPRESSO package [63]. In the last subsection I will also offer some comments on the importance of the derivative of the Hubbard interaction. In the remainder of this section I will present the implementation of energy derivatives in a code using a localized basis set of atomic orbitals taken from norm-conserving pseudo-potential. Mathematical complications deriving from the use of other kinds of pseudo-potentials (e.g., ultra-soft [77]) will not be addressed here.

4.1 The Hubbard forces

The Hubbard forces are defined as the derivative of the Hubbard energy with respect to the displacement of atoms. The force acting on the atom α in the direction i is defined as:

$$F^U_{\alpha,i} = -\frac{\partial E_U}{\partial \tau_{\alpha i}} = -\sum_{I,m,m',\sigma} \frac{\partial E_U}{\partial n^{I\sigma}_{m,m'}} \frac{\partial n^{I\sigma}_{m,m'}}{\partial \tau_{\alpha i}} = -\frac{U}{2} \sum_{I,m,m',\sigma} (\delta_{mm'} - 2n^{I\sigma}_{m'm}) \frac{\partial n^{I\sigma}_{m,m'}}{\partial \tau_{\alpha i}} \tag{20}$$

where $\tau_{\alpha i}$ is the component i of the position of atom α in the unit cell, E_U and $n^{I\sigma}_{m,m'}$ are the Hubbard energy and the elements of the occupation matrix as defined in Eq. (3). Based on that definition it is easy to derive the following formula:

$$\frac{\partial n^{I\sigma}_{m,m'}}{\partial \tau_{\alpha i}} = \sum_{k,v} f_{kv} [\frac{\partial}{\partial \tau_{\alpha i}} \left(\langle \varphi^I_{mk} | \psi^\sigma_{kv} \rangle \right) \langle \psi^\sigma_{kv} | \varphi^I_{m'k} \rangle + \langle \varphi^I_{mk} | \psi^\sigma_{kv} \rangle \frac{\partial}{\partial \tau_{\alpha i}} \langle \psi^\sigma_{kv} | \varphi^I_{m'k} \rangle] \tag{21}$$

(k and v being the k-point and band indexes, respectively) so that the problem is reduced to determine the quantities

$$\frac{\partial}{\partial \tau_{\alpha i}} \langle \varphi^I_{mk} | \psi^\sigma_{kv} \rangle \tag{22}$$

for each I, m, m', σ, k and v. Since the Hellmann-Feynman theorem applies, no response of the electronic wave function has to be taken into consideration for first derivatives of the energy. The quantities in Eq. (22) can thus be calculated considering only the derivative of the atomic wave functions:

$$\frac{\partial}{\partial \tau_{\alpha i}} \left\langle \varphi^I_{mk} | \psi^\sigma_{kv} \right\rangle = \left\langle \frac{\partial \varphi^I_{mk}}{\partial \tau_{\alpha i}} | \psi^\sigma_{kv} \right\rangle . \tag{23}$$

Although the atomic occupations are defined on localized atomic orbitals, the product with Kohn-Sham wavefunctions of a given **k**-vector (Eq. (3)) selects the Fourier component of the

atomic wavefunction at the same k-point. This component can be constructed as a Bloch sum of localized atomic orbitals:

$$\varphi^{at}_{i,\mathbf{k},I}(\mathbf{r}) = \frac{1}{\sqrt{N}} \sum_{\mathbf{R}} e^{-i\mathbf{k}\cdot\mathbf{R}} \varphi^{at}_{i,I}(\mathbf{r}-\mathbf{R}-\tau_I) = e^{-i\mathbf{k}\cdot\mathbf{r}} \frac{1}{\sqrt{N}} \sum_{\mathbf{R}} e^{i\mathbf{k}\cdot(\mathbf{r}-\mathbf{R})} \varphi^{at}_{i,I}(\mathbf{r}-\mathbf{R}-\tau_I). \quad (24)$$

In this equation i is the cumulative index for all the quantum numbers $\{n, l, m\}$ defining the atomic state, τ_I is the position of atom I inside the unit cell, N is the total number of k-points and the sum runs over all the N direct lattice vectors $\mathbf{R}$. The second factor in the right hand side of Eq. (24) is a function with the periodicity of the lattice. Its Fourier spectrum thus contains only reciprocal lattice vectors:

$$\varphi^{at}_{i,\mathbf{k},I}(\mathbf{r}) = \frac{1}{\sqrt{\Omega}} \sum_{\mathbf{G}} e^{-i(\mathbf{k}+\mathbf{G})\cdot\mathbf{r}} c_{i,I}(\mathbf{k}+\mathbf{G}). \quad (25)$$

In this equation $\mathbf{G}$ are reciprocal lattice vector ($\mathbf{G}\cdot\mathbf{R} = 2\pi n$), and V is the total volume of N unit cells: $V = N\Omega$). The response to the ionic displacement thus results:

$$\frac{\partial \varphi^{at}_{i,\mathbf{k},I}}{\partial \tau_{\alpha j}} = \delta_{I,\alpha} \frac{i}{\sqrt{\Omega}} \sum_{\mathbf{G}} e^{-i(\mathbf{k}+\mathbf{G})\cdot\mathbf{r}} c_{i,\alpha}(\mathbf{k}+\mathbf{G})(\mathbf{k}+\mathbf{G})_j \quad (26)$$

where $(\mathbf{k}+\mathbf{G})_j$ is the component of the vector along direction j and i is the imaginary unit. Due to the presence of the Kronecker δ in front of its expression, the derivative of the atomic wave function is different from zero only in the case it is centered on the atom which is being displaced. Thus, the derivative in Eq. (23) only contributes to forces on atoms subject to the Hubbard correction. Finite off-site terms in the expression of the forces arise when using ultrasoft pseudopotentials. However this case is not explicitly treated in this chapter.

4.2 The Hubbard stresses

Starting from the the expression for the Hubbard energy functional, given in Eq. (12), we can compute the contribution to the stress tensor as:

$$\sigma^U_{\alpha\beta} = -\frac{1}{\Omega} \frac{\partial E_U}{\partial \varepsilon_{\alpha\beta}} \quad (27)$$

where Ω is the volume of the unit cell (the energy is also given per unit cell), $\varepsilon_{\alpha\beta}$ is the strain tensor that describes the deformation of the crystal:

$$\mathbf{r}_\alpha \rightarrow \mathbf{r'}_\alpha = \sum_\beta (\delta_{\alpha\beta} + \varepsilon_{\alpha\beta}) \mathbf{r}_\beta \quad (28)$$

where $\mathbf{r}$ is the space coordinate internal to the unit cell. The procedure, already developed for the forces (see Eqs. (20), (21)), can be applied to the case of stresses as well. The problem thus reduces to evaluating the derivative

$$\frac{\partial}{\partial \varepsilon_{\alpha\beta}} \langle \varphi^I_{mk} | \psi^\sigma_{kv} \rangle. \quad (29)$$

In order to determine the functional dependence of atomic and KS wavefunctions on the strain we deform the lattice accordingly to Eq. (28) and study how these functions are modified by the distortion. Distortions will be assumed small enough to justify first order expansions of physical quantities around the values they have in the undeformed crystal. To linear order, the distortion of the reciprocal lattice is opposite to that of real space coordinates:

$$\mathbf{k}_\alpha \to \mathbf{k'}_\alpha = \sum_\beta (\delta_{\alpha\beta} - \varepsilon_{\alpha\beta})\mathbf{k}_\beta. \tag{30}$$

Thus, the products $(\mathbf{k}+\mathbf{G})\cdot\mathbf{r}$ appearing in the plane wave (PW) expansion of the wave functions (see, for example, Eq. (25)) remain unchanged.
Let's first study the modification of the atomic wavefunctions taking in consideration the expression given in Eq. (25). The volume appearing in the normalization factor transforms as follows:

$$V \to V' = |1+\varepsilon|V \tag{31}$$

where $|1+\varepsilon|$ is the determinant of the matrix $\delta_{\alpha\beta}+\varepsilon_{\alpha\beta}$ that describes the deformation of the crystal. Applying the strain defined in Eq. (28), to the expression of the $\mathbf{k}+\mathbf{G}$ Fourier component of the atomic wave function one obtains:

$$\begin{aligned} c'_{i,I}(\mathbf{k}'+\mathbf{G}') &= \frac{1}{\sqrt{|1+\varepsilon|}\sqrt{N\Omega}} e^{i(\mathbf{k}'+\mathbf{G}')\cdot\tau'_I} \int_{V'} d\mathbf{r}' e^{i(\mathbf{k}'+\mathbf{G}')\cdot\mathbf{r}'} \varphi^{at}_{i,\mathbf{k},I}(\mathbf{r}') \\ &= \frac{1}{\sqrt{|1+\varepsilon|}} \frac{1}{\sqrt{N\Omega}} e^{i(\mathbf{k}+\mathbf{G})\cdot\tau_I} \int_{V'} d\mathbf{r} e^{i(\mathbf{k}'+\mathbf{G}')\cdot\mathbf{r}} \varphi^{at}_{i,\mathbf{k},I}(\mathbf{r}). \end{aligned} \tag{32}$$

Since the integral appearing in this expression does not change upon distorting the integration volume, defining

$$\tilde{c}_{i,I}(\mathbf{k}+\mathbf{G}) = c_{i,I}(\mathbf{k}+\mathbf{G}) e^{-i(\mathbf{k}+\mathbf{G})\cdot\tau_I} \tag{33}$$

one obtains:

$$\tilde{c}'_{i,I}(\mathbf{k}'+\mathbf{G}') = \frac{1}{\sqrt{|1+\varepsilon|}} \tilde{c}_{i,I}(\mathbf{k}'+\mathbf{G}') = \frac{1}{\sqrt{|1+\varepsilon|}} \tilde{c}_{i,I}((1-\varepsilon)(\mathbf{k}+\mathbf{G})). \tag{34}$$

Thus, the "deformed" atomic wave function results:

$$\begin{aligned} \varphi^{at}_{i,\mathbf{k},I}(\mathbf{r}) &= \frac{1}{\sqrt{\Omega}} \sum_{\mathbf{G}} e^{-i(\mathbf{k}+\mathbf{G})\cdot\mathbf{r}} e^{i(\mathbf{k}+\mathbf{G})\cdot\tau_I} \tilde{c}_{i,I}(\mathbf{k}+\mathbf{G}) \to \\ &\quad \frac{1}{\sqrt{\Omega'}} \sum_{\mathbf{G}'} e^{-i(\mathbf{k}'+\mathbf{G}')\cdot\mathbf{r}'} e^{i(\mathbf{k}'+\mathbf{G}')\cdot\tau'_I} \tilde{c}'_{i,I}(\mathbf{k}'+\mathbf{G}') \\ &= \frac{1}{|1+\varepsilon|} \frac{1}{\sqrt{\Omega}} \sum_{\mathbf{G}} e^{-i(\mathbf{k}+\mathbf{G})\cdot\mathbf{r}} e^{i(\mathbf{k}+\mathbf{G})\cdot\tau_I} \tilde{c}_{i,I}((1-\varepsilon)(\mathbf{k}+\mathbf{G})). \end{aligned} \tag{35}$$

According to the Bloch theorem Kohn-Sham (KS) wavefunctions can be expressed as follows:

$$\psi^\sigma_{kv}(\mathbf{r}) = \frac{1}{\sqrt{V}} \sum_G e^{-i(\mathbf{k}+\mathbf{G})\cdot\mathbf{r}} a^\sigma_{kv}(\mathbf{G}) \tag{36}$$

where

$$a^{\sigma}_{kv}(\mathbf{G}) = \frac{1}{\sqrt{V}} \int_V d\mathbf{r} e^{i(\mathbf{k}+\mathbf{G})\cdot\mathbf{r}} \psi^{\sigma}_{kv}(\mathbf{r}). \tag{37}$$

Upon distorting the lattice as described in Eq. (28) the electronic charge density is expected to rescale accordingly. One can thus imagine the electronic wave function in a point of the strained space to be proportional to its value in the corresponding point of the undistorted lattice:

$$\psi^{\sigma}_{kv}(\mathbf{r}) \rightarrow \psi'^{\sigma}_{k'v}(\mathbf{r}') = \alpha \psi^{\sigma}_{kv}((1-\varepsilon)\mathbf{r}') \tag{38}$$

where the proportionality constant α is to be determined by normalizing the wave function in the strained crystal. By a simple change of the integration variable we obtain:

$$1 = \int_{V'} d\mathbf{r}' |\psi'^{\sigma}_{kv}|^2 = |1+\varepsilon| \int_V d\mathbf{r} |\alpha \psi^{\sigma}_{kv}|^2 = |1+\varepsilon|\alpha^2 \tag{39}$$

from which, choosing α real, we have

$$\alpha = \frac{1}{\sqrt{|1+\varepsilon|}}. \tag{40}$$

Using this result we can determine the variation of the $\mathbf{k}+\mathbf{G}$ Fourier component of ψ^{σ}_{kv} (Eq. (37)). We easily obtain:

$$\begin{aligned} a^{\sigma}_{k'v}(\mathbf{G}') &= \frac{1}{\sqrt{V'}} \int_{V'} d\mathbf{r}' e^{i(\mathbf{k}'+\mathbf{G}')\cdot\mathbf{r}'} \psi'^{\sigma}_{k'v}(\mathbf{r}') \\ &= \frac{1}{\sqrt{|1+\varepsilon|}} \frac{1}{\sqrt{V}} \int_V |1+\varepsilon| d\mathbf{r} e^{i(\mathbf{k}+\mathbf{G})\cdot\mathbf{r}} \frac{1}{\sqrt{|1+\varepsilon|}} \psi^{\sigma}_{kv}(\mathbf{r}) = a^{\sigma}_{kv}(\mathbf{G}). \end{aligned} \tag{41}$$

We can now compute the first order variation of the scalar products between atomic and Kohn-Sham wavefunctions:

$$\langle \varphi^I_{mk} | \psi^{\sigma}_{kv} \rangle' = \frac{1}{\sqrt{|1+\varepsilon|}} \sum_G e^{i(\mathbf{k}+\mathbf{G})\cdot\tau_I} [c^I_{mk}((1-\varepsilon)(\mathbf{k}+\mathbf{G}))]^* a^{\sigma}_{kv}(G). \tag{42}$$

The expression of the derivative follows immediately (for small strains $|1+\varepsilon| \sim 1 + Tr(\varepsilon)$):

$$\begin{aligned} \frac{\partial}{\partial \varepsilon_{\alpha\beta}} \langle \varphi^I_{mk} | \psi^{\sigma}_{kv} \rangle |_{\varepsilon=0} &= -\frac{1}{2}\delta_{\alpha\beta} \langle \varphi^I_{mk} | \psi^{\sigma}_{kv} \rangle \\ &\quad - \sum_G e^{i(\mathbf{k}+\mathbf{G})\cdot\tau_I} a^{\sigma}_{kv}(G) \partial_\alpha [c^I_{mk}(\mathbf{k}+\mathbf{G})]^* (\mathbf{k}+\mathbf{G})_\beta. \end{aligned} \tag{43}$$

The explicit expression of the derivative of the Fourier components of the atomic wavefunctions won't be detailed here. In fact this quantity depends on the particular definition of the atomic orbitals that can vary in different implementations.

4.3 Phonons and second energy derivatives

Many important properties of materials (such as, for example, their vibrational spectrum) are related to the second derivatives of their total energy. It was therefore important to develop

the capability to compute these quantities from first principles for correlated systems. The main linear response technique to obtain second derivatives of the DFT energies is Density Functional Perturbation Theory (DFPT). In this section I present the recent extension of DFPT to the LDA+U energy functional to compute the vibrational spectrum (and other linear-response properties) of materials from their correlated (LDA+U) ground state [76].
DFPT is based on the application of first-order perturbation theory to the self-consistent DFT ground state. I refer to Ref. [78] for an extensive description and for the definition of the notation used here. The displacement of atom L in direction α from its equilibrium position induces a (linear) response $\Delta^\lambda V_{SCF}$ in the KS potential V_{SCF}, leading to a variation $\Delta^\lambda n(\mathbf{r})$ of the charge density ($\lambda \equiv \{L\alpha\}$). The Hubbard potential,

$$V_{Hub} = \sum_{I\sigma m_1 m_2} U^I \left[\frac{\delta_{m_1 m_2}}{2} - n^{I\sigma}_{m_1 m_2}\right] |\phi^I_{m_2}\rangle\langle\phi^I_{m_1}|,$$

also responds to the shift of atomic positions and its variation, to be added to $\Delta^\lambda V_{SCF}$, reads:

$$\begin{aligned}\Delta V_{Hub} &= \sum_{I\sigma m_1 m_2} U^I \left[\frac{\delta_{m_1 m_2}}{2} - n^{I\sigma}_{m_1 m_2}\right] \left[|\Delta\phi^I_{m_2}\rangle\langle\phi^I_{m_1}| + |\phi^I_{m_2}\rangle\langle\Delta\phi^I_{m_1}|\right] \\ &- \sum_{I\sigma m_1 m_2} U^I \Delta n^{I\sigma}_{m_1 m_2} |\phi^I_{m_2}\rangle\langle\phi^I_{m_1}| \end{aligned} \tag{44}$$

where $\Delta\phi^I_m$ is the variation of atomic wavefunctions due to the shift in the position of their centers and

$$\begin{aligned}\Delta n^{I\sigma}_{m_1 m_2} &= \sum_i^{occ} \{\langle\psi^\sigma_i|\Delta\phi^I_{m_1}\rangle\langle\phi^I_{m_2}|\psi^\sigma_i\rangle + \langle\psi^\sigma_i|\phi^I_{m_1}\rangle\langle\Delta\phi^I_{m_2}|\psi^\sigma_i\rangle\} \\ &+ \sum_i^{occ} \{\langle\Delta\psi^\sigma_i|\phi^I_{m_1}\rangle\langle\phi^I_{m_2}|\psi^\sigma_i\rangle + \langle\psi^\sigma_i|\phi^I_{m_1}\rangle\langle\phi^I_{m_2}|\Delta\psi^\sigma_i\rangle\}. \end{aligned} \tag{45}$$

In Eq. (45) $|\Delta\psi^\sigma_i\rangle$ is the linear response of the KS state $|\psi^\sigma_i\rangle$ to the atomic displacement and is to be computed solving the DFPT equations [78].
It is important to note that, in the approach discussed in this section, the derivative of the Hubbard U is assumed to be small and neglected.
Once the self-consistent density response $\Delta n(\mathbf{r})$ is obtained, the dynamical matrix of the system can be computed to calculate the phonon spectrum and the vibrational modes of the crystal. The Hubbard energy contributes to the dynamical matrix with the following term

$$\Delta^\mu(\partial^\lambda E_{\rm Hub}) = \sum_{I\sigma m m'} U^I \left[\frac{\delta_{mm'}}{2} - n^{I\sigma}_{mm'}\right] \Delta^\mu\left(\partial^\lambda n^{I\sigma}_{mm'}\right) - \sum_{I\sigma m m'} U^I \Delta^\mu n^{I\sigma}_{mm'} \partial^\lambda n^{I\sigma}_{mm'} \tag{46}$$

which represents the total derivative of the Hellmann-Feynman Hubbard forces (Eq. (20)). In Eq. 46, the symbol ∂^λ indicates an explicit derivative (usually called "bare") with respect to atomic positions that does not involve linear-response terms (i.e., the variation of the Kohn-Sham wave functions).

When computing phonons in ionic insulators and semiconductor materials a non-analytical term $C^{na}_{I\alpha,J\beta}$ must be added to the dynamical matrix to account for the coupling of longitudinal vibrations with a macroscopic electric field generated by ion displacement [79, 80]. This term, responsible for the LO-TO splitting at $\mathbf{q} = \Gamma$, depends on the Born effective charge tensor $\mathbf{Z}^*$ and the high-frequency dielectric tensors ε^∞: $C^{na}_{I\alpha,J\beta} = \frac{4\pi e^2}{\Omega} \frac{(\mathbf{q}\cdot\mathbf{Z}^*_I)_\alpha (\mathbf{q}\cdot\mathbf{Z}^*_J)_\beta}{\mathbf{q}\cdot\overleftrightarrow{\varepsilon}^\infty\cdot\mathbf{q}}$. The calculation of $\mathbf{Z}^*_{I,\alpha\beta}$ and $\varepsilon^\infty_{\alpha\beta}$ is based on the response of the electronic system to a macroscopic electric field and requires the evaluation of the transition amplitudes between valence and conduction KS states, promoted by the commutator of the KS Hamiltonian with the position operator $\mathbf{r}$, $\langle\psi_{c,\mathbf{k}}|[H_{SCF},\mathbf{r}]|\psi_{v,\mathbf{k}}\rangle$ [81]. A contribution to this quantity from the Hubbard potential must be also included:

$$\langle\psi_{c,\mathbf{k}}|[V^\sigma_{\rm Hub}, r_\alpha]|\psi_{v,\mathbf{k}}\rangle = \sum_{Imm'} U^I \left[\frac{\delta_{mm'}}{2} - n^{I\sigma}_{mm'}\right] \left[-i\langle\psi_{c,\mathbf{k}}|\frac{d}{dk_\alpha}\left(|\phi^I_{m,\mathbf{k}}\rangle\langle\phi^I_{m',\mathbf{k}}|\right)|\psi_{v,\mathbf{k}}\rangle\right] \quad (47)$$

where $\phi^I_{m,\mathbf{k}}$ are Bloch sums of atomic wave functions and k_α represents one of the components of the Bloch vector $\mathbf{k}$.

To summarize, the extension of DFPT to the DFT+U functional requires three terms: the variation of the Hubbard potential $\Delta^\lambda V_{\rm Hub}$ to be added to $\Delta^\lambda V_{\rm SCF}$; the second derivative $\Delta^\mu(\partial^\lambda E_{\rm Hub})$ to be added to the analytical part of the dynamical matrix; and the commutator of the Hubbard potential with the position operator to contribute to the non analytical part of the dynamical matrix. This extension of DFPT, called DFPT+U, was introduced in Ref. [76] and implemented in the PHONON code of the QUANTUM ESPRESSO package [63]. As an example of application I present below the results obtained from the DFPT+U calculation of the vibrational spectrum of MnO and NiO, also discussed in Ref. [76]. The Hubbard U for both systems was computed using the linear-response method discussed in one of the previous sections and resulted 5.25 eV for Mn and 5.77 eV for Ni.

As other transition metal mono-oxides, MnO and NiO crystallize in the cubic rock-salt structure but acquire a rhombohedral symmetry due to their antiferromagnetic order (called AFII) consisting of ferromagnetic planes of cations alternating with opposite spin. Because of the lower symmetry, the directions corresponding to the cubic diagonals lose their equivalence which leads to the splitting of the transverse optical modes (with oxygen and metal sublattices vibrating against each other) around the zone center [82]. Figure 3 compares the phonon dispersions of MnO and NiO obtained from the GGA+U ground state with those resulting from GGA. As it can be observed, the Hubbard correction determines an overall increase in the phonon frequencies for both materials, significantly improving the agreement with available experimental results [83–86]. Moreover, the phonon frequencies computed from the GGA+U ground state lead to a decreased splitting between transverse optical modes compared to GGA, which also is in better agreement with experimental data (although for NiO the sign of the splitting is still controversial [83, 87, 88]).

These results demonstrate that, on the contrary to what is sometimes expected or assumed, electronic correlations have significant effects on the structural and vibrational properties of materials and a corrected functional should be used when calculating properties related to the

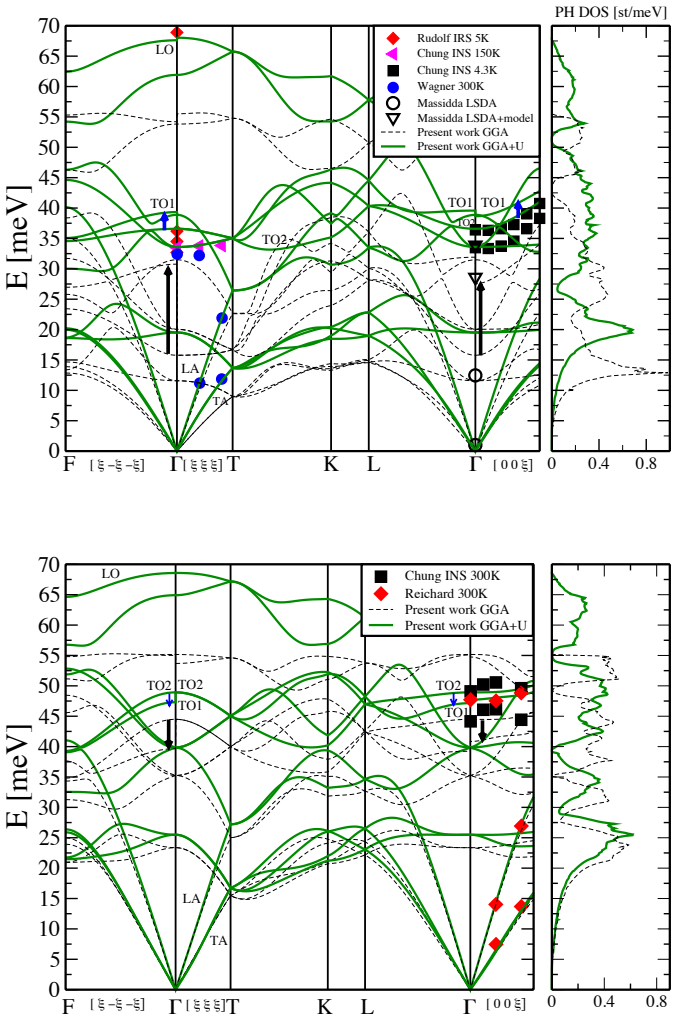

Fig. 3: *(From [76]) The phonon dispersion and the vibrational DOS of MnO (upper panel) and NiO (lower panel), calculated with GGA (dashed lines) and GGA+U (solid thick lines). Blue (black) arrows mark the GGA+U (GGA) magnetic splittings and their sign. Filled symbols: Experimental data [83–86]. Open symbols: Results of other calculations (at zone center) [82].*

vibrational spectrum, such as, e.g., Raman spectroscopy, or when integrating over the Brillouin zone to calculate thermodynamic quantities.

4.4 Derivatives of U

In all the preceding sections discussing the contribution of the Hubbard corrective functional to the first and second derivatives of the energy (forces, stresses, force-constant/dynamical matrices) the effective Hubbard U was held fixed. In fact, its dependence on the atomic positions and/or the cell parameters is usually assumed to be small and neglected. This is, of course, an approximation as the Hubbard U should be thought of as a functional of the charge density as well and thus depends on any factor able to change the electronic structure of the ground state. The validity of this approximation should be tested carefully, case by case. In fact, some recent

works have shown that accounting for the variation of the interaction parameter with the ionic positions and the lattice parameter can be quite important to obtain quantitatively predictive results. In Ref. [68], focused on the properties of the low-spin ground state of $LaCoO_3$ under pressure, the Hubbard U (necessary to reproduce the insulating character of this material and for a better description of its electronic and bonding structure) was recalculated for every volume explored. The structurally-consistent U proved crucial to predict the variation of the structural parameters of the material (lattice spacing, rhombohedral angle, Co-O distance and bond angles) with pressure in good agreement with experimental data. In Ref. [89] the linear-response calculation of the U as a function of the unit cell volume (or the applied pressure) allowed for a precise evaluation of the pressure-induced high-spin to low-spin transition in $(Mg_{1-x}Fe_x)O$ Magnesiowüstite for different Fe concentrations.
The lack of an analytic expression for the Hubbard U makes it very difficult to account for its variation with the atomic position and lattice parameters. However, a recent article [90] has introduced a method to efficiently compute the derivative dU^I/dR^J that allows to capture (at least at first order) the variation of U with the ionic position. This extension is based on the linear-response approach to compute U [19] that was discussed in section 3 and, in particular, on the calculation of the linear-response of the ionic forces to the external perturbation α (see Eq. 17). The same method could be easily generalized to stress and used to evaluate $dU^I/d\epsilon_{\alpha\beta}$. In Ref. [90] this approach is used to account for the variation of U with atomic positions during chemical interactions involving bi-atomic molecules. It is demonstrated that a configuration-dependent effective interaction parameter significantly improves the quantitative description of the potential energy surfaces that the system explores during these processes and eliminates the inaccuracies related to the use of the same (average) value of U for all the configurations, that has become quite common practice in literature. The promising results obtained in this work give hope that analogous implementations could actually be completed for the calculation of stresses and second derivatives and to improve the accuracy of molecular dynamics simulations based on LDA+U [74, 91].

5 The LDA+U+V approach: when covalency is important

5.1 Extended Hubbard model and formulation of LDA+U+V functional

In this section I would like to introduce and briefly discuss one of the latest extensions to the LDA+U functional: the LDA+U+V [34]. This modification is shaped on the "extended" Hubbard model and includes both on-site and inter-site electronic interactions. The extended formulation of the Hubbard Hamiltonian (Eq. (1)) has been considered since the early days of this model [10, 11] and can be expressed as follows:

$$H_{Hub} = t \sum_{\langle i,j\rangle,\sigma} (c^{\dagger}_{i,\sigma} c_{j,\sigma} + h.c.) + U \sum_{i} n_{i,\uparrow} n_{i,\downarrow} + V \sum_{\langle i,j\rangle} n_i n_j \tag{48}$$

where V represents the strength of the interaction between electrons on neighbor atomic sites.

The interest on the extended Hubbard model has been revamped in the last decades by the discovery of high T_c superconductors and the intense research activity focusing around them. Whether the inter-site coupling V has a determinant role in inducing superconductivity is, however, still matter of debate. Although the "resonating valence bond" model [92] predicts a superconducting state (at least within mean-field theory) for a doped Mott insulator with only on-site couplings [93], several numerical studies suggest that the inter-site interaction plays indeed an important role [94, 95] and superconductivity is predicted in a regime with repulsive on-site ($U > 0$) and attractive inter-site ($V < 0$) couplings [96–99]. Several studies have also demonstrated that the relative strength of U and V controls many properties of the ground state of correlated materials, as, for example, the occurrence of possible phase separations [100], the magnetic order [101, 102], the onset of charge-density and spin-density-wave regimes [103]. In Refs. [17, 104] the inter-site coupling (between d states) was recognized to be important to determine a charge-ordered ground state in mixed-valence systems, while in Ref. [105] the extended Hubbard model was used to calculate the Green's function of two particles on a lattice and to refine the Auger core-valence-valence line shapes of solids. More recently, the extended Hubbard model has been used to study the conduction and the structural properties of polymers and carbon nano-structures and the interplay between U and V was shown to control, for example, the dimerization of graphene nanoribbons [106].

Our motivation to include inter-site interactions in the formulation of the corrective Hubbard Hamiltonian was the attempt to define a more flexible and general computational scheme able to account for (rather than just suppress) the possible hybridization of atomic states on different atoms. In order to understand the implementation of the LDA+U+V [34] it is useful to start from the second-quantization expression of the site- and orbital- dependent electronic interaction energy:

$$E_{int} = \frac{1}{2} \sum_{I,J,K,L} \sum_{i,j,k,l} \sum_{\sigma} \langle \phi_i^I \phi_j^J | V_{ee} | \phi_k^K \phi_l^L \rangle \left(n_{ki}^{KI\sigma} n_{lj}^{LJ\sigma'} - \delta_{\sigma\sigma'} n_{kj}^{KJ\sigma} n_{li}^{LI\sigma'} \right) \tag{49}$$

where $n_{ki}^{KI\sigma}$ represent the average values of number operators ($\langle c_i^{I\sigma\dagger} c_k^{K\sigma} \rangle$), to be associated to occupations defined as in Eq. (3). Generalizing the approach described for the on-site case, the E_{Hub} of the DFT+U+V can be obtained from Eq. (49) supposing that a significant contribution to the corrective potential also comes from the interactions between orbitals on couples of distinct sites: $\langle \phi_i^I \phi_j^J | V_{ee} | \phi_k^K \phi_l^L \rangle \rightarrow \delta_{IK}\delta_{JL}\delta_{ik}\delta_{jl} V^{IJ} + \delta_{IL}\delta_{JK}\delta_{il}\delta_{jk} K^{IJ}$. Similarly to the on-site case, the effective inter-site interactions are assumed to be all equal to their atomic averages over the states of the two atoms: $\langle \phi_i^I \phi_j^J | V_{ee} | \phi_k^K \phi_l^L \rangle \rightarrow \delta_{IK}\delta_{JL}\delta_{ik}\delta_{jl} V^{IJ} = \frac{\delta_{IK}\delta_{JL}\delta_{ik}\delta_{jl}}{(2l_I+1)(2l_J+1)} \sum_{i',j'} \langle \phi_{i'}^I \phi_{j'}^J | V_{ee} | \phi_{i'}^I \phi_{j'}^J \rangle$. Within this hypothesis it is easy to derive the following expression ($V^{II} = U^I$):

$$E_{Hub} = \sum_I \frac{U^I}{2} \left[(n^I)^2 - \sum_{\sigma} Tr\left[(\mathbf{n}^{II\sigma})^2 \right] \right] + \sum_{IJ}^{\star} \frac{V^{IJ}}{2} \left[n^I n^J - \sum_{\sigma} Tr(\mathbf{n}^{IJ\sigma} \mathbf{n}^{JI\sigma}) \right] \tag{50}$$

where the star in the sum operator reminds that for each atom I, index J covers all its neighbors up to a given distance (or belonging to a given shell). Eq. (50) uses a generalized formulation of

the occupation matrix (Eq. (3)) to allow for the possibility that the two atomic wave functions involved in its definition belong to different atoms:

$$n^{IJ\sigma}_{m,m'} = \sum_{k,v} f^{\sigma}_{kv} \langle \psi^{\sigma}_{kv} | \phi^{J}_{m'} \rangle \langle \phi^{I}_{m} | \psi^{\sigma}_{kv} \rangle \tag{51}$$

where f^{σ}_{kv} are the occupations of the KS states. In Eq. (51) the indexes m and m' run over the angular momentum manifolds that are subjected to the Hubbard correction on atoms I and J respectively. It is important to notice that the occupation matrix defined in Eq. (51) contains information about all the atoms in the same unit cell and the on-site occupations defined in Eq. (3) correspond to its diagonal blocks ($\mathbf{n}^{I\sigma} = \mathbf{n}^{II\sigma}$). Generalizing the FLL expression of the on-site double-counting term we arrive at the following expression:

$$E_{dc} = \sum_{I} \frac{U^I}{2} n^I (n^I - 1) + \sum_{I,J}^{\star} \frac{V^{IJ}}{2} n^I n^J. \tag{52}$$

Subtracting Eq. (52) from Eq. (50) one finally gets:

$$E_{UV} = E_{Hub} - E_{dc} = \sum_{I,\sigma} \frac{U^I}{2} Tr\left[\mathbf{n}^{II\sigma}\left(\mathbf{1} - \mathbf{n}^{II\sigma}\right)\right] - \sum_{I,J,\sigma}^{*} \frac{V^{IJ}}{2} Tr\left[\mathbf{n}^{IJ\sigma}\mathbf{n}^{JI\sigma}\right]. \tag{53}$$

To better understand the effect of the inter-site part of the energy functional it is convenient to derive the contribution of the extended Hubbard correction to the KS potential (actually corresponding to $\frac{\delta E_{Hub}}{\delta(\psi^{\sigma}_{kv})^*}$):

$$V_{UV}|\psi^{\sigma}_{kv}\rangle = \sum_{I,m,m'} \frac{U^I}{2}\left(\delta_{mm'} - 2n^{II\sigma}_{m'm}\right)|\phi^{I}_{m}\rangle\langle\phi^{I}_{m'}|\psi^{\sigma}_{kv}\rangle - \sum_{I,J,m,m'}^{*} V^{IJ} n^{JI\sigma}_{m'm} |\phi^{I}_{m}\rangle\langle\phi^{J}_{m'}|\psi^{\sigma}_{kv}\rangle. \tag{54}$$

From Eq. (54) it is evident that while the *on-site* term of the potential is attractive for occupied states that are, at most, linear combinations of atomic orbitals of the *same atom* (resulting in on-site blocks of the occupation matrix, $\mathbf{n}^{II\sigma}$, dominant on others), the *inter-site* interaction stabilizes states that are linear combinations of atomic orbitals belonging to *different atoms* (e.g., molecular orbitals, that lead to large off-site blocks, $\mathbf{n}^{JI\sigma}$, of the occupation matrix). Thus, the two interactions are in competition with each other. The detailed balance between these quantities, controlling the character of the resulting ground state (e.g., the degree of localization), is guaranteed by the possibility to compute both parameters simultaneously through the linear-response approach described in [19]. In fact, the inter-site interaction parameters correspond to the off-diagonal terms of the interaction matrix defined in Eq. (19).

It is important to notice that the trace operator in the on-site functional guarantees the invariance of the energy only with respect to rotations of atomic orbitals *on the same atomic site*. In fact, the on-site corrective functional (Eq. (12)) is not invariant for general rotations of the atomic orbital basis set that mixes states from different atoms. In the inter-site term (Eq. (53)), the trace applied to the product of generalized occupation matrices is not sufficient to re-establish this invariance due to the lack of higher order terms (e.g., involving more than two sites) and to

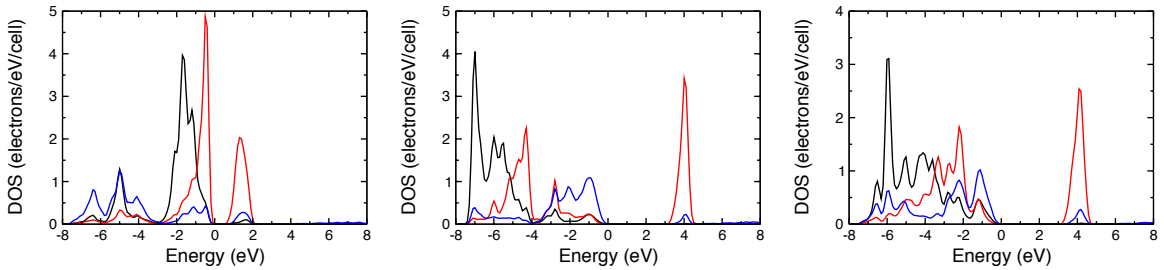

Fig. 4: *(From Ref. [34]) The density of states of NiO obtained with different approximations: GGA (left); GGA+U (center); GGA+U+V (right). The energies were shifted for the top of the valence band to correspond to the zero of the energy in all cases. The black line represents majority spin d states, the red line minority d states, the blue line oxygen p states.*

the use of site- and orbital- averaged interaction parameters. However, the inter-site extension of the corrective functional represents, with respect to the on-site case, a significant step towards general invariance as it contains, at least, some of the multiple-site terms that would be generated by the rotation of on-site ones. Site- and orbital-dependence of the corrective functional are implicitly included in Wannier-function-based implementations of the DFT+U [59, 107, 108] as it becomes evident by re-expressing Wannier functions on the basis of atomic orbitals. The two approaches would thus lead to equivalent results if all the relevant multiple-center interactions parameters are included in the corrective functionals and are computed consistently with the choice of the orbital basis. While on the basis of Wannier-functions the number of relevant electronic interactions to be computed is probably minimal (especially if maximally-localized orbitals are used [58]), the atomic orbital representation, besides providing a more intuitive and transparent scheme to select relevant interactions terms (e.g., based on inter-atomic distances), is more convenient to compute derivatives of the energy as, for example, forces and stresses that are crucial to evaluate the structural properties of systems.

In the implementation of Eq. (53) we have added the possibility for the corrective functional to act on two l manifolds per atom as, for example, the $3s$ and $3p$ orbitals of Si, or the $4s$ and $3d$ orbitals of Ni. The motivation for this extension consists in the fact that different manifolds of atomic states may require to be treated on the same theoretical ground in cases where hybridization is relevant (as, e.g., for bulk Si whose bonding structure is based on the sp^3 mixing of s and p orbitals).

5.2 LDA+U+V case studies: NiO, Si, and GaAs

The new LDA+U+V was first employed to study the electronic and structural properties of NiO, Si and GaAs [34], prototypical representatives of Mott or charge-transfer (NiO) and band insulators (Si and GaAs). The choice of these systems was made to test the ability of the new functional to bridge the description of Mott or charge-transfer insulators (NiO) with that of band insulators (Si and GaAs). In fact, the fundamental gap of a system is the sum of the KS gap and the discontinuity in the KS potential (usually missing in most approximate local or semi-local xc functionals) [109]. Since the main effect of the Hubbard correction consists in

	a	B	E_g
GGA	7.93	188	0.6
GGA+U	8.069	181	3.2
GGA+U+V	7.99	197	3.2
Exp	7.89	166-208	3.1-4.3

Table 1: *The equilibrium lattice parameter (a, in Bohr atomic radii), the bulk modulus (B, in GPa), and the band gap (E_g, in eV) of NiO obtained with different computational approaches: GGA, "traditional" GGA+U (with U only on the d states of Ni) and GGA+U+V with the interaction parameters computed "self-consistently" from the GGA+U+V ground state (see text). Comparison is made with experimental results on all the computed quantities.*

re-introducing the discontinuity of the KS potential at integer occupations it should be able to correct the description of the electronic properties for both classes of materials .

As mentioned in section 4.3, NiO has a cubic rock-salt structure with a rhombohedral symmetry brought about by its AFII ground state. Because of the balance between crystal field and exchange splittings of the d states of Ni, (nominally) occupied by 8 electrons, the material has a finite KS gap with oxygen p states occupying the top of the valence band. This gap, however, severely underestimates the one obtained from photoemission experiments (of about 4.3 eV [110]). LDA+U has been used quite successfully on this material (the spread of results is mostly due to the different values of U used) providing a band gap between 3.0 and 3.5 eV, and quite accurate estimates for both the magnetic moments and the equilibrium lattice parameter [111–113]. DFT+U has also been employed recently to compute the k-edge XAS spectrum of NiO using a novel, parameter-free computational approach [114] that has produced results consistent with experimental data. The use of GW on top of a LDA+U calculation has provided a better estimate of the energy gap compared to LDA+U, even though other details of the density of states were almost unchanged [115].

Besides the on-site U_{Ni}, the LDA+U+V calculations we performed also included the interactions between nearest neighbor Ni and O (V_{Ni-O}) and between second nearest neighbor Ni atoms (V_{Ni-Ni}). The corrective functional included interactions between d states, between d and p and between d and s (on-site). Other interactions were found to have a negligible effect on the results and were neglected. The numerical values of the interaction parameters, all determined through the linear-response approach discussed above, can be found in Ref [34]. Fig. 4 compares the density of states (DOS) of NiO as obtained from GGA, GGA+U and GGA+U+V calculations. It is easy to observe that the GGA+U+V obtains a band gap of the same width as GGA+U, also maintaining the charge-transfer character of the material with O p states at the top of the valence band, as observed in photoemission experiments. As anticipated, the GGA band gap is far too small if compared with experiments and also has Ni d states at the top of the valence band. As expected, the inter-site interactions between Ni and O electrons also results in a more significant overlap in energy between d and p states. In table 1 a comparison is made between experiments and calculations on the equilibrium lattice parameter, bulk modulus and

	U_{ss}	U_{sb}	U_{bs}	U_{bb}	V_{ss}	V_{sb}	V_{bs}	V_{bb}
Si-Si	2.82	3.18	3.18	3.65	1.34	1.36	1.36	1.40
Ga-Ga	3.14	3.56	3.56	4.17				
As-As	4.24	4.38	4.38	4.63				
Ga-As					1.72	1.68	1.76	1.75

Table 2: *Interaction parameters U and V (eV) for Si and GaAs (Ga $3d$ electrons as valence electrons). Inter-site terms are for first-neighbors and the listed values are for the equilibrium lattice parameters found with GGA+U+V. Indexes s and b stand for "standard" (higher l) and "background" (lower l) orbitals respectively.*

energy gap. One can see that while GGA provides the better estimate of the experimental lattice parameter, GGA+U+V improves on the result of GGA+U for the structural parameter and the bulk modulus is also corrected towards the experimental value. Thus, accounting for inter-site interactions does not destroy the quality of the LDA+U description of the ground state of correlated materials and has the potential to improve problematic aspects (e.g., structural properties) counter-balancing the effects of excessive electronic localization.

The application to Si and GaAs is, in some sense, the "proof of fire" for the LDA+U+V approach, as the insulating character of these materials is due to the hybridization of s and p orbitals) from neighbor atoms which leads to the formation of fully occupied bonding states and empty anti-bonding orbitals. The excessive stabilization of atomic orbitals induced by the on-site U suppresses the overlap with neighbor atoms and tends to reduces the gap between valence and conduction states [34]. While providing a quite good description of the ground state properties of these materials, the LDA and GGA functionals drastically underestimate the experimental band gap. A better estimate of the band gap has been obtained using SIC and hybrid functionals [116–118] or with the GW approach based on an LDA [119, 120] or a EXX [121] ground state.

As mentioned above, for the LDA+U+V method to work on these systems both on-site and inter-site interactions had to be computed for s and p states to account for the sp^3 hybridization. Table 2 collects all the interaction parameters computed for Si and GaAs. It is important to notice how, in virtue of the hybridization between s and p states the value of these parameters is almost constant both for on-site and inter-site interactions. In table 3, the equilibrium lattice parameter, the bulk modulus and the band energy gap obtained from GGA, GGA+U and GGA+U+V calculations on Si and GaAs can be directly compared with experimental measurements of the same quantities (we refer to the data collected in the web-database, Ref. [122]). As it can be observed from this table, the (on-site only) GGA+U predicts the equilibrium lattice parameter in better agreement with the experimental value than GGA for GaAs while it overcorrects GGA for Si; however, the bulk modulus is improved with respect to the GGA value only in the case of Si. Due to the suppression of the interatomic hybridization, in both cases, the energy band gap is lowered compared to GGA, further worsening the agreement with experiments. The use of the inter-site correction results in a systematic improvement for the evaluation

	Si			GaAs		
	a	B	E_g	a	B	E_g
GGA	5.479	83.0	0.64	5.774	58.4	0.19
GGA+U	5.363	93.9	0.39	5.736	52.6	0.00
GGA+U+V	5.370	102.5	1.36	5.654	67.7	0.90
Exp.	5.431	98.0	1.12	5.653	75.3	1.42

Table 3: *Comparative results for lattice parameter (a, in Å), bulk modulus (B, in GPa) and energy gap (E_g, in eV).*

of all these quantities. In fact, encouraging the occupations of hybrid states, the inter-site interactions not only enlarge the splittings between populated and empty orbitals (which increases the size of the band gap), but also make bonds shorter (so that hybridization is enhanced) and stronger, thus tuning both the equilibrium lattice parameter and the bulk modulus of these materials to values closer to the experimental results. Calculations on GaAs explicitly included Ga $3d$ states in the valence manifold as this was reported to produce a Ga pseudopotential of better quality [123].

Fig. 5 shows a comparison between the band structures of Si and GaAs obtained with GGA and GGA+U+V. As it can be observed, the increase in the band gap obtained with the "+U+V" correction is the result of an almost uniform shift of electronic energies (downwards for valence, upwards for conduction states) that maintains, however, the overall dispersion pattern.

These results confirm that the extended Hubbard correction is able to significantly improve the description of band insulators and semiconductors with respect to GGA, providing a more accurate estimate of structural and electronic properties. In view of the fact that these systems are normally treated with hybrid functionals or SIC approaches, the good results obtained with LDA+U+V are the demonstration that this approach has similar capabilities and the inaccuracy of the LDA+U (with on-site interactions only) is not inherent to the reference model but rather to the approximations used to obtain its final expression. These results also clarify that, within the single particle KS representation of the N-electron problem, band and Mott insulators can be treated within the same theoretical framework.

The fact that LDA+U+V can be equally accurate in the description of band and Mott insulators opens to the possibility to use it in a broad range of intermediate situations where (Mott) electronic localization coexists with or competes against the hybridization of atomic states from neighbor atoms, (as, e.g., in magnetic impurities in semiconductors or metals, high T_c superconductors, etc), or in the description of processes (such as, e.g., electronic charge transfers excitation [124]) involving a significant shift in the degree of electronic localization. In a recent work [90] LDA+U+V was used to study transition-metal dioxide molecules (e.g., MnO_2); the inclusion of the inter-site interaction was found to be crucial to predict the electronic configuration, the equilibrium structure and its deformations in agreement with experiments. The extended corrective functional has also been used as the starting point of DFT+DMFT calculations [125] and it has been demonstrated that the inclusion of the inter-site interaction in the

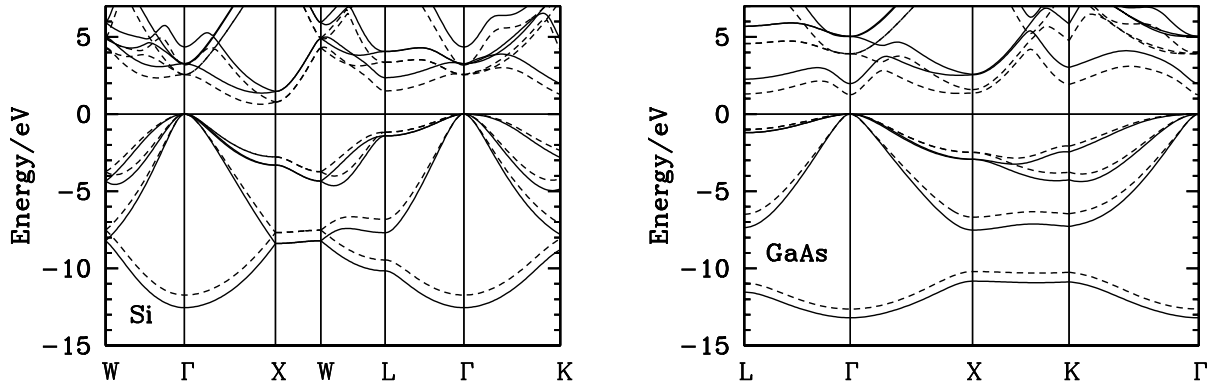

Fig. 5: *(From Ref. [34]) The band structure of Si (left) and GaAs (right). Continuous lines represent GGA+U+V results and dashed lines represent standard GGA results. All energies were shifted so that the top of valence bands are at zero energy.*

local part of the functional (not updated in the inner DMFT calculation) produced results of the same quality of cluster-DMFT but at the same computational cost of standard DMFT calculations.

6 Summary and outlook

Introduced as a simple correction to the DFT exchange-correlation functionals to improve the description of systems with strongly localized electrons, the LDA+U has become one of the most widely used numerical approaches to capture the effects of static electronic correlation. Much of the success this method continues to have in the scientific community is certainly related to the fact that it is quite easy to implement in existing DFT codes, it is very simple to use, allows to easily compute energy derivatives and also carries very limited additional computation costs. These characteristics, as also the availability of a single, easy-to-change interaction parameter to tune the strength of the correction, have encouraged the use of this scheme in a semiempirical way, as a first order, rough assessment of the (mostly qualitative) effects of electronic correlation on the physical properties of a given system. As a consequence, it has been regarded as a semiquantitative approach (as is the Hubbard model it is based on) or, at most, as a first order correction upon which to build higher level, more sophisticated approaches (as, for example, DMFT).

Notwithstanding the inherent limits of this approach (as, e.g., its static character and the consequent inability to capture dynamical, frequency dependent effects), I think it is important to stress the fact that it offers a unique possibility to compute properties related to energy derivatives from the correlated ground state of a system and thus allows to study (albeit in an approximate way) the effects of electronic correlation on equilibrium structural properties, on the dynamic evolution of systems, on phase stability and transitions, on the behavior at finite temperature. It also represents a better starting point than (uncorrected) approximate DFT func-

tionals for higher order corrections or to compute the excitation spectrum of materials (e.g., with TDDFT or GW) thanks to the corrections it introduces to the KS spectrum.
In the present chapter I have illustrated the theoretical foundation of the LDA+U corrective approach, its prerogatives and limits, its historical construction and recent refinements. Above all, I hope I have provided a strong evidence of how this approach can represent a useful framework to capture some effects of electronic correlation and of how relatively minor extensions to its formulation can significantly improve its quantitative predictivity and the quality and numerical efficiency of computational approaches that are based on this simple correction. Therefore, further theoretical work on the "+U" functional (e.g., to include higher order many-body terms or to automatize the calculation of effective interactions) is highly desirable and can have far-reaching consequences for the definition of more accurate and efficient computational approaches able to capture the physics of correlated systems.

References

[1] P. Hohenberg and W. Kohn, Phys. Rev. **136**, B864 (1964)

[2] W. Kohn and L.J. Sham, Phys. Rev. **140**, A1133 (1965)

[3] I.G. Austin and N.F. Mott, Science **168**, 71 (1970)

[4] J.P. Perdew and A. Zunger, Phys. Rev. B **23**, 5048 (1981)

[5] D.M. Ceperley and B.J. Alder, Phys. Rev. Lett. **45**, 566 (1980)

[6] J.P. Perdew and A. Zunger, Phys. Rev. B **23**, 5048 (1981)

[7] J. Hubbard, Proc. Roy. Soc. Lond. A **276**, 238 (1963)

[8] J. Hubbard, Proc. Roy. Soc. Lond. A **277**, 237 (1964)

[9] J. Hubbard, Proc. Roy. Soc. Lond. A **281**, 401 (1964)

[10] J. Hubbard, Proc. Roy. Soc. Lond. A **285**, 542 (1965)

[11] J. Hubbard, Proc. Roy. Soc. Lond. A **296**, 82 (1966)

[12] J. Hubbard, Proc. Roy. Soc. Lond. A **296**, 100 (1966)

[13] V.I. Anisimov and O. Gunnarsson, Phys. Rev. B **43**, 7570 (1991)

[14] V.I. Anisimov, J. Zaanen, and O.K. Andersen, Phys. Rev. B **44**, 943 (1991)

[15] V.I. Anisimov, I.V. Solovyev, M.A. Korotin, M.T. Czyżyk, and G.A. Sawatzky, Phys. Rev. B **48**, 16929 (1993)

[16] I.V. Solovyev, P.H. Dederichs, and V.I. Anisimov, Phys. Rev. B **50**, 16861 (1994)

[17] V.I. Anisimov, F. Aryasetiawan, and A.I. Lichtenstein, J. Phys.: Condens. Matter **9**, 767 (1997)

[18] T.L. Gilber, Phys. Rev. B **12**, 2111 (1975)

[19] M. Cococcioni and S. de Gironcoli, Phys. Rev. B **71**, 035105 (2005)

[20] B. Himmetoglu, R.M. Wentzcovitch, and M. Cococcioni, Phys. Rev. B **84**, 115108 (2011)

[21] A.I. Liechtenstein, V.I. Anisimov, and J. Zaanen, Phys. Rev. B **52**, R5467 (1995)

[22] S.L. Dudarev, G.A. Botton, S.Y. Savrasov, C.J. Humphreys, and A.P. Sutton, Phys. Rev. B **57**, 1505 (1998)

[23] E. Bousquet and N. Spaldin, Phys. Rev. B **82**, 220402 (2010)

[24] T. Jeong and W.E. Pickett, J. Phys.: Condens. Mattter **18**, 6289 (2006)

[25] L. de'Medici, Phys. Rev. B **83**, 205112 (2011)

[26] L. de'Medici, J. Mravlje, and A. Georges, Phys. Rev. Lett. **107**, 256401 (2011)

[27] F. Bultmark, F. Cricchio, O. Grånäs, and L. Nordström, Phys. Rev. B **80**, 035121 (2009)

[28] H. Nakamura, H. Hayashi, N. Nakai, M. Okumura, and M. Machida, Physica C **469**, 908 (2009)

[29] E.R. Ylvisaker, W.E. Pickett, and K. Koepernik, Phys. Rev. B **79**, 035103 (2009)

[30] M. Levy, Phys. Rev. A **26**, 1200 (1982)

[31] Y. Zhao and D. Truhlar, Theoretical Chemistry Accounts: Theory, Computation, and Modeling (Theoretica Chimica Acta) **120**, 215 (2008)

[32] T.M. Willis and H.P. Rooksby, Acta Crystallogr. **6**, 827 (1953)

[33] T. Yagi, T. Suzuki, and S. Akimoto, J. Geophys. Res. **90**, 8784 (1985)

[34] V. Leiria Campo Jr. and M. Cococcioni, J. Phys.: Condens. Matter **22**, 055602 (2010)

[35] L. Hedin, Phys. Rev. **139**, A796 (1965)

[36] B. Lundqvist, Z. Phys. B **6**, 193 (1967)

[37] B. Lundqvist, Z. Phys. B **6**, 206 (1967)

[38] B. Lundqvist, Z. Phys. B **7**, 117 (1968)

[39] L. Hedin and S. Lundqvist, *Solid State Physics*, Vol. 23 (Academic Press, New York, San Francisco, 1969)

[40] R.W. Godby, M. Schlüter, and L.J. Sham, Phys. Rev. Lett. **56**, 2415 (1986)

[41] M.S. Hybertsen and S.G. Louie, Phys. Rev. B **34**, 5390 (1986)

[42] R.W. Godby, M. Schlüter, and L.J. Sham, Phys. Rev. B **35**, 4170 (1987)

[43] R. Del Sole, L. Reining, and R.W. Godby, Phys. Rev. B **49**, 8024 (1994)

[44] S.V. Faleev, M. van Schilfgaarde, and T. Kotani, Phys. Rev. Lett. **93**, 126406 (2004)

[45] W. Metzner and D. Vollhardt, Phys. Rev. Lett. **62**, 324 (1989)

[46] E. Müller-Hartmann, Z. Phys. B **74** 507 (1989)

[47] U. Brandt and C. Mielsch, Z. Phys. B, **75**, 365 (1989)

[48] V. Janis, Z. Phys. B **83**, 227 (1991)

[49] A. Georges and G. Kotliar, Phys. Rev. B **45**, 6479 (1992)

[50] A. Georges, G. Kotliar, W. Krauth, and M.J. Rozenberg, Rev. Mod. Phys. **68**, 13 (1996)

[51] H. Jiang, R.I. Gomez-Abal, P. Rinke, and M. Scheffler, Phys. Rev. B **82**, 045108 (2010)

[52] C.C. Lee, H.C. Hsueh, and W. Ku, Phys. Rev. B **82**, 081106 (2010)

[53] A.G. Petukhov, I.I. Mazin, L. Chioncel, and A.I. Liechtenstein, Phys. Rev. B **67**, 153106 (2003)

[54] M.T. Czyźyk and G.A. Sawatzky, Phys. Rev. B **49**, 14211 (1994)

[55] Y.-M. Quan, L.-J. Zou, D.-Y. Liu, and H.-Q. Lin, `http://arxiv.org/abs/arXiv:1106.3487`

[56] J. Yoshitake and Y. Motome, `http://arxiv.org/abs/arXiv:1105.5757`

[57] E. Pavarini, E. Koch, D. Vollhardt, and A. Lichtenstein (eds.), *The LDA+DMFT approach to strongly correlated materials*, Reihe Modeling and Simulation, Vol. 1 (Forschungszentrum Jülich, 2011) `http://www.cond-mat.de/events/correl11`

[58] N. Marzari and D. Vanderbilt, Phys. Rev. B **56**, 12847 (1997)

[59] V.V. Mazurenko, S.L. Skornyakov, A.V. Kozhevnikov, F. Mila, and V.I. Anisimov, Phys. Rev. B **75**, 224408 (2007)

[60] D.D. O'Regan, N.D.M. Hine, M.C. Payne, and A.A. Mostofi, *Projector self-consistent DFT+U using non-orthogonal generalized Wannier functions*, in D.D. O'Regan, *Optimized Projections for the Ab Initio Simulation of Large and Strongly Correlated Systems*, (Springer, Heidelberg, 2012)

[61] W.E. Pickett, S.C. Erwin, and E.C. Ethridge, Phys. Rev. B **58**, 1201 (1998)

[62] F. Aryasetiawan, M. Imada, A. Georges, G. Kotliar, S. Biermann, and A.I. Lichtenstein, Phys. Rev. B **70**, 195104 (2004)

[63] P. Giannozzi, S. Baroni, N. Bonini, M. Calandra, R. Car, C. Cavazzoni, D. Ceresoli, G.L Chiarotti, M. Cococcioni, I. Dabo, A. Dal Corso, S. de Gironcoli, S. Fabris, G. Fratesi, R. Gebauer, U. Gerstmann, C. Gougoussis, A. Kokalj, M. Lazzeri, L. Martin-Samos, N. Marzari, F. Mauri, R. Mazzarello, S. Paolini, A. Pasquarello, L. Paulatto, C. Sbraccia, S. Scandolo, G. Sclauzero, A.P. Seitsonen, A. Smogunov, P. Umari, and R.M. Wentzcovitch, *QUANTUM ESPRESSO: a modular and open-source software project for quantum simulations of materials*, J. Phys.: Condens. Matter **21**, 395502 (2009)

[64] M.T. Czyżyk and G.A. Sawatzky, Phys. Rev. B **49**, 14211 (1994)

[65] J.P. Perdew, R.G. Parr, M. Levy, and J.L. Balduz, Phys. Rev. Lett. **49**, 1691 (1982)

[66] J.P. Perdew and M. Levy, Phys. Rev. Lett. **51**, 1884 (1983)

[67] I. Dabo, A. Ferretti, N. Poilvert, Y. Li, N. Marzari, and M. Cococcioni, Phys. Rev. B **82**, 115121 (2010)

[68] H. Hsu, K. Umemoto, M. Cococcioni, and R.M. Wentzcovitch, Phys. Rev. B **79**, 125124 (2009)

[69] H. Hsu, P. Blaha, M. Cococcioni, and R.M. Wentzcovitch, Phys. Rev. Lett. **106**, 118501 (2011)

[70] F. Zhou, C.A. Marianetti, M. Cococcioni, D. Morgan, and G. Ceder, Phys. Rev. B **69**, 201101(2004)

[71] F. Zhou, M. Cococcioni, C.A. Marianetti, D. Morgan, and G. Ceder Phys. Rev. B **70**, 235121 (2004)

[72] H.J. Kulik, M. Cococcioni, D.A. Scherlis, and N. Marzari, Phys. Rev. Lett. **97**, 103001 (2006)

[73] D.A. Scherlis, M. Cococcioni, H.-L. Sit, and N. Marzari, J. Phys. Chem. B **111**, 7384

[74] H.-L. Sit, M. Cococcioni, and N. Marzari. Phys. Rev. Lett. **97**, 028303 (2006)

[75] M. Cococcioni, Reviews in Mineralogy and Geochemistry **71**, 147 (2010)

[76] A. Floris, S. de Gironcoli, E.K.U. Gross, and M. Cococcioni, under review in Physical Review Letters, 2011.

[77] D. Vanderbilt, Phys. Rev. B **41**, 7892 (1990)

[78] S. Baroni, S. de Gironcoli, A. Dal Corso, and P. Giannozzi, Rev. Mod. Phys. **73**, 515 (2001)

[79] M. Born and K. Huang, *Dynamical Theory of Crystal Lattices* (Oxford University Press, Oxford, 1954)

[80] W. Cochran and R.A. Cowley, J. Phys. Chem. Solids **23**, 447 (1962)

[81] P. Giannozzi, S. de Gironcoli, P. Pavone, and S. Baroni, Phys. Rev. B **43**, 7231 (1991)

[82] S. Massidda, M. Posternak, A. Baldereschi, and R. Resta, Phys. Rev. Lett. **82**, 430 (1999)

[83] E.M.L. Chung, D. McK. Paul, G. Balakrishnan, M.R. Lees, A. Ivanov, and M. Yethiraj, Phys. Rev. B **68**, 140406 (2003)

[84] T. Rudolf, Ch. Kant, F. Mayr, and A. Loidl, Phys. Rev. B **77**, 024421 (2008)

[85] B.C. Haywood and M.F. Collins, J. Phys. C: Solid State Physics **4**, 1299 (1971)

[86] W. Reichardt, V. Wagner, and W. Kress, J. Phys. C: Solid State Physics **8**, 3955 (1975)

[87] W. Luo, P. Zhang, M.L. Cohen, Solid State Commun. **142**, 504 (2007)

[88] M.T. Hutchings and E.J. Samuelsen, Phys. Rev. B **6**, 3447 (1972)

[89] T. Tsuchiya, R.M. Wentzcovitch, C.R.S. da Silva, and S. de Gironcoli, Phys. Rev. Lett. **96**, 198501 (2006)

[90] H.J. Kulik and N. Marzari, J. Chem. Phys. **135**, 194105 (2011)

[91] P.H.-L. Sit, M. Cococcioni, and N. Marzari, J. Electroanalytical Chem. **607**, 107 (2007)

[92] P.W. Anderson, Science **235**, 1196 (1987)

[93] P.W. Anderson, G. Baskaran, Z. Zou, and T. Hsu, Phys. Rev. Lett. **58**, 2790 (1987)

[94] M. Imada. J. Phys. Soc. Jpn. **60**, 2740 (1991)

[95] J.E. Hirsch, E. Loch, D.J. Scalapino, and S. Tang, Physica C **153-155**, 549 (1988)

[96] J.S. Thakur and M.P. Das, Int. J. Mod. Phys. B **21**, 2371 (2007)

[97] R. Jursa, S. Wermbter, and G. Czycholl, Proceedings of the 21^{st} International Conference on Low Temperature Physics, p. 613, (1996)

[98] A. Szabo and N. S. Ostlund, *Modern Quantum Chemistry* (Dover, 1996)

[99] E.V.L. de Mello, Brazilian J. Phys **29**, 551 (1999)

[100] F. Mancini, F.P. Mancini, and A. Naddeo, Europ. Phys. J. B **68**, 309 (2009)

[101] S. Morohoshi and Y. Fukumoto, J. Phys. Soc. Jpn **77**, 105005 (2008)

[102] T. Watanabe, H. Yokoyama, Y. Tanaka, and J. Inoue, J. Phys. Chem. Sol. **69**, 3372 (2008)

[103] P.G.J. van Dongen, Phys. Rev. B **49**, 7904 (1994)

[104] V.I. Anisimov, I.S. Elfimov, N. Hamada, and K. Terakura, Phys. Rev. B **54**, 4387 (1996)

[105] C. Verdozzi and M. Cini, Phys. Rev. B **51**, 7412 (1995)

[106] L.Y. Zhu and W.Z. Wang, J. Phys.: Cond Matter **18**, 6273 (2006)

[107] F. Lechermann, A. Georges, A. Poteryaev, S. Biermann, M. Posternak, A. Yamasaki, and O. K. Andersen. Phys. Rev. B **74**, 125120 (2006)

[108] T. Miyake and F. Aryasetiawan, Phys. Rev. B **77**, 085122 (2008)

[109] R.M. Dreizler and E.K.U. Gross, *Density Functional Theory* (Springer, Heidelberg, 1990)

[110] G.A. Sawatzky and J.W. Allen, Phys. Rev. Lett. **53**, 2339 (1984)

[111] S.L. Dudarev, L.-M. Peng, S.Y. Savrasov, and J.-M. Zuo, Phys. Rev. B **61**, 2506 (2000)

[112] O. Bengone, M. Alouani, P. Blöchl, and J. Hugel, Phys. Rev. B **62**, 16392 (2000)

[113] A. Rohrbach, J. Hafner, and G. Kresse, Phys. Rev. B **69**, 075413 (2004)

[114] C. Gougoussis, M. Calandra, A. Seitsonen, Ch. Brouder, A. Shukla, and F. Mauri, Phys. Rev. B **79**, 045118 (2009)

[115] S. Kobayashi, Y. Nohara, S. Yamamoto, and T. Fujiwara, Phys. Rev. B **78**, 155112 (2008)

[116] M. Städele, M. Moukara, J. A. Majewski, P. Vogl, and A. Görling, Phys. Rev. B **59**, 10031 (1999)

[117] H.-V. Nguyen and S. de Gironcoli, Phys. Rev. B **79**, 205114 (2009)

[118] J. Heyd, J.E. Peralta, G.E. Scuseria, and R.L. Martin, J. Chem. Phys. **123**, 174101 (2005)

[119] M. Rohlfing, P. Krüger, and J. Pollmann, Phys. Rev. B **48**, 17791 (1993)

[120] W.G. Aulbur, L.Jöonson, and J.W. Wilkins, *Quasiparticle Calculations in Solids*, Solid State Phys. **54**, 1 (1999)

[121] W.G. Aulbur, M. Städele, and A. Görling, Phys. Rev. B **62**, 7121 (2000)

[122] Semiconductor physical properties database `http://www.ioffe.ru/SVA/NSM/Semicond/`

[123] O. Anatole von Lilienfeld and P.A. Schultz, Phys. Rev. B **77**, 115202 (2008)

[124] B. Himmetoglu, A. Marchenko, I. Dabo, and M. Cococcioni, *Role of electronic localization in the phosphorescence of iridium sensitizing dyes*, to be submitted to J. Chem. Phys.

[125] A.S. Belozerov, M.A. Korotin, V.I. Anisimov, and A.I. Poteryaev, Phys. Rev. B **85**, 045109 (2012)

5 The Gutzwiller Density Functional Theory

Jörg Bünemann
Computational Physics Group
BTU Cottbus

Contents

E. Pavarini, E. Koch, F. Anders, and M. Jarrell
Correlated Electrons: From Models to Materials
Modeling and Simulation Vol. 2
Forschungszentrum Jülich, 2012, ISBN 978-3-89336-796-2
http://www.cond-mat.de/events/correl12

1 Introduction

1.1 The electronic many-particle problem

The fundamental Hamiltonian for the electrons in solid-state theory has, in atomic units, the well-known form

$$\begin{aligned} \hat{H}_{\rm el} &= \sum_s \int \mathrm{d}^3 r\, \hat{\psi}_s^\dagger(\boldsymbol{r}) \left(-\frac{1}{2}\Delta_{\boldsymbol{r}} + V(\boldsymbol{r}) \right) \hat{\psi}_s(\boldsymbol{r}) \\ &\quad + \frac{1}{2} \sum_{s,s'} \int \mathrm{d}^3 r \int \mathrm{d}^3 r'\, \hat{\psi}_s^\dagger(\boldsymbol{r}) \hat{\psi}_{s'}^\dagger(\boldsymbol{r}') \frac{1}{|\boldsymbol{r}-\boldsymbol{r}'|} \hat{\psi}_{s'}(\boldsymbol{r}') \hat{\psi}_s(\boldsymbol{r}) \,. \end{aligned} \tag{1}$$

In these lecture notes, we assume that the potential $V(\boldsymbol{r})$, generated by the atomic nuclei, is perfectly lattice periodic. The operators $\hat{\psi}_s^{(\dagger)}(\boldsymbol{r})$ annihilate (create) an electron at the real-space position $\boldsymbol{r}$ with spin $s = \uparrow, \downarrow$. Despite the fact that the Hamiltonian (1) only describes the electronic degrees of freedom, the calculation of the electrons' properties poses a difficult many-particle problem which cannot be solved in general. The strategies to deal with the many-body problem (1) can be grouped into two main categories.

i) *Model-system approaches*:

In order to explain experiments, it is often sufficient to take into account only a limited number of degrees of freedom in the Hamiltonian (1). Therefore, the full problem is replaced by a simpler 'model Hamiltonian' which describes certain electronic properties of a material. Celebrated examples are the Heisenberg model for magnetic insulators and the BCS Hamiltonian for superconductors. In many-particle theory in general, and for transition metals and their compounds in particular, multi-band Hubbard Hamiltonians provide the standard models, see Sec. 1.3.

ii) *Ab-initio approaches*:

In order to cope with the full Hamiltonian (1), one has to resort to approximations which are necessarily cruder than those designed for the investigation of much simpler model systems. The most frequently used *ab-initio* approach is the Local-Density Approximation (LDA) to Density-Functional Theory (DFT), see Sec. 1.2.

1.2 Density-Functional Theory (DFT)

Density-Functional Theory (DFT) is based on a theorem by Hohenberg and Kohn [1]. It states that there exists a universal functional $W[n(\boldsymbol{r})]$ of the electronic density $n(\boldsymbol{r})$ such that

$$E[n(\boldsymbol{r})] = \int \mathrm{d}^3 r\, V(\boldsymbol{r}) n(\boldsymbol{r}) + W[n(\boldsymbol{r})] \,, \tag{2}$$

has its minimum, $E_0 \equiv E[n_0(\boldsymbol{r})]$, at the exact ground-state density $n_0(\boldsymbol{r})$ of the Hamiltonian (1) and E_0 is the corresponding ground-state energy. Since it is impossible to determine

the functional $W[n(\boldsymbol{r})]$ for many-particle systems exactly, it is necessary to develop reasonable approximations for it. Usually, one writes

$$W[n(\boldsymbol{r})] = T[n(\boldsymbol{r})] + \frac{1}{2}\int \mathrm{d}^3r \int \mathrm{d}^3r' \, \frac{n(\boldsymbol{r})n(\boldsymbol{r}')}{|\boldsymbol{r}-\boldsymbol{r}'|} + E_{\mathrm{xc}}[n(\boldsymbol{r})] \ , \tag{3}$$

where $T[n(\boldsymbol{r})]$ is the kinetic-energy functional and $E_{\mathrm{xc}}[n(\boldsymbol{r})]$ is the exchange-correlation functional, which contains all Coulomb-energy contributions apart from the Hartree term that was separated in (3). Both functionals are unknown. Approximate expressions for $T[n(\boldsymbol{r})]$ and $E_{\mathrm{xc}}[n(\boldsymbol{r})]$ are usually derived by considering a free electron gas. The kinetic energy of such electrons in the Hartree-Fock approximation is $\sim n^{5/3}$ where n is the density of the homogeneous electron gas. Therefore, a common approximation for the kinetic-energy functional in (3) is

$$T[n(\boldsymbol{r})] = \frac{3}{10m}(3\pi^2)^{2/3}\int \mathrm{d}^3r \; n(\boldsymbol{r})^{5/3} \ . \tag{4}$$

In the same way, one may approximate the exchange-correlation potential in the form

$$E_{\mathrm{xc}}[n(\boldsymbol{r})] = -\int \mathrm{d}^3r \frac{3e^2}{4\pi}(3\pi)^{1/3} n(\boldsymbol{r})^{4/3} \ . \tag{5}$$

To work with the energy functionals (4) and (5) is a simple example of a Local-Density Approximation (LDA) because only the local density appears in $W[n(\boldsymbol{r})]$ and corrections, e.g., involving gradients $\nabla n(\boldsymbol{r})$, are absent.

The DFT in a LDA, as introduced so far, provides an approximate way to determine the ground-state energy and the electronic density in the ground state. These quantities are of interest if one aims, e.g., to determine the ground-state lattice structure or lattice parameters of a material. Most practical applications of the DFT, however, rely on an additional concept, the *Kohn-Sham scheme*. This scheme is based on the assumption that, for each system of interacting particles, there exists an effective single-particle Hamiltonian

$$\begin{aligned} \hat{H}_0^{\mathrm{eff}} \ = \ & \sum_s \int \mathrm{d}^3r \, \hat{\psi}_s^\dagger(\boldsymbol{r}) \left(-\frac{1}{2}\Delta_{\boldsymbol{r}} + V(\boldsymbol{r}) \right) \hat{\psi}_s(\boldsymbol{r}) \\ & + \sum_s \int \mathrm{d}^3r \, \hat{\psi}_s^\dagger(\boldsymbol{r}) \left(\int \mathrm{d}^3r' \frac{n(\boldsymbol{r}')}{|\boldsymbol{r}-\boldsymbol{r}'|} + V_{\mathrm{xc}}^{\mathrm{KS}}[n(\boldsymbol{r})] \right) \hat{\psi}_s(\boldsymbol{r}) \ , \end{aligned} \tag{6}$$

which has the same ground-state density $n_0(\boldsymbol{r})$ as the original many-particle Hamiltonian (1). In general, one cannot prove rigorously that such a single-particle Hamiltonian exists; this poses the *v-representability* problem. If a system is v-representable, however, the Kohn-Sham potential in (6) is given by

$$V_{\mathrm{xc}}^{\mathrm{KS}}[n(\boldsymbol{r})] = \frac{\partial}{\partial \tilde{n}(\boldsymbol{r})} \Big(T\left[\tilde{n}(\boldsymbol{r})\right] - T'\left[\tilde{n}(\boldsymbol{r})\right] + E_{\mathrm{xc}}\left[\tilde{n}(\boldsymbol{r})\right] \Big) \Big|_{\tilde{n}(\boldsymbol{r})=n(\boldsymbol{r})} \ , \tag{7}$$

where $T'[n(\boldsymbol{r})]$ is the minimum kinetic energy of free non-interacting particles with the density distribution $n(\boldsymbol{r})$. Usually one assumes $T'[n(\boldsymbol{r})] = T[n(\boldsymbol{r})]$ such that both terms cancel each other in (7).

For our formulation of a self-consistent *Gutzwiller Density-Functional Theory* (GDFT) in Sec. 5, it will be convenient to introduce a basis of local (Wannier) orbitals $\phi_{i,\sigma}(\boldsymbol{r})$, which are centered around the L lattice sites i and carry the spin-orbital index σ. With this basis, the Hamiltonian (6) can be written as

$$\hat{H}_0^{\rm eff} = \sum_{i,j} \sum_{\sigma,\sigma'} t_{i,j}^{\sigma,\sigma'}[n(\boldsymbol{r})]\ \hat{c}_{i,\sigma}^\dagger \hat{c}_{j,\sigma'}\ . \tag{8}$$

Here, the *electron transfer* or *hopping* parameters

$$t_{i,j}^{\sigma,\sigma'}[n(\boldsymbol{r})] \equiv \int {\rm d}^3 r \phi_{i,\sigma}^*(\boldsymbol{r}) \left(-\frac{1}{2}\Delta_{\boldsymbol{r}} + V(\boldsymbol{r}) + \int {\rm d}^3 r' \frac{n(\boldsymbol{r}')}{|\boldsymbol{r}-\boldsymbol{r}'|} + V_{\rm xc}^{\rm KS}[n(\boldsymbol{r})] \right) \phi_{j,\sigma}(\boldsymbol{r}), \tag{9}$$

depend on the particle density

$$n(\boldsymbol{r}) = \sum_{i,j} \sum_{\sigma,\sigma'} \phi_{i,\sigma}^*(\boldsymbol{r}) \phi_{j,\sigma'}(\boldsymbol{r}) \langle \hat{c}_{i,\sigma}^\dagger \hat{c}_{j,\sigma'} \rangle_{\Psi_0}\ , \tag{10}$$

where $|\Psi_0\rangle$ is the ground state of (8),

$$\hat{H}_0^{\rm eff} |\Psi_0\rangle = E_0 |\Psi_0\rangle\ . \tag{11}$$

At least in principle, the self-consistent solution of the *Kohn-Sham equations* (8)-(11) is the central part of most DFT applications in solid-state physics. Note, however, that actual numerical implementations of the DFT usually do not work with Wannier functions, but use atomic orbitals or plane waves as basis sets.

Despite the rather drastic approximations which have led to the Kohn-Sham equations, a comparison of theoretical and experimental results has revealed a remarkable agreement for a large number of materials. Therefore, the LDA has become the most important tool for the investigation of electronic properties in solid-state physics. There are, however, well-known problems with certain classes of materials. For example, band gaps in insulators or semiconductors are usually found to be significantly smaller in DFT than in experiment. Even bigger discrepancies arise for materials with strong local Coulomb interactions. These are, in particular, transition metals, lanthanides, and their respective compounds. Such systems have been investigated in the past mostly based on model systems, which we discuss in the following section.

1.3 Multi-band Hubbard models

We distinguish *localised* orbitals, $\sigma \in \ell$, and *delocalised* orbitals, $\sigma \in {\rm d}$, where the localised orbitals are those which require a more sophisticated treatment of the local Coulomb interaction than provided by the LDA. The natural starting point for such a treatment is a multi-band Hubbard model of the form

$$\hat{H}_{\rm H} = \hat{H}_0 + \sum_i \hat{H}_{i;{\rm c}}\ , \tag{12}$$

$$\hat{H}_0 \equiv \sum_{i\neq j} \sum_{\sigma,\sigma'} t_{i,j}^{\sigma,\sigma'} \hat{c}_{i,\sigma}^\dagger \hat{c}_{j,\sigma'} + \sum_i \sum_{\sigma,\sigma'\in {\rm d}} \epsilon_i^{\sigma,\sigma'} \hat{c}_{i,\sigma}^\dagger \hat{c}_{i,\sigma'}\ , \tag{13}$$

$$\hat{H}_{i;{\rm c}} \equiv \sum_{\sigma,\sigma'\in\ell} \epsilon_i^{\sigma,\sigma'} \hat{c}_{i,\sigma}^\dagger \hat{c}_{i,\sigma'} + \sum_{\sigma_1,\sigma_2,\sigma_3,\sigma_4\in\ell} U_i^{\sigma_1,\sigma_2,\sigma_3,\sigma_4} \hat{c}_{i,\sigma_1}^\dagger \hat{c}_{i,\sigma_2}^\dagger \hat{c}_{i,\sigma_3} \hat{c}_{i,\sigma_4}\ . \tag{14}$$

#	Atomic eigenstate $\vert\Gamma\rangle$	Symmetry	energy E_Γ
1	$\vert\uparrow,\uparrow\rangle$	${}^3A_2$	$U'-J$
2	$(\vert\uparrow,\downarrow\rangle+\vert\downarrow,\uparrow\rangle)/\sqrt{2}$	${}^3A_2$	$U'-J$
3	$\vert\downarrow,\downarrow\rangle$	${}^3A_2$	$U'-J$
4	$(\vert\uparrow,\downarrow\rangle-\vert\downarrow,\uparrow\rangle)/\sqrt{2}$	${}^1E$	$U'+J$
5	$(\vert\uparrow\downarrow,0\rangle-\vert 0,\uparrow\downarrow\rangle)/\sqrt{2}$	${}^1E$	$U-J_{\rm C}$
6	$(\vert\uparrow\downarrow,0\rangle+\vert 0,\uparrow\downarrow\rangle)/\sqrt{2}$	${}^1A_1$	$U+J_{\rm C}$

Table 1: *Two-particle eigenstates with symmetry specifications and energies.*

This model contains a general two-particle interaction in the localised orbitals, and fixed hopping parameters, $t_{i,j}^{\sigma,\sigma'}$, and orbital energies, $\epsilon_i^{\sigma,\sigma'}=t_{i,i}^{\sigma,\sigma'}$. Since the parameters $t_{i,j}^{\sigma,\sigma'}$ are usually derived from a DFT calculation, see Eq. (9), they already contain the Coulomb interaction on a DFT level. For the localised orbitals this means that, through the on-site energies $\epsilon_i^{\sigma,\sigma'}$, the Coulomb interaction appears twice in the Hamiltonian $\hat{H}_{i;\mathrm{c}}$. We will address this so-called *double-counting problem* in Sec. 5.

In the context of the Gutzwiller variational theory we need the eigenstates $\vert\Gamma\rangle_i$ and the eigenvalues $E_{i,\Gamma}$ of the Hamiltonian $\hat{H}_{i;\mathrm{c}}$. They allow us to write $\hat{H}_{i;\mathrm{c}}$ as

$$\hat{H}_{i;\mathrm{c}}=\sum_{\Gamma}E_{i,\Gamma}\hat{m}_{i,\Gamma}\quad,\quad \hat{m}_{i,\Gamma}\equiv\vert\Gamma\rangle_{i\,i}\langle\Gamma\vert\ . \tag{15}$$

As a simple example, we consider a model with two degenerate e_{g}-orbitals in a cubic environment. In this case we may set $\epsilon_i^{\sigma,\sigma'}=0$, and the local Hamiltonian then has the form

$$\begin{aligned}\hat{H}_{i;\mathrm{c}} \;=\; & U\sum_{e}\hat{n}_{e,\uparrow}\hat{n}_{e,\downarrow}+U'\sum_{s,s'}\hat{n}_{1,s}\hat{n}_{2,s'}-J\sum_{s}\hat{n}_{1,s}\hat{n}_{2,s} \\ & +J\sum_{s}\hat{c}^{\dagger}_{1,s}\hat{c}^{\dagger}_{2,\bar{s}}\hat{c}_{1,\bar{s}}\hat{c}_{2,s}+J_C\Big(\hat{c}^{\dagger}_{1,\uparrow}\hat{c}^{\dagger}_{1,\downarrow}\hat{c}_{2,\downarrow}\hat{c}_{2,\uparrow}+\hat{c}^{\dagger}_{2,\uparrow}\hat{c}^{\dagger}_{2,\downarrow}\hat{c}_{1,\downarrow}\hat{c}_{1,\uparrow}\Big)\ ,\end{aligned} \tag{16}$$

where $e=1,2$ labels the e_{g}-orbitals, $s=\uparrow,\downarrow$ is the spin index and we use the convention $\bar{\uparrow}\equiv\downarrow$, $\bar{\downarrow}\equiv\uparrow$. For e_{g}-orbitals, only two of the three parameters in (16) are independent since the symmetry relations $U'=U-2J$ and $J=J_C$ hold. In our model, we have four spin-orbital states $\sigma=(e,s)$ per atom, leading to a $2^4=16$-dimensional atomic Hilbert space. All eigenstates $\vert\Gamma\rangle_i$ of $\hat{H}_{i;\mathrm{c}}$ with particle numbers $N\neq 2$ are simple Slater determinants of spin-orbital states $\vert\sigma\rangle$ and their energies are

$$\begin{aligned}&E_\Gamma=0 && (N=0,1)\ ,\\ &E_\Gamma=U+2U'-J && (N=3)\ ,\\ &E_\Gamma=2U+4U'-2J && (N=4)\ .\end{aligned} \tag{17}$$

The two-particle eigenstates are slightly more complicated because some of them are linear combinations of Slater determinants. We introduce the basis

$$\vert s,s'\rangle\equiv\hat{c}^{\dagger}_{1,s}\hat{c}^{\dagger}_{2,s'}\vert 0\rangle\quad,\quad\vert\uparrow\downarrow,0\rangle\equiv\hat{c}^{\dagger}_{1,\uparrow}\hat{c}^{\dagger}_{1,\downarrow}\vert 0\rangle\quad,\quad\vert 0,\uparrow\downarrow\rangle\equiv\hat{c}^{\dagger}_{2,\uparrow}\hat{c}^{\dagger}_{2,\downarrow}\vert 0\rangle \tag{18}$$

of two-particle states, which are used to set up the eigenstates of $\hat{H}_{i;\mathrm{c}}$, see table 1. The states of lowest energy are the three triplet states with spin $S = 1$, which belong to the representation A_2 of the cubic point-symmetry group. Finding a high-spin ground state is a simple consequence of Hund's first rule. Higher in energy are the two degenerate singlet states of symmetry E and the non-degenerate singlet state of symmetry A_1.
The eigenstates of the local Hamiltonian $\hat{H}_{i;\mathrm{c}}$ play an essential role in the formulation of the multi-band Gutzwiller theory in Sec. 2. Since in most applications only a finite (and not too large) number of localised orbitals is taken into account, these eigenstates can be readily calculated by standard numerical techniques. The special case of a $3d$-shell in a cubic environment has been discussed analytically in great detail in the textbook by Sugano, Ref. [2].

2 Gutzwiller wave functions

The single-band Hubbard model

To understand the main physical idea behind the Gutzwiller variational theory, it is instructive to start with a consideration of the single-band Hubbard model

$$\hat{H}_{1\mathrm{B}} = \sum_{i,j} \sum_{s=\uparrow,\downarrow} t_{i,j} \hat{c}^{\dagger}_{i,s} \hat{c}_{j,s} + U \sum_{i} \hat{d}_i \quad , \quad \hat{d}_i \equiv \hat{n}_{i,\uparrow} \hat{n}_{i,\downarrow} \, . \tag{19}$$

In Hartree-Fock theory, one uses a variational wave function which is a one-particle product state

$$|\Psi_0\rangle = \prod_{\gamma} \hat{h}^{\dagger}_{\gamma} \, |0\rangle \tag{20}$$

in order to investigate many-particle Hamiltonians such as (19). It is well known, however, that such wave functions are insufficient for systems with medium to strong Coulomb interaction effects, see, e.g, the discussion in Sec. 4. It is a particular problem of a Hartree-Fock treatment that local charge fluctuations can only be suppressed in that approach by a spurious breaking of symmetries. Therefore, it usually overestimates the stability of phases with a broken symmetry. Hartree-Fock wave functions, however, can still be a reasonable starting point in order to set up more sophisticated variational wave functions. This leads us to the general class of *Jastrow wave functions* [3, 4], which are defined as

$$|\Psi_{\mathrm{J}}\rangle = \hat{P}_{\mathrm{J}} \, |\Psi_0\rangle \quad . \tag{21}$$

Here, $|\Psi_0\rangle$ is again a one-particle product state and $\hat{P}_{\mathrm{J}}$ is a correlation operator, which can be chosen in various ways in order to minimise the variational ground-state energy. The *Gutzwiller wave function* (GWF) is a special Jastrow wave function with a particular choice of the correlation operator $\hat{P}_{\mathrm{J}}$. It was introduced by Gutzwiller [5–7] in the form

$$|\Psi'_{\mathrm{G}}\rangle \equiv \hat{P}'_{\mathrm{G}} \, |\Psi_0\rangle = \prod_{i} \hat{P}'_i \, |\Psi_0\rangle \, , \tag{22}$$

and with the purpose to study ferromagnetism in a single-band Hubbard model. The (local) *Gutzwiller correlation operator*

$$\hat{P}_i' \equiv g^{\hat{d}_i} = 1 - (1-g)\hat{d}_i \;, \tag{23}$$

for each lattice site i contains a variational parameter g (with $0 \leq g \leq 1$), which allows one to supress local double occupancies that are energetically unfavourable for a finite Hubbard interaction $U > 0$.

The Hilbert space of the local Hamiltonian for the one-band Hubbard model is four-dimensional, where a local basis $|I\rangle$ is given by the states $|\emptyset\rangle$, $|\uparrow\rangle$, $|\downarrow\rangle$, and $|d\rangle$ for empty, singly-occupied and doubly-occupied sites, respectively. By working with the occupation operator $\hat{d}_i$ in (23), Gutzwiller singled out the doubly-occupied state $|d\rangle$. A more symmetric definition of the *local* Gutzwiller correlator (23) is given by

$$\hat{P}_i = \prod_I \lambda_I^{\hat{m}_{i,I}} = \sum_I \lambda_I \hat{m}_{i,I} \tag{24}$$

where the operators $\hat{m}_{i,I} = |I\rangle_{i\,i}\langle I|$ are the projectors onto the four atomic eigenstates $|I\rangle$. The operator (24) contains four parameters λ_I instead of only one parameter g in Gutzwiller's definition (23). It can be readily shown, however, that the operators (23) and (24) define the same sets of variational wave functions as long as the respective one-particle states $|\Psi_0\rangle$ are also treated as variational objects. Therefore, the wave functions, defined by (24), contain more variational parameters than are actually needed. This surplus of parameters will turn out to be quite useful when we evaluate expectation values in the limit of infinite spatial dimensions. Moreover, for the multi-band generalisation of Gutzwiller wave functions in the following section, Eq. (24) is the most natural starting point.

Multi-band Hubbard models

It is pretty obvious [8, 9] how the Gutzwiller wave functions (22) can be generalised for the investigation of the multi-band Hubbard models (12). The starting point is again a (normalised) single-particle product state $|\Psi_0\rangle$ to which we apply a Jastrow factor that is a product of local correlation operators. Hence, the multi-band Gutzwiller wave functions are given as

$$|\Psi_{\mathrm{G}}\rangle = \hat{P}_{\mathrm{G}}\,|\Psi_0\rangle = \prod_i \hat{P}_i\,|\Psi_0\rangle \;\;, \tag{25}$$

where, as in (24), we might work with a local correlation operator of the form

$$\hat{P}_i = \sum_{\Gamma_i} \lambda_{i;\Gamma_i} \hat{m}_{i;\Gamma_i} \;\;,\;\; \hat{m}_{i;\Gamma_i} = |\Gamma\rangle_{i\,i}\langle\Gamma| \;\;. \tag{26}$$

The variational parameters $\lambda_{i;\Gamma_i}$ allow us to optimise the occupation of each eigenstate $|\Gamma\rangle$ of the local Hamiltonian $\hat{H}_{i;\mathrm{c}}$. In multi-orbital systems, however, these states are usually degenerate and not uniquely defined. Moreover, it is not clear whether, in a solid, the (atomic) eigenstates

$|\Gamma\rangle_i$ lead to the best variational ground state of the form (25). Instead of (26) it may therefore be better to work with the general local correlation operator

$$\hat{P}_i = \sum_{\Gamma_i,\Gamma_i'} \lambda_{i;\Gamma_i,\Gamma_i'} \, |\Gamma\rangle_{i\,i}\langle\Gamma'| \ , \tag{27}$$

which contains a matrix $\lambda_{i;\Gamma_i,\Gamma_i'}$ of variational parameters. The analytical evaluation of expectation values, which we discuss in the following section, can be carried out without additional efforts for the general correlation operator (27). In numerical applications, however, we often have to restrict ourself to the simpler operator (26) since the number of parameters $\lambda_{i;\Gamma_i,\Gamma_i'}$ may become prohibitively large. Alternatively, one can try to identify the relevant non-diagonal elements of $\lambda_{i;\Gamma_i,\Gamma_i'}$ and take only these into account. Such strategies have been discussed in more detail in Ref. [10].

For systems without superconductivity, the Gutzwiller wave function should be an eigenstate of the total particle number operator

$$\hat{N} = \sum_{i,\sigma} \hat{n}_{i,\sigma} \ . \tag{28}$$

This requires that $\hat{N}$ commutes with $\hat{P}_{\mathrm{G}}$, which leads to

$$\sum_{\Gamma,\Gamma'} \lambda_{i;\Gamma,\Gamma'}(|\Gamma| - |\Gamma'|) \, |\Gamma\rangle_{i\,i}\langle\Gamma'| = 0 \tag{29}$$

where $|\Gamma|$ is the number of particles in the state $|\Gamma\rangle_i$. From equation (29), we conclude that $\lambda_{i;\Gamma,\Gamma'}$ can only be finite for states $|\Gamma\rangle_i, |\Gamma'\rangle_i$ with the same particle number. In a similar way, one can show that these states have to belong to the same representation of the point symmetry group. To study superconducting systems, one works with BCS-type one-particle wave functions $|\Psi_0\rangle$ for which the particle number is not conserved. In this case, the variational-parameter matrix $\lambda_{i;\Gamma,\Gamma'}$ has to be finite also for states $|\Gamma\rangle_i, |\Gamma'\rangle_i$ with different particle numbers, see Refs. [9, 11].

To keep the notation simple in this tutorial presentation, we will restrict ourselves to the case of a diagonal and real variational-parameter matrix and do not consider superconducting states. Consequently, the local correlation operators are Hermitian, $\hat{P}_i^\dagger = \hat{P}_i$. Moreover, we work with a spin-orbital basis σ for which the non-interacting local density matrix

$$C_{i;\sigma,\sigma'} \equiv \langle \hat{c}_{i,\sigma}^\dagger \hat{c}_{i,\sigma'} \rangle_{\Psi_0} \tag{30}$$

is diagonal,

$$C_{i;\sigma,\sigma'} = \delta_{\sigma,\sigma'} n_{i,\sigma}^0 \ . \tag{31}$$

This can always be achieved (i.e., for any $|\Psi_0\rangle$) by a proper transformation of the local basis σ. To simplify the notation further, we will frequently drop lattice-site indices in purely local equations.

3 Gutzwiller energy functional in infinite dimensions

The evaluation of expectation values for Gutzwiller wave functions remains a difficult many-particle problem even in the simplest case of a single-band Hubbard model. It has been achieved for this model in one dimension both for paramagnetic and for ferromagnetic states [12–16]. In the opposite limit of infinite spatial dimensions, expectation values can be evaluated for the general class of wave-functions (25). In this section, we summarise the main technical ideas behind this evaluation and discuss the resulting energy functional. An application of this functional to finite-dimensional systems is usually denoted as the *Gutzwiller approximation* because, for the single-band model, Gutzwiller has derived the very same functional [5–7] by means of combinatorial techniques [17].

3.1 Diagrammatic expansion

In order to determine the expectation value

$$\langle \hat{H}_{\rm H} \rangle_{\Psi_{\rm G}} = \frac{\langle \Psi_{\rm G} | \hat{H}_{\rm H} | \Psi_{\rm G} \rangle}{\langle \Psi_{\rm G} | \Psi_{\rm G} \rangle}, \tag{32}$$

of the Hamiltonian (12) we need to evaluate the following quantities ($i \neq j$)

$$\langle \Psi_{\rm G} | \hat{c}^{\dagger}_{i,\sigma} \hat{c}_{j,\sigma'} | \Psi_{\rm G} \rangle = \left\langle (\hat{P}_i \hat{c}^{\dagger}_{i,\sigma} \hat{P}_i)(\hat{P}_j \hat{c}_{j,\sigma'} \hat{P}_j) \prod_{l \neq (i,j))} \hat{P}^2_l \right\rangle_{\Psi_0}, \tag{33}$$

$$\langle \Psi_{\rm G} | \hat{m}_{i;\Gamma} | \Psi_{\rm G} \rangle = \left\langle (\hat{P}_i \hat{m}_{i;\Gamma} \hat{P}_i) \prod_{l \neq i} \hat{P}^2_l \right\rangle_{\Psi_0}, \tag{34}$$

$$\langle \Psi_{\rm G} | \Psi_{\rm G} \rangle = \left\langle \prod_{l} \hat{P}^2_l \right\rangle_{\Psi_0}. \tag{35}$$

The r.h.s. of all three equations (33)-(35) can be evaluated by means of Wick's theorem because the wave function $|\Psi_0\rangle$ is a single-particle product state. In this way, we can represent all contributions by diagrams with internal vertices l (from operators $\hat{P}^2_l$), external vertices i in Eq. (34), or i and j in Eq. (33), and lines

$$P^{\sigma,\sigma'}_{l,l'} \equiv \langle \hat{c}^{\dagger}_{l,\sigma} \hat{c}_{l',\sigma'} \rangle_{\Psi_0} \tag{36}$$

which connect these vertices. This diagrammatic expansion, however, is still very complicated even in the limit of infinite spatial dimensions. As shown in more detail in Refs. [8,9], it is very beneficial, in this limit, to introduce the (local) constraints

$$1 = \langle \hat{P}^2_l \rangle_{\Psi_0}, \tag{37}$$

$$\langle \hat{c}^{\dagger}_{l,\sigma} \hat{c}_{l,\sigma'} \rangle_{\Psi_0} = \langle \hat{c}^{\dagger}_{l,\sigma} \hat{P}^2_l \hat{c}_{l,\sigma'} \rangle_{\Psi_0}. \tag{38}$$

These constraints do not restrict our total set of variational wave functions (25) because they merely exploit the fact that we have introduced more variational parameters λ_Γ than are actually

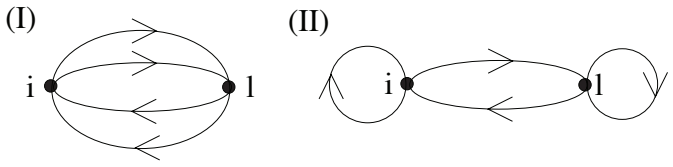

Fig. 1: *Two examples of double-occupancy diagrams ($l \neq i$). Diagram (II) vanishes due to the constraints (37), (38). Diagram (I) vanishes in the limit of infinite spatial dimensions.*

needed; see the discussion on the single-band model in Sec. 2. Note that moving the operator $\hat{P}_l^2$ relative to $\hat{c}^\dagger_{l,\sigma}$ and $\hat{c}_{l,\sigma'}$ does not alter the whole set of constraints (37), (38).
The constraints (37), (38) have an important consequence: Each diagram that results from (33)-(35) is non-zero only when all of its internal vertices l are connected to other vertices by at least four lines. As a simple example, Fig. 1 shows two (first order) diagrams which result from (34). While the constraints do not affect diagram (I), they ensure that diagram (II) vanishes.
In order to have a meaningful (i.e., finite) kinetic energy per lattice site our lines have to vanish like

$$P_{i,j}^{\sigma,\sigma'} \sim \frac{1}{\sqrt{2D}^{||i-j||}} \,, \tag{39}$$

on a hyper-cubic lattice in the limit of large spatial dimensions D. Here, we introduced the Manhattan metric

$$||i-j|| \equiv \sum_{k=1}^{D} |R_{i;k} - R_{j;k}| \,, \tag{40}$$

where $R_{i;k}$ is the k-th component of the lattice site vector $\boldsymbol{R}_i$. Note that the number of neighbouring sites with distance $||i-j||$ is given by

$$N_{\text{n.n.}}^{||i-j||} = 2D^{||i-j||} \,. \tag{41}$$

The scaling behaviour (39) in infinite dimensions has significant consequences for our diagrammatic expansion. As an example, we consider diagram (I) in Fig. 1. If we skip, for simplicity, any spin-orbital dependence of lines, this diagram leads to the contribution

$$\text{diagram (I)} \sim \sum_l P_{i,l}^4 = \mathcal{O}\left(\frac{1}{D}\right) \overset{D\to\infty}{\longrightarrow} 0 \,. \tag{42}$$

where the scaling $1/D$ results from equations (39) and (41). In general, one can show that in infinite dimensions a diagram vanishes if it contains an internal vertex that is connected to other vertices by three or more lines. The constraints (37), (38) ensure that this is the case for *all* diagrams which contain at least one internal vertex. Our arguments, so far, only apply to diagrams in which all internal vertices are connected to the external vertices i (or i and j). Of course, if we apply Wick's theorem to equations (33)-(34) we also obtain diagrams with internal vertices that are not connected to the external vertices. These diagrams, however, are exactly cancelled by the norm diagrams from Eq. (35) as shown in Ref. [8]. In summary, we therefore end up with the simple results

$$\langle \hat{c}^\dagger_{i,\sigma} \hat{c}_{j,\sigma'} \rangle_{\Psi_\text{G}} = \left\langle (\hat{P}_i \hat{c}^\dagger_{i,\sigma} \hat{P}_i)(\hat{P}_j \hat{c}_{j,\sigma'} \hat{P}_j) \right\rangle_{\Psi_0} \,, \tag{43}$$

$$\langle \hat{m}_{i;\Gamma} \rangle_{\Psi_\text{G}} = \left\langle (\hat{P}_i \hat{m}_{i;\Gamma} \hat{P}_i) \right\rangle_{\Psi_0} \,, \tag{44}$$

for expectation values in the limit of infinite spatial dimensions. These expectation values and the constraints (37), (38) will be further analysed in the following section and lead us to the Gutzwiller energy functional in infinite dimensions.

3.2 Energy functional for multi-band systems

Notation

We assume that the $2N$ (localised) spin-orbital states σ are ordered in some arbitrary way, $\sigma = 1, \ldots, 2N$ where N is the number of localised orbitals per lattice site. In order to set up a proper basis of the local Hilbert space which belongs to $\hat{H}_{i;\mathrm{c}}$, we introduce the following notation for the 2^{2N} possible electronic configurations (Slater determinants).

i) An atomic configuration I is characterised by the electron occupation of the orbitals,

$$I \in \{\emptyset; (1), \ldots, (2N); (1,2), \ldots, (2,3), \ldots (2N-1, 2N); \ldots; (1, \ldots, 2N)\} \ , \quad (45)$$

where the elements in each set $I = (\sigma_1, \sigma_2, \ldots)$ are ordered, i.e., it is $\sigma_1 < \sigma_2 < \ldots$. In general, we interpret the indices I as sets in the usual mathematical sense. For example, in the atomic configuration $I \backslash I'$ only those orbitals in I that are not in I' are occupied. The 'complement' $\bar{I}$ is defined as

$$\bar{I} \equiv (1, \ldots, 2N) \backslash I \ . \quad (46)$$

where $(1, \ldots, 2N)$ is the state with the maximum number of $2N$ electrons.

ii) A state with a specific configuration I is given as

$$|I\rangle = \hat{C}_I^\dagger \, |0\rangle \equiv \prod_{\sigma \in I} \hat{c}_\sigma^\dagger \, |0\rangle = \hat{c}_{\sigma_1}^\dagger \ldots \hat{c}_{\sigma_{|I|}}^\dagger \, |0\rangle \ , \quad (47)$$

where the operators $\hat{c}_\sigma^\dagger$ are in ascending order, i.e., it is $\sigma_1 < \sigma_2 \ldots < \sigma_{|I|}$ and $|I|$ is the number of particles in I. Products of annihilation operators, such as

$$\hat{C}_I \equiv \prod_{\sigma \in I} \hat{c}_\sigma = \hat{c}_{\sigma_1} \ldots \hat{c}_{\sigma_{|I|}}, \quad (48)$$

will be placed in descending order, i.e., with $\sigma_1 > \sigma_2 \ldots > \sigma_{|I|}$. Note that we have introduced the operators $\hat{C}_I^\dagger$ and $\hat{C}_I$ just as convenient abbreviations. They must not be misinterpreted as fermionic creation or annihilation operators. The sign function

$$f(\sigma, I) \equiv \langle I \cup \sigma | \hat{c}_\sigma^\dagger | I \rangle \quad (49)$$

counts whether an odd or even number of commutations is required to place σ in its proper position in I ($f(\sigma, I) = \mp 1$). It vanishes if $\sigma \in I$.

iii) The operator $\hat{m}_{I,I'} \equiv |I\rangle\langle I'|$ describes the transfer between configurations I' and I. It can be written as

$$\hat{m}_{I,I'} = \hat{C}_I^\dagger \hat{C}_{I'} \prod_{\sigma'' \in J} (1 - \hat{n}_{\sigma''}) \tag{50}$$

where $J \equiv \overline{I \cup I'}$. A special case, which derives from (50), is the occupation operator

$$\hat{m}_I \equiv |I\rangle\langle I| = \prod_{\sigma \in I} \hat{n}_\sigma \prod_{\sigma' \in \bar{I}} (1 - \hat{n}_{\sigma'}) \; . \tag{51}$$

The states $|I\rangle$ form a basis of the atomic Hamitonian's Hilbert space. Therefore, we can write the eigenstates of the local Hamiltonian (15) as

$$|\Gamma\rangle = \sum_I T_{I,\Gamma} \, |I\rangle \tag{52}$$

with coefficients $T_{I,\Gamma}$. For a simple example, see the two-particle states in table 1.

Local energy

The evaluation of the r.h.s. of Eq. (44) is straightforward if we use

$$\hat{P} \hat{m}_\Gamma \hat{P} = \lambda_\Gamma^2 \hat{m}_\Gamma \; . \tag{53}$$

This equation gives us

$$\langle \hat{m}_\Gamma \rangle_{\Psi_{\rm G}} = \lambda_\Gamma^2 m_\Gamma^0 \; , \tag{54}$$

where

$$m_\Gamma^0 = \langle \hat{m}_\Gamma \rangle_{\Psi_0} = \sum_I |T_{I,\Gamma}|^2 m_I^0 \quad , \quad m_I^0 = \prod_{\sigma \in I} n_\sigma^0 \prod_{\sigma \notin I} (1 - n_\sigma^0) \; . \tag{55}$$

Here we have used Eqs. (26), (31), and (51).

Hopping expectation values

For the evaluation of (43) we start with

$$\hat{P} \hat{c}_\sigma^\dagger \hat{P} = \sum_{\Gamma,\Gamma'} \lambda_\Gamma \lambda_{\Gamma'} \sum_{I_1,I_1',I_2,I_2'} \langle I_2 | \hat{c}_\sigma^\dagger | I_1' \rangle \, T_{I_1,\Gamma} T_{I_2,\Gamma}^* T_{I_1',\Gamma'} T_{I_2',\Gamma'}^* \, \hat{m}_{I_1,I_2'} \tag{56}$$

which follows from Eqs. (26), (50), (52). Note that the second operator $\hat{P} \hat{c}_{\sigma'} \hat{P}$ in (43) is just the conjugate of (56) with σ replaced by σ'. Hence, the only remaining expectation values which we need to evaluate in (43) have the form

$$E(I, I'; J, J') \equiv \langle \hat{m}_{i;I,I'} \hat{m}_{j;J,J'} \rangle_{\Psi_0} \; . \tag{57}$$

An application of Wick's Theorem to (57) leads, in general, to a number of diagrams with (potentially) several lines connecting the lattice sites i and j. At this point, however, we again apply the infinite-dimensional rule that all diagrams with three or more lines connecting i and j

can be discarded. Hence, the only remaining diagrams are those with exactly one line between i and j. Together with Eq. (31), we therefore find

$$E(I,I';J,J') = \sum_{\gamma} f(\gamma,I')\delta_{I,I'\cup\gamma}\frac{m^0_{I'}}{1-n^0_\gamma}\sum_{\gamma'} f(\gamma',J)\delta_{J\cup\gamma',J'}\frac{m^0_J}{1-n^0_{\gamma'}}\langle\hat{c}^\dagger_{i,\gamma}\hat{c}_{j,\gamma'}\rangle_{\Psi_0}\ . \tag{58}$$

Altogether, we obtain the following result for the hopping expectation value (43) in infinite dimensions

$$\langle\hat{c}^\dagger_{i,\sigma}\hat{c}_{j,\sigma'}\rangle_{\Psi_{\rm G}} = \sum_{\gamma,\gamma'} q^\gamma_\sigma q^{\gamma'}_{\sigma'}\langle\hat{c}^\dagger_{i,\gamma}\hat{c}_{j,\gamma'}\rangle_{\Psi_0} \tag{59}$$

with the *renormalisation matrix*

$$\begin{aligned} q^\gamma_\sigma &= \frac{1}{1-n^0_\gamma}\sum_{\Gamma,\Gamma'}\lambda_\Gamma\lambda_{\Gamma'}\sum_{I,I'} f(\sigma,I)f(\gamma,I')T^*_{I\cup\sigma,\Gamma}T_{I,\Gamma'}T^*_{I',\Gamma'}T_{I'\cup\gamma,\Gamma}m^0_{I'} &(60)\\ &= \frac{1}{n^0_\gamma}\sum_{\Gamma,\Gamma'}\lambda_\Gamma\lambda_{\Gamma'}\langle\Gamma|\hat{c}^\dagger_\sigma|\Gamma'\rangle\Big\langle\big(|\Gamma\rangle\langle\Gamma'|\hat{c}_\gamma\big)\Big\rangle_{\Psi_0}\ . &(61)\end{aligned}$$

Constraints

The explicit form of the correlation operator (26), together with Eq. (31), gives us directly the explicit form of the constraints (37), (38)

$$\begin{aligned} 1 &= \sum_\Gamma\lambda^2_\Gamma\sum_I T_{I,\Gamma}T^*_{I,\Gamma}m^0_I\ , &(62)\\ \delta_{\sigma,\sigma'}n^0_\sigma &= \sum_\Gamma\lambda^2_\Gamma\sum_{I(\sigma,\sigma'\in I)} f(\sigma,I\backslash\sigma)f(\sigma',I\backslash\sigma')T_{I\backslash\sigma,\Gamma}T^*_{I\backslash\sigma',\Gamma}m^0_I\ . &(63)\end{aligned}$$

Summary: Structure of the energy functional

In summary, we obtain the following Gutzwiller energy functional for the multi-band Hubbard models (12) in infinite dimensions

$$\begin{aligned} E^{\rm GA} &= \sum_{i\neq j}\sum_{\sigma,\sigma',\gamma,\gamma} t^{\gamma,\gamma'}_{i,j}q^\sigma_\gamma\left(q^{\sigma'}_{\gamma'}\right)^*\langle\hat{c}^\dagger_{i,\sigma}\hat{c}_{j,\sigma'}\rangle_{\Psi_0} + \sum_i\sum_{\sigma,\sigma'\in{\rm d}}\epsilon^{\sigma,\sigma'}_i\langle\hat{c}^\dagger_{i,\sigma}\hat{c}_{i,\sigma'}\rangle_{\Psi_0}\\ &\quad + L\sum_\Gamma E_\Gamma\lambda^2_\Gamma m^0_\Gamma \end{aligned}\tag{64}$$

where, for the delocalised orbitals, the renormalisation factors are $q^\sigma_\gamma = \delta_{\sigma,\gamma}$. The single-particle state $|\Psi_0\rangle$ enters (64) solely through the non-interacting density matrix $\tilde{\rho}$ with the elements

$$\rho_{(i\sigma),(j\sigma')} \equiv \langle\hat{c}^\dagger_{j,\sigma'}\hat{c}_{i,\sigma}\rangle_{\Psi_0}\ . \tag{65}$$

Hence, the Gutzwiller energy functional simplifies to

$$E^{\rm GA}(\tilde{\rho},\lambda_\Gamma) = \sum_{i\neq j}\sum_{\sigma,\sigma',\gamma,\gamma} t^{\gamma,\gamma'}_{i,j}q^\sigma_\gamma\left(q^{\sigma'}_{\gamma'}\right)^*\rho_{(j\sigma'),(i\sigma)} + \sum_{i;\sigma,\sigma'\in{\rm d}}\epsilon^{\sigma,\sigma'}_i\rho_{(i\sigma),(i\sigma)} + L\sum_\Gamma E_\Gamma\lambda^2_\Gamma m^0_\Gamma\ . \tag{66}$$

It has to be minimised with respect to all elements of $\tilde{\rho}$ and the variational parameters λ_Γ obeying the constraints (62), (63) and

$$\tilde{\rho}^2 = \tilde{\rho} \; . \tag{67}$$

The latter constraint ensures that $\tilde{\rho}$ belongs to a single-particle product state.
There are several ways, how the constraints (62), (63) may be implemented in numerical calculations [10]. In this tutorial introduction, we will simply assume that Eqs. (62), (63) are solved by expressing some of the parameters λ_Γ by the remaining 'independent' parameters $\lambda^{\rm i}_\Gamma$. Equation (67) is then the only remaining constraint in the minimisation of the resulting energy function $\bar{E}^{\rm GA}\left(\tilde{\rho}, \lambda^{\rm i}_\Gamma\right)$. If it is implemented by means of Lagrange parameters, see Appendix A, the minimisation with respect to $\tilde{\rho}$ leads to the effective single-particle Hamiltonian

$$\hat{H}_0^{\rm eff} = \sum_{i\neq j} \sum_{\sigma,\sigma',\gamma,\gamma} t_{i,j}^{\gamma,\gamma'} q_\gamma^\sigma \left(q_{\gamma'}^{\sigma'}\right)^* \hat{c}^\dagger_{i,\sigma}\hat{c}_{j,\sigma'} + \sum_{i,\sigma\in d} \epsilon_i^{\sigma,\sigma'} \hat{c}^\dagger_{i,\sigma}\hat{c}_{i,\sigma} + \sum_{i,\sigma\in \ell} \eta_\sigma \hat{c}^\dagger_{i,\sigma}\hat{c}_{i,\sigma} \tag{68}$$

which gives us $|\Psi_0\rangle$ as the ground state of (68),

$$\hat{H}_0^{\rm eff}|\Psi_0\rangle = E_0|\Psi_0\rangle \; . \tag{69}$$

The 'fields' η_σ for the localised orbitals in (68) are given as [18]

$$\eta_\sigma = \frac{\partial}{\partial n^0_\sigma} \bar{E}^{\rm GA}\left(\tilde{\rho}, \lambda^{\rm i}_\Gamma\right) \; . \tag{70}$$

The remaining numerical problem is the solution of Eqs. (68)-(70) together with the minimisation condition

$$\frac{\partial}{\partial \lambda^{\rm i}_\Gamma} \bar{E}^{\rm GA}\left(\tilde{\rho}, \lambda^{\rm i}_\Gamma\right) = 0 \; . \tag{71}$$

Numerical strategies to solve these equations have been discussed in detail in Ref. [10] to which we refer the interested reader.
Up to this point, the effective single-particle Hamiltonian (68),

$$\hat{H}_0^{\rm eff} = \sum_{\mathbf{k},\tau} E_{\mathbf{k},\tau} \hat{h}^\dagger_{\mathbf{k},\tau}\hat{h}_{\mathbf{k},\tau} \; , \tag{72}$$

and its eigenvalues (band-energies) $E_{\mathbf{k},\tau}$ in momentum space are just auxiliary objects which determine $|\Psi_0\rangle$. One can readily show, however, that the non-interacting Fermi-surfaces, defined by the Fermi energy $E_{\rm F}$,

$$E_{\mathbf{k},\tau} - E_{\rm F} = 0 \; , \tag{73}$$

are equal to the correlated Fermi surfaces because the momentum distribution

$$n_{\mathbf{k},\tau} \equiv \langle \hat{h}^\dagger_{\mathbf{k},\tau}\hat{h}_{\mathbf{k},\tau}\rangle_{\Psi_{\rm G}} \tag{74}$$

has step discontinuities exactly at the momenta given by Eq. (73). The Fermi surface defined by (73) may therefore be compared to those, e.g., from de-Haas-van-Alphen experiments. Moreover, within a Landau-Fermi-liquid theory, the eigenvalues $E_{\mathbf{k},\tau}$ turn out as the quasi-particle excitation energies which can be measured, e.g., in 'angle-resolved photoemission spectroscopy' (ARPES) experiments, see Refs. [9, 19].

3.3 Example: single-band Hubbard model

As a simple example we use the general results derived in Sec. 3.2, to recover the well-known Gutzwiller energy functional for the single-band Hubbard model [5]. For this model, the (local) Gutzwiller correlation operator (24) had the form

$$\hat{P} = \lambda_\emptyset \hat{m}_\emptyset + \lambda_\uparrow \hat{m}_\uparrow + \lambda_\downarrow \hat{m}_\downarrow + \lambda_d \hat{d} \,, \tag{75}$$

where

$$\hat{m}_\emptyset = (1-\hat{n}_\uparrow)(1-\hat{n}_\downarrow) = 1 - \hat{n}_\uparrow - \hat{n}_\downarrow + \hat{d} \,, \tag{76}$$

$$\hat{m}_s = \hat{n}_s(1-\hat{n}_{\bar{s}}) = \hat{n}_s - \hat{d} \,, \tag{77}$$

$\bar{\uparrow} = \downarrow$, $\bar{\downarrow} = \uparrow$, and $\hat{d}$ has been defined in Eq. (19). Equation (54) gives us the expectation value for the occupation of the four local eigenstates,

$$m_\emptyset \equiv \langle \hat{m}_\emptyset \rangle_{\Psi_{\rm G}} = \lambda_\emptyset^2 (1-n_\uparrow^0)(1-n_\downarrow^0) \,, \tag{78}$$

$$\hat{m}_s \equiv \langle \hat{m}_s \rangle_{\Psi_{\rm G}} = \lambda_s^2 n_s^0 (1-n_{\bar{s}}^0) \,, \tag{79}$$

$$d \equiv \langle \hat{d} \rangle_{\Psi_{\rm G}} = \lambda_d^2 n_\uparrow^0 n_\downarrow^0 \,. \tag{80}$$

With these equations, we can replace the original variational parameters $\lambda_\emptyset$, λ_s, λ_d by their corresponding expectation values $m_\emptyset$, m_s, d. This simplifies the expressions for the constraints (62), (63) which then read

$$1 = m_\emptyset + m_\uparrow + m_\downarrow + d \,, \tag{81}$$

$$n_s^0 = m_s + d \,. \tag{82}$$

Note that the second constraint (82) simply ensures that the correlated and the uncorrelated (spin-dependent) particle numbers are equal,

$$\langle \hat{n}_s \rangle_{\Psi_{\rm G}} = m_s + d = n_s^0 = \langle \hat{n}_s \rangle_{\Psi_0} \,. \tag{83}$$

Equations (81), (82) can be readily solved, e.g., by expressing $m_\emptyset$, m_s as functions of d,

$$m_\emptyset = 1 - n_\uparrow^0 - n_\downarrow^0 + d \,, \tag{84}$$

$$m_s = n_s^0 - d \,. \tag{85}$$

In this way, the only remaining variational parameter is the average number of doubly-occupied lattice sites d.

Finally, we can evaluate the hopping renormalisation factors (61),

$$q_s^{s'}(d) = \delta_{s,s'}(\lambda_d \lambda_{\bar{s}} n_{\bar{s}}^0 + \lambda_s \lambda_\emptyset (1-n_{\bar{s}}^0)) \tag{86}$$

$$= \delta_{s,s'} \frac{1}{\sqrt{n_s^0(1-n_s^0)}} (\sqrt{m_{\bar{s}} d} + \sqrt{m_s m_\emptyset}) \,, \tag{87}$$

where, in the second line, we have used Eqs. (78)-(80). In summary, we obtain the variational energy functional

$$\bar{E}^{\rm GA}(d, \Psi_0) = \sum_{s=\uparrow,\downarrow} (q_s^s(d))^2 \sum_{i,j} t_{i,j} \langle \hat{c}_{i,s}^\dagger \hat{c}_{j,s} \rangle_{\Psi_0} + LUd \tag{88}$$

for the single-band Hubbard model (19) in the Gutzwiller approximation.

4 Applications

4.1 Ferromagnetism in a two-band Hubbard model

Since Gutzwiller's ground-breaking work we know that the single-band energy functional (88) leads to ferromagnetic ground states only under very special circumstances, e.g., if the density of states has a sharp peak at the Fermi level and the Coulomb interaction is much larger than the band width. From this observation, we can already conclude that ferromagnetism, as it naturally appears in transition metals, is most probably related to the orbital degeneracy of the partially filled $3d$-shell in these systems. Therefore, it is quite instructive to study ferromagnetic instabilities in a system with two orbitals, as a first step from the simple one-band model towards a realistic description of materials with partially filled $3d$-shells.

A) Model specification

We consider a Hubbard model with two degenerate $e_{\rm g}$-orbitals per site on a simple three-dimensional cubic lattice. The local (atomic) Hamiltonian for this system is given in equation (16). We include realistic hopping parameters for transition metal energy bands to the nearest and second-nearest neighbours in (13). This choice avoids pathological features in the energy bands, such as perfect nesting at half band filling. The single-particle part of the Hamiltonian (13) is easily diagonalised in momentum space and leads to a density of states $D_0(\varepsilon)$ that is shown as a function of the band filling in Fig. 2.
The case $n_\sigma = n_\sigma^0 = 0.29$ corresponds to a maximum in the density of states at the Fermi energy. For this band filling, we expect the strongest tendency towards ferromagnetism.

B) Variational energy functional

For a two-band model, it is still possible to give a manageable explicit expression of the energy as a function of the variational parameters. The eigenstates of the two-particle spectrum all belong to different representations of the point symmetry group, see table 1. Therefore, one can safely assume that the variational-parameter matrix $\lambda_{\Gamma,\Gamma'} = \delta_{\Gamma,\Gamma'}$ is diagonal and we have $\lambda_\Gamma = \lambda_{\Gamma'}$ for all states $|\Gamma\rangle$, $|\Gamma'\rangle$ that are degenerate due to the cubic symmetry. Then, we are left with 11 (independent) variational parameters $m_\Gamma = \lambda_\Gamma^2 m_\Gamma^0$:

i) two parameters for an empty and a fully occupied site: $m_\emptyset$, f;

ii) four parameters for singly and triply occupied sites: m_s and t_s with $s = \uparrow, \downarrow$;

iii) five parameters for doubly-occupied sites: $d_t^{\uparrow,\uparrow}$, $d_t^{\downarrow,\downarrow}$, d_t^0 (for the triplet ${}^3A_2$), d_E (for the doublet ${}^1E$), and d_A (for the singlet ${}^1A_1$).

For our degenerate two-band model, the uncorrelated local density matrix (31) is automatically diagonal and orbital independent,

$$\left\langle \hat{c}^\dagger_{i,(b,s)} \hat{c}_{i,(b',s')} \right\rangle_{\Psi_0} = \delta_{s,s'} \delta_{b,b'} n_s^0 \ . \tag{89}$$

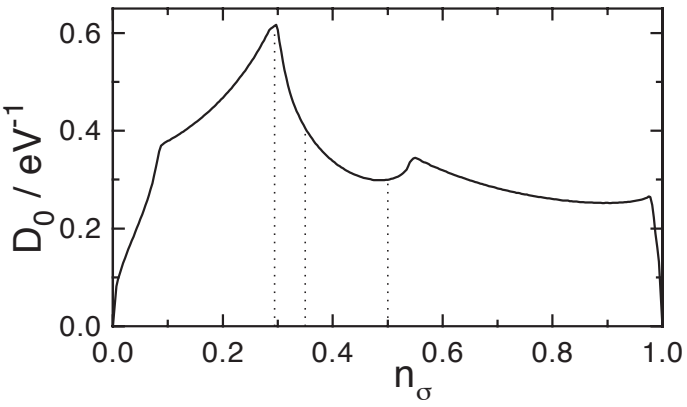

Fig. 2: *Model density of states at the Fermi energy as a function of the orbital filling n_σ. The dashed lines indicate the half-filled case ($n_\sigma = 0.5$ and the fillings used in this section ($n_\sigma = 0.29$ and $n_\sigma = 0.35$). The total bandwidth is $W = 6.8$ eV.*

As in the single-band case, the constraint equations (62), (63) can be solved explicitly, e.g., by considering the occupations

$$m_\emptyset = 1 - 2n_\uparrow^0 - 2n_\downarrow^0 + d_t^{\uparrow\uparrow} + d_t^{\downarrow\downarrow} + d_t^0 + d_A + 2d_E + 4t_\uparrow + 4t_\downarrow + 3f \;, \tag{90}$$

$$m_s = n_s^0 - \left[d_t^{ss} + t_{\bar{s}} + 2t_{\bar{s}} + f + \frac{1}{2}\left(d_A + 2d_E + d_t^0\right)\right], \tag{91}$$

as functions of the remaining nine independent parameters. The expectation value of the two-band Hubbard Hamiltonian is then given by

$$\begin{aligned} E_{\text{atom}}^{\text{2b}} &= \sum_s (q_s^s)^2 \varepsilon_{s,0} + (U' - J)(d_t^{\uparrow\uparrow} + d_t^{\downarrow\downarrow} + d_t^0) \\ &\quad + 2(U' + J)d_E + (U + J)d_A + (2U + 4U' - 2J)(t_\uparrow + t_\downarrow + f) \;, \end{aligned} \tag{92}$$

where we introduced the orbital-independent elements

$$\begin{aligned} q_s^s &= \frac{1}{\sqrt{n_s^0(1 - n_s^0)}} \Bigg[\left(\sqrt{t_s} + \sqrt{m_{\bar{s}}}\right) \frac{1}{2}\left(\sqrt{d_A} + 2\sqrt{d_E} + \sqrt{d_t^0}\right) \\ &\quad + \sqrt{m_s}\left(\sqrt{m_\emptyset} + \sqrt{d_t^{ss}}\right) + \sqrt{t_{\bar{s}}}\left(\sqrt{d_t^{\bar{s}\bar{s}}} + \sqrt{f}\right)\Bigg], \end{aligned} \tag{93}$$

of the diagonal renormalisation matrix and the bare band energies

$$\varepsilon_{s,0} = \int_{-\infty}^{E_{\text{F},s}} \mathrm{d}\varepsilon \, \varepsilon D_0(\varepsilon) \;. \tag{94}$$

For comparison, we will also consider the energy

$$\begin{aligned} E_{\text{dens}}^{(\text{2b})} &= \sum_s (\bar{q}_s^s)^2 \varepsilon_{s,0} + (U' - J)(d_1^{\uparrow\uparrow} + d_1^{\downarrow\downarrow}) \\ &\quad + 2U' d_0 + 2U d_c + (2U + 4U' - 2J)(t_\uparrow + t_\downarrow + f) \end{aligned} \tag{95}$$

of a two-band model without the terms in the second line of the atomic Hamiltonian (16) since this is an approximation that is often made in studies on multi-band models. In this case, there are seven variational parameters $d_1^{\uparrow\uparrow}$, $d_1^{\downarrow\downarrow}$, d_0, d_c, $t_\uparrow$, $t_\downarrow$, and f, which represent the occupation of

the configuration states $|I\rangle$. The probabilities for an empty site $m_\emptyset$ and a singly-occupied site m_s are related to the variational parameters by

$$m_s = n_s^0 - [d_1^{ss} + t_{\bar{s}} + 2t_s + f + d_c + d_0] \ , \tag{96}$$

$$m_\emptyset = 1 - 2n_\uparrow^0 - 2n_\downarrow^0 + d_1^{\uparrow\uparrow} + d_1^{\downarrow\downarrow} + 2d_0 + 2d_c + 4t_\uparrow + 4t_\downarrow + 3f \ . \tag{97}$$

The renormalisation factors have the form

$$\bar{q}_s^s = \frac{1}{\sqrt{n_s^0(1-n_s^0)}}\Big[\left(\sqrt{t_s}+\sqrt{m_{\bar{s}}}\right)\left(\sqrt{d_c}+\sqrt{d_0}\right) + \sqrt{m_s}\left(\sqrt{m_\emptyset}+\sqrt{d_1^{ss}}\right) + \sqrt{t_{\bar{s}}}\left(\sqrt{d_1^{\bar{s}\bar{s}}}+\sqrt{f}\right)\Big] \ . \tag{98}$$

C) Ground-state properties

The energies (92) and (95) have to be minimised with respect to their respective (nine or seven) independent variational parameters m_Γ and the magnetisation

$$M \equiv (n_\uparrow^0 - n_\downarrow^0)/2 \ , \tag{99}$$

for example, by means of the algorithm introduced in Ref. [10]. In Fig. 3 (left), the magnetisation M is shown as a function of U for fixed $J/U = 0.2$ ($U'/U = 0.6$). The critical interaction for the ferromagnetic transition, $U_{\rm F}^{\rm atom}$, is about a factor two larger than its value $U_{\rm F}^{\rm HF}$ as obtained from the Hartree-Fock-Stoner theory. The corresponding values $U_{\rm F}^{\rm dens}$ always lie somewhat below the values for the Gutzwiller wave function with full atomic correlations. In general, the relation $M_{\rm HF}(U) > M_{\rm dens}(U) > M_{\rm atom}(U)$ holds, i.e., for all interaction strengths, the tendency to ferromagnetism is the strongest within the Hartree-Fock theory and weakest for Gutzwiller wave functions with atomic correlations. Furthermore, the slopes of $M(U)$ are much steeper in the Hartree-Fock results than in the presence of correlations.

The properties of the ferromagnetic phase strongly depend on the spectrum of the atomic two-electron configurations. To further analyse this point, we have included the case of $J_{\rm C} = 0$, which changes only the excited two-electron states. A shift of the curve $M(U)$ results towards smaller interaction strengths; for a given magnetisation density, a smaller interaction strength is required as compared to the correct symmetry case $J = J_{\rm C}$, see Fig. 3 (left). The effect is more pronounced when we go to the Gutzwiller wave function with pure density correlations. These results indicate that itinerant ferromagnetism is strongly influenced by the atomic multiplet spectra.

In Fig. 3 (left/a), we chose the particle density per band to be $n^0 = (n_\uparrow^0 + n_\downarrow^0)/2 = 0.29$, right at the maximum of the density of state curve, compare Fig. 2. In this case, there are finite slopes of the $M(U)$ curves at $U_{\rm F}$, and a 'Stoner criterion' for the onset of ferromagnetism applies. In Fig. 3 (left/b), we chose the particle density per band as $n^0 = 0.35$. In this case, the density of states at the Fermi energy $D_0(E_{{\rm F},\uparrow}) + D_0(E_{{\rm F},\downarrow})$ first *increases* as a function of the magnetisation density. Therefore, a discontinuous transition thus occurs from the paramagnet to the ferromagnet.

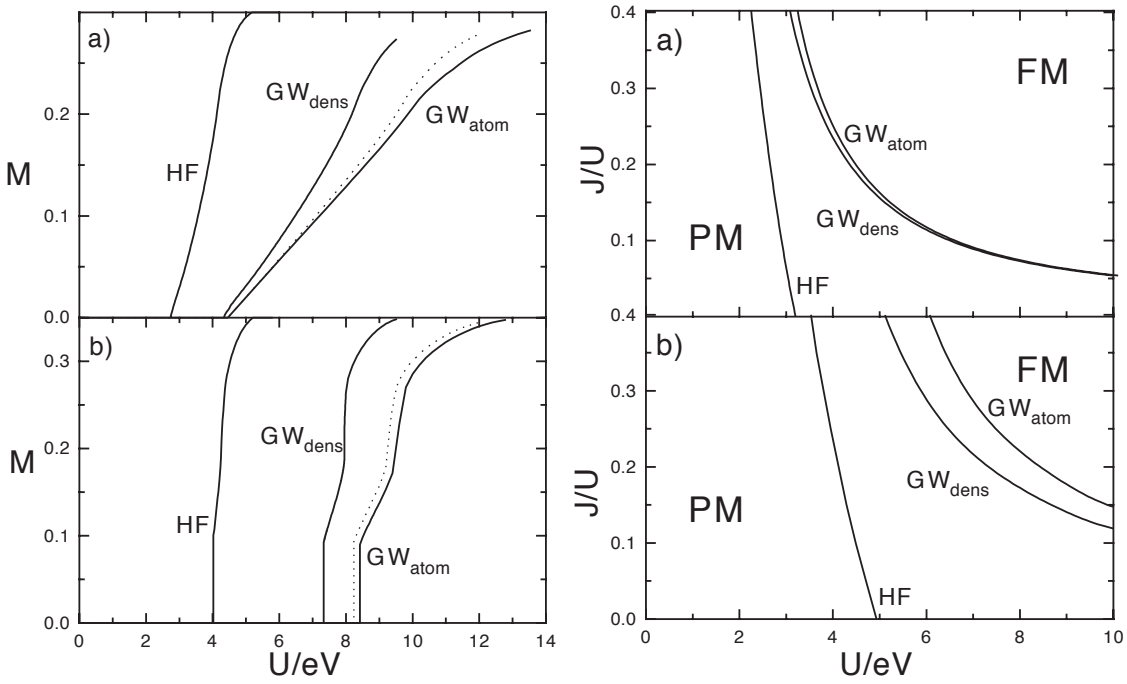

Fig. 3: *Left: Magnetisation density per band as a function of U for the Hartree-Fock solution (HF), the Gutzwiller wave function with pure density correlations (GW_{dens}), and the Gutzwiller wave function with atomic correlations (GW_{atom}) for (a) $n_s = 0.29$ and (b) $n_s = 0.35$. The dotted line indicates the results for GW_{atom} with $J_C = 0$. The local exchange interaction is $J = 0.2U$ in all curves. Right: Phase diagram as a function of U and J for the Hartree-Fock solution (HF) and the two Gutzwiller wave functions (GW_{dens}, GW_{atom}) for (a) $n^0 = 0.29$ and (b) $n^0 = 0.35$; PM: paramagnet, FM: ferromagnet.*

In the case of pure density correlations, a second jump in the $M(U)$ curve is observed that is absent in the other two curves. As discussed in Ref. [20], this jump is related to another feature of the density of states. In the Hartree-Fock theory, this feature is too weak to be of any significance in comparison to the interaction energy. When the full atomic correlations are taken into account, this first-order jump at a finite magnetisation density disappears due to the enhanced flexibility of the variational wave function.

Another remarkable difference between the Hartree-Fock and the Gutzwiller method lies in the approach to ferromagnetic saturation. In the Hartree-Fock theory, the magnetisation saturates at U values about 20% to 40% above the onset of ferromagnetism at $U_{\mathrm{F}}^{\mathrm{HF}}$. In contrast, in the variational approach saturation is reached at about twice the onset value, $U_{\mathrm{sat}} \lesssim 2U_{\mathrm{F}}$. However, even when the minority spin occupancies are zero and $\langle \hat{S}_z^{\mathrm{at}} \rangle$ is constant, the majority spin occupancies $s_\uparrow$ and $d_t^{\uparrow\uparrow}$ vary with U since the limit of zero empty sites is reached only for $U \to \infty$.

In Fig. 3 (right), we display the J-U phase diagram for both fillings. It shows that the Hartree-Fock theory always predicts a ferromagnetic instability. In contrast, the correlated electron approach strongly supports the idea that a substantial on-site Hund's rule exchange is required for the occurrence of ferromagnetism at realistic interaction strengths. For the case $n^0 = 0.29$, the differences between the phase diagrams for the two correlated electron wave functions are

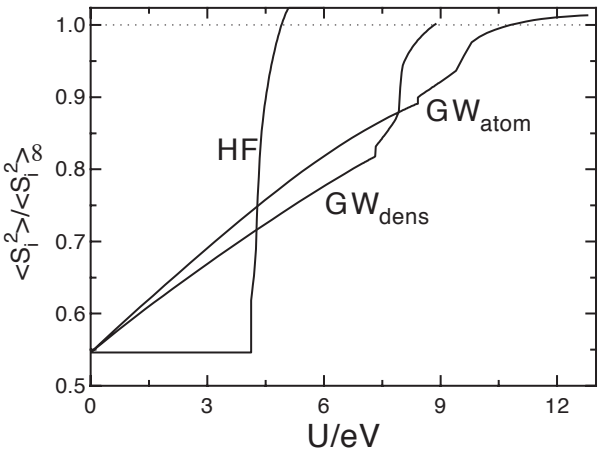

Fig. 4: *Size of the local spin $\langle\big(\hat{\vec{S}}_i\big)^2\rangle$ as a function of the interaction strength for $J = 0.2U$ and band filling $n^0 = 0.35$ for the Hartree-Fock theory (HF) and the Gutzwiller wave functions (GW_{dens}, GW_{atom}).*

minor. Due to the large density of states at the Fermi energy, the critical interaction strengths for the ferromagnetic transition are comparably small, and the densities for the double occupancies in both correlated wave functions do not differ much. For the larger band filling $n^0 = 0.35$, i.e., away from the peak in the density of states, the values for $U_{\rm F}$ are considerably larger and, in the atomic correlation case, the Gutzwiller wave functions can generate local spin triplets more easily while keeping the global paramagnetic phase.

The magnitude of the local spin as a function of U is shown in Fig. 4. For $U \to \infty$, each site is either singly occupied with probability $2 - 4n^0$ or doubly occupied (spin $S = 1$) with probability $4n^0 - 1$. Hence,

$$\langle(\vec{S}_i)^2\rangle_\infty = (3/4)(2 - 4n^0) + 2(4n^0 - 1) = 5n^0 - 1/2\ . \tag{100}$$

For the correlated wave functions, this limit is reached from *above* since, for $U < \infty$, charge fluctuations first increase the number of spin-one sites at the expense of spin-$1/2$ sites, which turn into empty sites. A further decrease of U will also activate the singlet double occupancies and higher multiple occupancies. Thus, the local spin eventually reduces below $\langle(\vec{S}_i)^2\rangle_\infty$. On the contrary, the Hartree-Fock theory does not give the proper large-U limit for the local spin. Instead, the Hartree-Fock limit is given by

$$\langle(\vec{S}_i)^2\rangle_\infty^{\rm HF} = n^0(3 + 2n^0)\ . \tag{101}$$

The change of $\langle(\vec{S}_i)^2\rangle$ at $U_{\rm F}$ is only a minor effect within the correlated electron approach. In particular, this holds true for the case of atomic correlations, where about 90% of the local spin saturation value is already reached in the paramagnetic state. Again, the Hartree-Fock results are completely different. There, the local spin sharply increases as a function of the interaction strength since the absence of correlations fixes

$$\langle(\vec{S}_i)^2\rangle^{\rm HF}(U < U_{\rm F}^{\rm HF}) = \langle(\vec{S}_i)^2\rangle(U = 0). \tag{102}$$

Finally, in Fig. 5, we display the energy differences between the paramagnetic and ferromagnetic ground states as a function of the interaction strength for $J = 0.1U$. For the correlated electron case, this quantity is of the order of the Curie temperature, which is in the range of

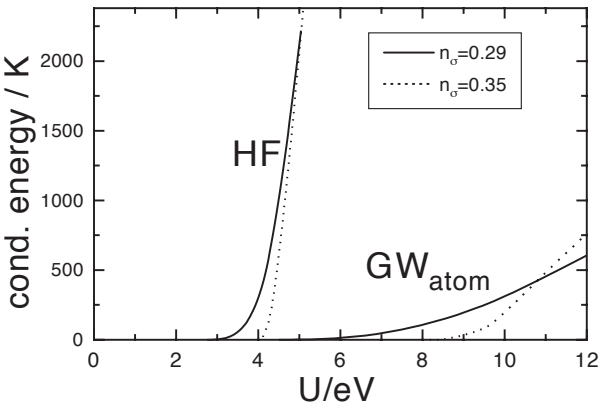

Fig. 5: *Condensation energy as a function of U for $J = 0.2U$ for the Hartree-Fock theory (HF) and the Gutzwiller wave function (GW_{atom}) for $n = 0.29$ (full lines) and $n = 0.35$ (dashed lines).*

$100\,\mathrm{K} - 1000\,\mathrm{K}$ in real materials. On the other hand, the Hartree-Fock theory yields small condensation energies only in the range of $U \approx 4\,\mathrm{eV}$; for larger U, the condensation energy is of order U. Including the correlation effects within the Gutzwiller theory, we have relatively small condensation energies even for interaction values as large as twice the bandwidth ($U \approx 10\,\mathrm{eV}$).

4.2 Antiferromagnetic order in iron-pnictide models

Since their recent discovery, the iron-based high-T_c superconductors, e.g., LaOFeAs, have attracted tremendous attention both in theory and experiment. From a theoretical point of view, these systems are of particular interest because their conduction electrons are less correlated than those of other high-T_c superconductors. In contrast to the cuprates, the pnictides' undoped parent compounds are antiferromagnetic metals at low temperatures, not insulators. However, the electronic mass is enhanced by a factor of two which indicates that electronic correlations are quite substantial in the pnictides, too.

The theoretical description of the pnictides' normal phases already turned out to be a difficult problem. Standard density-functional theory (DFT) grossly overestimates the size of their magnetic moment in the antiferromagnetic ground state. For example, in LaOFeAs experiment finds a staggered moment of $m = (0.4 \ldots 0.8)\mu_\mathrm{B}$ [21–23] whereas DFT calculations predict moments of $m \approx 1.8\mu_\mathrm{B}$, or larger [24, 25]. For other pnictide compounds, the comparison is equally unfavourable.

The electronic structure of LaOFeAs near the Fermi energy is fairly two-dimensional and the bands are dominantly of iron d and (partially) of arsenic p character. A complete tight-binding model for LaOFeAs should therefore consist of eight bands (i.e., five iron d- and three arsenic p-bands) [26], see Fig. 6 (left). For many-particle approaches, however, the study of such an eight-band model model is obviously quite challenging. Therefore, in many theoretical works on iron pnictides various simpler models have been proposed to study particular aspects of these materials. The fact that the bands near the Fermi energy are dominantly of iron d character suggest the study of an effective five-band model of pure iron d-bands. Such a model has been proposed, e.g., in Ref. [27], see Fig. 6 (middle). Even simpler models may be derived if one only aims to reproduce the Fermi surfaces of LaOFeAs. This is achieved, e.g., by the three-band model in Fig. 6 (right), which was investigated in Ref. [28].

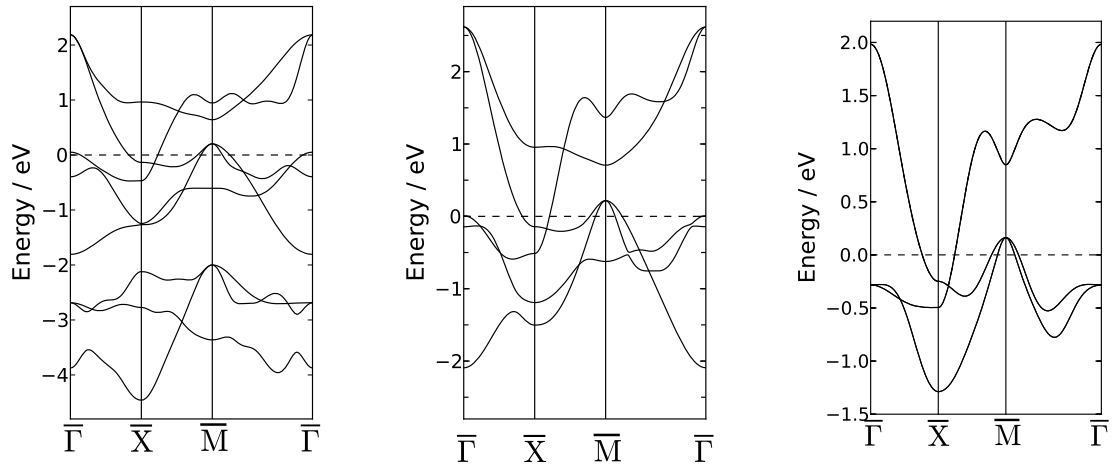

Fig. 6: *Model band structures for LaOFeAs with eight bands [26] (left), five bands [27] (middle) and three bands [28] (right).*

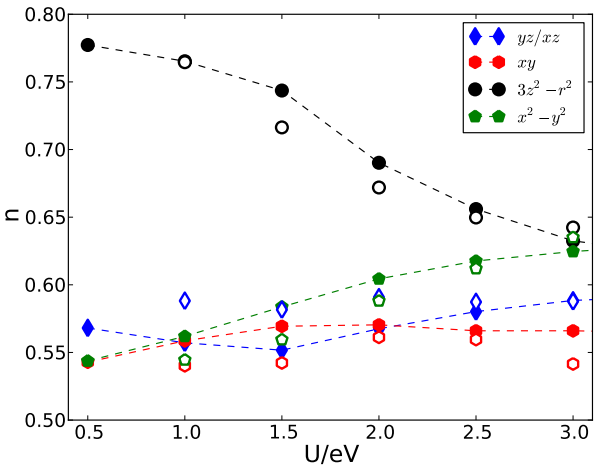

Fig. 7: *Orbital densities in Gutzwiller theory (full symbols) and in DMFT (open symbols) as a function of U (with $U/J = 4$) for the simplified local Hamiltonian $\hat{H}_{\rm c} = \hat{H}_{\rm c}^{(1)}$, see Eq. (103).*

In cases where a simplified model reproduces certain properties of a material correctly, there will often remain doubts whether this agreement is merely coincidental or an indication that the model indeed captures the relevant physics of a system. A big advantage of the Gutzwiller theory is its numerical simplicity that allows one to study even complicated multi-band models with modest numerical efforts. In this way, it is possible to test the quality of simplified models by comparing their properties with those of more realistic Hamiltonians. In this section, we will compare the magnetic properties of all three models, displayed in Figs. 6. This comparison provides an interesting example of the dangers that lie in the study of oversimplified model systems. Based on a Gutzwiller theory calculation it has been argued in Ref. [28] that the three-band model has a relatively small magnetic moment, in agreement with experiment. However, as we have shown in Ref. [29] the magnetic properties of the five-band model are very different from experiment and from those of the three-band model. One must therefore conclude that both models are insufficient in describing the magnetic properties of LaOFeAs. In fact, it turns out that an inclusion of the arsenic p-orbitals is essential, see below.

In many theoretical studies, the following Hamiltonian for the Hubbard interaction $\hat{H}_{i;\mathrm{c}}$ in (14) is used,

$$\begin{aligned}
\hat{H}_{\mathrm{c}}^{(1)} &= \hat{H}_{\mathrm{c}}^{\mathrm{dens}} + \hat{H}_{\mathrm{c}}^{\mathrm{sf}} \,, \\
\hat{H}_{\mathrm{c}}^{\mathrm{dens}} &= \sum_{b,s} U(b,b)\hat{n}_{b,s}\hat{n}_{b',\bar{s}} + \sum_{b(\neq)b'} \sum_{s,s'} \widetilde{U}_{s,s'}(b,b')\hat{n}_{b,s}\hat{n}_{b',s'} \,, \\
\hat{H}_{\mathrm{c}}^{\mathrm{sf}} &= \sum_{b(\neq)b'} J(b,b') \left(\hat{c}_{b,\uparrow}^{\dagger}\hat{c}_{b,\downarrow}^{\dagger}\hat{c}_{b',\downarrow}\hat{c}_{b',\uparrow} + \mathrm{h.c.} \right) + \sum_{b(\neq)b';s} J(b,b')\hat{c}_{b,s}^{\dagger}\hat{c}_{b',\bar{s}}^{\dagger}\hat{c}_{b,\bar{s}}\hat{c}_{b',s} \,.
\end{aligned} \tag{103}$$

Here, we introduced $\widetilde{U}_{s,s'}(b,b') = U(b,b') - \delta_{s,s'}J(b,b')$, where $U(b,b')$ and $J(b,b')$ are the local Coulomb and exchange interactions. For a system of five correlated d-orbitals in a cubic environment, however, the Hamiltonian (103) is incomplete [2]. The full Hamiltonian reads $\hat{H}_{\mathrm{c}} = \hat{H}_{\mathrm{c}}^{(1)} + \hat{H}_{\mathrm{c}}^{(2)}$ where

$$\begin{aligned}
\hat{H}_{\mathrm{c}}^{(2)} &= \Bigg[\sum_{t;s,s'} (T(t) - \delta_{s,s'}A(t))\hat{n}_{t,s}\hat{c}_{u,s'}^{\dagger}\hat{c}_{v,s'} + \sum_{t,s} A(t) \left(\hat{c}_{t,s}^{\dagger}\hat{c}_{t,\bar{s}}^{\dagger}\hat{c}_{u,\bar{s}}\hat{c}_{v,s} + \hat{c}_{t,s}^{\dagger}\hat{c}_{u,\bar{s}}^{\dagger}\hat{c}_{t,\bar{s}}\hat{c}_{v,s} \right) \\
&\quad + \sum_{t(\neq)t'(\neq)t''} \sum_{e,s,s'} S(t,t';t'',e)\hat{c}_{t,s}^{\dagger}\hat{c}_{t',s'}^{\dagger}\hat{c}_{t'',s'}\hat{c}_{e,s} \Bigg] + \mathrm{h.c.} \,.
\end{aligned} \tag{104}$$

Here, t and e are indices for the three t_{2g} orbitals with symmetries xy, xz, and yz, and the two e_g orbitals with symmetries $u = 3z^2 - r^2$ and $v = x^2 - y^2$. The parameters in (104) are of the same order of magnitude as the exchange interactions $J(b,b')$ and, hence, there is no a-priori reason to neglect them. Of all the parameters $U(b,b')$, $J(b,b')$, $A(t)$, $T(t)$, $S(t,t';t'',e)$ only ten are independent in cubic symmetry. In a spherical approximation, i.e., assuming that all orbitals have the same radial wave-function, all parameters are determined by, e.g., the three Racah parameters A, B, C. We prefer to work with the orbital averages $J \propto \sum_{b\neq b'} J(b,b')$, and $U' \propto \sum_{b\neq b'} U(b,b')$ of the exchange and the inter-orbital Coulomb interaction. They are related to the intra-orbital interaction $U = U(b,b)$ via $U' = U - 2J$. Due to this symmetry relation, the three values of U, U', and J do not determine the Racah parameters A, B, C uniquely. Therefore, we make use of the atomic relation $C/B = 4$ which is approximately satisfied in solids, too. In this way, the three Racah parameters and, consequently, all parameters in $\hat{H}_{\mathrm{c}}$ are functions of U and J. This permits a meaningful comparison of our results for all three model Hamiltonians.

In order to test the reliability of our approach we first compare our results for the partial densities of the five-band model with those from paramagnetic DMFT calculations. In Fig. 7 we show the density of electrons in each orbital as a function of U for fixed ratio $U/J = 4$. The full symbols give the Gutzwiller result for the simplified local Hamiltonian (103), $\hat{H} = \hat{H}_0 + \hat{H}_{\mathrm{c}}^{(1)}$; open symbols give the DMFT results [30]. Obviously, the agreement between the Gutzwiller theory and DMFT is very good. This comes not as a surprise because both methods are derived in the limit of infinite spatial dimensions.

Figure 7 shows a common feature of multi-band model systems. The local Coulomb interaction induces a substantial charge flow between the bands because, for the local Coulomb interaction, it is energetically more favourable to distribute electrons equally among the bands. However,

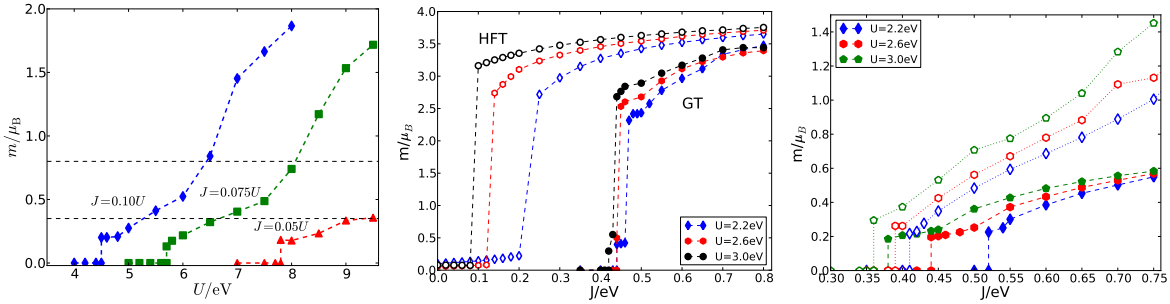

Fig. 8: *Magnetic moment as a function of U for: left: model with eight bands [26]; middle: model with five bands [27] (Hartree-Fock and Gutzwiller theory); right: model with three bands [28] and local Hamiltonians $\hat{H}_{\rm c}^{\rm dens}$ (dotted) and $\hat{H}_{\rm c}^{\rm sf}$ (dashed)* .

the bands described by $\hat{H}_0$ are extracted from a DFT calculation whose predictions for the Fermi surface reproduce experimental data reasonably well. Therefore, the artificial charge flow as seen in Fig. 7 is clearly a consequence of the double counting of Coulomb interactions. Since the (paramagnetic) Fermi surface found in DFT reproduces its experimentally determined shape, we assume that the same holds for the paramagnetic orbital densities. For each value of the interaction parameters we therefore choose orbital on-site energies $\epsilon_i^{\sigma,\sigma}$ which lead to a paramagnetic ground state with the same orbital densities as in DFT. Note that a more sophisticated calculation of orbital densities requires the self-consistent Gutzwiller DFT scheme which we shall introduce in the following section.

In Figs. 8 we display the magnetic moment as a function of U for all three model systems. As mentioned before, the three-band model shows relatively small magnetic moments over a large range of Coulomb- and exchange-interaction parameters, see Fig. 8 (right). This is in stark contrast to the results for the five-band model in Fig. 8 (middle). Here we find a transition to an antiferromagnet with a large moment, $m \gtrsim 2\mu_{\rm B}$ which is as abrupt as in a corresponding Hartree-Fock calculation. However, if one takes into account the arsenic p-bands, the magnetic moment is significantly smaller and in the range of experiment, without the need of fine-tuning the Coulomb- or exchange-interaction parameters, see Fig. 8 (left). In summary, we can conclude that a proper understanding of the magnetic order in LaOFeAs requires the study of an eight-band model of iron d- and arsenic p-bands. It it possible, of course, that other properties of this compound, e.g., the superconducting order, may be correctly described by simpler model Hamiltonians.

5 The Gutzwiller density-functional theory

5.1 The Gutzwiller DFT equations

The model-based Gutzwiller method, which we have used in the previous section, ignores the fact that the hopping parameters (9) are actually functions of the density $n(\boldsymbol{r})$. Taking this functional dependence into account defines the *Gutzwiller density functional theory* (GDFT). The explicit inclusion of the local Coulomb interaction within the Gutzwiller theory leads to

changes of the particle density $n(\boldsymbol{r})$ for three reasons:

i) The particle density $n(\boldsymbol{r})$ in the Gutzwiller-correlated ground state

$$n(\boldsymbol{r}) = \sum_{i \neq j} \sum_{\sigma,\sigma',\gamma,\gamma'} \phi^*_{i,\gamma}(\boldsymbol{r}) \phi_{j,\gamma'}(\boldsymbol{r}) q^{\sigma}_{\gamma} \left(q^{\sigma'}_{\gamma'}\right)^* \rho_{(j\sigma'),(i\sigma)} + \sum_i \sum_{\sigma} |\phi_{i,\sigma}(\boldsymbol{r})|^2 \rho_{(i\sigma),(i\sigma)} \quad (105)$$

differs from the corresponding DFT expression (10).

ii) Due to the renormalisation factors in (66) there will be an energy gain from changes of the hopping parameters $t^{\sigma,\sigma'}_{i,j} = t^{\sigma,\sigma'}_{i,j}[n(\boldsymbol{r})]$, which requires the re-adjustment of $n(\boldsymbol{r})$.

iii) The Coulomb interaction can lead to drastic changes of the occupation numbers $n^0_{i\sigma} = \rho_{(i\sigma),(i\sigma)}$ in the localised orbitals, e.g., when the ground state is magnetically ordered. This also changes the non-local elements of the single-particle density matrix $\tilde{\rho}$ and the particle density (105).

These correlation-induced changes of the particle density are taken into account in the self-consistent GDFT by including the dependence of the hopping parameters on $n(\boldsymbol{r})$. Equation (105) shows that $n(\boldsymbol{r})$ and, consequently, $t^{\sigma,\sigma'}_{i,j}$ are unique functions of $\tilde{\rho}$ and λ_Γ. Therefore, the GDFT energy functional has the form

$$E^{\mathrm{GDFT}}\left(\tilde{\rho}, \lambda_\Gamma\right) = \sum_{\sigma,\sigma',\gamma,\gamma'} q^{\sigma}_{\gamma} \left(q^{\sigma'}_{\gamma'}\right)^* \sum_{i \neq j} t^{\gamma,\gamma'}_{i,j}(\tilde{\rho}, \lambda_\Gamma) \rho_{(j\sigma'),(i\sigma)} + \sum_{i,\sigma \in \mathrm{d}} \epsilon^{\sigma,\sigma}_i \rho_{(i\sigma),(i\sigma)} + L \sum_\Gamma E_\Gamma \lambda^2_\Gamma m^0_\Gamma \; . \quad (106)$$

We assume again that the constraints (62) and (63) are solved by expressing some of the parameters λ_Γ by the remaining independent parameters $\lambda^{\mathrm{i}}_\Gamma$. The resulting energy functional $\bar{E}^{\mathrm{GDFT}}\left(\tilde{\rho}, \lambda^{\mathrm{i}}_\Gamma\right)$ has to be minimised with respect to the density matrix $\tilde{\rho}$ and the independent variational parameters $\lambda^{\mathrm{i}}_\Gamma$,

$$\frac{\partial}{\partial \rho_{(i\sigma),(j\sigma')}} \bar{E}^{\mathrm{GDFT}}\left(\tilde{\rho}, \lambda^{\mathrm{i}}_\Gamma\right) = 0 \quad , \quad \frac{\partial}{\partial \lambda^{\mathrm{i}}_\Gamma} \bar{E}^{\mathrm{GDFT}}\left(\tilde{\rho}, \lambda^{\mathrm{i}}_\Gamma\right) = 0 \; , \quad (107)$$

with the usual constraint (67) for the non-interacting density matrix $\tilde{\rho}$. The minimisation with respect to $\tilde{\rho}$ leads to renormalised Kohn-Sham equations of the form (8), (9), (11), and (105) with Eq. (8) replaced by

$$\hat{H}_0 = \sum_{i \neq j} \sum_{\sigma,\sigma',\gamma,\gamma'} q^{\sigma}_{\gamma} \left(q^{\sigma'}_{\gamma'}\right)^* t^{\gamma,\gamma'}_{i,j}(\tilde{\rho}, \lambda_\Gamma) \hat{c}^\dagger_{i,\sigma} \hat{c}_{j,\sigma'} + \sum_{i,\sigma \in \ell} \eta_\sigma \hat{c}^\dagger_{i,\sigma} \hat{c}_{i,\sigma}, \quad (108)$$

and by [18]

$$\eta_{\tilde{\sigma}} \equiv \frac{1}{L} \sum_{\sigma,\sigma',\gamma,\gamma'} \Big[\frac{\partial}{\partial n_{\tilde{\sigma}}} q^{\sigma}_{\gamma} \left(q^{\sigma'}_{\gamma'}\right)^* \Big] \sum_{i \neq j} t^{\gamma,\gamma'}_{i,j}(\tilde{\rho}, \lambda_\Gamma) \rho_{(j\sigma'),(i\sigma)} + \frac{\partial}{\partial n_{\tilde{\sigma}}} \sum_\Gamma E_\Gamma \lambda^2_\Gamma m^0_\Gamma \; , \quad (109)$$

respectively. The set of Eqs. (9), (105), and (106)-(109), which have to be solved self-consistently, constitute the GDFT. This approach was first proposed in Refs. [31–33] and has been applied

to various systems in Refs. [32–36]. In all these works, the authors report a remarkably better agreement with experiment than it could be obtained by a model-based Gutzwiller calculation for the same materials.

One of the main advantages of the DFT is its *ab-initio* character, i.e., the absence of any adjustable parameters. Unfortunately, this benefit of the DFT cannot be fully maintained in the GDFT because that would require the calculation of the two-particle interaction parameters $U_i^{\sigma_1,\sigma_2,\sigma_3,\sigma_4}$ in the localised orbitals from first principles. The straightforward *ab-initio* solution of this problem, namely to calculate these parameters from the Wannier orbitals $\phi_{i,\sigma}(\boldsymbol{r})$, is known to yield values which are much too large. Apparently, screening effects decrease the Coulomb-interaction parameters significantly. These effects, however, are not well understood and a quantitatively reliable technique for the calculation of screened Coulomb parameters does not exist. For this reason one usually applies the same strategy as in model-based calculations where the matrix elements $U_i^{\sigma_1,\sigma_2,\sigma_3,\sigma_4}$ are somehow parameterised, e.g., in spherical approximation by means of a few Racah parameters. These are chosen to obtain the best agreement with experiment. In this context, it is a big advantage that the GDFT provides one with more data, e.g., with structural properties, that can be compared to experiment, see Sec. 5.2.

As mentioned before, the local Coulomb interaction appears twice in the Hamiltonian (14) because it also affects the on-site energies $\epsilon_i^{\sigma,\sigma'}$. There are several ways to overcome this *double-counting problem* which have been proposed in the literature, see, e.g., Ref. [37]. According to Refs. [32–36], the subtraction of the mean-field operator

$$\hat{H}_{\rm dc} = 2 \sum_{\sigma,\sigma',\gamma\in\ell} (U_i^{\sigma,\gamma,\gamma,\sigma'} - U_i^{\gamma,\sigma,\gamma,\sigma'}) n_\gamma^0 \hat{c}_{i,\sigma}^\dagger \hat{c}_{i,\sigma'}, \tag{110}$$

from $\hat{H}_{i;\rm c}$ leads to good results within the GDFT.

5.2 Application

As an example for the relevance of the GDFT we show results on the iron-pnictides LaOFeAs and $BaFe_2As_2$ which have been presented in Ref. [35]. The failure to describe the magnetic order is not the only problem the DFT faces in its calculations on iron-pnictides. There are also substantial deviations between the experimental results and DFT predictions on lattice parameters, in particular for the distance between Fe and As. Taking correlations into account more properly, as it is done within the GDFT, changes these lattice parameters significantly. Figure 9 shows the interlayer distance $d_{\rm FeAs}^z$ as a function of J for several values of U. In both systems, the exchange interaction clearly plays an important role and needs to be included in order to reproduce the experimental value for $d_{\rm FeAs}^z$. As a consequence, other properties are also changed significantly as a function of J, see Ref. [35]. It should be noted that the calculations in Ref. [35] were carried out with the simplified local Hamiltonian $\hat{H}_c^{\rm dens}$ in Eq. (103). Taking the full atomic interaction into account may therefore change results, at least quantitatively. Nevertheless, these results already illustrate how important it is, in studies on transition metal compounds, to treat the local Coulomb interaction in a more sophisticated way than provided by state-of-the-art DFT methods.

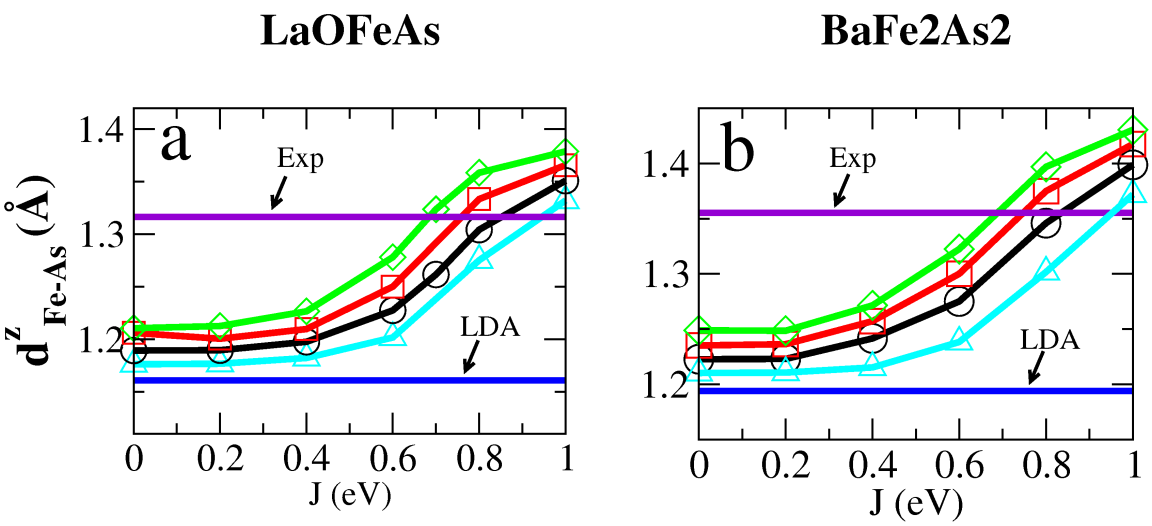

Fig. 9: *Interlayer distance d^z_{FeAs} in LaOFeAs and $BaFe_2As_2$ as a function of J for several values of U.*

6 Summary and Outlook

In this tutorial presentation, we have provided a comprehensive introduction into the Gutzwiller variational approach and its merger with the density functional theory. Numerically, the Gutzwiller method is rather cheap as compared to other many-particle approaches. It will therefore, quite likely, emerge as an important tool for the improvement of existing *ab-initio* methods. There are two more recent developments which we shall briefly mention as an outlook:

- **The time-dependent Gutzwiller theory**

  The Gutzwiller theory, as introduced in this presentation, can be used for the calculation of ground-state properties and of quasi-particle energies in the Fermi-liquid regime. For the description of experiments one often needs to calculate two-particle response functions such as the magnetic susceptibility or the optical conductivity. This is achieved by the so-called *time dependent Gutzwiller theory*. This method is derived in a very similar way, as the random-phase approximation can be introduced as a time-dependent generalisation of the Hartree-Fock theory. It was first developed for single-band Hubbard models by Seibold et al. [38, 39] and has been applied with astonishing success to quite a number of such models and response functions [40–50]. Recently, the method has been generalised for the study of multi-band models [51, 52].

- **Beyond the Gutzwiller approximation**

  As we have demonstrated in this presentation, the energy-functional which we derived in infinite dimensions (i.e., the Gutzwiller approximation), constitutes already a major improvement over, e.g., the Hartree-Fock theory. It is well-known, however, that the limit of infinite spatial dimensions has some severe limitations. For example, if we consider the Fermi surface of a single-band Hubbard model, it will be independent of U as long as

no symmetry-broken phases are considered. This cannot be correct in finite dimensions which becomes evident already from straightforward perturbation theory in U [53]. It is also known from a numerical evaluation of Gutzwiller wave functions in two dimensions that, for sufficiently large values of U, the variational ground states can be superconducting [54, 55]. This is also not reproduced within the Gutzwiller approximation. In a recent work, we have therefore proposed an efficient diagrammatic method for the evaluation of Gutzwiller wave functions in finite dimensions [56]. It has enabled us to study correlation-induced Fermi-surface deformations [56] as well as superconductivity (unpublished). The numerical effort of this method is still moderate and the investigation of more complicated multi-band models will therefore be feasible in the near future.

Acknowledgment

The proofreading of this manuscript by F. Gebhard is gratefully acknowledged. I also thank the authors of Ref. [35] for providing me with the data, shown in Fig. 9.

Appendix

A Minimisation of functions with respect to non-interacting density matrices

We consider a general function $E(\tilde{\rho})$ of a non-interacting density matrix $\tilde{\rho}$ with the elements

$$\rho_{\gamma,\gamma'} = \langle \hat{c}^\dagger_{\gamma'} \hat{c}_\gamma \rangle_{\Phi_0} \ . \tag{111}$$

The fact that $\tilde{\rho}$ is derived from a single-particle product wave function $|\Phi_0\rangle$ is equivalent to the matrix equation $\tilde{\rho}^2 = \tilde{\rho}$. Hence, the minimum of $E(\tilde{\rho})$ in the space of all *non-interacting* density matrices is determined by the condition

$$\frac{\partial}{\partial \rho_{\gamma',\gamma}} L(\tilde{\rho}) = 0 \ , \tag{112}$$

where we introduced the Lagrange functional

$$\begin{aligned} L(\tilde{\rho}) &\equiv E(\tilde{\rho}) - \sum_{l,m} \Omega_{l,m} \left[\tilde{\rho}^2 - \tilde{\rho} \right]_{m,l} & (113) \\ &= E(\tilde{\rho}) - \sum_{l,m} \Omega_{l,m} \Big(\sum_p \rho_{m,p} \rho_{p,l} - \rho_{m,l} \Big) & (114) \end{aligned}$$

and the matrix $\tilde{\Omega}$ of Lagrange parameters $\Omega_{l,m}$. The minimisation of (113) leads to the matrix equation

$$\tilde{H} = \tilde{\rho}\tilde{\Omega} + \tilde{\Omega}\tilde{\rho} - \tilde{\Omega} \tag{115}$$

for the Hamilton matrix $\tilde{H}$ with the elements

$$H_{\gamma,\gamma'} = \frac{\partial}{\partial \rho_{\gamma',\gamma}} E(\tilde{\rho}) \ . \tag{116}$$

For density matrices which satisfy $\tilde{\rho}^2 = \tilde{\rho}$, Eq. (115) leads to $[\tilde{H}, \tilde{\rho}] = 0$. Hence, $\tilde{H}$ and $\tilde{\rho}$ must have the same basis of (single-particle) eigenvectors and, consequently, $|\Phi_0\rangle$ is the ground state of

$$\hat{H}_0^{\text{eff}} = \sum_{\gamma,\gamma'} H_{\gamma,\gamma'} \hat{c}^\dagger_\gamma \hat{c}_{\gamma'} \ . \tag{117}$$

References

[1] P. Hohenberg and W. Kohn, Phys. Rev. **136**, 864 (1964)

[2] S. Sugano, Y. Tanabe, and H. Kamimura: *Multiplets of Transition-Metal Ions in Crystals*, Pure and Applied Physics 33 (Academic Press, New York, 1970)

[3] E. Feenberg: *Theory of Quantum Liquids* (Academic Press, New York, 1969)

[4] B.E. Clements, E. Krotscheck, J.A. Smith, and C.E. Campbell, Phys. Rev. B **47**, 5239 (1993)

[5] M.C. Gutzwiller, Phys. Rev. Lett **10**, 159 (1963)

[6] M.C. Gutzwiller, Phys. Rev. **134**, A923 (1964)

[7] M.C. Gutzwiller, Phys. Rev. **137**, A1726 (1965)

[8] J. Bünemann, W. Weber, and F. Gebhard, Phys. Rev. B **57**, 6896 (1998)

[9] J. Bünemann, F. Gebhard, and W. Weber,
in A. Narlikar (ed.), *Frontiers in Magnetic Materials* (Springer, Berlin, 2005)

[10] J. Bünemann, T. Schickling, F. Gebhard, and W. Weber,
physica status solidi (b) **249**, 1282 (2012)

[11] J. Bünemann, K. Jávorne-Radnóczi, P. Fazekas, and F. Gebhard,
J. Phys. Cond. Mat., **17**, 3807 (2005)

[12] W. Metzner and D. Vollhardt, Phys. Rev. B **37**, 7382 (1988)

[13] M. Kollar and D. Vollhardt, Phys. Rev. B **65**, 155121 (2002)

[14] F. Gebhard and D. Vollhardt, Phys. Rev. Lett. **59**, 1472 (1987)

[15] F. Gebhard and D. Vollhardt, Phys. Rev. B **38**, 6911 (1988)

[16] F. Gebhard, Phys. Rev. B **41**, 9452 (1990)

[17] J. Bünemann, Eur. Phys. J. B **4**, 29 (1998)

[18] Note that, in general, the fields η_σ are non-diagonal ($\eta_{\sigma,\sigma'}$) and given as the derivative of the energy-functional with respect to the elements of the non-interacting density matrix (30). This requires the evaluation of the more complicated energy functional without the condition (31), see Ref. [10]

[19] J. Bünemann, F. Gebhard, and R. Thul, Phys. Rev. B **67**, 75103 (2003)

[20] J. Bünemann and W. Weber, Physica B **230**, 412 (1997)

[21] C. de la Cruz, Q. Huang, J.W. Lynn, J. Li, W. Ratcliff, J.L. Zarestky, H.A. Mook, G.F. Chen, J.L. Luo, N.L. Wang, and P. Dai, Nature London **453**, 899 (2008)

[22] N. Qureshi, Y. Drees, J. Werner, S. Wurmehl, C. Hess, R. Klingeler, B. Büchner, M.T. Fernández-Díaz, and M. Braden, Phys. Rev. B **82**, 184521 (2010)

[23] H.F. Li, H.-F. Li, W. Tian, J.-Q. Yan, J.L. Zarestky, R.W. McCallum, T.A. Lograsso, and D. Vaknin, Phys. Rev. B **82**, 064409 (2010)

[24] I.I. Mazin, M.D. Johannes, L. Boeri, K. Koepernik, and D.J. Singh, Phys. Rev. B **78**, 085104 (2008)

[25] Y.-Z. Zhang, I. Opahle, H.O. Jeschke, and R. Valentí, Phys. Rev. B **81**, 094505 (2010)

[26] O.K. Andersen and L. Boeri, Ann. Physik (Berlin) **523**, 8 (2011)

[27] S. Graser, T. Maier, P. Hirschfeld, and D. Scalapino, New J. Phys. **11**, 025016 (2009)

[28] S. Zhou and Z. Wang, Phys. Rev. Lett. **105**, 096401 (2010)

[29] T. Schickling, F. Gebhard, and J. Bünemann, Phys. Rev. Lett. **106**, 146402 (2011)

[30] H. Ishida and A. Liebsch, Phys. Rev. B **81**, 054513 (2010)

[31] K.M. Ho, J. Schmalian, and C.Z. Wang, Phys. Rev. B **77**, 073101 (2008)

[32] X. Deng, X. Dai, and Z. Fang, Europhys. Lett. **83**, 37008 (2008)

[33] X. Deng, L. Wang, X. Dai, and Z. Fang, Phys. Rev. B **79**, 075114 (2009)

[34] G. Wang, X. Dai, and Z. Fang, Phys. Rev. Lett. **101**, 066403 (2008)

[35] G. Wang, Y. M. Qian, G. Xu, X. Dai, and Z. Fang, Phys. Rev. Lett. **104**, 047002 (2010)

[36] H. Weng, G. Xu, H. Zhang, S.-C. Zhang, X. Dai, and Z. Fang, Phys. Rev. B **84**, 060408 (2011)

[37] M. Karolak, G. Ulm, T. Wehling, V. Mazurenko, A. Poteryaev, and A. Lichtenstein, J. of Electron Spectroscopy and Related Phenomena **181**, 11, (2010)

[38] G. Seibold, E. Sigmund, and V. Hizhnyakov, Phys. Rev. B **57**, 6937 (1998)

[39] G. Seibold and J. Lorenzana, Phys. Rev. Lett. **86**, 2605 (2001)

[40] G. Seibold, Phys. Rev. B **58**, 15520 (1998)

[41] G. Seibold, F. Becca, and J. Lorenzana, Phys. Rev. B **67**, 085108 (2003)

[42] J. Lorenzana and G. Seibold, Phys. Rev. Lett. **90**, 066404 (2003)

[43] G. Seibold and J. Lorenzana, Phys. Rev. B **69**, 134513 (2004)

[44] G. Seibold, F. Becca, P. Rubin, and J. Lorenzana, Phys. Rev. B **69**, 155113 (2004)

[45] J. Lorenzana, G. Seibold, and R. Coldea, Phys. Rev. B **72**, 224511 (2005)

[46] G. Seibold and J. Lorenzana, Phys. Rev. Lett. **94**, 107006 (2005)

[47] G. Seibold and J. Lorenzana, Phys. Rev. B **73**, 144515 (2006)

[48] G. Seibold and J. Lorenzana, J. of Superconductivity and Novel Magnetism **20**, 619 (2007)

[49] G. Seibold, F. Becca, and J. Lorenzana, Phys. Rev. Lett. **100**, 016405 (2008)

[50] G. Seibold, F. Becca, and J. Lorenzana, Phys. Rev. B **78**, 045114 (2008)

[51] E. v. Oelsen, G. Seibold, and J. Bünemann, Phys. Rev. Lett. **107**, 076402 (2011)

[52] E. v. Oelsen, G. Seibold, and J. Bünemann, New J. Phys. **13**, 113031 (2011)

[53] C. J. Halboth and W. Metzner, Z. Phys. B **102**, 501 (1997)

[54] D. Eichenberger and D. Baeriswyl, Phys. Rev. B **76**, 180504 (2007)

[55] D. Eichenberger and D. Baeriswyl, Phys. Rev. B **79**, 100510 (2009)

[56] J. Bünemann, T. Schickling, and F. Gebhard, Europhys. Lett. **98**, 27006 (2012)

6 Crystal-Field Theory, Tight-Binding Method and Jahn-Teller Effect

Eva Pavarini
Institute for Advanced Simulation
Forschungszentrum Jülich GmbH

Contents

E. Pavarini, E. Koch, F. Anders, and M. Jarrell
Correlated Electrons: From Models to Materials
Modeling and Simulation Vol. 2
Forschungszentrum Jülich, 2012, ISBN 978-3-89336-796-2
http://www.cond-mat.de/events/correl12

1 Introduction

The central equation of solid-state physics is the eigenvalue problem $\hat{H}\Psi = E\Psi$, defined (in the non-relativistic limit) by the many-body Hamiltonian

$$\hat{H} = -\frac{1}{2}\sum_i \nabla_i^2 + \frac{1}{2}\sum_{i\neq i'} \frac{1}{|\boldsymbol{r}_i - \boldsymbol{r}_{i'}|} - \sum_{i,\alpha} \frac{Z_\alpha}{|\boldsymbol{r}_i - \boldsymbol{R}_\alpha|} - \sum_\alpha \frac{1}{2M_\alpha}\nabla_\alpha^2 + \frac{1}{2}\sum_{\alpha\neq\alpha'} \frac{Z_\alpha Z_{\alpha'}}{|\boldsymbol{R}_\alpha - \boldsymbol{R}_{\alpha'}|},$$

where $\{\boldsymbol{r}_i\}$ are the coordinates of the N_e electrons, $\{\boldsymbol{R}_\alpha\}$ those of the N_n nuclei, Z_α the atomic numbers, and M_α the nuclear masses.[1] The Born-Oppenheimer Ansatz

$$\Psi(\{\boldsymbol{r}_i\},\{\boldsymbol{R}_\alpha\}) = \psi(\{\boldsymbol{r}_i\};\{\boldsymbol{R}_\alpha\})\Phi(\{\boldsymbol{R}_\alpha\}), \tag{1}$$

splits the Schrödinger equation $\hat{H}\Psi = E\Psi$ into the system

$$\begin{cases} \hat{H}_e\psi(\{\boldsymbol{r}_i\};\{\boldsymbol{R}_\alpha\}) &= \varepsilon(\{\boldsymbol{R}_\alpha\})\psi(\{\boldsymbol{r}_i\};\{\boldsymbol{R}_\alpha\}), \\ \\ \hat{H}_n\Phi(\{\boldsymbol{R}_\alpha\}) &= E\Phi(\{\boldsymbol{R}_\alpha\}), \end{cases} \tag{2}$$

where the Hamilton operator for the electrons ($\hat{H}_e$) and that for the lattice ($\hat{H}_n$) are

$$\begin{aligned} \hat{H}_e &= -\frac{1}{2}\sum_i \nabla_i^2 + \frac{1}{2}\sum_{i\neq i'} \frac{1}{|\boldsymbol{r}_i - \boldsymbol{r}_{i'}|} - \sum_{i,\alpha} \frac{Z_\alpha}{|\boldsymbol{r}_i - \boldsymbol{R}_\alpha|} + \frac{1}{2}\sum_{\alpha\neq\alpha'} \frac{Z_\alpha Z_{\alpha'}}{|\boldsymbol{R}_\alpha - \boldsymbol{R}_{\alpha'}|} \\ &= \hat{T}_e + \hat{V}_{ee} + \hat{V}_{en} + \hat{V}_{nn}, \end{aligned} \tag{3}$$

$$\begin{aligned} \hat{H}_n &= -\sum_\alpha \frac{1}{2M_\alpha}\nabla_\alpha^2 + \varepsilon(\{\boldsymbol{R}_\alpha\}) \\ &= \hat{T}_n + \hat{U}_n, \end{aligned} \tag{4}$$

and where in (4) we neglect non-adiabatic corrections.[2] The electronic eigenvalue $\varepsilon(\{\boldsymbol{R}_\alpha\})$ acts as potential for the nuclei and defines a Born-Oppenheimer energy surface. While (3) describes the electronic structure, (4) yields the equilibrium crystal structure of the system and the phonon modes. If the equilibrium structure $\{\boldsymbol{R}_\alpha^0\}$ is known, for example experimentally, we can focus on (3). Because $\hat{V}_{ee}$ is not separable, with increasing N_e, finding the eigenvalues and eigenvectors of (3) becomes quickly an unfeasible task, even for a single atom. The modern approach to such many-body problems consists in building, starting from (3), minimal but material specific low-energy many-body models, which retain the essential physics of the phenomenon we want to understand [1].

The first step in model building consists in performing density-functional theory (DFT) calculations. DFT is based on the Hohenberg-Kohn theorem, which states that the ground-state energy of the many-body Hamiltonian (3) is a functional $E[n]$ of the electron density, minimized by

[1] In this lecture we use atomic units (see Appendix A).

[2] The neglected term is $\hat{\Lambda}_n = -\sum_\alpha \frac{1}{M_\alpha}\left[\frac{1}{2}\langle\psi|\nabla_\alpha^2\psi\rangle + \langle\psi|\nabla_\alpha\psi\rangle\cdot\nabla_\alpha\right]$.

the ground-state density. In the Kohn-Sham DFT scheme, the ground-state energy of (3) can be obtained by solving an auxiliary Schrödinger equation $\hat{h}_e\psi = \varepsilon\psi$, with

$$\hat{h}_e = \sum_i \left[-\frac{1}{2}\nabla_i^2 + v_R(\boldsymbol{r}_i)\right] = \sum_i \hat{h}_e(\boldsymbol{r}_i). \tag{5}$$

The auxiliary Hamiltonian describes N_e non-interacting electrons in an external potential, $v_R(\boldsymbol{r})$, chosen such that the ground-state electron density $n_0(\boldsymbol{r})$ of the auxiliary model equals $n(\boldsymbol{r})$, the ground-state electron density of the original interacting system. This potential can be written as

$$v_R(\boldsymbol{r}) = -\sum_\alpha \frac{Z_\alpha}{|\boldsymbol{r}-\boldsymbol{R}_\alpha|} + \int d\boldsymbol{r}' \frac{n(\boldsymbol{r}')}{|\boldsymbol{r}-\boldsymbol{r}'|} + \frac{\delta E_{\rm xc}[n]}{\delta n} = v_{en}(\boldsymbol{r}) + v_H(\boldsymbol{r}) + v_{xc}(\boldsymbol{r}), \tag{6}$$

where $v_H(\boldsymbol{r})$ is the long-range Hartree term and $E_{\rm xc}[n]$ is the so-called exchange-correlation functional. The main difficulty of DFT is that $E_{\rm xc}[n]$ is not know, and it is therefore necessary to find good approximations for it. Most common are the local-density approximation (LDA) and its extensions; they work remarkably well for several classes of materials and properties, as discussed in the lecture of David Singh. The class of systems at the center of this school, however, is made of compounds for which many-body effects *beyond* the LDA play a crucial role, leading to cooperative emergent phenomena; examples are transition-metal oxides with partially filled d-shells, Mott insulators, Kondo systems, and heavy fermions. For such *strongly correlated materials* simple approximations to $E_{\rm xc}[n]$ fail, even qualitatively.

For strongly correlated systems, the second step consists in using DFT to construct a *localized* one-electron basis; this is usually achieved building from the Bloch functions $\psi_{n\boldsymbol{k}\sigma}(\boldsymbol{r})$, obtained by solving (5) for a given crystal, material-specific Wannier functions

$$\psi_{in\sigma}(\boldsymbol{r}) = \frac{1}{\sqrt{N}} \sum_{\boldsymbol{k}} e^{-i\boldsymbol{R}_i\cdot\boldsymbol{k}}\, \psi_{n\boldsymbol{k}\sigma}(\boldsymbol{r}).$$

Localized Wannier functions can be constructed using different procedures: the downfolding approach, discussed in [2] and in the lecture of Ole Andersen, the maximally-localized Wannier functions algorithm of Marzari and Vanderbilt [3], and the projectors technique, described in the lecture of Sasha Lichtenstein.

The third step consists in writing the Hamiltonian (3) in second quantization using such localized Wannier functions as one-electron basis. The resulting many-body Hamiltonian is the sum of an LDA term $\hat{H}^{\rm LDA}$, a Coulomb term $\hat{U}$, and a double-counting correction $\hat{H}_{\rm DC}$

$$\hat{H}_e = \hat{H}^{\rm LDA} + \hat{U} - \hat{H}_{\rm DC}. \tag{7}$$

The LDA part of the Hamiltonian is given by

$$\hat{H}^{\rm LDA} = -\sum_\sigma \sum_{in,i'n'} t_{n,n'}^{i,i'} c_{in\sigma}^\dagger c_{i'n'\sigma}, \tag{8}$$

where $c_{in\sigma}^\dagger$ ($c_{in\sigma}$) creates (annihilates) an electron of spin σ in orbital n at site i, and

$$t_{n,n'}^{i,i'} = -\int d\boldsymbol{r}\, \overline{\psi}_{in\sigma}(\boldsymbol{r})[-\frac{1}{2}\nabla^2 + v_{\rm R}(\boldsymbol{r})]\psi_{i'n'\sigma}(\boldsymbol{r}). \tag{9}$$

The $i \neq i'$ contributions are the hopping integrals, while the on-site ($i = i'$) term yields the crystal-field matrix

$$\varepsilon^{i,i}_{n,n'} = -t^{i,i}_{n,n'} = \int d\boldsymbol{r}\, \overline{\psi}_{in\sigma}(\boldsymbol{r}) \left[-\frac{1}{2}\nabla^2 + v_{\rm R}(\boldsymbol{r}) \right] \psi_{in'\sigma}(\boldsymbol{r}). \tag{10}$$

The Coulomb interaction $\hat{U}$ is given by

$$\hat{U} = \frac{1}{2} \sum_{ii'jj'} \sum_{\sigma\sigma'} \sum_{nn'pp'} U^{ij\,i'j'}_{np\,n'p'} c^\dagger_{in\sigma} c^\dagger_{jp\sigma'} c_{j'p'\sigma'} c_{i'n'\sigma},$$

with

$$U^{iji'j'}_{np\,n'p'} = \int d\boldsymbol{r}_1 \int d\boldsymbol{r}_2\, \frac{\overline{\psi}_{in\sigma}(\boldsymbol{r}_1) \overline{\psi}_{jp\sigma'}(\boldsymbol{r}_2) \psi_{j'p'\sigma'}(\boldsymbol{r}_2) \psi_{i'n'\sigma}(\boldsymbol{r}_1)}{|\boldsymbol{r}_1 - \boldsymbol{r}_2|}. \tag{11}$$

The Coulomb tensor (11) is discussed in [4] and in the lecture of Robert Eder. The double counting term $\hat{H}_{\rm DC}$ cancels the part of the electron-electron interaction contained and already well accounted for in $\hat{H}^{\rm LDA}$, such as the mean-field part of the exchange-correlation interaction and the long-range Hartree term; the difference $\hat{U} - \hat{H}_{\rm DC}$ is therefore a short-range many-body correction to the LDA [4]. The Hamiltonian (7) still describes the full many-body problem and further approximations are necessary to make progress. Typically electrons are divided into two types, correlated or heavy electrons (e.g., d or f open shells) and uncorrelated or light electrons. For the correlated electrons the LDA fails qualitatively, and $\hat{U} - \hat{H}_{\rm DC}$ has to be accounted for explicitly; for the light electrons we can instead assume that LDA is overall a good approximations and no correction $\hat{U} - \hat{H}_{\rm DC}$ is needed. The main effect of the light electrons is assumed to be a renormalization of the Coulomb parameters (*screening*), which, as a consequence, cannot be calculated any more as in (11); since the exact screening is not known, approximated schemes such as the constrained LDA or the constrained random-phase approximation are commonly used. These schemes are discussed in the lecture of Olle Gunnarsson. The separation of electron in light and heavy is the most delicate aspect of model building, as only in few cases the distinction is really clear cut. In most cases we can only make a reasonable guess, that has to be tested *a posteriori*, e.g., comparing with experiments, or better, when doable, extending the basis of heavy electrons to include, e.g., other states close to the Fermi level.

In the last step, the minimal material-specific many-body model is solved using many-body methods. If we solve it with the dynamical mean-field theory (DMFT) approach, the procedure described above defines the LDA+DMFT method [4].

While strong-correlation effects arise from the Coulomb matrix (11), chemistry enters mostly through the hopping integrals (9) and the crystal-field matrix (10). The purpose of this lecture is to explain the physical origin of these parameters, and the role they can play. To do this we will use some basic results of group theory. For simplicity, in most derivations we will use atomic hydrogen-like orbitals as a basis; the generalization to Wannier functions is straightforward.

The lecture is organized as follows. In section 2 we introduce group theory; we discuss the case of a free atom and the covering operations of molecules and crystals. In section 3 we analyze

how and why, in a crystal or a molecule, the atomic l-shells split, becoming the crystal-field levels; we focus in particular on the splitting due to the electric field generated at a given site by the surrounding ions. In section 4 we discuss covalency effects, which lead to the formations of bonds and bands (hopping integrals), and contribute to the splitting of atomic levels. In the last section we analyze the Jahn-Teller effect, a cooperative distortion driven by the coupling between electrons and lattice, which leads to further crystal-field splitting.

2 Elements of group theory

A *group*[3] G is a set of elements $\{g_i\}$ plus an operation, $\star$, which satisfy the following conditions

1. G is closed under group multiplication, i.e., $g_i \star g_j = g_k \in G \ \forall g_i,\ g_j \in G$
2. the *associative law* holds, i.e., $g_i \star (g_j \star g_k) = (g_i \star g_j) \star g_k \ \forall g_i,\ g_j,\ g_k \in G$
3. there is an *identity element* $e \in G$, such that $g_i \star e = e \star g_i = g_i \, \forall g_i \in G$
4. there is an *inverse element* $g_i^{-1} \in G$ to each $g_i \in G$, such that $g_i \star g_i^{-1} = g_i^{-1} \star g_i = e$

If the operation $\star$ is commutative, so that $g_i \star g_j = g_j \star g_i \ \forall g_i,\ g_j \in G$, the group is called *Abelian*. Groups with a finite number h of elements are called *finite groups*, and h is said to be the *order* of the group. An element g_i in group G is said to be *conjugated* to g_j if

$$g_i = g_X \star g_j \star g_X^{-1},$$

where g_X is some element of G. The elements of G can be collected into *classes* $\mathcal{C}_k$, each of which is made of all N_k mutually conjugated elements. The identity forms a class by itself. A *subgroup* of G is a set of elements of G which forms a group with the same multiplication operation of G, $\star$. Every group has at least two trivial subgroups, the group itself and a group formed by the identity only. A subgroup N of G is *invariant* if $gNg^{-1} = N \ \forall g \in G$.
Two groups G and G' are *homomorphic* if there is a correspondence $g_i \rightarrow g_i{}'$ between the elements of the two groups, so that

$$(g_i \star g_j)' = g_i' \star' g_j' \qquad \forall g_i, g_j \in G,$$

where $\star$ and $\star'$ are the multiplication operations of G and G', respectively. A homomorphism is in general a many-to-one correspondence, $\{g_1, g_2, \dots\} \rightarrow g_i'$. The identity of G, e, has as image the identity of G', e'; however in general there are several elements of G, $\{a_1 = e, a_2, \dots a_e\}$ which have e' as image in G'. Furthermore, if $g_j \in G$ has the image $g_j' \in G'$, all elements $\{g_j a_i\}$ have the same image g_j' in G'. The set $\{a_1, a_2, \dots a_e\}$ forms an invariant subgroup of G. If the correspondence between the elements of G' and G is one-to-one, G and G' are said to be *isomorphic*. A finite group is specified by the *multiplication table* of its elements; two groups with the same multiplication table are isomorphic.

[3] This section is a short summary of results relevant for the topics treated; it does not aim to be a rigorous introduction to group theory. For the latter, we refer the interested reader to specialized books [5, 6].

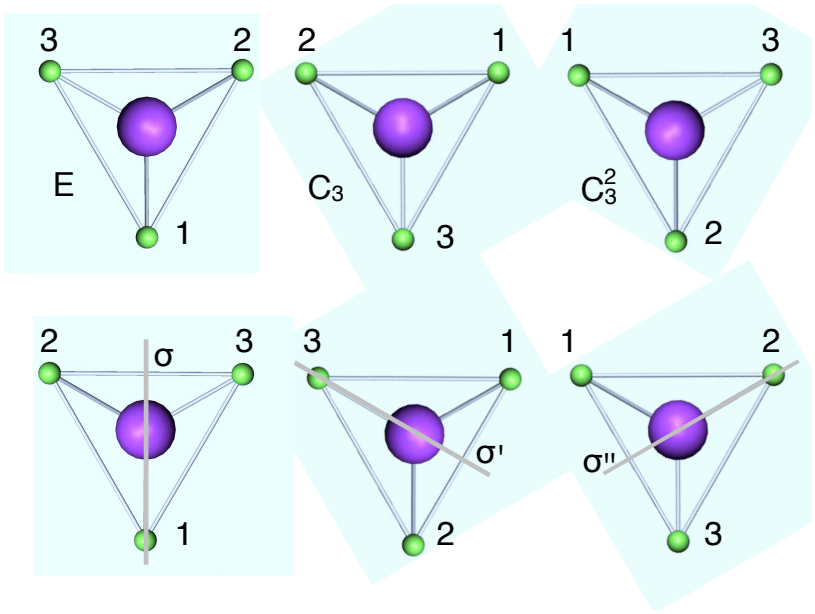

Fig. 1: *The symmetry operations which transform the ammonia molecule NH_3 into itself (viewed from the top). The point group is C_{3v}, the group of covering operations of a trigonal pyramid.*

Some of the groups relevant in physics are:

- $S(n)$, the group of permutations of n objects; $\star$ is the composition of permutations
- the group of vectors in three dimensions; $\star$ is the sum of vectors
- groups of matrices, with the matrix product as $\star$; in particular
  - $U(n)$, the group of unitary $n \times n$ matrices
  - $O(n)$, the group of orthogonal $n \times n$ matrices
  - $SU(n)$, the group of unitary $n \times n$ matrices with determinant 1
  - $SO(n)$, the group of orthogonal $n \times n$ matrices with determinant 1
  - finite groups of matrices

The group of all proper rotations in three dimensions is isomorphic to $SO(3)$. Every finite group of order n is isomorphic to a subgroup of $S(n)$. The set of all geometric symmetries that leave at least one point fixed (the origin) forms the *point group*. The point groups of crystals or molecules are isomorphic to finite subgroups of the orthogonal group $O(3)$; they are also the groups of covering operations of a given polyhedron. For example, the point group of the ammonia molecule NH_3 is the group of covering operations of a trigonal pyramid, and has six elements, shown in Fig. 1: the identity E, two rotations, by $2\pi/3$ and $4\pi/3$ (operations C_3 and $C_3^2 = C_3 \otimes C_3$), and three reflections (σ, σ', σ''). This group, called C_{3v}, has three classes, $\mathcal{C}_1 = \{E\}$, $\mathcal{C}_2 = \{C_3, C_3^2\}$, and $\mathcal{C}_3 = \{\sigma, \sigma', \sigma''\}$.

A *representation* of an abstract group G is any group G' homomorphic (or isomorphic) to G that is composed of specific operators acting on a given linear space $\mathcal{L}$. If G and G' are isomorphic the representation is said to be *faithful*. In this lecture we work with representations made of square matrices, which we indicate as $\Gamma(g_i)$; the multiplication operation of the group, $\star$, is the matrix product. As an example, we consider the group G of the rotations about the z axis. In this example, G is the abstract group. We can associate to each counterclockwise rotation by an angle θ (i.e., to each element $g = R(\theta)$ of G) a matrix $M(\theta)$

$$g = R(\theta) \rightarrow M(\theta) = \begin{pmatrix} \cos\theta & -\sin\theta \\ \sin\theta & \cos\theta \end{pmatrix}.$$

The elements of the matrix are the coefficients of the transformation

$$\begin{aligned} x' &= x\cos\theta - y\sin\theta, \\ y' &= y\sin\theta + x\cos\theta. \end{aligned}$$

The matrices $M(\theta)$ form a representation of G acting on the two-dimensional linear space $\mathcal{L}$ of vectors in the xy plane. The number of rows and columns of the matrices yields the *dimensionality* d of the representation; in the example just discussed $d = 2$.
A matrix representation Γ is called *reducible* if every matrix in the representation, $\Gamma(g_i)$, can be written in the same block form through the same *similarity transformation*.[4] If this cannot be done, the representation is said to be *irreducible*. For example if

$$\Gamma(g_i) = \begin{pmatrix} \Gamma_1(g_i) & 0 \\ 0 & \Gamma_2(g_i) \end{pmatrix} \quad \forall g_i \in G,$$

the representation Γ is said to be reducible. The number of irreducible representations is equal to the number of the classes. If the group is Abelian, the number of irreducible representations equals the number of elements and the irreducible representations are all one dimensional.
If the matrices of a representation are unitary, the representation is said to be *unitary*. A representation of a finite group made of non-singular $n \times n$ matrices is equivalent, through a similarity transformation, to a representation by unitary matrices. For finite groups, it is therefore always possible to work with unitary representations. There is nevertheless an infinite number of equivalent representations of a group G, and thus a large arbitrariness in the form of the representation. However the trace of a matrix is invariant under a similarity transformation; it is therefore useful to classify matrix representations through their *characters*, defined as

$$\chi(g_i) = \mathrm{Tr}\ \Gamma(g_i).$$

The matrix representations of all the elements g_k in a given class, $\mathcal{C}_k$, have the same character, $\chi(g_k) = \chi(\mathcal{C}_k)$, $\forall g_k \in \mathcal{C}_k$. Furthermore the following *orthogonality relations* hold for the

[4] A similarity transformation is the transformation of a $n \times n$ matrix Γ into another $n \times n$ matrix $\Gamma' = B^{-1}AB$, where B is an invertible $n \times n$ matrix.

irreducible representations Γ_j of a given group

$$\sum_i [\chi_{j_1}(g_i)]^* \chi_{j_2}(g_i) = \sum_k N_k [\chi_{j_1}(\mathcal{C}_k)]^* \chi_{j_2}(\mathcal{C}_k) = h\delta_{j_1,j_2}, \tag{12}$$

$$\sum_j [\chi_j(\mathcal{C}_k)]^* \chi_j(\mathcal{C}_l) = \frac{h}{N_k}\delta_{l,k}, \tag{13}$$

where $h = \sum_k N_k$ is the order of the group, N_k the number of elements in the class, and where for simplicity we have assumed that the irreducible representations are unitary matrices.
It is convenient to display the characters of irreducible representations in a *character table*. For the point group C_{3v} such character table is

C_{3v}	E	$2C_3$	$3\sigma_v$
Γ_1	1	1	1
Γ_2	1	1	-1
Γ_3	2	-1	0

where for each class a representative element and, in front of it, the number of elements in the class, N_k, are given (here $\mathcal{C}_1 \to E$, $\mathcal{C}_2 \to 2C_3$, $\mathcal{C}_3 \to 3\sigma_v$). The orthogonality relations tell us that different columns or different rows (the latter with weights N_k, see (12)) form orthogonal vectors. The first column of the character table is the trace of the identity and therefore yields the dimensionality of the irreducible representation. The first irreducible representation, Γ_1, has character 1 for every element of the group, and it is called *trivial representation*. The trivial representation exists for any group and is one dimensional. If an object (a molecule or a crystal) is invariant under all symmetry operations of a given group, we can say that it transforms according to the trivial representation.
A reducible representation can be decomposed in irreducible ones using the orthogonality relations of characters. One can show that, if $\chi(g_i)$ are the characters of the reducible representation, they must be given by a linear combination of the characters of irreducible representations

$$\chi(g_i) = \sum_j a_j \chi_j(g_i),$$

where the coefficients are determined from the orthogonality relations

$$a_j = \frac{1}{h}\sum_k N_k [\chi_j(\mathcal{C}_k)]^* \chi(\mathcal{C}_k).$$

Hence

$$\Gamma = a_1\Gamma_1 \oplus a_2\Gamma_2 \oplus \cdots = \bigoplus_j a_j \Gamma_j. \tag{14}$$

In quantum mechanics we are interested in the group of symmetry operators $O(g)$ which leave the Hamiltonian invariant, the *group of the Hamiltonian*, and in their action on wavefunctions. It is therefore important to know how a symmetry operator acts on a function $f(\boldsymbol{r})$ and on an operator $\hat{H}$. A function $f(\boldsymbol{r})$ is transformed by the symmetry operation $O(g)$ into the function

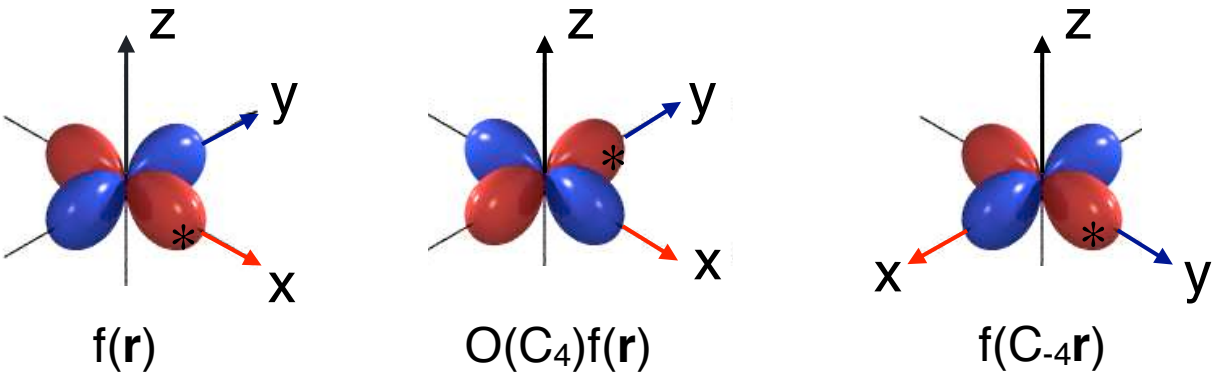

Fig. 2: *Rotation of an $x^2 - y^2$ atomic orbital by an angle $2\pi/4$ about the z axis (operation C_4).*

$O(g)f(\boldsymbol{r}) = f'(\boldsymbol{r}')$, where $\boldsymbol{r}' = g\boldsymbol{r}$ are the transformed coordinates, i.e.,

$$f'(\boldsymbol{r}') = O(g)f(\boldsymbol{r}) = f(g^{-1}\boldsymbol{r}). \tag{15}$$

This equation tells us how to construct an operator that corresponds to a given geometrical transformation. Fig. 2 shows (15) for an atomic $x^2 - y^2$ function and a rotation by $2\pi/4$ (operation C_4); the inverse operation is the rotation by $-2\pi/4$ (operation $C_{-4} = C_4^3$).
The Hamiltonian, or any other operator $\hat{H}$, transforms as follows

$$\hat{H}' = O(g)\hat{H}O(g^{-1}). \tag{16}$$

The group of the Hamiltonian is the group of h operators $\{O(g)\}$ which leave $\hat{H}$ unchanged ($\hat{H} = \hat{H}'$), i.e., which commute with the Hamiltonian. If $\psi(\boldsymbol{r})$ is an eigenvector of the Hamiltonian with eigenvalue ε_j, then for any operator in the group of the Hamiltonian

$$O(g)\hat{H}\psi(\boldsymbol{r}) = O(g)\varepsilon_j\psi(\boldsymbol{r}) = \varepsilon_j O(g)\psi(\boldsymbol{r}) = \hat{H}O(g)\psi(\boldsymbol{r}).$$

Thus $O(g)\psi(\boldsymbol{r})$ is an eigenvector of $\hat{H}$ with eigenvalue ε_j. The wavefunctions $\{O(g)\psi(\boldsymbol{r})\}$, where the $O(g)$ are operators in the group of the Hamiltonian, are all degenerate eigenvectors of $\hat{H}$. They define a linear space $\mathcal{L}_j$ of functions $f(x) = \sum_g c_g\ O(g)\psi(\boldsymbol{r})$, where the coefficients c_g are complex numbers. The space $\mathcal{L}_j$ is invariant under the action of the operators $O(g)$ in the group of the Hamiltonian, and has dimension $d_j \leq h$. If $\mathcal{L}_j$ includes all wavefunctions with eigenvalue ε_j, the degeneracy is said to be *essential*. If there are degenerate wavefunctions which are not in $\mathcal{L}_j$, this additional degeneracy is said to be *accidental*; accidental degeneracies sometime occur because of hidden symmetries. The symmetry group of the Hamiltonian is also the symmetry group of the solid or the molecule described by the Hamiltonian. The Hamiltonian, as the physical system, is invariant under all symmetry operations in the group and therefore transforms according to the trivial irreducible representation.
Let us assume that $\{\psi_j^i(\boldsymbol{r})\}$ is a set of $d_j \leq h$ linearly independent and essentially degenerate wavefunctions with eigenvalue ε_j which span $\mathcal{L}_j$. We can then construct a d_j-dimensional

irreducible matrix representation of the group of the Hamiltonian using the set $\{\psi^i_j(\boldsymbol{r})\}$ as a basis. The matrices of this representation, $\Gamma_j(g)$, are defined formally by

$$O(g)\psi^i_j(\boldsymbol{r}) = \sum_{i'} \Gamma^{i',i}_j(g)\psi^{i'}_j(\boldsymbol{r}).$$

The function $\psi^i_j(\boldsymbol{r})$ is said to belong to the *i-th* row of the *j-th* irreducible representation. If a function $\psi^i_j(\boldsymbol{r})$ belongs to the *i-th* row of the *j-th* irreducible representation with dimensionality d_j, the remaining $d_j - 1$ functions required to complete the basis for that irreducible representations are called *partners functions* of $\psi^i_j(\boldsymbol{r})$. Two functions belonging to different irreducible representations or to different rows of the same irreducibile representations are orthogonal

$$\langle\psi^i_j|\psi^{i'}_{j'}\rangle = \delta_{i,i'}\delta_{j,j'}\frac{1}{d_j}\sum_k \langle\psi^k_j|\psi^k_j\rangle.$$

Any function $f(\boldsymbol{r})$ in the space on which a group G of operators $\{O(g)\}$ acts can be decomposed as

$$f(\boldsymbol{r}) = \sum_j^{N_j}\sum_i^{d_j} f^i_j(\boldsymbol{r}),$$

where $j = 1, \ldots, N_j$ labels all distinct irreducible representations of G, and f^i_j belongs to the *i-th* row of the *j-th* irreducible representation. The components $f^i_j(\boldsymbol{r})$ can be obtained by means of the projection operator $\hat{\mathcal{P}}^{ii}_j$

$$\hat{\mathcal{P}}^{ii}_j = \frac{d_j}{h}\sum_g \left[\Gamma^{ii}_j(g)\right]^* O(g), \tag{17}$$

$$f^i_j(\boldsymbol{r}) = \hat{\mathcal{P}}^{ii}_j f(\boldsymbol{r}).$$

The symmetry group G of the Hamiltonian can be often written as a direct product of two subgroups G_a and G_b, of dimension h_a and h_b. The *direct product* $G = G_a \otimes G_b$ is the group G with elements $\{g\}$

$$\{g\} = \{E = (e_a, e_b), g_2 = (e_a, g_{2_b}), \ldots, g_h = (g_{h_a}, g_{h_b})\},$$

with group multiplication

$$g \star g' = (g_a, g_b) \star (g'_a, g'_b) = (g_a \star g'_a, g_b \star g'_b).$$

The matrices of the irreducible representations of G, $\Gamma_j(g)$, can be constructed as direct products of the matrices of the irreducible representations of G_a and G_b, $\Gamma_{j_a}(g_a)$ and $\Gamma_{j_a}(g_b)$

$$[\Gamma_j(g)]^{i\,,i'} = [\Gamma_{j_a}(g_a)]^{i_a,i'_a} \otimes [\Gamma_{j_b}(g_b)]^{i_b,i'_b} = [\Gamma_{j_a}(g_a) \otimes \Gamma_{j_b}(g_b)]^{i_a i_b, i'_a i'_b}.$$

The character of a direct product representation is the product of the characters

$$\chi_j(g) = \chi_{j_a}(g_a)\chi_{j_b}(g_b).$$

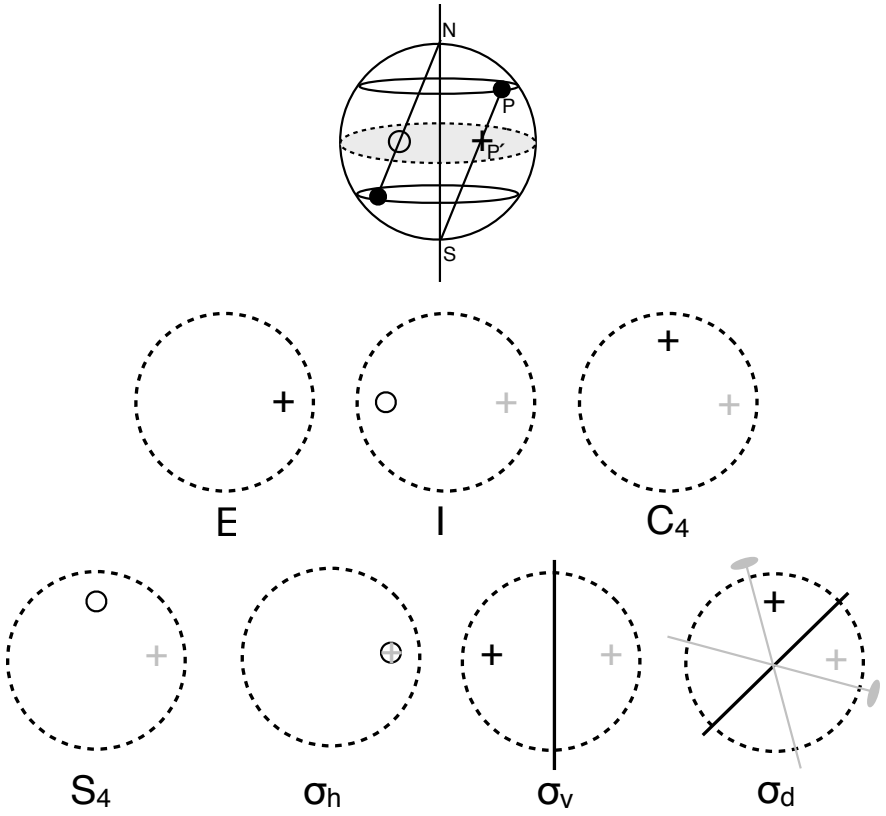

Fig. 3: *Stereographic projections illustrating the effect of some point symmetry operations. A point P at position $\mathbf{r}$ in the northern hemisphere is joint to the south pole S; the intersection of the line PS with the equatorial plane (+) is P', the stereographic projection of P. To treat the two hemispheres symmetrically, a point in the southern hemisphere is projected from the north pole N; the intersection with the equatorial plane is shown as an empty circle. Let us assume that P is in the northern hemisphere. The identity operation leaves P untouched; this is shown in the picture of the equatorial circle labeled with E. The operations $g = I, C_4, S_4, \sigma_v, \sigma_h, \sigma_d$ move P (grey +) to position $\mathbf{r}' = g\mathbf{r}$ (black circle or black +); this is shown in the pictures labeled with g. For $g = \sigma_d$, the two-fold axes (labeled with a digon) are also shown. The principal axis is perpendicular to the equatorial plane.*

Let us now consider the geometrical symmetry operations and symmetry groups relevant for atoms, molecules and solids. The symmetry group of an atom (central potential) is at least $O(3) = SO(3) \otimes C_i$, where $SO(3)$ is the group of proper rotations in three dimensions and $C_i = \{E, I\}$ is the group of order two, which has the identity E and the inversion I as only elements. The group $O(3)$ includes proper rotations and improper rotations; the latter are composed operations made of rotations and inversion. For molecules and crystals, only a subset of the proper and improper rotations are covering operations. These point group operations can include

- E, the identity
- C_n, a rotation by an angle $2\pi/n$; in a crystal, n can only take the values $n = 2, 3, 4, 6$

- σ reflection in a plane, classified as
  - σ_h, reflection through a plane perpendicular to the axis of highest rotation symmetry, called *principal axis*
  - σ_v, reflection through a plane to which the principal axis belongs
  - σ_d, reflection through a plane to which the principal axis belongs, and bisecting the angle between the two-fold axes perpendicular to the principal axis.
- $S_n = \sigma_h \otimes C_n$, improper rotation of an angle $2\pi/n$; in a crystal, n can only take the values $n = 3, 4, 6$.
- $I = S_2$, the inversion.

Some of these operations are illustrated in Fig. 3 using stereographic projections.
In a crystal, additional covering operations are

- lattice translations $\boldsymbol{T} = n_1\boldsymbol{a} + n_2\boldsymbol{b} + n_3\boldsymbol{c}$, where n_i are integers and $\boldsymbol{a}$, $\boldsymbol{b}$, $\boldsymbol{c}$ the primitive translations that define the unit cell.
- glide planes and screw axes, which are made by a point group operation R and a translation of a vector $\boldsymbol{f}$ which is a fraction of a lattice vector.

The lattice translations form the *translation group*. The complete set of covering operation of a crystal is known as *space group*. In three dimensions, there are 32 crystallographic point groups and 230 space groups. An operation in the space group is indicated as $\{\boldsymbol{\tau}|R\}$, where R is an element of the point group, and $\boldsymbol{\tau}$ a translation ($\boldsymbol{\tau} = \boldsymbol{T}$ or $\boldsymbol{\tau} = \boldsymbol{f}$). Space groups which do not include glide planes or screw axes are said to be *symmorphic*; the remaining space groups are said to be *non symmorphic*.
To understand solids and molecules, it is often useful to work in a basis of atomic orbitals. Atomic functions can be used, e.g., as a starting point to construct orbitals for molecules and crystals, as in the tight-binding method. These orbitals (see Appendix B) are defined as

$$\psi_{nlm}(\rho, \theta, \phi) = R_{nl}(\rho) Y^l_m(\theta, \phi),$$

where $R_{nl}(\rho)$ is the radial function, $Y^l_m(\theta, \phi)$ a spherical harmonic, $\rho = Zr$, Z the atomic number, and nlm the quantum numbers. In a hydrogen-like atom, the states with the same principal quantum number n but different angular momentum l are degenerate. This "accidental" degeneracy is caused by a hidden symmetry[5] of the Hamiltonian of the hydrogen atom. The $(2l+1)$-fold degeneracy of a given l shell is instead essential for any system with $O(3)$ symmetry. Thus we can construct irreducible representations of $O(3)$ with dimensionality $d = 2l + 1$

[5] It can be shown that the degeneracy is associated with rotational symmetry in 4 dimensions and that the group the Hamiltonian ($1/r$ potential) is actually $O(4)$. This additional symmetry is associated with the conservation of the Laplace-Runge-Lenz (LRL) vector; a generalization of the LRL vector to the case of an arbitrary central potential also exist.

using as basis set hydrogen-like atomic functions with principal quantum number n and angular momentum quantum number l.

Let us calculate the characters of such representations. The radial function is invariant under proper and improper rotations; thus we have only to consider the effect of these operations on the spherical harmonics. According to (15), the rotation of $Y_m^l(\theta,\phi)$ about the z axis by an angle α (C_α) is equivalent to the rotation of the xy axes by $-\alpha$. Thus

$$O(C_\alpha)Y_m^l(\theta,\phi) = Y_m^l(\theta,\phi-\alpha) = e^{-im\alpha}Y_m^l(\theta,\phi).$$

Therefore the matrix $\Gamma^l(C_\alpha)$ of the d-dimensional representation Γ^l has elements

$$[\Gamma^l(C_\alpha)]_{m,m'} = \delta_{m,m'}e^{-im\alpha}.$$

The character of the representation Γ^l for a rotation C_α is then

$$\chi^l(\alpha) = \sum_{m=-l}^{l} e^{-im\alpha} = \frac{\sin(l+\frac{1}{2})\alpha}{\sin\frac{\alpha}{2}}.$$

This result is valid for any direction of the rotation axis, and for any d-dimensional basis set obtained by making linear combinations of the $Y_m^l(\theta,\phi)$ functions, because the trace of a matrix is invariant under basis transformation; in particular the result is valid for real combinations of spherical harmonics (Appendix B), the basis usually adopted to study crystals and molecules, and for a set of Wannier functions with the symmetry of spherical or a real harmonics in a given l shell. The characters of the identity and the inversion are

$$\chi^l(E) = 2l+1,$$

$$\chi^l(I) = (-1)^l(2l+1).$$

The reflection through an horizontal plane, σ_h, can be written as $\sigma_h = I \otimes C_2$; thus

$$\chi^l(\sigma_h) = (-1)^l.$$

This result is also valid for σ_v and σ_d, since it is alway possible to choose the quantization axis perpendicular to the reflection plane. Finally, an improper rotation $S_\alpha = \sigma_h \otimes C_\alpha$ can be also obtained as $S_\alpha = I \otimes C_{\alpha+\pi}$; thus

$$\chi^l(S_\alpha) = (-1)^l\frac{\sin(l+\frac{1}{2})(\alpha+\pi)}{\sin\frac{\alpha+\pi}{2}}.$$

In Tab. 1 we summarize the characters of Γ^l. Since $O(3) = SO(3)\otimes C_i$, the characters in Tab. 1 can also be obtained as product of the characters of the same representation in $SO(3)$, $\Gamma^l_{SO(3)}$, and one of the irreducible representations of the group C_i, A_g (even) and A_u (odd). The characters of $\Gamma^l_{SO(3)}$ and the table of characters of C_i are shown below

$SO(3)$	E	C_α
$\Gamma^l_{SO(3)}$	$2l+1$	$\sin(l+\frac{1}{2})\alpha/\sin\frac{\alpha}{2}$

C_i	E	I
A_g	1	1
A_u	1	-1

$O(3)$	E	C_α	I	S_α	σ
Γ^l	$2l+1$	$\sin(l+\frac{1}{2})\alpha/\sin\frac{\alpha}{2}$	$(-1)^l(2l+1)$	$(-1)^l\sin(l+\frac{1}{2})(\alpha+\pi)/\sin\frac{\alpha+\pi}{2}$	$(-1)^l$

Table 1: *Characters of the irreducible representations Γ^l of group* O(3).

The direct product representation $\Gamma^l_{SO(3)} \otimes A_g$ with l even yields Γ^l with $l = 0, 2, 4, \ldots$, while $\Gamma^l_{SO(3)} \otimes A_u$ with l odd yields Γ^l with $l = 1, 3, 5, \ldots$.
The representation Γ^l is reducible in crystallographic or molecular point groups; we can find its decomposition in irreducible representations using the decomposition formula (14). Thus Tab. 1 can be viewed as the starting point to go from atoms to molecules and crystals.

3 Crystal-field theory

In an atom, the potential $v_{\rm R}(\boldsymbol{r})$ which determines the one-electron energies (10) is central and has (at least) all the symmetries of $O(3)$. In a molecule or a solid, $v_{\rm R}(\boldsymbol{r})$ has in general lower symmetry, the symmetry of a finite point group. Thus electronic states that are degenerate in an atom can split in a solid or a molecule. The symmetry reduction arises from the *crystal field*; the latter has two components, the Coulomb potential generated by the surrounding ions and the *ligand field* due to the bonding neighbors. In this section we will analyze the first contribution; the second effect will be discussed in the next section.
Let us assume that the crystal is ionic and the ions can be treated as point charges q_α (point charge model), and let us neglect $v_{\rm H}(\boldsymbol{r})$ and $v_{\rm xc}(\boldsymbol{r})$ in (6). Then, the one-electron potential can be written as

$$v_{\rm R}(\boldsymbol{r}) = \sum_\alpha \frac{q_\alpha}{|\boldsymbol{R}_\alpha - \boldsymbol{r}|} = v_0(r) + \sum_{\alpha\neq 0} \frac{q_\alpha}{|\boldsymbol{R}_\alpha - \boldsymbol{r}|} = v_0(r) + v_c(\boldsymbol{r}), \tag{18}$$

where $\boldsymbol{R}_\alpha$ are the positions of the ions and q_α their charges. The term $v_0(r)$ is the ionic central potential at site $\boldsymbol{R}_0$, and has spherical symmetry. The term $v_c(\boldsymbol{r})$ is the electric field generated at a given site $\boldsymbol{R}_0$ by all the surrounding ions in the crystal and it is called *crystal-field potential*.
Let us consider a crystal with the perovskite structure ABC_3, shown in Fig. 4. We want to calculate the crystal-field potential at the site of the transition metal, B. Let us first assume that only the contribution of nearest neighbors (the negative C ions, usually oxygens) is relevant. The C ions are located at positions $(\pm a, 0, 0), (0, \pm a, 0), (0, 0, \pm a)$, where a is the lattice constant, and have all the same charge q_C. Expanding around $\boldsymbol{r} = 0$, we find that the first contribution to $v_{\rm c}(\boldsymbol{r})$ with less than spherical symmetry is

$$v_{\rm oct}(\boldsymbol{r}) = \frac{35}{4}\frac{q_C}{a^5}\left(x^4 + y^4 + z^4 - \frac{3}{5}r^4\right) = D\left(x^4 + y^4 + z^4 - \frac{3}{5}r^4\right).$$

We can rewrite this potential as

$$v_{\rm oct}(\boldsymbol{r}) = \frac{7}{6}\frac{1}{\sqrt{\pi}}\frac{q_C}{a^5}r^4\left[Y_0^4(\theta,\phi) + \sqrt{\frac{5}{14}}\left(Y_4^4(\theta,\phi) + Y_{-4}^4(\theta,\phi)\right)\right], \tag{19}$$

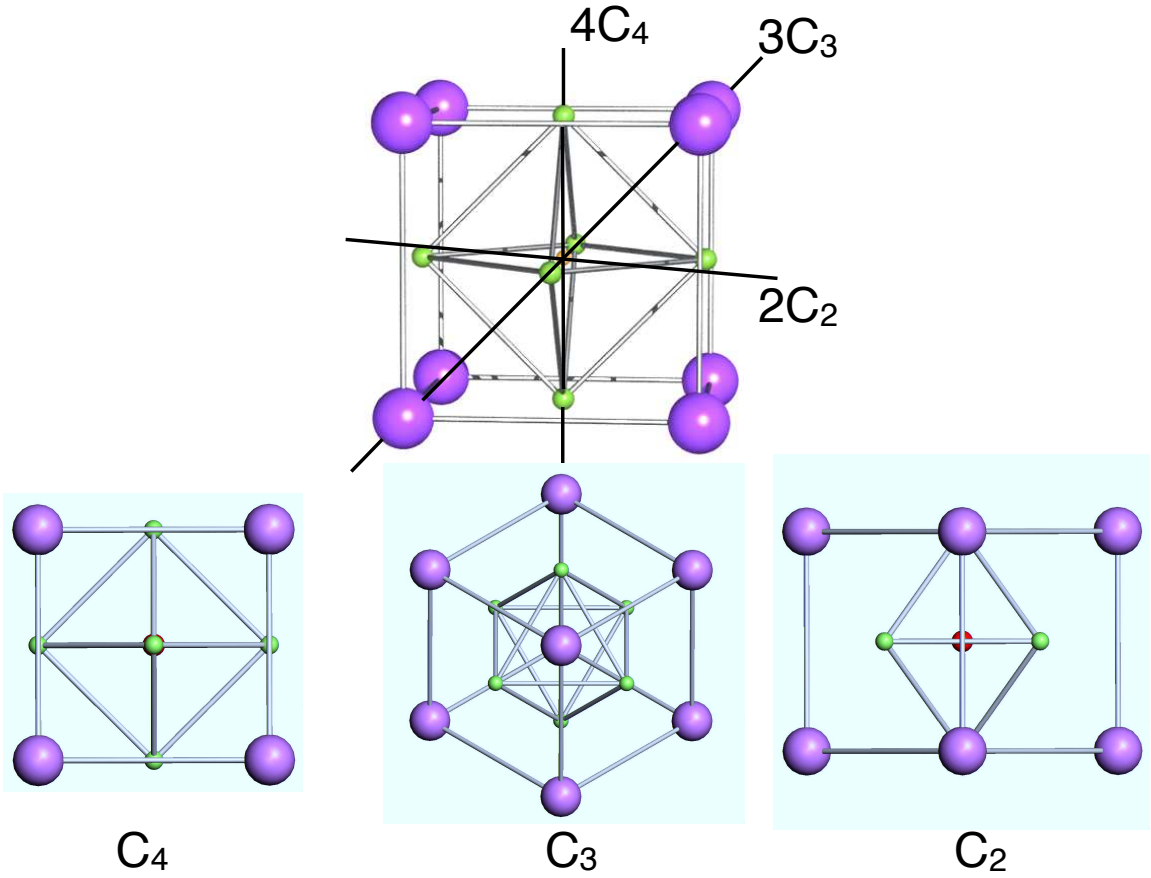

Fig. 4: *The unit cell of a cubic perovskite ABC_3 and its symmetry axes; the lattice constant is a. The transition metal B (red) is at $(0,0,0)$; the ligands C (green) are located at $(\pm a,0,0)$, $(0,\pm a,0)$,$(0,0,\pm a)$, forming an octahedron; the cations A are located at $(\pm a/2,\pm a/2,\pm a/2)$, $(\pm a/2,\mp a/2,\pm a/2)$, $(\mp a/2,\pm a/2,\pm a/2)$, $(\pm a/2,\pm a/2,\mp a/2)$, forming a cube. The bottom figures show different views illustrating the rotational symmetries of the cell.*

where

$$\begin{aligned} Y_0^4(\theta,\phi) &= \frac{3}{16}\frac{1}{\sqrt{\pi}}(35\cos^4\theta - 30\cos^2\theta + 3), \\ Y_{\pm 4}^4(\theta,\phi) &= \frac{3}{16}\frac{35}{\sqrt{2\pi}}\sin^4\theta e^{\pm 4i\phi}. \end{aligned}$$

Let us now calculate the crystal field due to the cubic cage of cations A (with charge q_A), shown in Fig. 4. One can show that

$$v_{\rm cube}(\boldsymbol{r}) = -\frac{8}{9}\frac{q_A}{q_C}v_{\rm oct}(\boldsymbol{r}),$$

i.e., $v_{\rm cube}(\boldsymbol{r})$ has the same form as $v_{\rm oct}(\boldsymbol{r})$; this happens because a cube and an octahedron are dual polyhedra[6] and have therefore the same symmetry properties. If $q_A/q_C > 0$, $v_{\rm cube}(\boldsymbol{r})$ has opposite sign than $v_{\rm oct}(\boldsymbol{r})$; however, in the case of a perovskite, cations are positive ions; thus the crystal field due to the A cage has the same sign of the field generated by the B octahedron.

[6]Every polyhedron has a dual which can be obtained by exchanging the location of faces and vertices.

The crystal-field potential $v_{\rm c}(\boldsymbol{r})$ can split the $(2l+1)$-fold degeneracy of the atomic levels. To calculate how the l manifold splits, we use group theory. We assume for simplicity that the symmetry is only O (group of the proper rotations which leave a cube invariant); using the full symmetry group of the cube, $O_h = O \otimes C_i$, does not change the result, because the spherical harmonics have fixed parity. The character table of group O is

	O	E	$8C_3$	$3C_2$	$6C_2$	$6C_4$
$(x^2+y^2+z^2)$	A_1	1	1	1	1	1
	A_2	1	1	1	-1	-1
$(x^2-y^2, 3z^2-r^2)$	E	2	-1	2	0	0
(x,y,z)	T_1	3	0	-1	-1	1
(xy,xz,yz)	T_2	3	0	-1	1	-1

(20)

We want to calculate the characters of the reducible matrix representation Γ^l constructed using spherical harmonics with quantum numbers lm as a basis. From Tab. 1

$$\begin{aligned}
\chi^l(C_2) &= (-1)^l \\
\chi^l(C_3) &= \begin{cases} 1 & l = 0,3,\ldots \\ 0 & l = 1,4,\ldots \\ -1 & l = 2,5,\ldots \end{cases} \\
\chi^l(C_4) &= \begin{cases} 1 & l = 0,1,4,5,\ldots \\ -1 & l = 2,3,6,7,\ldots \end{cases}
\end{aligned}$$

For the s,p,d,f shells we can therefore write for representations Γ^l

O	E	$8C_3$	$3C_2$	$6C_2$	$6C_4$
Γ^s	1	1	1	1	1
Γ^p	3	0	-1	-1	1
Γ^d	5	-1	1	1	-1
Γ^f	7	1	-1	-1	-1

We can now determine how the reducible representations Γ^l splits using the decomposition formula Eq. (14). Hereafter for convenience the symmetry representations of electronic terms are written in lower case to distinguish them from capital letters used for the nuclear displacements and the general irreducible representations. We find

$$\begin{aligned}
\Gamma^s &= a_1 \\
\Gamma^p &= t_1 \\
\Gamma^d &= e \oplus t_2 \\
\Gamma^f &= a_2 \oplus t_1 \oplus t_2
\end{aligned}$$

Thus, the s- and the p-functions do not split, because the a_1 irreducible representation is one-dimensional and the t_1 irreducible representation is 3-dimensional. However, d-functions split

into a doublet and a triplet, while f-functions into a singlet and two triplets. To calculate which functions belong to which representation we can, e.g., use the projector (17). For d-electrons, relevant for the case of a transition-metal ion, we find that the d-shell splits into e ($x^2-y^2, 3z^2-r^2$) and t_2 (xy, xz, yz). The partner functions for the representations of group O are given in the first column of the character table (20), on the left.

The full symmetry of the B site is O_h. The group O_h can be obtained as direct product, $O_h = O \otimes C_i$; with respect to O, the group O_h has twice the number of elements and classes, and thus twice the number of irreducible representations. The latter split into even ($a_{1g}, a_{2g}, e_g, t_{1g}, t_{2g}$) and odd ($a_{1u}, a_{2u}, e_u, t_{1u}, t_{2u}$) representations. The d-functions are even, and therefore x^2-y^2 and $3z^2-r^2$ are partners functions for the e_g irreducibile representation, while xy, xz, yz are partner functions for the t_{2g} irreducible representation. The p-orbitals are odd, and are partners functions for the t_{1u} representation.

Group theory tells us *if* the degenerate $2l+1$ levels split at a given site in a lattice, but not of *how much* they do split, and which orbitals are higher in energy. We can however calculate the crystal-field splitting approximately using (19). Let us consider first the case in which the central atom B is a transition-metal ion in a $3d^1$ configuration (e.g., Ti^{3+} or V^{4+}), which has degeneracy $2l+1=5$. In the perovskite structure, the octahedral potential $v_{\rm oct}(\boldsymbol{r})$ yields the following element of matrix between states in the d^1 manifold

$$\begin{aligned}
\langle\psi_{n20}\ |\hat{v}_{\rm oct}|\psi_{n20}\ \rangle &= +6Dq \\
\langle\psi_{n2\pm1}|\hat{v}_{\rm oct}|\psi_{n2\pm1}\rangle &= -4Dq \\
\langle\psi_{n2\pm2}|\hat{v}_{\rm oct}|\psi_{n2\pm2}\rangle &= +\ Dq \\
\langle\psi_{n2\pm2}|\hat{v}_{\rm oct}|\psi_{n2\mp2}\rangle &= +5Dq
\end{aligned}$$

where $Dq = -q_C\langle r^4\rangle/6a^5$. The crystal-field splitting between e_g and t_{2g}-states can be the obtained by diagonalizing the crystal-field matrix

$$H_{\rm CF} = \begin{pmatrix} Dq & 0 & 0 & 0 & 5Dq \\ 0 & -4Dq & 0 & 0 & 0 \\ 0 & 0 & 6Dq & 0 & 0 \\ 0 & 0 & 0 & -4Dq & 0 \\ 5Dq & 0 & 0 & 0 & Dq \end{pmatrix}.$$

We find two degenerate e_g eigenvectors with energy $6Dq$

$$\begin{aligned}
|\psi_{n20}\rangle &= |3z^2-r^2\rangle, \\
\frac{1}{\sqrt{2}}\left[|\psi_{n22}\rangle + |\psi_{n2-2}\rangle\right] &= |x^2-y^2\rangle,
\end{aligned}$$

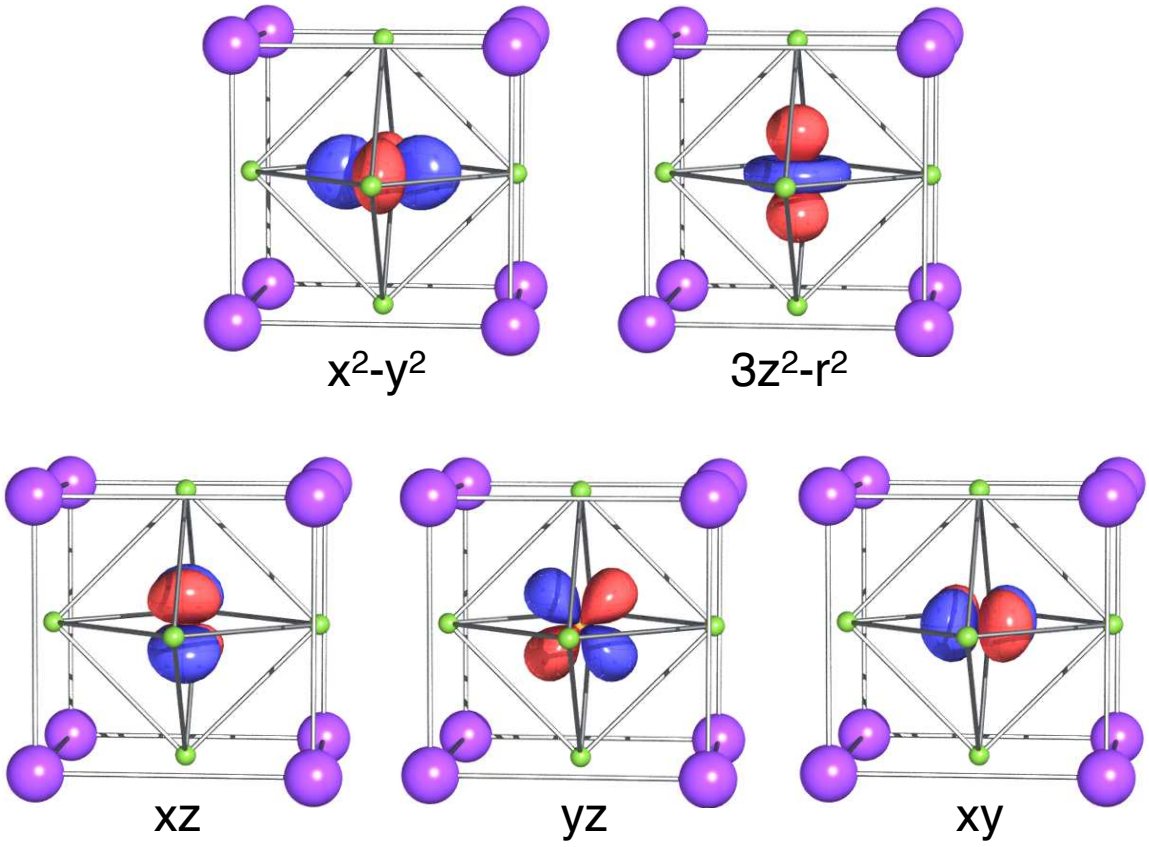

Fig. 5: *The Cu e_g and t_{2g} Wannier orbitals for the cubic perovskite $KCuF_3$, obtained from first principles calculations, using a Wannier basis that spans all bands.*

and three degenerate t_{2g} eigenvectors with energy $-4Dq$

$$\begin{aligned}
\frac{i}{\sqrt{2}}\left[|\psi_{n22}\rangle - |\psi_{n2-2}\rangle\right] &= |xy\rangle,\\
\frac{1}{\sqrt{2}}\left[|\psi_{n21}\rangle - |\psi_{n2-1}\rangle\right] &= |xz\rangle,\\
\frac{i}{\sqrt{2}}\left[|\psi_{n21}\rangle + |\psi_{n2-1}\rangle\right] &= |yz\rangle.
\end{aligned}$$

The splitting is

$$\Delta = E_{e_g} - E_{t_{2g}} = 10Dq.$$

Thus the e_g-states are higher in energy than the t_{2g}-states. This happens because e_g electrons point towards the negative C ions (see Fig. 5), and will therefore feel a larger Coulomb repulsion than t_{2g} electrons, which point between the negative C ions.
For a generic lattice, we can expand the crystal-field potential (18) in spherical harmonics using

$$\frac{1}{|\boldsymbol{r}_1 - \boldsymbol{r}_2|} = \sum_{k=0}^{\infty} \frac{r_<^k}{r_>^{k+1}} \frac{4\pi}{2k+1} \sum_{q=-k}^{k} Y_q^k(\theta_2,\phi_2)\overline{Y}_q^k(\theta_1,\phi_1),$$

where $r_<$ ($r_>$) is the smaller (larger) of r_1 and r_2. The crystal-field potential can then be written

as

$$v_c(\boldsymbol{r}) = \sum_{k=0}^{\infty} \sum_{q=-k}^{k} B_q^k Y_q^k, \tag{21}$$

where $B_q^k = (-1)^q \bar{B}_{-q}^k$. Although the series in (21) is in principle infinite, one can terminate it by specifying the wavefunctions, since

$$\langle Y_m^l | Y_q^k | Y_{m'}^l \rangle = 0 \quad \text{if} \quad k > 2l.$$

For example, for p electrons $k \leq 2$, for d-electrons, $k \leq 4$, and f electrons $k \leq 6$. Thus, for d-electrons and O_h symmetry, the terms that appear in the potential (19) are actually also the only ones to be taken into account.

The derivation of (19) and (21) presented here might let us think that the first nearest neighbors are those that determine the crystal field. However, this is often not the case, because Coulomb repulsion is a long-range interaction; for example, in some systems the first nearest neighbors yield cubic symmetry at a given site but further neighbors lower the symmetry.[7]

The point charge model discussed in this section is useful to explain the relation between crystal field and site symmetry, however yields unsatisfactory results for the crystal-field splitting in real materials. Corrections beyond the point-charge approximation turn out to be important. In addition, as we will see in the next section, in many systems the crystal field has a large, sometimes dominant, covalent contribution, the ligand field. The modern approach to calculate crystal-field splittings including the ligand-field contribution is based on material-specific DFT potentials and DFT localized Wannier functions as one-electron basis. We will discuss this approach at the end of the next section.

Let us now analyze the splitting of energy levels in a many-electron $3d^n$ manifold. Apart from the crystal field (21), in calculating the energies of states in such manifold, we have also to take into account the electron-electron Coulomb repulsion. This will be treated in detail in the lecture of Robert Eder. Here we briefly discuss some simple examples: $3d^1$, $3d^9$ and $3d^2$. We have seen that for a d-electron surrounded by an octahedron of negative ions, $\Delta = 10Dq$; the energy difference between the electronic configuration e_g^1 and electronic configuration t_{2g}^1 is therefore Δ. In the case of a single hole in the d-shell ($3d^9$ ion, e.g., Cu^{2+}), the energy difference between $t_{2g}^6 e_g^3$ and $t_{2g}^5 e_g^4$, is then just $-\Delta$, because of electron-hole symmetry. The d crystal-field orbitals (Wannier functions) for the $3d^9$ perovskite $KCuF_3$ (cubic structure) are shown in Fig. 5. For a generic $3d^n$ configuration we can consider two limit cases, strong or weak crystal field. If the crystal field is *strong*, one can treat Coulomb electron-electron interaction as a perturbation, and classify the atomic states according to the crystal field. Let us consider the case of a perovskite in which the central ion has electronic configuration $3t_{2g}^2$ (e.g., V^{3+}); if we neglect the electron-electron repulsion, the excited states are $t_{2g}^1 e_g^1$, with energy Δ, and e_g^2, with energy 2Δ. We can obtain a representation of the group O_h in the basis of two-electron states from the direct product of the representations in the basis of single-electron states. By using the decomposition

[7] This means that O_h is not the point group.

formula (14), we can then show that

$$\begin{aligned} t_{2g} \otimes t_{2g} &= a_{1g} \oplus e_g \oplus t_{1g} \oplus t_{2g} \\ e_g \otimes t_{2g} &= t_{1g} \oplus t_{2g} \\ e_g \otimes e_g &= a_{1g} \oplus a_{2g} \oplus e_g \end{aligned}$$

The Coulomb repulsion acts as a perturbation and can split degenerate states belonging to different irreducible representations. In particular, the manifold t_{2g}^2 splits into ${}^1a_{1g}$, ${}^1e_g$,${}^1\,t_{2g}$, and ${}^3t_{1g}$ (ground state), where ${}^{(2S+1)}$ indicates the spin degeneracy of the state.

If the crystal field is *weak*, the opposite approach can be used; the crystal field is treated as a perturbation of the atomic Coulomb multiplets, labeled as ${}^{2S+1}L$. In this case the two-electron ground state is the triplet ${}^3F$ and the O_h crystal field splits it into ${}^3t_{1g}$,${}^3\,t_{2g}$, and ${}^3a_{2g}$.

Up to here we have neglected the spin-orbit interaction. The latter plays an important role, e.g., in $5d$- or f-systems. In the case in which the crystal field is weak with respect to the spin-orbit coupling, as it happens in many f-electron compounds, the total angular momentum J is a good quantum number. It is therefore useful to construct a reducible representation of the point group, Γ^J, in the basis of the eigenvectors of total angular momentum. The character of Γ^J for a rotation is

$$\chi^J(\alpha) = \frac{\sin(J+\frac{1}{2})\alpha}{\sin\frac{\alpha}{2}},$$

For half-integral values of J (odd number of electrons), $\chi^J(\alpha)$ has the property

$$\chi^J(\alpha + 2\pi) = -\chi^J(\alpha).$$

We therefore expand the original point group to include a new element, R, which represents the rotation by 2π. The new group has twice the number of elements of the original group and is known as *double group*. In the case of the group O the double group is labeled with O' and its character table is

O'	E	$8C_3$	$3C_2+3RC_2$	$6C_2+6RC_2$	$6C_4$	R	$8RC_3$	$6RC_4$
Γ_1	1	1	1	1	1	1	1	1
Γ_2	1	1	1	-1	-1	1	1	-1
Γ_3	2	-1	2	0	0	2	-1	0
Γ_4	3	0	-1	-1	1	3	0	1
Γ_5	3	0	-1	1	-1	3	0	-1
Γ_6	2	1	0	0	$\sqrt{2}$	-2	-1	$-\sqrt{2}$
Γ_7	2	1	0	0	$-\sqrt{2}$	-2	-1	$\sqrt{2}$
Γ_8	4	-1	0	0	0	-4	1	0

To determine if the atomic levels in a given J manifold split we use the same procedure adopted

for the l-shell. First we calculate the characters of all elements in the group

$$\begin{aligned}
\chi^J(E) &= 2J+1 \\
\chi^J(R) &= -(2J+1) \\
\chi^J(C_2) &= 0 \\
\chi^J(RC_2) &= 0 \\
\chi^J(C_3) &= \begin{cases} 1 & J = 1/2, 7/2, \ldots \\ -1 & J = 3/2, 9/2, \ldots \\ 0 & J = 5/2, 11/2 \ldots \end{cases} \\
\chi^J(RC_3) &= \begin{cases} -1 & J = 1/2, 7/2, \ldots \\ 1 & J = 3/2, 9/2, \ldots \\ 0 & J = 5/2, 11/2 \ldots \end{cases} \\
\chi^J(C_4) &= \begin{cases} \sqrt{2} & J = 1/2, 9/2 \ldots \\ 0 & J = 3/2, 7/2, \ldots \\ -\sqrt{2} & J = 5/2, 13/2, \ldots \end{cases} \\
\chi^J(RC_4) &= \begin{cases} -\sqrt{2} & J = 1/2, 9/2 \ldots \\ 0 & J = 3/2, 7/2, \ldots \\ +\sqrt{2} & J = 5/2, 13/2, \ldots \end{cases}
\end{aligned}$$

Next we use the decomposition formula (14) to find how the reducible representation Γ^J is decomposed in irreducible ones. One can show that

$$\begin{aligned}
\Gamma^{\frac{1}{2}} &= \Gamma_6 \\
\Gamma^{\frac{3}{2}} &= \Gamma_8 \\
\Gamma^{\frac{5}{2}} &= \Gamma_7 \oplus \Gamma_8 \\
\Gamma^{\frac{7}{2}} &= \Gamma_6 \oplus \Gamma_7 \oplus \Gamma_8 \\
\Gamma^{\frac{9}{2}} &= \Gamma_6 \oplus 2\Gamma_8
\end{aligned}$$

Since $\Gamma_6, \Gamma_7, \Gamma_8$ have dimensionality $d \geq 2$, all levels remain at least two-fold degenerate. This is an example of *Kramers degeneracy*. Kramers theorem states that, in the presence of (only) electric fields, the energy levels of a system with odd number of fermions are at least two-fold degenerate. Kramers degeneracy is a consequence of time-reversal symmetry.

4 Tight-binding method

In solids, electrons delocalize to form bonds and bands. In the Hamiltonian (8), these arise from the elements of matrix (9), the hopping integrals. But what is the specific form of the Hamiltonian (8) for a given system? Which parameters are large? Which are zero? The simplest way to answer these questions is to use the tight-binding method, which consists in expanding the crystal wavefunctions in the basis of functions centered at each atomic site; here we use

as a basis atomic orbitals,[8] $\{\psi_{nlm}(\boldsymbol{r})\}$. Let us first consider a simple example, a homonuclear molecular ion formed by two hydrogen nuclei, located at $\boldsymbol{R}_1$ and $\boldsymbol{R}_2$, and one electron. The electronic Hamiltonian for such an H_2^+ molecular ion is

$$\hat{h}_e(\boldsymbol{r}) = -\frac{1}{2}\nabla^2 - \frac{1}{|\boldsymbol{r}-\boldsymbol{R}_1|} - \frac{1}{|\boldsymbol{r}-\boldsymbol{R}_2|} = -\frac{1}{2}\nabla^2 + v(\boldsymbol{r}-\boldsymbol{R}_1) + v(\boldsymbol{r}-\boldsymbol{R}_2) = -\frac{1}{2}\nabla^2 + v_R(\boldsymbol{r}).$$

We take as atomic basis the ground state $1s$ atomic orbitals, $\psi_{1s}(\boldsymbol{r}-\boldsymbol{R}_1)$ and $\psi_{1s}(\boldsymbol{r}-\boldsymbol{R}_2)$; in the free hydrogen atom they have energy ε^0_{1s}. In this basis, the Hamiltonian and the overlap matrix have the form

$$H = \varepsilon^0_{1s}\, O + \begin{pmatrix} \Delta\varepsilon_{1s} & V_{ss\sigma} \\ V_{ss\sigma} & \Delta\varepsilon_{1s} \end{pmatrix} \qquad O = \begin{pmatrix} 1 & S \\ S & 1 \end{pmatrix}$$

where

$$\begin{aligned}
\Delta\varepsilon_{1s} &= \int d\boldsymbol{r}\, \psi_{1s}(\boldsymbol{r}-\boldsymbol{R}_\alpha)\left[v_R(\boldsymbol{r}) - v(\boldsymbol{r}-\boldsymbol{R}_\alpha)\right]\psi_{1s}(\boldsymbol{r}-\boldsymbol{R}_\alpha), \quad \alpha = 1,2 \\
V_{ss\sigma} &= \int d\boldsymbol{r}\, \psi_{1s}(\boldsymbol{r}-\boldsymbol{R}_\alpha) v(\boldsymbol{r}-\boldsymbol{R}_\alpha)\psi_{1s}(\boldsymbol{r}-\boldsymbol{R}_{\alpha'}), \quad \alpha \neq \alpha' \\
S &= \int d\boldsymbol{r}\, \psi_{1s}(\boldsymbol{r}-\boldsymbol{R}_\alpha)\psi_{1s}(\boldsymbol{r}-\boldsymbol{R}_{\alpha'}), \quad \alpha \neq \alpha'.
\end{aligned}$$

The hopping integral $t = -V_{ss\sigma} > 0$ is a Slater-Koster two-center integral (Appendix B).
The ground state of the molecular ion is the *bonding* linear combination

$$\phi^B_{1s}(\boldsymbol{r}) = \left[\psi_{1s}(\boldsymbol{r}-\boldsymbol{R}_1) + \psi_{1s}(\boldsymbol{r}-\boldsymbol{R}_2)\right]/\sqrt{2(1+S)},$$

and has energy

$$E_B = \varepsilon^0_{1s} + \frac{\Delta\varepsilon_{1s} + V_{ss\sigma}}{1+S}.$$

The label σ in $V_{ss\sigma}$ indicates that the bonding state is symmetrical with respect to rotations about the bond axis (see Fig. 6). The excited state is the *antibonding* state

$$\phi^A_{1s}(\boldsymbol{r}) = \left[\psi_{1s}(\boldsymbol{r}-\boldsymbol{R}_1) - \psi_{1s}(\boldsymbol{r}-\boldsymbol{R}_2)\right]/\sqrt{2(1-S)},$$

and has energy

$$E_A = \varepsilon^0_{1s} + \frac{\Delta\varepsilon_{1s} - V_{ss\sigma}}{1-S}.$$

Let us now consider a crystal. If we neglect $v_{\rm H}(\boldsymbol{r})$ and $v_{\rm xc}(\boldsymbol{r})$ in (6), the one-electron Hamiltonian $\hat{h}_e(\boldsymbol{r})$ in (5) becomes

$$\hat{h}_e(\boldsymbol{r}) = -\frac{1}{2}\nabla^2 - \sum_{i,\alpha}\frac{Z_{i,\alpha}}{|\boldsymbol{r}-\boldsymbol{T}_i-\boldsymbol{R}_\alpha|} = -\frac{1}{2}\nabla^2 + \sum_{i,\alpha} v(\boldsymbol{r}-\boldsymbol{T}_i-\boldsymbol{R}_\alpha) = -\frac{1}{2}\nabla^2 + v_R(\boldsymbol{r}),$$

[8] Linear Combination of Atomic Orbitals (LCAO) approach.

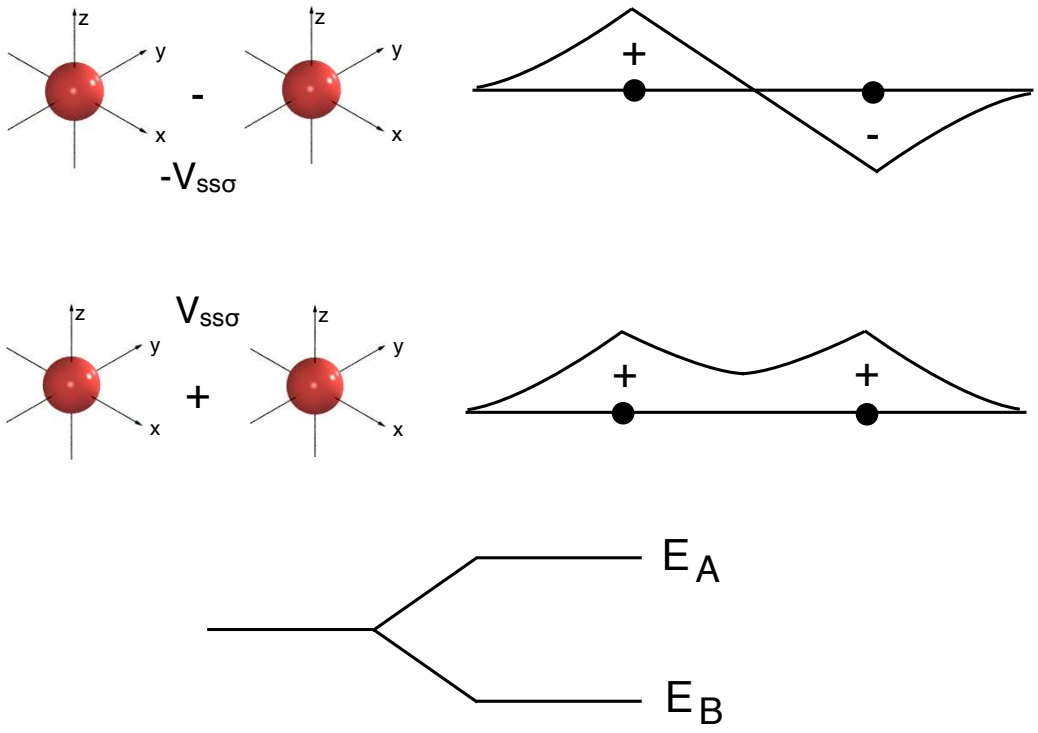

Fig. 6: *Pictorial view of the antibonding (top) and bonding (bonding) state of H_2^+.*

where $\boldsymbol{R}_\alpha$ are the positions of the basis $\{\alpha\}$ atoms in the unit cell and $\boldsymbol{T}_i$ lattice vectors. For each atomic orbital with quantum numbers lm we construct a Bloch state

$$\psi^\alpha_{lm}(\boldsymbol{k},\boldsymbol{r}) = \frac{1}{\sqrt{N}}\sum_i e^{i\boldsymbol{T}_i\cdot\boldsymbol{k}}\,\psi_{lm}(\boldsymbol{r}-\boldsymbol{T}_i-\boldsymbol{R}_\alpha). \tag{22}$$

In the Bloch basis (22), the Hamiltonian and the overlap matrix are given by

$$\begin{aligned} H^{\alpha,\alpha'}_{lm,l'm'}(\boldsymbol{k}) &= \langle\psi^\alpha_{lm}(\boldsymbol{k})|\hat{h}_e|\psi^{\alpha'}_{l'm'}(\boldsymbol{k})\rangle, \\ O^{\alpha,\alpha'}_{lm,l'm'}(\boldsymbol{k}) &= \langle\psi^\alpha_{lm}(\boldsymbol{k})|\psi^{\alpha'}_{l'm'}(\boldsymbol{k})\rangle. \end{aligned}$$

They define a generalized eigenvalue problem, the solution of which yields the band structure. The Hamiltonian matrix is given by

$$H^{\alpha,\alpha'}_{lm,l'm'}(\boldsymbol{k}) = \varepsilon^0_{l'\alpha'}O^{\alpha,\alpha'}_{lm,l'm'}(\boldsymbol{k}) + \Delta\varepsilon^\alpha_{lm,l'm'}\delta_{\alpha,\alpha'} - \frac{1}{N}\sum_{i\alpha\neq i'\alpha'} e^{i(\boldsymbol{T}_{i'}-\boldsymbol{T}_i)\cdot\boldsymbol{k}}\,t^{i\alpha,i'\alpha'}_{lm,l'm'}.$$

Here $\varepsilon^0_{l\alpha}$ are atomic levels, and $\Delta\varepsilon^\alpha_{lm,l'm'}$ the crystal-field matrix

$$\Delta\varepsilon^\alpha_{lm,l'm'} = \int d\boldsymbol{r}\,\overline{\psi}_{lm}(\boldsymbol{r}-\boldsymbol{R}_\alpha)[v_R(\boldsymbol{r}) - v(\boldsymbol{r}-\boldsymbol{R}_\alpha)]\psi_{l'm'}(\boldsymbol{r}-\boldsymbol{R}_\alpha), \tag{23}$$

which, as in the case of the H_2^+ ion, is a two-center integral. Finally

$$t^{i\alpha,i'\alpha'}_{lm,l'm'} = -\int d\boldsymbol{r}\,\overline{\psi}_{lm}(\boldsymbol{r}-\boldsymbol{R}_\alpha-\boldsymbol{T}_i)[v_R(\boldsymbol{r}) - v(\boldsymbol{r}-\boldsymbol{R}_{\alpha'}-\boldsymbol{T}_{i'})]\psi_{l'm'}(\boldsymbol{r}-\boldsymbol{R}_{\alpha'}-\boldsymbol{T}_{i'}). \tag{24}$$

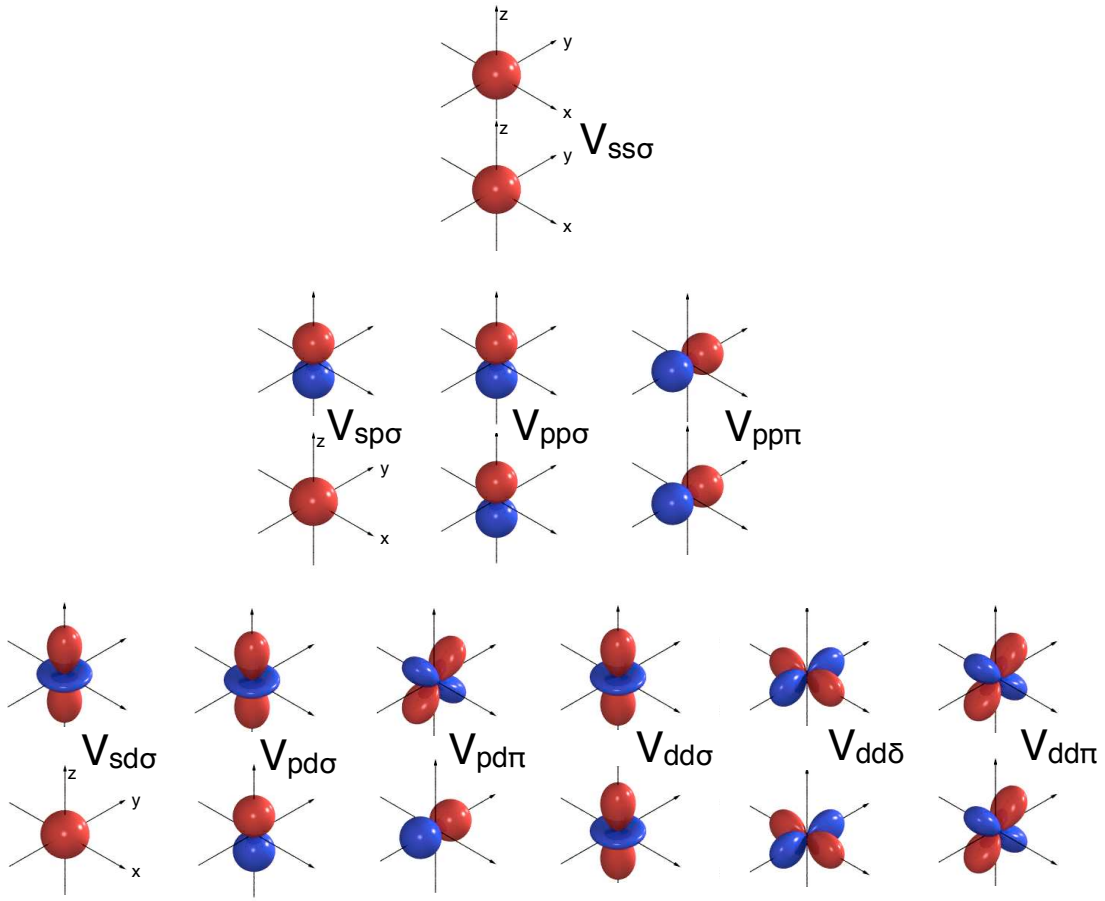

Fig. 7: *Independent Slater-Koster two-center integrals for s, p and d atomic orbitals (Appendix B). The label σ indicates that the bonding state is symmetrical with respect to rotations about the bond axis; the label π that the bond axis lies in a nodal plane; the label δ that the bond axis lies in two nodal planes.*

The hopping integrals (24) contain two-center and three-center terms; if the basis is localized, we can neglect the three-center contributions and assume that $t^{i\alpha,i'\alpha'}_{lm,l'm'} \sim -V^{i\alpha,i'\alpha'}_{lm,l'm'}$, where

$$V^{i\alpha,i'\alpha'}_{lm,l'm'} = \int d\boldsymbol{r}\, \overline{\psi}_{lm}(\boldsymbol{r}-\boldsymbol{R}_\alpha-\boldsymbol{T}_i)v(\boldsymbol{r}-\boldsymbol{R}_\alpha-\boldsymbol{T}_i)\psi_{l'm'}(\boldsymbol{r}-\boldsymbol{R}_{\alpha'}-\boldsymbol{T}_{i'})$$

is a two-center integral. A general Slater-Koster two-center integral can be expressed as a function of few independent two-center integrals, shown in Fig. 7 for s, p, and d-functions. A part from the σ bond, which is the strongest, other bonds are possible; the π bonds are made of orbitals which share a nodal plane to which the bond axis belongs, and the δ bond, which has two nodal planes which contain the bond axis and the two ions; furthermore, if the ions on the two sites are different, the bond is *polar*. Fig. 8 shows how to obtain a generic two-center integral involving p and s orbitals.

Let us now consider as an example the e_g and t_{2g} bands of $KCuF_3$; we assume for simplicity that the system is an ideal cubic perovskite (point group O_h), as in Fig. (4). Let us use as a basis only Cu d and F p atomic orbitals, and as matrix elements only on-site terms and pd hopping integrals. We label the p-orbitals on different F sites as μ^ν, where $\nu = a, b, c$ identifies

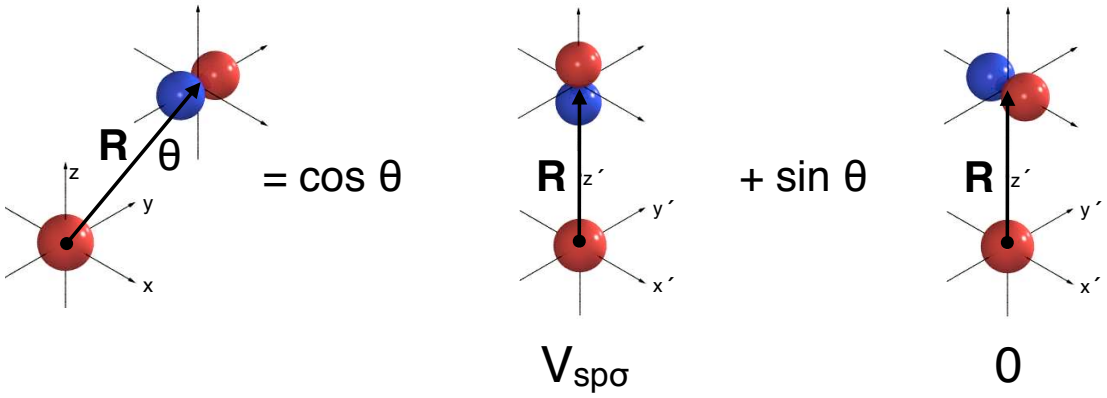

Fig. 8: *Illustration of the decomposition of a general s-p two-center integral in terms of $V_{sp\sigma}$.*

the direction of the unit cell axis along which the F atom lies and $\mu = x, y, z$ the orbital; we then construct the corresponding Bloch states $|\boldsymbol{k}\ \mu^{\nu}\rangle$, as well as the Cu e_g Bloch states $|\boldsymbol{k}\ \mu\rangle$, $\mu = 3z^2 - r^2, x^2 - y^2$. We neglect the overlap matrix for simplicity.
The tight-binding Hamiltonian in this basis has then the form

$H^{\rm TB}_{e_g}$	$\lvert\boldsymbol{k}\ z^c\rangle$	$\lvert\boldsymbol{k}\ x^a\rangle$	$\lvert\boldsymbol{k}\ y^b\rangle$	$\lvert\boldsymbol{k}\ 3z^2-r^2\rangle$	$\lvert\boldsymbol{k}\ x^2-y^2\rangle$
$\lvert\boldsymbol{k}\ z^c\rangle$	ε_p	0	0	$-2V_{pd\sigma}s_z$	0
$\lvert\boldsymbol{k}\ x^a\rangle$	0	ε_p	0	$V_{pd\sigma}s_x$	$-\sqrt{3}V_{pd\sigma}s_x$
$\lvert\boldsymbol{k}\ y^b\rangle$	0	0	ε_p	$V_{pd\sigma}s_y$	$\sqrt{3}V_{pd\sigma}s_y$
$\lvert\boldsymbol{k}\ 3z^2-r^2\rangle$	$-2V_{pd\sigma}\overline{s}_z$	$V_{pd\sigma}\overline{s}_x$	$V_{pd\sigma}\overline{s}_y$	ε_d	0
$\lvert\boldsymbol{k}\ x^2-y^2\rangle$	0	$-\sqrt{3}V_{pd\sigma}\overline{s}_x$	$\sqrt{3}V_{pd\sigma}\overline{s}_y$	0	ε_d

where $s_\alpha = ie^{-ik_\alpha a/2}\sin k_\alpha a/2$, $\alpha = x, y, z$, $\varepsilon_p < \varepsilon_d = \varepsilon_p + \Delta_{pd}$, and $V_{pd\sigma} < 0$. If $|V_{pd\sigma}|/\Delta_{pd}$ is small, the occupied bonding-like bands have mostly F p character, while the partially filled antibonding-like bands have mostly Cu e_g character. The energies ε_d and ε_p include the crystal-field term (23). We now calculate the e_g-like bands along high-symmetry lines.[9] Along the Γ-X direction we find the dispersion relations for the e_g-like bands

$$\begin{aligned} \varepsilon_2(\boldsymbol{k}) &= \varepsilon_d \\ \varepsilon_1(\boldsymbol{k}) &= \varepsilon_p + \frac{\Delta_{pd}}{2} + \frac{\sqrt{\Delta_{pd}^2 + 16V_{pd\sigma}^2|s_x|^2}}{2} \\ &\sim \varepsilon_d + 2t - 2t\cos k_x a \end{aligned} \tag{25}$$

where $t = V_{pd\sigma}^2/\Delta_{pd}$; in the last step (25) we have assumed that $|V_{pd\sigma}|/\Delta_{pd}$ is small. We can repeat the calculation for the t_{2g} bands. In this case the simplest tight-binding Hamiltonian is

$H^{\rm TB}_{t_{2g}}$	$\lvert\boldsymbol{k}\ y^a\rangle$	$\lvert\boldsymbol{k}\ x^b\rangle$	$\lvert\boldsymbol{k}\ xy\rangle$
$\lvert\boldsymbol{k}\ y^a\rangle$	ε_p	0	$2V_{pd\pi}s_x$
$\lvert\boldsymbol{k}\ x^b\rangle$	0	ε_p	$2V_{pd\pi}s_y$
$\lvert\boldsymbol{k}\ xy\rangle$	$2V_{pd\pi}\overline{s}_x$	$2V_{pd\pi}\overline{s}_y$	ε_d

[9] Special points: $\Gamma = (0,0,0)$, Z$= (0,0,\pi/a)$, X$= (\pi/a,0,0)$, M$= (\pi/a,\pi/a,0)$, R$= (\pi/a,\pi/a,\pi/a)$.

and cyclic permutations of x, y, z. In the Γ-X direction we find

$$\begin{aligned}
\varepsilon_{2'}(\boldsymbol{k}) &= \varepsilon_d \\
\varepsilon_5(\boldsymbol{k}) &= \varepsilon_p + \frac{\Delta_{pd}}{2} + \frac{\sqrt{\Delta_{pd}^2 + 16 V_{pd\pi}^2 |s_x|^2}}{2} \\
&\sim \varepsilon_d + 2t - 2t \cos k_x a
\end{aligned}$$

where $t = V_{pd\pi}^2/\Delta_{pd}$. The tight-binding model we have used so far is oversimplified, but it already qualitatively describes the e_g and t_{2g} bands in Fig. 9. A more accurate description can be obtained including other Slater-Koster integrals, such as the hopping to apical F s states, or between neighboring F p-states. With increasing number of parameters, it becomes progressively harder to estimate them, e.g. from comparison with experiments; furthermore a large number of fitting parameters makes it impossible to put a theory to a test. However, modern techniques allow us to calculate hopping integrals and crystal-field splittings *ab-initio*, using localized Wannier functions as basis instead of atomic orbitals, and the DFT potential $v_R(\boldsymbol{r})$ as one electron potential; because Wannier functions are orthogonal, the corresponding overlap matrix is diagonal. This leads to the expression (8) for the Hamiltonian, with hopping and crystal-field integrals defined as in (9) and (10).

In the simple model discussed above we could diagonalize the Hamiltonian analytically; this is, in general, not doable for models describing the full band structure of a given material in a large energy window. Group theory helps us in determining the degeneracy of states along high symmetry directions. For simplicity we first restrict ourselves to symmorphic space groups, which do not contain glide planes and screw axes; these groups are the direct product of the translational subgroup and one of the crystallographic point groups.

To understand how symmetries affect bands, we have first to introduce some new concepts. The *group of the wavevector*, $G_{\boldsymbol{k}}$, is the set of space group operations which transform $\boldsymbol{k}$ into itself or an equivalent vector $\boldsymbol{k} + \boldsymbol{G}$, where $\boldsymbol{G}$ is a reciprocal space lattice vector.

$$R\boldsymbol{k} = \boldsymbol{k} + \boldsymbol{G}.$$

The set of distinct non-equivalent vectors in $\{R\boldsymbol{k}\}$ is instead called the *star* of the $\boldsymbol{k}$ point. The group of the Γ point is the point group of the crystal, G, as every operation R transforms Γ into itself. The group of a generic $\boldsymbol{k}$ point in the first Brillouin zone is a subgroup of G, and might contain only the identity. Because the scalar product is a scalar, it is invariant under any operation. Thus

$$\boldsymbol{r} \cdot R\boldsymbol{k} = R^{-1}\boldsymbol{r} \cdot \boldsymbol{k}.$$

The effect of a point group operation on a Bloch state $\psi_{\boldsymbol{k}}(\boldsymbol{r}) = u_{\boldsymbol{k}}(\boldsymbol{r}) e^{i\boldsymbol{r}\cdot\boldsymbol{k}}$ is then

$$O(R)\psi_{\boldsymbol{k}}(\boldsymbol{r}) = O(R)u_{\boldsymbol{k}}(r)e^{i\boldsymbol{r}\cdot\boldsymbol{k}} = u_{\boldsymbol{k}}(R^{-1}\boldsymbol{r})e^{i\boldsymbol{r}\cdot R\boldsymbol{k}} = u'_{R\boldsymbol{k}}(\boldsymbol{r})e^{i\boldsymbol{r}\cdot R\boldsymbol{k}} = \psi_{R\boldsymbol{k}}(\boldsymbol{r}).$$

If $O(R)$ is in the group G of the Hamiltonian, the Bloch functions $\psi_{R\boldsymbol{k}}$ are degenerate. Under an operation in $G_{\boldsymbol{k}} \subseteq G$, the Bloch function $\psi_{\boldsymbol{k}}(\boldsymbol{r}) = u_{\boldsymbol{k}}(\boldsymbol{r}) e^{i\boldsymbol{r}\cdot\boldsymbol{k}}$ might be transformed into

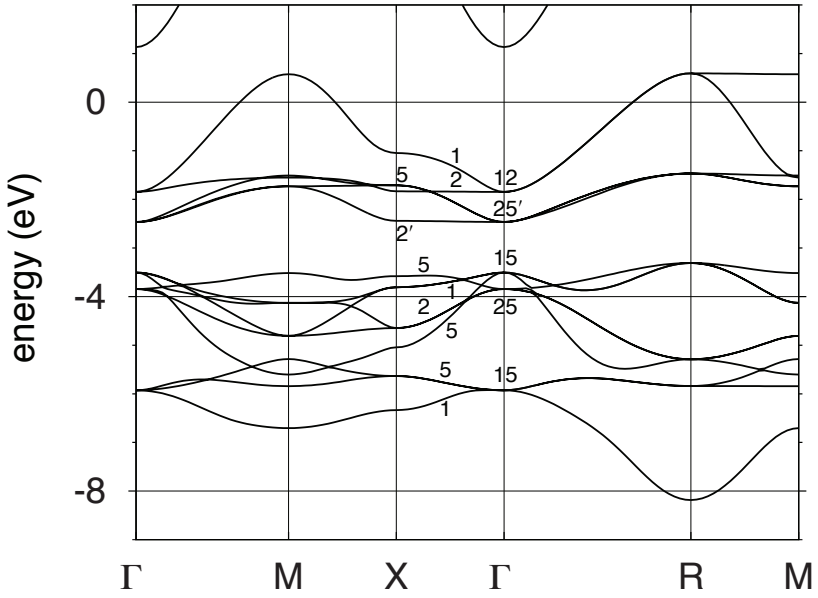

Fig. 9: *LDA band structure of cubic KCuF$_3$. Labels along the direction X-Γ indicate the corresponding irreducible representations for the e_g bands.*

a degenerate distinct function $\psi'_{\boldsymbol{k}}(\boldsymbol{r}) = u'_{\boldsymbol{k}}(\boldsymbol{r})e^{i\boldsymbol{r}\cdot\boldsymbol{k}}$ with the same wavevector; the basis of the linear space defined by the set $\{O(R)\psi_{\boldsymbol{k}}(\boldsymbol{r})\}$ builds an irreducible representation of $G_{\boldsymbol{k}}$, called the *small representation*. Thus, for symmorphic space groups, once we identified the group of the wavevector, we can use directly the character table of the point group to classify energy levels. For non-symmorphic space groups, the character table should be modified because some point group operations $\{R|0\}$ are replaced by $\{R|\boldsymbol{f}\}$; one can however show that the character for an operation $\{R|\boldsymbol{f}\}$ is $e^{i\boldsymbol{f}\cdot\boldsymbol{k}}\,\chi(R)$; at the Γ point the factor $e^{i\boldsymbol{f}\cdot\boldsymbol{k}}$ is one.
Let us analyze band-degeneracy in the case of the cubic perovskite KCuF$_3$. The space group is symmorphic and the point group is O_h; the group of the Γ point is therefore O_h. We write below the character table of O_h and the irreducible representations at the Γ point

	O_h	E	$3C_4^2$	$6C_4$	$6C_2'$	$8C_3$	I	$3IC_4^2$	$6IC_4$	$6IC_2'$	$8IC_3$
	$\Gamma_1(g)$	1	1	1	1	1	1	1	1	1	1
	$\Gamma_2(g)$	1	1	−1	−1	1	1	1	−1	−1	1
$(x^2-y^2, 3z^2-r^2)$	$\Gamma_{12}(g)$	2	2	0	0	−1	2	2	0	0	−1
(x,y,z)	$\Gamma_{15}(u)$	3	−1	1	−1	0	−3	1	−1	1	0
	$\Gamma_{25}(u)$	3	−1	−1	1	0	−3	1	1	−1	0
	$\Gamma_1'(u)$	1	1	1	1	1	−1	−1	−1	−1	−1
	$\Gamma_2'(u)$	1	1	−1	−1	1	−1	−1	1	1	−1
	$\Gamma_{12}'(u)$	2	2	0	0	−1	−2	−2	0	0	1
	$\Gamma_{15}'(g)$	3	−3	1	−1	0	3	−3	1	−1	0
(xy, xz, yz)	$\Gamma_{25}'(g)$	3	−3	−1	−1	0	3	−3	−1	−1	0

Here g are the even and u the odd representations. The e_g-bands are in the $E_g = \Gamma_{12}$ irreducible

representation, and the t_{2g} in the $T_{2g} = \Gamma'_{25}$ irreducible representation.
For a wavevector $\Delta = \frac{2\pi}{a}(k_x, 0, 0)$ the group is C_{4v}, the symmetry group of a square. The character table of point-group C_{4v} is given below

	C_{4v}	E	C_4^2	$2C_4$	$2IC_4^2$	$2IC'_2$
$1, x, 3x^2 - r^2$	Δ_1	1	1	1	1	1
$y^2 - z^2$	Δ_2	1	1	-1	1	-1
yz	Δ'_2	1	1	-1	-1	1
$yz(y^2 - z^2)$	Δ'_1	1	1	1	-1	-1
$y, z; xy, xz$	Δ_5	2	-2	0	0	0

The representations of t_{2g}-states ($T_{2g} = \Gamma'_{25}$) and that of e_g-states ($E_g = \Gamma_{12}$) in the O_h group are reducible in C_{4v} and split as follows

$$\begin{aligned} \Gamma_{12} &\to \Delta_1 \oplus \Delta_2 \\ \Gamma'_{25} &\to \Delta'_2 \oplus \Delta_5 \end{aligned}$$

Thus the e_g-states split into $3x^2 - r^2$ and $y^2 - z^2$, and the t_{2g} into yz and into xy, xz.
To analyze the F p-bands at the Γ-point, we have first to construct all 9 F p-Bloch states $|\boldsymbol{k}\ \mu^\nu\rangle$, and then construct the linear combinations which belong to specific irreducible representations of O_h. The first step is to build a reducible 9×9 odd representation, Γ^F using the states $|\boldsymbol{k}\ \mu^\nu\rangle$ as a basis. We do not need, however, to construct the full matrices, because the characters are the sum of the diagonal elements $\langle \boldsymbol{k}\ \mu^\nu | O(g) | \boldsymbol{k}\ \mu^\nu \rangle$. By adding the non-zero terms, we find

	E	$3C_4^2$	$6C_4$	$6C'_2$	$8C_3$	I	$3IC_4^2$	$6IC_4$	$6IC'_2$	$8IC_3$
Γ^F	9	-3	1	-1	0	-9	3	-1	1	0

The Γ^F representation can be decomposed in irreducible representations of the group O_h as $\Gamma^F = 2\Gamma_{15} \oplus \Gamma_{25}$. Along Γ-X the decomposition is $2\Delta_1 \oplus \Delta_2 \oplus 3\Delta_5$.
Let us now return to the crystal-field splitting. In the point charge model discussed in the previous section, the neighboring sites are viewed as ions, and their nature and tendency towards covalent bondings are ignored. In the tight-binding approach described in this section, this corresponds to calculate the terms $\Delta\varepsilon_{lm,l'm'}$ in a basis of atomic orbitals; in the simple tight-binding model considered, this gives the splitting of e_g and t_{2g} bands at the Γ point. However, the ligands do matter, because they can form bonding and antibonding states with the central atom. In the case of a cubic perovskite, the t_{2g} and e_g bands are antibonding-like bands; because $V_{pd\sigma}$ (σ bond), relevant for the e_g bands, is larger than $V_{pd\pi}$ (π bond), relevant for the t_{2g} bands, the latter are lower in energy, in agreement with the results of the point-charge model. This ligand field, differently from the crystal field in the point-charge model, is mostly determined by the first shells of neighbors, because the hopping integrals decay fast with distance (Appendix B). We can understand better the effect of the ligands by considering the e_g and t_{2g} tight-binding Hamiltonians $H^{\rm TB}_{e_g}$ and $H^{\rm TB}_{t_{2g}}$ at the $\boldsymbol{k} = M = (\pi/a, \pi/a, 0)$ point. The d-like

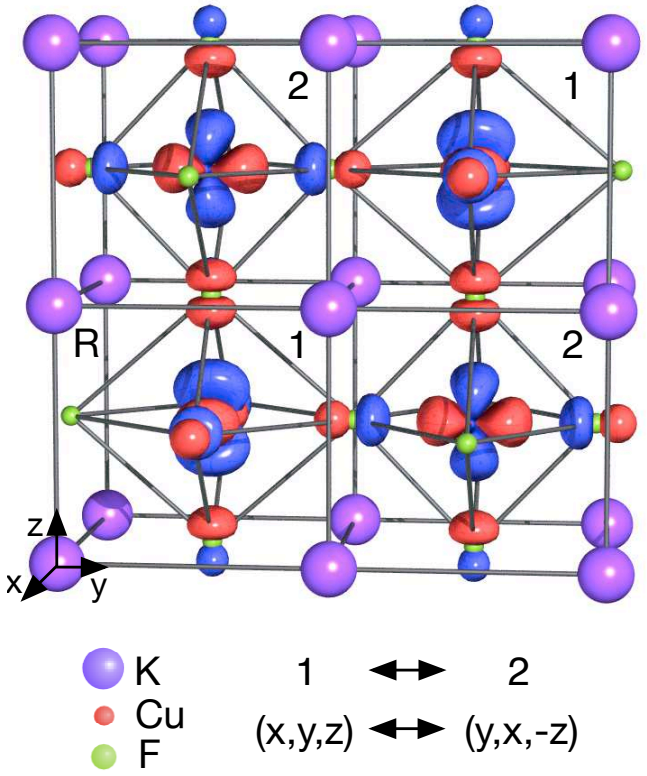

Fig. 10: *Cooperative Jahn-Teller distortion and ordering of the e_g hole orbitals in $KCuF_3$. Adapted from Ref. [7]. The Wannier function of the hole orbitals is obtained by downfolding all states but the Cu e_g; therefore, differently than the orbitals in Fig. 5, it has p-tails at F sites.*

states that diagonalize the Hamiltonians are antibonding combinations of ligand p-functions and transition-metal d-functions. Two of such states can be written as

$$\begin{aligned} |M\psi_{x^2-y^2}\rangle &= c_{1d}|M\ x^2-y^2\rangle + c_{1p}\left[|M\ x^a\rangle - |M\ y^b\rangle\right], \\ |M\psi_{xy}\rangle &= c_{2d}|M\ xy\rangle - c_{2p}\left[|M\ y^a\rangle + |M\ x^b\rangle\right], \end{aligned}$$

where c_{id}, c_{ip} define the mixing, $i = 1, 2$ and $c_{id}^2 + c_{ip}^2 = 1$. If the atomic xy and $x^2 - y^2$ orbitals are degenerate, the difference in the energy of the two states depends only on the degree of mixing and the Slater-Koster integrals $V_{pd\sigma}$ and $V_{pd\pi}$. For the simple tight-binding models presented for $KCuF_3$, the additional e_g-t_{2g} splitting due to the ligands can thus be estimated as $(W_{e_g} - W_{t_{2g}})/2$, where W_{e_g} and $W_{t_{2g}}$ are the e_g and t_{2g} band width, respectively.

As previously discussed, the modern approach to tight-binding theory consists in using localized Wannier functions, instead of atomic orbitals, as a basis. In this case, one can build Wannier functions which span the e_g and t_{2g} bands only, and which have therefore the effects of the ligands built-in. This can be seen, e.g., in Fig. 10 for the empty orbital of $KCuF_3$; the Wannier function, obtained by downfolding all states but e_g, has p tails on the neighboring F sites. In the basis of such Wannier functions, the crystal-field splitting, including ligand-field effects, can be obtained directly from the on-site elements (10) of the Hamiltonian.

5 Jahn-Teller effect

The Jahn-Teller theorem states that any electronically degenerate system can lower its energy under some structural distortions, and therefore is unstable. The only exceptions are linear molecules and Kramers degeneracy. To explain this effect we have to go back to the Born-Oppenheimer Ansatz and the system of coupled Schrödinger equations for the electrons and the lattice, (3) and (4). Let us consider a system in a high symmetry structure, $\{\boldsymbol{R}^0_\alpha\}$, for which the electronic ground state has energy $\varepsilon(\{\boldsymbol{R}^0_\alpha\})$ with degeneracy m; the corresponding degenerate electronic wavefunctions are $\psi_m(\{\boldsymbol{r}_i\};\{\boldsymbol{R}^0_\alpha\})$. Thus there are m Born-Oppenheimer potential energy surfaces $\hat{U}_n = \varepsilon(\{\boldsymbol{R}_\alpha\})$ which are degenerate for $\{\boldsymbol{R}_\alpha\} = \{\boldsymbol{R}^0_\alpha\}$. Let us consider one of these surfaces, and expand the potential around $\{\boldsymbol{R}^0_\alpha\}$. We find

$$\hat{H}_n = \hat{T}_n + \varepsilon(\{\boldsymbol{R}^0_\alpha\}) + \sum_{\alpha\mu}\left[\frac{\partial \hat{U}_n}{\partial u_{\alpha\mu}}\right]_{\{\boldsymbol{R}^0_\alpha\}} u_{\alpha\mu} + \frac{1}{2}\sum_{\alpha\mu,\alpha'\mu'}\left[\frac{\partial^2 \hat{U}_n}{\partial_{\alpha\mu}\partial_{\alpha'\mu'}}\right]_{\{\boldsymbol{R}^0_\alpha\}} u_{\alpha\mu}u_{\alpha'\mu'} + \ldots,$$

where $\boldsymbol{u}_\alpha = \boldsymbol{R}_\alpha - \boldsymbol{R}^0_\alpha$ are displacement vectors, and $\mu = x, y, z$. If $\{\boldsymbol{R}^0_\alpha\}$ is an equilibrium structure, the gradient is zero. In this case, the Hamiltonian can be written as

$$\hat{H}_n \sim \hat{T}_n + \frac{1}{2}\sum_{\alpha\mu,\alpha'\mu'}\left[\frac{\partial^2 \hat{U}_n}{\partial_{\alpha\mu}\partial_{\alpha'\mu'}}\right]_{\{\boldsymbol{R}^0_\alpha\}} u_{\alpha\mu}u_{\alpha'\mu'} + \cdots = \hat{T}_n + \hat{U}^{\rm PH}_n(\{\boldsymbol{R}^0_\alpha\}) + \ldots, \tag{26}$$

where we have defined $\varepsilon(\{\boldsymbol{R}^0_\alpha\})$ as the energy zero. It is convenient to rewrite (26) in *normal coordinates* $\{Q_{\beta\nu}\}$ and associated canonically conjugated momenta $\{P_{\beta\nu}\}$. The normal coordinates are the linear combination of displacements, $Q_{\beta\nu} = \sum_{\alpha\mu} a_{\beta\nu,\alpha\mu}u_{\alpha\mu}$, with $\beta = 1,\ldots N_n$, $\nu = x, y, z$, which bring (26) in the diagonal form

$$\hat{H}_n \sim \frac{1}{2}\sum_{\beta\nu}(P^2_{\beta\nu} + \omega^2_{\beta\nu}Q^2_{\beta\nu}). \tag{27}$$

In a crystal, this Hamiltonian yields the phonon dispersions. In general, the high-symmetry structure might or might not be a stationary point. The behavior of the energy surfaces close to the high symmetry point in which they are degenerate allows us to separate them into two classes, the first one in which $\{\boldsymbol{R}^0_\alpha\}$ is a stationary point for all m (Renner-Teller intersection), and the second in which the surface is not a stationary point at least for some of the surfaces (Jahn-Teller intersection). The classical Jahn-Teller systems are those for which $\nabla\hat{U}_n(\{\boldsymbol{R}^0_\alpha\}) \neq 0$ at least in some direction (see, e.g., Fig. (11)). Let us now consider the first order correction to the m degenerate eigenvalues due to a small distortion around $\{\boldsymbol{R}^0_\alpha\}$. The electronic Hamiltonian (3) has matrix elements

$$\begin{aligned}\langle\psi_m|\hat{H}_e(\{\boldsymbol{R}_\alpha\})|\psi_{m'}\rangle &= \varepsilon(\{\boldsymbol{R}^0_\alpha\}) + \sum_{\alpha\mu}\langle\psi_m|\left[\frac{\partial \hat{H}_e}{\partial u_{\alpha\mu}}\right]_{\{\boldsymbol{R}^0_\alpha\}}|\psi_{m'}\rangle u_{\alpha\mu} + \ldots \\ &= \varepsilon(\{\boldsymbol{R}^0_\alpha\}) + \hat{U}^{\rm JT}_{m,m'} + \ldots.\end{aligned}$$

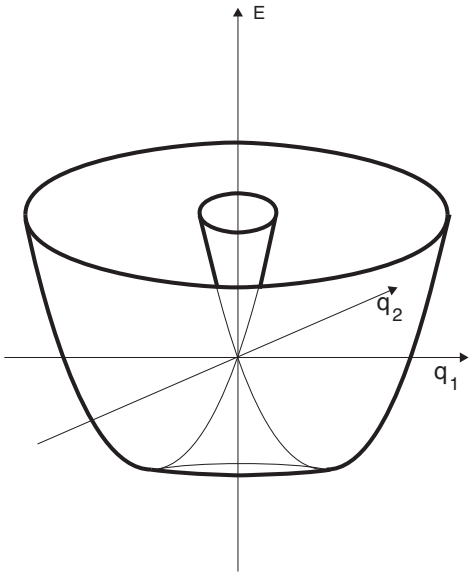

Fig. 11: *Born-Oppenheimer potential-energy surface exhibiting the form of a mexican hat. The slope of the curve at small distortions q_1, q_2 yields the Jahn-Teller coupling constant λ.*

Since the perturbation $\hat{U}^{\rm JT}$ couples the degenerate functions, we generalize the Born-Oppenheimer Ansatz as follows

$$\Psi(\{\boldsymbol{r}_i\},\{\boldsymbol{R}_\alpha\}) \;=\; \sum_m \psi_m(\{\boldsymbol{r}_i\};\{\boldsymbol{R}_\alpha\})\Phi_m(\{\boldsymbol{R}_\alpha\}).$$

To find the equations for the functions $\{\hat{\Phi}_m\}$, we write the Schödinger equation $H\Psi = E\Psi$, multiply on the left by $\overline{\psi}_m$, and integrate over the coordinates of the electrons.[10] We obtain

$$\hat{H}_n\Phi_m(\{\boldsymbol{R}_\alpha\}) = [\hat{T}_n + \hat{U}_n^{\rm PH}]\Phi_m(\{\boldsymbol{R}_\alpha\}) + \sum_{m,m'} U^{\rm JT}_{m,m'}\Phi_{m'}(\{\boldsymbol{R}_\alpha\}) = E\Phi_m(\{\boldsymbol{R}_\alpha\}). \qquad (28)$$

The Jahn-Teller potential couples degenerate Born-Oppenheimer sheets, and the dynamic of the system close to the degeneracy point is determined by all degenerate sheets. The ground state of (28) yields a new structure $\{\tilde{\boldsymbol{R}}^0_\alpha\}$ in which the electronic states are not any more degenerate. Let us consider a classical example of a Jahn-Teller material, $KCuF_3$. In the high-symmetry cubic perovskite structure shown in Fig. 12, the two Cu $3d^9$ configurations with a hole in one of the e_g orbitals ($3t_{2g}^6e_g^3$ states), are degenerate. The Jahn-Teller theorem tells us that there must be a geometrical instability. Let us consider a single octahedron and the normal modes that could lead to such an instability through coupling to the e_g-states. These are the modes Q_1 and Q_2 shown in Fig. 12. They are defined as

$$\begin{aligned}\boldsymbol{Q}_1 &= [\boldsymbol{u}_1(q_1) - \boldsymbol{u}_4(q_1) - \boldsymbol{u}_2(q_1) + \boldsymbol{u}_5(q_1)],\\ \boldsymbol{Q}_2 &= [\boldsymbol{u}_3(q_2) - \boldsymbol{u}_6(q_2) - \boldsymbol{u}_1(q_2) + \boldsymbol{u}_4(q_2) - \boldsymbol{u}_2(q_2) + \boldsymbol{u}_5(q_2)],\end{aligned}$$

[10] We neglect non adiabatic corrections, i.e., the operator $\hat{\Lambda}_n$, with elements $\langle m|\hat{\Lambda}_n|m'\rangle = -\sum_\alpha \frac{1}{M_\alpha}\left[\frac{1}{2}\langle\psi_m|\nabla^2_\alpha\psi_{m'}\rangle + \langle\psi_m|\nabla_\alpha\psi_{m'}\rangle\cdot\nabla_\alpha\right]$

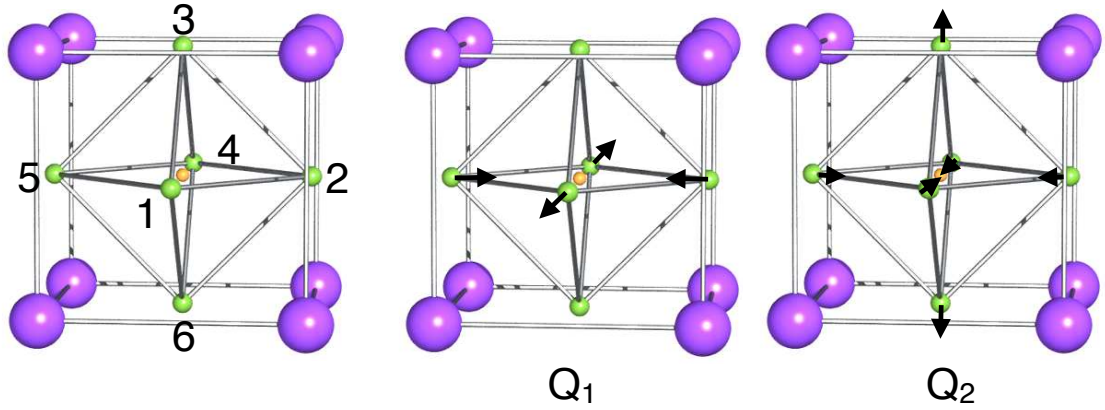

Fig. 12: *Unit cell (left) and degenerate vibrational modes Q_1 and Q_2 of cubic $KCuF_3$.*

where the displacements are

$$\begin{array}{rclrcl}
\boldsymbol{u}_1(q_1) &=& \frac{1}{\sqrt{2}}q_1(1,0,0) & \boldsymbol{u}_1(q_2) &=& -\frac{1}{\sqrt{6}}q_2(1,0,0)\\
\boldsymbol{u}_2(q_1) &=& -\frac{1}{\sqrt{2}}q_1(0,1,0) & \boldsymbol{u}_2(q_2) &=& -\frac{1}{\sqrt{6}}q_2(0,1,0)\\
\boldsymbol{u}_3(q_1) &=& (0,0,0) & \boldsymbol{u}_3(q_2) &=& \frac{2}{\sqrt{6}}q_2(0,0,1)\\
\boldsymbol{u}_4(q_1) &=& -\frac{1}{\sqrt{2}}q_1(1,0,0) & \boldsymbol{u}_4(q_2) &=& \frac{1}{\sqrt{6}}q_2(1,0,0)\\
\boldsymbol{u}_5(q_1) &=& \frac{1}{\sqrt{2}}q_1(0,1,0) & \boldsymbol{u}_5(q_2) &=& \frac{1}{\sqrt{6}}q_2(0,1,0)\\
\boldsymbol{u}_6(q_1) &=& (0,0,0) & \boldsymbol{u}_6(q_2) &=& -\frac{2}{\sqrt{6}}q_2(0,0,1)
\end{array}$$

For the Q_1 and Q_2 modes, the quadratic potential has the form

$$\hat{U}_n^{\rm PH} = \frac{1}{2}C(q_1^2+q_2^2).$$

$KCuF_3$ is thus an example of a $e\otimes E$ Jahn-Teller system, a system in which an electronic doublet (e) interacts with a doublet of degenerate normal modes (E). The form[11] of the Jahn-Teller potential $\hat{U}^{\rm JT}$ can be obtained from the effect of the perturbation due to Q_1 and Q_2 on the crystal-field matrix (23). The linear order correction is

$$\Delta\varepsilon_{lm,l'm'}(\mathbf{0},\boldsymbol{R}_\alpha+\boldsymbol{u}) - \Delta\varepsilon_{lm,l'm'}(\mathbf{0},\boldsymbol{R}_\alpha) \sim \nabla\Delta\varepsilon_{lm,l'm'}(\mathbf{0},\boldsymbol{R}_\alpha)\cdot\boldsymbol{u}$$

For e_g-states we use for simplicity the following approximations[12]

$$\begin{aligned}
\Delta\varepsilon_{3z^2-r^2,3z^2-r^2} &\sim \left[n^2-\frac{1}{2}(l^2+m^2)\right]^2\tilde{V}_{dd\sigma},\\
\Delta\varepsilon_{3z^2-r^2,x^2-y^2} &\sim \frac{\sqrt{3}}{2}(l^2-m^2)\left[n^2-\frac{1}{2}(l^2+m^2)\right]\tilde{V}_{dd\sigma},\\
\Delta\varepsilon_{x^2-y^2,x^2-y^2} &\sim \frac{3}{4}(l^2-m^2)^2\tilde{V}_{dd\sigma}.
\end{aligned}$$

[11] The covalent contribution yields the same form of the potential.

[12] The crystal-field integrals are also two-center integrals; the table of Slater-Koster integrals in Appendix B is thus still valid, provided that $V_{ll'\alpha}$ are replaced by the corresponding crystal-field terms, which we indicate as $\tilde{V}_{ll'\alpha}$.

By summing all relevant contributions, we obtain

$$\hat{U}^{\rm JT}(q_1,q_2) = -\lambda \begin{pmatrix} q_2 & q_1 \\ q_1 & -q_2 \end{pmatrix} = -\lambda\left(q_1\hat{\tau}_x + q_2\hat{\tau}_z\right), \quad \lambda \propto |\tilde{V}'_{dd\sigma}|$$

where λ is the Jahn-Teller coupling and $\hat{\tau}_z$, $\hat{\tau}_x$ are pseudospin operators in orbital space, with

$$\begin{array}{llll} \hat{\tau}_z|3z^2-r^2\rangle & = -|3z^2-r^2\rangle, & \hat{\tau}_z|x^2-y^2\rangle & = |x^2-y^2\rangle, \\ \hat{\tau}_x|3z^2-r^2\rangle & = \ \ |x^2-y^2\rangle, & \hat{\tau}_x|x^2-y^2\rangle & = |3z^2-r^2\rangle. \end{array}$$

In matrix form

$$\hat{\tau}_z = \begin{pmatrix} 1 & 0 \\ 0 & -1 \end{pmatrix} \quad \hat{\tau}_x = \begin{pmatrix} 0 & 1 \\ 1 & 0 \end{pmatrix}.$$

If we neglect the kinetic energy of the nuclei (limit $M_\alpha \to \infty$), the ground state of the system can be obtained minimizing the potential energy

$$U(q_1,q_2) = \hat{U}^{\rm JT} + \hat{U}_n^{\rm PH} = -\lambda \begin{pmatrix} q_2 & q_1 \\ q_1 & -q_2 \end{pmatrix} + \frac{1}{2}C(q_1^2+q_2^2). \tag{29}$$

To find the minimum of (29), it is convenient to introduce polar coordinates, which we define as $q_2 = q\cos\theta, q_1 = q\sin\theta$. In these coordinates

$$U^{\rm JT} = -\lambda q \begin{pmatrix} \cos\theta & \sin\theta \\ \sin\theta & -\cos\theta \end{pmatrix}.$$

We find two eigenvalues; the lowest energy branch $E(q) = -\lambda q + \frac{1}{2}q^2$ takes the form of a mexican hat, shown in Fig. 11. The minimum of $E(q)$ is obtained for $q = q_0 = \lambda/C$ and has value $E_{\rm JT} = -\lambda^2/2C$; the quantity $E_{\rm JT}$ is defined as the Jahn-Teller energy of the system. The electronic ground state can be written as

$$|\theta\rangle_G = -\sin\frac{\theta-\pi}{2}|x^2-y^2\rangle + \cos\frac{\theta-\pi}{2}|3z^2-r^2\rangle.$$

The excited state (hole orbital), with energy $\lambda q + \frac{1}{2}q^2$, is

$$|\theta\rangle_E = -\sin\frac{\theta}{2}|x^2-y^2\rangle + \cos\frac{\theta}{2}|3z^2-r^2\rangle.$$

The states $|\theta\rangle_E$ with different θ are shown in Fig. 13. In the simple model discussed so far, all states $|\theta\rangle_G$ have the same Jahn-Teller energy. Cubic symmetry however only requires that θ, $\theta + 2\pi/3$, and $\theta - 2\pi/3$ yield degenerate states. The additional degeneracy is removed when we take into account anharmonic terms, the lowest order of which has the form

$$U^{\rm anh}(q_1,q_2) = -\beta(Q_2^3 - 3Q_2Q_1^2) \propto \cos 3\theta,$$

and yields, for positive β, the tetragonal distortions ($\theta = 0, \pm 2\pi/3$) as ground state configuration. Higher order terms or a negative β can reverse the sign of the potential, making the Q_1 Jahn-Teller distortion ($\theta = 2\pi/4, 2\pi/4 \pm 2\pi/3$) more stable [8].

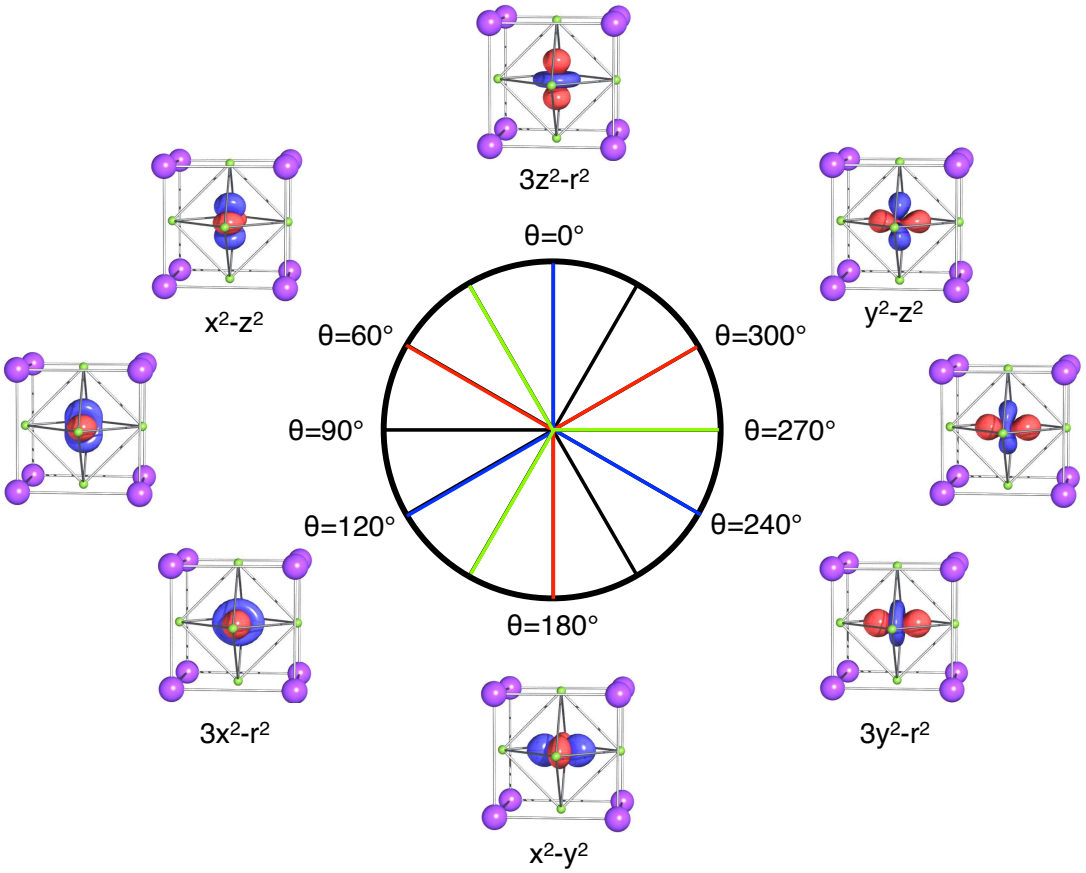

Fig. 13: *Linear combinations of e_g-states, $|\theta\rangle = -\sin\frac{\theta}{2}|x^2-y^2\rangle + \cos\frac{\theta}{2}|3z^2-r^2\rangle$. The $\theta = 0^o$ orbital is the excited state in the presence of a tetragonal compression along the z axis, while $\theta = \pm 2\pi/3$ are excited states for a tetragonal compression along x or y. This three-fold degeneracy (rotation of $\pm 2\pi/3$) is due to cubic symmetry.*

In the presence of Jahn-Teller distortions and/or many-body super-exchange effects, orbital-order phenomena can take place. Super-exchange phenomena are discussed in the lecture of Erik Koch. The order of orbitals in $KCuF_3$, calculated using the LDA+DMFT approach, is shown in Fig. 10. The origin of orbital order in $KCuF_3$ and $LaMnO_3$, and the related interplay between Jahn-Teller effect and many-body super-exchange, are discussed in Refs. [7, 9].

Let us now analyze the different electronic configurations that can occur in perovskites. For the electronic configuration $3d^1 = 3t_{2g}^1$, the procedure is as the one illustrated above, except that t_{2g}-states are 3-fold degenerate and form π bonds, which are weaker, therefore the splitting introduced by the Jahn-Teller effect is smaller than for e_g-states. In the case of electronic configurations $3d^n$ with $n > 1$, to determine if the ion is Jahn-Teller active one has to consider the degeneracies of the many-body state, including Coulomb repulsion. Weak Jahn-Teller states are $3d^1$ (Ti^{3+} in $LaTiO_3$) and $3d^2$ (V^{3+} in $LaVO_3$), as also $3t_{2g}^4$, $3t_{2g}^5$, $3t_{2g}^4 e_g^2$, $3t_{2g}^5 e_g^2$; strong Jahn-Teller configurations are, e.g., $3d^9$ (Cu^{2+} in $KCuF_3$) and $3t_{2g}^3 e_g^1$ (Mn^{3+} in $LaMnO_3$); the configurations $3t_{2g}^3$ and $3t_{2g}^3 e_g^2$ are not degenerate and therefore not Jahn-Teller active.

6 Conclusions

The parameters of the one-electron Hamiltonian are essential ingredients of many-body models. The crystal-field splittings and the hopping integrals carry the information on the lattice and the covalency, and determine to a large extent what makes a system different from the others. The color of a transition-metal complex is for example often determined by the e_g-t_{2g} crystal-field splitting. For a given system, the hopping integrals determine the band structure and the shape of the Fermi surface; the crystal-field splitting plays a crucial role for the local properties, such as the local magnetic moments or spin states, competing with spin-orbit interaction and Coulomb repulsion. In strongly correlated systems, the competition between hopping integrals and Coulomb interaction decides if the system is a metal or a Mott insulator; the crystal-field splitting can however help the formation of a Mott insulating state by reducing the degeneracy of the relevant many-body states [2].

In this lecture we have discussed simple approaches to determine the one-electron parameters for a given system. Such approaches are based on atomic orbitals and symmetries. They are easier to use for high-symmetry systems, in which the number of parameters to determine are small; once the model is constructed, the parameters can be obtained, e.g., by fitting to experiment. In the age of massively parallel supercomputers and standard *ab-initio* codes, it might seem anachronistic to study approximate methods to calculate one-electron parameters. However, these approaches are very useful for understanding qualitatively the behavior of a given system, and the results of complex calculations. It is indeed astonishing how far we can often go in understanding a system with these methods alone. One of the reasons of the successes of tight-binding and crystal-field theory is that symmetries are fully accounted for. In developing approximations to describe numerically complex many-body effects, we should always remember that symmetries are crucial, and taking them into account is essential to understand the properties of a given material.

The modern approach to calculate one-electron parameters is based on *ab-initio* localized Wannier functions; they are built from DFT calculations (e.g., in the LDA approximation), and used as a one-electron basis to construct material-specific many-body models. The choice of LDA Wannier functions as a basis relies on the success of the LDA in describing the properties of weakly correlated systems. These successes let us hope that the long-range and the mean-field part of the electron-electron interaction are already well accounted for by the LDA. Thanks to *ab-initio* Wannier functions it is possible to build many-body models even for low-symmetry materials, accounting, e.g., for the effects of small distortions that split the t_{2g} levels [2], a very hard task with semiempirical tight binding. When using Wannier functions as a one-electron basis to build many-body models, we should however never forget what are the assumptions behind; simple models and symmetry considerations remind us where all comes from.

Acknowledgment

Support of the Deutsche Forschungsgemeinschaft through FOR1346 is gratefully acknowledged.

Appendices

A Constants and units

In this lecture, formulas are given in atomic units. The unit of mass m_0 is the electron mass ($m_0 = m_e$), the unit of charge e_0 is the electron charge ($e_0 = e$), the unit of length a_0 is the Bohr radius ($a_0 = a_B \sim 0.52918$ Å), and the unit of time is $t_0 = 4\pi\varepsilon_0\hbar a_0/e^2$. In these units, m_e, a_B, e and $1/4\pi\varepsilon_0$ have the numerical value 1, the speed of light is $c = 1/\alpha \sim 137$, and the unit of energy is $1\text{Ha} = e^2/4\pi\varepsilon_0 a_0 \sim 27.211$ eV.

B Atomic orbitals

B.1 Radial functions

The nlm hydrogen-like atomic orbital is given by

$$\psi_{nlm}(\rho,\theta,\phi) = R_{nl}(\rho)Y_l^m(\theta,\phi),$$

where $R_{nl}(\rho)$ is the radial function and $Y_m^l(\theta,\phi)$ a spherical harmonic, $\rho = Zr$ and Z the atomic number. In atomic units, the radial functions are

$$R_{nl}(\rho) = \sqrt{\left(\frac{2Z}{n}\right)^3 \frac{(n-l-1)!}{2n[(n+l)!]^3}} e^{-\rho/n} \left(\frac{2\rho}{n}\right)^l L_{n-l-1}^{2l+1}\left(\frac{2\rho}{n}\right),$$

where L_{n-l-1}^{2l+1} are generalized Laguerre polynomials of degree $n-l-1$.
The radial function for $n = 1, 2, 3$ are

$$\begin{aligned}
R_{1s}(\rho) &= 2 \; Z^{3/2} && e^{-\rho} \\
R_{2s}(\rho) &= \tfrac{1}{2\sqrt{2}} \; Z^{3/2} && (2-\rho)\, e^{-\rho/2} \\
R_{2p}(\rho) &= \tfrac{1}{2\sqrt{6}} \; Z^{3/2} && \rho\, e^{-\rho/2} \\
R_{3s}(\rho) &= \tfrac{2}{3\sqrt{3}} \; Z^{3/2} && (1-2\rho/3+2\rho^2/27)\, e^{-\rho/3} \\
R_{3p}(\rho) &= \tfrac{4\sqrt{2}}{9\sqrt{3}} \; Z^{3/2} && \rho(1-\rho/6)\, e^{-\rho/3} \\
R_{3d}(\rho) &= \tfrac{2\sqrt{2}}{81\sqrt{15}} \; Z^{3/2} && \rho^2\, e^{-\rho/3}
\end{aligned}$$

where we used the standard notation s for $l = 0$, p for $l = 1$ and d for $l = 2$.

B.2 Real harmonics

To study solids, it is usually convenient to work in the basis of real harmonics. The latter are defined in terms of the spherical harmonics as follows:

$$y_{l0} = Y_0^l, \quad y_{lm} = \frac{1}{\sqrt{2}}(Y_{-m}^l + (-1)^m Y_m^l), \quad y_{l-m} = \frac{i}{\sqrt{2}}(Y_{-m}^l - (-1)^m Y_m^l), \quad m > 0.$$

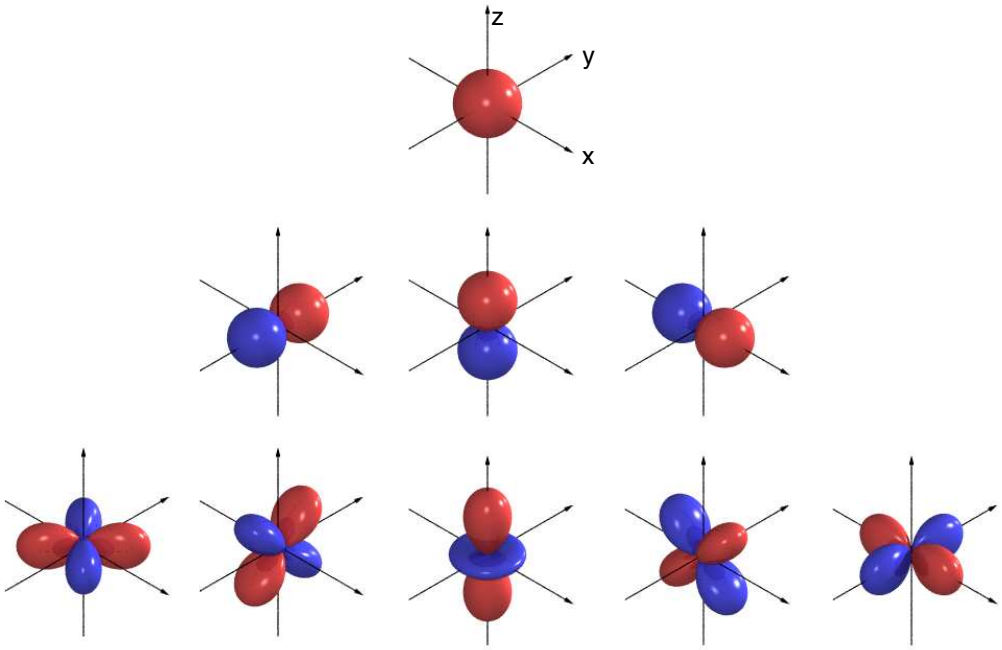

Fig. 14: *The s (first row), p_y, p_z, p_x (second row), and d_{xy}, d_{yz}, $d_{3z^2-r^2}$, d_{xz}, $d_{x^2-y^2}$ (last row) real harmonics.*

Using the definitions $x = r\sin\theta\cos\phi$, $y = r\sin\theta\sin\phi$, $z = r\cos\theta$, we can express the $l = 0, 1, 2$ real harmonics (Fig. 14) as

$$
\begin{aligned}
s \quad &= y_{00} \quad = Y_0^0 \qquad\qquad = \sqrt{\tfrac{1}{4\pi}} \\
p_y \quad &= y_{1-1} = \tfrac{i}{\sqrt{2}}(Y_1^1 + Y_{-1}^1) = \sqrt{\tfrac{3}{4\pi}} \qquad y/r \\
p_z \quad &= y_{10} \quad = Y_2^0 \qquad\qquad = \sqrt{\tfrac{3}{4\pi}} \qquad z/r \\
p_x \quad &= y_{11} \quad = \tfrac{1}{\sqrt{2}}(Y_1^1 - Y_{-1}^1) = \sqrt{\tfrac{3}{4\pi}} \qquad x/r \\
d_{xy} \quad &= y_{2-2} = \tfrac{i}{\sqrt{2}}(Y_2^2 - Y_{-2}^2) = \sqrt{\tfrac{15}{4\pi}} \qquad xy/r^2 \\
d_{yz} \quad &= y_{2-1} = \tfrac{i}{\sqrt{2}}(Y_1^2 + Y_{-1}^2) = \sqrt{\tfrac{15}{4\pi}} \qquad yz/r^2 \\
d_{3z^2-r^2} \quad &= y_{20} \quad = Y_2^0 \qquad\qquad = \sqrt{\tfrac{15}{4\pi}}\tfrac{1}{2\sqrt{3}}\,(3z^2 - r^2)/r^2 \\
d_{xz} \quad &= y_{21} \quad = \tfrac{1}{\sqrt{2}}(Y_1^2 - Y_{-1}^2) = \sqrt{\tfrac{15}{4\pi}} \qquad xz/r^2 \\
d_{x^2-y^2} \quad &= y_{22} \quad = \tfrac{1}{\sqrt{2}}(Y_2^2 + Y_{-2}^2) = \sqrt{\tfrac{15}{4\pi}}\tfrac{1}{2} \qquad (x^2 - y^2)/r^2
\end{aligned}
$$

B.3 Slater-Koster integrals

The interatomic Slater-Koster two-center integrals are defined as

$$E_{lm,l'm'} = \int d\boldsymbol{r}\, \overline{\psi}_{lm}(\boldsymbol{r}-\boldsymbol{d}) V(\boldsymbol{r}-\boldsymbol{d}) \psi_{l'm'}(\boldsymbol{r}).$$

They can be expressed as a function of radial integrals $V_{ll'\alpha}$, which scale with the distance d roughly as $d^{-(l+l'+1)}$ [10], and direction cosines, defined as

$$l = \boldsymbol{d}\cdot\hat{x}/d, \quad m = \boldsymbol{d}\cdot\hat{y}/d, \quad n = \boldsymbol{d}\cdot\hat{z}/d.$$

The Slater-Koster integrals for s-, p-, and d-orbitals [10] are listed below.

$$
\begin{array}{lcrrr}
E_{s,s} & = & V_{ss\sigma} & & \\
E_{s,x} & = & lV_{sp\sigma} & & \\
E_{x,x} & = & l^2V_{pp\sigma} & +(1-l^2)V_{pp\pi} & \\
E_{x,y} & = & lmV_{pp\sigma} & -lmV_{pp\pi} & \\
E_{x,z} & = & lnV_{pp\sigma} & -lnV_{pp\pi} & \\
E_{s,xy} & = & \sqrt{3}lmV_{sd\sigma} & & \\
E_{s,x^2-y^2} & = & \frac{1}{2}\sqrt{3}(l^2-m^2)V_{sd\sigma} & & \\
E_{s,3z^2-r^2} & = & [n^2-\frac{1}{2}(l^2+m^2)]V_{sd\sigma} & & \\
E_{x,xy} & = & \sqrt{3}l^2mV_{pd\sigma} & +m(1-2l^2)V_{pd\pi} & \\
E_{x,yz} & = & \sqrt{3}lmnV_{pd\sigma} & -2lmnV_{pd\pi} & \\
E_{x,zx} & = & \sqrt{3}l^2nV_{pd\sigma} & +n(1-2l^2)V_{pd\pi} & \\
E_{x,x^2-y^2} & = & \frac{\sqrt{3}}{2}l[(l^2-m^2)]V_{pd\sigma} & +l(1-l^2+m^2)V_{pd\pi} & \\
E_{y,x^2-y^2} & = & \frac{\sqrt{3}}{2}m[(l^2-m^2)]V_{pd\sigma} & -m(1+l^2-m^2)V_{pd\pi} & \\
E_{z,x^2-y^2} & = & \frac{\sqrt{3}}{2}n[(l^2-m^2)]V_{pd\sigma} & -n(l^2-m^2)V_{pd\pi} & \\
E_{x,3z^2-r^2} & = & l[n^2-\frac{1}{2}(l^2+m^2)]V_{pd\sigma} & -\sqrt{3}ln^2V_{pd\pi} & \\
E_{y,3z^2-r^2} & = & m[n^2-\frac{1}{2}(l^2+m^2)]V_{pd\sigma} & -\sqrt{3}mn^2V_{pd\pi} & \\
E_{z,3z^2-r^2} & = & n[n^2-\frac{1}{2}(l^2+m^2)]V_{pd\sigma} & +\sqrt{3}n(l^2+m^2)V_{pd\pi} & \\
E_{xy,xy} & = & 3l^2m^2V_{dd\sigma} & +(l^2+m^2-4l^2m^2)V_{dd\pi} & +(n^2+l^2m^2)V_{dd\delta} \\
E_{xy,yz} & = & 3lm^2nV_{dd\sigma} & +ln(1-4m^2)V_{dd\pi} & +ln(m^2-1)V_{dd\delta} \\
E_{xy,zx} & = & 3l^2mnV_{dd\sigma} & +mn(1-4l^2)V_{dd\pi} & +mn(l^2-1)V_{dd\delta} \\
E_{xy,x^2-y^2} & = & \frac{3}{2}lm(l^2-m^2)V_{dd\sigma} & 2lm(m^2-l^2)V_{dd\pi} & \frac{1}{2}lm(l^2-m^2)V_{dd\delta} \\
E_{yz,x^2-y^2} & = & \frac{3}{2}mn(l^2-m^2)V_{dd\sigma} & -mn[1+2(l^2-m^2)]V_{dd\pi} & +mn[1+\frac{1}{2}(l^2-m^2)]V_{dd\delta} \\
E_{zx,x^2-y^2} & = & \frac{3}{2}nl(l^2-m^2)V_{dd\sigma} & +nl[1-2(l^2-m^2)]V_{dd\pi} & -nl[1-\frac{1}{2}(l^2-m^2)]V_{dd\delta} \\
E_{xy,3z^2-r^2} & = & \sqrt{3}lm[n^2-\frac{1}{2}(l^2+m^2)]V_{dd\sigma} & -2\sqrt{3}lmn^2V_{dd\pi} & \frac{\sqrt{3}}{2}lm(1+n^2)V_{dd\delta} \\
E_{yz,3z^2-r^2} & = & \sqrt{3}mn[n^2-\frac{1}{2}(l^2+m^2)]V_{dd\sigma} & +\sqrt{3}mn(l^2+m^2-n^2)V_{dd\pi} & -\frac{\sqrt{3}}{2}mn(l^2+m^2)V_{dd\delta} \\
E_{zx,3z^2-r^2} & = & \sqrt{3}ln[n^2-\frac{1}{2}(l^2+m^2)]V_{dd\sigma} & +\sqrt{3}ln(l^2+m^2-n^2)V_{dd\pi} & -\frac{\sqrt{3}}{2}ln(l^2+m^2)V_{dd\delta} \\
E_{x^2-y^2,x^2-y^2} & = & \frac{3}{4}(l^2-m^2)^2V_{dd\sigma} & +[l^2+m^2-(l^2-m^2)^2]V_{dd\pi} & +[n^2+\frac{1}{4}(l^2-m^2)^2]V_{dd\delta} \\
E_{x^2-y^2,3z^2-r^2} & = & \frac{\sqrt{3}}{2}(l^2-m^2)[n^2-\frac{1}{2}(l^2+m^2)]V_{dd\sigma} & +\sqrt{3}n^2(m^2-l^2)V_{dd\pi} & +\frac{1}{4}\sqrt{3}(1+n^2)(l^2-m^2)V_{dd\delta} \\
E_{3z^2-r^2,3z^2-r^2} & = & [n^2-\frac{1}{2}(l^2+m^2)]^2V_{dd\sigma} & +3n^2(l^2+m^2)V_{dd\pi} & \frac{3}{4}(l^2+m^2)^2V_{dd\delta}
\end{array}
$$

References

[1] E. Pavarini, E. Koch, A. Lichtenstein, D. Vollhardt (eds.)
The LDA+DMFT approach to strongly correlated materials,
Reihe Modeling and Simulation, Vol. 1 (Forschungszentrum Jülich, 2011)
`http://www.cond-mat.de/events/correl11`

[2] E. Pavarini, S. Biermann, A. Poteryaev, A.I. Lichtenstein, A. Georges, O.K. Andersen, Phys. Rev. Lett. **92**, 176403 (2004)
E. Pavarini A. Yamasaki, J. Nuss and O.K. Andersen, New J. Phys. **7**, 188 (2005)

[3] J. Kunes: *Wannier functions and construction of model Hamiltonians*, in [1]

[4] E. Pavarini: *The LDA+DMFT Approach*, in [1]

[5] M.S. Dresselhaus, G. Dresselhaus, A. Jorio:
Group Theory: Application to the Physics of Condensed Matter
(Springer, Berlin Heidelberg, 2008)

[6] M. Tinkham: *Group Theory and Quantum Mechanics* (McGraw-Hill, 1964)

[7] E. Pavarini, E. Koch, and A.I. Lichtenstein, Phys. Rev. Lett. **101**, 266405 (2008)

[8] J. Kanamori, J. Appl. Phys. **31**, S14 (1960)

[9] E. Pavarini and E. Koch, Phys. Rev. Lett. **104**, 086402 (2010)
A. Flesch, G. Zhang, E. Koch, and E. Pavarini, Phys. Rev. B **85**, 035124 (2012)

[10] W.A. Harrison: *Electronic Structure and The Properties of Solids* (Dover, 1989)

7 Exchange Mechanisms

Erik Koch
Computational Materials Science
German Research School for Simulation Sciences

Contents

E. Pavarini, E. Koch, F. Anders, and M. Jarrell
Correlated Electrons: From Models to Materials
Modeling and Simulation Vol. 2
Forschungszentrum Jülich, 2012, ISBN 978-3-89336-796-2
http://www.cond-mat.de/events/correl12

1 Introduction

One of the profound *Surprises in Theoretical Physics* [1] is that magnetism is an inherently quantum mechanical effect. Classically, magnetic moments originate from electric currents: A current density $\vec{j}(\vec{r})$ generates a magnetic moment

$$\vec{\mu} = \frac{1}{2}\int \vec{r}\times\vec{j}\,d^3r\,. \tag{1}$$

These moments interact via the dipole-dipole interaction. The magnetostatic interaction energy between two dipoles at a distance R, $\hat{R}$ being the unit-vector from the position of the first to that of the second dipole,

$$\Delta E = \frac{\mu_0}{4\pi}\,\frac{\vec{\mu}_1\cdot\vec{\mu}_2 - 3(\hat{R}\cdot\vec{\mu}_1)(\hat{R}\cdot\vec{\mu_2})}{R^3} = \frac{\vec{\mu}_1\cdot\vec{\mu}_2 - 3(\hat{R}\cdot\vec{\mu}_1)(\hat{R}\cdot\vec{\mu_2})}{4\pi\varepsilon_0 c^2\;R^3} \tag{2}$$

depends on their distance and relative orientation. This can, however, not be the origin of the magnetism found in actual materials: In a classical system charges cannot flow in thermodynamic equilibrium, the celebrated Bohr-van Leuween theorem, and hence there are no magnetic moments to begin with [2].
In quantum mechanics, however, non-vanishing charge currents in the ground state are not uncommon: An electron in state $\Psi(\vec{r})$ corresponds to a current density

$$\vec{j}(\vec{r}) = -\frac{e\hbar}{2im_e}\left(\overline{\Psi(\vec{r})}\nabla\Psi(\vec{r}) - \Psi(\vec{r})\nabla\overline{\Psi(\vec{r})}\right) \tag{3}$$

which, for complex wave function $\Psi(\vec{r})$, is usually non-vanishing. According to (1) it produces a magnetic moment proportional to the expectation value of the angular momentum

$$\vec{\mu}_L = -\frac{e\hbar}{2m_e}\,\langle\vec{L}\,\rangle = -\mu_B\,\langle\vec{L}\,\rangle\,. \tag{4}$$

The constant of proportionality is the Bohr magneton μ_B. In particular, an atomic orbital $|n,l,m\rangle$ has a magnetic moment proportional to the magnetic quantum number $\vec{\mu} = -\mu_B\,m\,\hat{z}$. Also the electron spin $\vec{S}$ carries a magnetic moment

$$\vec{\mu}_S = -g_e\mu_B\,\langle\vec{S}\,\rangle\,. \tag{5}$$

The constant of proportionality between spin and magnetic moment differs from that between orbital momentum and moment by the gyromagnetic ratio g_0. Dirac theory gives $g_e = 2$, which is changed to $g_e \approx 2.0023\ldots$ by QED corrections.
Atomic moments are thus of the order of μ_B. For two such moments at a distance of 1 Å the magnetostatic energy (2) is of the order of 0.05 meV, corresponding to a temperature of less than 1 K. Therefore, magnetic ordering which, e.g., in magnetite (Fe_3O_4), persists till about 860 K, must originate from an interaction other that the magnetostatic interaction of dipoles. Indeed, it is the interplay of electronic properties which are apparently unrelated to magnetism, the Pauli principle in combination with the Coulomb repulsion (Coulomb exchange) as well

as the hopping of electrons (kinetic exchange) that leads to an effective coupling between the magnetic moments in a solid.

The basic mechanisms of the exchange coupling are quite simple: Since many-body wave functions must change sign under the permutation of Fermions, electrons of the same spin cannot be at the same position. Electrons of like spin thus tend to avoid each other, i.e., the probability of finding them close to each other tends to be lower than for electrons of opposite spin (exchange hole). In that sense the Coulomb energy between two electrons depends on their relative spins. By this argument, aligning electron spins tends be energetically favorable. This *Coulomb exchange* is the basis of Hund's first rule. When more than one atom is involved, electrons can hop from one site to the neighbor. This kinetic term is, again, modified by the Pauli principle, as the hopping to an orbital on the neighboring atom will only be possible, if there is not already an electron of the same spin occupying that orbital and by the Coulomb repulsion among the electrons. This is the idea of *kinetic exchange*. When Coulomb exchange and kinetic terms work together we speak of *double exchange*. In that case the electron-hopping serves to mediate the spin-correlation created on an atom to its neighbors.

Exchange mechanisms are idealizations of characteristic situations found in real materials. As such they are merely approximations, but they afford a simplification of the complicated realistic description, which provides a good basis for thinking about the relevant effects in a real material. We will start by discussing the effect of Coulomb exchange matrix elements (Sec. 2). To keep things simple, we will discuss a two-orbital model and only mention atomic multiplets and Hund's rule, while the full Coulomb vertex is discussed in the lecture of R. Eder. Next we turn to exchange mechanisms involving also hopping (Sec. 3). We start by looking at the a simple two-site model with two electrons. Focussing on the limit of strong electronic correlations (Coulomb repulsion dominating electron hopping), we introduce the method of downfolding to derive an effective Hamiltonian in which an explicit coupling of the electron spins appears. While conceptually simple, this direct exchange mechanism is rarely found in real materials. There hopping between correlated orbitals is usually mediated by a weakly correlated orbital. This is the superexchange mechanism. The derivation is very similar to that of kinetic exchange. However, the number of states involved, makes explicit book-keeping tedious. To simplify our work, we introduce second quantization as a simple notation of many-electron states. This also enables us to easily discuss double exchange, which combines direct exchange on an atom with coupling to the neighbors via electron hopping. Examples are the superexchange between transition metal atoms bridged by an oxygen at a right angle, which arises from the Coulomb exchange on the oxygen, as well as the exchange in mixed-valence compounds (Sec. 4). The competition between kinetic and double exchange is described by the Goodenough-Kanamori rules. Finally we show that exchange is not restricted to coupling spins, but can also produce interactions between orbital occupations (Sec. 5).

How exchange gives rise to an effective coupling of momenta is most easily shown for single- or two-site models. To see how these results carry over to solids, we consider the case of direct exchange (Sec. 6). Starting from the Hubbard model we show how taking the limit of strong correlations leads to the t-J-model, which, for half-filling, simplifies to the Heisenberg model.

2 Coulomb exchange

The Coulomb repulsion between electrons,

$$H_U = \sum_{i<j} \frac{1}{|\vec{r}_i - \vec{r}_j|}\,, \tag{6}$$

is manifestly spin-independent. Nevertheless, because of the antisymmetry of the many-electron wave function, the eigenenergies of H_U depend on the spin. This is the basis of the multiplet structure in atoms and of Hund's first two rules.

To understand the mechanism of this Coulomb exchange we consider a simple two-electron model. In the spirit of tight-binding (see the lecture of E. Pavarini), we assume that we have solved the two-electron Hamiltonian H_0, replacing the interaction term H_U, e.g. as a self-consistent potential $\sum_i U(\vec{r}_i)$, obtaining an orthonormal set of one-electron eigenstates $\varphi_\alpha(\vec{r})$ with eigenvalues ε_α. We now ask for the effect of re-introducing the interaction $H_U - \sum_i U(\vec{r}_i)$. The largest effect we will find for states that are degenerate.

Let us consider two orbitals $\alpha = a,\, b$. Then the two-electron Slater determinants with spins σ and σ'

$$\begin{aligned} \Psi_{a,\sigma;\,b\sigma'}(\vec{r}_1, s_1;\, \vec{r}_2, s_2) &= \frac{1}{\sqrt{2}} \begin{vmatrix} \varphi_a(\vec{r}_1)\,\sigma(s_1) & \varphi_a(\vec{r}_2)\,\sigma(s_2) \\ \varphi_b(\vec{r}_1)\,\sigma'(s_1) & \varphi_b(\vec{r}_2)\,\sigma'(s_2) \end{vmatrix} \\ &= \frac{1}{\sqrt{2}} \Big(\varphi_a(\vec{r}_1)\,\varphi_a(\vec{r}_2)\;\sigma(s_1)\,\sigma'(s_2) - \varphi_b(\vec{r}_1)\,\varphi_a(\vec{r}_2)\;\sigma'(s_1)\,\sigma(s_2) \Big) \end{aligned} \tag{7}$$

are degenerate eigenstates of H_0 with eigenvalue $\varepsilon_a + \varepsilon_b$, independent of the spin orientations. To see how this degeneracy is lifted, we calculate the matrix elements of H_U in the basis of the Slater determinants $\Psi_{a,\sigma;\,b\sigma'}$.

When both electrons have the same spin ($\sigma = \sigma'$), we can factor out the spin functions

$$\Psi_{a,\sigma;\,b\sigma} = \frac{1}{\sqrt{2}} \Big(\varphi_a(\vec{r}_1)\varphi_b(\vec{r}_2) - \varphi_b(\vec{r}_1)\varphi_a(\vec{r}_2) \Big)\; \sigma(s_1)\sigma(s_2) \tag{8}$$

and obtain

$$\left\langle \Psi_{a,\sigma;\,b,\sigma} \left| \frac{1}{|\vec{r}_1 - \vec{r}_2|} \right| \Psi_{a,\sigma;\,b,\sigma} \right\rangle = \frac{1}{2}\,(U_{ab} - J_{ab} - J_{ba} + U_{ba}) = U_{ab} - J_{ab} \tag{9}$$

where the direct terms are the Coulomb integral

$$U_{ab} = \int d^3r_1 \int d^3r_2\, \frac{|\varphi_a(\vec{r}_1)|^2\;|\varphi_b(\vec{r}_1)|^2}{|\vec{r}_1 - \vec{r}_2|} \tag{10}$$

while the cross terms give the exchange integral

$$J_{ab} = \int d^3r_1 \int d^3r_2\, \frac{\overline{\varphi_a(\vec{r}_1)}\,\varphi_b(\vec{r}_1)\;\overline{\varphi_b(\vec{r}_2)}\,\varphi_a(\vec{r}_2)}{|\vec{r}_1 - \vec{r}_2|}\,. \tag{11}$$

For the states where the electrons have opposite spin ($\sigma' = -\sigma$)

$$\left\langle \Psi_{a,\sigma;\,b,-\sigma} \left| \frac{1}{|\vec{r}_1 - \vec{r}_2|} \right| \Psi_{a,\sigma;\,b,-\sigma} \right\rangle = U_{ab} \tag{12}$$

the diagonal matrix element has no exchange contribution, as the overlap of the spin functions for the cross terms vanish. There are however off-diagonal matrix elements

$$\left\langle \Psi_{a\uparrow;\,b\downarrow} \left| \frac{1}{|\vec{r}_1 - \vec{r}_2|} \right| \Psi_{a\downarrow;\,b\uparrow} \right\rangle = -J_{ab} \ . \tag{13}$$

Since H_U does not change the spins, these are the only non-zero matrix elements. In the basis of the states $\Psi_{\uparrow\uparrow}$, $\Psi_{\uparrow\downarrow}$, $\Psi_{\downarrow\uparrow}$ and $\Psi_{\downarrow\downarrow}$ the Coulomb term is thus given by

$$H_U = \begin{pmatrix} U_{ab} - J_{ab} & 0 & 0 & 0 \\ 0 & U_{ab} & -J_{ab} & 0 \\ 0 & -J_{ab} & U_{ab} & 0 \\ 0 & 0 & 0 & U_{ab} - J_{ab} \end{pmatrix} . \tag{14}$$

The triplet states $\Psi_{\uparrow\uparrow}$ and $\Psi_{\downarrow\downarrow}$ are obviously eigenstates of H_U with eigenenergy

$$\Delta\varepsilon_{\text{triplet}} = U_{ab} - J_{ab} \ . \tag{15}$$

Diagonalizing the 2×2 submatrix, we obtain the third triplet state $(\Psi_{\uparrow\downarrow} + \Psi_{\downarrow\uparrow})/\sqrt{2}$ and the singlet state $(\Psi_{\uparrow\downarrow} - \Psi_{\downarrow\uparrow})/\sqrt{2}$

$$\frac{1}{\sqrt{2}}\left(\Psi_{\uparrow\downarrow} - \Psi_{\downarrow\uparrow}\right) = \frac{1}{\sqrt{2}}\Big(\varphi_a(\vec{r}_1)\varphi_b(\vec{r}_2) + \varphi_b(\vec{r}_1)\varphi_a(\vec{r}_2)\Big)\ \frac{1}{\sqrt{2}}\Big(|\downarrow\uparrow\rangle - |\uparrow\downarrow\rangle\Big) \tag{16}$$

with energy

$$\Delta\varepsilon_{\text{singlet}} = U_{ab} + J_{ab} \ . \tag{17}$$

To see whether the triplet or the singlet is lower in energy, we need to know the sign of the exchange matrix element. While the Coulomb integral U_{ab}, having a positive integrand, is obviously positive, it is less obvious that also $J_{ab} > 0$. Introducing $\Phi(\vec{r}) = \overline{\varphi_a(\vec{r})}\varphi_b(\vec{r})$ and rewriting the integral using the convolution theorem as well as the Fourier transform of $1/r$, we obtain [3, 4]:

$$\begin{aligned} J_{ab} &= \int d^3r_1\, \overline{\Phi(\vec{r}_1)} \underbrace{\int d^3r_2\, \frac{1}{|\vec{r}_1 - \vec{r}_2|}\, \Phi(\vec{r}_2)}_{=\int dk\, e^{ikr_1} 4\pi/k^2 \Phi(k)\,/(2\pi)^3} && (18) \\ &= \frac{1}{(2\pi)^3} \int d^3k \underbrace{\int d^3r_1\ e^{i\vec{k}\cdot\vec{r}_1} \overline{\Phi(\vec{r}_1)}}_{=\overline{\Phi(-k)}}\, \Phi(\vec{k}\,)\, \frac{4\pi}{k^2} && (19) \\ &= \frac{1}{(2\pi)^3} \int d^3k\ |\Phi(\vec{k}\,)|^2\, \frac{4\pi}{k^2} > 0 && (20) \end{aligned}$$

Thus the triplet states are below the singlet state by an energy $2J_{ab}$. If the φ_α are degenerate atomic orbitals, this is an example of Hund's first rule: For an atomic shell, the lowest state will have maximum spin.

Since H_U only contains interactions within the system of electrons, it commutes with the total orbital momentum $[H_U, \vec{L}_{\text{tot}}] = 0$. Obviously it also commutes with the total spin $\vec{S}_{\text{tot}}$. The

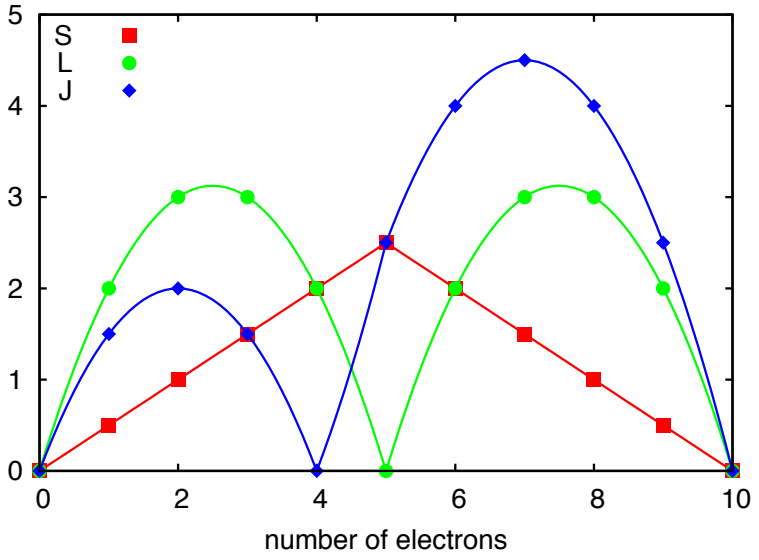

Fig. 1: *Angular momenta of the Hund's rules ground state* $^{2S+1}L_J$ *for* d*-shells.*

eigenstates of $H_0 + H_U$ can thus be classified by their quantum numbers L and S. These terms are written as ^{2S+1}L. For p- and d-shells they are listed in table 1. Hund's rules give the multiplet term with the lowest energy: For a given shell, this lowest state has the largest possible spin (Hund's first rule). If there are several terms of maximum multiplicity, the one with lowest energy has the largest total orbital momentum (Hund's second rule). There is a third Hund's rule, which, however, is not related with the electron-electron repulsion but with spin-orbit coupling: Within L-S coupling H_{SO} splits the atomic orbitals into eigenstates of the total angular momentum $\vec{J} = \vec{L}_{\text{tot}} + \vec{S}_{\text{tot}}$. The multiplets ^{2S+1}L thus split into $^{2S+1}L_J$. The term with the lowest energy is the one with smallest J if the shell is less than half-filled and largest J if it is more than half-filled (Hund's third rule). These rules are illustrated for d-shells in Fig. 2. A more detailed discussion of multiplet effects and the Coulomb interaction in atomic-like systems is given in the lecture of R. Eder and in [5, 6]

s		$^2\mathbf{S}$				
p^1 or p^5		$^2\mathbf{P}$				
p^2 or p^4	^1S ^1D		$^3\mathbf{P}$			
p^3		^2P ^2D		$^4\mathbf{S}$		
d^1 or d^9		$^2\mathbf{D}$				
d^2 or d^8	^1S ^1D ^1G		^3P $^3\mathbf{F}$			
d^3 or d^7		^2P $\overset{2\times}{^2D}$ ^2F ^2G ^2H		^4P $^4\mathbf{F}$		
d^4 or d^6	$\overset{2\times}{^1S}$ $\overset{2\times}{^1D}$ ^1F $\overset{2\times}{^1G}$ ^1I		$\overset{2\times}{^3P}$ ^3D $\overset{2\times}{^3F}$ ^3G ^3H		$^5\mathbf{D}$	
d^5		^2S ^2P $\overset{3\times}{^2D}$ $\overset{2\times}{^2F}$ $\overset{2\times}{^2G}$ ^2H ^2I		^4P ^4D ^4F ^4G		$^6\mathbf{S}$

Table 1: *Atomic multiplets for open* s*-,* p*-, and* d*-shells. For terms that appear multiple times the number of distinct terms is indicated. The Hund's rules ground state is indicated in bold.*

3 Kinetic exchange

When electron-hopping plays the main role in the exchange mechanism, we speak of kinetic exchange. In contrast to Coulomb exchange the resulting interactions are usually antiferromagnetic, i.e., they prefer antiparallel spins. The physical principle of kinetic exchange can be understood in a simple two-site system. We discuss this problem in some detail and introduce two key concept along the way: downfolding and second quantization. More realistic exchange mechanisms are then natural generalizations of this simple mechanism [7–9].

3.1 A toy model

As a toy model, we consider the minimal model of an H_2 molecule. We restrict ourselves to two (orthogonal) orbitals, φ_1 and φ_2, separated by some distance. If we add an electron to the system, that electron will be able to move between the two orbitals, with a matrix element $-t$. Because we allow the electron to only occupy two s-orbitals, the Hamiltonian is a 2×2 matrix

$$H = \begin{pmatrix} 0 & -t \\ -t & 0 \end{pmatrix} . \tag{21}$$

This tight-binding Hamiltonian is easily diagonalized giving the linear combinations

$$\varphi_\pm = \frac{1}{\sqrt{2}} \Big(\varphi_1 \pm \varphi_2 \Big) \tag{22}$$

as eigenstates with eigenenergies $\varepsilon_\pm = \mp t$. We have written the hopping matrix element as $-t$, so that for $t > 0$ the state without a node, φ_+, is the ground state.
Pictorially we can write the basis states by specifying which orbital the electron occupies. For a spin-up electron we then write

$$\varphi_1 = |\uparrow , \cdot \rangle \qquad \text{and} \qquad \varphi_2 = | \cdot , \uparrow \rangle \tag{23}$$

where we now represent the basis states by where the electron is located.
If there are two electrons in the system, i.e., one electron per orbital, we can again use basis states which just specify, which orbitals the electrons occupy. For two electrons of opposite spin we then find two states where the electrons are in different orbitals

$$|\uparrow , \downarrow \rangle \qquad |\downarrow , \uparrow \rangle \qquad \text{“covalent states”}$$

and two states where the electrons are in the same orbital

$$|\updownarrow , \cdot \rangle \qquad | \cdot , \updownarrow \rangle \qquad \text{“ionic states”.}$$

In this basis the Hamiltonian matrix for our simple model of the H_2 molecule has the form

$$H = \begin{pmatrix} 0 & 0 & -t & -t \\ 0 & 0 & +t & +t \\ -t & +t & U & 0 \\ -t & +t & 0 & U \end{pmatrix} \qquad \begin{matrix} |\uparrow , \downarrow \rangle \\ |\downarrow , \uparrow \rangle \\ |\updownarrow , \cdot \rangle \\ | \cdot , \updownarrow \rangle \end{matrix} \tag{24}$$

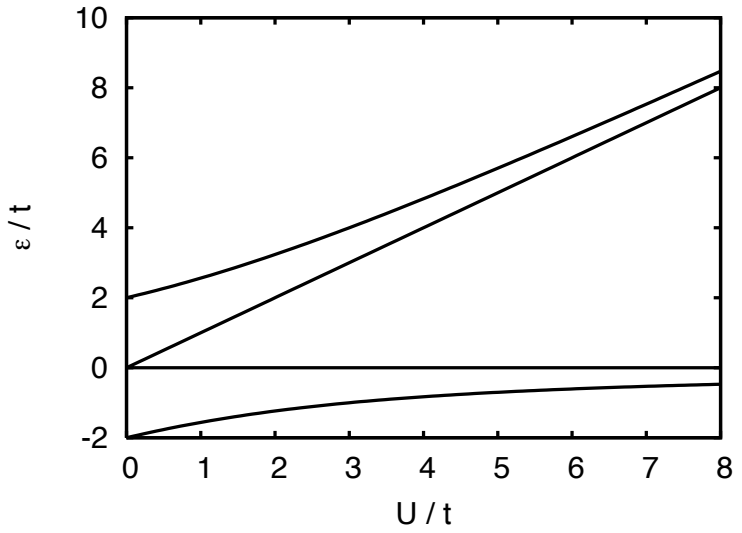

Fig. 2: *Spectrum of the two-site Hubbard model as a function of U. For large U there are two levels with energy close to zero. Their energy difference corresponds to the exchange energy. The remaining two states with ionic character have an energy roughly proportional to U.*

As before, moving an electron to a neighboring orbital gives a matrix element $-t$, with an additional sign when the order of the electrons is changed (Fermi statistics!). For the ionic states, where both electrons are in the same orbital, we have the Coulomb matrix element U. Coulomb matrix elements involving electrons on different sites are, for reasonably large distance between the sites, negligible. So there is no Coulomb exchange, just the local Coulomb repulsion in our model. Diagonalizing H we find the energy spectrum and the corresponding eigenstates:

$$\varepsilon_\pm = \frac{U}{2} \pm \frac{\sqrt{U^2+16\,t^2}}{2} \quad , \quad \Psi_\pm = \frac{\Big(|{\uparrow}\,,{\downarrow}\rangle - |{\downarrow}\,,{\uparrow}\rangle - \frac{\varepsilon_\pm}{2t}\big[\,|{\uparrow\downarrow}\,,\,\cdot\,\rangle + |\,\cdot\,,{\uparrow\downarrow}\rangle\,\big]\Big)}{\sqrt{2+\varepsilon_\pm^2/(2t^2)}}$$

$$\varepsilon_{\rm cov} = 0 \quad , \quad \Psi_{\rm cov} = \frac{1}{\sqrt{2}}\Big(|{\uparrow}\,,{\downarrow}\rangle + |{\downarrow}\,,{\uparrow}\rangle\Big)$$

$$\varepsilon_{\rm ion} = U \quad , \quad \Psi_{\rm ion} = \frac{1}{\sqrt{2}}\Big(|{\uparrow\downarrow}\,,\,\cdot\,\rangle - |\,\cdot\,,{\uparrow\downarrow}\rangle\Big)$$

The eigenenergies as a function of U are shown in figure 2.

3.2 Direct exchange

Again, we have found that the energy of two-electron states depends on the relative spin of the electrons. To understand this more clearly we analyze the limit when U is much larger than t. From Fig. 2 we see that there are two states with energies that increase with U. They are the states $\Psi_{\rm ion}$ and Ψ_+ that have considerable contributions of the ionic states. Then there are two states whose energy is close to zero. They are the states that have mainly covalent character. To find the energy and the character of these levels in the limit $U \to \infty$ we can just expand $\varepsilon_- \to -4t^2/U$ and $\varepsilon_+ \to U + 4t^2/U$. We thus see that while the purely covalent state, the spin-triplet state $\Psi_{\rm cov}$, is independent of U, Ψ_- has a slightly lower energy due to some small

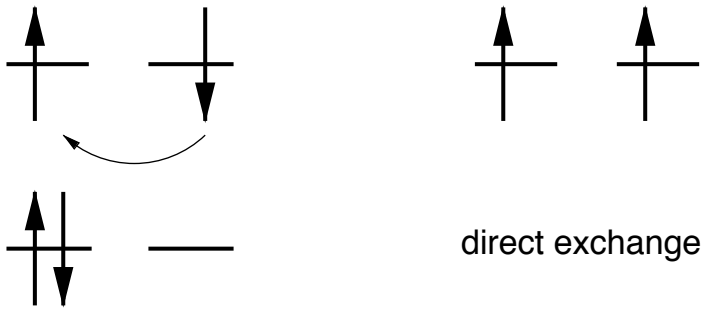

Fig. 3: *Simple picture of direct exchange: The antiparallel alignment of the spins (left) is favored, since it allows the electrons to hop to the neighboring site. For parallel spins (right) hopping is suppressed by the Pauli principle.*

admixture of the ionic states. In the limit $U \to \infty$ it becomes the maximally entangled state $(|\uparrow,\downarrow\rangle - |\downarrow,\uparrow\rangle)/\sqrt{2}$. We see that for large U, Ψ_- cannot be expressed, even approximately, as a Slater determinant, see also Sec. 3.4. This is the reason why strongly correlated systems are so difficult to describe.

A more instructive method to analyze the large-U limit, which can readily be generalized to more complex situations, where we can no longer diagonalize the full Hamiltonian, is the downfolding technique. The mathematical background is explained in the appendix. The idea of downfolding is to partition the Hilbert space into parts that are of interest, here the low-energy convalent type states, and states that should be projected out, here the high-energy ionic states. With this partitioning we can view the Hamitonian matrix (24) as built of 2×2 submatrices. Calculating the inverse on the space of covalent states (see Eqn. (84) in the appendix) we find an *effective Hamiltonian* which now operates on the covalent states only:

$$H_{\text{eff}}(\varepsilon) = \begin{pmatrix} -t & -t \\ +t & +t \end{pmatrix} \begin{pmatrix} \varepsilon - U & 0 \\ 0 & \varepsilon - U \end{pmatrix}^{-1} \begin{pmatrix} -t & +t \\ -t & +t \end{pmatrix} \approx -\frac{2t^2}{U} \begin{pmatrix} 1 & -1 \\ -1 & 1 \end{pmatrix}. \qquad (25)$$

In the last step we have made an approximation by setting ε to zero, which is roughly the energy of the states with covalent character.

The process of eliminating the ionic states thus gives rise to an effective interaction between the covalent states, which was not present in the original Hamiltonian (24). Diagonalizing the effective Hamiltonian, we find

$$\varepsilon_s = -\frac{4t^2}{U} \quad , \qquad \Psi_s = \frac{1}{\sqrt{2}}\Big(|\uparrow,\downarrow\rangle - |\downarrow,\uparrow\rangle\Big)$$
$$\varepsilon_t = 0 \qquad , \qquad \Psi_t = \frac{1}{\sqrt{2}}\Big(|\uparrow,\downarrow\rangle + |\downarrow,\uparrow\rangle\Big)$$

These states correspond to the singlet and triplet states in the hydrogen molecule. Here the singlet-triplett splitting is $J = -4t^2/U$. The other states in the triplet are those with two electrons of parallel spin: $|\uparrow,\uparrow\rangle$ and $|\downarrow,\downarrow\rangle$. They, of course, also have energy zero, as hopping is impossible due to the Pauli principle.

To understand the nature of the effective interaction in the low-energy Hamiltonian we observe that the off-diagonal matrix elements in (25) correspond to flipping the spin of both electrons ("exchange"). Remembering that

$$\vec{S}_1 \cdot \vec{S}_2 = S_1^z S_2^z + \frac{1}{2}\Big(S_1^+ S_2^- + S_1^- S_2^+ \Big) \tag{26}$$

we see that the effective interaction will contain a spin-spin coupling term.

3.3 Second quantization for pedestrians

A more systematic way for obtaining the form of the effective interaction is by using second quantization, which will also help us simplify our notation. In second quantization we use operators to specify in which orbital an electron is located. As an example, $c^\dagger_{1,\uparrow}$ puts a spin-up electron in orbital φ_1. Denoting the system with no electrons by $|0\rangle$, the basis states that we have considered so far are written as

$$\begin{aligned} |\uparrow,\cdot\rangle &= c^\dagger_{1\uparrow}|0\rangle \\ |\cdot,\uparrow\rangle &= c^\dagger_{2\uparrow}|0\rangle \end{aligned}$$

for the single-electron states, and

$$\begin{aligned} |\uparrow,\downarrow\rangle &= c^\dagger_{2\downarrow}c^\dagger_{1\uparrow}|0\rangle \\ |\downarrow,\uparrow\rangle &= c^\dagger_{2\uparrow}c^\dagger_{1\downarrow}|0\rangle \\ |\updownarrow,\cdot\rangle &= c^\dagger_{1\downarrow}c^\dagger_{1\uparrow}|0\rangle \\ |\cdot,\updownarrow\rangle &= c^\dagger_{2\downarrow}c^\dagger_{2\uparrow}|0\rangle \end{aligned} \tag{27}$$

for the two-electron states. In order to describe the hopping of an electron from one orbital to another, we introduce operators that annihilate an electron. For example $c_{1\uparrow}$ removes a spin-up electron from orbital φ_1. The hopping of an up electron from φ_1 to φ_2 is thus described by the operator $c^\dagger_{2\uparrow}c_{1\uparrow}$ that first takes an electron out of orbital 1 and then creates one in orbital 2. The Hamiltonian for a spin-up electron hopping between two orbitals can thus be written as

$$H = -t\Big(c^\dagger_{1\uparrow}c_{2\uparrow} + c^\dagger_{2\uparrow}c_{1\uparrow} \Big) \,. \tag{28}$$

Calculating the matrix elements with the single-electron basis states, we recover the matrix (21). For the calculation we need to know that the operators that describe the electrons *anticommute*. This reflects the fact that a many-electron wave function changes sign when two electrons are exchanged. Using the notation $\{a,b\} = ab + ba$ we have

$$\Big\{ c_{i\sigma},\, c_{j\sigma'} \Big\} = 0 \qquad \Big\{ c^\dagger_{i\sigma},\, c^\dagger_{j\sigma'} \Big\} = 0 \qquad \Big\{ c_{i\sigma},\, c^\dagger_{j\sigma'} \Big\} = \delta_{i,j}\delta_{\sigma,\sigma'}$$

Moreover, trying to annihilate an electron in a state where there is no electron, results in zero: $c_{i\sigma}|0\rangle = 0$. Finally, as the notation implies, $c^\dagger_{i\sigma}$ is the adjoint of $c_{i\sigma}$ and $\langle 0|0\rangle = 1$.

To describe the Coulomb repulsion between two electrons in the same orbital we use that $n_{i\sigma} = c^\dagger_{i\sigma} c_{i\sigma}$ returns 0 when operating on a basis state with no spin-σ electron in orbital φ_i, and has eigenvalue 1 for a basis state with a spin-σ electron in orbital φ_i. It is thus called the occupation-number operator. The Coulomb repulsion in orbital φ_1 is then described by the operator $U n_{1\uparrow} n_{1\downarrow}$, which is non-zero only when there is a spin-up *and* a spin-down electron in φ_1. The Hamiltonian for our two-orbital model, where both up- and down-spin electrons can hop, and including the Coulomb repulsion for two electrons in the same orbital, is thus given by

$$\begin{aligned} H &= -t\left(c^\dagger_{1\uparrow}c_{2\uparrow} + c^\dagger_{2\uparrow}c_{1\uparrow} + c^\dagger_{1\downarrow}c_{2\downarrow} + c^\dagger_{2\downarrow}c_{1\downarrow}\right) + U\left(n_{1\uparrow}n_{1\downarrow} + n_{2\uparrow}n_{2\downarrow}\right) \\ &= -t\sum_{i,j,\sigma} c^\dagger_{j\sigma}c_{i\sigma} + U\sum_i n_{i\uparrow}n_{i\downarrow}\ . \end{aligned} \tag{29}$$

You should convince yourself that when you calculate the matrix elements for the two-electron states, you recover the matrix (24). The great advantage of writing the Hamiltonian in second-quantized form is that it is valid for any number of electrons, while the matrix form is restricted to a particular number of electrons.

Coming back to the effective Hamiltonian (25), we can rewrite H_{eff} in second quantized form:

$$\begin{aligned} H_{\text{eff}} &= -\frac{2t^2}{U}\left(c^\dagger_{2\uparrow}c^\dagger_{1\downarrow}c_{1\downarrow}c_{2\uparrow} - c^\dagger_{2\downarrow}c^\dagger_{1\uparrow}c_{1\downarrow}c_{2\uparrow} - c^\dagger_{2\uparrow}c^\dagger_{1\downarrow}c_{1\uparrow}c_{2\downarrow} + c^\dagger_{2\downarrow}c^\dagger_{1\uparrow}c_{1\uparrow}c_{2\downarrow}\right) \\ &= -\frac{2t^2}{U}\left(c^\dagger_{1\downarrow}c_{1\downarrow}c^\dagger_{2\uparrow}c_{2\uparrow} - c^\dagger_{1\uparrow}c_{1\downarrow}c^\dagger_{2\downarrow}c_{2\uparrow} - c^\dagger_{1\downarrow}c_{1\uparrow}c^\dagger_{2\uparrow}c_{2\downarrow} + c^\dagger_{1\uparrow}c_{1\uparrow}c^\dagger_{2\downarrow}c_{2\downarrow}\right) \end{aligned} \tag{30}$$

Looking at equation (89) in the appendix we see that the spin operators are given in second quantization by

$$S^x_i = \frac{1}{2}\left(c^\dagger_{i\uparrow}c_{i\downarrow} + c^\dagger_{i\downarrow}c_{i\uparrow}\right) \qquad S^y_i = -\frac{i}{2}\left(c^\dagger_{i\uparrow}c_{i\downarrow} - c^\dagger_{i\downarrow}c_{i\uparrow}\right) \qquad S^z_i = \frac{1}{2}\left(n_{i\uparrow} - n_{i\downarrow}\right). \tag{31}$$

From this we find (after some calculation) that the effective Hamiltonian can be written in terms of the spin operators

$$H_{\text{eff}} = \frac{4t^2}{U}\left(\vec{S}_1 \cdot \vec{S}_2 - \frac{n_1\, n_2}{4}\right). \tag{32}$$

To conclude, we again find that the completely spin-independent Hamiltonian (29), in the limit of large U, gives rise to a spin-spin interaction. Since the exchange coupling $J = 4t^2/U$ is positive, states with antiparallel spins have lower energy. Thus direct exchange leads to *antiferromagnetism*.

It is important to realize that the singlet-triplet splitting for the effective Hamiltonian really arises from the admixture of ionic states into the singlet. By downfolding we eliminate the high-energy ionic states, i.e., charge fluctuations, from our Hilbert space. The eliminated states then give rise to an effective spin-spin interaction on the new reduced low-energy Hilbert space. We must therefore keep in mind that, when working with the effective Hamiltonian (32), we are considering slightly different states than when working with the original Hamiltonian (29).

3.4 Mean-field treatment

To conclude our discussion of the simplest kinetic exchange mechanism, it is instructive to consider the results of a mean-field treatment. For the two-electron Hamiltonian (24) it is straightforward to find the Hartree-Fock solution by directly minimizing the energy expectation value for a two-electron Slater determinant. The most general ansatz is a Slater determinant constructed from an orbital $\varphi(\theta_\uparrow) = \sin(\theta_\uparrow)\,\varphi_1 + \cos(\theta_\uparrow)\,\varphi_2$ for the spin-up, and $\varphi(\theta_\downarrow) = \sin(\theta_\downarrow)\,\varphi_1 + \cos(\theta_\downarrow)\,\varphi_2$ for the spin-down electron:

$$|\Psi(\theta_\uparrow,\theta_\downarrow)\rangle = \left(\sin(\theta_\downarrow)\,c^\dagger_{1\downarrow} + \cos(\theta_\downarrow)\,c^\dagger_{2\downarrow}\right)\,\left(\sin(\theta_\uparrow)\,c^\dagger_{1\uparrow} + \cos(\theta_\uparrow)\,c^\dagger_{2\uparrow}\right)\,|0\rangle\ . \tag{33}$$

Translating the second quantized states via (27) into the basis used for writing the Hamiltonian matrix (24), we find the expectation value

$$\begin{aligned}\langle\Psi(\theta_\uparrow,\theta_\downarrow)|H|\Psi(\theta_\uparrow,\theta_\downarrow)\rangle \;=\;& -2t\,(\sin\theta_\uparrow\sin\theta_\downarrow + \cos\theta_\uparrow\cos\theta_\downarrow)\,(\cos\theta_\uparrow\sin\theta_\downarrow + \sin\theta_\uparrow\cos\theta_\downarrow)\\ & +U\left(\sin^2\theta_\uparrow\sin^2\theta_\downarrow + \cos^2\theta_\uparrow\cos^2\theta_\downarrow\right)\ .\end{aligned} \tag{34}$$

If the Slater determinant respects the symmetry of the molecule under the exchange of sites (mirror symmetry of the H_2 molecule), it follows that the Hartree-Fock orbitals for both spins are the bonding state φ_+ ($\theta = \pi/4$). This is the *restricted Hartree-Fock* solution. The corresponding energy is $E(\pi/4,\pi/4) = -2t + U/2$. The excited states are obtained by replacing occupied orbitals φ_+ with φ_-. Alltogether we obtain the restricted Hartree-Fock spectrum

$$\begin{aligned} E(\ \ \pi/4,\ \ \pi/4) &= -2t + U/2\\ E(\ \ \pi/4,-\pi/4) &= \qquad U/2\\ E(-\pi/4,\ \ \pi/4) &= \qquad U/2\\ E(-\pi/4,-\pi/4) &= \ \ 2t + U/2 \end{aligned} \tag{35}$$

Comparing to the energy for a state with both electrons of the same spin ($E = 0$), we see that there is no spin-triplet, i.e., Hartree-Fock breaks the spin symmetry. The states (35) are *spin-contaminated* [10]. Even worse, the Hartree-Fock ground state, and consequently all the states, are independent of U. The weight of the ionic states is always $1/2$, leading to an increase of the energy with $U/2$.

To avoid this, we can allow the Hartree-Fock solution to break the symmetry of the molecule (*unrestricted Hartree-Fock*), putting, e.g., more of the up-spin electron in the orbital on site 1 and more of the down-spin electron in orbital 2. For $U < 2t$ this does not lead to a state of lower energy. For larger U there is a symmetry-broken ground state

$$\Psi_{UHF} = \Psi(\theta,\pi/2-\theta)\ \text{ with }\quad \theta(U) = \frac{\pi}{4} \pm \frac{1}{2}\arccos\left(\frac{2t}{U}\right)\ . \tag{36}$$

Its energy is $E_{UHF} = -2t^2/U$. This looks similar to the singlet energy ε_s, however, with a different prefactor. Still there is no triplet state (spin contamination) and, for $U \to \infty$, the overlap with the true singlet ground state goes to $|\langle\Psi_{UHF}|\Psi_-\rangle|^2 = 1/2$. In an extended system the breaking of the symmetry implies long-range order.

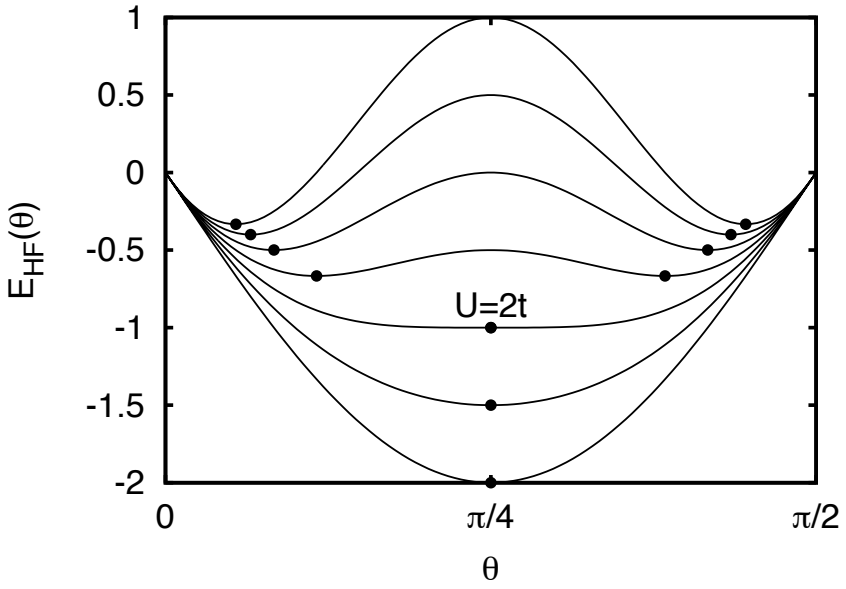

Fig. 4: *Energy expectation value for a Slater determinant $\Psi(\theta, \pi/2-\theta)$ for $U=0,\ t,\ 2t,\ \ldots,\ 6t$. When $U \leq 2t$ the minimum is at $\theta = \pi/4$. This is the Hartree-Fock solution with the bonding orbitals φ_+ occupied. For $U \geq 2t$, $\theta = \pi/4$ is still an extremal point (restricted Hartree-Fock solution), but an energy minimum is only attained when the symmetry is broken (unrestricted Hartree-Fock solution).*

3.5 Superexchange

For the direct exchange mechanism discussed above, it is crucial that there is hopping between the orbitals. These orbitals are typically localized d-orbitals of transition-metals. However, direct exchange cannot explain the antiferromagnetism of most transition-metal compounds: Since the d-orbitals are so localized, hopping can only occur between orbitals on different atoms that are very close to each other. But most antiferromagnetic insulators are transition-metal *oxides*, so that the transition-metal cations are separated by large oxygen anions. In such a situation, shown in figure 5, direct hopping between the d-orbitals is very unlikely. The concept of direct exchange can, however, be extended to these cases by taking into account hopping via the intermediate p-orbital. This mechanism is called superexchange.

To understand superexchange, we consider two d-orbitals with an oxygen p-orbital in between. We introduce the operator $c^\dagger_{i\sigma}$, which creates a spin-σ electron in the d-orbital at site i, where $i = 1$ denotes the d-orbital on the left and $i = 2$ the one on the right (see figure 5). Likewise $c^\dagger_{p\sigma}$ creates an electron in the p-orbital. The energy of an electron in a d- or p-orbital is ε_d and ε_p, respectively. The Coulomb repulsion between two electrons in a d-orbital is U_d, while we neglect the repulsion between electrons in the p-orbital. Finally, $-t_{pd}$ is the hopping between p and d orbitals. The Hamiltonian for the system of figure 5 is then given by

$$H = \sum_\sigma \left(\varepsilon_d \sum_i n_{i\sigma} + \varepsilon_p \, n_{p\sigma} - t_{pd} \sum_i \left(c^\dagger_{i\sigma} c_{p\sigma} + c^\dagger_{p\sigma} c_{i\sigma} \right) \right) + U_d \sum_i n_{i\uparrow} n_{i\downarrow} \, . \qquad (37)$$

In the absence of hopping, the ground state will have singly occupied d-orbitals, corresponding

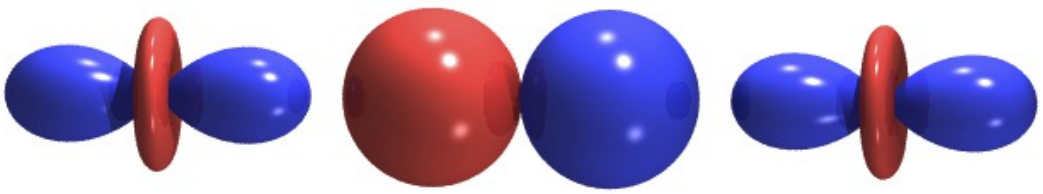

Fig. 5: *In superexchange an oxygen p-orbital mediates the exchange interaction between two transition-metal d-orbitals.*

to a positively charged transition-metal ion, and a doubly occupied p-orbital, corresponding to an O^{2-} ion. To study a possible coupling between the spins on the d-orbitals, we first look at the case where both d-spins point upwards (see the far right of Fig. 6). The Hamiltonian matrix in the corresponding Hilbert space is then given by

$$H = \left(\begin{array}{c|cc} 0 & t_{pd} & t_{pd} \\ \hline t_{pd} & U_d + \Delta_{pd} & 0 \\ t_{pd} & 0 & U_d + \Delta_{pd} \end{array}\right) \begin{array}{l} c^\dagger_{2\uparrow} c^\dagger_{p\downarrow} c^\dagger_{p\uparrow} c^\dagger_{1\uparrow} |0\rangle \\ c^\dagger_{2\uparrow} c^\dagger_{p\uparrow} c^\dagger_{1\downarrow} c^\dagger_{1\uparrow} |0\rangle \\ c^\dagger_{2\downarrow} c^\dagger_{2\uparrow} c^\dagger_{p\uparrow} c^\dagger_{1\uparrow} |0\rangle \end{array} \tag{38}$$

where we have chosen $2(\varepsilon_p + \varepsilon_d)$ as the zero of our energy scale and defined $\Delta_{pd} = \varepsilon_d - \varepsilon_p$. The basis states of the Hilbert space are given on the right and the lines indicate the partitioning of the Hilbert space for downfolding. The effective Hamiltonian for parallel spins on d-orbitals is then

$$H_{\text{eff}} = (t_{pd}, t_{pd}) \begin{pmatrix} \varepsilon - (U_d + \Delta_{pd}) & 0 \\ 0 & \varepsilon - (U_d + \Delta_{pd}) \end{pmatrix} \begin{pmatrix} t_{pd} \\ t_{pd} \end{pmatrix} \approx -\frac{2t_{pd}^2}{U_d + \Delta_{pd}} \tag{39}$$

where in the last step we have set ε to zero.

For antiparallel spins the Hilbert space is nine-dimensional. We sort the basis states into groups that are connected by the hopping of one electron. Starting from the two states with singly occupied d-orbitals, the second group has one of the p-electrons transfered to a d-orbital, leading to one doubly occupied d, while the last group has a second electron hopped, leading to either an empty p- or an empty d-orbital. The corresponding Hamiltonian matrix is

$$\left(\begin{array}{cc|cccc|ccc} 0 & 0 & +t_{pd} & +t_{pd} & 0 & 0 & 0 & 0 & 0 \\ 0 & 0 & 0 & 0 & +t_{pd} & +t_{pd} & 0 & 0 & 0 \\ \hline +t_{pd} & 0 & U_d + \Delta_{pd} & 0 & 0 & 0 & -t_{pd} & 0 & -t_{pd} \\ +t_{pd} & 0 & 0 & U_d + \Delta_{pd} & 0 & 0 & 0 & -t_{pd} & -t_{pd} \\ 0 & +t_{pd} & 0 & 0 & U_d + \Delta_{pd} & 0 & +t_{pd} & 0 & +t_{pd} \\ 0 & +t_{pd} & 0 & 0 & 0 & U_d + \Delta_{pd} & 0 & +t_{pd} & +t_{pd} \\ \hline 0 & 0 & -t_{pd} & 0 & +t_{pd} & 0 & U_d & 0 & 0 \\ 0 & 0 & 0 & -t_{pd} & 0 & +t_{pd} & 0 & U_d & 0 \\ 0 & 0 & -t_{pd} & -t_{pd} & +t_{pd} & +t_{pd} & 0 & 0 & 2(U_d + \Delta_{pd}) \end{array}\right) \begin{array}{l} c^\dagger_{2\downarrow} c^\dagger_{p\downarrow} c^\dagger_{p\uparrow} c^\dagger_{1\uparrow} |0\rangle \\ c^\dagger_{2\uparrow} c^\dagger_{p\downarrow} c^\dagger_{p\uparrow} c^\dagger_{1\downarrow} |0\rangle \\ c^\dagger_{2\downarrow} c^\dagger_{p\uparrow} c^\dagger_{1\downarrow} c^\dagger_{1\uparrow} |0\rangle \\ c^\dagger_{2\downarrow} c^\dagger_{2\uparrow} c^\dagger_{p\downarrow} c^\dagger_{1\uparrow} |0\rangle \\ c^\dagger_{2\uparrow} c^\dagger_{p\downarrow} c^\dagger_{1\downarrow} c^\dagger_{1\uparrow} |0\rangle \\ c^\dagger_{2\downarrow} c^\dagger_{2\uparrow} c^\dagger_{p\uparrow} c^\dagger_{1\downarrow} |0\rangle \\ c^\dagger_{p\downarrow} c^\dagger_{p\uparrow} c^\dagger_{1\downarrow} c^\dagger_{1\uparrow} |0\rangle \\ c^\dagger_{2\downarrow} c^\dagger_{2\uparrow} c^\dagger_{p\downarrow} c^\dagger_{p\uparrow} |0\rangle \\ c^\dagger_{2\downarrow} c^\dagger_{2\uparrow} c^\dagger_{1\downarrow} c^\dagger_{1\uparrow} |0\rangle \end{array}$$

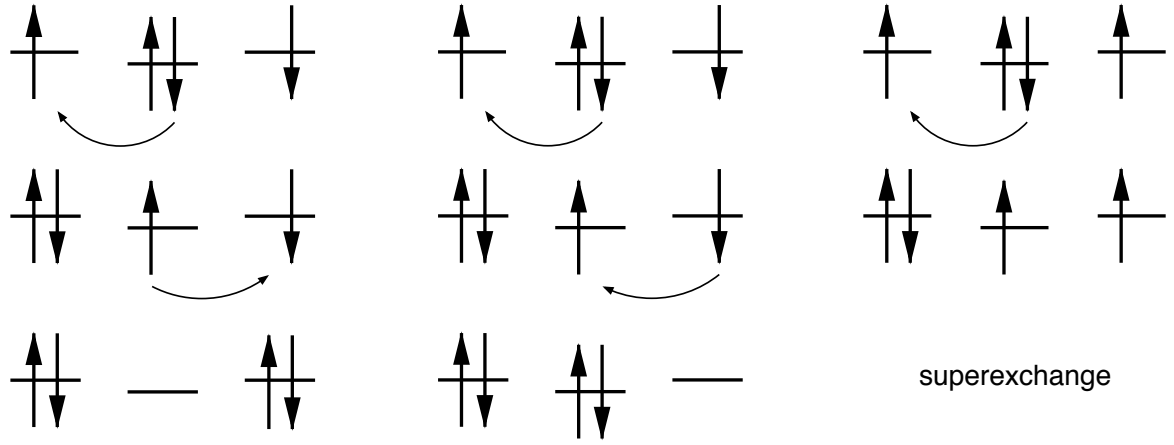

Fig. 6: *Simple picture of superexchange. Here the orbital on the central site is different from the orbitals on the sides. Typically, in the center there is a oxygen p-orbital coupling two d-orbitals. This situation is illustrated in Fig. 5. For antiparallel spins on the d-orbitals there are two ways that two consecutive hopping processes are possible. For parallel spins the Pauli principle suppresses the second hopping process.*

Downfolding the high energy states with at least one doubly occupied d-orbital, setting $\varepsilon = 0$ and expanding in $1/U_d$ (remembering $(A + \Delta)^{-1} \approx A^{-1}(1 - \Delta A^{-1})$), which is equivalent to second-order perturbation theory, leads to

$$\begin{aligned} H_{\text{eff}} &= H_{00} + T_{01}\left(\varepsilon - \left(H_{11} + T_{12}\left(\varepsilon - H_{22}\right)^{-1} T_{21}\right)\right)^{-1} T_{10} \\ &\approx H_{00} - T_{01}H_{11}^{-1}T_{10} - T_{01}H_{11}^{-1}T_{12}H_{22}^{-1}T_{21}H_{11}^{-1}T_{10} \qquad (40) \\ &= -\frac{2t_{pd}^2}{U_d + \Delta_{pd}}\begin{pmatrix} 1 & 0 \\ 0 & 1 \end{pmatrix} - \frac{2t_{pd}^4}{(U_d + \Delta_{pd})^2}\left(\frac{1}{U_d} + \frac{1}{U_d + \Delta_{pd}}\right)\begin{pmatrix} 1 & -1 \\ -1 & 1 \end{pmatrix}. \qquad (41) \end{aligned}$$

The first term is the same as for parallel spins (39). The additional term is of the same type as that found for the direct exchange mechanism. Again, it can be written in terms of spin operators. In the present case they are the spin operators for the d-orbitals, while the p-orbital does no longer appear in the spin Hamiltonian. The spin coupling is now given by

$$J = \frac{4t_{pd}^4}{(U_d + \Delta_{pd})^2}\left(\frac{1}{U_d} + \frac{1}{U_d + \Delta_{pd}}\right), \qquad (42)$$

which reflects that the superexchange mechanism involves four hopping processes (see Fig. 6), while direct exchange only involves two hoppings (see Fig. 3). The hopping process involving only a single doubly occupied d-orbital (middle of Fig. 6) is a generalization of the simple direct exchange with an effective hopping $t_{\text{eff}} = t_{pd}^2/(U_d + \Delta_{pd})$ between the d-orbitals and gives the first term, $4t_{\text{eff}}^2/U_d$, in (42), while the hopping process involving two occupied d-orbitals (left in Fig. 6) gives the second term $4t_{pd}^4/(U_d + \Delta_{pd})^3$.

3.6 Ferromagnetic superexchange

In the discussion of superexchange we have, so far, assumed that the oxygen ion lies between the two d-orbitals. This 180^o geometry is shown on the left of Fig. 7. The situation is quite different, when the oxygen forms a 90^o bridge between the two d-orbitals, see the right of Fig. 7. By symmetry, there is only hopping between the d- and the p-orbital that point towards each other (see, e.g., the discussion of the Slater-Koster integrals in the lecture of E. Pavarini). As there is also no hopping between the p-orbitals on the same site, the Hamiltonian for the system separates into two parts, one involving only the d orbital on site 1 and the p_x orbital and the other only involving d on site 2 and p_y, e.g.:

$$H_1 = \begin{pmatrix} 0 & +t_{pd} \\ +t_{pd} & U_d + \Delta_{pd} \end{pmatrix} \qquad \begin{matrix} c^\dagger_{x\downarrow} c^\dagger_{x\uparrow} c^\dagger_{1\downarrow} |0\rangle \\ c^\dagger_{x\downarrow} c^\dagger_{1\downarrow} c^\dagger_{1\uparrow} |0\rangle \end{matrix} \tag{43}$$

Since it is not possible for an electron on site 1 to reach site 2, none of the superexchange processes discussed above are operational. Nevertheless, the energy for the system depends on the relative orientation of the electron spins in the two d-orbitals. To see this, we have to remember that Coulomb exchange prefers a triplet for two electrons in different orbitals on the same site (Hund's first rule). Including J_{xy} on the oxygen (but neglecting U_p for simplicity), we get, for the triplet state with two up-electrons, the Hamiltonian

$$\left(\begin{array}{c|cc|c} 0 & t_{pd} & t_{pd} & 0 \\ \hline t_{pd} & U_d + \Delta_{pd} & 0 & t_{pd} \\ t_{pd} & 0 & U_d + \Delta_{pd} & t_{pd} \\ \hline 0 & t_{pd} & t_{pd} & 2(U_d + \Delta_{pd}) - J_{xy} \end{array}\right) \qquad \begin{matrix} c^\dagger_{1\uparrow} c^\dagger_{x\downarrow} c^\dagger_{x\uparrow} c^\dagger_{y\downarrow} c^\dagger_{y\uparrow} c^\dagger_{2\uparrow} |0\rangle \\ c^\dagger_{1\downarrow} c^\dagger_{1\uparrow} c^\dagger_{x\uparrow} c^\dagger_{y\downarrow} c^\dagger_{y\uparrow} c^\dagger_{2\uparrow} |0\rangle \\ c^\dagger_{1\uparrow} c^\dagger_{x\downarrow} c^\dagger_{x\uparrow} c^\dagger_{y\uparrow} c^\dagger_{2\downarrow} c^\dagger_{2\uparrow} |0\rangle \\ c^\dagger_{1\downarrow} c^\dagger_{1\uparrow} c^\dagger_{x\uparrow} c^\dagger_{y\uparrow} c^\dagger_{2\downarrow} c^\dagger_{2\downarrow} |0\rangle \end{matrix} . \tag{44}$$

The first state has the two up-electrons on the d-orbitals. The second group of states has one d-orbital doubly occupied, while the last state has both d doubly occupied, i.e., two electrons on the two p-orbitals – the situation discussed in Sec. 2. Calculating the effective Hamiltonian as in (40) gives the energy of the triplet state

$$H_{\text{eff}} = -\frac{2t_{pd}^2}{U_d + \Delta_{pd}} - \frac{4t_{pd}^4}{(U_d + \Delta_{pd})^2} \frac{1}{2(U_d + \Delta_{pd}) - J_{xy}} . \tag{45}$$

Starting from singly occupied d orbitals with opposite spin, we obtain

$$\left(\begin{array}{cc|cccc|cc} 0 & 0 & t_{pd} & 0 & t_{pd} & 0 & 0 & 0 \\ 0 & 0 & 0 & t_{pd} & 0 & t_{pd} & 0 & 0 \\ \hline t_{pd} & 0 & U_d + \Delta_{pd} & 0 & 0 & 0 & t_{pd} & 0 \\ 0 & t_{pd} & 0 & U_d + \Delta_{pd} & 0 & 0 & 0 & t_{pd} \\ t_{pd} & 0 & 0 & 0 & U_d + \Delta_{pd} & 0 & t_{pd} & 0 \\ 0 & t_{pd} & 0 & 0 & 0 & U_d + \Delta_{pd} & 0 & t_{pd} \\ \hline 0 & 0 & t_{pd} & 0 & t_{pd} & 0 & 2(U_d + \Delta_{pd}) & -J_{xy} \\ 0 & 0 & 0 & t_{pd} & 0 & t_{pd} & -J_{xy} & 2(U_d + \Delta_{pd}) \end{array}\right) \qquad \begin{matrix} c^\dagger_{1\uparrow} c^\dagger_{x\downarrow} c^\dagger_{x\uparrow} c^\dagger_{y\downarrow} c^\dagger_{y\uparrow} c^\dagger_{2\downarrow} |0\rangle \\ c^\dagger_{1\downarrow} c^\dagger_{x\downarrow} c^\dagger_{x\uparrow} c^\dagger_{y\downarrow} c^\dagger_{y\uparrow} c^\dagger_{2\uparrow} |0\rangle \\ c^\dagger_{1\downarrow} c^\dagger_{1\uparrow} c^\dagger_{x\uparrow} c^\dagger_{y\downarrow} c^\dagger_{y\uparrow} c^\dagger_{2\downarrow} |0\rangle \\ c^\dagger_{1\downarrow} c^\dagger_{1\uparrow} c^\dagger_{x\downarrow} c^\dagger_{y\downarrow} c^\dagger_{y\uparrow} c^\dagger_{2\uparrow} |0\rangle \\ c^\dagger_{1\uparrow} c^\dagger_{x\downarrow} c^\dagger_{x\uparrow} c^\dagger_{y\downarrow} c^\dagger_{2\downarrow} c^\dagger_{2\uparrow} |0\rangle \\ c^\dagger_{1\downarrow} c^\dagger_{x\downarrow} c^\dagger_{x\uparrow} c^\dagger_{y\uparrow} c^\dagger_{2\downarrow} c^\dagger_{2\uparrow} |0\rangle \\ c^\dagger_{1\downarrow} c^\dagger_{1\uparrow} c^\dagger_{x\uparrow} c^\dagger_{y\downarrow} c^\dagger_{2\downarrow} c^\dagger_{2\uparrow} |0\rangle \\ c^\dagger_{1\downarrow} c^\dagger_{1\uparrow} c^\dagger_{x\downarrow} c^\dagger_{y\uparrow} c^\dagger_{2\downarrow} c^\dagger_{2\uparrow} |0\rangle \end{matrix}$$

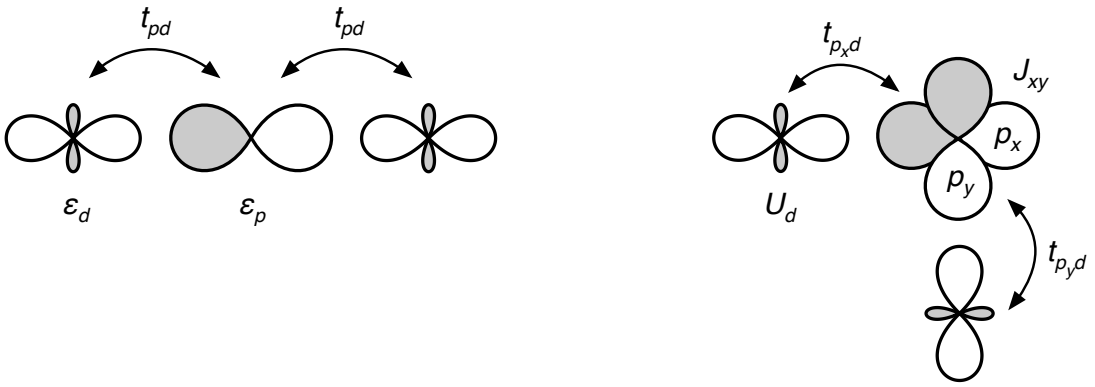

Fig. 7: *Dependence of superexchange on geometry: When the d-orbitals interact via an oxygen in-between (the 180^o geometry shown on the left), both d-orbitals couple to the same p-orbital, while the hopping to the two other p-orbitals vanishes by symmetry. The result is antiferromagnetic superexchange. When the angle of the M-O-M group is 90^o (right), the d-orbitals couple to orthogonal p-orbitals, making it impossible for an electron on one d-orbital to reach the d-orbital on the other site. In this case, superexchange is mediated via the Coulomb exchange on the connecting oxygen.*

giving the effective Hamiltonian

$$H_{\text{eff}} = -\frac{2t_{pd}^2}{U_d+\Delta_{pd}}\begin{pmatrix}1&0\\0&1\end{pmatrix} - \frac{4t_{pd}^4}{(U_d+\Delta_{pd})^2}\frac{1}{4(U_d+\Delta_{pd})^2-J_{xy}^2}\begin{pmatrix}2(U_d+\Delta_{pd}) & +J_{xy}\\ +J_{xy} & 2(U_d+\Delta_{pd})\end{pmatrix}.$$

Rearranging the matrices, we can bring this to the canonical form

$$\begin{aligned} H_{\text{eff}} = &-\left(\frac{2t_{pd}^2}{U_d+\Delta_{pd}} + \frac{4t_{pd}^4}{(U_d+\Delta_{pd})^2}\frac{1}{2(U_d+\Delta_{pd})-J_{xy}}\right) \\ &+ \frac{4t_{pd}^4}{(U_d+\Delta_{pd})^2}\frac{J_{xy}}{4(U_d+\Delta_{pd})^2-J_{xy}^2}\begin{pmatrix}1&-1\\-1&1\end{pmatrix}. \end{aligned} \tag{46}$$

The first term is just the energy of the triplet state (45). The second gives the difference in energy to the singlet. Despite the fact that the electrons cannot be transferred between the d orbitals we thus get a singlet-triplet splitting. This coupling of the spins originates from the states with both d-orbitals doubly occupied: the two remaining electrons, one each on the p_x- and p_y-orbital, respectively, form a triplet of energy $2J_{xy}$ lower than that of the singlet (see Eqn. (15)). When the electrons hop back from the d-orbital, the entanglement of the spins is transferred to the remaining electron on the d. Originating from the Coulomb exchange on the oxygen, the exchange coupling is ferromagnetic

$$J = -\frac{4t_{pd}^4}{(U_d+\Delta_{pd})^2}\frac{2J_{xy}}{4(U_d+\Delta_{pd})^2-J_{xy}^2}. \tag{47}$$

It tends to be significantly weaker than the antiferromagnetic 180^o superexchange coupling (42). When the angle of the M-O-M group is larger than 90^o, hopping to both p-orbitals becomes possible according to the Slater-Koster rules and the antiferromagnetic superexchange processes of Fig. 6 start to compete with the ferromagnetic superexchange mediated by the Coulomb exchange on the oxygen. This is one basis of the Goodenough-Kanamori rules [7, 11].

4 Double exchange

Double exchange takes its name from the fact that it results from a combination of Coulomb- and kinetic-exchange. In that sense the 90^o superexchange mechanism discussed above is a double exchange mechanism. More commonly, double exchange is encountered in mixed-valence compounds. So far we have considered systems with an integer number of electrons per site. When correlations are strong the lowest energy state will essentially have the same number of electrons on every site and hopping will be strongly suppressed by the Coulomb repulsion energy U as we have seen for the simple two-site model of kinetic exchange. In a mixed valence system the number of electrons per site is non-integer, so even for large U some site will have more electrons than others. Thus electrons can hop between such sites without incurring a cost U. Hence these compounds are usually metallic.

As a simple example we consider two sites with two orbitals of the type discussed in Sec. 2. We assume that each site has one electron in orbital a, and that there is only a single electron in the b-orbitals. This electron can hop between the sites via a hopping matrix element t_{bb}. The situation is illustrated in Fig. 8.

When all three spins are up, $S^z_{\rm tot} = 3/2$, we have a simple 2×2 Hamiltonian, taking U_{ab} as our zero of energy

$$H = \begin{pmatrix} -J_{ab} & -t_{bb} \\ -t_{bb} & -J_{ab} \end{pmatrix} . \tag{48}$$

The eigenstates are the bonding/antibonding linear combinations of the Hund's rule triplets. Their dispersion is $\pm t$:

$$\varepsilon_\pm = -J_{ab} \pm t_{bb} . \tag{49}$$

We see that the hopping couples the two sites into a state with the electrons in the a-orbital in a triplet state:

$$\Psi_\pm = \frac{1}{\sqrt{2}}\Big(|\uparrow,\uparrow\rangle_1 \, |\cdot,\uparrow\rangle_2 \pm |\cdot,\uparrow\rangle_1 \, |\uparrow,\uparrow\rangle_2 \Big) = \frac{1}{\sqrt{2}}\Big(|\uparrow,\cdot\rangle_b \pm |\cdot,\uparrow\rangle_b \Big) \, |\uparrow,\uparrow\rangle_a \tag{50}$$

In the language of quantum information (see the lecture of D. DiVincenzo), the hopping electron teleports the local triplet from the sites to the a-orbitals.

To obtain the Hamiltonian for the $S^z_{\rm tot} = 1/2$ states, we arrange the basis states in the order they are connected by matrix elements, see Fig. 8. We obtain the tridiagonal Hamiltonian

$$H = \begin{pmatrix} -J_{ab} & -t_{bb} & 0 & 0 & 0 & 0 \\ -t_{bb} & 0 & -J_{ab} & 0 & 0 & 0 \\ 0 & -J_{ab} & 0 & -t_{bb} & 0 & 0 \\ 0 & 0 & -t_{bb} & 0 & -J_{ab} & 0 \\ 0 & 0 & 0 & -J_{ab} & 0 & -t_{bb} \\ 0 & 0 & 0 & 0 & -t_{bb} & -J_{ab} \end{pmatrix} \tag{51}$$

The ground-state is the equally weighted linear combination of all basis states. It has energy $\varepsilon = -J_{ab} - t_{bb}$ and belongs to the sector with $S_{\rm tot} = 3/2$. Again, the hopping electron teleports

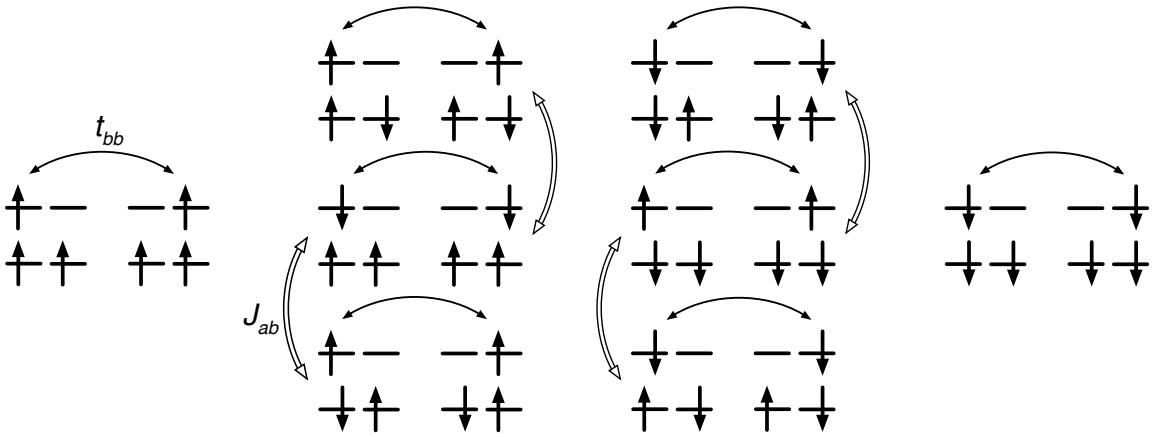

Fig. 8: *Matrix elements entering the double-exchange Hamiltonian. Hopping matrix elements t_{bb} are indicated as double arrows, Coulomb-exchange matrix elements J_{ab} as double lines. Note that the right half of the states are obtained from the left by flipping all spins.*

the triplets from the sites into a triplet state of the spins in the a-orbitals:

$$\frac{1}{\sqrt{6}}\Big(|\uparrow,\uparrow\rangle_1|\cdot,\downarrow\rangle_2+|\cdot,\uparrow\rangle_1|\uparrow,\downarrow\rangle_2+|\cdot,\uparrow\rangle_1|\downarrow,\uparrow\rangle_2+|\downarrow,\uparrow\rangle_1|\cdot,\uparrow\rangle_2+|\uparrow,\downarrow\rangle_1|\cdot,\uparrow\rangle_2+|\cdot,\downarrow\rangle_1|\uparrow,\uparrow\rangle_2\Big)$$
$$= \frac{1}{\sqrt{2}}\Big(|\uparrow,\cdot\rangle_b+|\cdot,\uparrow\rangle_b\Big)\,\frac{1}{\sqrt{2}}\Big(|\uparrow,\downarrow\rangle_a+|\downarrow,\uparrow\rangle_a\Big)+\frac{1}{\sqrt{2}}\Big(|\downarrow,\cdot\rangle_b+|\cdot,\downarrow\rangle_b\Big)\,|\uparrow,\uparrow\rangle_a$$

As in the $S^z_{\rm tot}=3/2$-sector, there is a corresponding eigenstate of energy $\varepsilon=-J_{ab}+t_{bb}$ with the b-electron antibonding. Again, we find that the triplet state is centered at $-J_{ab}$ with dispersion $\pm t_{bb}$. Thus the hopping electron in orbital b tends to align the spins in orbital a.
While the total spin is conserved, this is not true for the spin on site i, $\vec{S}_{i,a}+\vec{S}_{i,b}$ or for the spin in the a-orbitals $\vec{S}_{1a}+\vec{S}_{2a}$. Consequently the hopping mixes the Hund's rule singlets and triplets and therefore does not produce a singlet state of the a electrons. Instead, for $t_{bb}\ll J_{ab}$, we find in first order perturbation theory

$$\begin{array}{ll}
-J_{ab}-t_{bb} & \big(\ 1,\ \ 1,\ \ 1,\ \ 1,\ \ 1,\ \ 1\big)^T/\sqrt{6}\\
-J_{ab}-t_{bb}/2 & \big(\ 2,\ \ 1,\ \ 1,-1,-1,-2\big)^T/\sqrt{12}\\
-J_{ab}+t_{bb}/2 & \big(\ 2,-1,-1,-1,-1,\ \ 2\big)^T/\sqrt{12}\\
-J_{ab}+t_{bb} & \big(\ 1,-1,-1,\ \ 1,\ \ 1,-1\big)^T/\sqrt{6}\\
\\
+J_{ab}-t_{bb}/2 & \big(\ 0,\ \ 1,-1,-1,\ \ 1,\ \ 0\big)^T/2\\
+J_{ab}+t_{bb}/2 & \big(\ 0,\ \ 1,-1,\ \ 1,-1,\ \ 0\big)^T/2
\end{array}\qquad (52)$$

While the triplet states, $S_{\rm tot}=3/2$, are centered around $-J_{ab}$ with dispersion $\pm t_{bb}$, states with singlet character are centered at the same energy, but have smaller dispersion, $\pm t_{bb}/2$.
We can look at the situation from a different perspective, focusing on the effect of the spins in the a-orbitals on the hopping electron. This is another source of Goodenough-Kanamori rules [11]. We choose the quantization-axis on site 2 rotated relative to that on site 1 by an angle ϑ. Taking the original quantization axis as $\hat{z}$ and the direction from site 1 to site 2 as $\hat{x}$,

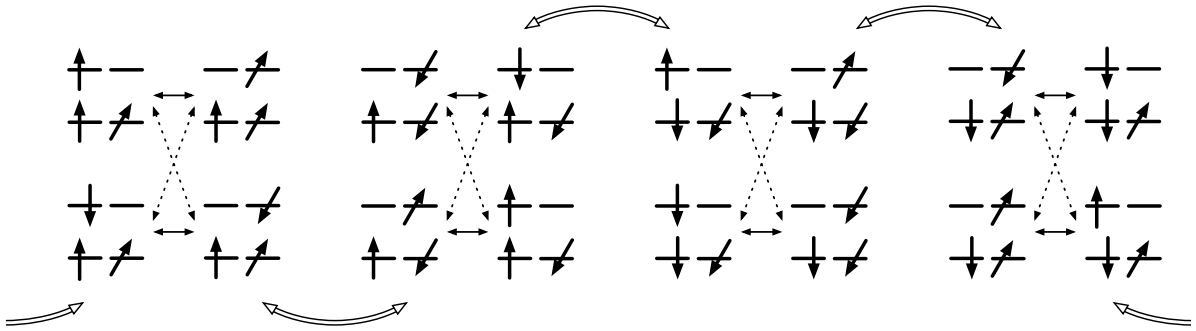

Fig. 9: *With quantization axes tilted between the sites, all states couple. Matrix elements are indicated by arrows: Hopping only couples sites with the same occupation of the a-orbitals. Full lines stand for $t_{bb}\cos(\vartheta/2)$, dotted lines for matrix elements proportional to $t_{bb}\sin(\vartheta/2)$. These states are coupled by off-diagonal Coulomb exchange matrix elements J_{ab}, shown as double lines.*

the rotation in spin space is given by $exp(-i\sigma_y\,\vartheta/2)$ (see appendix C). Introducing operators $d_{2b\sigma}$ in the rotated basis, we have, in terms of the original operators,

$$d_{2b\uparrow} = \cos(\vartheta/2)\,c_{2b\uparrow} - \sin(\vartheta/2)\,c_{2b\downarrow} \tag{53}$$

$$d_{2b\downarrow} = \sin(\vartheta/2)\,c_{2b\uparrow} + \cos(\vartheta/2)\,c_{2b\downarrow} \tag{54}$$

so the hopping becomes

$$-t_{bb}\,c^\dagger_{2b\uparrow}c_{1b\uparrow} = -t_{bb}\left(+\cos(\vartheta/2)\,d^\dagger_{2b\uparrow} + \sin(\vartheta/2)\,d^\dagger_{2b\downarrow}\right)c_{1b\uparrow} \tag{55}$$

$$-t_{bb}\,c^\dagger_{2b\downarrow}c_{1b\downarrow} = -t_{bb}\left(-\sin(\vartheta/2)\,d^\dagger_{2b\uparrow} + \cos(\vartheta/2)\,d^\dagger_{2b\downarrow}\right)c_{1b\downarrow}\,. \tag{56}$$

Obviously, such a change of basis does not change the spectrum of the resulting Hamiltonian. We do get a new situation, however, when we assume that the spin on orbital a is *fixed*. This is, e.g., a good approximation when the spin in the a-orbital arises actually not a from a single electron, but from many electrons coupled by Hund's rule, e.g., in a half-filled t_{2g}-level, like in the manganites. Then there are no off-diagonal exchange terms (double lines in Fig. 9) and the Hamiltonian splits into 4×4 blocks with only hopping (solid and dotted lines in Fig. 9) and on-site Coulomb exchange J_{ab}. The Hamiltonian then becomes

$$H = \left(\begin{array}{cc|cc} -J_{ab} & +t_{bb}\,\cos(\vartheta/2) & +t_{bb}\,\sin(\vartheta/2) & 0 \\ +t_{bb}\,\cos(\vartheta/2) & -J_{ab} & 0 & -t_{bb}\,\sin(\vartheta/2) \\ \hline +t_{bb}\,\sin(\vartheta/2) & 0 & 0 & +t_{bb}\,\cos(\vartheta/2) \\ 0 & -t_{bb}\,\sin(\vartheta/2) & +t_{bb}\,\cos(\vartheta/2) & 0 \end{array}\right), \tag{57}$$

where the a-spin simply produces a Zeeman splitting of orbital b, proportional to the exchange coupling J_{ab}. In the limit $t_{bb} \ll J_{ab}$ we can neglect the states with misaligned spins and obtain

$$\varepsilon = -J_{ab} \pm t_{bb}\,\cos(\vartheta/2)\,, \tag{58}$$

i.e., for parallel spins, $\vartheta = 0$, the gain in kinetic energy is maximized, giving the ground-state energy of the full Hamiltonian, while for anti-parallel spins, $\vartheta = \pi$ the dispersion vanishes.

5 Orbital-ordering

Exchange mechanisms are not restricted to the coupling of spins. As pointed out by Kugel and Khomskii [12], also orbital occupations can interact. Such a coupling leads, besides an ordering of the spins, to an ordering of the orbitals.

To understand the mechanism of orbital-ordering, we consider an e_g-molecule, i.e., two sites with two orbitals a and b, as discussed in Sec. 2. The Hamiltonian on the sites is thus given by (14). In addition, the two sites are coupled by hopping matrix elements t_{aa} and t_{bb}, i.e., hopping does not change the type, a or b, of the occupied orbital. We now consider the case of one electron in orbital a and the other in orbital b.

First, we consider the situation when both electrons have the same spin, e.g., spin-up. The basis states are shown in Fig. 10. Setting up the Hamiltonian is analogous to setting up (24)

$$H = \left(\begin{array}{cc|cc} 0 & 0 & -t_{bb} & -t_{aa} \\ 0 & 0 & +t_{aa} & +t_{bb} \\ \hline -t_{bb} & +t_{aa} & U_{ab}-J_{ab} & 0 \\ -t_{aa} & +t_{bb} & 0 & U_{ab}-J_{ab} \end{array}\right). \tag{59}$$

Downfolding to the states without doubly occupied sites, we obtain

$$H_{\text{eff}} \approx -\frac{1}{U_{ab}-J_{ab}} \begin{pmatrix} t_{aa}^2+t_{bb}^2 & -2t_{aa}t_{bb} \\ -2t_{aa}t_{bb} & t_{aa}^2+t_{bb}^2 \end{pmatrix} = -\frac{(t_{aa}-t_{bb})^2}{U_{ab}-J_{ab}} - \frac{2t_{aa}t_{bb}}{U_{ab}-J_{ab}} \begin{pmatrix} 1 & -1 \\ -1 & 1 \end{pmatrix}. \tag{60}$$

Thus we find that there is an interaction between the states with exchanged orbital-occupation, i.e., an orbital-exchange. For the present case of ferromagnetically aligned spins, the exchange coupling favors the orbital singlet, when the hopping matrix elements are of the same sign. In analogy with the situation in kinetic exchange, this is called antiferro orbital exchange. To make the relation with kinetic exchange even more explicit, we can introduce, in analogy to (31), pseudo-spin operators $\vec{T}_{i\sigma}$

$$T_{i\sigma}^x = \frac{1}{2}\left(c_{ai\sigma}^\dagger c_{bi\sigma} + c_{bi\sigma}^\dagger c_{ai\sigma}\right),\ T_{i\sigma}^y = -\frac{i}{2}\left(c_{ai\sigma}^\dagger c_{bi\sigma} - c_{bi\sigma}^\dagger c_{ai\sigma}\right),\ T_{i\sigma}^z = \frac{1}{2}\left(n_{ai\sigma} - n_{bi\sigma}\right) \tag{61}$$

so that we can write

$$H_{\text{eff}} = -\frac{(t_{aa}-t_{bb})^2}{U_{ab}-J_{ab}} + \frac{4t_{aa}t_{bb}}{U_{ab}-J_{ab}}\left(\vec{T}_{1\uparrow}\cdot\vec{T}_{2\uparrow} - \frac{1}{4}\right). \tag{62}$$

Fig. 10: *Basis states for an up-electron in orbital a and another up-electron in orbital b. Note that the states are ordered as in Eqn. (24).*

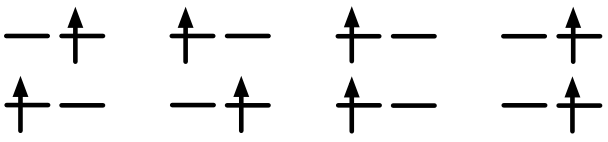

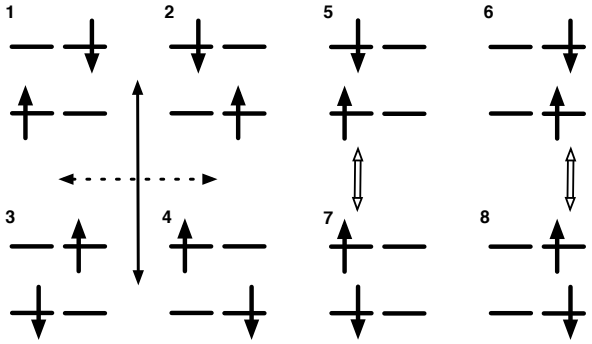

Fig. 11: *Basis states for electrons of opposite spin. The numbering used for the matrix (63) is indicated. Spin exchange is indicated by the full, orbital exchange by the dotted arrow. The states with both electrons on the same site are coupled via Coulomb exchange (double arrows).*

When the two electrons have opposite spin, we can study the interplay of spin- and orbital-exchange. The basis states shown in Fig. 11. We expect orbital exchange to operate between the first two states in each row and spin exchange between the states between the rows. The Hamiltonian is

$$H = \left(\begin{array}{cccc|cccc} 0 & 0 & 0 & 0 & -t_{bb} & -t_{aa} & 0 & 0 \\ 0 & 0 & 0 & 0 & +t_{aa} & +t_{bb} & 0 & 0 \\ 0 & 0 & 0 & 0 & 0 & 0 & -t_{bb} & -t_{aa} \\ 0 & 0 & 0 & 0 & 0 & 0 & +t_{aa} & +t_{bb} \\ \hline -t_{bb} & +t_{aa} & 0 & 0 & U_{ab} & 0 & -J_{ab} & 0 \\ -t_{aa} & +t_{bb} & 0 & 0 & 0 & U_{ab} & 0 & -J_{ab} \\ 0 & 0 & -t_{bb} & +t_{aa} & -J_{ab} & 0 & U_{ab} & 0 \\ 0 & 0 & -t_{aa} & +t_{bb} & 0 & -J_{ab} & 0 & U_{ab} \end{array}\right) \tag{63}$$

from which we obtain

$$\begin{aligned} H_{\text{eff}} &\approx -\frac{1}{U_{ab}^2 - J_{ab}^2} \begin{pmatrix} (t_{aa}^2 + t_{bb}^2)U_{ab} & -2t_{aa}t_{bb}\, U_{ab} & (t_{aa}^2 + t_{bb}^2)J_{ab} & -2t_{aa}t_{bb}\, J_{ab} \\ -2t_{aa}t_{bb}\, U_{ab} & (t_{aa}^2 + t_{bb}^2)U_{ab} & -2t_{aa}t_{bb}\, J_{ab} & (t_{aa}^2 + t_{bb}^2)J_{ab} \\ (t_{aa}^2 + t_{bb}^2)J_{ab} & -2t_{aa}t_{bb}\, J_{ab} & (t_{aa}^2 + t_{bb}^2)U_{ab} & -2t_{aa}t_{bb}\, U_{ab} \\ -2t_{aa}t_{bb}\, J_{ab} & (t_{aa}^2 + t_{bb}^2)J_{ab} & -2t_{aa}t_{bb}\, U_{ab} & (t_{aa}^2 + t_{bb}^2)J_{ab} \end{pmatrix} \\ &= -\frac{1}{U_{ab}^2 - J_{ab}^2} \begin{pmatrix} U_{ab} & J_{ab} \\ J_{ab} & U_{ab} \end{pmatrix} \otimes \begin{pmatrix} t_{aa}^2 + t_{bb}^2 & -2t_{aa}t_{bb} \\ -2t_{aa}t_{bb} & t_{aa}^2 + t_{bb}^2 \end{pmatrix} \\ &= -\frac{1}{U_{ab}^2 - J_{ab}^2} \left[U_{ab} + J_{ab} - J_{ab} \begin{pmatrix} 1 & -1 \\ -1 & 1 \end{pmatrix}\right] \otimes \left[(t_{aa} - t_{bb})^2 + 2t_{aa}t_{bb} \begin{pmatrix} 1 & -1 \\ -1 & 1 \end{pmatrix}\right]. \end{aligned} \tag{64}$$

I.e., we get a simultaneous coupling of the spin- and orbital degrees of freedom. The first term describes the coupling of the spins, which is antiferromagnetic, while the coupling of the orbitals is, for hopping matrix elements of the same sign, ferro, i.e., orbital triplet. In terms of the spin and pseudo-spin operators we can write, with $\vec{T}_i = \sum_\sigma \vec{T}_{i\sigma}$ and $\vec{S}_i = \sum_{\alpha\in\{a,b\}} \vec{S}_{\alpha,i}$

$$H_{\text{eff}} = -\frac{1}{U_{ab}^2 - J_{ab}^2} \left[(U_{ab} + J_{ab}) + 2J_{ab}\left(\vec{S}_1 \cdot \vec{S}_2 - \frac{1}{4}\right)\right] \left[(t_{aa} - t_{bb})^2 - 4t_{aa}t_{bb}\left(\vec{T}_1 \cdot \vec{T}_2 - \frac{1}{4}\right)\right].$$

There will be additional terms when we allow states with both electrons in the same orbital.

6 Extended systems

6.1 Hubbard model

We now turn to *extended* systems. For this we consider the Hubbard model [13] on an infinite lattice. Note that now the Hilbert space is infinitely dimensional, so we can no longer write down the Hamiltonian in its matrix form but have to rely on the second quantized form (29)

$$H = -t \sum_{i,j,\sigma} c^\dagger_{j\sigma} c_{i\sigma} + \; U \; \sum_i n_{i\uparrow} n_{i\downarrow} \; . \tag{65}$$

As in our toy model we still assume that each atom has only a single relevant orbital. There are links between the neighboring atoms with matrix elements t, which can be intuitively interpreted as hopping from site to site. In the absence of other terms the hopping gives rise to a band. A second energy scale is given by the Coulomb repulsion U between two electrons on the same atom. If this on-site Coulomb repulsion is comparable to or even larger than the band width, the electrons can no longer be considered independent; since the double occupation of an atom is energetically very costly, the movement of an electron will be hindered by the Coulomb repulsion. One says that the electrons move in a *correlated* way. We should note that also the Pauli principle hinders the movement of an electron. This effect can, however, be efficiently described by constructing a Slater determinant of independent-electron wave functions. Correlations, on the other hand, are notoriously difficult to describe since no simple wave functions for such systems are available. In the case of strong correlations, i.e., for $U \gg t$, we will treat the hopping as a perturbation. This is called the *atomic limit*, since the sites are almost independent atoms. Thus it is most appropriate to describe strongly correlated electrons in a local picture, i.e., in terms of electron configurations, which are the states that diagonalize the Coulomb term.

6.2 Mott transition

The physics described by the Hubbard model is the interplay between kinetic energy and Coulomb repulsion. Writing the Hubbard-Hamiltonian either in real or in k-space

$$\begin{aligned} H = \; & -t \sum_{i,j,\sigma} c^\dagger_{j\sigma} c_{i\sigma} \qquad + U \sum_i n_{i\uparrow} n_{i\downarrow} \\ = \; & \sum_{k\sigma} \varepsilon_k \, c^\dagger_{k\sigma} c_{k\sigma} \; + \frac{U}{M} \sum_{k,k',q} c^\dagger_{k\uparrow} c_{k-q\uparrow} c^\dagger_{k'\downarrow} c_{k'+q\downarrow} \, , \end{aligned}$$

where M is the number of lattice sites, we see that there are obviously two limiting cases: There is the non-interacting- or band-limit, when $t \gg U$. In that case, only the hopping term survives, i.e., there are no interactions, and the Hamiltonian can be solved easily in k-space. The energy levels then form a band and the system is metallic, except when the band is completely filled. In the opposite case, the atomic limit, the interaction term dominates. In that limit, to minimize the Coulomb energy, the electrons will be distributed over the lattice sites as uniformly

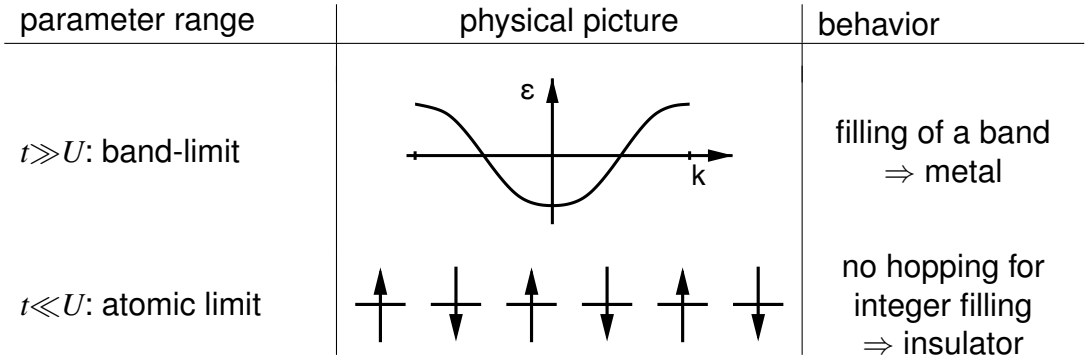

Fig. 12: *Metal-insulator transition for half-filling, i.e., one electron per site.*

as possible. For a non-degenerate, half-filled system this means, that every site carries exactly one electron, and hopping is suppressed, because it would create a doubly occupied site, which would increase the energy by $U \gg t$. Thus in the atomic limit the half-filled system will be an insulator. Clearly, in-between these two limiting cases there must be, at some value U_c, the so-called *critical* U, a transition from a metallic to an insulating state — the Mott transition [14]. Usually this transition is expected when U becomes of the order of the (non-interacting) band width W.

As the criterion for determining the metal-insulator transition we can use the opening of the gap for charge-carrying single-electron excitations

$$E_g = E(N+1) - 2E(N) + E(N-1)\,, \tag{66}$$

where $E(N)$ denotes the total energy of a cluster of M atoms with N electrons. For the half-filled system we have $N = M$. It is instructive to again consider the two limiting cases. In the non-interacting limit the total energy is given by the sum over the eigenvalues of the hopping Hamiltonian $\sum_{n:\mathrm{occ}} \varepsilon_n$. Thus, in the non-interacting limit $E_g^{\mathrm{band}} = \varepsilon_{N+1} - \varepsilon_N$, which, for a partly filled band, will vanish in the limit of infinite system size. On the other hand, in the atomic limit, the Coulomb energy for a single site with n electrons is $Un(n-1)/2$. Thus, for half-filling of we have

$$E_g^{\mathrm{atml}} = U\,, \tag{67}$$

i.e., the insulating state in the atomic limit is characterized by a finite gap.

For an infinite system the gap E_g can be rewritten in terms of the chemical potential. In the thermodynamic limit ($M \to \infty$ with N/M constant) we have to distinguish two types: the energy needed to add an electron to the system (electron affinity)

$$\mu^+ = \lim(E(N+1) - E(N)) = \left.\frac{d\varepsilon(n)}{dn}\right|_{n\searrow 1}\,, \tag{68}$$

and the energy required to extract an electron from the system (ionization energy)

$$\mu^- = \lim(E(N) - E(N-1)) = \left.\frac{d\varepsilon(n)}{dn}\right|_{n\nearrow 1}\,. \tag{69}$$

The gap is then given by the discontinuity in the left- and right-derivative of the energy per site $\varepsilon(n) = \lim E(N)/M$: $E_g = \mu^+ - \mu^-$.

6.3 Heisenberg model

We now consider the Hubbard model in the limit of large U. This is the generalization of the discussion of direct kinetic exchange in Sec. 3.2 to an extended system. For large U we work with the electron configurations, in which the interaction term is diagonal. Configurations with doubly occupied sites will have energies of the order of U or larger, so these are the configurations that we would like to project out. For downfolding we thus partition the configuration basis, and hence the Hilbert space, into the set of low-energy states which have no doubly occupied sites

$$S = \left\{ |n_{1\uparrow}, n_{1\downarrow}, n_{2\uparrow}, n_{2\downarrow}, \ldots\rangle \,\middle|\, \forall i : \, n_{i\uparrow} + n_{i\downarrow} \leq 1 \right\} \tag{70}$$

and the set of high-energy states with one or more doubly occupied sites

$$D = \left\{ |n_{1\uparrow}, n_{1\downarrow}, n_{2\uparrow}, n_{2\downarrow}, \ldots\rangle \,\middle|\, \exists i : \, n_{i\uparrow} + n_{i\downarrow} = 2 \right\} \, . \tag{71}$$

The hopping term T, which for large U is a perturbation to the interaction term I, couples the subspaces by hopping an electron into or out of a doubly occupied site. In addition it lifts the degeneracies within the subspaces. Hence the Hamiltonian can be partitioned as (note that $I \equiv 0$ on subspace S)

$$\hat{H} = \begin{pmatrix} P_S \, T \, P_S & P_S \, T \, P_D \\ P_D \, T \, P_S & P_D \, (T + I) \, P_D \end{pmatrix} \, , \tag{72}$$

Since we are dealing with an extended system, the subspaces are infinite, so we cannot write the Hamiltonian on the subspaces as matrices. Instead we restrict the operators to the appropriate subspace by using projection operators, P_S projecting on the low-energy configurations S, P_D projecting on D. Just like in 3.2 we can then write down an effective Hamiltonian operating on the low-energy configurations only:

$$H_{\text{eff}} = P_S \, T \, P_S + P_S \, T \, P_D \, \left[P_D \, (\varepsilon - (I + T)) \, P_D \right]^{-1} P_D \, T \, P_S \, , \tag{73}$$

Unlike in the derivation of direct exchange, for the extended system we have no way of calculating the inverse in the second term explicitly. We can, however, expand in powers of t/U. This is Kato's method for perturbation theory (see, e.g., section 16.3 of [15]). Essentially we only need to consider configurations with a *single* double-occupancy – these correspond to the states of lowest energy in D. On this subspace the interaction term is diagonal with eigenvalue U and can thus be easily inverted. We then obtain the Hamiltonian

$$H_{t-J} = P_S \left[T - \frac{t^2}{U} \sum_{\langle ij \rangle \langle jk \rangle \sigma\sigma'} c^\dagger_{k\sigma'} c_{j\sigma'} \, n_{j\uparrow} n_{j\downarrow} \, c^\dagger_{j\sigma} c_{i\sigma} \right] P_S \, , \tag{74}$$

which is called the t-J Hamiltonian. The first term describes the hopping, constrained to configurations with no doubly occupied sites. Thus it essentially describes the hopping of empty sites (holes). To understand what the second term does, we observe that, because of the operators $n_{j\uparrow} n_{j\downarrow}$, there are only contributions for states with a singly occupied site j: $n_{j\sigma} = 0$ and $n_{j,-\sigma} = 1$. After applying the second term, site j will again be singly occupied with $n_{j\sigma'} = 0$

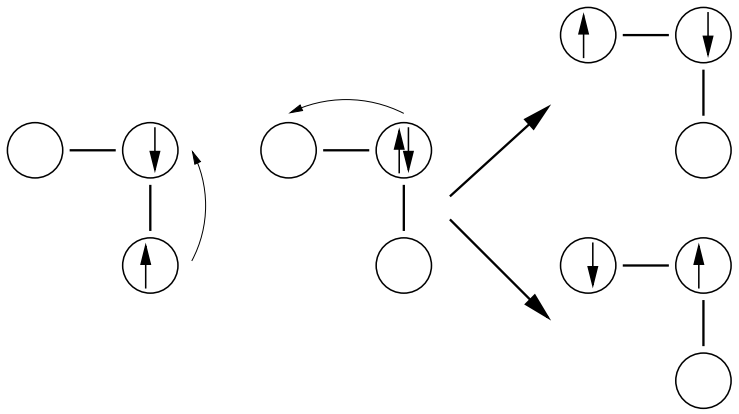

Fig. 13: *Processes contained in the three-site term T': indirect hopping processes to a second-nearest neighbor site with an intermediate (virtual) doubly occupied state. In the first process the two hopping processes are performed by the same electron, in the second process each electron hops once and thus the spin on the intermediate site is flipped.*

and $n_{j,-\sigma'} = 1$. Hence, for $\sigma \neq \sigma'$ the spin on site j will be flipped. Moreover, we distinguish the contributions where only two different sites are involved ($k = i$) from the three-site terms ($k \neq i$). The terms for $k = i$ are just the ones we already know from the kinetic exchange mechanism. The three-site terms describe a second-nearest neighbor hopping of an electron from site i to site k via a singly occupied intermediate site j. For $\sigma = \sigma'$ the spin of the hopping electron is opposite to that on the intermediate site. For $\sigma \neq \sigma'$ the spin of the intermediate site is flipped – as is that of the hopping electron. This is shown in Fig. 13. The t-J Hamiltonian is

$$H_{t-J} = P_S \left[T + H_H + T'\right] P_S \tag{75}$$

with

$$T = -t \sum_{\langle ij\rangle,\sigma} c^\dagger_{j\sigma} c_{i\sigma} \tag{76}$$

$$H_H = \frac{4t^2}{U} \sum_{\langle ij\rangle} \left(\vec{S}_j \cdot \vec{S}_i - \frac{n_i n_j}{4}\right) \tag{77}$$

$$T' = -\frac{t^2}{U} \sum_{\substack{\langle ij\rangle\langle jk\rangle \\ i\neq k}} \sum_{\sigma} \left(c^\dagger_{k\sigma}(1-n_{j\sigma})c_{i\sigma} - c^\dagger_{k,-\sigma}c^\dagger_{j\sigma}c_{j,-\sigma}c_{i\sigma}\right) n_{j,-\sigma} \tag{78}$$

In the case of half-filling, when $n_i = 1$, all hopping processes are suppressed, i.e., the projection P_S annihilates T and T'. Thus for a Mott insulator the t-J model reduces to the spin $1/2$ Heisenberg model

$$H_H = J \sum_{\langle ij\rangle} \vec{S}_j \cdot \vec{S}_i + \text{const.} \tag{79}$$

with the exchange coupling $J = 4t^2/U$ given by the direct kinetic exchange mechanism. We again stress that the spin-spin interaction is a result of projecting out the states with double occupancies.

7 Conclusion

We have seen that magnetic interactions in matter arise from the interplay of the Pauli principle and Coulomb interaction, kinetic energy, or both. The resulting effective couplings between magnetic moments are thus not fundamental interactions and, usually, take quite complex forms. However, in limiting cases they can become quite simple and transparent. These scenarios are called exchange mechanisms, of which we have discussed here a small selection. They give an idea of what magnetic interactions can be expected in real materials. Thus, despite their simplicity, exchange mechanisms provide vital guides for understanding the physics of complex ordering phenomena, of spins and orbital-occupations, from simple concepts.

Acknowledgment

Support of the Deutsche Forschungsgemeinschaft through FOR1346 is gratefully acknowledged.

Appendices

A Atomic units

Practical electronic structure calculations are usually done in atomic units, a. u. for short. While the idea behind the atomic units is remarkably simple, in practice there is often some confusion when trying to convert to SI units. We therefore give a brief explanation.
The motivation for introducing atomic units is to simplify the equations. For example, in SI units the Hamiltonian of a hydrogen atom is

$$H = -\frac{\hbar^2}{2m_e}\nabla^2 - \frac{e^2}{4\pi\epsilon_0\, r}\ . \tag{80}$$

To avoid having to keep track of the constants, we would like to simplify this to

$$H = -\frac{1}{2}\nabla^2 - \frac{1}{r}\ . \tag{81}$$

To this end we invent units in which the *numerical values* of the electron mass m_e, the elementary charge e, the Planck-constant $\hbar$, and the dielectric constant $4\pi\epsilon_0$ are all equal to one. This immediately tells us: 1 a.u. mass $= m_e$ and 1 a.u. charge $= e$. To complete the set of basis units we still need the atomic unit of length, which we call a_0, and of time, t_0. To find the values of a_0 and t_0 we write $\hbar$ and $4\pi\epsilon_0$ (using simple dimensional analysis) in atomic units: $\hbar = 1\, m_e a_0^2/t_0$ and $4\pi\epsilon_0 = 1\, t_0^2 e^2/(m_e a_0^3)$. Solving this system of equations, we find

1 a.u. length	$= a_0 =$	$4\pi\epsilon_0\hbar^2/m_e e^2$	$\approx 5.2918\cdot 10^{-11}$	m
1 a.u. mass	$= m_e =$		$\approx 9.1095\cdot 10^{-31}$	kg
1 a.u. time	$= t_0 =$	$(4\pi\epsilon_0)^2\hbar^3/m_e e^4$	$\approx 2.4189\cdot 10^{-17}$	s
1 a.u. charge	$= e =$		$\approx 1.6022\cdot 10^{-19}$	C

The atomic unit of length, a_0, is the Bohr radius. As the dimension of energy is mass times length squared divided by time squared, its atomic unit is $m_e a_0^2/t_0^2 = m_e e^4/(4\pi\epsilon_0)^2\hbar^2$. Because of its importance the atomic unit of energy has a name, the Hartree. One Hartree is minus twice the ground-state energy of the hydrogen atom (80), about 27.211 eV. The speed of light c in atomic units is given by $c\ t_0/a_0 = 4\pi\varepsilon_0\hbar c/e^2 = 1/\alpha$, where α is the fine structure constant. Thus $c = \alpha^{-1}$ a.u. ≈ 137 a.u. The Bohr magneton is $\mu_B = 1/2$ a.u.

B Downfolding

To integrate-out high-energy degrees of freedom, we partition the Hilbert space of the full system into states of interest (low-energy states) and 'other' states, which will be integrated out. The Hamiltonian is then written in blocks

$$H = \begin{pmatrix} H_{00} & T_{01} \\ T_{10} & H_{11} \end{pmatrix} , \tag{82}$$

where H_{00} is the Hamiltonian restricted to the states of interest (reduced Hilbert space), H_{11} the Hamiltonian for the 'other' states, and the T matrices describe transitions between the two subspaces. The resolvent is partitioned likewise

$$G(\varepsilon) = (\varepsilon - H)^{-1} = \begin{pmatrix} \varepsilon - H_{00} & T_{01} \\ T_{10} & \varepsilon - H_{11} \end{pmatrix}^{-1} . \tag{83}$$

Calculating the inverse of the 2×2 matrix, taking into account that the entries are matrices themselves and thus do not commute, we obtain

$$G_{00}(\varepsilon) = \left(\varepsilon - [H_{00} + \underbrace{T_{01}(\varepsilon - H_{11})^{-1} T_{10}}_{=H_{\text{eff}}}] \right)^{-1} . \tag{84}$$

This expression looks just like the resolvent for a Hamiltonian

$$\begin{aligned} H_{\text{eff}} &= H_{00} + T_{01}(\varepsilon - H_{11})^{-1} T_{10} && (85) \\ &\approx H_{00} + T_{01}(\varepsilon_0 - H_{11})^{-1} T_{10} && (86) \end{aligned}$$

on the reduced Hilbert space. This effective Hamiltonian describes the physics of the full system, but operates only on the small reduced Hilbert space. Of course, this drastic simplification comes at a price: the effective Hamiltonian is energy dependent. If the hopping matrix elements in T_{01} are small, and/or if the states in the part of the Hilbert space that has been integrated out are energetically well-separated from the states that are explicitly considered, this energy dependence can, to a good approximation, be neglected. We can then replace ε by a typical energy ε_0 for the states in the reduced Hilbert space to obtain an energy-independent Hamiltonian $H_{\text{eff}}(\varepsilon_0)$ that gives a good description of the electrons in the reduced Hilbert space, i.e., the states with an energy close to ε_0.

C Pauli matrices

Here we collect the most important properties of the Pauli matrices. The Pauli or spin matrices are defined as

$$\sigma_x = \begin{pmatrix} 0 & 1 \\ 1 & 0 \end{pmatrix} \quad \sigma_y = \begin{pmatrix} 0 & -i \\ i & 0 \end{pmatrix} \quad \sigma_z = \begin{pmatrix} 1 & 0 \\ 0 & -1 \end{pmatrix} \tag{87}$$

They are hermitean, i.e. $\sigma_i^\dagger = \sigma_i$, and $\sigma_i^2 = 1$. Therefore their eigenvalues are ± 1. The eigenvectors of σ_z are $|m_z\rangle$, $m_z = \pm 1$:

$$|+1\rangle = \begin{pmatrix} 1 \\ 0 \end{pmatrix} \quad \text{and} \quad |-1\rangle = \begin{pmatrix} 0 \\ 1 \end{pmatrix}. \tag{88}$$

For these vectors we find

$$\sigma_x|\,m_z\rangle = |\,-m_z\rangle \quad \sigma_y|\,m_z\rangle = i m_z|\,-m_z\rangle \quad \sigma_z|\,m_z\rangle = m_z|\,m_z\rangle \tag{89}$$

The products of the Pauli matrices are $\sigma_x\,\sigma_y = i\sigma_z$, where the indices can be permuted cyclically. From this follows for the commutator

$$[\sigma_x, \sigma_y] = 2i\sigma_z \tag{90}$$

while the anticommutator vanishes:

$$\{\sigma_x, \sigma_y\} = 0 \tag{91}$$

Finally a rotation by an angle φ about the axis $\hat{n}$ changes the spin matrices

$$R_{\hat{n}}(\varphi) = e^{-i\hat{n}\cdot\vec{\sigma}\,\varphi/2} = cos(\varphi/2) - i\sin(\varphi/2)\,\hat{n}\cdot\vec{\sigma} \tag{92}$$

References

[1] R. Peierls: *Surprises in Theoretical Physics* (Princeton University Press, 1979)

[2] J.H. van Vleck: *Quantum Mechanics: The Key to Understanding Magnetism*, in S. Lundqvist (ed.): *Nobel Lectures, Physics 1971-1980* (World Scientific, Singapore, 1992) http://www.nobelprize.org/nobel_prizes/physics/laureates/1977

[3] Patrik Fazekas: *Lecture Notes on Electron Correlation and Magnetism* (World Scientific, Singapore, 1999)

[4] A. Auerbach: *Interacting Electrons and Quantum Magnetism* (Springer, Heidelberg, 1994)

[5] E. Pavarini: *The LDA+DMFT Approach*, in [16]

[6] M. Weissbluth: *Atoms and Molecules* (Academic Press, San Diego, 1978)

[7] P.W. Anderson: *Theory of Magnetic Exchange Interactions*, in F. Seitz and D. Turnbull (eds.): *Solid State Physics* **14**, 99 (1963)

[8] D.C. Mattis: *The Theory of Magnetism Made Simple* (World Scientific, Singapore, 2006)

[9] S. Blundell: *Magnetism in Condensed Matter* (Oxford University Press, 2001)

[10] A. Szabo and N.S. Ostlund: *Modern Quantum Chemistry* (Dover Publications, 1996)

[11] J.B. Goodenough: *Goodenough-Kanamori rule*, Scholarpedia **3**, 7382 (2008) http://scholarpedia.org/article/Goodenough-Kanamori_rule

[12] K.I. Kugel and D.I. Khomskii, Zh. Eksp. Teor. Fiz. **64**, 1429 (1973) [Sov. Phys. JETP **37**, 725 (1973)]

[13] A. Montorsi (Ed.): *The Hubbard Model*, (World Scientific, Singapore, 1992)

[14] F. Gebhard: *The Mott Metal-Insulator Transition* (Springer, Heidelberg, 1997)

[15] A. Messiah: *Méchanique Quantique* (Dunond, Paris, 1964)

[16] E. Pavarini, E. Koch, D. Vollhardt, and A.I. Lichtenstein: *The LDA+DMFT approach to strongly correlated materials* Reihe Modeling and Simulation, Vol. 1 (Forschungszentrum Jülich, 2011) http://www.cond-mat.de/events/correl11

8 Multiplets in Transition Metal Ions

Robert Eder
Institut für Festkörperphysik
Karlsruhe Institute of Technology

Contents

E. Pavarini, E. Koch, F. Anders, and M. Jarrell
Correlated Electrons: From Models to Materials
Modeling and Simulation Vol. 2
Forschungszentrum Jülich, 2012, ISBN 978-3-89336-796-2
http://www.cond-mat.de/events/correl12

1 Introduction

Compounds containing $3d$ transition metal – or iron group – ions have been intriguing solid state physicists ever since the emergence of solid state physics as a field of research. In fact, already in the 1930's NiO became the first known example of a correlated insulator in that it was cited by deBoer and Verwey as a counterexample to the then newly invented Bloch theory of electron bands in solids [1]. During the last 25 years $3d$ transition metal compounds have become one of the central fields of solid state physics, following the discovery of the cuprate superconductors, the colossal magnetoresistance phenomenon in the manganites and, most recently, the iron-pnictide superconductors.

It was conjectured early on that the reason for the special behaviour of these compounds is the strong Coulomb interaction between electrons in the partially filled $3d$ shells of the iron group elements. These $3d$ wave functions are orthogonal to those of the inner-shells – $1s$, $2s$ and $2p$ – solely due to their angular part $Y_{2,m}(\Theta, \phi)$. Their radial part $R_{3,2}(r)$ thus is not pushed out to regions far from the nucleus by the requirement to be orthogonal to the inner shell wave functions and therefore is concentrated close to the nucleus (the situation is exactly the same for the $4f$ wave functions in the Rare Earth elements). Any two electrons in the $3d$ shell thus are forced to be close to each other on average so that their mutual Coulomb repulsion is strong (the Coulomb repulsion between two $3d$ electrons is weak, however, when compared to the Coulomb force due to the nucleus and the inner shells so that the electrons *have to* stay close to one another!). For clarity we also mention that the Coulomb repulsion between two electrons in the inner shells of most heavier elements is of course much stronger than between the $3d$ electrons of the iron group elements. This, however, is irrelevant because these inner shells are several 100 - 1000 eV below the Fermi energy so that they are simply completely filled. The $3d$-orbitals in the iron group elements or the $4f$-orbitals in the Rare Earths on the other hand participate in the bands at the Fermi level so that the strong Coulomb interaction in these orbitals directly influences the conduction electrons. This is why the Coulomb repulsion in these shells dominates the physical properties of these compounds and gives rise to such a wide variety of interesting phenomena. Let us therefore discuss the Coulomb interaction in a partially filled atomic shell in more detail.

2 Multiplets of a free ion

2.1 General considerations

For definiteness we consider NiO. The atomic electron configurations are [Ar]$3d^8 4s^2$ for Nickel and [He]$2s^2 2p^4$ for Oxygen. In a purely ionic picture the oxgen atom will want to fill its $2p$ shell and become O^{2-}, rendering Ni to be Ni^{2+} with electron configuration [Ar]$3d^8$. Accordingly let us first consider a Ni^{2+} ion *in vacuum*. It is a standard exercise in textbooks of atomic physics to show that the d^8 configuration, which is equivalent to d^2, has the following multiplets: ${}^3F$, ${}^3P$, ${}^1G$, ${}^1D$ and ${}^1S$. The energies of these multiplets differ and can be observed experimentally, e.g.,

in the spectrum of Ni vapor. The first two Hund's rules state that the multiplet with the lowest energy, i.e., the ground state of the Ni^{2+} ion, is ${}^3F$. Then we may ask: what is the physical mechanism that leads to the multiplet splitting and makes ${}^3F$ the ground state? The answer is that it is the Coulomb repulsion between $3d$ electrons which splits the multiplets energetically and enforces the first two Hund's rules. When being asked for the energy of the d^n configuration one might give be tempted to give the following answer:

$$E[d^n] \approx n \cdot \epsilon_d + U \cdot \frac{n(n-1)}{2}.$$

The first term, where ϵ_d is the energy of the d-orbital, is the single-particle energy. The second term obviously counts the number of electron pairs and multiplies them by the parameter U which accordingly has the meaning of an average Coulomb repulsion energy between two electrons. For a non-degenerate orbital, instead of the five-fold degenerate d-orbital, n can take only the values 0, 1 and 2, with corresponding Coulomb energies 0, 0 and U. In this case the second term therefore reduces to the expression $Un_\uparrow n_\downarrow$ familiar from the Hubbard or Anderson model.

In a degenerate situation, however, the Coulomb interaction between electrons has additional aspects. Let us first consider a classical picture where the electrons are taken as charged mass points orbiting around the nucleus. In this case the Colomb force $\boldsymbol{F}_{ij}$ acting on electron i due to electron j in general is not parallel to the position vector $\boldsymbol{r}_i$ of electron i and thus exerts a nonvanishing torque $\boldsymbol{\tau}_{ij} = \boldsymbol{r}_i \times \boldsymbol{F}_{ij}$. This means that the angular momentum of any given electron changes constantly but since $\boldsymbol{F}_{ij} = -\boldsymbol{F}_{ji} = f(|\boldsymbol{r}_i - \boldsymbol{r}_j|)\ (\boldsymbol{r}_i - \boldsymbol{r}_j)$ it is easy to see that $\boldsymbol{\tau}_{ij} = -\boldsymbol{\tau}_{ji}$ so that the two electrons i and j merely 'exchange angular momentum' and the total angular momentum is conserved. The quantum mechanical version of this exchange of angular momentum is shown in Fig. 1: The 8 d-electrons are initially distributed over the 5 d-orbitals which are labeled by the m-value in the angular part of their wave functions, $Y_{2,m}(\Theta, \phi)$. Then, two electrons scatter from each other due to their Coulomb interaction and after the scattering find themselves in orbitals with a different m-value. The sum over the m-values of the occupied orbitals, which gives the z-component of the total orbital angular momentum L^z, must remain constant during the scattering process so that the two scattering electrons move

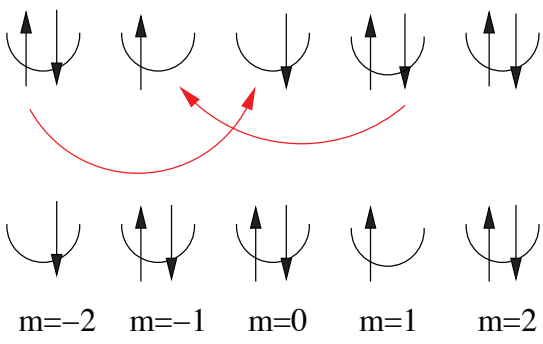

Fig. 1: *A scattering process between two electrons in a partly filled d-shell.*

along the 'm-ladder' in opposite direction and by an equal number of steps. The single particle energy of the electrons, which is $8\epsilon_d$ in Fig. 1, is unchanged by the scattering. This means that scattering processes of the type shown in Fig. 1 connect all states with a given z-component of the total spin and orbital angular momentum and all of these states are degenerate with respect to their single particle energy. If we think of an unperturbed Hamiltonian H_0 which consists of the single particle energies of the various levels and consider the Coulomb interaction between the $3d$ electrons as perturbation H_1 we have exactly the situation of degenerate first order perturbation theory. The textbook procedure then is to set up the secular determinant, i.e., the matrix $\langle\mu|H_1|\nu\rangle$ where $|\mu\rangle$ and $|\nu\rangle$ run over the set of degenerate eigenstates of H_0, and diagonalize this.

To formulate this in a more quantitative fashion we first introduce Fermionic creation (and annihilation) operators $c^\dagger_{n,l,m,\sigma}$ which create an electron with z-component of spin σ in the orbital with principal quantum number n, orbital angular momentum l, and z-component of orbital angular momentum m. In the following we will often contract (n,l,m,σ) to the 'compound index' ν for brevity, so that e.g. $c^\dagger_{\nu_i} = c^\dagger_{n_i,l_i,m_i,\sigma_i}$. In our case the degenerate states $|\nu\rangle$ can be written as

$$|\nu\rangle = |\nu_1,\nu_2\ldots\nu_n\rangle = c^\dagger_{\nu_1}c^\dagger_{\nu_2}\ldots c^\dagger_{\nu_n}|0\rangle. \tag{1}$$

In the case of a partly filled $3d$-shell all $n_i = 3$ and all $l_i = 2$ identically, so that these two indices could be omitted, but we will keep them for the sake of later generalizations. In writing the basis states as in (1) we need to specify an ordering convention for the creation operators on the right hand side. For example, only states are taken into account where $m_1 \le m_2 \le m_3 \cdots \le m_n$. Moreover, if two m_i are equal the $c^\dagger_{m_i\downarrow}$-operator is assumed to be to the left of the $c^\dagger_{m_i\uparrow}$-operator. If we adopt this convention, every possible state obtained by distributing the n electrons over the $2(2l+1)$ spin-orbitals is included exactly once in the basis. If the n_i and l_i were to take different values we could generalize this by demanding that the (n_i,l_i,m_i)-triples be ordered lexicographically. As will be seen below, strict application of an ordering convention for the Fermi operators is necessary to determine the correct Fermi signs for the matrix elements. In second quantization the Coulomb Hamiltonian H_1 then reads (in atomic units)

$$\begin{aligned} H_1 &= \frac{1}{2}\sum_{i,j,k,l} V(\nu_i,\nu_j,\nu_k,\nu_l)\; c^\dagger_{\nu_i}c^\dagger_{\nu_j}c_{\nu_k}c_{\nu_l}, \\ V(\nu_1,\nu_2,\nu_3,\nu_4) &= \int dx \int dx'\; \psi^*_{\nu_1}(x)\;\psi^*_{\nu_2}(x')\;V_c(x,x')\;\psi_{\nu_4}(x)\;\psi_{\nu_3}(x'), \\ V_c(x,x') &= \frac{1}{|\boldsymbol{r}-\boldsymbol{r}'|}. \end{aligned} \tag{2}$$

Here $x = (\boldsymbol{r},\sigma)$ is the combined position and spin coordinate and V_c is the Coulomb interaction between electrons. Note the factor of $1/2$ in front of H_1 and the correspondence of indices and integration variables $\nu_4 \leftrightarrow x$ and $\nu_3 \leftrightarrow x'$ in the Coulomb matrix element, see textbooks of many-particle physics such as Fetter-Walecka [2]. In the next paragraph we will calculate the matrix elements $V(\nu_1,\nu_2,\nu_3,\nu_4)$.

2.2 Calculation of the Coulomb matrix elements

First, we use the fact that the single-particle basis we are using consists of atomic spin-orbitals so if we parameterize the vector $\boldsymbol{r}$ by its polar coordinates (r, Θ, ϕ) we have

$$\psi_{\nu_i}(x) \;\; = \;\; R_{n_i,l_i}(r)\; Y_{l_i,m_i}(\Theta,\phi)\; \delta_{\sigma,\sigma_i}. \tag{3}$$

The radial wave functions R_{n_i,l_i} are assumed to be real, as is the case for the true radial wave function of bound states in a central potential. Apart from this we do not really specify them. In fact, it would be rather difficult to give a rigorous prescription for their determination. It will turn out, however, that these radial wave functions enter the matrix elements only via a discrete and rather limited set of numbers which are very often obtained by fit to experiment.
In addition to (3), we use the familiar multipole expansion of the Coulomb interaction

$$\frac{1}{|\boldsymbol{r}-\boldsymbol{r}'|} \;\; = \;\; \sum_{k=0}^{\infty}\sum_{m=-k}^{k} Y^*_{k,m}(\Theta',\phi')\; \frac{4\pi}{2k+1}\; \frac{r_<^k}{r_>^{k+1}}\; Y_{k,m}(\Theta,\phi). \tag{4}$$

We now evaluate the matrix element $V(\nu_1,\nu_2,\nu_3,\nu_4)$ and first note that the sum over spin variables simply gives the prefactor $\delta_{\sigma_1,\sigma_4}\;\delta_{\sigma_2,\sigma_3}$. Next we pick one term with given k and m from the multipole expansion (4) and proceed to the integration over the spatial variables (r,Θ,ϕ) and (r',Θ',ϕ'). Let us first consider the angular variables (Θ,ϕ). Obviously these always come as arguments of spherical harmonics and there is one from $\psi^*_{\nu_1}(x)$, i.e., the bra, one from the multipole expansion (4), i.e., H_1, and one from $\psi_{\nu_4}(x)$, i.e., the ket. We thus find a factor of

$$\int_0^{2\pi} d\phi \;\int_{-1}^{1} dcos(\Theta)\; Y^*_{l_1,m_1}(\Theta,\phi)\; Y_{k,m}(\Theta,\phi)\; Y_{l_4,m_4}(\Theta,\phi) \tag{5}$$

Such a dimensionless integral over three spherical harmonics is called a Gaunt coefficient and can be shown to be proportional to a Clebsch-Gordan coefficient [3,4]. An interesting property can be seen if we note the ϕ-dependence of $Y_{l,m}(\Theta,\phi) = P_{l,m}(\Theta)\; e^{im\phi}$ whence we find that the Gaunt coefficient (5) is different from zero only if $m_1 = m_4 + m$. Moreover, the Θ-dependent factors $P_{l,m}(\Theta)$ are all real [3,4], so that all nonvanishing Gaunt coefficients are real. In exactly the same way the integration over (Θ',ϕ') gives

$$\int_0^{2\pi} d\phi' \;\int_{-1}^{1} dcos(\Theta')\; Y^*_{l_2,m_2}(\Theta',\phi')\; Y^*_{k,m}(\Theta',\phi')\; Y_{l_3,m_3}(\Theta',\phi'), \tag{6}$$

which by similar arguments is different from zero only if $m_2 + m = m_3$. Since (5) and (6) must be different from zero for the same m in order to obtain a nonvanishing contribution we must have $m_1 + m_2 = m_3 + m_4$. This is simply the condition, stated already above, that L^z be conserved.
It remains to do the integral over the two radial variables r and r'. These two integrations cannot be disentangled and we find a last factor

$$R^k(n_1l_1,n_2l_2,n_3l_3,n_4l_4) = \int_0^{\infty} dr\, r^2 \int_0^{\infty} dr' r'^2\; R_{n_1l_1}(r) R_{n_2l_2}(r')\; \frac{r_<^k}{r_>^{k+1}}\; R_{n_4l_4}(r) R^l_{n_3l_3}(r'). \tag{7}$$

These integrals, which have the dimension of energy, are labeled by the multipole index k and in the present case of Coulomb scattering within a d-shell the number of relevant multipole orders is severely limited by the properties of the Gaunt coefficients. First, since the latter are proportional to Clebsch-Gordan coefficients the three l-values appearing in them have to obey the so-called *triangular condition* [5] whence $k \leq \min(|l_1 + l_4|, |l_2 + l_3|)$. For a d-shell where $l_i = 2$ it follows that $k \leq 4$. Second, the parity of the spherical harmonic Y_{lm} is $(-1)^l$, i.e., even for the case $l_i = 2$. For integrals such as (5) or (6) to be different from zero the spherical hamonic Y_{km} from the multipole expansion must have even parity, too, so that for Coulomb scattering within a d-shell only R^0, R^2 and R^4 are relevant. This shows that the sloppy definition of the wave function $R_{n_i,l}(r)$ is not a real problem – details of this wave function are irrelevant anyway. In a way, these three parameters may be viewed as a generalization of the Hubbard-U in that R^k is something like the 'the Hubbard-U for k-pole interaction'.
Next, we introduce the following short notation for nonvanishing Gaunt coefficients

$$c^k(lm; l'm') = \sqrt{\frac{4\pi}{2k+1}} \int_0^{2\pi} d\phi \int_{-1}^{1} dcos(\Theta)\, Y^*_{lm}(\Theta,\phi)\, Y_{k,m-m'}(\Theta,\phi)\, Y_{l',m'}(\Theta,\phi). \tag{8}$$

These coefficients are tabulated in Appendix 20a of the textbook by Slater [3] or Table 4.4 of the textbook by Griffith [4], see also the Appendix of the present note. Using this notation we can write the complete Coulomb matrix element as

$$V(\nu_1,\nu_2,\nu_3,\nu_4) = \delta_{\sigma_1,\sigma_4}\,\delta_{\sigma_2,\sigma_3}\,\delta_{m_1+m_2,m_3+m_4} \sum_{k=0}^{\infty} c^k(l_1m_1; l_4m_4)\, c^k(l_3m_3; l_2m_2)\, R^k(n_1l_1, n_2l_2, n_3l_3, n_4l_4). \tag{9}$$

To conclude this paragraph we discuss *particle-hole symmetry*. This phrase expresses the fact that in a shell with angular momentum l the configurations with n electrons and $2(2l+1) - n$ electrons, i.e., n holes, have the same multiplets and that the energies of the multiplets are the same up to an overall additive constant. We consider the following transformation:

$$\begin{aligned} |0\rangle &\rightarrow |0'\rangle = c^\dagger_{l,-l,\downarrow} c^\dagger_{l,-l,\uparrow} c^\dagger_{l,-l+1,\downarrow} c^\dagger_{l,-l+1,\uparrow} \ldots c^\dagger_{l,l,\downarrow} c^\dagger_{l,l,\uparrow} |0\rangle \\ c^\dagger_\nu &\rightarrow h_\nu, \\ c_\nu &\rightarrow h^\dagger_\nu. \end{aligned} \tag{10}$$

This transformation replaces the empty state $|0\rangle$ by the filled shell $|0'\rangle$ and the electron creation/annihilation operators $c^\dagger/c$ by *hole* annihilation/creation operators $h/h^\dagger$. We will now show that the Hamiltonian H_1, when expressed in terms of the hole operators, up to a constant, has the same form as the original Hamiltonian. Once this is shown, we can define basis states $h^\dagger_{\nu_1} \ldots h^\dagger_{\nu_n} |0'\rangle$ which have n holes in the filled shell but have exactly the same matrix elements between them as states of n electrons.
To show the equivalence we assume that in the Coulomb Hamiltonian (2) all Fermion c-operators are replaced by h-operators according (10). Then, in each term we can permute the Fermion

operators according to

$$h_{\nu_1}h_{\nu_2}h^\dagger_{\nu_3}h^\dagger_{\nu_4} = h^\dagger_{\nu_4}h^\dagger_{\nu_3}h_{\nu_2}h_{\nu_1} + \delta_{\nu_2\nu_3}h_{\nu_1}h^\dagger_{\nu_4} - \delta_{\nu_1\nu_3}h_{\nu_2}h^\dagger_{\nu_4} + \delta_{\nu_2\nu_4}h^\dagger_{\nu_3}h_{\nu_1} - \delta_{\nu_1\nu_4}h^\dagger_{\nu_3}h_{\nu_2}$$

where the terms quadratic in h-operators originate from anticommutations. The quartic terms now have the original form, but with the replacement $c \to h$ and

$$V(\nu_4, \nu_3, \nu_2, \nu_1) \to V(\nu_1, \nu_2, \nu_3, \nu_4).$$

As can be seen from (2), however, this replacement is equivalent to complex conjugation of the matrix elements, and since the matrix elements V are real – see (9) – the quartic terms of the Hamiltonian expressed in terms of the hole-operators have the same form as the original Hamiltonian in terms of electron operators.
As for the quadratic terms it can be shown by a somewhat lengthy calculation, see for example Chapter 14 of Slaters textbook [3], that they can be brought to the form $C_1 n + C_2$ with real constants C_1 and C_2 and n the number of holes. For fixed n this is just a constant shift.
This theorem shows that the energies of the d^8 multiplets are, up to an additive constant, identical to those of the d^2 multiplets. Some terms in the Hamiltonian which will be discussed later do not remain invariant under the particle-hole transformation but change sign.

2.3 Solution of the Coulomb problem by exact diagonalization

We now describe how the problem of the partly filled $3d$-shell can be solved numerically, using the method of exact diagonalization. As already noted this may also be viewed as first order degenerate perturbation theory with respect to the Coulomb interaction between the electrons within a given shell. Our basis states (1) obviously correspond to all possible ways of distributing n electrons over the 10 spin-orbitals of the $3d$-shell (two spin directions for each $m \in \{-2, -1 \ldots 2\}$). As shown in Fig. 2 we can code each of these basis states by an integer $0 \le i \le 2^{10}$. If we really use all these integers we are actually treating all states with

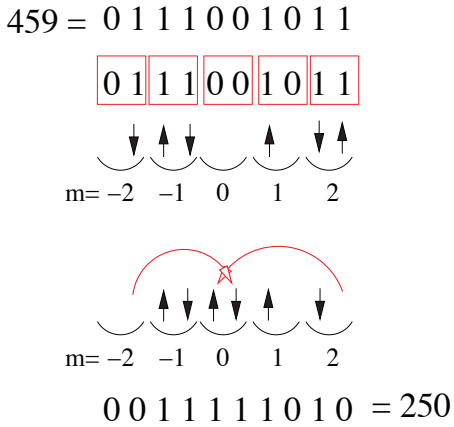

Fig. 2: *The coding of basis states by integers and a scattering process.*

$0 \leq n \leq 10$ simultaneously but this will be convenient for latter generalizations. Next, for a given initial state $|\nu_1, \nu_2, \ldots \nu_n\rangle$ we can let the computer search for all possible transitions of the type shown in Fig. 2 and compute the corresponding matrix elements from (9) using, say, the $c^k(lm; l'm')$ copied from Slater's textbook and some given R^0, R^2 and R^4. Let us consider the following matrix element

$$\langle 0|c_{\mu_n} \ldots c_{\mu_1}\ V(\lambda_1, \lambda_2, \lambda_3, \lambda_4)\ c^\dagger_{\lambda_1} c^\dagger_{\lambda_2} c_{\lambda_3} c_{\lambda_4}\ c^\dagger_{\nu_1} c^\dagger_{\nu_2} \ldots c^\dagger_{\nu_n}|0\rangle.$$

For this to be nonzero, the operators $c^\dagger_{\lambda_3}$ and $c^\dagger_{\lambda_4}$ must be amongst the $c^\dagger_{\nu_i}$, otherwise the annihilation operators in the Hamiltonian could be commuted to the right where they annihilate $|0\rangle$. In order for these pairs of operators to cancel each other, c_{λ_4} must first be commuted to the position right in front of $c^\dagger_{\lambda_4}$. If this takes n_4 interachanges of Fermion operators we get a Fermi sign of $(-1)^{n_4}$. Bringing next c_{λ_3} right in front of $c^\dagger_{\lambda_3}$ by n_3 interchanges of Fermion operators gives a sign of $(-1)^{n_3}$. Next, the creation operators $c^\dagger_{\lambda_1}$ and $c^\dagger_{\lambda_2}$ have to be commuted to the right to stand at their proper position as required by the ordering convention – see the discussion after (1). If this requires an additional number of Fermion interchanges n_2 for $c^\dagger_{\lambda_2}$ and and n_1 for $c^\dagger_{\lambda_1}$ there is an additional Fermi sign of $(-1)^{n_1+n_2}$. The total matrix element for this transition then is $(-1)^{n_1+n_2+n_3+n_4} V(\lambda_1, \lambda_2, \lambda_3, \lambda_4)$. The correct Fermi sign thereby is crucial for obtaining correct results and must be computed by keeping track of all necessary interchanges of Fermion operators. This is perhaps the trickiest part in implementing the generation of the Hamilton matrix or any other operator as a computer program.

Once the matrix has been set up it can be diagonalized numerically. Thereby it is a good check to evaluate the expectation values of the square of the orbital angular momentum and spin, $\boldsymbol{L}^2$ and $\boldsymbol{S}^2$, which also allow to assign the standard term symbols. The operator of orbital angular momentum can be written down by noting that the only nonvanishing matrix elements of the spin raising/lowering operator are $\langle l, m \pm 1|L^\pm|l, m\rangle = \sqrt{(l \mp m)(l \pm m + 1)}$ [5] whence

$$\begin{aligned} L^z &= \sum_{m=-l}^{l} \sum_{\sigma}\ m\ c^\dagger_{l,m,\sigma} c_{l,m,\sigma}, \\ L^+ &= \sum_{m=-l}^{l-1} \sum_{\sigma}\ \sqrt{(l-m)(l+m+1)}\ c^\dagger_{l,m+1,\sigma} c_{l,m,\sigma}, \end{aligned}$$

and similar for $L^- = (L^+)^+$. If $|\Psi\rangle$ then is a normalized eigenstate, that means a linear combination of basis states like (1), we define $|\Psi_1\rangle = L^z|\Psi\rangle$, $|\Psi_2\rangle = L^+|\Psi\rangle$ and $|\Psi_3\rangle = L^-|\Psi\rangle$ whence $\langle\Psi|\boldsymbol{L}^2|\Psi\rangle = \langle\Psi_1|\Psi_1\rangle + \frac{1}{2}(\langle\Psi_2|\Psi_2\rangle + \langle\Psi_3|\Psi_3\rangle)$. The procedure for $\boldsymbol{S}^2$ is completely analogous. The resulting expectation values $\langle\boldsymbol{L}^2\rangle$ and $\langle\boldsymbol{S}^2\rangle$ first have to assume the proper quantized values $L(L+1)$ and $S(S+1)$ with integer L and half-integer S and secondly have to be the same for *all* eigenfunctions belonging to a given degenerate eigenvalue. This – and the proper level of degeneracy of each eigenvalue – provides a stringent test for the correctness of the program.

Table 1 gives the resulting multiplet energies for d^8 and d^7, the resulting L and S for each multiplet, as well as the degeneracy n. The values of the R^k parameters have been calculated by using Hartree-Fock wave functions for Ni^{2+} and Co^{2+} in (7). The energy of the lowest

E	S	L	n	Term	E	S	L	n	Term
0.0000	1	3	21	^3F	0.0000	3/2	3	28	^4F
1.8420	0	2	5	^1D	1.8000	3/2	1	12	^4P
1.9200	1	1	9	^3P	2.1540	1/2	4	18	^2G
2.7380	0	4	9	^1G	2.7540	1/2	5	22	^2H
13.2440	0	0	1	^1S	2.7540	1/2	1	8	^2P
					3.0545	1/2	2	10	^2D
					4.5540	1/2	3	14	^2F
					9.9774	1/2	2	10	^2D

Table 1: *Energies of the d^8 multiplets calculated with $R^2 = 10.479\ eV$, $R^4 = 7.5726\ eV$ (Left), and energies of the d^7 multiplets calculated with $R^2 = 9.7860\ eV$, $R^4 = 7.0308\ eV$ (Right).*

multiplet is taken as the zero of energy and it turns out that all *energy differences* depend only on R^2 and R^4. Note the increasing complexity of the level schemes with increasing number of holes in the d-shell. Moreover, the multiplets do span a range of several eV. Finally, the Table shows that the ground states indeed comply with the first two of Hund's rules: they have maximum spin and maximum orbital angular momentum for this spin. It can be shown this is indeed always the case as long as one uses Coulomb and exchange integrals with the correct, i.e. positive, sign [3, 4].

2.4 Special case: Diagonal matrix elements

As will become apparent later, the diagonal elements $\langle\nu|H_1|\nu\rangle$ are of particular importance, so we give explicit expressions for them. We have seen that in a matrix element of H_1 $n-2$ creation operators in the ket $|\nu\rangle = |\nu_1, \nu_2, \ldots \nu_n\rangle$ must be simply cancelled by their Hermitean conjugate in the bra $\langle\nu|$ without ever 'touching' the Hamiltonian. We may then think of the remaining two Fermion operators, which are the ones which *are* paired with Fermion operators in the Hamiltonian, as having been commuted to the first and second position in the ket. This will give uns a Fermi sign, but in a diagonal matrix element this Fermi sign is the same for the ket and for the bra and cancels. Accordingly the $n-2$ creation and annihilation operators in the ket and bra which are paired with their own Hermitean conjugate can be simply ignored. It follows, that it is sufficient to compute the diagonal matrix element of H_1 between products of only two Fermion operators. Using (2) one finds

$$\begin{aligned}\langle 0|c_{\nu_2}c_{\nu_1}\ H_1\ c^\dagger_{\nu_1}c^\dagger_{\nu_2}|0\rangle &= \frac{1}{2}\left[V(\nu_1,\nu_2,\nu_2,\nu_1)+V(\nu_2,\nu_1,\nu_1,\nu_2)\right.\\ &\qquad \left.-V(\nu_1,\nu_2,\nu_1,\nu_2)-V(\nu_2,\nu_1,\nu_2,\nu_1)\right]\\ &= V(\nu_1,\nu_2,\nu_2,\nu_1)-V(\nu_1,\nu_2,\nu_1,\nu_2).\end{aligned}$$

Here the identity $V(\nu_1,\nu_2,\nu_3,\nu_4) = V(\nu_2,\nu_1,\nu_4,\nu_3)$, which follows from exchanging the integration variables $x \leftrightarrow x'$ in (2), has been used. The second term in the last line is called the

exchange integral and is different from zero only if $\sigma_1 = \sigma_2$. From (9) we have

$$\begin{aligned} V(\nu_1,\nu_2,\nu_2,\nu_1) &= \sum_{k=0}^{\infty} c^k(l_1m_1;l_1,m_1)\; c^k(l_2m_2;l_2,m_2)\; R^k(n_1l_1,n_2l_2,n_2l_2,n_1l_1), \\ V(\nu_1,\nu_2,\nu_1,\nu_2) &= \delta_{\sigma_1\sigma_2} \sum_{k=0}^{\infty} c^k(l_1m_1;l_2,m_2)\; c^k(l_1m_1;l_2,m_2)\; R^k(n_1l_1,n_2l_2,n_1l_1,n_2l_2). \end{aligned}$$

It is customary to introduce the following abbreviations

$$\begin{aligned} a^k(lm;l'm') &= c^k(lm;lm)\;\; c^k(l'm';l'm') \\ b^k(lm;l'm') &= c^k(lm;l'm')\; c^k(lm;l'm') \\ F^k(nl;n'l') &= R^k(nl,n'l',n'l',nl) \\ G^k(nl;n'l') &= R^k(nl,n'l',nl,n'l') \end{aligned}$$

The F^k and G^k are called Slater-Condon parameters. It can be easily verified using (7) that F^k is a Coulomb-integral whereas G^k is an exchange integral. For the case of a partly filled d-shell all n_i and l_i are equal so for each k there is only one F^k and one G^k and, in fact, $G^k = F^k$. The a^k and b^k are listed for example in Appendix 20a of Slater's textbook [3] or in Appendix B of the lecture notes [6].

Finally, since ν_1 and ν_2 can be any two out of the n Fermion operators in the ket, the total diagonal matrix element of H_1 is obtained by summing over all $\frac{n(n-1)}{2}$ pairs:

$$\langle\nu|H_1|\nu\rangle = \sum_{i<j} \sum_{k=0}^{\infty} \left(a^k(l_im_i;l_jm_j)\; F^k - \delta_{\sigma_i\sigma_j}\; b^k(l_im_i;l_jm_j)\; G^k \right) \tag{11}$$

As will be seen in the next paragraph, this formula is sufficient for the analytical calculation of multiplet energies.

2.5 Analytical calculation of multiplet energies by diagonal sum-rule

The exact diagonalization procedure outlined above can be used to obtain all eigenenergies and the corresponding eigenstates of the Coulomb problem. It is a flexible numerical method of solution into which crystalline electric field, hybridization with ligand orbitals, spin-orbit coupling, and Coulomb interaction with holes in core shells, which is important for the discussion of X-ray absorption spectra, can be incorporated easily. On the other hand, multiplet theory was invented during the 1920's to explain the spectra of free atoms or ions, and at that time computers were not available. It turns out, however, that despite the apparent complexity of the problem the energies of the multiplets can be obtained analytically and this will be explained in the following.

The first ingredient is the so-called diagonal sum-rule. This is simply the well-known theorem that the sum of the eigenvalues of a Hermitean matrix H is equal to its trace $tr(H) = \sum_i H_{ii}$. This follows immediately by noting that the trace of a matrix is invariant under basis transformations, i.e., $tr(H) = tr(UHU^{-1})$ for any unitary matrix U. By choosing U to be the matrix which transforms to the basis of eigenvectors of H the diagonal sum-rule follows.

Next, one uses the fact that the Hamilton matrix is block-diagonal, with blocks defined by their values of L^z and S^z. The diagonal sum-rule then can be applied for each of the blocks separately. In addition, the dimension of these blocks decreases as L^z and S^z approach their maximum values so that the number of multiplets contained in a given block decreases.
As an example for the procedure let us consider a p^2 configuration (by particle-hole symmetry this is equivalent to a p^4 configuration). We write the Fermion operators in the form $c_{l,m,\sigma}$, i.e., we suppress the principal quantum number n. Since we have 6 possible states for a single p-electron – three m-values with two spin directions per m-value – we have 15 states for two electrons. The triangular condition implicit in the Gaunt coefficients now restricts the multipole order k to be ≤ 2. Again, only even k contribute, so that we have two Slater-Condon parameters, F^0 and F^2. The following Table which is taken from Slater's textbook [3] gives the values of the coefficients $a^k(1,m;1,m')$ and $b^k(1,m;1,m')$: We first consider the sector with $S^z = 1$.

m	m'	a^0	$25a^2$	b^0	$25b^2$
±1	±1	1	1	1	1
±1	0	1	-2	0	3
0	0	1	4	1	4
±1	∓1	1	1	0	6

Table 2: *The coefficients a^k and b^k for two p-electrons.*

The highest possible L^z is $L^z = 1$ which is obtained for a single state, $|1\rangle = c^\dagger_{1,0,\uparrow} c^\dagger_{1,1,\uparrow}|0\rangle$. We can conclude that one of the multiplets is ${}^3P$ and its energy is equal to the diagonal matrix element of $|1\rangle$ which by (11) is

$$E({}^3P) = \sum_{k\in\{0,2\}} \left(a^k(1,1;1,0) - b^k(1,1;1,0)\right) F^k = F^0 - \frac{5}{25}F^2.$$

We proceed to the sector $S^z = 0$. Here the highest possible L^z is $L^z = 2$ again obtained for only single state namely $c^\dagger_{1,1,\downarrow} c^\dagger_{1,1,\uparrow}|0\rangle$. We conclude that we also have ${}^1D$ with energy

$$E({}^1D) = \sum_{k\in\{0,2\}} a^k(1,1;1,1)\, F^k = F^0 + \frac{1}{25}F^2.$$

The two multiplets that we found so far, ${}^1D$ and ${}^3P$, comprise $5 + 9 = 14$ states - we thus have just one state missing, which can only be ${}^1S$. To find its energy, we need to consider the sector $S^z = 0$ and $L^z = 0$. There are three states in this sector: $c^\dagger_{1,0,\downarrow} c^\dagger_{1,0,\uparrow}|0\rangle$, $c^\dagger_{1,-1,\uparrow} c^\dagger_{1,1,\downarrow}|0\rangle$ and $c^\dagger_{1,-1,\downarrow} c^\dagger_{1,1,\uparrow}|0\rangle$. Two out of the three eigenvalues of the 3×3 Hamiltonian in the basis spanned by these states must be $E({}^3P)$ and $E({}^1D)$, because these multiplets also have members with $S^z = 0$ and $L^z = 0$. To obtain $E({}^1S)$ we accordingly compute the sum of the diagonal elements of the 3×3 matrix and set

$$\begin{aligned} E({}^3P) + E({}^1D) + E({}^1S) &= \sum_{k\in\{0,2\}} \left(a^k(1,0;1,0) + 2\, a^k(1,-1;1,1)\right) F^k \\ \rightarrow\ E({}^1S) &= F^0 + \frac{10}{25}F^2. \end{aligned}$$

This example shows the way of approach for multiplet calculations using the diagonal sum-rule: one starts out with a state with maximum L^z or S^z for which there is usually only a single basis state. This basis state belongs to some multiplet whose energy simply equals the 'diagonal element' of the 1×1 Hamiltonmatrix. Then one proceeds to lower S^z and/or L^z and obtains energies of additional multiplets by calculating the trace of the respective block of the Hamilton matrix and using the known energies of multiplets with higher L^z or S^z. It turns out that in this way the energies of *all* multiplets involving s, p, d, or f electrons can be expressed in terms of the Slater-Condon parameters by analytical formulas. A rather complete list can be found for example in the Appendices 21a and 21b of the textbook by Slater [3].

One point which may be helpful when reading the literature is the following: for the special case of a partly filled d-shell many authors use the so-called Racah parameters A, B and C instead of the 3 Slater-Condon parameters F^0, F^2 and F^4. The rule for conversion is simple:

$$A = F^0 - \frac{49}{441}F^4 \qquad B = \frac{1}{49}F^2 - \frac{5}{441}F^4 \qquad C = \frac{35}{441}F^4.$$

The Racah-parameters have been introduced because the analytical formulas for the energies of the multiplets of d^n as derived by the diagonal sum-rule look nicer when they are expressed in terms of them. For example Griffith [4] gives multiplet energies in terms of the Racah-parameters in his Table 4.6.

As stated above, multiplet theory was originally developed to discuss the spectra of atoms or ions in the gas phase. The question then arises, as to what are the values of the Slater-Condon parameters. Of course one might attempt to compute these parameters using, e.g., Hartree-Fock wave functions in the expression (7). It turns out, however, that very frequently the number of multiplets considerably exceeds the number of relevant Slater-Condon parameters. In the case of the p^2 configuration we had three multiplets, ^3P, ^1D and ^1S, but only two Slater-Condon parameters F^0 and F^2. This would suggest to obtain the values of the Slater-Condon parameters by fit to the spectroscopic data and the textbook by Slater [3] contains a vast amount of data which are analyzed in this way. For the p^2 configuration we restrict ourselves to a simple cross check. Using the above formulae and eliminating the F's we find:

$$r = \frac{E(^1S) - E(^1D)}{E(^1D) - E(^3P)} = \frac{3}{2}. \tag{12}$$

This relation should be obeyed by all ions with two p-electrons outside filled shells, e.g., the series C, N^{1+} and O^{2+} or two holes in a filled p-shell such as the series O and F^+. The energies of these multiplets have been measured with high precision and are available in databases [7] and Table 3 shows the resulting values of r. For the first row elements the deviation is about 25%, for the second row only about 5%. We recall that multiplet theory in its simplest form corresponds to first order degenerate perturbation theory, where H_0 contains the orbital energies and H_1 the Coulomb interaction between electrons in one shell. It therefore ignores various scattering processes which may lead to inaccuracies.

p^2	C	N^+	O^{2+}	Si	P^+	S^{2+}
	1.124	1.134	1.130	1.444	1.430	1.399
p^4	O	F^+	S	Cl^+		
	1.130	1.152	1.401	1.392		

Table 3: *The ratio (12) for various Atoms and Ions with p^2 and p^4 configurations ouside a closed shell.*

2.6 Spin-orbit coupling

As the last problem in this section on free atoms or ions we briefly discuss spin-orbit coupling. The corresponding Hamiltonian is

$$H_{SO} = \lambda_{SO} \sum_{i=1}^{n} \boldsymbol{L}_i \cdot \boldsymbol{S}_i = \lambda_{SO} \sum_{i=1}^{n} \left(L_i^z S_i^z + \frac{1}{2}(L_i^+ S_i^- + L_i^- S_i^+) \right).$$

where $\boldsymbol{L}_i$ ($\boldsymbol{S}_i$) are the operator of orbital (spin) angular momentum of the i^{th} electron. The first term on the right hand side can be translated into second quantized form easily:

$$H_{SO}^{\parallel} = \frac{\lambda_{SO}}{2} \sum_{m=-l}^{l} m \, (c_{l,m,\uparrow}^{\dagger} c_{l,m,\uparrow} - c_{l,m,\downarrow}^{\dagger} c_{l,m,\downarrow}). \tag{13}$$

As regards the transverse part, we note [5] that the only nonvanishing matrix elements of the orbital angular momentum raising/lowering operator are $\langle l, m \pm 1 | l^{\pm} | l, m \rangle = \sqrt{(l \mp m)(l \pm m + 1)}$ whence

$$H_{SO}^{\perp} = \frac{\lambda_{SO}}{2} \sum_{m=-l}^{l-1} \sqrt{(l-m)(l+m+1)} \, (c_{l,m+1,\downarrow}^{\dagger} c_{l,m,\uparrow} + c_{l,m,\uparrow}^{\dagger} c_{l,m+1,\downarrow}). \tag{14}$$

It is easy to see that H_{SO} changes sign under the particle-hole transformation (10). This means that, e.g., the multiplets of d^n and d^{10-n} have the same Coulomb energies, but the splitting due to spin-orbit coupling is opposite. Since the value of λ_{SO} is positive [5], this means that for less than half-filled shells the ground state has the minimum value of J possible, whereas for more than half-filled shells the ground state has the maximum possible value of J, i.e., Hund's third rule.

Spin-orbit coupling can be implemented rather easily into the numerical procedure, the main difficulty again is keeping track of the Fermi sign. Due to the fact that neither L^z nor S^z are conserved anymore the corresponding reduction of the Hilbert space is no longer possible. In transition metal compounds the spin-orbit coupling constant λ_{SO} for the $3d$ shell is rather small, of order $\lambda_{SO} \approx 0.05$ eV. Still, if the ground state of a given ion has a nonvanishing spin, spin orbit coupling will determine how this spin orients itself in an ordered phase, i.e., *magnetic anisotropy*. In the rare earth elements spin-orbit coupling in the $4f$ shell is of comparable magnitude as the Coulomb repulsion. There, taking spin-orbit coupling into account is mandatory.

3 Effects of the environment in the crystal

So far we have considered a single ion in vacuum. Clearly, one might ask if the results obtained in this limit retain any relevance once the ion is embedded into a solid and this will be discussed in the following. It will become apparent that the small spatial extent of the $3d$ radial wave function $R_{3,2}(r)$ strongly suppresses any effect of the environment in a solid, so that in many cases the main effect of embedding the ion into a solid is the partial splitting of the multiplets of the free ion.

In many transition metal compounds the $3d$ ions are surrounded by an approximately octahedral or tetrahedral 'cage' of nonmetal ions such as Oxygen, Sulphur, Arsenic. An example for octahedral coordination is provided by the perovskite structure. These nearest neighbor ions, which will be called 'ligands' in the following, have a twofold effect: first, they produce a static electric field – the so-called *crystalline electric field* or CEF – and second there may be *charge transfer* that means electrons from a filled ligand orbital may tunnel into a $3d$-orbital of the transition metal ion due to the overlap of the respective wave functions.

3.1 Crystalline electric field

Let us first consider the crystalline electric field, whereby we model the ligands simply by n_c point charges $Z_i e$ at the positions $\boldsymbol{R}_i$. We denote the electrostatic potential due to these point charges by $V_{\mathrm{CEF}}(\boldsymbol{r})$ and find for the respective Hamiltonian [2]

$$\begin{aligned} H_{\mathrm{CEF}} &= \sum_{i,j} V_{\mathrm{CEF}}(\nu_i,\nu_j)\; c^\dagger_{\nu_i} c_{\nu_j}, \\ V_{\mathrm{CEF}}(\nu_1,\nu_2) &= \int dx\; \psi^*_{\nu_1}(x)\; V_{\mathrm{CEF}}(\boldsymbol{r})\; \psi_{\nu_2}(x). \end{aligned} \tag{15}$$

The radial dependence of the $3d$ wave functions $\psi_\nu(x)$ is given by $R_{3,2}(r)$ which differs appreciably from zero only in a narrow range $r \leq r_{3d}$. Assuming that $r_{3d} < R_i$ for all i we obtain $V_{\mathrm{CEF}}(\boldsymbol{r})$ from the multipole expansion (4)

$$\begin{aligned} V_{\mathrm{CEF}}(\boldsymbol{r}) &= -\frac{Z_{av}e^2}{R_{av}} \sum_{k=0}^{\infty} \sum_{m=-k}^{k} \gamma_{k,m} \left(\frac{r}{R_{av}}\right)^k \sqrt{\frac{4\pi}{2k+1}}\, Y_{k,m}(\Theta,\phi), \\ \gamma_{k,m} &= \sqrt{\frac{4\pi}{2k+1}} \sum_{i=1}^{n_c} \frac{Z_i}{Z_{av}} \left(\frac{R_{av}}{R_i}\right)^{k+1} Y^*_{k,m}(\Theta_i,\phi_i). \end{aligned} \tag{16}$$

Here we have introduced the avergage distance and charge of the ligands, R_{av} and Z_{av}. In calculating the matrix elements $V_{\mathrm{CEF}}(\nu_1,\nu_2)$ the integral over the polar angles (Θ,ϕ) again gives a Gaunt coefficient. For a d-shell it again follows from the triangular condition that $k \leq 4$ and from parity that k be even. The term with $k = 0$ gives only a constant shift and can be

omitted so that

$$\begin{aligned} V_{\mathrm{CEF}}(\nu_1,\nu_2) &= \sum_{k\in\{2,4\}} \gamma_{k,m_1-m_2}\; c^k(2,m_1;2,m_2)\; I_k, \\ I_k &= -\frac{Z_{av}e^2}{R_{av}}\;\left(\frac{r_{3d}}{R_{av}}\right)^k \int_0^\infty d\rho\;\rho^{k+2}\;\tilde{R}^2_{nl}(\rho), \end{aligned}$$

with the rescaled and normalized radial wave function $\tilde{R}_{nl}(\rho) = r_{3d}^{3/2} R_{nl}(\rho r_{3d})$. Note that I_k has the correct dimension of energy and that the integral is dimensionless and of order unity. For $r_{3d}/R_{av} \ll 1$, which we expect to hold due to the small extent of the $3d$ radial wave function, the sum can be terminated after the lowest $k > 0$ for which there is a nonvanishing contribution, i.e., where $\gamma_{k,m}$ does not vanish. As was the case for the Coulomb interaction, the CEF can be described by very few – in fact only one if only the lowest order in r_{3d}/R_{av} is kept – parameters which depend on the radial wave function $R_{3,2}(r)$. These parameters again are frequently fitted to experiment.

The actual form of the matrix elements depends on the geometry of the cage of ligands via the sum in $\gamma_{k,m}$. For the frequently considered case of an ideal octahedron of identical charges where $R_i = R = R_{av}$ and $Z_i = Z = Z_{av}$ one finds $\gamma_{k,m} = 0$ for $0 < k < 4$ and

$$\begin{aligned} \gamma_{4,4} &= \sqrt{\frac{35}{8}} \\ \gamma_{4,0} &= \sqrt{\frac{49}{4}} \end{aligned} \tag{17}$$

as well as $\gamma_{4,-4} = \gamma_{4,4}$. Using the tabulated values of the $c^4(2,m;2,m')$ (see Appendix), $V_{\mathrm{CEF}}(\nu_1,\nu_2)$ can be written down as a matrix in the indices m_1 and m_2:

$$V_{\mathrm{CEF}}(\nu_1,\nu_2) = \frac{I_4}{6}\begin{pmatrix} 1 & 0 & 0 & 0 & 5 \\ 0 & -4 & 0 & 0 & 0 \\ 0 & 0 & 6 & 0 & 0 \\ 0 & 0 & 0 & -4 & 0 \\ 5 & 0 & 0 & 0 & 1 \end{pmatrix}. \tag{18}$$

This matrix has the eigenvalues I_4 (twofold degenerate) and $-2I_4/3$ (threefold degenerate). If the ligands are O^{2-} ions, $Z = -2$ and $I_4 > 0$. For historical reasons the splitting between the eigenvalues is frequently called $10Dq$ so that in our point charge model $Dq = I_4/6$. The two eigenfunctions belonging to the eigenvalue $6Dq$ are the real valued e_g-type spherical harmonics, the three eigenvalues belonging to the eigenvalue $-4Dq$ are the real valued t_{2g}-type spherical harmonics, see the lecture by E. Pavarini. Lastly, we note that H_{CEF} changes sign under the particle-hole transformation (10). In a solid the multiplets of d^n and d^{10-n} thus are split in opposite ways.

The implementation of the CEF in an exact diagonalization program is rather obvious. As an example Fig. 3 shows the eigenenergies of the d^8 and d^7 configuration with Coulomb interaction and octahedral CEF as $10Dq$ is increasing. Such plots of crystal field levels versus $10Dq$ are

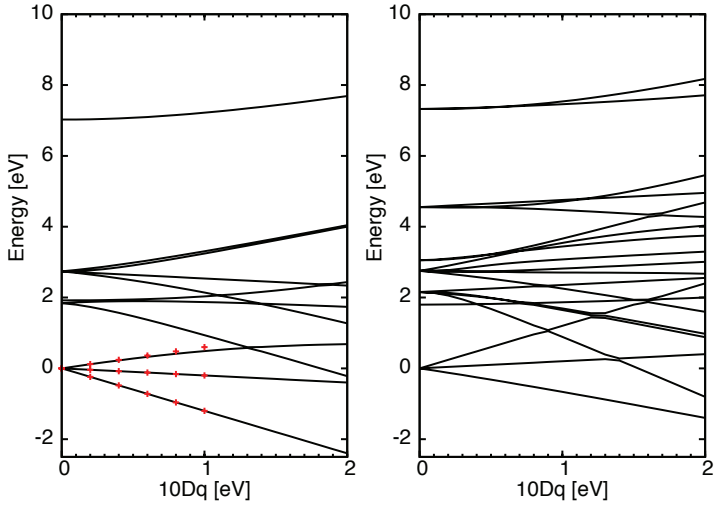

Fig. 3: *Examples for Tanabe-Sugano diagrams: the splitting of multiplets of d^8 (left) and d^7 (right) for increasing $10Dq$. The Slater-Condon parameters have the values given in Table 2. The symbols in the diagram for d^8 give the energies calculated analytically by use of the Wigner-Eckart theorem.*

called Tanabe-Sugano diagrams after the authors who first derived them [8]. One realizes that the highly degenerate multiplets of the free ion are split into several levels of lower degeneracy by the CEF, which is to be expected for a perturbation which lowers the symmetry. Note that the components into which a given multiplets splits up all have the same spin as the multiplet itself. This is because the spin of an electron does not 'feel' an electrostatic potential – or, more precisely, because the operator of total spin commutes with any operator which acts only on the real-space coordinates $\boldsymbol{r}_i$ of the electrons. Only the introduction of spin-orbit coupling, as discussed in the preceding section, leads to a coupling between spin and environment of a given ion and thus may lead to magnetic anisotropy.

3.2 Analytical results by application of the Wigner-Eckart theorem

In addition to the purely numerical approach, many results can be obtained by invoking the Wigner-Eckart theorem. To formulate this theorem we first need to define a tensor operator. Let $\boldsymbol{J}$ be some angular momentum operator with eigenfunctions $|j,m\rangle$. This means that the three components of $\boldsymbol{J}$ have to obey the commutation relations $[J_\alpha, J_\beta] = i\epsilon_{\alpha\beta\gamma}J_\gamma$. It follows [5] that the kets $|j,m\rangle$ obey $\boldsymbol{J}^2|j,m\rangle = j(j+1)|j,m\rangle$, $J^z|j,m\rangle = m|j,m\rangle$ and $J^\pm|j,m\rangle = \sqrt{(j\mp m)(j\pm m+1)}|j,m\pm 1\rangle$.
A rank-j tensor operator then is a set of $2j+1$ operators $O_{j,m}$ which obey $[J^z, O_{j,m}] = mO_{j,m}$ and $[J^\pm, O_{j,m}] = \sqrt{(j\mp m)(j\pm m+1)}O_{j,m\pm 1}$. This means that these operators transform amongst themselves like eigenfunctions of angular momentum. Note that a tensor operator always needs to refer to some angular momentum operator. As an example we choose $\boldsymbol{J}$ to be the orbital angular momentum of a single particle. Then, the set of $2l+1$ spherical harmonics $Y_{l,m}(\Theta,\phi)$ forms a rank-l tensor operator. Namely by acting with a component of $\boldsymbol{J}$ onto

the product $Y_{l,m}(\Theta,\phi)|\Psi(r,\Theta,\phi)\rangle$ with an arbitrary wave function Ψ, the differential operators included in $\boldsymbol{J}$ will always produce two terms $JY_{l,m}|\Psi\rangle = (JY_{l,m})|\Psi\rangle + Y_{l,m}J|\Psi\rangle$ so that $[J,Y_{l,m}]|\Psi\rangle = (JY_{l,m})|\Psi\rangle$ and since $|\Psi\rangle$ is arbitrary the tensor operator property of $Y_{l,m}$ follows. In exactly the same way, if $\boldsymbol{J}$ is the total angular momentum of n electrons the $2l+1$ functions $\sum_{i=1}^{n} Y_{l,m}(\Theta_i,\phi_i)$ form a rank-l tensor operator as well. For a $3d$ shell with n electrons the operator describing the CEF is $H_{\mathrm{CEF}} = \sum_{i=1}^{n} V_{\mathrm{CEF}}(\boldsymbol{r}_i)$ with $V_{\mathrm{CEF}}(\boldsymbol{r})$ given by (16). H_{CEF} therefore is a sum of components of a tensor operator and this property makes the Wigner-Eckart theorem useful in the present case.

The theorem itself states that the matrix elements of *any two* rank-j tensor operators between eigenstates of their respective angular momentum operator are proportional to one another, whereby the constant of proportionality is *independent of the values of* m

$$\langle\alpha,j',m'|O_{J,M}|\alpha,j,m\rangle = C(\alpha,\beta,j',j,J)\langle\beta,j',m'|\bar{O}_{J,M}|\beta,j,m\rangle.$$

The symbols α and β stand for some unspecified 'additional' quantum numbers. Note that neither m', nor M, nor m appear in the constant of proportionality C. The deeper reason for this theorem is that the dependence of the matrix elements on m', M and m is given solely by Clebsch-Gordan coefficients. More precisely, an alternative way of stating the theorem [5] is that

$$\langle\alpha,j',m'|O_{J,M}|\alpha,j,m\rangle = A(\alpha,j,j',J)\langle j'm'Jj|JMjm\rangle$$

where $\langle j'm'Jj|JMjm\rangle$ is a Clebsch-Gordan coefficient. The above version then follows with $C(\alpha,\beta,j,j',J) = A(\beta,j,j',J)/A(\alpha,j,j',J)$. The quantity $A(\alpha,j,j',J)$ is known as the reduced matrix element.

To illustrate the application of the theorem we now use it to calculate the splitting of the ${}^3F$ ground state multiplet of d^8, which is equivalent to d^2, in ideal octahedral coordination. On the left hand side we accordingly choose $|\alpha,j,m\rangle = |{}^3F,m\rangle$ where $|{}^3F,m\rangle$ is the member of the ${}^3F$ multiplet with $L^z = m$ and $S^z = 1$ (the value of S^z is arbitrary and the final results of course must not depend on this choice). The $|{}^3F,m\rangle$ are eigenfunctions of the total orbital momentum operator. For O_{JM} we choose $\sum_{i=1}^{n} V_{\mathrm{CEF}}(\boldsymbol{r}_i)$, where $V_{\mathrm{CEF}}(\boldsymbol{r})$ is the CEF potential (16) and the sum is over all n electrons. For ideal octahedral coordination this is a linear combination of components of a tensor operator of rank 4, see (16) and (17).

On the right hand side we choose $|\beta,j,m\rangle = Y_{3,m}(\Theta,\phi)$ and for the tensor operator $\bar{O}_{J,M}$ the expression

$$\tilde{V}_{\mathrm{CEF}}(\Theta,\phi) = \sum_{m=-4}^{4} \gamma_{4,m} Y_{4,m}(\Theta,\phi),$$

i.e., the dimensionless version of the CEF potential (16) but now *for a single particle*. The Wigner-Eckart theorem then tells us that the secular determinant of the CEF potential between the $|{}^3F,m\rangle$ is, up to a constant factor C, the same as the matrix $\langle Y_{3,m'}|\tilde{V}_{\mathrm{CEF}}|Y_{3,m}\rangle$. Above we found that the matrix elements of $\tilde{V}_{\mathrm{CEF}}$ are $\gamma_{4,m'-m}\ c^4(3,m';3,m)$ and using the tabulated

$c^4(3m;3m')$ (see Appendix) this becomes

$$\tilde{V}_{\rm CEF} = \frac{7}{66}\begin{pmatrix} 3 & 0 & 0 & 0 & \sqrt{15} & 0 & 0 \\ 0 & -7 & 0 & 0 & 0 & 5 & 0 \\ 0 & 0 & 1 & 0 & 0 & 0 & \sqrt{15} \\ 0 & 0 & 0 & 6 & 0 & 0 & 0 \\ \sqrt{15} & 0 & 0 & 0 & 1 & 0 & 0 \\ 0 & 5 & 0 & 0 & 0 & -7 & 0 \\ 0 & 0 & \sqrt{15} & 0 & 0 & 0 & 3 \end{pmatrix}. \tag{19}$$

Since we are not interested in constant factors we drop the factor of $7/66$. The matrix on the right hand side then can be decomposed into 2×2 blocks and we obtain the eigenvalues -12 (once), -2 (three times) and $+6$ (three times). The Wigner-Eckart theorem now tells us that the ${}^3F$ ground state multiplet of both d^2 and of d^8 splits up in the same way, namely into three levels, with degeneracies $1, 3$ and 3 and energies $-12C$, $-2C$ and $6C$.

To 'gauge' the calculation and determine the constant C we now need to evaluate the CEF energy of *one* particular state of the true ${}^3F$ multiplet. To that end we note that the CEF eigenstates originating from the ${}^3F$ multiplet are expressed in terms of the $|{}^3F,m\rangle$ in *exactly the same way* as the eigenstates of the matrix (19). By inspection of the matrix (19) we see, however, that the eigenvalue $+6$ has one particularly simple eigenvector, namely $(0,0,0,1,0,0,0)$. This corresponds to the state $|{}^3F,m=0\rangle$. This special state now can be calculated as follows: by starting with the member of ${}^3F$ with maximum m, namely $|{}^3F,3\rangle = c^\dagger_{2,1,\uparrow}c^\dagger_{2,2,\uparrow}|0\rangle$, acting repeatedly with L^- and normalizing we can work ourselves down to $m=0$:

$$\begin{aligned}
|{}^3F,3\rangle &= c^\dagger_{2,1,\uparrow}c^\dagger_{2,2,\uparrow}|0\rangle, \\
|{}^3F,2\rangle &= c^\dagger_{2,0,\uparrow}c^\dagger_{2,2,\uparrow}|0\rangle, \\
|{}^3F,1\rangle &= \left(\sqrt{\frac{2}{5}}\,c^\dagger_{2,0,\uparrow}c^\dagger_{2,1,\uparrow} + \sqrt{\frac{3}{5}}\,c^\dagger_{2,-1,\uparrow}c^\dagger_{2,2,\uparrow}\right)|0\rangle, \\
|{}^3F,0\rangle &= \left(\sqrt{\frac{4}{5}}\,c^\dagger_{2,-1,\uparrow}c^\dagger_{2,1,\uparrow} + \sqrt{\frac{1}{5}}\,c^\dagger_{2,-2,\uparrow}c^\dagger_{2,2,\uparrow}\right)|0\rangle.
\end{aligned}$$

From the Wigner-Eckart theorem we now know that the last state, $|{}^3F,0\rangle$, is an eigenstate of the Coulomb energy plus CEF. Accordingly, its CEF-energy is simply the expectation value $\langle{}^3F,0|H_{\rm CEF}|{}^3F,0\rangle$ with $H_{\rm CEF}$ given by (15) with (18). This is easily calculated and we obtain the constant C as:

$$6C = \frac{I_4}{6}\left(\frac{4}{5}\,(-8) + \frac{1}{5}\,2\right) = -I_4,$$

so that $C = -I_4/6 = -Dq$. We thus find that in octahedral coordination ${}^3F$ of d^2 splits into three levels with $E=-6Dq$ (3-fold degenerate), $E=2Dq$ (3-fold) and $E=12Dq$ (1-fold). For d^8 particle-hole symmetry tells us that the sign of the CEF splitting has to be inverted whence we find the energies and degeneracies $E=-12Dq$ (1-fold), $E=-2Dq$ (3-fold) and $E=6Dq$ (3-fold). This splitting of the lowest multiplet can be nicely seen in Fig. 3. In the

result obtained by exact diagonalization the upper level with $E = 6Dq$ 'bends downward' for larger $10Dq$. The reason is that the CEF mixes the ${}^3F$ and ${}^3P$ multiplets and the resulting level repulsion for large $10Dq$ leads to the deviation from the linear behaviour, which gives only the asymptotic behaviour for $10Dq \to 0$. Note the tremendous simplification which occurs in this way, because the $|{}^3F, m\rangle$ actually are linear combinations of Slater-determinants (1) with coefficients which have to be obtained from diagonalizing the full Coulomb-Hamiltonian! Historically, by using the Wigner-Eckart theorem together with skilfull application of group theory, the energies and wave functions of transition metal ions in various coordinations in fact were calculated analytically and without the use of a computer. This is how the Tanabe-Sugano diagrams were obtained originally.

3.3 Charge transfer

We proceed to a discussion of charge transfer. This means that electrons can tunnel from ligand orbitals into $3d$ orbitals, so that the number of electrons in the d-shell fluctuates. To deal with this we need to enlarge our set of Fermion operators $c^\dagger_\nu / c_\nu$ by operators $l^\dagger_\mu / l_\mu$ which create/annihilate electrons in orbitals centered on ligands. The compound index μ for the ligand operators also must include the index i of the ligand: $\mu = (i, n, l, m, \sigma)$. The Hamiltonian then would read

$$H = \sum_{i,j} \left(t_{\nu_i,\mu_j}\ c^\dagger_{\nu_i} l_{\mu_j} + H.c. \right) + \sum_j \epsilon_{\mu_j} l^\dagger_{\mu_j} l_{\mu_j} + \sum_i \epsilon_{\nu_i} c^\dagger_{\nu_i} c_{\nu_i}. \tag{20}$$

The *hybridization integrals* t_{ν_i,μ_j} may be expressed in terms of relatively few parameters by using the famous *Slater-Koster tables*, see the lecture by E. Pavarini. For example, if only the p-orbitals of the ligands are taken into account, which applies to oxides of transition metals such as perovskites, there are just two relevant parameters, $V_{pd\sigma}$ and $V_{pd\pi}$. Estimates for these may be obtained from fits to LDA band structures. If electrons are allowed to tunnel between d-shell and ligand orbitals the site energies ϵ_{μ_j} become relevant as well. Estimating the d-shell site energies from LDA calculations is tricky due to the *double counting problem*: the energies of the d-orbitals extracted from band structure calculations involve the Hartree-potential, which is also included in the diagonal matrix elements of the multiplet Hamiltonian and thus must be subtracted in some way. Recently, considerable interest has emerged in the determination of such parameters.

The use of the Slater-Koster tables brings about a slight complication in that these are formulated in terms of the real-valued spherical harmonics $Y_\alpha(\Theta, \phi)$ which are linear combinations of the original $Y_{2,m}(\Theta, \phi)$. However, these sets of functions are related by a simple unitary transformation. We again specialize to the case where the ligands are oxygen ions which form an ideal octahedron with the transition metal ion in the center of gravity of the octahedron. In this case the number of relevant ligand orbitals can be reduced considerably. Namely, for each of the real-valued transition metal $3d$ orbitals $Y_\alpha(\Theta, \phi)$ there is precisely one linear combination of O $2p$ orbitals on the ligands, L_α, which hybridizes with them. The Hamiltonian then simplifies

to

$$H_{\rm hyb} = 2\,V_{pd\pi}\,\sum_{\alpha\in t_{2g}}\sum_{\sigma}\left(c^{\dagger}_{\alpha,\sigma}l_{\alpha\sigma}+H.c.\right)+\sqrt{3}\,V_{pd\sigma}\,\sum_{\alpha\in e_g}\sum_{\sigma}\left(c^{\dagger}_{\alpha,\sigma}l_{\alpha\sigma}+H.c.\right).$$

By inserting the unitary transformation $c^{\dagger}_{\alpha}=\sum_{m=-2}^{2}\,U_{\alpha,m}c^{\dagger}_{m,\sigma}$ to transform to the original complex spherical harmonics this is easily included into the formalism. In the exact diagonalization program this means that the number of orbitals has to be doubled, because we have the five combinations L_α, each of which can accomodate an electron of either spin direction. This leads to a quite drastic increase in the dimension of the Hilbert space but using, e.g., the Lanczos algorithm, see the lecture by E. Koch [9], the problem still is tractable. $H_{\rm hyb}$ then simply transfers electrons from ligand orbitals to d-orbitals and vice versa and is easy to implement.

4 Cluster calculation of photoemission and X-ray absorption spectra

In the preceding section we have discussed the general formalism for exact diagonalization of a cluster consisting of a transition metal ion and its nearest neighbor ions ('ligands'). Thereby the following terms were included into the Hamiltonian: the Coulomb repulsion between the electrons in the $3d$ shell, the electrostatic field produced by the ligands, charge transfer between the ligands and the transition metal d orbitals and, possibly, the spin orbit coupling in the $3d$ shell. By diagonalizing the resulting Hamilton matrix we can obtain the eigenfunctions $|\Psi_\nu\rangle$ and their energies E_ν and these can be used to simulate various experiments on transition metal compounds such as electron spectroscopy, optical spectroscopy, electron spin resonance or inelastic neutron scattering. It has turned out that these simulations are in fact spectacularly successful. In many cases calculated spectra can be overlayed with experimental ones and agree peak by peak. Nowadays complete packages for such cluster simulations are available, and these are used routinely for the interpretation of, e.g., electron spectroscopy [10]. This shows in particular that the multiplets of the free ion – suitably modified by the effects of crystalline electric field and charge transfer – persist in the solid and thus are essential for a correct description of transition metal compounds. In the following, we want to explain this in more detail and consider photoelectron spectroscopy. In this lecture only a very cursory introduction can be given, there are however several excellent reviews on the application of multiplet theory to the simulation of photoelectron spectroscopy [11–13].

In a valence-band photoemission experiment electromagnetic radiation impinges on the sample which then emits electrons – this is nothing but the well-known photo-electric effect. 'Valence band photoemission' means that the photoelectrons are ejected from states near the Fermi level so that, to simplest approximation, an ion in the solid undergoes the transition $d^n \rightarrow d^{n-1}$ (note that this ignores charge transfer, which in fact is quite essential!). What is measured is the current I of photoelectrons as a function of their kinetic energy E_{kin} and possibly the polar angles (Θ,ϕ) relative to the crystallographic axes of the sample. Frequently one measures the angle-integrated spectrum, obtained by averaging over (Θ,ϕ), or rather: measuring a polycrystalline

sample. A further parameter which strongly influences the shape of the spectrum $I(E_{kin})$ is the energy $h\nu$ of the incident photons. At sufficiently high $h\nu$ the photoionization cross-section for the transition metal $3d$-orbitals is significantly larger than for the other orbitals in the solid so that the photoelectrons in fact are emitted almost exclusively the $3d$-orbitals. This is often called XPS – for X-ray photoemission spectroscopy.

The theory of the photoemission process is complicated [14, 15] but with a number of simplifying assumptions one can show that the photocurrent $I(E_{kin})$ measured in an angle-integrated photoemission at high photon energy is proportional to the so-called single-particle spectral function

$$\begin{aligned} A(\omega) &= -\frac{1}{\pi Z}\Im \sum_{m=-2}^{2}\sum_{\mu} e^{-\beta E_\mu} \left\langle \Psi_\mu \left| c^\dagger_{3,2,m,\sigma} \frac{1}{\omega + (H - E_\mu) + i0^+} c_{3,2,m,\sigma} \right| \Psi_\mu \right\rangle \\ &= \frac{1}{Z}\sum_{m=-2}^{2}\sum_{\mu,\nu} e^{-\beta E_\mu} |\langle \Psi_\nu | c_{3,2,m,\sigma} | \Psi_\mu \rangle|^2 \delta(\omega + (E_\nu - E_\mu)). \end{aligned} \tag{21}$$

Here H is the Hamiltonian describing the solid, $|\Psi_\mu\rangle$ and E_μ denote the eigenstates of H with a fixed electron number N_e. Moreover $\beta = (k_B T)^{-1}$ where k_B is the Boltzmann constant, T the temperature, and $Z = \sum_\mu \; exp(-\beta E_\mu)$. The operator $c_{3,2,m,\sigma}$ removes an electron from a $3d$-orbital. In the thermodynamical limit the results will not depend on the position of the ion in the sample and accordingly we have suppressed the site index on $c_{3,2,m,\sigma}$. After removal of the electron the sample then remains in an eigenstate $|\Psi_\nu\rangle$ with $N_e - 1$ electrons and energy E_ν. The relation between E_{kin} and ω follows from energy conservation:

$$h\nu + E_\mu = E_{kin} + \Phi + E_\nu$$

The left and right hand sides of this equation are the energies of the system before (solid+photon) and after (solid + photo-electron) the photoemission process. Here Φ is the so-called work function, i.e., the energy needed to transverse the potential barrier at the surface of the solid (this needs to be introduced because the measured kinetic energy E_{kin} is the one *in vacuum*). It follows from the δ function in the second line of (21) that we have to put $I(E_{kin}) \propto A(E_{kin} + \Phi - h\nu)$.

We now make the approximation, introduced by Fujimori and Minami [16], and evaluate $A(\omega)$ by replacing the energies and wave functions of the solid by those of the octahedral cluster. If we moreover let $T \to 0$ the sum over μ becomes a sum over the m denerate gound states of the cluster and $e^{-\beta E_\mu}/Z \to 1/m$. The underlying assumption is that the coupling of the clusters to a solid will predominantly broaden the ionization states of the cluster to 'bands' of not too large bandwidth. This broadening is usually simulated by replacing the δ-functions by Lorentzians. To compare to a measured spectrum the calculated spectrum often is convoluted with a Gaussian to simulate the finite energy resolution of the photoelectron detector. The upper version of the equation (21) is suitable for using the Lanczos algorithm whereas the lower one is better suited if the eigenstates and energies have been obtained by full diagonalization of the eigenvalue problem.

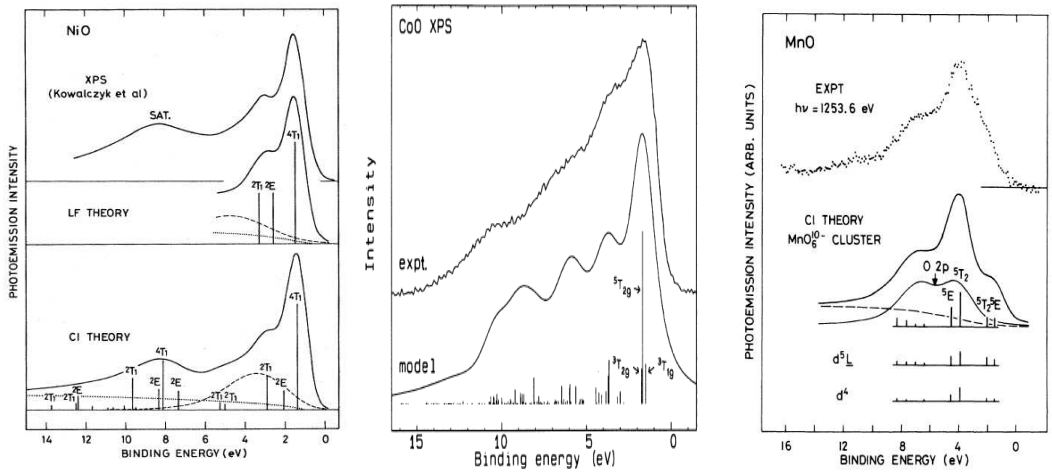

Fig. 4: *Comparison of experimental valence band photoemission spectra and results from cluster calculations: NiO (left), CoO(center), MnO(right). Reprinted with permission from [16], Copyright 1984, from [17], Copyright 1991, and from [18], Copyright 1990 by the American Physical Society.*

Fig. 4 shows various examples from the literature where measured XPS-spectra are compared to spectra calculated by the procedure outlined above. The sticks in some of the theoretical spectra mark the final state energies E_ν and are labeled by the symbols of the irreducible representation of the octahedral group, see the lecture by E. Pavarini, to which the corresponding final state wave function $|\Psi_\nu\rangle$ belongs. The figure shows that the agreement between the theoretical spectra and experiment is usually rather good. It is interesting to note that the three oxides shown in the figure all have the same crystal structure, namely the rock-salt structure. Since, moreover, Ni, Co and Mn are close neighbors in the periodic table, LDA predicts almost identical band structures, the main difference being an upward shift of the chemical potential with increasing nuclear charge of the transition metal. Despite this, the XPS spectra differ considerably and this change is reproduced very well by the theoretical spectra. This is clear evidence that the shape of the spectra is determined not so much by the single particle band structure, but by the multiplet structure of the transition metal ion, which in turn depends on its valence and spin state.

Next, we discuss X-ray absorption. In an X-ray absorption experiment an electron from either the $2p$ or the $3p$ shell absorbs an incoming X-ray photon and is promoted to the $3d$-shell via a dipole transition. In terms of electron configurations, the transition thus is $2p^6 3d^n \rightarrow 2p^5 3d^{n+1}$ (for definiteness we will always talk about the $2p$ shell from now on). Of particular interest here is the range of photon energies just above the threshold where the energy of the photon is sufficient to lift the core electron to an unoccupied state. Above this threshold the X-ray absorption coefficient $\kappa(\omega)$ rises sharply, which is called an absorption edge. The energy of the edge thereby is characteristic for a given element so that one can determine unambiguously which atom in a complex solid or molecule is probed. The ω-dependence of $\kappa(\omega)$ in an energy range of a few eV above the absorption edge – called NEXAFS for 'Near Edge X-ray Absorption Fine

Struture' – contains information about the initial state of the $3d$ shell, that means its valence and spin state, and this information can be extracted by using cluster calculations. The measured quantity in this case is

$$\begin{aligned}\kappa(\omega) &= -\frac{1}{\pi Z}\Im \sum_{m=-2}^{2}\sum_{\mu} e^{-\beta E_\mu} \left\langle \Psi_\mu \left| D(\boldsymbol{n}) \frac{1}{\omega-(H-E_\mu)+i0^+} D(\boldsymbol{n}) \right| \Psi_\mu \right\rangle \\ &= \frac{1}{Z}\sum_{m=-2}^{2}\sum_{\mu,\nu} e^{-\beta E_\mu} |\langle \Psi_\nu | D(\boldsymbol{n}) | \Psi_\mu \rangle|^2 \delta(\omega-(E_\nu-E_\mu)). \end{aligned} \tag{22}$$

This is very similar to the single-particle spectral function (21), the only difference is that now the dipole operator $D(\boldsymbol{n})$ (which will be defined later on) appears in place of the electron annihilation operator $c_{3,2,m,\sigma}$. This also implies that the number of electrons in the final states $|\Psi_\nu\rangle$ now is equal to that in the initial states $|\Psi_\mu\rangle$.

We again make the approximation to use the octahedral cluster to simulate this experiment. The initial state for this experiment – $2p^6 3d^n$ – is simply the ground state of the cluster. More difficult is the final state, $2p^5 3d^{n+1}$. This has a hole in the $2p$ shell so that the single-particle basis has to be enlarged once more to comprise also the 6 spin-orbitals available for $2p$ electrons. We may restrict the basis, however, to include only states with 5 electrons in these 6 spin-orbitals, so that the dimension of the Hilbert space increases only by a moderate factor of 6. The spin-orbit coupling constant $J_{SO,2p}$ in the $2p$ shell of $3d$ transition metals is of order 10 eV so we definitely need to include spin orbit coupling in the $2p$-shell. Here the forms (13) and (14) with $l=1$ can be used. The orbital angular momentum $l=1$ and the spin of $\frac{1}{2}$ can be coupled to a total angular momentum of either $J=\frac{3}{2}$ or $J=\frac{1}{2}$. Using the identity

$$\langle \boldsymbol{L}\cdot\boldsymbol{S}\rangle = \frac{1}{2}\left(J(J+1)-L(L+1)-S(S+1)\right)$$

we expect a splitting of $E_{\frac{3}{2}}-E_{\frac{1}{2}}=\frac{\lambda_{SO}}{2}(\frac{15}{4}-\frac{3}{4})=\frac{3\lambda_{SO}}{2}$. This means that we actually have two edges, separated by $\frac{3\lambda_{SO}}{2}\approx 10-15$ eV for $2p$ core levels. The one for lower photon energy – called the L_3 edge – is due to electrons coming from ${}^2P_{3/2}$, the one for higher photon energy (L_2-edge) due to electrons from ${}^2P_{1/2}$. Since there are 4 ${}^2P_{3/2}$ states but only 2 ${}^2P_{1/2}$ states the L_3 edge has roughly twice the intensity of the L_2 edge.

Next, there is the Coulomb interaction between the core-hole and the electrons in the d-shell. For example, there may now be Coulomb scattering between a $2p$ and a $3d$ electron as shown in Fig. 5. Let us consider the expression for the corresponding Coulomb matrix element (9). Here one of the indices ν_1 and ν_2 and one of the indices ν_3 and ν_4 must now refer to the $2p$ orbital and there are two possible combinations. If ν_2 and ν_3 refer to the $2p$ orbital we have

$$c^k(2,m_1;2,m_4)\; c^k(1,m_3;1,m_2) F^k(3,2;2,1).$$

The triangular condition for $c^k(1,m_3;1,m_2)$ requires $k\le 2$. Since only Y_{lm} with equal l and hence with equal parity are combined in one c^k only even k give non-vanishing contributions and we have two Coulomb integrals, $F^0(3,2;2,1)$ and $F^2(3,2;2,1)$.

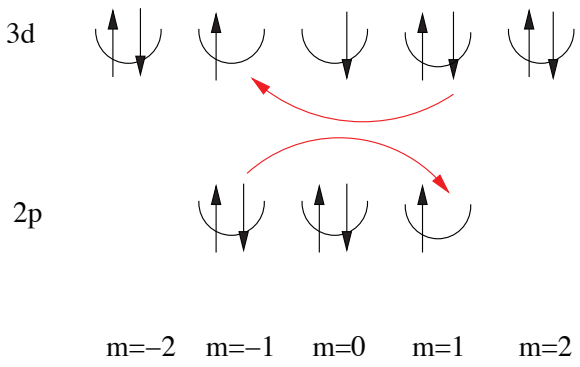

Fig. 5: *An electron in the $3d$ shell and an electron in the $2p$ shell scatter from one another.*

If ν_2 and ν_4 refer to the $2p$ orbital we have

$$c^k(2, m_1; 1, m_4)\ c^k(2, m_3; 1, m_2) G^k(3, 2; 2, 1).$$

The triangular condition for both c^k requires $k \leq 3$. Since now Y_{1m} and Y_{2m} are combined in one Gaunt coefficient only odd k contribute, so that we have two relevant exchange integrals, $G^1(3, 2; 2, 1)$ and $G^3(3, 2; 2, 1)$. Apart from these minor changes, the implementation of the d-p Coulomb interaction is exactly the same as the d-d interaction.

The Coulomb interaction between electrons in the $2p$ shell is definitely very strong – but it is irrelevant because we are considering only states with a *single hole* in this shell. Since this hole has no second hole to scatter from, the only effect of the Coulomb repulsion between electrons in the $2p$ shell is via the diagonal matrix elements which give a shift of the orbitals energy ϵ_{2p}. On the other hand ϵ_{2p} merely enters the position of the absorption edge, which would be $\approx \epsilon_{3d} - \epsilon_{2p}$ but not its spectral shape. Since we are not really interested in computing the onset of the edge, the precise value of ϵ_{2p} and hence the Coulomb interaction between $2p$ electrons is not important. Lastly we mention that the CEF effect on the inner-shell electrons is usually neglected.

Lastly, we discuss the dipole operator $D(\boldsymbol{n})$. This involves the matrix element of $\boldsymbol{n} \cdot \boldsymbol{r}$, where $\boldsymbol{n}$ is the vector which gives the polarization of the X-rays. This can be rewritten as

$$\boldsymbol{n} \cdot \boldsymbol{r} \ = \ r \sqrt{\frac{4\pi}{3}} \sum_{m=-1}^{1} \tilde{n}_m\ Y_{1,m}(\Theta, \phi)$$

where $\tilde{n}_1 = (-n_x + i n_y)/\sqrt{2}$, $\tilde{n}_0 = n_z$ and $\tilde{n}_{-1} = (n_x + i n_y)/\sqrt{2}$. It follows that

$$\begin{aligned} D(\boldsymbol{n}) &= \sum_{m,m'} \sum_{\sigma} d_{m,m'}\ c^\dagger_{3,2,m,\sigma} c_{2,1,m',\sigma} \\ d_{m,m'}(\boldsymbol{n}) &= d\ \tilde{n}_{m-m'}\ c^1(2, m; 1, m') \\ d &= \int_0^\infty dr\ r^3\ R_{3,2}(r) R_{2,1}(r). \end{aligned}$$

The factor of d merely scales the overall intensity of the spectrum and is largely irrelevant.

Combining all of the above one can compute X-ray absorption spectra. Fig. 6 shows examples

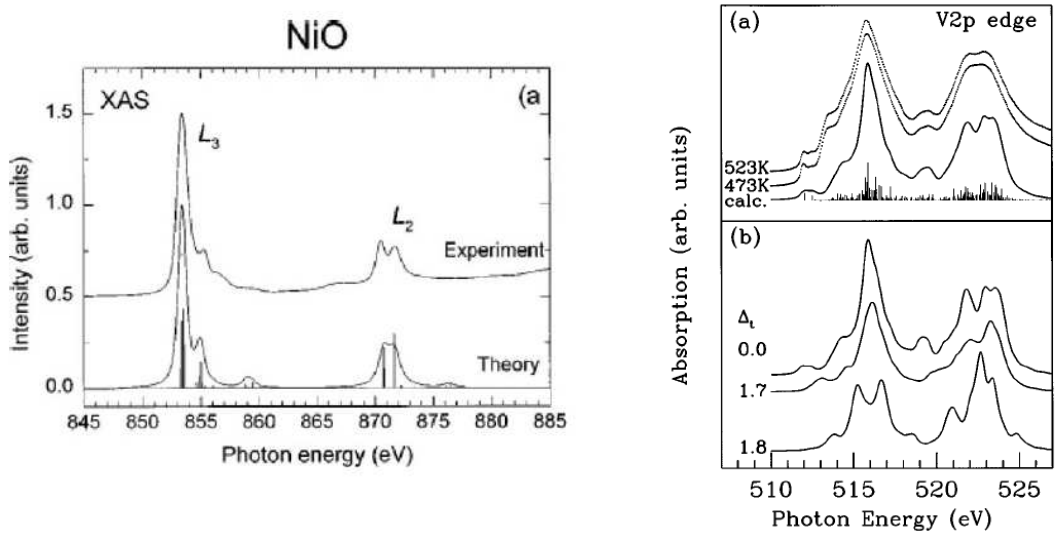

Fig. 6: *Comparison of experimental $2p$ XAS-spectra and results from cluster calculations: NiO (left) and $LiVO_2$ (right). The bottom part of the right-hand figure shows theoretical spectra calculated with different values of the CEF-strength Δ_t. Reprinted with permission from [19], Copyright 1999 and from [20], Copyright 1997 by the American Physical Society.*

from the literature where experimental $2p$-XAS spectra for NiO and $LiVO_2$ are compared to spectra obtained from multiplet theory. In both cases one can see the splitting of approximately 10-15 eV between the L_3 and L_2 edges. The edges do have an appreciable fine structure, however, and this is reproduced well by theory. The figure also illustrates the amount of information contained in XAS-spectra: the lower panel on the right hand side shows theoretical spectra calculated with different values of the CEF parameter, Δ_t. The strong difference between the spectra for $\Delta_t = 1.7$ and $\Delta_t = 1.8$ is due to a level crossing from a high-spin ground state of the Vanadium ion for $\Delta_t = 1.7$ to a low-spin ground state for $\Delta_t = 1.8$. In fact, $LiVO_2$ undergoes a phase transition at a temperature of ≈ 500 K whereby the magnetic susceptiblity drops almost to zero in the low temperature phase. A low-spin to high-spin transition of the Vanadium ion – for example caused by a change of the CEF due to thermal expansion – could be a possible explanation. It is obvious, however, that the spectrum for the low-spin ground state has no similarity whatsoever to the experimental spectrum at either 473 K or 523 K, rather these spectra a very similar to the spectrum of the high-spin ground state with $\Delta_t \approx 0$. A high-spin to low-spin transition therefore can be ruled out as the origin of the drop in magnetic susceptibility. This is one example how XAS can be used to determine the valence and spin of a given transition metal ion.

Let us discuss this in more detail. Photoelectron spectroscopies are often performed because for example the valence or the spin state of the transition metal ion in a given solid or molecule is unknown. Let us assume that we have two possible states of the ion, $|\Psi_0\rangle$ and $|\Psi_0'\rangle$, with energies E_0 and E_0' (for simplicity we assume that these are nondegenerate). Then we may ask: how will the spectrum change if we go from one ground state to the another? We note first that the final states $|\Psi_\nu\rangle$ and their energies E_ν in (21) and (22) are unchanged. What differs is first the energy

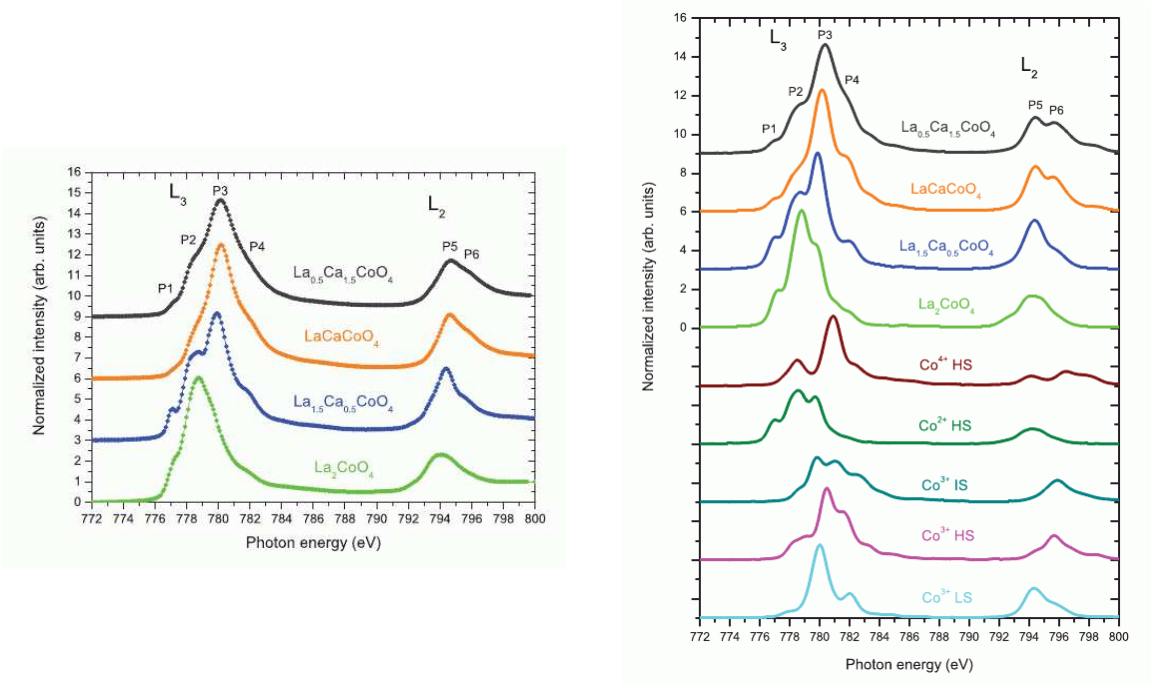

Fig. 7: *Left: Experimental Co 2p-XAS-Spectra for different Cobalt compounds with Perovskite structure. Right: The bottom part shows theoretical spectra calculated for different valence and spin states of Cobalt. By combining these spectra the actual experimental spectra can be reproduced almost quantitatively, see the four spectra at the top. Reprinted with permission from [21], Copyright 2011 by the American Physical Society.*

differences $E_\nu - E_0$. However, since we do not know E_0 and E_0' – otherwise we would know which one of them is lower in energy and hence the ground state – the absolute position of the peaks in the spectrum is of no significance. What is really relevant, however, is the *intensity* of the peaks which involves the matrix elements $|\langle\Psi_\nu|c|\Psi_0\rangle|^2$ or $|\langle\Psi_\nu|D(\boldsymbol{n})|\Psi_0\rangle|^2$. These matrix elements may change drastically when the ground state wave function $|\Psi_0\rangle$ changes and by comparing with cluster simulations the shape of the spectrum can give information about the valence and spin state of the transition metal ion. This is illustrated in Fig. 7, which shows experimental Cobalt $2p$ XAS-spectra of various Co-compounds with perovskite structure as well as theoretical spectra calculated by using the CTM4XAS package [10] for different valence and spin states of the Cobalt-ion. The experimental spectra obviously can be reproduced quite well by a superposition of such spectra for 'pure' valence and spin states of the Cobalt-ion. This implies that different Cobalt ions in the sample are in different valence and spin states whereby the percentages are simply given by the weight of the corresponding spectrum in the superposition.

To summarize this section: multiplet theory is of considerable importance in the interpretation of photoelectron spectroscopy. The simulated spectra usually show very good agreement with experimental ones. All of this shows that the multiplets of the free ion persist in the solid and that the proper desciption of the Coulomb interaction is crucial for the description of these compounds.

5 Conclusion

We have seen that the Coulomb repulsion between electrons in partially filled atomic shells leads to multiplet splitting. The simple estimate

$$E[d^n] \approx n \cdot \epsilon_d + U \cdot \frac{n(n-1)}{2}.$$

given in the introduction describes only the center of gravity of the energies of the d^n-derived states, and superimposed over this the Coulomb repulsion creates a multiplet spectrum with a width of several eV. While multiplet theory was derived originally for the discussion of spectroscopic data of atoms and ions in the gas phase, it has turned out that it is essential also for the understanding of many experiments on transition-metal compounds. Photoelectron spectroscopy, optical spectroscopy, electron spin resonance and inelastic neutron scattering all can be interpreted in terms of multiplets. The often excellent agreement between theory and experiment which can be obtained thereby is clear evidence that the multiplets of the free ion are a reality also in solids, with the only modification being some additional splitting due to CEF and modification of spectral intensities due to charge transfer. Any realistic description of $3d$ transition metal compounds therefore must take multiplet splitting into account.

Appendix

m	m'	c^0	$7\,c^2$	$21\,c^4$	a^0	$49\,a^2$	$441\,a^4$	b^0	$49\,b^2$	$441\,b^4$
±2	±2	1	-2	1	1	4	1	1	4	1
±2	±1	0	$\sqrt{6}$	$-\sqrt{5}$	1	-2	-4	0	6	5
±2	0	0	-2	$\sqrt{15}$	1	-4	6	0	4	15
±1	±1	1	1	-4	1	1	16	1	1	16
±1	0	0	1	$\sqrt{30}$	1	2	-24	0	1	30
0	0	1	2	6	1	4	26	1	4	36
±2	∓2	0	0	$\sqrt{70}$	1	4	1	0	0	70
±2	∓1	0	0	$-\sqrt{35}$	1	-2	-4	0	0	35
±1	∓1	0	$-\sqrt{6}$	$-\sqrt{40}$	1	1	16	0	6	40

Table 4: *The Gaunt coeficients* $c^k(2,m;2,m')$*, the coefficients* $a^k(2,m;2,m')$ *and* $b^k(2,m;2,m')$

m	m'	c^0	$15\,c^2$	$33\,c^4$	$\frac{429}{5}\,c^6$
±3	±3	1	-5	3	-1
±3	±2	0	5	$-\sqrt{30}$	$\sqrt{7}$
±3	±1	0	$\sqrt{10}$	$\sqrt{54}$	$-\sqrt{28}$
±3	0	0	0	$-\sqrt{63}$	$\sqrt{84}$
±2	±2	1	0	-7	6
±2	±1	0	$\sqrt{15}$	$\sqrt{32}$	$-\sqrt{105}$
±2	0	0	$-\sqrt{20}$	$-\sqrt{3}$	$4\sqrt{14}$
±1	±1	1	3	1	-15
±1	0	0	$\sqrt{2}$	$\sqrt{15}$	$5\sqrt{14}$
0	0	1	4	6	20
±3	∓3	0	0	0	$-\sqrt{924}$
±3	∓2	0	0	0	$\sqrt{462}$
±3	∓1	0	0	$\sqrt{42}$	$-\sqrt{210}$
±2	∓2	0	0	$\sqrt{70}$	$\sqrt{504}$
±2	∓1	0	0	$-\sqrt{14}$	$-\sqrt{378}$
±1	∓1	0	$-\sqrt{24}$	$-\sqrt{40}$	$-\sqrt{420}$

Table 5: *The Gaunt coeficients* $c^k(3,m;3,m')$

References

[1] J.H. de Boer and E.J.W. Verwey, Proc. Phys. Soc. London 49, 59 (1937)

[2] A.L. Fetter and J.D. Walecka: *Quantum Theory of Many Particle Systems* (McGraw-Hill, San Francisco, 1971)

[3] J.C. Slater: *Quantum Theory of Atomic Structure* (McGraw-Hill, New York, 1960)

[4] J.S. Griffith: *The Theory of Transition Metal Ions* (Cambridge University Press, Cambridge, 1961)

[5] L.D. Landau and E.M. Lifshitz: *Lehrbuch der Theoretischen Physik* (Akademie Verlag Berlin, 1988)

[6] E. Pavarini: The LDA+DMFT Approach, in [22]

[7] Yu. Ralchenko, A.E. Kramida, J. Reader, and NIST ASD Team (2011). NIST Atomic Spectra Database (ver. 4.1.0), `http://physics.nist.gov/asd`

[8] S. Sugano, Y. Tanabe, and H. Kitamura: *Multiplets of Transition Metal Ions* (Academic Press, New York 1970) (Dover, 1989)

[9] E. Koch: *The Lanczos Method*, in [22]

[10] See, e.g., the CTM4XAS package `http://www.anorg.chem.uu.nl/CTM4XAS`

[11] F.M.F. de Groot, J. of Electron Spectroscopy and Related Phenomena, **67** 525 (1994)

[12] F.M.F. de Groot, Coordination Chemistry Reviews, **249** 31 (2005)

[13] F.M.F. de Groot and A. Kotani: *Core Level Spectroscopy of Solids* (Taylor And Francis, 2008)

[14] C. Caroli, D. Lederer-Rozenblatt, B. Roulet, and D. Saint-James, Phys. Rev. B **8**, 4552 (1973)

[15] P.J. Feibelman and D.E. Eastman, Phys. Rev. B **10**, 4932 (1974)

[16] A. Fujimori and F. Minami, Phys. Rev. B **30**, 957 (1984)

[17] J. van Elp, J.L. Wieland, H. Eskes, P. Kuiper, G.A. Sawatzky, F.M.F. de Groot, and T.S. Turner, Phys. Rev. B **44**, 6090 (1991)

[18] A. Fujimori, N. Kimizuka, T. Akahane, T. Chiba, S. Kimura, F. Minami, K. Siratori, M. Taniguchi, S. Ogawa, and S. Suga, Phys. Rev. B **42**, 7580 (1990)

[19] M. Finazzi, N.B. Brookes, and F.M.F. de Groot, Phys. Rev. B **59**, 9933 (1999)

[20] H.F. Pen, L.H. Tjeng, E. Pellegrin, F.M.F. de Groot, G.A. Sawatzky, M.A. van Veenendaal, and C.T. Chen, Phys. Rev. B **55**, 15500 (1997)

[21] M. Merz, D. Fuchs, A. Assmann, S. Uebe, H. v.Löhneysen, P. Nagel, and S. Schuppler, Phys. Rev. B **84**, 014436 (2011)

[22] E. Pavarini, E. Koch, D. Vollhardt, and A. Lichtenstein (eds.):
The LDA+DMFT approach to strongly correlated materials,
Reihe Modeling and Simulation, Vol. 1 (Forschungszentrum Jülich, 2011)
`http://www.cond-mat.de/events/correl11`

9 Strongly Correlated Electrons: Estimates of Model Parameters

Olle Gunnarsson
Max-Planck-Institut für Festkörperforschung
Heisenbergstraße 1, 70569 Stuttgart, Germany

Contents

E. Pavarini, E. Koch, F. Anders, and M. Jarrell
Correlated Electrons: From Models to Materials
Modeling and Simulation Vol. 2
Forschungszentrum Jülich, 2012, ISBN 978-3-89336-796-2
http://www.cond-mat.de/events/correl12

1 Introduction

For weakly or moderately correlated systems *ab initio* methods, such as the density functional formalism [1, 2] or the GW method [3, 4], are often quite successful. For strongly correlated systems, however, these methods are often not sufficient. It is then necessary to treat correlation effects in a more accurate way. Such systems are often quite complicated with large unit cells. It is then very hard to treat correlation effects within an *ab initio* approach, and one often turns to model Hamiltonians. The idea is then to focus on states and interactions believed to be particularly important for the physics of interest. This has the additional advantage that it may then be easier to understand the physics, since less important effects do not confuse the interpretation. On the other hand, there is a risk of oversimplifying the model and thereby missing the correct physics. The purpose of this lecture is to discuss this approach.
In principle it is straightforward to construct a model. We can produce a complete basis set and then calculate matrix elements of the real space Hamiltonian (in atomic units)

$$H = \sum_i \left(-\frac{1}{2} \bigtriangledown_i^2 + V_{ext}(\mathbf{r}_i) \right) + \sum_{i<j} \frac{1}{|\mathbf{r}_i - \mathbf{r}_j|}. \tag{1}$$

For atoms or small molecules, this Hamiltonian may then be solved using various many-body methods, e.g., configuration interaction (CI), where the many-body wave function is written as a linear combination of determinants. For strongly correlated solids, however, a Hamiltonian obtained in this way is often too complicated to allow reasonably accurate calculations. We are then forced to use substantially simpler models. This usually involves a drastic reduction of the basis set and the neglect of many interactions. Typical examples are the Anderson [5], the Hubbard [6] and the t-J [7] models.
This approach involves the neglect of interactions which are large. For instance, the Anderson impurity model is often used for a $3d$ impurity in a weakly correlated host. We define a direct Coulomb integral

$$F_{ij} = \int d^3r \int d^3r' \frac{|\Phi_i(\mathbf{r})|^2 |\Phi_j(\mathbf{r}')|^2}{|\mathbf{r} - \mathbf{r}'|}, \tag{2}$$

where $\Phi_i(\mathbf{r})$ is the wave function of a state i. Then the Coulomb integral $F_{3d,3d}$ between $3d$ electrons is kept, while, for instance, the integral $F_{3d,4s}$ between a $3d$ and a $4s$ electron is neglected. For a free Mn atom $F_{3d,3d} = 21$ eV and $F_{3d,4s} = 10$ eV. Such an approximation is clearly highly questionable. An essential task is then to try to include the explicitly neglected interactions or states implicitly as a renormalization of parameters in the model. As we show later, this leads to an effective Coulomb interaction between the $3d$ electrons which is much smaller than the calculated value for a free atom. A basic assumption of such simple models is then that all the neglected interactions can, with a reasonable accuracy, be included implicitly as a renormalization of various model parameters. In this approach it is important to keep track of what effects are explicitly included in the model. These should not be included in the calculation of renormalized parameters, since this would involve double-counting.
There are various ways of obtaining parameters. One approach has been indicated above. We use *ab initio* calculations to calculate parameters and then we try to estimate how these are

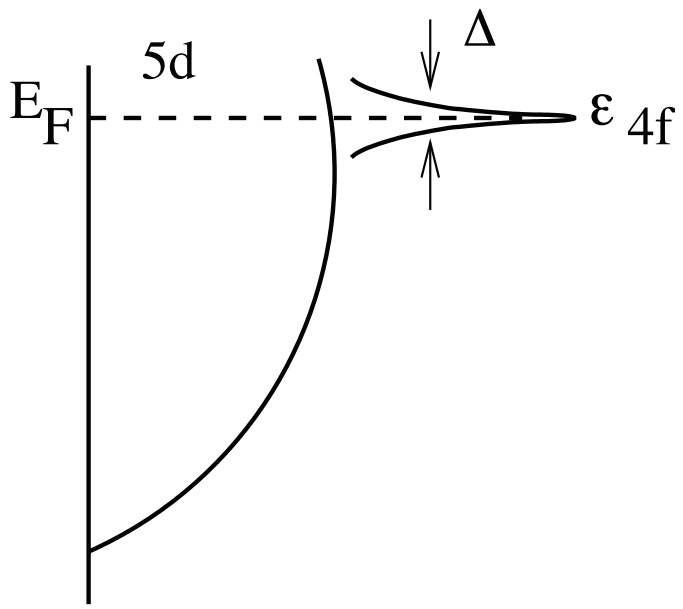

Fig. 1: *Schematic density of state for a Ce compound according to the promotional model.*

renormalized by neglected interactions. Another is to calculate certain properties of the model, compare with experiment and then adjust parameters until the experimental value is obtained. This approach then automatically gives renormalized parameters. It is important to try to obtain as much independent information as possible about the parameters, both from calculations and from different experiments, and to check if the various pieces of information are consistent.

The importance of obtaining theoretical information about parameters can be illustrated by the historical development of the theory of Ce compounds. Traditionally, Ce compounds were described in the so called promotional model [8]. It was assumed that the Ce $4f$ level was located very close to the Fermi level, E_F, and that it had a very weak interaction with other states. A mean-field theory was then used to show that this leads to a very narrow resonance, as indicated in Fig. 1. The narrowness of the resonance could explain the large susceptibility and specific heat of Ce compounds, and the closeness of the $4f$ level to E_F the change of apparent valence when the pressure or temperature are changed. Thermodynamic considerations, however, showed that the $4f$ level ought to be about 2 eV below E_F [9], in strong disagreement with the model. This result was later reconciled with experiment in a many-body approach [10, 11], showing that even if the $4f$ level is far below E_F it can form a Kondo-like many-body resonance at E_F leading to very large values of the susceptibility and the specific heat. This illustrates how an oversimplified (mean-field) method can nevertheless lead to reasonable results if it is combined with a bad choice of parameters. Correcting the parameters then forces us to use a better method and to find out more about the correct physics.

2 Projecting out states

2.1 One-particle Hamiltonian

One approach to the construction of models is to project out stateswhich are believed not to be essential for the physics. We can illustrate this for a one-particle Hamiltonian

$$H = \sum_i \varepsilon_i n_i + \sum_{i \neq j} t_{ij} \psi_i^\dagger \psi_j \tag{3}$$

We introduce a projection operator

$$P = \sum_{\nu \in P} |\nu\rangle\langle\nu|, \tag{4}$$

where $|\nu\rangle$ are states we want to keep. We introduce the resolvent operator

$$(z-H)^{-1} = \sum_\nu |\nu\rangle\langle\nu|(z-H)^{-1}\sum_\mu |\mu\rangle\langle\mu| = \sum_n |n\rangle \frac{1}{z-E_n}\langle n|, \tag{5}$$

which has poles for $z = E_n$ at the eigenvalues, where $H|n\rangle = E_n|n\rangle$. Introducing the complement $Q = (1-P)$, we can write the Hamiltonian as [12, 13]

$$\begin{pmatrix} H_{PP} & H_{PQ} \\ H_{QP} & H_{QQ} \end{pmatrix}, \tag{6}$$

where, e.g., $H_{PP} = PHP$. Then we can derive the exact result (Löwdin downfolding)

$$P(z-H)^{-1}P = [z - H_{PP} - H_{PQ}(z-H_{QQ})^{-1}H_{QP}]^{-1}. \tag{7}$$

The operator $P(z-H)^{-1}P$ has the same poles as the original operator $(z-H)^{-1}$, if the corresponding eigenstates have weight inside the space P. The new operator has a smaller dimension, but because of the z dependence it is not simpler. To simplify the expression, we put z equal to an energy (ε_0) in the range of interest. The operator is then energy independent. As an additional simplification, we may assume that the off-diagonal elements of H_{QQ} can be neglected. Then the matrix elements of the new operator become

$$t_{ij} \rightarrow t_{ij} - \sum_{\mu \in Q} \frac{t_{i\mu}t_{\mu j}}{\varepsilon_0 - E_\mu}. \tag{8}$$

This latter approximation is accurate if the states being projected out are much higher in energy than the states of interest and if the off-diagonal elements are small compared with the energy difference $\varepsilon_0 - E_\mu$. The assumption about H_{QQ} being diagonal can also be relaxed. This approach reduces the size of the Hamiltonian matrix, i.e., the number of states, at the cost of obtaining more long-range hopping. For a one-particle Hamiltonian, this approach is a controlled and systematic procedure for reducing the size of the Hamiltonian.

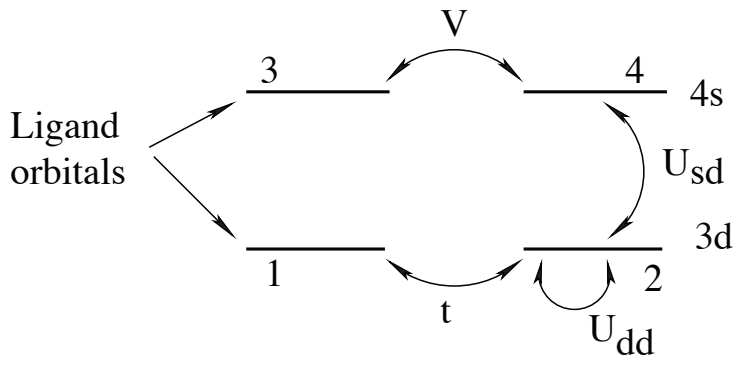

Fig. 2: *Schematic picture of a very simple model of a transition metal compound, with a* $3d$ *atom (levels 2 and 4) coupling to a ligand (with levels 1 and 3).*

2.2 Many-body Hamiltonian

We now consider a many-body Hamiltonian, with a two-body interaction in the form of a Coulomb interaction. We then define P as projecting out states that have no electron in certain (high-lying) one-particle states $|\mu\rangle$, and $Q = 1 - P$. We consider a Coulomb interaction with four (creation and annihilation) operators and project out a state with one electron in $|\mu\rangle$. Then H_{QP} contains an operator $c^\dagger_{\mu\sigma}$ and H_{PQ} an operator $c_{\mu\sigma}$. Even if we assume H_{QQ} to be diagonal, we are left with an operator $H_{PQ}H_{QP}$ acting on a state without electrons in $|\mu\rangle$. Then $c_{\mu\sigma}c^\dagger_{\mu\sigma} \equiv 1$, and two operators drop out. But we are still left with six other operators, which in the general case are all different. We have then generated a three-body operator. This is too complicated, and all such operators need to be neglected. Unless it can be shown that these terms are small, this means that there is not a controlled systematic procedure for reducing the number of states. We then have to rely on more intuitive approaches.

As an example we consider a very simple model which is relevant for $3d$ impurities. The model is constructed so that an exact solution can be found. We want to illustrate how this model can be projected down to a simpler model with renormalized parameters. We introduce the Hamiltonian [14]

$$H = \sum_\sigma \left(\sum_{i=1}^{4} \varepsilon_i n_{i\sigma} + (t\psi^\dagger_{1\sigma}\psi_{2\sigma} + V\psi^\dagger_{3\sigma}\psi_{4\sigma} + \text{H.c.}) \right) + U_{dd} n_{2\uparrow} n_{2\downarrow} + U_{sd} \sum_{\sigma\sigma'} n_{2\sigma}\, n_{4\sigma'} \quad (9)$$

where level 2 corresponds to a $3d$ level and level 4 to a $4s$ level on a transition metal atom. Level 1 and 3 correspond to a ligand coupling to the transition metal atom via the hopping integrals t and V. On the transition metal atom there is a large Coulomb interaction U_{dd} between electrons in the $3d$ level and a weaker U_{sd} interaction between the $3d$ and $4s$ levels. We assume that orbital 2 is quite localized, so that t is small, but that levels 3 and 4 are delocalized, so that V is large. The level structure is shown schematically in Fig. 2.

We first consider the spinless case, and put one electron in each of the spaces 1+2 and 3+4. We derive parameters in an intuitive approach, and then compare with a controlled projection approach, possible in this case. We introduce the eigenstates of the space 3+4 with the electron in space 1+2 on site 1 or 2. With the electron on level 1 the bonding and antibonding eigenstates

in the 3+4 space are

$$\psi_{b1} = a_3\psi_3 + a_4\psi_4 \tag{10}$$
$$\psi_{a1} = a_4\psi_3 - a_3\psi_4,$$

with the energies ε_{b1} and ε_{a1}. With the electron in 1+2 on level 2 the states are

$$\psi_{b2} = \cos\phi\,\psi_{b1} + \sin\phi\psi_{a1} \tag{11}$$
$$\psi_{a2} = \sin\phi\,\psi_{b1} - \cos\phi\psi_{a1}, \tag{12}$$
$$\tag{13}$$

with the energies ε_{b2} and ε_{a2}. Here ϕ is of the order U_{sd}/V which is small in the limit we consider below. We assume that the electron in the space 3+4 can adjust completely to the movement of the electron in space 1+2 due to $|V| \gg |t|$. We then replace the four-level model in Eq. (9) by a two-level model with the effective level positions

$$\varepsilon_1^{\rm eff} = \varepsilon_1 + \varepsilon_{b1}; \quad \varepsilon_2^{\rm eff} = \varepsilon_2 + \varepsilon_{b2} \tag{14}$$

To test this, we now solve the full model exactly. We introduce a complete basis set

$$\begin{aligned} |\tilde{1}\rangle &= \psi_1^\dagger\psi_{b1}^\dagger|0\rangle \\ |\tilde{2}\rangle &= \psi_2^\dagger\psi_{b2}^\dagger|0\rangle \\ |\tilde{3}\rangle &= \psi_1^\dagger\psi_{a1}^\dagger|0\rangle \\ |\tilde{4}\rangle &= \psi_2^\dagger\psi_{a2}^\dagger|0\rangle, \end{aligned} \tag{15}$$

where we have chosen the basis set so that only the first two states are relevant if the assumptions above are correct. We now calculate the resolvent operator [14]

$$(z-H)^{-1} = \begin{pmatrix} z-\varepsilon_1-\varepsilon_{b1} & -t\cos\phi & 0 & t\sin\phi \\ -t\cos\phi & z-\varepsilon_2-\varepsilon_{b2} & -t\sin\phi & 0 \\ 0 & -t\sin\phi & z-\varepsilon_1-\varepsilon_{a1} & -t\cos\phi \\ t\sin\phi & 0 & -t\cos\phi & z-\varepsilon_2-\varepsilon_{a2} \end{pmatrix}^{-1}. \tag{16}$$

We now focus on the upper left 2×2 corner and use Löwdin folding [12] to project out the two high-lying states. For instance, the 11 element takes the form

$$\tilde{H}_{11} = \varepsilon_1 + \varepsilon_{b1} + \frac{t^2\,(z-\varepsilon_1-\varepsilon_{a1})\sin^2\phi}{(z-\varepsilon_1-\varepsilon_{a1})(z-\varepsilon_2-\varepsilon_{a2}) - t^2\cos^2\phi}. \tag{17}$$

For simplicity, we put $\varepsilon_1 = \varepsilon_2$ and assume that the term $t^2\cos^2\phi$ in the denominator can be neglected. Putting $z \approx \varepsilon_1 + \varepsilon_{b1}$, we then find that the correction term in Eq. (17) is of the order $t(t/V)(U_{sd}/V)^2$. If $|V| \gg |t|$ and $|V| \gg U_{sd}$, it is indeed justified to neglect the correction term. We then find that the level positions difference, $\varepsilon_1^{\rm eff} - \varepsilon_2^{\rm eff}$, have corrections to zeroth order in $(1/V)$, due to ε_{b1} and ε_{b2}. These corrections are included in our intuitive approach above.

V	$\varepsilon_2^{\rm eff}$-$\varepsilon_1^{\rm eff}$	$U^{\rm eff}$	E_0+2V		n_2		χ	
			Renorm.	Exact	Renorm.	Exact	Renorm.	Exact
1.0	1.17	3.18	-1.05	-0.95	0.380	0.364	0.314	0.312
1.5	1.39	3.21	-0.97	-0.90	0.339	0.326	0.266	0.262
2.0	1.53	3.29	-0.92	-0.88	0.317	0.307	0.240	0.237
3.0	1.68	3.44	-0.87	-0.85	0.292	0.287	0.214	0.213
4.0	1.75	3.55	-0.85	-0.84	0.280	0.277	0.202	0.201
6.0	1.83	3.68	-0.83	-0.82	0.268	0.267	0.190	0.190
10.0	1.90	3.80	-0.81	-0.81	0.259	0.258	0.181	0.181
20.0	1.95	3.90	-0.80	-0.80	0.252	0.252	0.174	0.174

Table 1: *Ground-state energy E_0, occupancy n_2 of level 2 and susceptibility χ of the spin-degenerate model (9). The parameters are $\varepsilon_1 = \varepsilon_2 = \varepsilon_3 = \varepsilon_4 = 0$, $t = 1$, $U_{dd} = 4$ and $U_{sd} = 2$.*

Then there is a second order correction to the hopping integral due to $\cos\phi$. This correction is due to the fact that the electron in the space 3+4 cannot completely follow the electron in space 1+2 in the optimum way. This correction is usually neglected.
We now turn to the same model with spin degeneracy. The exact solution can then be obtained from a 16×16 matrix. In this case the analytical calculation is to complicated to illustrate what happens, and we focus on a numerical calculation. We first calculate the energy $E(n_2)$ of the 3+4 space as a function of the occupancy of level 2. We then obtain

$$\begin{aligned} \varepsilon_1^{\rm eff} &= \varepsilon_1 + E(0) \\ \varepsilon_2^{\rm eff} &= \varepsilon_2 + E(1) \\ U^{\rm eff} &= E(2) + E(0) - 2E(1) \end{aligned} \tag{18}$$

in analogy with the spinless case. We then calculate the ground-state energy, E_0, the occupancy n_2 of level 2 and the spin susceptibility $\chi = -\partial^2 E_0(H)/\partial H^2$, where the model couples to an external magnetic field via the term $-H(n_{2\uparrow} - n_{2\downarrow})$. The results are shown in Table 1. We have added a contribution $2V$ to the total energy E_0, since there would have been a trivial contribution $-2V$ if there had been no interaction between spaces 1+2 and 3+4. As expected, the agreement between the approximate (Renorm.) and exact results improves as $|V|$ is increased. However, the agreement is surprisingly good even for $V = t$.

3 Effective Coulomb interaction

The essential point of the model from the previous section is that we can distinguish between two types of electrons, "slow" electrons (space 1+2) and "fast" electrons (space 3+4), in the following referred to as "localized" and "delocalized". The idea is that the delocalized electrons are assumed to adjust in an optimum way to the movements of the localized electrons. We can then estimate effective parameters in a similar way as in the previous section. For each system we then have to decide which electrons we consider localized and include explicitly in the model

System	Localized	Delocalized
$4f$ compounds	$4f$	$5d$
$3d$ compounds	$3d$	$4s$, $4p$

Table 2: *"Slow" ("localized") and "fast" ("delocalized") electrons for* $3d$ *and* $4f$ *compounds.*

and which are delocalized and only included implicitly as a renormalization of the parameters. This is illustrated in Table 2. For $4f$ compounds the $4f$ DFT band width is about 1/10 of the $5d$ band-width, and we may reasonably talk about two types of electrons. For $3d$ compounds this distinction is much less clear cut.

3.1 Perfect screening

We now focus on the calculation of an effective Coulomb integral $U^{\rm eff}$ as an essential model parameter. We apply the approach of the previous section to a real system. For that reason, we need to know how the energy of the system varies with the occupancy of, e.g., a $3d$ or $4f$ level, Eq. (18). Herring [15] estimated these energies using atomic data, assuming that any change in the number of localized electrons on an atom is compensated by the opposite change in the number of delocalized electrons on the same atom. For a $3d$ metal this can be written as

$$U = E(3d^{n+1}4s^0) + E(3d^{n-1}4s^2) - 2E(3d^n4s^1), \tag{19}$$

where $E(3d^n4s^m)$ is the energy of an atom (ion) with n 3d electrons and m 4s electrons. In this approach it is assumed that the variation in the number of $3d$ electrons is perfectly screened by a change in the number of $4s$ electrons. We refer to this as "perfect screening".
A similar method was used by Cox *et al.* [16] who studied transition metals and Herbst *et al.* [17] who studied the rare earths. They performed Hartree-Fock calculations for renormalized atoms with Wigner-Seitz boundary conditions.

3.2 Constrained density functional formalism

Dederichs *et al.* [18] calculated U using a constrained density functional formalism. The functional for a $3d$ compound is written as

$$E[n^i_{3d}] = F[n] + \int d^3r\, V_{\rm ext}(\mathbf{r})n(\mathbf{r}) + \mu\left(\int d^3r\, n(\mathbf{r}) - N\right) + \mu^i_{3d}\left(\int d^3r\, n^i_{3d}(\mathbf{r}) - n^i_{3d}\right). \tag{20}$$

Here $F[n]$ describes the kinetic and potential energy of the system, $V_{\rm ext}(\mathbf{r})$ is an external potential, μ is the chemical potential and μ^i_{3d} is a Lagrange parameter. n^i_{3d} is the number of localized electrons on site i, referred to as the central site in the following. A stationary point of the energy functional to density variations is searched

$$0 = \frac{\partial F}{\partial n} + V_{\rm ext}(\mathbf{r}) + \mu + \mu^i_{3d}P^i_{3d}, \tag{21}$$

where P^i_{3d} is a projection operator acting on the localized electrons. From this a new Kohn-Sham equation can be derived, where μ^i_{3d} enters as an additional nonlocal potential acting only on the localized electrons. μ^i_{3d} is varied until the prescribed number of $3d$ electrons is obtained. This requires a definition of localized electrons. For instance, in methods based on an expansion in spherical waves in a region around each nucleus a natural definition can be introduced. This way an effective U^{eff} is calculated, using a formula equivalent to Eq. (18).
In the approach above, U^{eff} contains a change of the kinetic energy of the electrons included explicitly in the model. This contribution needs to be subtracted. Hybertson *et al.* [19] did this by considering the model Hamiltonian in which U^{eff} will be used, e.g.,

$$H = \sum_{ij\sigma} t_{ij} \psi^\dagger_{i\sigma} \psi_{j\sigma} + \sum_i U^{\text{eff}} n_{i\uparrow} n_{i\downarrow}, \tag{22}$$

where t_{ij} are hopping integrals. This model is then solved in a constrained mean-field theory to simulate the constrained density functional approach. The energy as a function of the constrained occupancies is calculated, and U^{eff} is varied until the constrained DFT result is reproduced. We refer to this as cLDA. Cococcioni and Giroconcoli [20] used a similar approach. An alternative approach was used by McMahan *et al.* [21] and by Gunnarsson *et al.* [22]. They performed a band structure calculation with a large unit cell [21–23]. Then the hopping integrals from the orbital with localized electrons is cut off for the central atom in the unit cell. Then the occupation of the orbital can be trivially varied without a variation of the kinetic energy for hopping in and out of the orbital, since this energy is zero. Double-counting is also explicitly avoided, contrary to claims elsewhere [24]. This method is referred to as "cut off' LDA. In a different method, the hopping between the localized orbitals and the delocalized orbitals was cut on all sites, not only on the central site [28].

3.3 Constrained RPA

A different approach was taken by Aryasetiawan *et al.* [25]. They calculated the Coulomb interaction using a constrained random phase screening. In the random phase approximation (RPA) the polarizability is written as

$$P(\mathbf{r}, \mathbf{r}'; \omega) = \sum_i^{\text{occ}} \sum_j^{\text{unocc}} \psi_i(\mathbf{r}) \psi^*_i(\mathbf{r}') \psi^*_j(\mathbf{r}) \psi_j(\mathbf{r}') \left(\frac{1}{\omega - \varepsilon_j + \varepsilon_i + i0^+} - \frac{1}{\omega + \varepsilon_j - \varepsilon_i - i0^+} \right),$$

where $\psi_i(\mathbf{r})$ and ε_i are one-particle eigenfunctions and eigenvalues. Calculating the effective Coulomb interaction by using this screening would be incorrect, since it would involve double-counting. The Hubbard model explicitly allows localized electrons to screen the interaction between localized electrons, and the use of Eq. (23) would then lead to double counting. Aryasetiawan *et al.* [25] therefore excluded contributions to Eq. (23) where both i and j stand for Bloch states containing mainly localized states. For a transition metal compound they then excluded states within an energy window where the states are mainly of $3d$ character and for a rare earth compound a window where the states are mainly of $4f$ character. The definition of the energy window involves uncertainties [25]. This method is referred to as cRPA.

Unrenormalized (F^0)	21.4 eV
Relaxation of $3d$ orbital	-5.2 eV
Relaxation of $4s$, $4p$ orbitals	-2.2 eV
Relaxation core, XC effects	-1.2 eV
Atomic U	12.8 eV

Table 3: *Contribution to U for a free Mn atom with the configuration $3d^{5.1}4s^{0.64}4p^{0.70}$. This corresponds to the configuration for Mn in CdTe.*

On-site relaxation	15.4 eV
Charge transfer to Mn	-7.6 eV
Charge transfer to n.n. ligand	-0.4 eV
Solid state U	7.4 eV

Table 4: *Contribution to U for a Mn impurity in CdTe.*

3.4 Screening and breathing

The definition of U can be approximately rewritten as

$$U = E(n+1) + E(n-1) - 2E(n) \approx \frac{\delta\varepsilon}{\delta n} , \tag{23}$$

where $E(n)$ is the energy of the system with n localized electrons and ε is the energy eigenvalue of the localized orbital and n is the occupancy. If the system were not allowed to relax, this would lead to $U = F$, where F, given in Eq. (2), is the direct Coulomb integral of the orbital. In reality, the charge density relaxes and the corresponding change in the electrostatic potential acts back on the orbital eigenvalue, reducing the shift as n is varied and leading to a renormalized U. We can illustrate this for the case of a Mn impurity in CdTe [26]. First a free Mn atom is studied (Table 3). The spherical part $F^0_{3d,3d}$ of the direct Coulomb integral is large, 21 eV. The main renormalizing process is a breathing of the $3d$ orbital, where the orbital expands as the $3d$ occupancy is increased [26, 29]. This reduces U by about 5 eV. Breathing of the $4s$, $4p$ and core orbitals contribute less. The net result is a reduction of U from about 21 eV to about 13 eV. In the solid there are similar breathing effects, reducing U to about 15 eV (see Table 4). However, now there is additional charge transfer from the surrounding to the Mn atom, reducing the U by almost 8 eV. Charge transfer to near neighbors (n.n.) plays a smaller role. The result is reduction of U to about 7 eV according to this calculation.

The breathing effect can also be understood from Slater's rules [30]. According to these rules, the effective nuclear charge for a $3d$ orbital is $Z^* = Z - 18 - 0.35(n_{3d} - 1)$, where Z is the true nuclear charge and n_{3d} is the $3d$ occupancy. This illustrates how the effective nuclear charge is reduced and the orbital expands as n_{3d} is increased. According to Slater's rules, the occupancy of the $4s$ and $4p$ orbitals do not influence Z^* for the $3d$ orbital. This then suggests that the charge transfer in the solid to $4s$ and $4p$ should not influence breathing very much. This is also supported by a comparison of Tables 3 and 4.

System	cLDA	"cut-off"	cRPA	"perfect screening"	Exp
Fe	2.2 [20]	6 [23]	4 [25]	2.7 [16]	2 [31, 32]
Ce	4.5 [20]	6 [23]	3.2-3.3 [25]	5 [17]	5-7 [35]

Table 5: *Results for U for Fe as an example of a $3d$ metal and Ce illustrating a $4f$ metal.*

3.5 Results

We now consider results obtained using the methods above for $3d$ and $4f$ metals. Specifically, we consider Fe and Ce as examples of $3d$ and $4f$ metals. The results are shown in Table 5. "Perfect screening" provides a rather good estimate for both Fe and Ce. The "cut-off" method gives a substantially too large U for Fe. It was found [23] that only about half the screening charge is on the Fe atom, as one would expect from the energetics of the screening process [23]. It is then to be expected that U is substantially larger than the "perfect screening" result. cLDA gives a very good result compared with experiment, and actually somewhat smaller than "perfect screening". It is not clear why this result is so different from the "cut-off" method, and it would be interesting to study the screening in cLDA. The U in cRPA is a bit too large. Interestingly, the "cut-off" method gives a good estimate of U towards the end of the $3d$ series, e.g., for the cuprates [34].
For Ce "perfect screening" provides a fairly accurate estimate of U. The "cut off" method gives only a slightly larger U, in good agreement with experiment. In this case it is found that the screening charge on Ce is approximately unity [23], so it is not surprising that there is rather good agreement with "perfect screening". cLDA gives a U slightly smaller than "perfect screening" and U in cRPA is substantially smaller. It is not clear why cRPA implies such an effective screening and gives a U that is only roughly half the experimental estimate.

4 Neglected renormalizations

In this section we discuss two renormalizations of parameters, which are usually neglected. The purpose is not to argue that these effects should be included. This could be done, but it would result in more parameters and the results would probably be less transparent. The purpose is rather to illustrate that the parameters of effective models contain complicated renormalizations, and that *ab initio* estimates of such parameters may neglect several such effects. The purpose is also to show that if we insist on a rather simple model, which is advocated here, the effective parameters may actually be different for different properties.

4.1 Configuration dependence of hopping integrals

We already discussed in Sec. 3.4 that there is a substantial breathing of the localized orbital when the occupancy is changed. This changes the hopping integral into this orbital. In the LMTO method [36], used here, the hopping integral V is related to a potential parameter $\tilde{\Delta}$,

$$V^2 \sim \tilde{\Delta} \approx \frac{s}{2}[\phi_l(C,s)]^2, \tag{24}$$

n_l	n_c	Mn	Ce	U
n_l^0-1	n_c^0	51	8	72
n_l^0	n_c^0	85	19	91
n_l^0+1	n_c^0	129	38	112
n_l^0	n_c^0-1	40	5	53
n_l^0+1	n_c^0-1	67	11	69

Table 6: *Potential parameter $\tilde{\Delta}$ for different configurations of Mn, Ce and U in non-spin-polarized calculations. The localized orbital is $3d$ (Mn), $4f$ (Ce) and $5f$ (U), and we consider a core hole in the $1s$ (Mn), $3d$ (Ce) and $4f$ (U) orbital. The occupancy of the localized and core orbital is n_l and n_c, respectively. We introduce n_l^0, which is 5 (Mn), 1 (Ce) and 3 (U) and n_c^0 which is 2 (Mn), 10 (Ce) and 14 (U). All energies are in mRy.*

where $\phi_l(C,s)$ is the value of the localized orbital at the Wigner-Seitz radius s. The localized orbital with the angular momentum l is solved for an energy C, which gives the logarithmic derivative $-l-1$ at s. The value of $\tilde{\Delta}$ is shown in Table 6 for a few metals with and without a core hole [27]. The table illustrates the strong dependence of the hopping on the configuration used to calculate $\tilde{\Delta}$. For instance, if we want to describe how a host electron hops into a Ce atom, should we then use the initial configuration or the final configuration to calculate $\tilde{\Delta}$ or should we use an average? Table 6 shows that the difference could be even as much as a factor of two.

To address this issue, we temporarily introduce an impurity model with two orbitals [27]

$$\varphi_l^0 \equiv \varphi_l(r, n_l^0) \qquad (25)$$
$$\varphi_l^1 \equiv A\frac{\partial}{\partial n_l}\varphi_l(r,n_l)|_{n_l=n_l^0},$$

where A is chosen so that ϕ_l^1 is normalized. By forming linear combinations of φ_l^0 and φ_l^1, we can obtain an appropriate orbital for different occupancies, i.e., describing breathing. In, for instance, an Anderson impurity model we then introduce a term leading to transitions between these two orbitals

$$\tilde{U}\sum_{m\sigma}(\psi_{1m\sigma}^\dagger\psi_{0m\sigma}+\text{H.c.})(n_0+n_1-n_l^0), \qquad (26)$$

where $n_i=\sum_{m\sigma}n_{im\sigma}$. If the occupancy of the two levels adds up to n_l^0, the orbital φ_l^0 is appropriate and there is no mixing of the orbital φ_l^1. For any other occupancy, transitions to φ_l^1 are induced and the system has the freedom to adjust to the occupancy. For Mn in CdTe we find that $\tilde{U}=0.16$ Ry. The energies of the two orbitals are quite different, $\varepsilon_0=-0.45$ Ry and $\varepsilon_1=1.68$ Ry. The model then tends to have two sets of states, one set at ε_0 and one set at ε_1. We can then project out all high-lying states, having a substantial weight in φ_l^1. The result is then that we recover the normal Anderson impurity model, with just one localized orbital. But in this process the hopping matrix elements are modified. Since the mixing matrix element $\tilde{U}/(\varepsilon_1-\varepsilon_0)=0.08\ll 1$, this approach should be rather accurate.

We can then answer the question of how to calculate these elements. Let us consider a host electron hopping into a configuration with n_l localized electrons, resulting in a configuration

with $n_l + 1$ localized electrons. The projection procedure then shows that the matrix element should be calculated using $n_l + 1$ electrons, i.e., the end configuration [27]. For $n_l = 0$ this is easy to understand. In the initial state there is no localized electron and the extent of the localized wave function then plays no role. It is then natural that it is the wave function in the final configuration that matters. In a similar way it is the initial configuration that matters when an electron hops out of the localized orbital.

We then should be using different hopping integrals for different experiments. For Ce compounds, for instance, $f^0 - f^1$-hopping is particularly important for valence photoemission, and we would use $n_l = 1$ for calculating these hopping matrix elements. For inverse photoemission, we are often interested in the relative weights of the f^1 and f^2 peaks. We then need to distinguish between the calculation of the ground-state and the calculation of the final states, resulting from the inverse photoemission process. In the ground-state calculation the important matrix elements would be calculated for $n_l = 1$ and in the final state for $n_l = 2$. For core level spectroscopies we should in addition include a core hole for the calculation of matrix elements for the final states but not for the ground-state.

As argued above, this would lead to a complicated model. It seems questionable if the possible additional gain in physics would justify such a complicated model with additional parameters. However, the example illustrates one source of uncertainty in models with configuration independent hopping parameters. It also illustrates how parameters can be different for different experiments.

4.2 Many-body renormalization of hopping integrals

In Secs. 2.2 and 3 we discussed how the effective level energies and Coulomb integrals can be obtained by letting delocalized electrons adjust to the movements of localized electrons. This approach, however, raises questions about other many-body effects. One issue is the Anderson orthogonality catastrophe [37]. Consider the case when delocalized electrons interact with a (truly) localized electron via the Coulomb interaction. Let us then change the occupancy of the localized level by one and let $|0\rangle$ and $|1\rangle$ be the lowest states of the delocalized electrons in the presence of 0 or 1 localized electrons, respectively. Then $\langle 0|1\rangle = 0$ for an infinite system [37]. One might then think that the hopping integrals should be reduced by such effects. When a delocalized electron hops into a localized level, all the other electrons would adjust their wave functions to the new potential. Then one might expect that the overlap $\langle 0|1\rangle = 0$ enters the effective hopping integral. This is, however, not the appropriate comparison. Anderson's orthogonality catastrophe refers to the case when the localized electron is removed from the system. Here it hops into or out of delocalized states. The appropriate comparison is then X-ray absorption (XAS) or X-ray emission (XES). In addition to the Anderson effect there is then an exciton like effect, transferring spectral weight towards the Fermi energy. For instance, the XES spectrum looks like

$$S(\omega) \sim \left(\frac{\widetilde{\omega}}{\omega - \omega_0}\right)^{\alpha} \Theta(\omega - \omega_0), \tag{27}$$

		$-\Delta E$					n_d							
ε_d	U_{sd}	Ex.	Ren.	Unre.	Fit	XAS	Ex.	Ren.	Unre.	Fit	XAS	$\varepsilon_d^{\rm calc}$	$\varepsilon_d^{\rm fit}$	$t_{\rm eff}^{\rm fit}$
-1.5	1	1.33	1.28	1.66	1.33	1.31	0.89	0.91	0.94	0.89	0.89	-1.09	-1.09	1.12
-1.5	2	1.12	1.02	1.66	1.12	1.08	0.82	0.87	0.94	0.83	0.81	-0.79	-0.81	1.18
-1.5	3	0.98	0.83	1.66	0.99	0.94	0.76	0.81	0.94	0.78	0.74	-0.57	-0.64	1.21
-1.5	5	0.83	0.62	1.66	0.88	0.78	0.66	0.70	0.94	0.69	0.62	-0.29	-0.41	1.30
-1.0	3	0.64	0.48	1.20	0.69	0.62	0.57	0.55	0.90	0.55	0.53	-0.07	-0.09	1.31
-0.5	3	0.42	0.29	0.78	0.44	0.41	0.33	0.24	0.79	0.31	0.31	0.43	0.36	1.22
0.0	3	0.29	0.21	0.44	0.30	0.29	0.18	0.11	0.50	0.17	0.17	0.93	0.76	1.15
10	3	.043	.040	.043	.044	.043	.004	.003	.004	.004	.004	10.9	10.1	1.00

Table 7: *Energy lowering ΔE and occupancy of the d level n_d in the exact calculation ("Ex.") compared with results of calculations for the model (28) with $U_{sd} = 0$. The unrenormalized d level position was used for "Unre." and the calculated renormalized position for "Ren." and "XAS". For "XAS" the effective hopping integral was renormalized [Eq. (29)] and for "Fit" both the level position and the hopping were adjusted to obtain the best agreement with the exact results. The parameters are $t = 1$, $B = 5$ $N = 17$ and $N_{\rm el} = 9$.*

where $\tilde{\omega}$ is a typical energy and ω_0 is the threshold energy. The exponent α is positive and determined by the phase shift due to the Coulomb interaction between localized and delocalized electrons. From Eq. (27) we might then expect hopping integrals for states close to the Fermi energy to be enhanced. This would then in particular influence thermodynamic properties.
To check these ideas we have considered the spinless model [38]

$$H = \sum_{k=1}^{N} \varepsilon_k n_k + \varepsilon_d n_d + \frac{t}{\sqrt{N}} \sum_{k=1}^{N} (\psi_k^\dagger \psi_d + \text{H.c.}) + \frac{U_{sd}}{N} \sum_{k=1}^{N} \sum_{l=1}^{N} \psi_k^\dagger \psi_l \, n_d, \tag{28}$$

where we have introduced N delocalized states with the energies ε_k and a localized state with the energy ε_d. There is a hopping integral t, connecting the localized and delocalized states. When the localized level is occupied the delocalized electrons feel a scattering potential U_{sd}. The delocalized levels are equally spaced over an energy $2B$.
This model can be solved using exact diagonalization for finite N [38]. We have used $N = 17$ and the number of electrons $N_{el} = 9$. Although this is far from an infinite system, Anderson's orthogonality catastrophe already has an effect. For $B = 5$, $\varepsilon_d = -1.5$ and $U_{sd} = 5$, the overlap between the lowest states of delocalized electrons in the presence or absence of a localized electron is $0.85 < 1$. We then calculate the energy lowering $\Delta E = E_0 - \sum_k{}' \varepsilon_k$, where E_0 is the ground-state energy and the sum goes over the N_{el} lowest states. We have also calculated the $3d$ occupancy, n_d and the charge susceptibility $\chi_c = -\partial n_d / \partial \varepsilon_d$. The results are shown in Table 7 and 8.
We compare the exact results with several approximations [38]. In all these calculations U_{sd} was put to zero and its effects were approximately included via renormalized parameters. The column "Ren." shows results where ε_d was replaced by $\varepsilon_d^{\rm calc} = \tilde{E}_0(1) - \tilde{E}_0(0)$. Here $\tilde{E}_0(n_d)$ is the energy of the model as a function of the occupancy n_d. In this calculation the hopping to the

		χ_c							
ε_d	U_{sd}	Ex.	Ren.	Unre.	Fit	XAS	$\varepsilon_d^{\rm calc}$	$\varepsilon_d^{\rm fit}$	$t_{\rm eff}^{\rm fit}$
-1.5	1	0.12	0.10	0.05	0.12	0.13	-1.09	-1.09	1.12
-1.5	2	0.20	0.19	0.05	0.20	0.23	-0.79	-0.81	1.18
-1.5	3	0.27	0.30	0.05	0.28	0.32	-0.57	-0.64	1.21
-1.5	5	0.36	0.55	0.05	0.38	0.40	-0.29	-0.41	1.30
-1.0	3	0.47	0.74	0.12	0.50	0.47	-0.07	-0.09	1.31
-0.5	3	0.41	0.41	0.35	0.43	0.37	0.43	0.36	1.22
0.0	3	0.21	0.14	0.75	0.22	0.19	0.93	0.76	1.15
10	3	.0006	.0005	.0006	.0006	.0006	10.9	10.1	1.00

Table 8: *Same as Table 7 but for calculating χ.*

localized level was cut to avoid double-counting. The Table also shows results for unrenormalized parameters ("Unre."). We then treated the $\varepsilon_d^{\rm fit}$ and $t_{\rm eff}^{\rm fit}$ as fitting parameters, and adjusted these parameters to obtain the best possible agreement ("Fit") with the exact results. Finally we have performed calculations where the hopping matrix element to a level ε_k

$$\big(t_{\rm eff}(\varepsilon_k)\big)^2 = t^2 S(|\varepsilon_k - \varepsilon_F + \omega_0|), \tag{29}$$

was related to the X-ray absorption or emission spectra. $t_{\rm eff}(\varepsilon_k)^2$, summed over all states, is unrenormalized, but the hopping parameters to states close to the Fermi energy, ε_F, are enhanced at the cost of hopping to the band edges. In calculations with $t_{\rm eff}(\varepsilon_k)$ we used the renormalized level position $\varepsilon_d^{\rm calc}$.

We first compare the exact results with the unrenormalized and renormalized results. The renormalization improves the agreement with the exact results substantially. For most parameter sets the agreement is relatively good. For U_{sd} large and for $|\varepsilon_d|$ rather small, there are still substantial deviations. "XAS" shows the results when the hopping is renormalized as well, using Eq. (29). There is then a substantial additional improvement, and the agreement is now generally rather good. Finally, we have treated both the hopping and the level position as adjustable parameters. This gives only a marginal improvement and sometimes the results are even worse. This is remarkable, since the d-level position is now also a fit parameter and $\varepsilon_d^{\rm calc}$ is sometimes rather different from $\varepsilon_d^{\rm fit}$. On the other hand, hopping is energy-dependent, and "XAS" presumably describes this better than "Fit". This suggests that Eq. (29) gives a quite good renormalization.

In the case of Ce the delocalized states are primarily of $5d$ character. According to the Friedel sum rule we can then estimate the phase shift as $\delta \sim \pi/10$. This then gives a singularity index of the order $\alpha \sim 0.1$. For thermodynamic properties we may then expect an enhancement of the order of $(\tilde{\omega}/T_K)^{0.1}$, where T_K is the Kondo temperature. For, e.g., $CeCu_2Si_2$ $T_K = 0.001$ eV, and t^2 may then be enhanced by a factor of two, if we assume $\tilde{\omega} \sim 1$ eV. As discussed above, we do not advocate including these effects explicitly in a model. However, one should be aware that thermodynamic and spectroscopic properties may be renormalized differently.

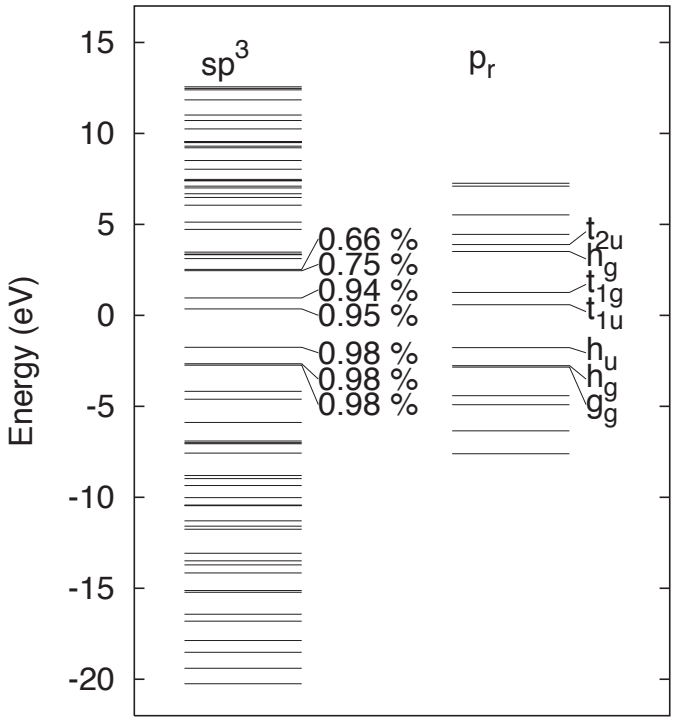

Fig. 3: *Levels of the C_{60} molecule. The left-hand part shows the levels obtained by using a basis of one $2s$ and three $2p$ orbitals per carbon atom (sp^3). The right-hand part shows the levels obtained by using just one radial $2p$ orbital per atom ($2p_r$). The numbers give the amount of radial $2p$ character ($2p_r$) in the full calculation (after Ref. [39]).*

5 Fullerenes

In this section we discuss the parameters for a molecular solid. As an example we use fullerenes [39]. Similar work has been done for TTF-TCNQ [40].

5.1 Hopping

The important levels in a C_{60} molecule can be described in a tight-binding picture including a $2s$ and three $2p$ orbitals on each of the 60 C atoms. The corresponding molecular levels are shown in Fig. 3. The molecule forms approximate sp^2 hybrids on each C atom which point towards the neighboring C atoms and radial orbitals p_r pointing out of the molecule. The former orbitals interact strongly and form bonding and antibonding molecular orbitals at the lower and upper end of the spectrum, respectively. The p_r orbitals interact much less and form molecular orbitals in the middle of the spectrum. The figure illustrates that these molecular orbitals can be described rather well using only the p_r orbitals. In the neutral molecule all orbitals up to and including the h_u orbital are filled.

C_{60} molecules condense to a solid of rather weakly bound molecules. Thus the distance (~ 3 Å) between the closest C atoms on two neighboring molecules is much larger than the distance (~ 1.4 Å) between two C atoms on the same C_{60} molecule. The molecular levels then essentially

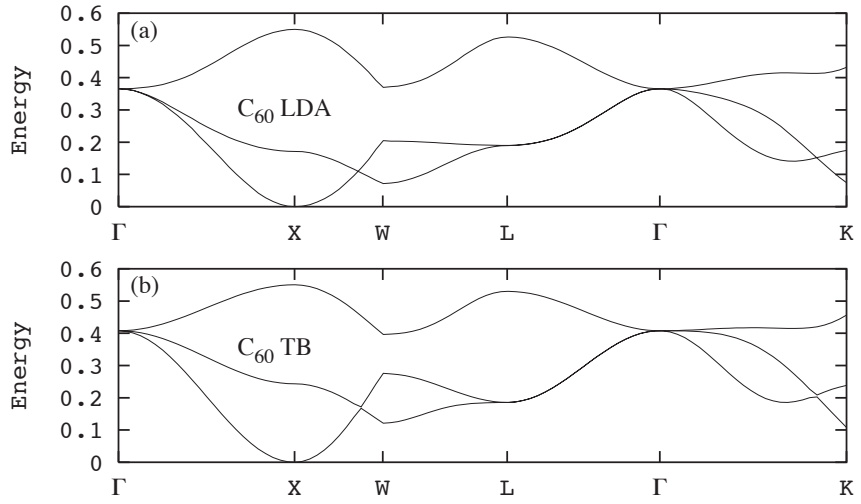

Fig. 4: *Band structure for a C_{60} solid in the $Fm\bar{3}$ structure (a) according to an ab initio LDA and (b) according to a TB calculation (after Gunnarsson et al. [43]).*

preserve their identity in the solid, but the discrete molecular levels are broadened to narrow, essentially non-overlapping bands. The alkali-doped fullerenes are of particular interest. In these systems the t_{1u} band is partly filled. Therefore the three-fold degenerate t_{1u} molecular level is particularly interesting.

The band structure can be described in a tight-binding (TB) scheme. We first form a molecular orbital corresponding to the t_{1u} level. The hopping between the molecules is described by hopping integrals $V_{pp\sigma}$ and $V_{pp\pi}$ corresponding to hopping between orbitals pointing directly towards each other or orbitals pointing perpendicular to the connecting line of the centers. Following Harrison [41], we assume that the ratio of the $\pi-$ and σ-integrals is -1/4. Then

$$V_{pp\sigma} = v_\sigma \frac{R}{R_0} e^{-\lambda(R-R_0)}; \quad \frac{V_{pp\pi}}{V_{pp\sigma}} = -\frac{1}{4} \quad R_0 = 3.1 \text{ Å}, \tag{30}$$

where R is the separation of the carbon atoms. The prefactor R has been included to simulate the r-dependence of a $2p$ orbital as described by Slater's rules [30]. The overall hopping strength, determined by v_σ, is adjusted to the band-width in a band structure calculation, and the decay length λ is determined from the dependence of the band width on the lattice parameter. Here we use the parameters [42, 43]

$$\lambda = 1.98 \text{ Å}^{-1} \text{and} \quad v_\sigma = 0.917 \text{ eV}. \tag{31}$$

The resulting TB band structure is compared with an *ab initio* band structure calculation in Fig. 4. The agreement is quite good. The resulting band structure $\varepsilon_{\mathbf{k}}$ has a simple parameterization [42, 44]. The dominating hopping between two molecules in this structure is given by two equivalent hopping integrals, with all other hopping integrals being substantially smaller. Effectively, we have therefore adjusted this parameter, requiring that the TB band width should agree with the LDA band width. The shape of the band structure in Fig. 4 is therefore primarily determined by the geometry of the C_{60} molecule and by the relative positions and orientations of the C_{60} molecules in the $Fm\bar{3}$ symmetry.

5.2 Coulomb interaction

We first consider the Coulomb integral U_0 between two t_{1u}-electrons for a free C_{60} molecule. A very simple estimate is obtained by assuming that the charge density of the t_{1u} orbital forms a thin shell of charge on a sphere with the radius of the C_{60} molecule $R \sim 3.5$ Å. Then $U_0 = 1/R \approx 4$ eV. This neglects that the orbitals breath when the occupancy is changed. To obtain a better estimate one can calculate how the t_{1u} eigenvalue changes with occupancy, using Eq. (23) and LDA. This leads to values of the order 2.7-3.0 eV [45–47]. U_0 for a free molecule can also be estimated from experimental results using

$$U_0 = I_p(C_{60}^-) - A(C_{60}^-) = E_0(2) + E_0(0) - 2E_0(1), \tag{32}$$

where $E_0(n)$ is the energy of a C_{60} molecule with n t_{1u} electrons. This leads to $U_0 \sim 2.7$ eV, in fairly good agreement with theory [39, 48].

We next consider U for a C_{60} solid, following Antropov *et al.* [47]. U is strongly screened by the polarization of the surrounding molecules. To describe this, we put the C_{60} molecules on an fcc lattice and assign a polarizability α to each molecule. An electron is added to the central molecule, and the surrounding molecules are allowed to polarize in a self-consistent way. This polarization acts back on the electron and reduces the energy-increase of the t_{1u} level by an amount δU. The summation over neighboring molecules is extended until it is converged. The U for the solid is then

$$U = U_0 - \delta U. \tag{33}$$

The value of α can be determined from the experimental value, $\varepsilon = 4.4$, of the dielectric function [51]. Using the Clausius-Mossotti relation and the lattice parameter $a = 14.04$ Å, this leads to $\alpha = 90$ Å^3. *Ab initio* calculations using the density functional formalism give $\alpha = 83$ Å^3 [46]. Using $\alpha = 90$ Å^3, Antropov *et al.* [47] found $\delta U = 1.7$ eV. Together with $U_0 = 2.7$ eV, this gives $U = 1.0$ eV. These values of U do not include the metallic screening from the t_{1u} electrons in A_3C_{60} compounds, and they are appropriate for models where the metallic screening is treated explicitly when solving the corresponding model.

We next consider the nearest neighbor interaction V, which is obtained by calculating the increase of the energy of a t_{1u} orbital on a molecule 1 when an electron is added to a neighboring molecule 2. This leads to the result

$$V = 1/R_{nn} - \delta V, \tag{34}$$

where R_{nn} is the nearest neighbor separation and $-\delta V$ is the lowering of the t_{1u} orbital on molecule 1 due to the polarization of the surrounding molecules when an electron is added to molecule 2. For $a = 14.04$ Å, Antropov *et al.* [47] estimated that δV=1.12 eV, resulting in $V = 0.3$ eV for the polarizability $\alpha = 90$ Å^3. The same value $V = 0.3$ eV was also obtained by Pederson and Quong [46]. We can see that U is indeed substantially larger than V, and that it is justified to focus on the effects of U at first.

U can be estimated experimentally from Auger spectroscopy [49, 50]. A carbon $1s$ electron is emitted in a photoemission process. This is followed by an Auger process, where a carbon

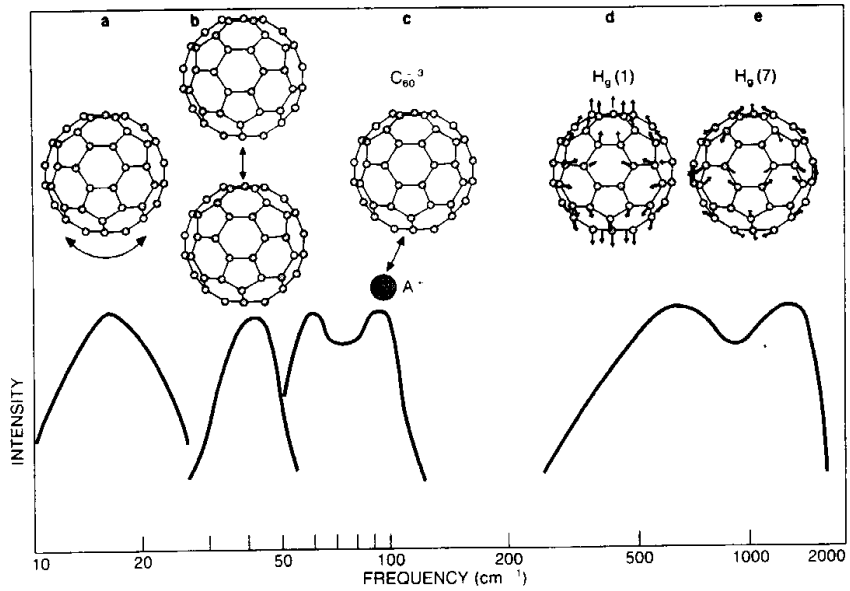

Fig. 5: *Schematic representation of various phonons in A_3C_{60} compounds. The figure shows, from left to right, (a) librations, (b) intermolecular C_{60}-C_{60} phonons, (c) A-C_{60} phonons and (d)-(e) intramolecular H_g modes. The figure indicates the radial and tangential character of the low-lying and and high-lying H_g modes, respectively (After Hebard [52]).*

$2p$ electron falls down into the $1s$ hole and another $2p$ electron is emitted. For noninteracting electrons, the Auger spectrum is just the self-convolution of the photoemission spectrum. For the interacting system, the Auger spectrum is expected to be shifted due to the interaction of the two holes in the final state. Indeed, Lof *et al.* [49] found good agreement with the self-convoluted curve when this was shifted by 1.6 eV. The experimental estimate of the Coulomb interaction is then $U = 1.6 \pm 0.2$ eV [49] as an average over all orbitals and about 1.4 eV for the highest occupied orbital. Since Auger is rather surface sensitive, this number may be more representative for U at the surface. One can estimate that U at the surface is about 0.3 eV larger than in the bulk, due to fewer neighbors and less efficient screening [47]. This suggests that the bulk value of U for the t_{1u} and h_u orbitals may be on the order $U = 1.1$ eV, which is close to the theoretical estimate. U has also been estimated for K_6C_{60} in a similar way [50], giving a similar value $U = 1.5$ eV.

5.3 Electron-phonon interaction

The electron-phonon interaction plays an important role for many properties of the alkali-doped fullerides. For instance, superconductivity is believed to be due the electron-phonon interaction. Fig. 5 indicates the different types of phonons in alkali-doped C_{60} compounds. The low-lying modes are librations (4-5 meV) and intermolecular modes (energies up to about 17 meV) involving alkali-C_{60} and C_{60}-C_{60} modes. The high-lying modes (34-195 meV) are intramolecular modes, where the molecules are deformed. All the low-lying modes have a rather weak coupling to the t_{1u} electrons, and the main coupling is to the intramolecular phonons. Here, we

therefore focus on the the coupling to these phonons. These phonons couple primarily to the level energies in contrast to the intermolecular phonons which couple to the hopping integrals. The C_{60} molecule has $60 \times 3 - 6 = 174$ intramolecular modes. For symmetry reasons, however, the t_{1u} electrons only couple to modes with A_g or H_g symmetry. There are eight five-fold degenerate H_g modes and two nondegenerate A_g modes. The coupling to the t_{1u}-level takes the form [53]

$$\begin{aligned} H_{el-ph} &= \sum_{\nu=1}^{8} g_\nu \sum_{M=1}^{5} \sum_{\sigma} \sum_{m=1}^{3} \sum_{m'=1}^{3} \left(V_{H_g}^{(M)}\right)_{m\,m'} \psi_{m\sigma}^\dagger \psi_{m'\sigma} \left(b_{\nu M} + b_{\nu M}^\dagger\right) \\ &+ \sum_{\nu=9}^{10} g_\nu \sum_{\sigma} \sum_{m=1}^{3} \sum_{m'=1}^{3} \left(V_{A_g}\right)_{m\,m'} \psi_{m\sigma}^\dagger \psi_{m'\sigma} \left(b_\nu + b_\nu^\dagger\right), \end{aligned} \tag{35}$$

where $\psi_{m\sigma}^\dagger$ creates a t_{1u} electron with quantum number m and $b_{\nu M}^\dagger$ creates a phonon in mode ν with quantum number M. The first eight modes are H_g Jahn-Teller phonons and the next two are A_g phonons. The coupling constants are g_ν and the coupling to the H_g phonons is given by the matrices

$$V_{H_g}^{(1)} = \frac{1}{2}\begin{pmatrix} -1 & 0 & 0 \\ 0 & -1 & 0 \\ 0 & 0 & 2 \end{pmatrix} \quad V_{H_g}^{(2)} = \frac{\sqrt{3}}{2}\begin{pmatrix} 1 & 0 & 0 \\ 0 & -1 & 0 \\ 0 & 0 & 0 \end{pmatrix} \quad V_{H_g}^{(3)} = \frac{\sqrt{3}}{2}\begin{pmatrix} 0 & 1 & 0 \\ 1 & 0 & 0 \\ 0 & 0 & 0 \end{pmatrix}$$

$$V_{H_g}^{(4)} = \frac{\sqrt{3}}{2}\begin{pmatrix} 0 & 0 & 1 \\ 0 & 0 & 0 \\ 1 & 0 & 0 \end{pmatrix} \quad V_{H_g}^{(5)} = \frac{\sqrt{3}}{2}\begin{pmatrix} 0 & 0 & 0 \\ 0 & 0 & 1 \\ 0 & 1 & 0 \end{pmatrix} \tag{36}$$

and the coupling to the A_g phonons by

$$V_{A_g}^{(1)} = \begin{pmatrix} 1 & 0 & 0 \\ 0 & 1 & 0 \\ 0 & 0 & 1 \end{pmatrix}. \tag{37}$$

The corresponding dimensionless electron-phonon coupling constant is [53]

$$\lambda = \frac{5}{3} N(0) \sum_{\nu=1}^{8} \frac{g_\nu^2}{\hbar\omega_\nu} + \frac{2}{3} N(0) \sum_{\nu=9}^{10} \frac{g_\nu^2}{\hbar\omega_\nu}, \tag{38}$$

where $N(0)$ is the density of states per spin and molecule and ω_ν is the frequency of mode ν. The theoretical calculation of the electron-phonon coupling for a solid is very complicated. Lannoo *et al.* [54] showed that for intramolecular modes in fullerides, important simplifications follow from the large difference between the intramolecular (E_I) and intermolecular (W) energy scales. The coupling for a solid can then be obtained approximately from a calculation for a free molecule and the density of states $N(0)$ of the solid. Thus, it is sufficient to calculate the shift $\Delta\varepsilon_{\nu\alpha}$ of the t_{1u} levels α for a free C_{60} molecule per unit displacement of the νth phonon coordinate. One then finds that

$$\lambda \sim N(0) \sum_{\nu\alpha} \frac{\Delta\varepsilon_{\nu\alpha}^2}{\omega_\nu^2}. \tag{39}$$

		$\lambda_\nu/N(0)$						
		Theory				Photoemission		Raman
Mode	ω_ν	Antrop. [55]	Faul. [56]	Man. [57]	Iwa. [60]	Gun. [58]	Iwa. [60]	Kuz. [61]
$H_g(8)$	1575	.022	.009	.014	.018	.023	.011	.003
$H_g(7)$	1428	.020	.015	.015	.023	.017	.028	.004
$H_g(6)$	1250	.008	.002	.003	.002	.005	.007	.001
$H_g(5)$	1099	.003	.002	.004	.005	.012	.009	.001
$H_g(4)$	774	.003	.010	.004	.006	.018	.007	.003
$H_g(3)$	710	.003	.001	.009	.012	.013	.015	.003
$H_g(2)$	437	.006	.010	.011	.011	.040	.012	.020
$H_g(1)$	273	.003	.001	.005	.006	.019	.007	.048
$\sum H_g$		.068	.049	.065	.083	.147	.096	.083

Table 9: *Partial electron-phonon coupling constants $\lambda_\nu/N(0)$ (in eV) according to different theoretical calculations and derived from photoemission and Raman scattering. The energies ω_ν (in cm^{-1}) of the modes for the undoped system are shown.*

This gives a molecule-specific quantity which is multiplied by $N(0)$. Table 9 shows results for the electron-phonon coupling. The theoretical calculations by Antropov *et al* [55], Faulhaber *et al.* [56] and Manini *et al.* [57] are based on *ab initio* LDA calculations. The work of Iwahara *et al.* is based on the B3LYP functional with some Hartree-Fock exchange mixed in. There are substantial deviations between the distribution of coupling strength to the different modes in the different calculations. This distribution is very sensitive to the precise form of the phonon eigenvectors. The deviations between the total coupling strengths are smaller. The work of Iwahara *et al.* gives a stronger coupling than the other three calculations. This is not so surprising, since this work is based on a rather different functional.

An experimental method for estimating the electron-phonon coupling is the use of photoemission data. Because of the relatively strong electron-phonon coupling, we expect to see satellites due to the excitation of phonons. The weights of the satellites give information about the strength of the coupling. This is essentially the Franck-Condon effect, but because of the Jahn-Teller effect the calculation of the satellite structure is rather complicated. The photoemission spectra of K_3C_{60} and Rb_3C_{60} have been analyzed along these lines [62]. Due to the broadening effects in a solid and due to the complications in the theoretical treatment of bands with dispersion, however, it was not possible to derive reliable, quantitative values for the electron-phonon coupling.

Photoemission spectra have also been measured for free C_{60}^- ions. In this case the theoretical treatment is substantially simpler [58]. In these experiments, a beam of C_{60}^- ions was created and a photoemission experiment was performed using a laser light source ($\hbar\omega = 4.025$ eV) and a time of flight spectrometer. The spectrum resulting from emission from the t_{1u} level was measured. To analyze the results, we use the couplings in Eq. (35) of the t_{1u} level to the two A_g and the eight five-fold degenerate H_g modes. For this model the ground-state can be calculated by numerical diagonalization to any desired accuracy [58]. Furthermore, within

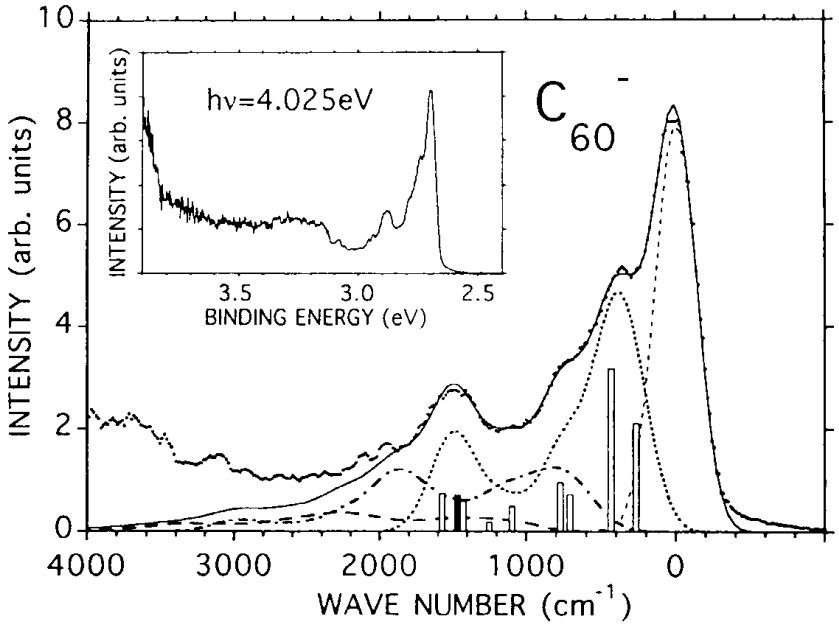

Fig. 6: *Experimental (dots) and theoretical (full line) photoemission spectrum of C_{60}^-. The theoretical no-loss (dashed), single-loss (dotted) and double-loss (dashed-dotted) curves are also shown. The contributions of the different modes to the single-loss curve are given by bars (H_g: open, A_g: solid). The inset shows the experimental spectrum over a larger energy range (after Gunnarsson et al. [58]).*

the sudden approximation [63], the photoemission spectrum can easily be calculated. A set of coupling constants is then assumed and the resulting spectrum is compared with experiment. The coupling parameters are varied until good agreement with experiment is obtained, thereby providing an estimate of the couplings. The resulting spectrum is compared with experiment in Fig. 6 and the corresponding parameters are shown in Table 9. An uncertainty in this approach is that with the available resolution, it is not possible to distinguish between the coupling to A_g modes and H_g modes with similar energies. The couplings to the A_g modes were therefore taken from a calculation [55]. With this assumption, the couplings to the H_g modes can then be determined. An equally good fit can, however, be obtained using other couplings to the A_g modes if the couplings to the H_g modes are changed correspondingly.

Substantially later the experiments in Ref. [58] were repeated by Wang *et al.* [59]. It was now possible to obtain a better resolution. These data have been analyzed in a similar way as in Ref. [58] by Iwahara *et al.* [60]. Their results are also shown in Table 9. The total coupling is weaker than in Ref. [58], but still substantially larger than in the *ab initio* LDA calculations. The agreement with the calculation using the B3LYP is better.

Raman scattering provides a different method of estimating the coupling strength. The electron-phonon coupling allows phonons to decay into an electron-hole pair in the metallic fullerides. This decay contributes to the width of the phonon and can be measured in Raman scattering. Other factors may also contribute to the width, but one can try to eliminate these by subtracting the width of the phonons for a nonmetallic system, where a decay in electron-hole pairs is not

possible. This was done by Winter and Kuzmany [61], and Table 9 shows results adapted [39] from the experiments [61]. The total weight does not differ much from what was obtained from photoemission [60], but the distribution of weight between the different modes differs dramatically. Theoretically, it is found that in the solid there is a transfer of weight to lower modes, due to the coupling to electron-hole pairs [64]. This mechanism is operative for the Raman data but not for the photoemission data (taken for a free molecule). This may explain some of the discrepancy between the photoemission and Raman data.

6 Conclusions

For complicated systems with strong correlation effects it is often not possible to obtain accurate *ab initio* solutions, but it is instead useful to turn to models. An important issue is then how to obtain parameters and how to renormalize parameters to include as much physics as possible. We have discussed how the basic principle is to try to include, implicitly as a renormalization of parameters, all effects not explicitly included in the model. On the other hand, we should not allow effects included explicitly in the model to renormalize parameters. For many-body systems there is no general systematic and controlled way of doing this. The basic assumption is often that the electrons can be put into two groups of "fast" (delocalized) and "slow" (localized) electrons, where the "fast" electrons are assumed to adjust to the "slow" electrons, and therefore can be projected out. Such a division is, however, often not very clear cut. Nevertheless some methods have been relatively successful in obtaining parameters for certain classes of systems. We have, however, shown simple examples of many-body effects that are usually not included, but can have an appreciable effect on the parameters. In particular, renormalization effects may work differently for different experiments. We have also argued that it is important to try to extract parameters from different sources, both theory and experiment, to obtain a better understanding of the accuracy of the parameters.

References

[1] P. Hohenberg and W. Kohn, Phys. Rev. **136**, B864 (1964)

[2] W. Kohn and L.J. Sham, Phys. Rev. **140**, A1133 (1965)

[3] L. Hedin, Phys. Rev. **139**, A796 (1965)

[4] F. Aryasetiawan and O. Gunnarsson, Reports on Progress in Physics, **61**, 237 (1998)

[5] P.W. Anderson, Phys. Rev. **124**, 41 (1961)

[6] J. Hubbard, Proc. Royal Society (London) **276**, 238 (1963)

[7] F.C. Zhang and T.M. Rice, Phys. Rev. B **37** 3759, (1988)

[8] A. Iandelli and A. Palenzona: *Chrystal chemistry of intermetallic compounds* in *Handbook on the Physics and Chemistry of Rare Earths*, Vol. 3, Eds.: K.A. Gschneider Jr. and L. Eyring (North-Holland, Amsterdam, 1979) p. 1

[9] B. Johansson, J. Phys. F **4**, L 169 (1979)

[10] J.W. Allen and R.M. Martin, Phys. Rev. Lett. **49**, 1106 (1982)

[11] K. Held, A.K. McMahan and R.T. Scalettar, Phys. Rev. Lett. **87**, 276404 (2001)

[12] P.O. Löwdin, J. Chem. Phys. **19**, 1396 (1951)

[13] O.K. Andersen, O. Jepsen and D. Glötzel: *Canonical Description of the Band Structure of Metals.*, in *Highlights of Condensed Matter Theory*, Eds. F. Bassani, F. Fumi and M.P. Tosi (North-Holland, Amsterdam 1985)

[14] O. Gunnarsson, Phys. Rev. **41**, 514 (1990)

[15] C. Herring: *Magnetism*, Vol. 4, Eds. G.T. Rado and H. Suhl (Academic Press, New York, 1966)

[16] B.N. Cox, M.A. Coultard and P. Loyd, J. Phys. F: Metal Physics **4**, 807 (1974)

[17] J.F. Herbst, R.E. Watson, and J.W. Wilkins, Phys. Rev. B **13**, 1439 (1976) and Phys. Rev. B **17**, 3089 (1978)

[18] P.H. Dederichs, S. Blügel, R. Zeller, and H. Akai, Phys. Rev. Lett. **53**, 2512 (1984)

[19] M.S. Hybertsen, M. Schlüter, N.E. Christensen, Phys. Rev. B **39**, 9028 (1989)

[20] M. Cococcioni and S. de Giroconcoli, Phys. Rev. B **71**, 035105 (2005)

[21] A.K. McMahan, R.M. Martin, S. Satpathy, Phys. Rev. B **38**, 6650 (1988)

[22] O. Gunnarsson, O.K. Andersen, O. Jepsen, J. Zaanen, Phys. Rev. B **39**, 1708 (1989)

[23] V.I. Anisimov and O. Gunnarsson, Phys. Rev. B **43**, 7570 (1991)

[24] Ref. [25] (Sec. IIID) argues that the "cut off" LDA [21, 22] for, e.g., a transition metal, incorrectly includes on-site $3d$-$3d$ transitions to describe breathing (cf. Sec. 3.4) of the central $3d$ orbitals. This is incorrect, since $3d$-$3d$ transitions would not change the radial extent of the $3d$ orbital. It was further implied that metallic $3d$ screening is included, i.e., transfer of charge to the central $3d$ orbitals, already included explicitly in the Hubbard model. This is, however, excluded by keeping the total occupancy of the $3d$ orbitals at the prescribed value. Finally, it was argued that breathing of the $3d$ orbital should not be included. Since breathing is not explicitly included in the Hubbard model, it should be included in the calculation of U. It is an important effect [26, 27].

[25] F. Aryasetiawan, K. Karlsson, O. Jepsen, and U. Schönberger, Phys. Rev. B **74**, 125106 (2006)

[26] O. Gunnarsson, O.K. Andersen, O. Jepsen, and J. Zaanen, Phys. Rev. B **39**, 1708 (1989)

[27] O. Gunnarsson and O. Jepsen, Phys. Rev. B **38**, 3568 (1988)

[28] I.V. Solovyev and M. Imada, Phys. Rev. B **71**, 045103 (2005)

[29] I.V. Solovyev and P.H. Dederichs, Phys. Rev. B **49**, 6736 (1994)

[30] J.A. Pople and D.L. Beveridge: *Approximate Molecular Orbital Theory* (McGraw-Hill, New York, 1970), p. 27-29

[31] M.I. Katsnelson abd A.I. Lichtenstein, J.Phys.: Condens. Matter **11**, 1037 (1999) and references therein

[32] Similar results were found for other system containing atoms from the middle of the $3d$ series [33].

[33] V. Drchal, O. Gunnarsson, and O. Jepsen, Phys. Rev. B **44**, 3518 (1991)

[34] O. Gunnarsson *et al.*, Phys. Rev. B **41**, 4811 (1990)

[35] J.W. Allen, S.J. Oh, O. Gunnarsson, K. Schönhammer, M.B. Maple, M.S. Torikachvili, and I. Lindau, Adv. Phys. **35**, 275 (1986)

[36] O.K. Andersen, Phys. Rev. B **12**, 3060 (1975)

[37] P.W. Anderson, Phys. Rev. Lett. **18**, 1049 (1967)

[38] O. Gunnarsson and K. Schönhammer, Phys. Rev. B **40**, 4160 (1989)

[39] O. Gunnarsson, *Alkali-doped Fullerides* (World Scientific, Singapore, 2004)

[40] L. Cano-Cortes, A. Dolfen, J. Merino, J. Behler, B. Delley, K. Reuter, and E. Koch, Eur. Phys. J. B **56**, 173 (2007)

[41] W. Harrison, *Electronic structure and the properties of solids*, (Freeman, San Francisco, 1980)

[42] O. Gunnarsson, S. Satpathy, O. Jepsen, and O.K. Andersen, Phys. Rev. Lett. **67**, 3002 (1991)

[43] O. Gunnarsson, S.C. Erwin, E. Koch, and R.M. Martin, Phys. Rev. B **57**, 2159 (1998)

[44] N. Laouini, O. K. Andersen, and O. Gunnarsson, Phys. Rev. B **51**, 17446 (1995)

[45] V. de Coulon, J.L. Martins, and F. Reuse, Phys. Rev. B **45**, 13671 (1992)

[46] M.R. Pederson and A.A. Quong, Phys. Rev. B **46**, 13584 (1992)

[47] V.P. Antropov, O. Gunnarsson, and O. Jepsen, Phys. Rev. B **46**, 13647 (1992)

[48] R.L. Hettich, R.N. Compton, and R.H. Ritchie, Phys. Rev. Lett. **67**, 1242 (1991)

[49] R.W. Lof, M.A. van Veenendaal, B. Koopmans, H.T. Jonkman, and G.A. Sawatzky, Phys. Rev. Lett. **68**, 3924 (1992)

[50] P.A. Brühwiler, A.J. Maxwell, A. Nilsson, N. Mårtensson, and O. Gunnarsson, Phys. Rev. B **48**, 18296 (1993)

[51] A.F. Hebard, R.C. Haddon, R.M. Fleming, and R. Kortan, Appl. Phys. Lett. **59**, 2109 (1991)

[52] A.F. Hebard, Phys. Today **45**, No. 11, p. 26 (1992)

[53] O. Gunnarsson, Phys. Rev. B **51**, 3493 (1995)

[54] M. Lannoo, G.A. Baraff, M. Schlüter, and D. Tomanek, Phys. Rev. B **44**, 12106 (1991)

[55] V.P. Antropov, O. Gunnarsson, and A.I. Liechtenstein, Phys. Rev. B **48**, 7651 (1993)

[56] J.C.R. Faulhaber, D.Y.K. Ko, and P.R. Briddon, Phys. Rev. B **48**, 661 (1993)

[57] N. Manini, A.D. Corso, M. Fabrizio, and E. Tosatti, Phil. Mag. B **81**, 793 (2001)

[58] O. Gunnarsson, H. Handschuh, P.S. Bechthold, B. Kessler, G. Ganteför, and W. Eberhardt, Phys. Rev. Lett. **74**, 1875 (1995)

[59] X.B. Wang, H.K. Woo, and L.S. Wang, J. Chem. Phys. **123**, 051106 (2005)

[60] N. Iwahara, T. Sato, K. Tanaka, L.F. Chibotaru, Phys. Rev. B **82**, 245409 (2010)

[61] J. Winter and H. Kuzmany, Phys. Rev. B **53**, 655 (1996)

[62] M. Knupfer, M. Merkel, M.S. Golden, J. Fink, O. Gunnarsson, V.P. Antropov, Phys. Rev. B **47**, 13944 (1993)

[63] L. Hedin and S. Lundqvist, in *Solid State Physics*, Vol. 23, p. 1, Eds. H. Ehrenreich, D. Turnbull, and F. Seitz (Academic, New York, 1969)

[64] J.E. Han and O. Gunnarsson, Phys. Rev. B **61**, 8628 (2000)

10 DFT-based Green Function Approach for Impurity Calculations

Rudolf Zeller
Institute for Advanced Simulation
Forschungszentrum Jülich GmbH

Contents

E. Pavarini, E. Koch, F. Anders, and M. Jarrell
Correlated Electrons: From Models to Materials
Modeling and Simulation Vol. 2
Forschungszentrum Jülich, 2012, ISBN 978-3-89336-796-2
http://www.cond-mat.de/events/correl12

1 Introduction

If one wants to apply density functional theory (DFT) to study the electronic structure of materials locally perturbed by defect atoms or more generally of disordered dilute and concentrated alloys, the standard approach is to use band structure methods developed for periodic systems. The defect atoms are periodically repeated so that a periodic crystal with a large unit cell (supercell) is obtained. The supercell must be large to minimize spurious interactions between the defect atoms in adjacent supercells. Supercells with a few hundred atoms can be treated routinely today and sophisticated corrections for some of the unwanted interactions have been developed. The situation was considerably different in the 1970s and 1980s when the computing power was orders of magnitude smaller than today. Then Green function methods were mandatory to investigate the electronic structure of defect atoms more efficiently. The advantage of Green function methods is that the potential must be determined self-consistently only in the region where it noticeably differs from the one of the unperturbed host crystal. As a consequence Green function methods correctly describe the embedding of the local environment of the defect atoms in the otherwise unperturbed surrounding perfect crystal. It is the aim of this chapter to give an introduction into the concept of Green function methods for studying locally perturbed crystals. For illustration of the concept and its advantages some key results will be presented. These results were mainly obtained by a Green function (GF) technique which is based on the Korringa-Kohn-Rostoker (KKR) band structure method [1, 2] and which was developed in Jülich over the last decades. This technique, the KKR-GF method, is particularly suited for metallic systems, but can be applied also for semiconductors and insulators.

2 Green function of the Kohn-Sham equation

The basic quantity in density functional theory [3, 4] is the electronic density. The density can be determined, if the Kohn-Sham single-particle equations

$$\left[-\nabla_{\mathbf{r}}^2 + v_{\text{eff}}(\mathbf{r})\right] \varphi_i(\mathbf{r}) = \epsilon_i \varphi_i(\mathbf{r}) \tag{1}$$

are solved.[1] The normalized Kohn-Sham wavefunctions $\varphi_i(\mathbf{r})$ can then be used to calculate the density by

$$n(\mathbf{r}) = 2 \sum_i |\varphi_i(\mathbf{r})|^2 \tag{2}$$

where for a system with N electrons the sum is over the $N/2$ orbitals with the lowest values of ϵ_i. The ϵ_i are the eigenvalues of the Hamiltonian $\mathcal{H} = -\nabla_{\mathbf{r}}^2 + v_{\text{eff}}(\mathbf{r})$. The factor two accounts for the assumed spin degeneracy. Alternatively to (2), the density can be calculated from the Green function of the Kohn-Sham system. This Green function is defined as the solution of

$$\left[-\nabla_{\mathbf{r}}^2 + v_{\text{eff}}(\mathbf{r}) - \epsilon\right] G(\mathbf{r}, \mathbf{r}'; \epsilon) = -\delta(\mathbf{r} - \mathbf{r}') \,. \tag{3}$$

[1] To simplify the notation, Rydberg atomic units $\hbar^2/2m = 1$ are used throughout this chapter and usually the equations are given only for non-spin-polarized systems. The generalization to spin-polarized (magnetic) systems is straightforward.

Here the boundary condition $G(\mathbf{r},\mathbf{r}';\epsilon) \to 0$ for $|\mathbf{r}-\mathbf{r}'| \to \infty$ is assumed and the symbol ϵ denotes a continuous complex variable in contrast to the real discrete variables ϵ_i. The result for the density is

$$n(\mathbf{r}) = -\frac{2}{\pi}\mathrm{Im}\int_{-\infty}^{E_F} G(\mathbf{r},\mathbf{r};\epsilon)\mathrm{d}\epsilon \tag{4}$$

where the integral is understood as an integral in the complex ϵ plane on a contour infinitesimally above the real ϵ axis. The Fermi level E_F is obtained by the condition that the density $n(\mathbf{r})$ integrated over all space gives the correct number of electrons. For instance, in neutral systems, this number is determined by the sum of the nuclear charges. The result (4) can be derived as follows. In operator notation (3) can be written as

$$[\mathcal{H}-\epsilon]G = -I \tag{5}$$

where $\mathcal{H}$ is the Hamiltonian and I the unity operator. In terms of eigenvalues ϵ_i and eigenfunctions $\varphi_i(\mathbf{r})$ the Hamiltonian $\mathcal{H}$ can be expressed as

$$\mathcal{H} = \sum_i \epsilon_i \varphi_i(\mathbf{r})\varphi_i^\star(\mathbf{r}')\,. \tag{6}$$

This is true because the right hand of this equation acting on $\varphi_i(\mathbf{r})$ leads to $\epsilon_i\varphi_i(\mathbf{r})$ which is the required result for $\mathcal{H}\varphi_i(\mathbf{r})$. This follows from

$$\sum_j \epsilon_j\varphi_j(\mathbf{r})\int \mathrm{d}\mathbf{r}'\varphi_j^\star(\mathbf{r}')\varphi_i(\mathbf{r}') = \sum_j \epsilon_j\varphi_j(\mathbf{r})\delta_{ij} = \epsilon_i\varphi_i(\mathbf{r}) \tag{7}$$

where the orthonormality constraint $\int \mathrm{d}\mathbf{r}'\varphi_j^\star(\mathbf{r}')\varphi_i(\mathbf{r}') = \delta_{ij}$ for the eigenfunctions was used. By using that G is the inverse operator of $\epsilon - \mathcal{H}$ the so called spectral representation

$$G(\mathbf{r},\mathbf{r}';\epsilon) = \sum_i \frac{\varphi_i(\mathbf{r})\varphi_i^\star(\mathbf{r}')}{\epsilon-\epsilon_i} \tag{8}$$

for the Green function is obtained. If this representation is inserted in (4) and the identity

$$\lim_{y\to 0^+}\frac{1}{x+\mathrm{i}y} = \mathrm{P}\frac{1}{x} - \mathrm{i}\pi\delta(x) \tag{9}$$

is applied to evaluate the imaginary part of (8), a delta function $\delta(\epsilon-\epsilon_i)$ appears which then can be used to perform the integration in (4). The upper integration limit E_F restricts the sum to eigenfunctions with $\epsilon_i \le E_F$ and the equivalence of (2) and (4) is demonstrated.
Equation (8) shows that the Green function has poles on the real ϵ axis at discrete values ϵ_i. These values represent the discrete part of the eigenvalue spectrum. In general, also a continuous part of the eigenvalue spectrum is possible. For instance in free space, with $v_{\mathrm{eff}}(\mathbf{r}) = 0$, the eigenfunctions are plane waves $\mathrm{e}^{\mathrm{i}\mathbf{k}\mathbf{r}}$ with eigenvalues given by k^2. These eigenvalues continuously cover the non-negative part of the real ϵ axis. Then (8) must be generalized into

$$G(\mathbf{r},\mathbf{r}';\epsilon) = \sum_i \frac{\varphi_i(\mathbf{r})\varphi_i^\star(\mathbf{r}')}{\epsilon-\epsilon_i} + \int_{-\infty}^{\infty}\frac{\varphi(\mathbf{r};\epsilon')\varphi^\star(\mathbf{r}';\epsilon')}{\epsilon-\epsilon'}\mathrm{d}\epsilon' \tag{10}$$

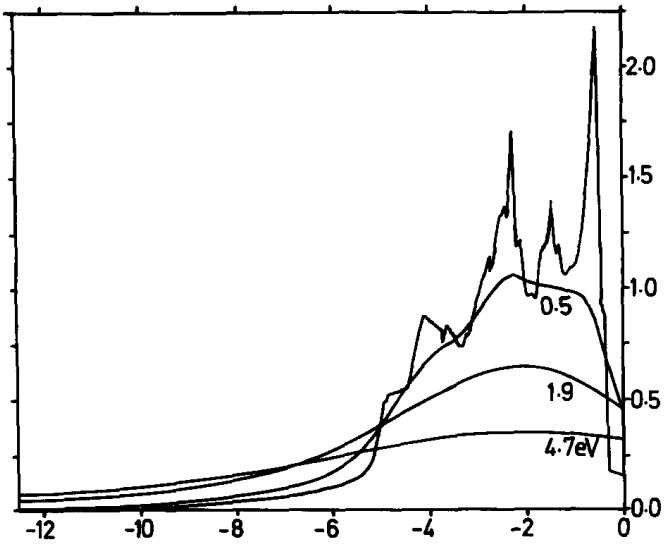

Fig. 1: *Density of states for Ni (here only for majority electrons) and the corresponding quantity along paths parallel to the real axis with distance 0.5, 1.8 and 4.7 eV. The picture is taken from Ref. [8]. It illustrates the increasing smoothness of the integrand with increasing distance from the real axis.*

where the integral is over the continuous part of the spectrum. In periodic crystals the continuous part of the spectrum is realized by bands, for instance by the valence and conduction bands in semiconductors. For the numerical evaluation of (4) it is important that the Green function is an analytical function[2] of ϵ except for the singularities on the real axis. This means that the integration (4) can be performed on a contour in the complex ϵ plane where the integrand is much smoother than just above the real axis as illustrated in Fig. 1. This procedure was suggested in a number of papers [6–9] and leads to considerable savings of computing time. Usually 30 to 40 points in the complex ϵ plane are enough for accurate evaluations of (4) provided that the points are chosen dense enough near E_F, where the contour necessarily approaches the real axis.
An important quantity, which is often used to provide an understanding of the electronic structure of materials in a single-particle picture, is the local density of states within in a volume V. It is defined as

$$n_V(\epsilon) = 2\sum_i \delta(\epsilon_i - \epsilon) \int_V \mathrm{d}\mathbf{r}\, |\varphi_i(\mathbf{r})|^2 \tag{11}$$

and gives the distribution of occupied and unoccupied electronic states within the volume V, for instance the local volume corresponding to one atom in the system. In terms of the Green function the local density of states is given by

$$n_V(\epsilon) = -\frac{2}{\pi} \operatorname{Im} \int_V \mathrm{d}\mathbf{r}\, G(\mathbf{r}, \mathbf{r}; \epsilon) \tag{12}$$

as can be verified by using the spectral representation (8). The total density of states is obtained if the integrals in (11) or (12) are done over all space.

[2]For an elementary introduction to classical Green functions and their analytical properties the textbook of Economou [5] is a good source.

3 Green function method for impurities

Historically the Green function method is attributed to Koster and Slater [10] who expanded the Green function in terms of Wannier functions. Because of the difficult construction of Wannier functions at that time the capabilities of this approach were rather limited. At the end of the 1970s Green function methods for the calculation of the electronic structure of impurities in solids received new attention. Inspired by the success of DFT calculations for periodic solids, several groups invested a considerable amount of work into the development of Green function methods for impurity calculations. They used a number of different techniques to calculate the the Green function of the periodic host crystal which is needed for the subsequent impurity calculations. The LCAO-GF method [11,12] was based on an expansion in linear combinations atomic orbitals, the LCGO-GF method [13] on an expansion in linear combination of Gaussian orbitals, the LMTO-GF method [14,15] on the linear muffin-tin orbital method and the KKR-GF method [16, 17] on the Korringa-Kohn-Rostoker band structure method.
In the beginning the Green functions were calculated mostly by using the spectral representation (8). This is easy for the imaginary part of the Green function because according to (9) the imaginary part of the denominator $\epsilon - \epsilon_i$ leads to a delta function so that only ϵ_i values contribute which are in the ϵ range for which the Green function is needed. From the imaginary part the real part was then obtained by the Kramers-Kronig relation

$$\mathrm{Re}\, G(\mathbf{r}, \mathbf{r}'; \epsilon) = -\frac{1}{\pi} P \int_{-\infty}^{\infty} \mathrm{d}\epsilon' \frac{1}{\epsilon - \epsilon'} \mathrm{Im}\, G(\mathbf{r}, \mathbf{r}'; \epsilon') \,. \tag{13}$$

Here in principle, the imaginary part is needed along the entire real ϵ axis. In practice, approximations were used, either the imaginary part in the integrand was neglected for higher ϵ values or it was replaced by an analytical approximation [18]. Another possibility is to use basis functions in a finite Hilbert space [15].
The problem that an infinite number of eigenstates contributes in (8) can be avoided if the host Green function is directly calculated by Brillouin zone integrations. This technique, which directly calculates the Green function for a given energy, is used in the KKR coherent potential approximation (KKR-CPA) [19, 20] and has been implemented also in the KKR-GF method. This procedure is perhaps most easily understood in terms of reference Green functions. Instead of using the defining differential equation (3) or the spectral representation (8), the Green function is calculated from the integral equation

$$G(\mathbf{r}, \mathbf{r}'; \epsilon) = G^r(\mathbf{r}, \mathbf{r}'; \epsilon) + \int \mathrm{d}\mathbf{r}'' G^r(\mathbf{r}, \mathbf{r}''; \epsilon) \Delta v(\mathbf{r}'') G(\mathbf{r}'', \mathbf{r}'; \epsilon) \,. \tag{14}$$

Here G^{r} is the Green function of a suitably chosen reference system with reference potential $v^{\mathrm{r}}(\mathbf{r})$ and $\Delta v(\mathbf{r}) = v_{\mathrm{eff}}(\mathbf{r}) - v^{\mathrm{r}}(\mathbf{r})$ is the perturbation of the potential given by the difference of the Kohn-Sham potential and the reference potential. The Green function G^{r} is determined by

$$\left[-\nabla^2_{\mathbf{r}} + v^{\mathrm{r}}(\mathbf{r}) - \epsilon\right] G^{\mathrm{r}}(\mathbf{r}, \mathbf{r}'; \epsilon) = -\delta(\mathbf{r} - \mathbf{r}') \,. \tag{15}$$

The calculation of Green functions by using reference systems is a powerful concept for the calculation of the electronic structure for systems with a complicated geometric structure. An

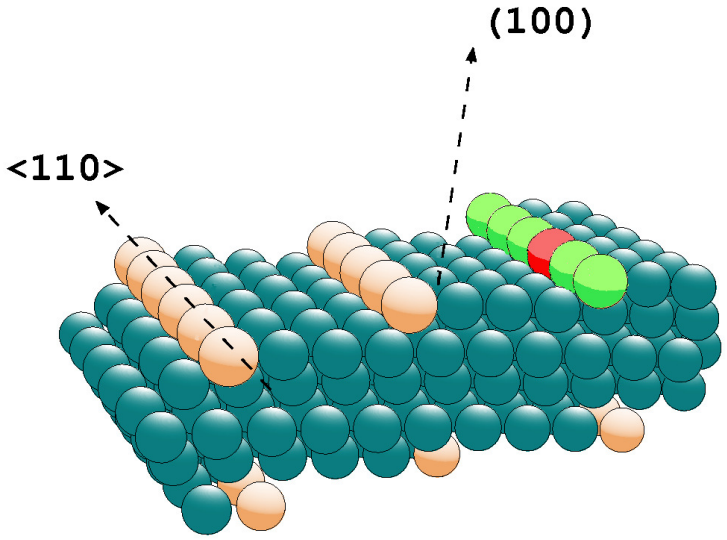

Fig. 2: *Illustration for the geometry of one impurity atom in an atomic chain which consists of other atoms than the otherwise periodically repeated chains at the step edges of a vicinal (711) surface of an fcc crystal.*

example for such a system, shown in Fig. 2, is a vicinal (711) surface of a face-centered-cubic crystal decorated with adatoms at step edges and within step edges. The Green function for this system can be constructed by the successive calculation of Green functions of simpler systems. i) Starting from free space the Green function for the bulk crystal is calculated treating the full bulk potential as perturbation using periodicity in three dimensions. ii) Several layers of the bulk crystal are removed, the removed potential is treated as perturbation using the two-dimensional surface periodicity. As a consequence of the fact the electrons cannot tunnel through several empty layers one obtains a slab which is decoupled from the rest of the bulk crystal. iii) Atomic chains are added at step edges. The potential perturbation is periodic in two dimension, but locally restricted to the vicinity of the step edges. iv) A chain of different atoms is inserted, only one-dimensional periodicity along the considered step edge is preserved, but the potential perturbation is confined to the vicinity of the considered chain. v) Finally, an impurity atom is inserted, periodicity is fully lost, but the potential perturbation is essentially confined to atoms in the vicinity of the impurity.

During this successive construction, periodicity can be used in the dimensions where it exists while in the remaining dimensions the potential perturbation is localized in the vicinity of the replaced atoms. In each successive step the integral equation must be solved only within a region of space where the potential differs non-negligibly from the one of the reference system. Once the Green function has been obtained for $\mathbf{r}$ and $\mathbf{r}'$ in this region, the Green function in all space can be obtained simply by multiplications and integrations. This represents an enormous advantage of Green function methods over supercell methods because the size of the region for which the integral equation must be solved is determined by the extent of the potential perturbation and not by the usually much larger extent of the perturbed wavefunctions or Green functions.

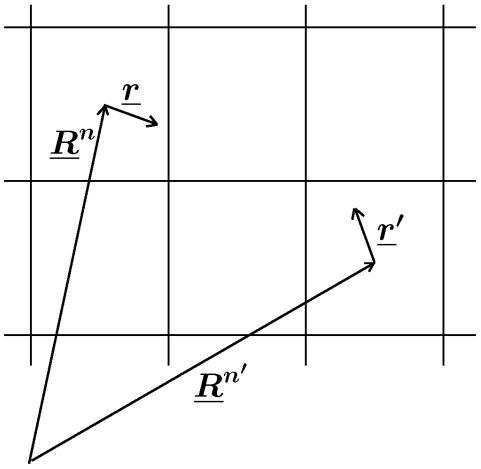

Fig. 3: *Partitioning of space and illustration for the definition of* $\mathbf{R}^n$ *and* $\mathbf{R}^{n'}$*, which define the positions of the cell centers, and* $\mathbf{r}$ *and* $\mathbf{r}'$*, which are vectors within the cells.*

An effective way to solve the integral equation (14) is provided by the KKR-GF method which does not rely on the determination of eigenvalues and eigenfunctions with their orthonormality constraints, but uses ideas of multiple-scattering theory. In this theory space is divided into non-overlapping regions, for instance cells around each atom, and the calculation of the Green function is broken up into two parts. First, *single-scattering* quantities, which depend only on the potential in a single cell, are determined. Second, the *multiple-scattering problem* is solved to obtain the correct combination of all single-scattering events.
The mathematical basis for the KKR-GF method is the fact that the Green function for free space, which is given by

$$G^0(\mathbf{r},\mathbf{r}';\epsilon) = -\frac{1}{4\pi}\frac{\exp(\mathrm{i}\sqrt{\epsilon}|\mathbf{r}-\mathbf{r}'|)}{|\mathbf{r}-\mathbf{r}'|}, \tag{16}$$

can be written in cell-centered coordinates as

$$G^0(\mathbf{r}+\mathbf{R}^n,\mathbf{r}'+\mathbf{R}^{n'};\epsilon) = \delta_{nn'}G^0(\mathbf{r},\mathbf{r}';\epsilon) + \sum_{LL'} J_L(\mathbf{r};\epsilon)G^{0,nn'}_{LL'}(\epsilon)J_{L'}(\mathbf{r}';\epsilon) \tag{17}$$

with analytically known Green function matrix elements $G^{0,nn'}_{LL'}(\epsilon)$ which do not depend on the radial coordinates r or r'. Here $\mathbf{R}^n$ and $\mathbf{R}^{n'}$ are the coordinates of the cell centers, usually the atomic positions, and $\mathbf{r}$ and $\mathbf{r}'$ are coordinates within the cells which originate at the cell centers. An illustration for these coordinates is given in Fig. 3. The functions

$$J_L(\mathbf{r};\epsilon) = j_l(r\sqrt{\epsilon})Y_{lm}(\hat{\mathbf{r}}) \tag{18}$$

are products of spherical harmonics Y_{lm} with spherical Bessel functions. Angular variables are denoted by $\hat{\mathbf{r}} = \mathbf{r}/r$ and radial variables by $r = |\mathbf{r}|$. The symbol L is used as compact notation for the angular momentum indices l and m and sums over L denote double sums over l and $|m| \leq l$.

If one proceeds as in [21], it is straightforward to show that the solution of (14) is given by

$$G(\mathbf{r}+\mathbf{R}^n,\mathbf{r}'+\mathbf{R}^{n'};\epsilon)=\delta_{nn'}G^n_{\rm s}(\mathbf{r},\mathbf{r}';\epsilon)+\sum_{LL'}R^n_L(\mathbf{r};\epsilon)G^{nn'}_{LL'}(\epsilon)R^{n'}_{L'}(\mathbf{r}';\epsilon)\;. \tag{19}$$

Here $G^n_{\rm s}$ is the single-site Green function for cell n which satisfies the integral equation

$$G^n_{\rm s}(\mathbf{r},\mathbf{r}';\epsilon)=G^{\rm r}(\mathbf{r},\mathbf{r}';\epsilon)+\int_n {\rm d}\mathbf{r}''G^{\rm r}(\mathbf{r},\mathbf{r}'';\epsilon)\Delta v^n(\mathbf{r}'')G^n_{\rm s}(\mathbf{r}'',\mathbf{r}';\epsilon) \tag{20}$$

and R^n_L are the single-site solutions which satisfy the integral equations

$$R^n_L(\mathbf{r};\epsilon)=J_L(\mathbf{r};\epsilon)+\int_n {\rm d}\mathbf{r}'G^{\rm r}(\mathbf{r},\mathbf{r}';\epsilon)\Delta v^n(\mathbf{r}')R^n_L(\mathbf{r}';\epsilon)\;. \tag{21}$$

In (20-21) the integration is only over the volume of cell n and $\Delta v^n(\mathbf{r})=\Delta v(\mathbf{r}+\mathbf{R}^n)$ is the potential perturbation in this cell n. The Green function matrix elements $G^{nn'}_{LL'}$ used in (19) satisfy the matrix equation

$$G^{nn'}_{LL'}(\epsilon)=G^{r,nn'}_{LL'}(\epsilon)+\sum_{n''}\sum_{L''L'''}G^{r,nn''}_{LL''}(\epsilon)\Delta t^{n''}_{L''L'''}(\epsilon)G^{n''n'}_{L'''L'}(\epsilon) \tag{22}$$

which computationally represents a linear algebra problem. The difference Δt^n of the so-called single-site t matrices is given by

$$\Delta t^n_{LL'}(\epsilon)=\int_n {\rm d}\mathbf{r}\;J_L(\mathbf{r};\epsilon)\Delta v^n(\mathbf{r})R^n_{L'}(\mathbf{r};\epsilon)\;. \tag{23}$$

Together (19-23) provide a computationally convenient solution of the integral equation (14) without the need to determine eigenvalues and eigenfunctions. The only real approximation which must be made is the truncation of the infinite sums over L to a finite number of terms. This determines the angular momentum cutoff $l_{\rm max}$ used in the KKR-GF method. Usually $l_{\rm max}=3$ or $l_{\rm max}=4$ is sufficient for accurate results.

If the density of states integrated over all space is needed, for instance for the total energy calculations, it is important that the integration in (12) can be performed analytically if the volume V extends over all space. This is the essence of Lloyd's formula [22] which gives the difference of the integrated density of states

$$\Delta N(\epsilon)=\int^{\epsilon}{\rm d}\epsilon'\Delta n(\epsilon') \tag{24}$$

of the perturbed and unperturbed systems by logarithms of determinants. The formula can be written as

$$\Delta N(\epsilon)=\frac{1}{\pi}{\rm Im}\sum_n \Delta\ln\det|\alpha^n_{LL'}(\epsilon)|-\frac{1}{\pi}{\rm Im}\ln\det|\delta^{nn'}_{LL'}-\sum_{L'}G^{{\rm r},nn'}_{LL'}(\epsilon)\Delta t^{n'}_{L'L}(\epsilon)| \tag{25}$$

which is the KKR equivalent of the operator identity (61) derived in the appendix. The matrix α in (25) is defined by [23]

$$\alpha^n_{LL'}(\epsilon)=\delta_{LL'}+\int_n d\mathbf{r}H_L(\mathbf{r};\epsilon)v^n(\mathbf{r})R^n_{L'}(\mathbf{r};\epsilon) \tag{26}$$

for the potential $v^n(\mathbf{r})$ and analogously for the reference potential, where the functions

$$H_L(\mathbf{r};\epsilon)=h^{(1)}_l(r\sqrt{\epsilon})Y_{lm}(\hat{\mathbf{r}}) \tag{27}$$

are products of spherical harmonics with spherical Hankel functions of the first kind.

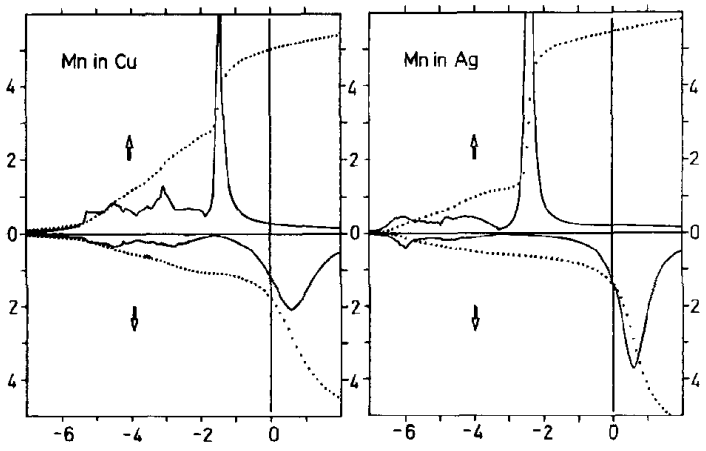

Fig. 4: *Local density of states (within the impurity cell) for Mn impurities in Cu and Ag as function of energy (in eV) relative to the Fermi level. The minority spin density of states is plotted downwards so that it does not overlap with the majority one. The dotted curves show the integrated density of states. The picture is taken from Ref. [25].*

3.1 Density of states

Although the single-particle eigenvalues ϵ_i and the density of states $n(\epsilon)$ calculated in density functional theory are only formal mathematical quantities, they often agree qualitatively with experiment and even more often they are used to provide a single-particle understanding of the chemical and physical mechanisms which lead to the observed behaviour of materials. Among the first systems studied by the KKR-GF method were $3d$ transition metal impurity atoms in noble metals which are the classical systems considered by Anderson in his famous paper on the Anderson impurity model [24].

In Fig. 4 the local density of states calculated with the local density approximation (LDA) of DFT is shown for Mn impurities in Cu and Ag. The differences for the two spin directions are caused by the fact that transition metal atoms of the Fe series can gain magnetic exchange energy by spin alignment. Anderson has discussed this behaviour in terms of Lorentzian type virtual bound states. Fig. 4 shows that these virtual bound states are reproduced in LDA-DFT calculations. In particular, the minority density of states shows almost Lorentzian type features with peak positions just above the Fermi level. However, also distortions from the Lorentzian form are clearly visible. They are caused by band structure effects arising from hybridization of the $3d$-states of the impurity atoms with the host d-states. Interestingly, in 1980 when Ref. [25] was published, it was seriously doubted that the observed splitting of the peak positions was the correct density functional answer, because conflicting results with much smaller splitting existed [26]. One criticism was that the observed spin splitting could be an artifact of the fact that only a potential perturbation in the impurity cell was used. Later calculations [27], where potential perturbations were also used in neighboring cells, confirmed the results shown in Fig. 4. Moreover, measurements [28,29] with various electron-spectroscopy techniques showed similar spin splittings as calculated. Fully quantitative agreement between calculations and experiment, of course, cannot be expected because states calculated with LDA are not to be identified as measurable quantities.

3.2 Defect formation energies

An important problem in the study of defects is the calculation of total energy differences which are the basic quantities necessary for understanding the microscopic origin of the formation of alloys and many other physical processes such as diffusion, short-range ordering, segregation. This is particularly true for vacancy formation and migration energies, which are difficult to measure, but important quantities to understand the thermodynamic and kinetic behaviour of metals and semiconductors. In supercell methods these numbers are difficult to calculate as expressed, for instance, in the following sentences taken from Puska *et al.* [30], who used supercells with up to 216 atoms. These authors write in the introduction *The vacancy in Si can be considered as the simplest example of a point defect in a semiconductor lattice* and in the conclusions *The convergence of the results is shown to be very slow* and *If the supercell is not large enough the long-range ionic relaxation pattern, especially in the [110] zigzag direction, may not be properly described*. Since then the vacancy in Si has been reinvestigated several times by supercell calculations, where due to the ever increasing computer power the supercell size has gradually increased. However, the convergence problem remains as stated in one of the most recent articles by Corsetti and Mostofi [31]. These authors who used supercells with up to 1000 atoms write in the conclusions *Our calculations confirm the slow finite size convergence of defect formation energies and transition levels, ...* They also argue that future increase of supercell sizes can reduce the spurious interactions between the vacancies in different cells, but that then another problem must be considered seriously. The problem is that total energy differences due to defect atoms are not calculated directly, but are obtained by numerical subtraction of supercell energies with and without defect. With increasing supercell size the numbers to be subtracted become larger which puts heavy demands on the numerical precision.

In contrast to supercell methods, Green function calculations are not plagued by these problems. The formation energy is calculated directly, not by energy differences, spurious interactions do not exist, and the region in space where the self-consistent calculations must be done is determined by the range of the potential perturbation and not by the usually much larger range of wavefunctions or Green function perturbations. Actually, the Si vacancy was considered as one of the earliest systems in Green function impurity calculations [11, 12]. At that time, however, it was not possible to calculate accurate total energies. Green function methods using basis sets suffered from insufficiently accurate basis functions and the KKR-GF method from the spherical approximation for the potential used in each cell. Only at the beginning of the 1990s accurate total energy calculations became possible, both due to the increased computing power and even more so because of the development of advanced numerical techniques. Results for some vacancy formation energies calculated by the KKR-GF method [32] are shown in Table 1. Compared to the original publication [33] the values for Cu and Ni contain corrections of about -0.04 and -0.08 eV which are energy gains obtained if the atoms relax to the correct equilibrium positions.

For the calculation of defect formation energies it is very important that Lloyd's formula is used to obtain the single-particle contribution. Within density functional theory the total energy con-

Table 1: *Calculated and experimental values for the vacancy formation energy of selected transition metals (in eV). The calculations for Cu and Ni include the effect of lattice relaxations.*

	Cu	Ag	Ni	Pd
Theory	1.37	1.20	1.68	1.57
Experiment	1.28	1.11	1.79, 1.63	1.85, 1.54

Table 2: *Solution energy (in eV) for a V impurity in Cu calculated using potential perturbations in the vanadium cell and in different numbers of shells of surrounding Cu neighbors.*

shells	0	1	2	3	4
cells	1	13	19	43	55
E_{Lloyd}	1.44	0.73	0.73	0.73	0.73
E_{local}	1.60	1.93	1.38	0.75	0.52

sists of a sum of the kinetic energy $T[n(\mathbf{r})]$, the electrostatic Hartree energy and the exchange correlation energy. The kinetic energy is usually evaluated as

$$T[n(\mathbf{r})] = \sum_i \epsilon_i - \int \mathrm{d}\mathbf{r}\, n(\mathbf{r}) v_{\mathrm{eff}}(\mathbf{r}) = \int^{E_F} \mathrm{d}\epsilon\, \epsilon\, n(\epsilon) - \int \mathrm{d}\mathbf{r}\, n(\mathbf{r}) v_{\mathrm{eff}}(\mathbf{r}) \tag{28}$$

$$= E_F N(E_F) - \int^{E_F} \mathrm{d}\epsilon\, N(\epsilon) - \int \mathrm{d}\mathbf{r}\, n(\mathbf{r}) v_{\mathrm{eff}}(\mathbf{r})$$

by using the single-particle energies ϵ_i, where the last result is obtained from integration by parts over ϵ. If the density of states $n(\epsilon)$ or the integrated density of states $N(\epsilon)$ is calculated from the Green function by (11) and (24), an explicit summation over all cells of the infinite crystal is required. This problem is avoided if Lloyd's formula (25) is used which already contains the integration over all space.

The different behaviour of the shell convergence of energies calculated with and without Lloyd's formula is illustrated in Table 2 where results for the solution energy for a vanadium impurity in copper are shown. While the use of Lloyd's formula leads to a converged result already for 13 cells, the use of (11) with summation over cells only gives poor results. This behaviour reflects the fact that wavefunction or Green function perturbations are much longer ranged than the potential perturbation. Density changes, which contribute, for instance, in the last term of (28) and in other parts of the energy functional, exist outside of the perturbed potential region, but these changes are unimportant because of the variational properties of the energy functional.

3.3 Forces and lattice relaxations

Substitutional impurities, in general, have a different size than the host atoms. This causes displacements of the neighboring atoms away from their ideal positions which they occupy in the unperturbed host crystal. In metals, because of the high coordination number, the displacements

are rather small and can be neglected in the calculations of many physical properties. However, sometimes the displacements have significant effects and their size and direction should be calculated. In electronic structure methods displacements are calculated usually from the condition that the forces on the atoms should vanish and the forces are determined usually by the Hellmann-Feynman theorem

$$\mathbf{F}^n = -\frac{\partial E}{\partial \mathbf{R}^n}\bigg|_{n(\mathbf{r};\mathbf{R^n})} - \int \mathrm{d}\mathbf{r}\, \frac{\delta E}{\delta n(\mathbf{r})} \frac{\partial n(\mathbf{r};\mathbf{R}^n)}{\partial \mathbf{R}^n} \tag{29}$$

which means that the force $\mathbf{F}^n$ on atom n is determined by the derivative of the total energy E with respect to the coordinate $\mathbf{R}^n$ of atom n. Here the first term, evaluated at constant density $n(\mathbf{r};\mathbf{R}^n)$, is the Hellmann-Feynman (HF) force and the second term is necessary if approximations are made in the solution of the Kohn-Sham equations. The second term vanishes in an exact treatment, because then $\frac{\delta E}{\delta n(\mathbf{r})} = E_F$ is constant and because the total number of electrons $N_{\mathrm{el}} = \int \mathrm{d}\mathbf{r}\, n(\mathbf{r};\mathbf{R}^n)$ does not depend on the atomic positions. Within a full potential KKR formalism, the Kohn-Sham equations for the valence electrons are solved rather accurately, the only approximation is the $l_{\max}$ cutoff. This means that the second term usually contains a negligible contribution from the valence electrons. For the core electrons, however, this term gives a considerable contribution if the core states are calculated as usual in an atomic fashion using only the spherical part of the potential. With a spherical ansatz n_{core} for the core density, the resulting expression for the force is

$$\mathbf{F}^n = Z^n \left.\frac{\partial V_{\mathrm{M}}(\mathbf{r})}{\partial \mathbf{r}}\right|_{\mathbf{r}=\mathbf{R}^n} - \int d^3r\, n_{\mathrm{core}}(|\mathbf{r}-\mathbf{R}^n|)\, \frac{\partial v_{\mathrm{eff}}(\mathbf{r})}{\partial \mathbf{r}} \tag{30}$$

where Z^n is the nuclear charge, $V_{\mathrm{M}}(\mathbf{r})$ the Madelung potential and $v_{\mathrm{eff}}(\mathbf{r})$ the Kohn-Sham potential. Due to the vector character of the potential derivatives in (30), only the $l = 1$ components of V_{M} and v_{eff} are needed. Since these quantities are anyhow calculated in a full-potential KKR treatment, the calculation of forces is easy. There are also no Pulay corrections [34] required which arise in basis set methods if the basis functions depend on the atomic positions.

While force calculation are simple, calculations of atomic displacements, which occur if the impurity atoms are smaller or larger than the host atoms, are more complicated in the KKR method. The main reason is the site-centered angular momentum expansion used in the Green function expression (19) which is needed around the displaced sites. While original undisplaced and new displaced sites can be used together in the calculation of the Green function with appropriate artificial zero potentials on non-participating sites, it is numerically simpler to transform the Green function matrix elements from undisplaced to displaced sites [35, 36]. The reference Green function matrix elements are transformed by

$$\tilde{G}^{\mathrm{r},nn'}_{LL'}(\epsilon) = \sum_{L''L'''} U_{LL''}(\mathbf{s}^n;\epsilon) G^{\mathrm{r},nn'}_{L''L'''}(\epsilon) U_{L'L'''}(\mathbf{s}^{n'};\epsilon) \tag{31}$$

where $\mathbf{s}^n$ is the shift of atom at site $\mathbf{R}^n$ to the new site $\mathbf{R}^n + \mathbf{s}^n$. The transformation matrix is given by

$$U_{L'L}(\mathbf{s}^n;\epsilon) = 4\pi \sum_{L''} \mathrm{i}^{l'+l''-l} C_{LL'L''} j_{l''}(\sqrt{\epsilon} s^n) Y_{L''}(\hat{\mathbf{s}}^n) \tag{32}$$

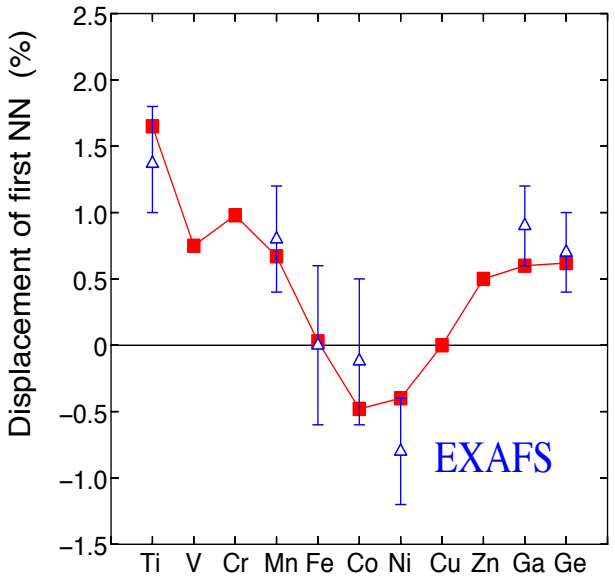

Fig. 5: *Displacements of the nearest Cu neighbors around impurities from Ti to Ge in Cu. The displacements are given in percent of the nearest neighbor distance between the atoms in unperturbed Cu. Experimental results obtained by EXAFS measurements are shown by triangles with error bars. The picture is taken from Ref. [37].*

where $C_{LL'L''} = \int_{4\pi} \mathrm{d}\hat{\mathbf{r}}\, Y_L(\hat{\mathbf{r}}) Y_{L'}(\hat{\mathbf{r}}) Y_{L''}(\hat{\mathbf{r}})$ are Gaunt coefficients, j_l spherical Bessel functions and Y_L spherical harmonics. Together with a similar transformation for the t matrix, the following algebraic Dyson equation

$$G = \tilde{G}^{\mathrm{r}} + \tilde{G}^{\mathrm{r}}[t - \tilde{t}^{\mathrm{r}}]G \tag{33}$$

must be solved. While the transformation (31) is exact, if the sums over L'' and L''' are extended over infinite angular momenta, in practical calculations these sums must be truncated. For large displacements a relatively high l_{max} value is needed, but $l_{\max} = 4$ is sufficient for displacements up to 10 % of the nearest neighbor distance as they occur around the substitutional impurities considered here.

Fig. 5 shows calculated displacements of nearest neighbor Cu atoms around impurities from the 3rd series of the periodic table together with experimental data derived from extended x-ray absorption fine structure (EXAFS) measurements. Most of the impurities lead to an outward displacement of the Cu neighbors which means that these impurities are *bigger* than Cu. Only Ni and Co are *smaller* with inward displacements. The displacements induced by Fe are very small and for a Cu impurity they are, of course, zero.

In contrast to metals, lattice relaxations in semiconductors are usually considerably larger because of more open structures and lower coordination numbers. For the defect pairs shown in Fig. 6 the displacements reach up to 10 % of the nearest neighbor distance which is about the limit for the U transformations. The figure shows a comparison of displacements calculated for donor-acceptor pairs in Si by the full-potential KKR-GF method and a pseudopotential *ab-initio* molecular dynamics program applied to a supercell with 64 atoms [38]. The displaced positions

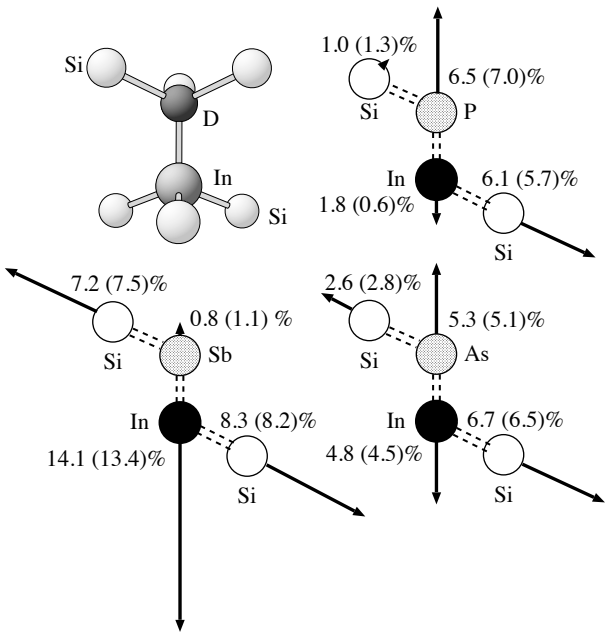

Fig. 6: *Calculated displacements for InSb, InP and InAs defect pairs in Si. The results are given in percent of the nearest neighbor distance between the bulk Si atoms. Two sets of numbers are given. The number in parentheses have been calculated by a pseudopotential method, the other number by the KKR-GF method.*

obtained by the two methods are essentially the same, but the KKR-GF method can give more information, in particular for properties that are determined by the core electrons, like hyperfine fields or electric field gradients.

The considered defect pairs are electrically and magnetically inactive and experimental information about the structure is difficult to obtain. One of the few methods to investigate such defects are perturbed angular correlation (PAC) experiments which measure the electric field gradients. The calculated electric field gradients depend sensitively on the lattice relaxations of the defect complex. While calculations without lattice relaxations give the wrong trend with respect to the atomic numbers of the donor atoms, the agreement greatly improves, if the relaxed configurations are considered [39], as for instance given in Fig. 6 for donor-acceptor pairs in Si. Thus a reliable calculation of the relaxations is crucial for understanding the electric field gradients.

Efficient and accurate force calculations open the possibility to study phonon dispersion relations. Within a Green function impurity method the calculations can be done in real space by directly determining the Born-von Karman force constants according to their definition. One atom is displaced by a finite amount and the induced forces on all atoms are calculated. Fourier transformation gives the dynamical matrix and phonon frequencies and eigenstates in the Brillouin zone are easily obtained. For cubic crystals a single self-consistent calculation is enough to determine the whole phonon spectrum. Fig. 7 shows the phonon dispersion curves of Al calculated in this way by the KKR-GF method. As can be seen a calculation including 6th near-

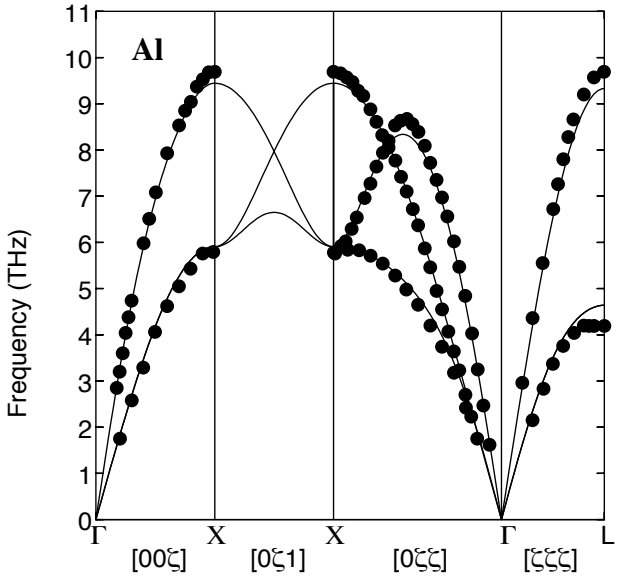

Fig. 7: *Calculated phonon spectrum (continuous lines) of fcc Al and experimental results (full dots). The central Al atom is shifted by 0.5% and the forces on six shells of neighboring atoms are calculated self-consistently, yielding force constant parameters for six nearest neighbor shells. The figure is taken from Ref. [37].*

est neighbor interactions reproduces the experimental data quite well. A disadvantage of this approach is that a relatively big cluster, including many atoms, must be used to account for long range elastic interactions present for example in semiconductors.

3.4 Long range perturbations

Magnetic impurities in non-magnetic materials induce magnetic polarization oscillations on the surrounding host atoms. Usually these oscillations are small effects. Typically a Cu atom as nearest neighbor of an impurity from the $3d$ series carries an induced moment of about $10^{-2}\mu_{\rm B}$ and the size of the moments decreases with increasing distance from the impurity as the third power of distance. Despite of this, as discussed in Ref. [40], very nice experimental information about the magnetization oscillations in Cu exists due to measurements of Knight shift satellites by the Slichter group. The measured Knight shift satellites can be related to calculated hyperfine fields as detailed in Ref. [40]. Fig. 8 shows calculated hyperfine fields on twelve shells of Cu neighbors around a Mn impurity, which means that potentials for 225 atoms have been calculated self-consistently. The corresponding experimental results derived from the Knight shift measurement are shown by red squares. Calculation and experiment nicely agree if the correct assignment of the experimentally observed peaks to the different shells has been made. While the assignment of calculated hyperfine fields to the different shells is unambiguous, the assignment of experimental peaks is more difficult. It relies on the symmetry of the shells, on the intensity of the peaks arising from the number of atoms in the shells and on the magnitude of the derived hyperfine field according to the rapid decrease with distance.

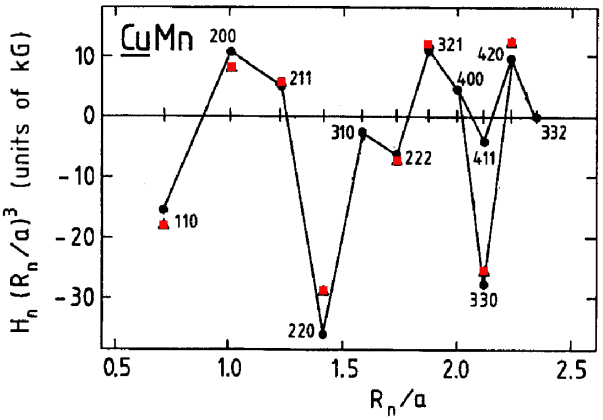

Fig. 8: *Hyperfine fields of Cu atoms in different shells around a Mn impurity in Cu. The calculated values (solid curve) were multiplied with $(R_n/a)^3$, where R_n is the distance from the Mn nucleus and a the lattice constant of Cu. The numbers indicate the different shells and the experimental values are shown as red squares. The picture is taken from Ref. [41].*

3.5 Parameters for model Hamiltonians

Green function impurity calculations can be used to obtain parameters for model Hamiltonians if constraints are applied in density functional theory [42]. Constraints are already used in the formal development of density functional theory, for instance the density is constrained to give the correct number of electrons and the Kohn-Sham orbitals must be normalized as $\sum_\alpha(\varphi_i^\alpha, \varphi_i^\alpha) = 1$. Another example is Levy's [43] explicit definition of the energy by constrained minimization over all many-electron wavefunctions which give the same density. The idea of constrained density-functional theory [42] is the extension to quite arbitrary constraints. This idea is useful if one wants to calculate total energy differences which depend on a parameter, for instance on N_V, the number of electrons inside a volume V. The constraint can be taken into account by modifying the energy functional $E[n(\mathbf{r})]$ into

$$\tilde{E}[n(\mathbf{r})] = E[n(\mathbf{r})] + v\left[N_V - \int_V n(\mathbf{r})\mathrm{d}\mathbf{r}\right] \tag{34}$$

where the constraint is guaranteed by the Lagrange parameter v. The minimization of (34) with respect to $n(\mathbf{r})$ leads to an additional potential v in the Kohn-Sham equations, which is constant and only acts in V and is zero elsewhere. This potential must be adjusted such that the resulting density $n(\mathbf{r})$ gives exactly N_V electrons in volume V. Instead of calculating the energy differences from the functional $\tilde{E}[n(\mathbf{r})]$ by subtracting the energies for different values of the parameter N_V, it is computationally easier to calculate the difference directly by the Hellmann-Feynman theorem

$$\frac{\mathrm{d}\tilde{E}(N_V)}{\mathrm{d}N_V} = v \qquad \Rightarrow \qquad \Delta\tilde{E}(N_V) = \int_{N_0}^{N_V} v(N')\,\mathrm{d}N' \tag{35}$$

which only requires the knowledge of the potential $v(N')$. Physically, the potential v can be viewed as the *force* necessary to constrain the system to the desired state and ΔE as the *strain energy* of the system.

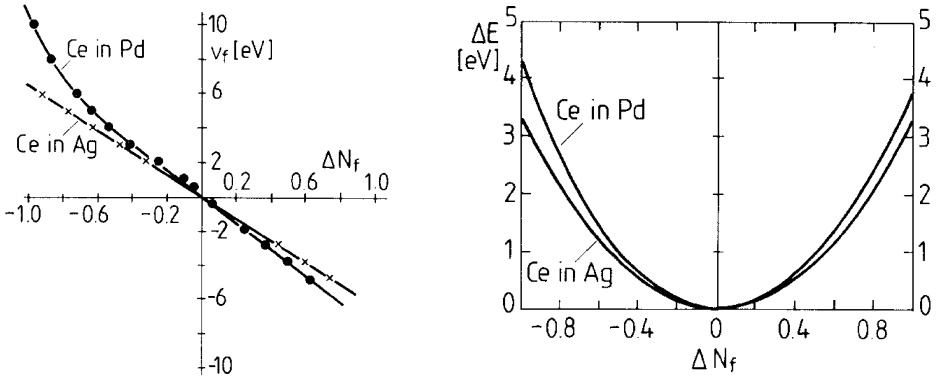

Fig. 9: *Constraining field (left) and energy difference (right) as function of the deviation of the occupation number N_f from its ground state value N_f^0. Pictures are taken from Ref. [42].*

Instead of varying the total charge it is more interesting to vary partial charges, for instance the number of d- or f-electrons in the impurity cell. Minimization then leads to a constant projection potential $v(N_{d,f})$ which acts only on states with $l = 2$ or $l = 3$ character in the considered cell. The energy differences obtained in this way can be related to the screened Coulomb parameters U_d and U_f (Hubbard *U*), for instance as

$$U_f = \Delta E(N_f^0 + 1) + \Delta E(N_f^0 - 1) \tag{36}$$

where N_f^0 is the number of f-electrons in equilibrium. In the calculation the screening is provided by the the s- and p-states which can adjust to the changed number of d- or f-electrons.
An early application of constrained density functional theory was the calculation of the Coulomb parameter U_f for Ce impurities in Ag and Pd [42]. The number N_f of f-electrons was determined by integrating the local density of states (12) using only $l = 3$ angular momentum components for $n(\epsilon)$. The ground state values of N_f were determined as $N_f^0 = 1.18$ for Ce in Pd and as $N_f^0 = 1.25$ for Ce in Ag. A constraining projection potential v_f was applied within the muffin-tin sphere around the Ce impurity and the dependence of N_f on v_f was determined. Both the constraining potential and the energy difference are plotted in Fig. 9. The dependence of v_f on N_f is almost linear except for Pd near $\Delta N_f = -1$, where it becomes increasingly difficult to remove all f-states due to their strong hybridization with d-states of Pd. The energy differences depend almost quadratically on ΔN_f and the screened Coulomb parameters according to (36) turned out be 6.6 eV for Ce in Ag and 8.1 eV in Pd.
Another early application of constrained density functional theory was the calculation of interaction energy differences between the ferromagnetic and antiferromagnetic configuration of impurity pairs in metals [44]. In these calculations the local magnetic moment of one of the impurities is constrained to an arbitrary value M and the lowest energy compatible with the constraint is determined by a modified functional

$$\tilde{E}[n(\mathbf{r}), m(\mathbf{r})] = E[n(\mathbf{r}), m(\mathbf{r})] + H\left[M - \int_V m(\mathbf{r})\mathrm{d}\mathbf{r}\right]$$

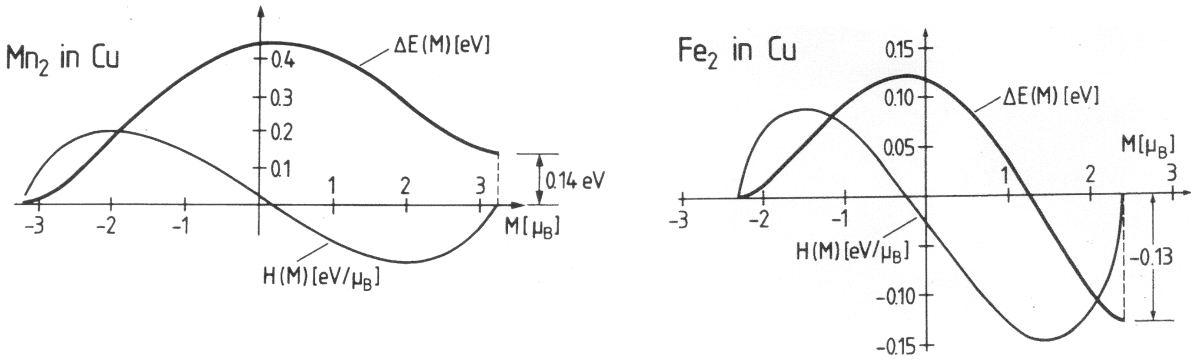

Fig. 10: *Difference of the magnetic interaction energy difference $\Delta E(M)$ and the constraining magnetic field $H(M)$ as function of the prescribed local impurity moment. The results are for pairs of Mn and Fe impurities on nearest neighbor sites in a Cu crystal (from Ref. [44]).*

where the Lagrange parameter H is a constraining longitudinal magnetic field, which is constant in the cell of one impurity with volume V and zero elsewhere. This field is chosen such that the integral of the magnetization $m(\mathbf{r})$ over the cell gives the desired value of the moment.
Similar to (35) the energy difference is given by

$$\Delta E(M) = \int_{M_0}^{M} H(M')\mathrm{d}M'$$

where M_0 is the value of M in the reference state. For instance in Fig. 10, the reference state is the antiferromagnetic configuration, for which the moments for the two impurities have opposite sign. This state corresponds to the left minima of the $\Delta E(M)$ curves in Fig. 10, while the right minima correspond to the ferromagnetic configuration. Both configurations are stable as the energy minima with vanishing constraining field H indicate. The energy differences between different magnetic configurations determine exchange parameters J_{ij} which may be used in a Heisenberg model

$$\hat{H} = -\sum_{i,j} J_{ij}\underline{\hat{S}}_i\underline{\hat{S}}_j \,,$$

which can be treated much faster for large and complex systems than fully self-consistent spin density functional calculations.

4 Random Alloys and CPA

For real alloys the consideration of one or even two impurities is relevant only for the very dilute limit where interactions between impurity clusters can safely be neglected. For increasing impurity concentration these interactions become more and more important. Instead of calculating the Green function for a single configuration realized in a particular system, one is then interested in spatial or configurational averages $\langle G\rangle$ of the Green function over many different possible configurations [45]. For the derivation of expressions for the averaged Green function

$\langle G\rangle$ it is convenient to consider first the single-site problem and then the interaction between the different sites. The single-site problem can be written in operator notation as

$$G_\alpha = g + gV_\alpha G_\alpha \tag{37}$$

where all quantities are considered as integral operators[3] and g and V_α are used as shorter notations for G^{r} and Δv^n. In order to emphasize that in this section single-site quantities are integral operators, the sites are labelled here by Greek letters. With the definition $t_\alpha g = V_\alpha G_\alpha$ the last equation can be solved as

$$G_\alpha = g + gt_\alpha g\ . \tag{38}$$

Multiplication with V_α from the left leads to

$$V_\alpha G_\alpha = t_\alpha g = V_\alpha g + V_\alpha g t_\alpha g\ . \tag{39}$$

This is valid if t_α is determined by

$$t_\alpha = V_\alpha + V_\alpha g t_\alpha\ . \tag{40}$$

Using spatial variables the last equation can be written as

$$t_\alpha(\mathbf{r},\mathbf{r}') = V_\alpha(\mathbf{r})\delta(\mathbf{r}-\mathbf{r}') + \int \mathrm{d}\mathbf{r}''\, V_\alpha(\mathbf{r}) g(\mathbf{r},\mathbf{r}'') t_\alpha(\mathbf{r}'',\mathbf{r}') \tag{41}$$

where the potential operator is local as characterized by the delta function. By iterating (40) as $t_\alpha = V_\alpha + V_\alpha g V_\alpha + V_\alpha g V_\alpha g V_\alpha \ldots$ one sees that t_α is a single-site quantity. It is only needed in cell α because all terms contain factors V_α on the left and right and V_α is restricted to cell α.
For the multiple-site problem, where the potential perturbation is given by $V = \sum_\alpha V_\alpha$, it is convenient to introduce an operator F which connects G and its average $\langle G\rangle$ by

$$G = F\langle G\rangle\ . \tag{42}$$

If this is used in $G = g + gVG$, which is (14) in operator notation, the result is

$$F\langle G\rangle = g + gVF\langle G\rangle \tag{43}$$

Averaging gives

$$\langle G\rangle = g + g\langle VF\rangle\langle G\rangle \tag{44}$$

where $\langle F\rangle = 1$ was used which follows from (42). The last equation contains only averaged quantities and could be solved easily if $\langle VF\rangle$ is known.[4]
The task is now to derive an equation for $\langle VF\rangle$. Subtraction of (43) and (44) and omitting the common operator $\langle G\rangle$ on both sides of the resulting equation gives

$$F - 1 = g(VF - \langle VF\rangle)\ . \tag{45}$$

[3] Integral operators, for instance g, act on arbitrary functions $f(\mathbf{r})$ as $\int \mathrm{d}\mathbf{r}' g(\mathbf{r},\mathbf{r}') f(\mathbf{r}')$.
[4] The quantity $\langle VF\rangle$ is usually called self-energy and labelled by the letter Σ.

which multiplied with V leads to

$$VF = V + Vg(VF - \langle VF \rangle) \tag{46}$$

This is the basic result used for further considerations. Now the crucial point is that VF can be written as a sum of single-site terms. For that purpose operators f_α are defined by the equation $V_\alpha F = t_\alpha f_\alpha$. With $V = \sum_\alpha V_\alpha$ one obtains $VF = \sum_\alpha V_\alpha F = \sum_\alpha t_\alpha f_\alpha$ and (46) can be written as

$$\sum_\alpha t_\alpha f_\alpha = \sum_\alpha V_\alpha + \sum_\alpha \sum_\beta V_\alpha g t_\beta f_\beta - \sum_\alpha \sum_\beta V_\alpha g \langle t_\beta f_\beta \rangle \; . \tag{47}$$

On the other hand, if (40) is multiplied with f_α and summed over α, the result is

$$\sum_\alpha t_\alpha f_\alpha = \sum_\alpha V_\alpha f_\alpha + \sum_\alpha V_\alpha g t_\alpha f_\alpha \; . \tag{48}$$

Subtraction of (47) and (48) gives

$$0 = \sum_\alpha V_\alpha (f_\alpha - 1 - \sum_{\beta \neq \alpha} g t_\beta f_\beta + \sum_\beta g \langle t_\beta f_\beta \rangle) \tag{49}$$

where the restriction $\beta \neq \alpha$ arises from the subtraction of the last term of (48). The last equation is satisfied if f_α is determined by the implicit equation

$$f_\alpha = 1 + \sum_{\beta \neq \alpha} g t_\beta f_\beta - \sum_\beta g \langle t_\beta f_\beta \rangle \; . \tag{50}$$

In general, this equation cannot be solved exactly, but it can be used to obtain approximations. Iteration of (50) starting with $f_\alpha = 0$ leads to

$$\begin{aligned} f_\alpha = {} & 1 \\ & + \sum_{\beta \neq \alpha} g t_\beta - \sum_\beta g \langle t_\beta \rangle \\ & + \sum_{\beta \neq \alpha} \sum_{\gamma \neq \beta} g t_\beta g t_\gamma - \sum_{\beta \neq \alpha} \sum_\gamma g t_\beta g \langle t_\gamma \rangle - \sum_\beta \sum_{\gamma \neq \beta} g \langle t_\beta g t_\gamma \rangle + \sum_\beta \sum_\gamma g \langle t_\beta \rangle g \langle t_\gamma \rangle \\ & + \ldots \end{aligned} \tag{51}$$

where terms containing three or more t operators are not shown. In order to obtain approximations for $\langle VF \rangle$ the last equation is multiplied with t_α, summed over α and averaged. This leads to

$$\begin{aligned} \langle VF \rangle = {} & \sum_\alpha \langle t_\alpha \rangle \\ & + \sum_\alpha \sum_{\beta \neq \alpha} \langle t_\alpha g t_\beta \rangle - \sum_\alpha \sum_\beta \langle t_\alpha \rangle g \langle t_\beta \rangle \\ & + \sum_\alpha \sum_{\beta \neq \alpha} \sum_{\gamma \neq \beta} \langle t_\alpha g t_\beta g t_\gamma \rangle - \sum_\alpha \sum_{\beta \neq \alpha} \sum_\gamma \langle t_\alpha g t_\beta \rangle g \langle t_\gamma \rangle \\ & - \sum_\alpha \sum_\beta \sum_{\gamma \neq \beta} \langle t_\alpha \rangle g \langle t_\beta g t_\gamma \rangle + \sum_\alpha \sum_\beta \sum_\gamma \langle t_\alpha \rangle g \langle t_\beta \rangle g \langle t_\gamma \rangle + \ldots \; . \end{aligned} \tag{52}$$

Here it is important to note that this expression is still exact although only terms up to third order in t_α are written down.
Now approximations can be made. An important approximation, which leads to a considerable simplification, is the neglect of correlations between different sites. While electronic structure calculations for alloys nowadays do not necessarily need this approximation, for instance in the non-local CPA of Rowlands *et al.* [46, 47], these advanced techniques are difficult to discuss and will not be considered here. The neglect of correlations means that averages $\langle t_\alpha g t_\beta \rangle$ can be factorized as $\langle t_\alpha \rangle \langle t_\beta \rangle$ if the sites α and β are different. This leads to

$$\begin{aligned} \langle VF \rangle = & \sum_\alpha \langle t_\alpha \rangle - \sum_\alpha \langle t_\alpha \rangle g \langle t_\alpha \rangle \\ & + \sum_\alpha \langle t_\alpha \rangle g \langle t_\alpha \rangle g \langle t_\alpha \rangle + \sum_\alpha \sum_{\beta \neq \alpha} \langle t_\alpha g \langle t_\beta \rangle g t_\alpha \rangle - \sum_\alpha \sum_{\beta \neq \alpha} \langle t_\alpha \rangle g \langle t_\beta \rangle g \langle t_\alpha \rangle - \dots . \end{aligned} \tag{53}$$

From this expression a number of approximations can be derived which are far better than the most simple approximation which replaces $\langle VF \rangle$ by $\langle V \rangle = \sum_\alpha \langle V_\alpha \rangle$. This approximation which only uses the averaged potential is called the virtual crystal approximation (VCA). It is easy to handle because it leads to a real potential, but has serious deficits for describing real disordered systems. A major improvement on the VCA is to use the first term of (53) or (52). This approximation is called average t matrix approximation (ATA) and takes into account all effects up to first order in the t operator. The ATA has been extensively discussed in the literature, in particular in connection with multiple-scattering theory [48, 49]. A simple way to go beyond the ATA is to use all terms of (53) which contain only a single site α. The result can written as $\sum_\alpha (1 + g\langle t_\alpha \rangle)^{-1} \langle t_\alpha \rangle$ and corresponds to the optical potential discussed by Goldberger and Watson [51]. This method is correct to second order in the t operator, the third order terms not treated are the last two ones shown in (53). An even better approximation is obtained by realizing that the above equations are valid for quite arbitrary Green functions g provided that the corresponding reference system shows no disorder. In a self-consistent procedure the reference Green function g is chosen in such a way that as many terms as possible vanish in (53). In principle, one could demand $\langle t_\alpha(\mathbf{r}, \mathbf{r}') \rangle = 0$. In general this is, however, not possible because the integral operator $t_\alpha(\mathbf{r}, \mathbf{r}')$ is a complicated function of $\mathbf{r}$ and $\mathbf{r}'$. In the multiple-scattering KKR method the situation is somewhat simpler because it relies on algebraic matrices t^n instead of integral operators t_α. Then, as shown by Soven [50] self-consistency can be implemented by choosing an effective reference medium with the requirement that the scattering of the electrons averaged over the constituent atoms vanishes in the effective medium. The resulting approximation called KKR-CPA has been widely applied to study the electronic structure of disordered alloys.
As an example for extensive KKR-CPA calculations Fig. 11 shows results [52] for the averaged local magnetic moments in alloys of Fe, Co, and Ni and alloys of these elements with other transition metals. The diagrams obtained on the left for the experimental results and on the right for the calculated results are referred to as Slater-Pauling curves. The Slater-Pauling curve has two main branches with slopes of 45^o and -45^o which meet in the middle where a maximal

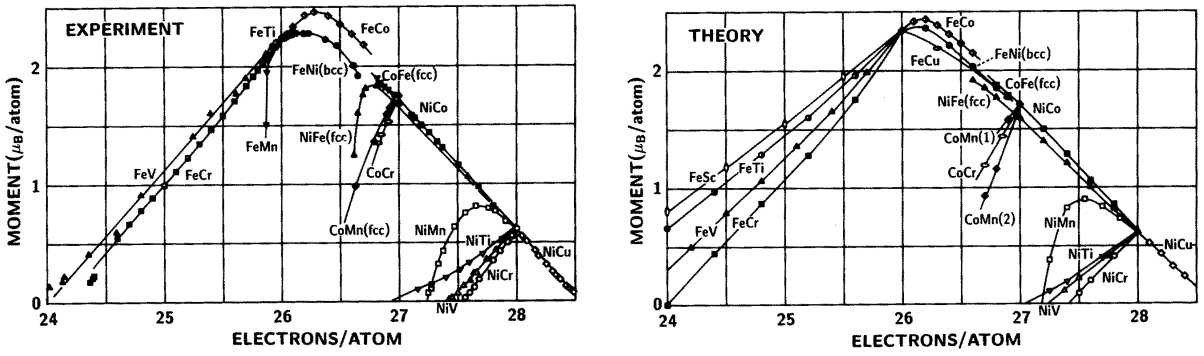

Fig. 11: *Slater-Pauling curve for the averaged magnetic moment per atom as function of the averaged number of electrons per atom. The picture is taken from Ref. [52].*

moment of about 2.4 μ_{B} occurs. The left main branch consists of Fe alloys, whereas Co and Ni alloys form the right main branch and the subbranches. The main reason for the two different slopes is a different electronic screening behavior. Alloys on the main branch on the right have a full majority spin band so that the screening of the valence difference introduced by the impurity atoms is provided by minority spin electrons. This leads to a reduced number of minority d-electrons which gives increased moments. Alloys on the other branches are characterized by the occurrence of antiparallel moments of the impurities which lead to reduced averaged moments with increasing concentration. Here the screening is mainly provided by the majority spin electrons. Although the agreement between experiment and calculation is not perfect, Fig. 11 shows that spin density functional theory is a powerful tool to understand and explain magnetic properties of materials.

Appendix

A Useful Green function properties

The Green function $G(\epsilon)$ for a Hamiltonian $\mathcal{H}$ is defined by the operator equation

$$G = \frac{1}{\epsilon - \mathcal{H}} \,. \tag{54}$$

For real ϵ it is necessary to perform a limiting process. Then the real quantity ϵ is replaced by a complex quantity $\epsilon + i\gamma$ and all equations are understood in the sense that the limit $\gamma \to 0+$ must be performed in the end. The relation

$$\lim_{\gamma \to 0+} \frac{1}{\epsilon + i\gamma - \mathcal{H}} = P\frac{1}{\epsilon - \mathcal{H}} - i\pi\delta(\epsilon - \mathcal{H}) \tag{55}$$

where P denotes the principal value, establishes the connection between the imaginary part of the Green function and the density of states $n(\epsilon) = \delta(\epsilon - \mathcal{H})$ and also the Kramers-Kronig relation between the imaginary and the real part of the Green function

$$\operatorname{Im} G(\epsilon) = -\pi n(\epsilon) \,, \qquad \operatorname{Re} G(\epsilon) = -\frac{1}{\pi} P \int_{-\infty}^{\infty} \frac{1}{\epsilon - \epsilon'} \operatorname{Im} G(\epsilon') \, \mathrm{d}\epsilon' \,. \tag{56}$$

where the last equation is a Hilbert transform.
While the above equations in this appendix are valid for real values of ϵ, complex values of ϵ are considered below. Then the last equation can be generalized to

$$G(\epsilon) = -\frac{1}{\pi} \int_{-\infty}^{\infty} \frac{1}{\epsilon - \epsilon'} \operatorname{Im} G(\epsilon') \, \mathrm{d}\epsilon' \,. \tag{57}$$

Another useful relation for the Green function is given by

$$\frac{\mathrm{d}G(\epsilon)}{\mathrm{d}\epsilon} = \frac{\mathrm{d}}{\mathrm{d}\epsilon} \frac{1}{\epsilon - \mathcal{H}} = -\frac{1}{\epsilon - \mathcal{H}} \frac{1}{\epsilon - \mathcal{H}} = -G(\epsilon)\, G(\epsilon) \,. \tag{58}$$

The electronic density of states can formally be expressed as

$$n(\epsilon) = -\frac{1}{\pi} \operatorname{Im} \, \operatorname{Tr} G\,(\epsilon) \,. \tag{59}$$

The difference between the density of states for two systems characterized by two Green-function operators $G(\epsilon)$ and $g(\epsilon)$ is given by

$$\Delta n(\epsilon) = -\frac{1}{\pi} \operatorname{Im} \operatorname{Tr}[G(\epsilon) - g(\epsilon)] = -\frac{1}{\pi} \operatorname{Im} \operatorname{Tr}[g(\epsilon) V G(\epsilon)] = -\frac{1}{\pi} \operatorname{Im} \operatorname{Tr} \left[g(\epsilon) V \frac{1}{1 - g(\epsilon) V} g(\epsilon) \right] .$$

Here and below V denotes the difference between the two potentials. By use of (58) for $g(\epsilon)$ this can be expressed as

$$\Delta n(\epsilon) = \frac{1}{\pi} \operatorname{Im} \operatorname{Tr} \left[\frac{\mathrm{d}g(\epsilon)}{\mathrm{d}\epsilon} V \frac{1}{1 - g(\epsilon) V} \right] = -\frac{1}{\pi} \operatorname{Im} \operatorname{Tr} \frac{\mathrm{d}}{\mathrm{d}\epsilon} \ln(1 - g(\epsilon) V) \,. \tag{60}$$

The difference between the integrated densities of states is thus given by

$$\Delta N(\epsilon) = \int^{\epsilon} d\epsilon' \, \Delta n(\epsilon') = -\frac{1}{\pi} \operatorname{Im} \operatorname{Tr} \ln(1 - g(\epsilon) V) \tag{61}$$

References

[1] J. Korringa 1947 Physica **13**, 392 (1947)

[2] W. Kohn and N. Rostoker, Phys. Rev. **94**, 1111 (1954)

[3] P. Hohenberg and W. Kohn, Phys. Rev. **136**, B864 (1964)

[4] W. Kohn and L.J. Sham, Phys. Rev. **140**, A1133 (1965)

[5] E.N. Economou: *Green's Functions in Quantum Physics* (Springer, Berlin, 2011)

[6] C. Koenig, J. Phys. F: Metal Phys. **3**, 1497 (1973)

[7] H. Dreysse and R. Riedinger, J. Physique **42**, 437 (1981)

[8] R. Zeller, J. Deutz and P.H. Dederichs, Solid State Commun. **44**, 993 (1982)

[9] A.R. Williams, P.J. Feibelman and N.D. Lang, Phys. Rev. B **26**, 5433 (1982)

[10] G.F. Koster and J.C. Slater, Phys. Rev. **94**, 1392 (1954); Phys. Rev. **95**, 1164 (1954)

[11] G.A. Baraff and M. Schlüter, Phys. Rev. Lett. **41**, 892 (1978)

[12] J. Bernholc, N.O. Lipari and S.T. Pantelides, Phys. Rev. Lett. **41**, 895 (1978)

[13] S.P. Singhal and J. Callaway, Phys. Rev. B **19**, 5049 (1979)

[14] C. Koenig and E. Daniel, J. Phys. (Paris) **42**, L193 (1981)

[15] O. Gunnarsson, O. Jepsen and O.K. Andersen, Phys. Rev. B **27**, 7144 (1983)

[16] R. Zeller and P.H. Dederichs, Phys. Rev. Lett. **42**, 1713 (1979)

[17] R. Podloucky, R. Zeller and P.H. Dederichs, Phys. Rev. B **22**, 5777 (1980)

[18] R. Zeller and P.J. Braspenning, Solid State Commun. **42**, 701 (1982)

[19] G.M. Stocks, W.M. Temmerman and B.L. Gyorffy, Phys. Rev. Lett. **41**, 339 (1978)

[20] A. Bansil, Phys. Rev. Lett. **41**, 1670 (1978)

[21] R. Zeller, J. Phys. C: Solid State Phys. **20**, 2347 (1987)

[22] P. Lloyd, Proc. Phys. Soc. London **90**, 207 (1967)

[23] R. Zeller, J. Phys. Condens. Matter **16**, 6453 (2004)

[24] P.W. Anderson, Phys. Rev. **124**, 41 (1961)

[25] R. Zeller, R. Podloucky and P.H. Dederichs, Z. Phys. **38**, 165 (1980)

[26] K.H. Johnson, D.D. Vvedensky and R.P. Messmer, Phys. Rev. B **19**, 1519 (1979)

[27] P.J. Braspenning, R. Zeller, A. Lodder and P.H. Dederichs, Phys. Rev. B **29**, 703 (1984)

[28] D. van der Marel, G.A. Sawatzky and F.U. Hillebrecht, Phys. Rev. Lett. **41**, 206 (1984)

[29] D. van der Marel, C. Westra, G.A. Sawatzky and F.U. Hillebrecht, Phys. Rev. B **31**, 1936 (1985)

[30] M.J. Puska, S. Pöykkö, M. Pesola and R.M. Nieminen, Phys. Rev. B **58**, 1318 (1998)

[31] F. Corsetti and A.A. Mostofi, Phys. Rev. B **84**, 035209 (2011)

[32] P.H. Dederichs, B. Drittler and R. Zeller, in: *Applications of Multiple Scattering Theory to Materials Science*, ed. by W.H. Butler, P.H. Dederichs, A. Gonis and R. Weaver, MRS Symposia Proceedings No. 253, (Materials Research Society, Pittsburgh, 1992)

[33] B. Drittler, M. Weinert, R. Zeller and P.H. Dederichs, Solid State Commun. **79**, 31 (1991)

[34] P. Pulay, Mol. Phys. **17**, 153 (1969)

[35] N. Stefanou, P.J. Braspenning, R. Zeller and P.H. Dederichs, Phys. Rev. B **36**, 6372 (1987)

[36] N. Papanikolaou, R. Zeller, P.H. Dederichs and N. Stefanou, Phys. Rev. B **55**, 4157 (1997)

[37] N. Papanikolaou, R. Zeller and P.H. Dederichs, J. Phys Condens. Matter **14**, 2799 (2002)

[38] A. Settels, K. Schroeder, T. Korhonen, N. Papanikolaou, M. Aretz, R. Zeller and P.H. Dederichs, Solid State Commun. **113**, 239 (2000)

[39] A. Settels, T. Korhonen, N. Papanikolaou, R. Zeller and P.H. Dederichs, Phys. Rev. Lett **83**, 4369 (1999)

[40] B. Drittler, H. Ebert, R. Zeller and P.H. Dederichs, Phys. Rev. B **39**, 6334 (1989)

[41] P.H Dederichs, P. Lang, K. Willenborg, R. Zeller, N. Papanikolaou and N. Stefanou, Hyperfine Interact. **78**, 341 (1993)

[42] P.H. Dederichs, S. Blügel, R. Zeller and H. Akai, Phys. Rev. Lett **53**, 2512 (1984)

[43] M. Levy, Proc. Natl. Acad. Sci. U.S.A. **76**, 6062 (1979)

[44] A. Oswald, R. Zeller and P.H. Dederichs, J. Magn. Magn. Mater. **140-144**, 1247 (1986)

[45] R.J. Elliot, J.A. Krumhansl and P.L. Leath, Rev. Mod. Phys. **46**, 465 (1974)

[46] D.A. Rowlands, J.B. Staunton, B.L. Györffy, E. Bruno and B. Ginatempo, Phys. Rev. B **72**, 045101 (2005)

[47] D.A. Rowlands, Rep. Prog. Phys. **72**, 086501 (2009)

[48] J. Korringa, J. Phys. Chem. Solids **7**, 252 (1958)

[49] J.L. Beeby and S.F. Edwards, Proc. R. Soc. (Lond.) A **274**, 395 (1963)

[50] P. Soven, Phys. Rev. **156**, 809 (1967)

[51] M.L. Goldberger and K.M. Watson, *Collision Theory* (Wiley, New York, 1964)

[52] P.H. Dederichs, R. Zeller, H. Akai and H. Ebert, J. Magn. Magn. Mater. **100**, 241 (1991)

11 The Kondo Effect

Frithjof B. Anders
Theoretische Physik II
Technische Universität Dortmund

Contents

E. Pavarini, E. Koch, F. Anders, and M. Jarrell
Correlated Electrons: From Models to Materials
Modeling and Simulation Vol. 2
Forschungszentrum Jülich, 2012, ISBN 978-3-89336-796-2
http://www.cond-mat.de/events/correl12

1 Introduction

Jun Kondo was intrigued [1, 2] by the puzzling experimental observation [3] that the resistance in noble or divalent metals typically shows a minimum at low temperatures when containing small concentrations of transition metals. It was expected that the inelastic scattering is reduced with decreasing temperature and, therefore, the resistance should be a monotonic function of T, which reaches a finite temperature-independent value for $T \to 0$ proportional to the remaining lattice imperfections. It had been noted that the increase of the residual resistance is proportional to the transition metal concentration [3, 4] and only occurs when those impurities are magnetic. In 1961, Anderson [5] proposed a simple model for the understanding of the formation of stable magnetic moments in transition metals ions. Since the Coulomb interactions is only weakly screened on atomic length scales, valence fluctuations on unfilled d and f shells are suppressed at integer fillings, and a finite total angular momentum is formed according to Hund's rules. The Anderson model, which we will discuss in Sec. 1.2, provides a microscopic understanding of the Friedel sum rule [6] which relates the phase shifts of the conduction electrons scattered on the impurity to the number of displaced electrons.
The overwhelming experimental evidence hints towards the generic nature of this effect: the details of the conduction bands actually do only enter into a single material-dependent low energy scale T_K, the so-called Kondo scale. Kondo realized that the position of the resistance minimum remains unaltered when reducing the concentration of the magnetic impurities which rules out interaction induced correlation effects between different localized spins. From the first observation [3] in 1934, it took three decades until Kondo [1, 2] proposed his seminal Hamiltonian, which provides a simple physical picture and explains the experimental data. In the Kondo model,

$$H = H_b + H_K \,, \tag{1}$$

the conduction electrons are described by a non-interacting electron gas

$$H_b \;=\; \sum_{\vec{k}\sigma} \varepsilon_{\vec{k}\sigma} c^\dagger_{\vec{k}\sigma} c_{\vec{k}\sigma} \tag{2}$$

and the interaction with a localized magnetic moment $\vec{S}$ is modelled by a simple Heisenberg term

$$H_K \;=\; J \vec{S} \vec{s}_b \,. \tag{3}$$

$c^\dagger_{\vec{k}\sigma}$ ($c_{\vec{k}\sigma}$) generates (destroys) a conduction electron with momentum $\vec{k}$ and spin σ, $\vec{S}$ represents the impurity spin, $\vec{s}_b$

$$\vec{s}_b = \frac{1}{2}\frac{1}{N} \sum_{\vec{k}\vec{k}'} \sum_{\alpha\beta} c^\dagger_{\vec{k}\alpha} \, \underline{\underline{\vec{\sigma}}}_{\alpha\beta} \, c_{\vec{k}'\beta} \tag{4}$$

is the spin of the conduction electrons at the impurity site and $\underline{\underline{\vec{\sigma}}}$ are the Pauli matrices. The lattice has a finite size of N sites which are sent to $N \to \infty$ in the thermodynamic limit.
Over the period of the last 50 years we have learned that the Kondo problem is not restricted to magnetically doped noble or divalent metals: it has turned out to be one of the most fundamental

problems in solid state physics. It involves the change of ground states when going from high-energy to low energy physics indicated by the infrared divergent perturbation theory.

1.1 Resistance minimum

Before we proceed to the Kondo problem itself, let us investigate the scattering of free conduction electrons on a finite number of impurities. The N_{imp} identical impurities are located at positions $\{\vec{R}_i\}$, and each contributes a potential $V(\vec{r}-\vec{R}_i)$ to H_b generating the additional potential scattering term

$$V = \sum_i \sum_{\vec{k}\vec{q}\sigma} e^{i\vec{q}\vec{R}_i}\, V(\vec{q})\, c^\dagger_{\vec{k}+\vec{q},\sigma} c_{\vec{k}\sigma}\,, \tag{5}$$

where $V(\vec{q})$ is the Fourier transform of $V(\vec{r})$. For a given configuration of impurities, $\{\vec{R}_i\}$, the single-particle Green function of the conduction electrons is determined by Dyson's equation [7],

$$G_{\vec{k},\vec{k}'}(z) = \frac{\delta_{\vec{k},\vec{k}'}}{z-\varepsilon_{\vec{k}\sigma}} + \sum_i \sum_{\vec{q}\sigma} e^{i\vec{q}\vec{R}_i}\, V(\vec{q})\, G^0_{\vec{k}}(z) G_{\vec{k}-\vec{q},\vec{k}'}(z)\,, \tag{6}$$

where $G^0_{\vec{k}}(z) = [z-\varepsilon_{\vec{k}\sigma}]^{-1}$. After expanding this equation in powers of $V(\vec{q})$, we need to average over the different configurations $\{\vec{R}_i\}$ in order to obtain the configuration averaged Green function $\langle G_{\vec{k},\vec{k}'}(z)\rangle_{\rm conf}$. In linear order, we obtain

$$\left\langle \sum_i e^{i\vec{q}\vec{R}_i} V(\vec{q}) \right\rangle = N_{imp} V(0)\, \delta_{\vec{q},0}\,, \tag{7}$$

while in second order, two terms [4] arise

$$\left\langle \sum_i e^{i\vec{q}\vec{R}_i} V(\vec{q}) \sum_j e^{i\vec{q}'\vec{R}_j} V(\vec{q}') \right\rangle = N_{imp} V(q) V(q') \delta_{\vec{q}+\vec{q}',0} + N_{imp}(N_{imp}-1) V^2(0) \delta_{\vec{q},0}\delta_{\vec{q}',0}\,. \tag{8}$$

The first describes two scattering events on a single impurity and the other a single scattering of two different impurities. Summing up all these zero momentum transfers $V(0)$ produces a uniform background which we absorb into the dispersion $\varepsilon_{\vec{k}\sigma}$. In higher order, there are two types of skeleton diagrams [8] generated: either the diagram describes multiple scattering on a single impurity, or several impurities are involved. The latter include interference effects which can be neglected if the mean free path is shorter than the average distance between two impurities. In the following, we assume such a small concentration of c_{imp} that the condition $c_{imp} = N_{imp}/N \ll 1$ is always fulfilled. Then $G_{\vec{k}}(z) = [z-\varepsilon_{\vec{k}\sigma}-\Sigma_{\vec{k}}(z)]^{-1}$ acquires a self-energy

$$\Sigma_{\vec{k}}(z) = c_{imp} T_{\vec{k}}(z), \tag{9}$$

which is proportional to the impurity concentration. The scattering matrix $T_{\vec{k}}(z)$ accounts for the sum of all multi-scattering processes on a single impurity.

The imaginary part of the self-energy is related to the single-particle life-time $\tau_{\vec{k}}$:

$$\Im m\Sigma_{\vec{k}}(\varepsilon_k - i\delta) = 1/2\tau(\vec{k})\,,$$

whose value close to the Fermi energy might be mistaken for a transport life-time entering the simple Drude model for the conductance,

$$\sigma \;=\; \frac{ne^2\tau_{Drude}}{m}\,, \tag{10}$$

where n is the concentration of electrons. According to Kubo's transport theory [7], however, the conductance is obtained from the current-current correlation function. A closer inspection reveals immediately that this correspondence of single-particle and transport life-time is incorrect in general: Clearly, forward scattering by the T-matrix contributes less to resistance than backward scattering. Hence, the average over the momentum transfer directions is required to connect τ_{Drude} with $T_k(z)$. However, we can employ the optical theorem to connect the imaginary part of the forward scattering $\Im m T_{\vec{k}}(z)$ to the angular integrated matrix elements $\Im m T_k(z) \propto \int d\Omega |\langle\vec{k}|\hat{T}|\vec{k}'\rangle|^2$. Since we deal with isotropic s-wave scattering in the Kondo problem, the T-matrix becomes angular independent and the angular averaging yields $\tau_{Drude} = \tau_{k_F}$.

Just taking the contribution linear in J, the spin-diagonal scattering of conduction electrons reads JS_z and the spin flip terms yields $\langle\vec{k}\uparrow|\hat{T}|\vec{k}'\downarrow\rangle = JS^-$, so that all three contributions from the scalar product $J\vec{S}\vec{s}_b$ add up to $\Im m T = J^2S(S+1) + O(J^3)$ using the optical theorem. In second order in J, we just find a constant contribution similar to a residual potential scattering term. Its magnitude, however, is proportional to the square of the effective moment.

In order to understand Kondo's theory of the resistance minimum, the second order contribution to the T-matrix [1]

$$\langle\vec{k}\sigma|\hat{T}|\vec{k}'\sigma'\rangle|_{(2)} = \left\langle \vec{k}\sigma \left| H_K \frac{1}{z-\hat{H}_0} H_K \right| \vec{k}'\sigma' \right\rangle \tag{11}$$

is needed. Since the details of the calculation can be found in Hewson's book [4], and a similar calculation is presented in the Sec. 2.1 below, we will only state the final result for the resistivity contribution of a single impurity:

$$\rho_{imp} = \frac{3\pi m J^2 S(S+1)}{2e^2\hbar\varepsilon_F}\left[1 - J\rho(\varepsilon_F)\ln\left(\frac{k_BT}{D}\right) + O(J^3)\right]\,, \tag{12}$$

where m is the electron mass, $\rho(\varepsilon_F)$ the conduction band density of state at the Fermi energy ε_F and D the band width. The infrared divergent logarithm arises from the integration of the resolvent $1/(z-\hat{H}_0) \propto 1/(z-\varepsilon)$ over all intermediate conduction electron states since the spin-flipped local states are degenerate. In a magnetic field, however, the logarithmic divergency will be cut off on the energy scale given by the Zeeman energy.

Typically, the bare coupling $g = J\rho(\varepsilon_F) \ll 1$ is small. However, the logarithmic corrections causes an increase in ρ_{imp} for decreasing temperatures and $J > 0$, which diverges for $T \to 0$. The effective scattering rate becomes of the order $\mathcal{O}(1)$ at temperatures of an exponentially small energy scale T_K

$$T_K \propto De^{-\frac{1}{\rho J}}\,, \tag{13}$$

which is non perturbative in the bare coupling constant ρJ. This scale indicates the breakdown of the perturbation theory and is called the Kondo scale. At the heart of the problem are divergent spin-flip contributions, which occur in quantum impurity problems with degenerate local quantum states.

1.2 Anderson model

As mentioned already in the introduction, Anderson proposed a model [5] for the understanding of local moment formation in 1961. Its simplest version comprises of a single localized spin-degenerate level with energy ε^d and a Coulomb repulsion U when the level is filled with two electrons of opposite spin. This local Hamiltonian

$$H_{imp} = \sum_{\sigma} \varepsilon^d d^\dagger_\sigma d_\sigma + U n_\uparrow n_\downarrow \tag{14}$$

is then trivially diagonalized by the four atomic states $|0\rangle, |\sigma\rangle, |2\rangle$. For the single particle energy we use the notation ε^d which is identical to ε_f in Bulla's lecture. This different notation roots historically in the modeling of either d-electron or f-electron systems.
Such an atomic orbital [5] is then coupled to a single conduction band

$$H_b = \sum_{\vec{k}\sigma} \varepsilon_{\vec{k}\sigma} c^\dagger_{\vec{k}\sigma} c_{\vec{k}\sigma} \tag{15}$$

via a hybridization term

$$H_{mix} = \sum_{\vec{k}\sigma} V_{\vec{k}} \left(c^\dagger_{\vec{k}\sigma} d_\sigma + d^\dagger_\sigma c_{\vec{k}\sigma} \right) . \tag{16}$$

The local dynamics of the single-impurity Anderson model (SIAM), defined by the Hamiltonian

$$H_{SIAM} = H_{imp} + H_b + H_{mix} \tag{17}$$

is completely determined by the hybridization function

$$\Gamma_\sigma(\omega) = \pi \sum_{\vec{k}} |V_{\vec{k}}|^2 \delta(\omega - \varepsilon_{\vec{k}\sigma}) . \tag{18}$$

The SIAM and the Kondo model belong to the class of quantum impurity models (QIM) which are defined by a finite number of local degrees of freedom, which are coupled to one or more bath continua.
In the regime $\varepsilon^d < 0$ and $\varepsilon^d + U > 0$, the energies of the empty and double occupied state, $|0\rangle$ and $|2\rangle$, lie above the $|\sigma\rangle$ states and can be neglected at low temperatures: a local moment represented by a spin $1/2$ is formed. Although local charge fluctuations on the d-level are suppressed at low temperatures and odd integer fillings, virtual exchange of electrons with the conduction are still possible, leading to spin-flip processes. Using a unitary transformation, Schrieffer and Wolff have derived [9] an effective energy dependent Kondo coupling $J_{\rm eff}$ between the local conduction electron and the two local moment states $|\sigma\rangle$. First, the Fock space

is partitioned into a low energy sector, which contains $|\sigma\rangle$, projected out by $\hat{P}_L$ and its complement $\hat{P}_H = (\hat{1} - \hat{P}_L)$ which includes $|0\rangle$ and $|2\rangle$. The Hamiltonian can then be divided into a diagonal part $H_d = \hat{P}_L H \hat{P}_L + \hat{P}_H H \hat{P}_H$ and an off-diagonal part $\lambda V = \hat{P}_L H \hat{P}_H + \hat{P}_H H \hat{P}_L$. The subsequent unitary transformation $U = \exp(\lambda S)$

$$H' = e^{\lambda S} H e^{-\lambda S} = H_d + \frac{\lambda^2}{2}[S, \bar{V}] + \sum_{n=2} \lambda^{n+1} \frac{n}{n+1!}[S, \bar{V}]_n \,, \tag{19}$$

is defined by the requirement of eliminating V in first order. The generator S is determined by the condition $[S, H_d] = -V$. Then, the effective Hamiltonian of the low energy subspace

$$H'_{LL} = \hat{P}_L H' \hat{P}_L = \hat{P}_L H \hat{P}_L + P_L \frac{\lambda^2}{2}[S, \bar{V}] P_L + O(\lambda^3) \tag{20}$$

acquires renormalized parameters and additional interaction terms via virtual transitions between the low and the high energy sectors mediated by V up to second order in λ. By applying this transformation to the H_{SIAM}, $H_K = \hat{P}_L \frac{\lambda^2}{2}[S, \bar{V}] \hat{P}_L$ takes the form of the Kondo interaction [9]

$$\begin{aligned} H_K &= \frac{1}{2} \sum_{\vec{k},\vec{k}'} \sum_{\alpha\beta} J_{\vec{k}\vec{k}'} c^\dagger_{\vec{k}\alpha} \vec{\sigma}_{\alpha\beta} c_{\vec{k}'\beta} \vec{S} \\ J_{\vec{k}\vec{k}'} &= -V_{\vec{k}} V_{\vec{k}'} \left(\frac{1}{\varepsilon_{\vec{k}} - (\varepsilon^d + U)} + \frac{1}{\varepsilon_{\vec{k}'} - (\varepsilon^d + U)} - \frac{1}{\varepsilon_{\vec{k}} - \varepsilon^d} - \frac{1}{\varepsilon_{\vec{k}'} - \varepsilon^d} \right) \end{aligned} \tag{21}$$

since the local low energy sector is only comprised of the two singly occupied spin states $|\sigma\rangle$ while $|0\rangle, |2\rangle \in P_H$.

For a constant hybridization $|V_{\vec{k}}|^2 = V^2$ and conduction band energies close to the Fermi energy, $\varepsilon_{\vec{k}}$ can be neglected, and $J_{\vec{k}\vec{k}'} \to J = -2V^2 U/[\varepsilon^d(\varepsilon^d + U)] > 0$ for the local moment regime where $\varepsilon^d < 0$ and $\varepsilon^d + U > 0$. At the particle-hole symmetric point $\varepsilon^d = -U/2$ the dimensionless Kondo coupling $\rho J = 8\Gamma_0/(\pi U)$ determines the charge fluctuation scale at, where $\Gamma_0 = \Gamma(0)$.

We have demonstrated that the Schrieffer-Wolff transformation generates an effective Kondo Hamiltonian for the low energy sector of the SIAM in second order in the hybridization. This clearly reveals the connection between the SIAM, which includes all orbital and spin degrees of freedom, and the Kondo model focusing solely on the local spin degrees of freedom. The numerical renormalization group approach [10, 11], discussed in the lecture of R. Bulla, is able to explicitly track the flow from a free-orbital fixed point for $\beta = 1/T \to 0$ to the Kondo model at intermediate temperatures $T/\Gamma_0 \approx 0.1$ and odd integer fillings of the orbital by iteratively eliminating the high energy degrees of freedom, which involve charge fluctuations.

More realistic descriptions of $3d$ and $4f$-shell dynamics requires more than one orbital. H_{imp} is easily generalized from a single to many orbitals:

$$H_{imp} = \sum_{i\sigma} \varepsilon^d_i n^d_{i\sigma} + \sum_{\substack{\sigma\sigma' \\ mnpq}} U_{mnpq} d^\dagger_{n\sigma} d^\dagger_{m\sigma'} d_{p\sigma'} d_{n\sigma} \,. \tag{22}$$

The direct and exchange Coulomb matrix elements U_{mnpq} will differ but are related by symmetry in the absence of relativistic effects, such as the spin-orbit interaction. This is discussed in more detail in the lecture of R. Eder. The Coulomb interaction in H_{imp} takes the rotational invariant form

$$\begin{aligned} H^U &= \frac{U}{2}\sum_{i\sigma} n^d_{i\sigma} n^d_{i-\sigma} + \frac{2U'-J}{4}\sum_{\substack{m\neq m'\\ \sigma\sigma'}} n^d_{m\sigma} n^d_{m'\sigma'} - J\sum_{m\neq m'} \vec{S}_m \vec{S}_{m'} \\ &\quad -\frac{J}{2}\sum_{\substack{m\neq m'\\ \sigma}} d^\dagger_{m\sigma} d^\dagger_{m-\sigma} d_{m'-\sigma} d_{m'\sigma} \end{aligned} \tag{23}$$

in spin-space by identifying $U_{nnnn} = U$, $U_{nmmn} = U - 2J = U'$, $U_{nmnm} = J$, $U_{nnmm} = -J$. Clearly, neglecting the orbital pair-transfer term $d^\dagger_{m\sigma} d_{m-\sigma} d_{m'-\sigma} d_{m'\sigma}$ breaks this rotational invariance. Since $J > 0$, the $\vec{S}_m \vec{S}_{m'}$ term is responsible for the Hund's rules, which favor the maximizing of the local spin and of the angular momentum by a ferromagnetic alignment.

2 Renormalization group

We have learned several important points in the previous sections: (i) The low energy physics of the Kondo effect shows universality and is characterized by a single energy scale T_K. (ii) The universality suggests that the problem can be tackled by approaches which were developed in the context of phase transitions: the renormalization group approach. (iii) The perturbative analysis breaks down due to infrared divergencies.
These divergencies indicate that the ground state of the starting point, a free conduction band coupled to a single spin, is orthogonal to the ground state of the strong-coupling fixed-point which governs the low energy physics.

2.1 Anderson's poor man's scaling

This section covers the simplest perturbative renormalization group (RG) approach to the Kondo model developed by Anderson [12] 1970. Although it does not solve the problem, it sets the stage for the deeper understanding of the physics provided by Wilson's numerical renormalization group approach.
We begin with the definition of s-wave conduction band annihilation operators $c_{\varepsilon\sigma}$

$$c_{\varepsilon\sigma} = \sqrt{\frac{1}{N\rho(\varepsilon)}}\sum_{\vec{k}} \delta(\varepsilon - \varepsilon_{\vec{k}}) c_{\vec{k}\sigma}\,, \tag{24}$$

which are obtained by angular integrating on a shell of constant energy ε. Starting from the anti-commutator $\left\{c_{\vec{k}\sigma}, c^\dagger_{\vec{k}'\sigma'}\right\} = \delta_{\sigma\sigma'}\delta_{\vec{k},\vec{k}'}$ of a discretized system, the prefactor $[\sqrt{N\rho(\varepsilon)}]^{-1}$ ensures the proper normalization of

$$\left\{c_{\varepsilon\sigma}, c^\dagger_{\varepsilon'\sigma'}\right\} = \delta_{\sigma\sigma'}\delta(\varepsilon - \varepsilon') \tag{25}$$

in the continuum limit since the density of state $\rho(\varepsilon)$ is defined as

$$\rho(\varepsilon) \;=\; \frac{1}{N}\sum_{\vec{k}}\delta(\varepsilon-\varepsilon_{\vec{k}})\,. \tag{26}$$

By supplementing the δ-function with some suitable symmetry adapted form factor $B(\vec{k})$, $\delta(\varepsilon-\varepsilon_{\vec{k}})\to\delta(\varepsilon-\varepsilon_{\vec{k}})B(\vec{k})$, such as a spherical harmonics $Y_{lm}(\Omega)$ or a Fermi surface harmonics [13], we could generalize these operators to the appropriate symmetry beyond simple s-wave scattering considered here. With those operators, the Hamiltonian (1) takes on the continuous form

$$H=\sum_{\sigma}\int_{-\infty}^{\infty}d\varepsilon\;\varepsilon c^{\dagger}_{\varepsilon\sigma}c_{\varepsilon\sigma}+\int_{-\infty}^{\infty}d\varepsilon\int_{-\infty}^{\infty}d\varepsilon' J(\varepsilon,\varepsilon')\sum_{\alpha\beta}c^{\dagger}_{\varepsilon\alpha}\vec{\sigma}c_{\varepsilon'\beta}\vec{S}_{imp} \tag{27}$$

where we have defined $J(\varepsilon,\varepsilon')=\frac{1}{2}J\sqrt{\rho(\varepsilon)\rho(\varepsilon')}$.
This formulation is still very general. It turns out, however, that the occurrence of the infrared divergence is linked to finite density of states at the Fermi energy. For simplicity, we assume a constant density of states restricted to the interval $\varepsilon\in[-D,D]$. $\rho_0=1/(2D)$ on this energy interval, and the Fermionic operator c_ε has the dimension of $1/\sqrt{E}$. After introducing the dimensionless coupling constant $g=\rho_0 J/2$, the dimensionless energy $x=\varepsilon/D$ and the dimensionless operators $c_{x\sigma}=\sqrt{D}c_{\varepsilon\sigma}$, we obtain the dimensionless isotropic Kondo Hamiltonian

$$\tilde{H}=\frac{H}{D}=\sum_{\sigma}\int_{-1}^{1}dx\;xc^{\dagger}_{x\sigma}c_{x\sigma}+g\int_{-1}^{1}dx\int_{-1}^{1}dx'\sum_{\alpha\beta}c^{\dagger}_{x\alpha}\vec{\sigma}c_{x'\beta}\vec{S}_{imp} \tag{28}$$

which will be subject to a perturbative renormalization group treatment. Since $\delta(\varepsilon-\varepsilon')=\delta([x-x']D)=\delta(x-x')(1/D)$, the rescaled operators also obey a normalized anti-commutator relation

$$\{c_{x\sigma},c^{\dagger}_{x'\sigma'}\} \;=\; (\sqrt{D})^2\{c_{\varepsilon\sigma},c_{\varepsilon'\sigma'}\}=D\delta_{\sigma\sigma'}\delta(\varepsilon-\varepsilon')=\delta_{\sigma\sigma'}\delta(x-x')\,. \tag{29}$$

The key ingredients to any renormalization group (RG) transformation are

1. separation of energy scale
2. eliminating high energy contributions by renormalizing low energy coupling constants
3. rescaling of all parameters and quantum fields

In the first step we define the appropriate low and high energy sector $\hat{P}_L$ and $\hat{P}_H=1-\hat{P}_L$ by partitioning the Fock-space appropriately. In the second step we perform the same transformations as outlined in Eq. (19). By eliminating the coupling between these sectors up to quadratic order, the effective Hamiltonian of the low energy subspace

$$H'_{LL}=\hat{P}_L H'\hat{P}_L=\hat{P}_L H\hat{P}_L+\hat{P}_L\frac{\lambda^2}{2}[S,\bar{V}]\hat{P}_L+O(\lambda^3)=H_{LL}+\Delta H^{(2)}_{LL}+O(\lambda^3) \tag{30}$$

acquires renormalized parameters via virtual transitions between the low and the high energy sectors mediated by V up to the second order in λ.

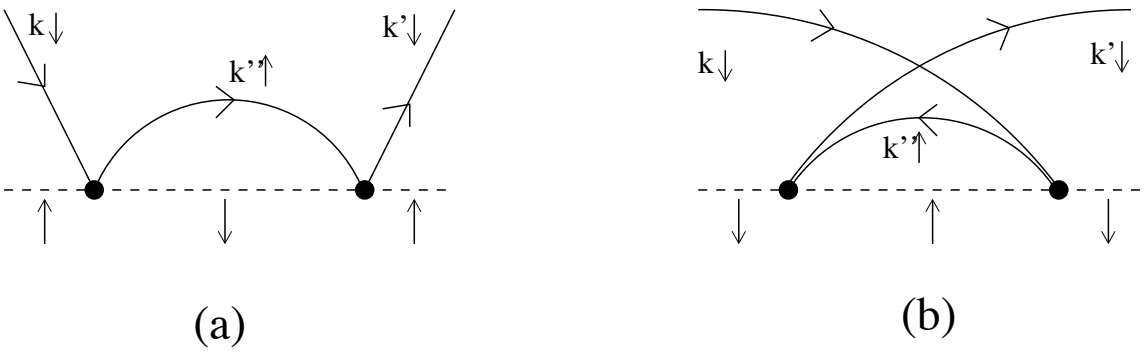

Fig. 1: *The particle (a) and the hole (b) spin-flip processes in second order in J contributing to the renormalization of J.*

Since the procedure is rather trivial for the free electron gas, we illustrate the steps on this part of the Hamiltonian. We introduce a dimensionless parameter $s > 1$ and split H_b into two contributions:

$$\frac{H_b}{D} = \sum_\sigma \int_{-1/s}^{1/s} dx\ x c^\dagger_{x\sigma} c_{x\sigma} + \sum_\sigma \left(\int_{-1}^{-1/s} dx + \int_{1/s}^{1} dx \right)\ x\, c^\dagger_{x\sigma} c_{x\sigma}\,. \tag{31}$$

One contribution contains all low energy modes $|x| < 1/s$ and the other all high energy modes $1/s < |x| < 1$. Defining $\hat{P}_L$ as the operator which projects onto all modes $|x| < 1/s$, the Hamiltonian is written as $H_b = \hat{P}_L H_b \hat{P}_L + \hat{P}_H H_b \hat{P}_H$ and, therefore, $V = 0$. Focusing on the low energy part

$$H'_b = H_{LL} = \hat{P}_L H_b \hat{P}_L = \sum_\sigma \int_{-1/s}^{1/s} dx\ x\, c^\dagger_{x\sigma} c_{x\sigma} \tag{32}$$

we have to rescale the energy modes x to $x' = sx$ in order to restore the original mode distribution $|x'| < 1$ and obtain

$$H'_b = \sum_\sigma s^{-2} \int_{-1}^{1} dx'\ x' c^\dagger_{x(x')\sigma} c_{x(x')\sigma}\,. \tag{33}$$

Since original Fermionic operators have the dimension $1/\sqrt{E}$, they must also be scaled as $c_{x'} = \sqrt{s} c_{x(x')\sigma}$ on expansion of the scale from $1/s \to 1$, which leads to

$$H'_b = \frac{1}{s} \sum_\sigma \int_{-1}^{1} dx'\ x' c^\dagger_{x'\sigma} c_{x'\sigma}\,. \tag{34}$$

This completes the third and last step of the RG procedure.

The dimensionful Hamiltonian H_b remains invariant under the mode elimination procedure if $H_b/D = H'_b/D'$. Comparing the rescaling of the integrals and fields after the mode elimination, Eq. (34) yields the scaling equation of the band width: $D' = D/s$. Such an invariance is called a fixed point under the RG transformation, and the Hamiltonian of the free electron gas is obviously such a fixed point Hamiltonian.

Before we come back to the Kondo interaction, we briefly review the scaling of an additional local Coulomb interaction $H_U \propto c^\dagger_{x_1\sigma}c^\dagger_{x_2\sigma'}c_{x_3\sigma'}c_{x_4\sigma}$ under the RG transformation. Performing the same RG steps in linear order, we accumulate $[s^{1/2}]^4$ for the rescaling of the four fields and $[s^{-1}]^4$ for the four integral transformation, s^{-2} in total. The Coulomb interaction is irrelevant since it vanishes under the RG flow. As a consequence, we, therefore, expect a local Fermi-liquid with vanishing scattering cross sections $\propto \omega^2$ at $T \to 0$, described by the strong-coupling fixed-point. Since we have understood the transformation of the free electron gas, we can add the dimensionless Kondo interaction H_K

$$H_K = \frac{1}{2}\sum_{\alpha,\beta}\sum_{i=x,y,z}\int_{-1}^{1} dx_1 \int_{-1}^{1} dx_2\, c^\dagger_{x_1\alpha}c_{x_2\beta}\, g^i \underline{\underline{\sigma}}^i_{\alpha\beta}\tau^i\,, \tag{35}$$

to the H_b and investigate $H = H_b + H_K$ under this RG transformation. In this expression, the local spin is represented by $\vec{S}_{loc} = \vec{\tau}/2$ and $g = \rho_0 J/2$ is generalized to three components g^i which include the anisotropic Kondo models.

Performing the unitary transformation (20), the low energy sector of H_K contributes to H in linear order via $\Delta H_d = \hat{P}_L H_{int}\hat{P}_L + \hat{P}_H H_{int}\hat{P}_H$. Additionally it generates the off-diagonal part $V = \hat{P}_L H_K \hat{P}_H + \hat{P}_H H_K \hat{P}_L$ for the Schrieffer-Wolff type transformation. Since the term linear in g, ΔH_d is invariant under the RG transformation, H_K is called a marginal operator in the vicinity of the local moment fixed point defined by $H_K = 0$.

In order to decide whether it is a relevant or irrelevant marginal operator, we have to go to second order in g. Using the eigenstates of H_d, $|p\rangle$ of the low-energy and $|q\rangle$ of the high-energy sector of the Fock space, we derive with the condition, $[S, H_d] = -V$

$$\Delta H^{(2)}_{LL} = \sum_{p,p'} |p\rangle\langle p'| \frac{1}{2}\sum_q V_{pq}V_{qp'}\left(\frac{1}{E_p - E_q} + \frac{1}{E_{p'} - E_q}\right)\,. \tag{36}$$

H_K contains a spin-spin interaction bilinear in the conduction electron operators. Therefore, one of the operators in $c^\dagger_{x_1\alpha}c_{x_2\beta}$ must contain a high-energy particle or hole excitation in V which is connected with the same conduction electron mode to one conduction electron line integrated out by mode elimination. Those matrix elements of $\Delta H^{(2)}_{LL}$ can be calculated diagrammatically using the two diagrams depicted in Fig. 1(a) and (b). Again, we eliminate a very thin shell of high energy excitations of width $\Delta l = 1 - 1/s = -\Delta D/D$, and the two diagrammatic contributions yield the quadratic corrections to g^i

$$\Delta H^{(2)}_{LL} = \Delta l \sum_{\alpha\beta}\int_{-1/s}^{1/s}\int_{-1/s}^{1/s} dx_1 dx_2\, c^\dagger_{x_1\alpha}c_{x_2\beta}\,\left(g^x g^y \tau^z\sigma^z + g^y g^z \tau^x\sigma^x + g^x g^z \tau^y\sigma^y\right)\,. \tag{37}$$

In the derivation of these equations, we have used the eigenstates of H_b and neglected the correction generated by H_K. This is a further approximation since the construction of S requires eigenstates of H_d and not only of H_b. This clearly restricts the validity of the flow equations derived below to small values of g^i.

The flow of the effective band width $dD/D = -dl$ is used to eliminate Δl. The combination of the infinitesimal change $\Delta H^{(2)}_{LL}$ in the limit $\Delta l \to dl$ with the linear contribution of H_K to the

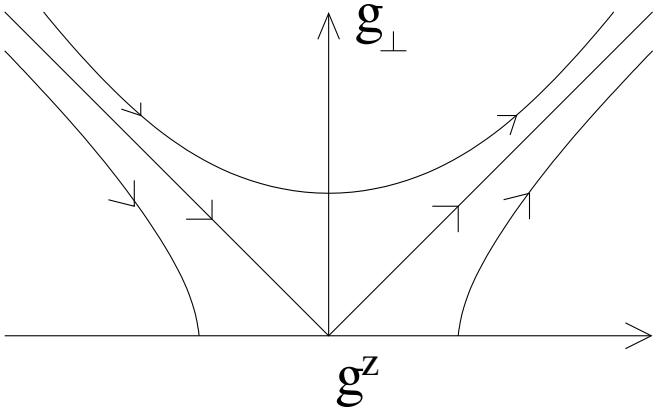

Fig. 2: *Flow of the coupling constants g^z and $g_\perp$, which is given by a set of hyperbolic curve as show in Eq. (39). For transverse coupling $|g_\perp| > g_z$, the Kondo coupling always flows to the strong-coupling fixed-point $g^z, g_\perp \to \infty$. For a ferromagnetic $g^z < 0$, $g_\perp$ renormalized to $g_\perp = 0$ where the RG-flow stops.*

low-energy sector, $P_L H_K P_L$, yields the three perturbative RG equations

$$\frac{dg^x}{d\ln\mathcal{D}} = -2g^y g^z \tag{38a}$$

$$\frac{dg^y}{d\ln\mathcal{D}} = -2g^x g^z \tag{38b}$$

$$\frac{dg^z}{d\ln\mathcal{D}} = -2g^x g^y \tag{38c}$$

for the parameter flow of the coupling constants. Fixed points of those flow equations are defined by $dg^i/d\ln\mathcal{D} = 0$ for all $i = x, y, z$. These equations are called poor man's scaling in the literature.

In the transversal Kondo model defined by two independent parameters g^z and $g_\perp = g^x = g^y$ these equations reduce to

$$\frac{dg_\perp}{d\ln\mathcal{D}} = -2g_\perp g^z \quad ; \qquad \frac{dg^z}{d\ln\mathcal{D}} = -2g_\perp^2\,, \tag{39}$$

from which we obtain by integration $[g^z]^2 - g_\perp^2 = \text{const}$. Therefore, the flow of the parameters g^z and $g_\perp$ are located on a hyperbolic curve in the parameter space $(g^z, g_\perp)$ which is depicted in figure 2. Since the RG-flow in Eq. (39) alway stops when $g_\perp$ vanishes, $(g^z, 0)$ defines a line of fixed points for $[g^z]^2 - g_\perp^2 > 0$ and $g^z < 0$. If the transverse coupling is larger than the ferromagnetic coupling g^z, $g^z < 0$, the transversal coupling $g_\perp$ remains finite for $g^z = 0$ and induces a sign change of g^z. The couplings flow to the strong-coupling fixed-point $(g_\perp, g^z) \to (\infty, \infty)$. These flow equations have one stable fixed point $(g^z, g_\perp) = (\infty, \infty)$ and one line of fixed points $(g^z, 0)$. The latter are stable for a ferromagnetic $g_z < 0$ and unstable for $g_z > 0$. For a fully isotropic Kondo coupling, $g = g^z = g_\perp$, we only need to integrate the single differential equation

$$\frac{dg}{d\ln\mathcal{D}} = \beta(g) = -2g^2\,. \tag{40}$$

The function $\beta(g)$ is called the β-function in the literature and determines how the coupling constants flow while reducing the band width: a negative β-function is a signature of weak interactions at high-energies and a growing interaction strength while reducing the band width. With the initial values of the model D_0, g_0, we integrate this differential equation to

$$g(D') = \frac{g_0}{1 + 2g_0 \ln(D_0/D')} \,. \tag{41}$$

This solution obviously breaks down at a low energy scale $T_K = D$ at which the denominator diverges:

$$T_K = D_0 e^{-1/2g_0} = D_0 e^{-1/\rho_0 J} \,. \tag{42}$$

However, the poor-man scaling approach is only valid for small coupling constants g, since higher order processes will modify the β-function. Nevertheless, we can use the new energy scale to express the running coupling constant $g(\mathcal{D}')$ as function of T_K

$$g(D') = \frac{1}{\ln(D'/T_K)} \tag{43}$$

which removes all reference to the original parameters. The coupling constant became an universal function of the ratio between cutoff and the new characteristic low energy scale T_K.
How can we understand the divergence of the effective coupling constant? If we let $g \to \infty$, we can ignore the kinetic energy of the conduction electrons for a moment and focus on the local Kondo interaction (35):

$$H_K = \frac{1}{2} \sum_{\alpha,\beta}^{\mu=x,y,z} c^\dagger_{0\alpha} c_{0\beta} g^\mu \underline{\underline{\sigma}}^\mu_{\alpha\beta} \tau^\mu \,, \tag{44}$$

where $c_{0\sigma} = \int_{-1}^{1} dx c_{x\sigma}$. Since H_K conserves spin and charge, a singlet and a triplet state is formed for $n_c = 1$, while the empty and doubly occupied conduction electron state does not couple to the local spin. The singlet has the energy of $-3/2g$, the three triplet states lie at the energy $g/2$ and the other two at $E = 0$. In the anti-ferromagnetic case $g > 0$, the ground state is a singlet, which is energetically decoupled from the rest of the conduction electrons for $g \to \infty$. The ground state in this strong-coupling limit will be a free electron gas with one electron removed and absorbed into this bound state. Hence, the ground state is orthogonal to the ground state of the local moment fixed point we started with. That is the reason why these ground states cannot be connected via perturbation theory. Since the scattering turns out to be irrelevant in the vicinity of this so-called strong-coupling fixed-point, it is a stable fixed point under the RG transformation.
Although the presented perturbative RG fails to solve the Kondo problem, it already proves that the original Kondo Hamiltonian is unstable in second order of g and predicts the correct crossover scale T_K. However, the divergence of the coupling constant happens already at a finite cutoff $D = T_K$ which must be an artifact of the approximation used since the model cannot have any phase transition at finite temperature. The correct solution can only be obtained by the numerical renormalization group [14, 15] or the Bethe ansatz [16].

2.2 Wilson's numerical renormalization group approach

Although Anderson's perturbative RG has already provided some deeper physical insight, its perturbative nature restricts its validity to a close range around its starting point: it cannot access the crossover regime from high to low temperature.
The Hamiltonian of a quantum impurity system is generally given by

$$H = H_{\rm bath} + H_{\rm imp} + H_{\rm mix} \ , \tag{45}$$

where $H_{\rm bath}$ models the continuous bath, $H_{\rm imp}$ represents the decoupled impurity, and $H_{\rm mix}$ accounts for the coupling between the two subsystems.
Such a system can be accurately solved using Wilson's numerical renormalization group (NRG) [14, 15]. At the heart of this approach is a logarithmic discretization of the continuous bath, controlled by the discretization parameter $\Lambda > 1$. The continuum limit is recovered for $\Lambda \to 1$. Using an appropriate unitary transformation, the Hamiltonian is then mapped onto a semi-infinite chain, with the impurity coupled to the open end. The nth link along the chain represents an exponentially decreasing energy scale: $D_n \sim \Lambda^{-n/2}$ for a fermionic bath [14] and $D_n \sim \Lambda^{-n}$ for a bosonic bath [17]. Using this hierarchy of scales, the sequence of dimensionless finite-size Hamiltonians

$$\begin{aligned} \Lambda^{-(N-1)/2} H_N &= \frac{2}{D\,(1+\Lambda^{-1})}(H_{\rm imp} + H_{\rm mix}) \\ &\quad + \sum_\alpha \sum_{n=0}^{N} \Lambda^{-(n-1)/2}\, \bar{\varepsilon}_{n\alpha} f^\dagger_{n\alpha} f_{n\alpha} \\ &\quad + \sum_\alpha \sum_{n=0}^{N-1} \Lambda^{-n/2}\, \bar{t}_{n\alpha} (f^\dagger_{n\alpha} f_{n+1\alpha} + f^\dagger_{n+1\alpha} f_{n\alpha}) \end{aligned} \tag{46}$$

for the N-site chain is solved iteratively, discarding the high-energy states at the conclusion of each step to maintain a manageable number of states. This reduced basis set of H_N is expected to faithfully describe the spectrum of the full Hamiltonian on a scale of D_N, corresponding to a temperature $T_N \sim D_N$.
Note that the dimensionless energies $\bar{\varepsilon}_{n\alpha}$ and tight-binding parameters $\bar{t}_{n\alpha}$ are of the order $O(1)$. In general, α labels all independent flavor and spin degrees of freedoms of the bath Hamiltonian. In the case of the single-band Kondo model, α denotes only the two spin states of the conduction electron band. The parameters $\bar{\varepsilon}_{n\alpha}$ and $\bar{t}_{n\alpha}$ encode all relevant details of a non-constant density of states.
Therefore, the NRG can be applied to pseudo-gap systems and used as an impurity solver for the dynamical mean field theory where in the self-consistently obtained coupling function $\Gamma(\omega)$ the lattice information and the formation of a Mott-Hubbard insulator is encoded [15]. The details on the connection between the coupling function $\Gamma(\omega)$ and the NRG parameters $\bar{\varepsilon}_{n\alpha}$ and $\bar{t}_{n\alpha}$ will be connected in R. Bulla's subsequence lecture.
We have followed the notation of Ref. [10, 11] where a mapped bath electron of flavor α is created (annihilated) by $f^\dagger_{n\alpha}(f_{n\alpha})$ at chain link n while in Bulla's lecture $c^\dagger_{n\sigma}(c_{n\sigma})$ is used for the

same operators. We also defined the Hamiltonian H_N in accordance with the original literature, while Bulla kept the factor $D/[2(1+\Lambda^{-1})]$ in his definition of H_N. We also emphasize the energy hierarchy by making the exponential decay of the tight binding parameters explicitly. The dimensionless parameters $\bar{\varepsilon}_{n\alpha}$ and $\bar{t}_{n\alpha}$ and those used in Bulla's lecture are connected by

$$\varepsilon_n = \frac{D\,(1+\Lambda^{-1})}{2}\Lambda^{-(n-1)/2}\,\bar{t}_{n\alpha} \tag{47a}$$

$$t_n = \frac{D\,(1+\Lambda^{-1})}{2}\Lambda^{-n/2}\,\bar{t}_{n\alpha} \tag{47b}$$

Due to the exponential form of the Boltzmann factors in the density operator, $\hat{\rho} = \exp(-\beta H)/Z$, the reduced NRG basis set of $\mathcal{H}_N$ is sufficient for an accurate calculation of thermodynamic quantities at temperature T_N. The fixed points under the RG transformation

$$H_{N+1} = \sqrt{\Lambda} H_N + \sum_\alpha \left(\bar{\varepsilon}_{N+1\alpha} f^\dagger_{N+1\alpha} f_{N+1\alpha} + \bar{t}_{N\alpha} (f^\dagger_{N\alpha} f_{N+1\alpha} + f^\dagger_{N+1\alpha} f_{N\alpha}) \right) \tag{48}$$

determines the thermodynamics properties and allows deep insight into the physics of the system. In SIAM, they have been explicitly stated in Refs. [10, 11]. It has been shown [14] that the Kondo temperature indeed determines the crossover scale from the local moment fixed point to the strong-coupling fixed-point. T_K is the only relevant energy scale at low temperatures so that all physical properties can be obtained from universal scaling functions for T/T_K and $\omega/T_K < 1$.

More details on the NRG and its power can be found in the lecture by R. Bulla or the NRG review [15] he co-authored.

2.3 Exotic Kondo effects in metals

In the previous section we have focused on the simplest case of a single spin-degenerate band coupled anti-ferromagnetically to a single local spin $S = 1/2$. The Kondo temperature T_K defines the crossover scale below which a singlet ground state emerges and the local spin is asymptotically screened.

How does the physics change if we couple a local spin with $S > 1/2$ to a single conduction band, or a spin $S = 1/2$ to more than one spin-degenerate conduction electron band?

We have discussed above that a Kondo Hamiltonian can be derived as an effective low energy Hamiltonian by applying a Schrieffer-Wolff (SW) transformation to the SIAM. If we consider its multi-orbital extension, Eq. (22), a much richer variety of impurity ground states emerge after freezing out the charge fluctuations. In Mn, Co, or other transition metal ions, Hund's rules generate a ground state spin $S > 1/2$, while point group symmetries in lattices or ligand symmetries in molecules [18] can suppress the hybridization to more than one conduction band. After a SW-transformation we could end up with an under-compensated Kondo model, schematically depicted in Fig. 3(c). The single conduction electron band will partially screen the local spin S to an effective spin $S' = S - 1/2$ which asymptotically decouples from the conduction band. It turns out that the RG fixed point is similar to the strong-coupling fixed-point,

but with a degeneracy of $2S$ remaining. The remaining very weakly coupled magnetic scatterer significantly modifies the universal functions describing the physical properties at temperatures $T < T_K$, and corrections to the T^2 behavior of a Fermi liquid are found. Hence, it is also called a singular Fermi-liquid which is characterized by a residual impurity entropy $S_{\rm loc} = \log(2S)$. The impurity entropy $S_{\rm loc}$ is defined as the difference of the total entropy and the entropy of the conduction band without impurity.

In the overcompensated Kondo model ($M > 1$)

$$H_K = \sum_{\alpha=1}^{M} J_\alpha \vec{S}\vec{s}_{b,\alpha} \,, \tag{49}$$

no Kondo singlet ground state can be formed by the local $S = 1/2$ impurity spin and the local conduction electron spins $\vec{s}_{b,\alpha}$, a consequence of the flavor conservation in such models. However, such flavor conservation is very hard to obtain from the SW transformation and might only occur in very exotic systems due to symmetry restrictions. Such models are characterized by an additional unstable intermediate-coupling fixed-point which can be understood by a simple argument: In very weak coupling $g_\alpha = \rho_0 J_\alpha/2 \to 0$, the poor man's scaling is applicable and g_α increases as we have discussed in the previous section. However, in the opposite limit, $1/g_\alpha \to 0$, we only need to consider one localized conduction electron in each channel α coupled to the local spin and treat the kinetic energy as perturbation. The ground state for anti-ferromagnetic g is formed by a composite $S' = M - S$ spin, which remains coupled to the rest of the conduction electrons by an effective matrix element of the order of the band width. Hence, an effective Kondo model is generated in which the coupling has been reduced from $g_\alpha \gg 1$ to $g_{\rm eff} \approx 1$. A detailed analysis proves [19] that the large coupling flows to smaller couplings, and the small couplings increase. Hence, both must flow to a fixed point of intermediate coupling strength. This requires the inclusion of the third order contributions to the β-function in Eq. (40). In the case of the isotropic two-channel Kondo model, $S = 1/2$ and $M = 2$, it takes the simple form $\beta(g) = -g^2 + g^3$ for a uniform Kondo coupling. In addition to the trivial fixed-point, $g = 0$, it has an intermediate fixed-point $\beta(g_c = 1) = 0$ [19]. It is interesting to note that the intermediate-coupling fixed-point impurity entropy reaches $(k_B/2)\log(2)$, indicating that a Majorana fermion decouples [20] from the system in the low energy limit. However, this fixed point is unstable against breaking of channel and spin symmetry. Under channel symmetry breaking, i.e. $J_1 \neq J_2$, the RG flow renormalizes $J_{\rm max} = \max(J_1, J_2) \to \infty$ and $J_{\rm min} = \min(J_1, J_2) \to 0$: the channel with the larger coupling forms a normal Kondo singlet while the other channel decouples.

In Fig. 3(a), the temperature dependent local entropy $S_{\rm loc}$ for the three cases, the compensated (black), the under-compensated (red) and the overcompensated (blue) model is depicted. For the compensated Kondo model, $S_{\rm loc} \approx k_B \log(2)$ at high temperature, which is reduced to $S_{\rm loc} \to 0$ for $T \to 0$ indicating the Kondo singlet formation. This corresponds to a vanishing effective local moment on the temperature scale $T_K \approx 10^{-5} D$.

The under-compensated model presented here comprises of a two-orbital Anderson model with a ferromagnetic Hund's rule coupling in Eq. (22), coupled to single conduction electron band.

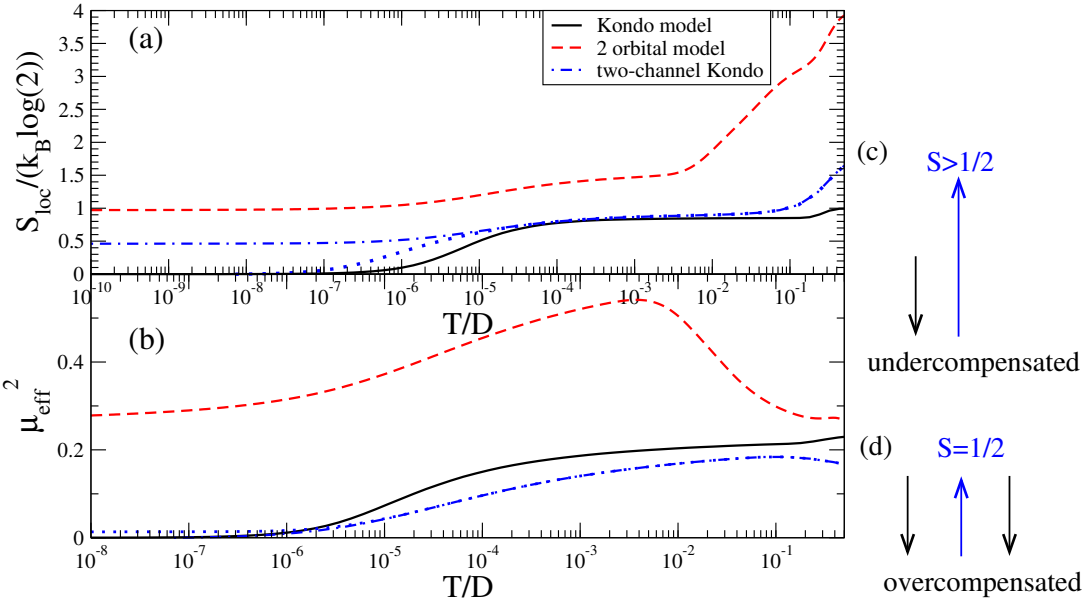

Fig. 3: *(a) Impurity entropy of the $S = 1/2$ Kondo model (black line), the under-compensated $S = 1$ model (red line) and the two-channel Kondo model (blue) line. (b) The local effective moment $\mu^2_{\rm eff}$ defined as $\mu^2_{\rm eff} = \langle S^2_z\rangle_H - \langle S^2_z\rangle_{H_b}$ for the same three models as in (a). (c) the local $S > 1/2$ coupled to one conduction spin is under-compensated, (d) a spin $S = 1/2$ is coupled to two conduction bands which is described by the two-channel Kondo model.*

For $T \to \infty$, the free orbital fixed point is 2^4-fold degenerate resulting in $S_{\rm loc}(\beta = 0) = 4k_B \log(2)$. As depicted in Fig. 3(a), it approaches $k_B \log(2)$ for $T \to 0$, indicating an unscreened decoupled $S = 1/2$ degree of freedom.

$S_{\rm loc}(T)$ for the overcompensated two-channel Anderson model [21–23] is shown as a blue curve. Starting from 4-fold degenerate local orbital fixed point, an effective two-channel Kondo model is found in the interval $10^{-3} < T/D < 10^{-1}$, and approaches the intermediate-coupling two-channel Kondo fixed point value of $S_{\rm loc} \approx k_B \log(2)/2$. By applying a weak external magnetic field of $H = 10^{-4}\Gamma_0$, the two-channel symmetry is broken and a crossover to the strong-couping fixed point is observed – blue dotted line in Fig. 3(a). The crossover is governed by the scale $T^* \propto H^2/T_K$. The effective magnetic moment $\mu^2_{\rm eff}$ tracks the $H = 0$ curve up T^* and approaches a finite value induced by the finite magnetic field.

This model has originally been proposed by Cox [21] for uranium-based Heavy Fermions in which the U $5f$-shell is doubly occupied. It predicts an orbital Kondo effect where the non-magnetic Γ_3 doublet is screened by a four-fold degenerate Γ_8 conduction band. Experimentally, however, there is still no evidence for the realization of such a two-channel Kondo fixed point.

3 Kondo effect in lattice systems

3.1 Heavy Fermion materials

Heavy Fermions [24] are Ce and U based metallic compounds which show a strongly enhanced γ-coefficient of the specific heat. Typically an enhancement over simple Cu of a factor of $300 - 6000$ is found. Since $\gamma \propto m^*$ in a simple effective Fermi-liquid theory, the name Heavy Fermions was coined for this material class. It has been noted that the additional magnetic contribution to the specific heat scales with the number of magnetic ions upon substitution with non-magnetic elements such as La [24]. Apparently the major contribution in such strongly correlated materials stems from the electrons in the localized $4f$ or $5f$-shells. Early on, local approximations were proposed [25, 26] in which each Ce or U site is treated as an independent Kondo scatterer interacting with an averaged conduction band. Coherence is recovered by summing up all single particle scattering events on a periodic lattice [24].
The most simplified description starts from a singly occupied $4f$-shell of Ce. Employing Hund's rules, spin-orbit coupling yields a $J = 5/2$ ground state multiplet which is quenched by the lattice point group symmetry either to a quartet and doublet in cubic crystal, or three Kramers doublets in a tetragonal environment. Taking into account only a single Kramers doublet on each $4f$-shell and hybridizing the orbital with one effective conduction band defines the periodic extension of the Anderson model (PAM)

$$H = \sum_{i\sigma} \varepsilon_i^f f_{i\sigma}^\dagger f_{i\sigma} + U n_{i\uparrow} n_{i\downarrow} + \sum_{\vec{k}\sigma} \varepsilon_{\vec{k}\sigma} c_{\vec{k}\sigma}^\dagger c_{\vec{k}\sigma} + \sum_{i,\vec{k},\sigma} V_k \left(e^{i\vec{k}\vec{R}_i} f_{i\sigma}^\dagger c_{\vec{k}\sigma} + e^{-i\vec{k}\vec{R}_i} c_{\vec{k}\sigma}^\dagger f_{i\sigma} \right) , \quad (50)$$

where $f_{i\sigma}$ annihilates an f-electron at lattice site i with spin σ. Although this model can already explain some basic properties of HF materials [24], a more realistic description requires the full $J = 5/2$ ground state multiplet structure, since experimentally the influence of crystal-field effects are clearly seen in the specific heat or transport measurements [24].
As mentioned above, experimental evidence has indicated that the magnetic contribution to the specific heat scales with number of magnetic Lanthanide ions, hinting towards locally generated strong correlations. It was proposed that the single-particle dispersion can be calculated using a local t-matrix which accounts for all local correlations, while different lattice [25] sites are linked only by a free propagation of electrons. A physically intuitive picture emerges: at the chemical potential, the electrons are mainly trapped in local Kondo-resonances and propagate only rather rarely from site to site. On a larger length scale, a very slow coherent motion is generated which is equivalent to a quasi-particle with a large effective mass.

3.2 Dynamical mean field theory (DMFT)

The combination of local-density approximation (LDA) and DMFT for realistic description of material properties of a large variety of strongly correlated electron systems has been the topic of the last year's school [27] entitled *The LDA+DMFT approach to strongly correlated materials.*

In DMFT, the k-dependence of the lattice self-energy is neglected. The original idea for such a local approximation dates back to the mid 1980s [25, 26, 28] and has been applied to Heavy Fermion systems. In 1989, it was proven that such an approximation has an exact limit in infinite spatial dimensions [29–31] which broaden the applicability of this approximation to a much larger range of problems.

The basic idea of the DMFT [32, 33] can be summarized as follows: One picks out a single lattice site or a unit-cell. Instead of solving the local dynamics embedded in the full lattice exactly, which is usually not possible, the rest of the interacting lattice is replaced by a fictitious tight-binding model. This implies that two-particle and higher order correlation functions are treated as factorized, which imposes restrictions on the applicability of the theory to phase-transitions. This is augmented by a self-consistency condition (SCC) which equates the local lattice Green function $G_{\rm lat}(z)$

$$G_{\rm lat}(z) = \frac{1}{N}\sum_{\vec{k}} G_{\vec{k}}(z) = \frac{1}{N}\sum_{\vec{k}} \frac{1}{z-\varepsilon_{\vec{k}}-\Sigma(z)} = G_{\rm loc}(z) \tag{51}$$

with the local Green function $G_{\rm loc}(z)$ of such an effective site. This effective site of the DMFT is equivalent to an Anderson impurity model as defined in Sec. (1.2), and its local dynamics is determined by $G_{\rm loc}(z) = [z-\varepsilon^d-\Sigma(z)-\tilde{\Delta}(z)]^{-1}$. It requires the knowledge of the local orbital energy ε^d, the local Coulomb repulsion U and the hybridization function $\tilde{\Gamma}(\omega) = \Im m\tilde{\Delta}(\omega-i\delta)$. In the subsequent lecture by Bulla, the notation $\bar{\Delta}(z)$ will be used instead of $\Delta(z)$ ($\tilde{\Delta}(z)$) for a single impurity problem (effective DMFT site). Since $\Gamma(\omega)$ can be interpreted as energy dependent single orbital decay rate in the absence of any Coulomb interaction, we used the letter Γ in this lecture while Bulla denotes the same quantity as $\Delta(\omega)$. In the literature, both notations are found for the same quantity.

For single band lattice models such as the PAM, Eq. (50), or the Hubbard model

$$H = \sum_{i\sigma} \varepsilon_i^d c_{i\sigma}^\dagger c_{i\sigma} - \sum_{ij} t_{ij}(c_{i\sigma}^\dagger c_{j\sigma} + c_{j\sigma}^\dagger c_{i\sigma}) + U n_{i\uparrow}n_{i\downarrow} \tag{52}$$

the effective site is given by Eq. (17) and can be easily extended to multi-orbital models [27] required for realistic transition metal compounds with partially filled $3d$-shells. In the latter case, Eq. (51) acquires a matrix form and the multi-orbital SIAM introduced in Sec. (1.2) is used to describe the effective site.

The self-consistent solution is obtained iteratively: after an initial guess of $\Delta(z)$, the dynamics of effective SIAM is calculated. Then its local self-energy $\Sigma(z)$ is used to obtain $G_{\rm lat}(z)$ via Eq. (51). Equating it with $G_{\rm loc}(z)$ yields a new $\tilde{\Delta}'(z)$ for the next step of the iteration. Usually convergence can be achieved in 10-20 iterations.

3.3 Impurity solver

It turns out that the k-summation in Eq. (51) is the computationally least expensive part of the DMFT iteration, even for multi-orbital problems. The calculation of local self-energy of a

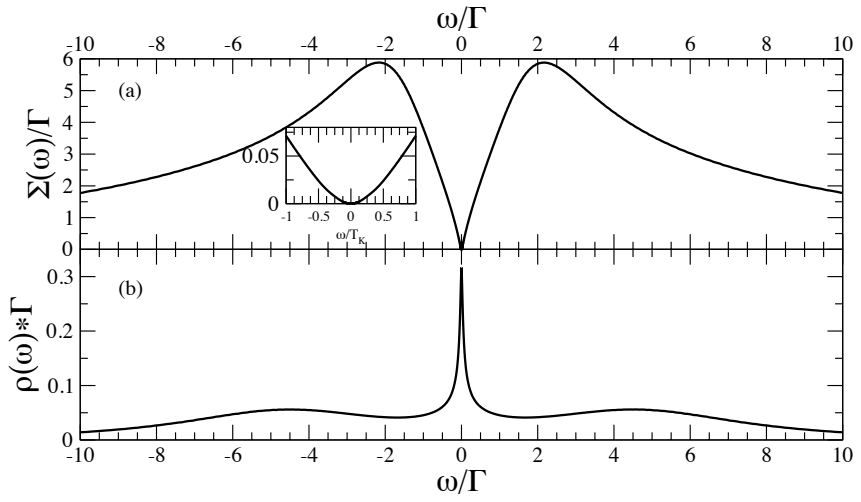

Fig. 4: *(a) Impurity self-energy $\Sigma(\omega)$ and (b) spectral function for a symmetric single orbital Anderson impurity model with $\varepsilon^d = -5\Gamma, U = 10\Gamma$ and a symmetric featureless band of width $D = 30\Gamma$ calculated using the NRG [40] for $T = 0$. $T_K = 0.021\Gamma$. The inset in (a) shows the behavior of $\Sigma(\omega)$ for $|\omega/T_K| < 1$.*

single or multi-orbital SIAM remains the major challenge since the Kondo problem lies at the heart of these quantum impurity problems.

In the 1970s, it was shown that equation-of-motion techniques fail to describe the Kondo physics of the Anderson model. The perturbation expansion in U [34] was successful in accounting for the local Fermi liquid properties which develop adiabatically from the solution of the resonant level model. However, such conserving approximations [35,36] are not able to generate the correct energy scale T_K which is exponentially dependent on U; they remain restricted to the weakly correlated regime $U/(\pi\Gamma) \leq 1$. In the early 1980s, the non-crossing approximation [37–39] was developed. It starts out from the atomic limit and includes the local Coulomb interaction exactly. The hybridization is then considered as small compared to other energy scales, so it only included in the leading-order diagrams. Although this approach contains the correct energy scale up to some small correction, it remains essentially a high-temperature expansion, since the local Fermi-liquid is not described correctly. Friedel's sum rule is violated and the extracted $\Im m\Sigma(\omega - i\delta)$ becomes negative at low temperatures $T \ll T_K$. Only for the two-channel Anderson model, this approach yields remarkably good results [21, 19] such as the correct power law of the self-energy.

Huge progress was made with the advent of quantum Monte Carlo algorithms [41] which yield, at least in principle, the correct dynamics. In practice, such approaches have two drawbacks: (i) they rely on a Trotter decomposition which limits the lowest accessible temperature. For typical parameters in high-temperature superconductors, this would often correspond to 500-1000K. (ii) The results are obtained on the imaginary time axis leaving an ill-defined problem of reconstructing the spectral function [42].

Nevertheless, new QMC approaches, based the expansion of the partition function Z rather

than on a Trotter decomposition, the so-called continuous-time QMC algorithms (CT-QMC) boosted the applicability range considerably and became standard within a few years (for a detailed comprehensive review see [43] and P. Werner's lecture in Ref. [27]). In the CT-QMC, the partition function Z is either expanded in the Coulomb-interaction, called the weak-coupling CT-QMC, or, similarly to the NCA, in the hybridization, called the strong-coupling CT-QMC. One of the big advantages of those solvers are that they scale very well with the number of the local orbitals. However, the sign problem of the fermionic determinants often restricts the applicability of QMC solvers to density-density type inter-orbital interactions, which breaks rotational invariance in spin-space.

Wilson's NRG has also been successfully employed as an impurity solver. While this approach includes the correct solution of any Kondo problem, the numerical effort scales exponentially with the number of conduction bands, which essentially limits the approach to two-band models, far from the five-band multi-orbitial models required, e.g., for FeAs based superconductors. A typical result for the dynamical properties of the single-orbital symmetric SIAM obtained using the NRG is shown in Fig. 4. The spectral function exhibits reminiscences of the two charge excitation peaks at $\omega \approx \varepsilon^d$ and ε^d+U each carrying half of the spectral weight and are broadened by $2\Gamma(0)$. Clearly visible is a narrow peak called Kondo or Abrikosov-Suhl resonance.

The peak height is pinned to approximately $1/(\pi\Gamma(0))$ due to the Friedel sum rule [44]. We have discussed already that the strong-coupling fixed-point is a Fermi-liquid, since asymptotically the electron-electron scattering is freezing out for $|\omega| \to 0$. As a consequence, the imaginary self-energy shows a quadratic behavior $\Im m\Sigma(\omega - i\delta) \propto (\omega/T_K)^2$ for frequencies $(\omega/T_K)^2 \ll 1$ which is depicted in the inset of Fig. 4(a). Recovering a local Fermi-liquid on exponentially small energy scales $T_K \propto \exp(-1/\rho J_{\text{eff}})$ with a pinned resonance close to $\omega = 0$ in accordance with the Friedel sum rule remains the biggest challenge for any impurity solver. This low energy spectral behavior converts immediately into the quasi-particle band formation in the DMFT as can be seen from the analytic form of the lattice Green function $G_{\vec{k}}(z) = [z - \varepsilon_{\vec{k}} - \Sigma(z)]^{-1}$. For a true lattice solution, the full energy dependence of the self-consistently obtained hybridization function $\Gamma(\omega)$ plays a crucial role. This is neglected in Fig. 4 as it is beyond the scope of this lecture.

4 Kondo effect in nano-devices

In this section, a brief introduction to the Kondo-effect in nano-devices such as single-electron transistors (SET) is given. In the 1980s huge progress has been made in structuring semiconductors which opened new possibilities for designing nano-devices using semiconductor hetero-junctions. In 1998, David Goldhaber-Gordon demonstrate in a seminal paper [45] that the Kondo effect can also be observed in single-electron transistors [46]. We illustrate the connection to the Anderson model and also discuss how in larger quantum boxes a two-channel charge Kondo effect has been predicted by Matveev [47]. Combining a single-electron transistor with a quantum box might yield the first physical realization of a two-channel Kondo model [48].

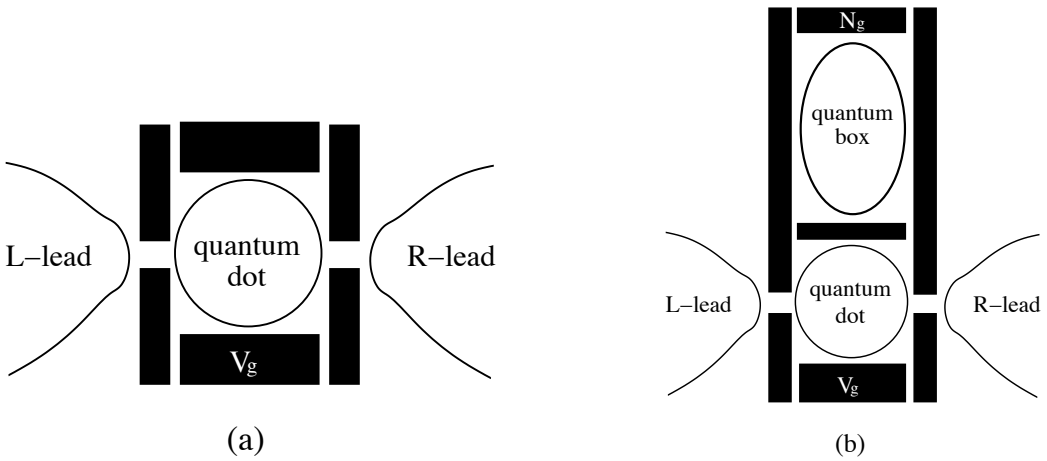

Fig. 5: *(a) Schematic picture of a quantum dot which is weakly coupled to two leads. The filling of the confined region can be controlled by the gate voltage V_g. (b) Schematic picture of a quantum dot coupled to a larger quantum box and to two leads. The filling in the quantum box is controlled by N_g, the filling in the quantum dot is controlled by the gate voltage V_g.*

4.1 Kondo effect in single-electron transistors

A typical realization of a single-electron transistor is schematically depicted in Fig. 5(a). It consists of negatively charged gates which are added on top of an insulating layer covering a GaAs hetero-junction. Those gates partition the underlying 2D electron gas and confine some of the electron gas in smaller areas, forming the quantum dot. These confinement regions have a diameter of $d = 10 - 100$ nm, and their filling is controlled by a gate voltage. The tunneling matrix elements between the leads can be individually tuned by a set of gates. Nowadays, molecules and carbon nano-tubes are also used to form SETs, giving additional complexity due to their internal degrees of freedom. The single-particle levels in the confined area are discrete and randomly distributed. They can be characterized by a finite average level-spacing $\Delta\varepsilon$. The leading contribution from the Coulomb interaction is given by the classical charging energy of a capacitor $E_{\rm charge} = (\hat{Q} - eN_g)^2/(2C) = (e^2/2C)(\hat{N} - N_g)^2$, where $\hat{Q} = e\hat{N}$ is the charge operator of the quantum dot, C its classical capacitance, and $N_g \propto V_g$ controls the filling.Then, the so-called constant interaction model for a quantum dot reads

$$H_{\rm dot} = \sum_i \varepsilon_i \hat{n}_i + \frac{1}{2} E_c (\hat{N} - N_g)^2 \,, \tag{53}$$

where n_i is the number operator of the i^{th} level with energy ε_i and the Coulomb interaction enters only via the charging energy $E_c = e^2/C$, ignoring the details of the individual single-electron wave functions.

At high temperatures $\langle \hat{Q} \rangle \propto V_g$, and we recover the classical limit. At low temperatures, $\beta E_c \gg 1$, the quantization of the charge becomes relevant. The transport through the quantum dot can only occur by single-electron hopping processes, from which the name single-electron transistor [46] was coined. At low temperatures, current-transport only occurs when the gate

voltage V_g is tuned such that the charging energy $E_{\rm charge}$ become energetically degenerate for states with N and $N+1$ electrons.
The coupling to the leads generates the additional energy scale $\Gamma = \pi \sum_\alpha \rho_\alpha(0) t_\alpha^2$, the charge fluctuation scale. t_α is the tunneling matrix element between the dot and the lead α. We can distinguish two different regimes: (i) the level spacing is large compared to the charge fluctuation scale, i. e. $\Delta\varepsilon > \Gamma$, or (ii) $\Delta\varepsilon \ll \Gamma$ which will be discussed in Sec. 4.2.
In the first case, all levels up to some level $\varepsilon_i < \varepsilon_l$ are filled and all levels $\varepsilon_i > \varepsilon_l$ are empty. The charge fluctuations just involve the spin-degenerate level $i = l$, and the Hamiltonian is identical to (14) after identifying $U = E_c$ and $\varepsilon^d = \varepsilon_l + (N_0 - N_g + \frac{1}{2})E_c$, where N_0 counts the number of occupied levels $\varepsilon_i < \varepsilon_l$. The single particle level ε^d is tuned by the external gate voltage $V_g \propto N_g$; the tunneling matrix elements take the role of the hybridization in the SIAM. In equilibrium, one can define a linear combination of both lead electrons

$$f_{0\sigma} = \frac{1}{\sqrt{t_L^2 + t_R^2}} \sum_\alpha t_\alpha c_{0\alpha\sigma} \tag{54}$$

which couples to the quantum-dot level,

$$H_T = t_0 \sum_\sigma (d_\sigma^\dagger f_{0\sigma} + f_{0\sigma}^\dagger d_\sigma) \tag{55}$$

while the orthogonal linear combination can be eliminated; $t_0 = \sqrt{t_L^2 + t_R^2}$. Hence the local dynamics is complete determined by the solution of the SIAM which contains the Kondo effect. Meir and Wingreen have shown [49] that the transmission matrix $T(z)$ governing the current transport through such a quantum dot is proportional to the local Green function of the dot, $T(z) \propto G_{\rm loc}(z)$. At high temperatures, the transport is favored when $\varepsilon^d \approx 0$ or $\varepsilon^d + U \approx 0$. At low temperatures and $n_l \approx 1$, the Kondo effect yields a pinned maximum of the spectral function which opens up a new correlation induced transport channel: the conductance increases in the Coulomb blockade valley when lowering the temperature, which is one of the hallmarks of the Kondo-effect in SETs.
Although, this connection had been understood quite early on, the mesoscopic community believed for a long time that the exponentially smallness of the Kondo scale prevents this effect from being observed. Realizing that the Kondo resonance is adiabatically connected to the resonant-level model, David Goldhaber-Gordon was the first to see that the Kondo temperature in nano-devices can be pushed into a reasonable regime by increasing the tunneling matrix elements t_α. In a seminal paper [45], he proved the existence of the Kondo effect in a quantum dot, stimulating a huge amount of research in Kondo-related physics in nano-devices.

4.2 Charge Kondo effect

Now we discuss the opposite limit of very small level spacings, i. e. $\Delta\varepsilon \ll \Gamma$. In this regime, the levels on the quantum dot are treated as continuum, and the single-particle dynamics is modeled by two electron gases, indexed by $\alpha = L(D)$ for the single lead (states on the dot)

$$H = \sum_{k\alpha\sigma} \varepsilon_{k\alpha\sigma} c_{k\alpha\sigma}^\dagger c_{k\alpha\sigma} + \frac{t}{N} \sum_{k,q} (c_{kL\sigma}^\dagger c_{kD\sigma} + c_{kD\sigma}^\dagger c_{kL\sigma}) + E_{\rm charge} \tag{56}$$

which are coupled by a tunneling matrix element t. To distinguish this limit from the SET, this type of quantum dot is called a quantum box since the small level spacing occurs only in devices with much larger diameters. The filling of the dot remains controlled by the charging energy $E_{\rm charge}$. A fixed dot filling and, therefore, a fixed $E_{\rm charge}$ still enables many different configurations which share approximately the same kinetic energy. Therefore, a mapping of the electronic occupation number operator to a new charge operator $\hat{N}_c = \sum_n n|n\rangle\langle n|$ has been introduced [50]. This new operator acts on a fictitious space of charge degrees of freedom, and the mapped charging energy is given by $E_{\rm charge} = 1/2E_c(\hat{N}_c - N_g)^2$. Since the number of electrons in the quantum box can only change by the tunneling term, the latter requires a modification

$$H_T = \frac{t}{N}\sum_{k,q}(c^\dagger_{kL\sigma}c_{kD\sigma} + c^\dagger_{kD\sigma}c_{kL\sigma}) \quad \rightarrow \quad \frac{t}{N}\sum_{k,q}(c^\dagger_{kL\sigma}c_{kD\sigma}N_c^- + N_c^+c^\dagger_{kD\sigma}c_{kL\sigma})\,, \quad (57)$$

where N_c^+ is the charge raising operator $\hat{N}_c^+ = \sum_n |n+1\rangle\langle n|$ and $\hat{N}_c^-$ its adjoint operator. Assigning the lead flavor up, the box flavor down, on can show that H conserves flavor, since it commutes with the flavor operator

$$\hat{N}_f \;=\; \frac{1}{2}(\hat{N}_L - \hat{N}_D) + \hat{N}_c \quad (58)$$

where $\hat{N}_\alpha = \sum_{k\sigma} n_{k\alpha\sigma}$ account for the total number of fermions in the lead or the box.

Due to the quantization of the charge, $E_{\rm charge}$ can only take discrete values on a parabola with its minimum at N_g. The two lowest charge states become energetically degenerate at half-integer values of N_g. Therefore, charge fluctuations are restricted to $N, N+1$ close to $N_g = N+1/2+\Delta n_g$ and $\beta E_c \gg 1$. With this restriction, the charging energy $E_{\rm charge} = \frac{E_c}{2}(\frac{1}{4} - \Delta n_g\sigma_z + \Delta n_g^2)$ is converted to a Zeeman term $-E_c/2\Delta n_g\sigma_z$, since Δn_g acts as a magnetic field in the iso-spin space of the two charge states $N, N+1$ [51]. The tunneling term H_T translates to a transversal Kondo interaction for the charge iso-spin and the physical spin, being a conserved number, converts into the conserved channel of the two-channel Kondo Hamiltonian. The effective capacitance $C(N_g,T) = -\partial\langle e\hat{N}\rangle/\partial N_g$ diverges logarithmically at $N_g = N+1/2$ for $T \rightarrow 0$ where the prefactor $C(N_g,T) \propto -1/(T_K)\log(T/T_K)$ is governed by the two-channel Kondo scale T_K. In turned out that the NRG is the optimal tool to investigate the crossover from the classical high temperature regime to the two-channel Kondo model [52].

By coupling an additional small quantum dot to the larger quantum box as depicted in Fig. 5(b), the charging energy of the quantum box can generate a dynamical channel conservation. It has been conjectured [48] that this might be the way to experimentally realize a spin two-channel Kondo model. Interestingly, it turned out that the two-channel charge Kondo effect discussed above and the spin Kondo effect are adiabatically connected in such a complex nano-device by the two gate voltages controlling the filling in the quantum dot and the quantum box.

5 Conclusion

In this lecture, we have presented a chronological introduction to the Kondo problem. We have started with Kondo's explanation of the resistance minimum in metals weakly doped with magnetic scatterers. In the late 1960s, it was shown that Kondo's model is related to a much more general class of models, the Anderson models: Removing charge fluctuations on partially filled $3d$ and $4f$-shells, effective Kondo models can be derived using the Schrieffer-Wolff transformation.

Major progress toward a deeper understanding of the Kondo problem and its inaccessibility to perturbative approaches was made in the 1970s. In Sec. 2.1, we derived Anderson's poor man's scaling using a perturbative renormalization group approach. The first accurate solution of the problem was given by Ken Wilson in 1975 [14]. He applied his newly developed numerical renormalization group approach which elegantly circumvents the weaknesses of the perturbative treatment by using a discretized many-body Fock space. In this discrete basis, any arbitrarily complex Hamiltonian is simply defined by its matrix elements while perturbative RG approaches rely on an a-priori known low-energy field theory. We also included a discussion of exotic Kondo effects in metals where the local spin is over- or under-compensated by the coupling to conduction electron channels.

In the 1980s and 1990s, it was realized that correlated electron systems such as Heavy Fermions, High-T_c superconductors, or Mott-Hubbard are connected to the Kondo problem. In Sec. 3, we briefly introduced the dynamical mean field theory. Within DMFT, the lattice self-energy is approximated by a $\vec{k}$-independent function. Then, the complex lattice problem is mapped onto an effective impurity problem which is supplemented by the lattice self-consistency condition. This effective impurity comprises of the unit cell which is embedded in a fictitious bath of non-interaction conduction electron. Again, at the heart of its solution lies the Kondo problem: the calculation of the local self-energy requires an adequate impurity solver which remains valid for all temperature and parameter regimes of interest.

Sec. 4 has been devoted to a brief introduction of the Kondo-effect in nano-devices. We have covered two extreme limits of nano-structured quantum dots: small dots with large level spacing are used as single electron transistors. At odd fillings, the Kondo effect opens up a new transport channel which lifts the Coulomb blockade. In large dots, the level spacing is treated as continuous: the low energy physics should be governed by a two-channel Kondo model [19, 47, 48].

Acknowlegment

This work was supported by the German-Israeli Foundation through Grant No. 1035-36.14, and by the Deutsche Forschungsgemeinschaft through AN 275/6-2, 275/7-1.

References

[1] J. Kondo, Prog. Theor. Phys **32**, 37 (1964)

[2] J. Kondo, J. Phys. Soc. Jpn. **74**, 1 (2005)

[3] W. de Haas, J. de Boer, and G. van den Berg, Physica **1**, 1115 (1934)

[4] A.C. Hewson, *The Kondo Problem to Heavy Fermions* (Cambridge University Press, 1993)

[5] P.W. Anderson, Phys. Rev. **124**, 41 (1961)

[6] D.C. Langreth, Phys. Rev. **150**, 516 (1966)

[7] G. Mahan, *Many-Particle Physics* (Plenum Press, New York, 1981)

[8] J.M. Luttinger and J.C. Ward, Phys. Rev. **118**, 1417 (1960)

[9] J.R. Schrieffer and P.A. Wolff, Phys. Rev. **149**, 491 (1966)

[10] H.R. Krishna-murthy, J.W. Wilkins, and K.G. Wilson, Phys. Rev. B **21**, 1003 (1980)

[11] H.R. Krishna-murthy, J.W. Wilkins, and K.G. Wilson, Phys. Rev. B **21**, 1044 (1980)

[12] P.W. Anderson, J. Phys. C **3**, 2436 (1970)

[13] J.W. Allan and B. Mitrovic, Solid State Phys. **37**, 1 (1982), for a review on Eliashberg theory

[14] K.G. Wilson, Rev. Mod. Phys. **47**, 773 (1975)

[15] R. Bulla, T.A. Costi, and T. Pruschke, Rev. Mod. Phys. **80**, 395 (2008)

[16] N. Andrei, K. Furuya, and J.H. Lowenstein, Rev. Mod. Phys. **55**, 331 (1983)

[17] R. Bulla, N. Tong, and M. Vojta, Phys. Rev. Lett. **91**, 170601 (2003)

[18] L.H. Yu *et al.*, Phys. Rev. Lett. **95**, 256803 (2005)

[19] D.L. Cox and A. Zawadowski, Advances in Physics **47**, 599 (1998), for a review on the multi-channel models

[20] V.J. Emery and S. Kivelson, Phys. Rev. B **46**, 10812 (1992)

[21] D.L. Cox, Phys. Rev. Lett. **59**, 1240 (1987)

[22] C.J. Bolech and N. Andrei, Phys. Rev. Lett. **88**, 237206 (2002)

[23] F.B. Anders, Phys. Rev. B **71**, 121101 (2005)

[24] N. Grewe and F. Steglich, in *Handbook on the Physics and Chemistry of Rare Earths*, edited by K. A. Gschneidner, Jr. and L. Eyring (North-Holland, Amsterdam, 1991), Vol. 14, p. 343

[25] N. Grewe, Solid State Communications **50**, 19 (1984)

[26] Y. Kuramoto, in *Theory of Heavy Fermions and Valence Fluctuations*, edited by T. Kasuya and T. Saso (Springer, Berlin, 1985), p. 152

[27] E. Pavarini, E. Koch, D. Vollhardt, and A.I. Lichtenstein (eds.)
The LDA+DMFT approach to strongly correlated materials,
Reihe Modeling and Simulation, Vol. 1 (Forschungszentrum Jülich, 2011)
`http://www.cond-mat.de/events/correl11`

[28] N. Grewe, Z. Phys. B **67**, 323 (1987)

[29] W. Metzner and D. Vollhardt, Phys. Rev. Lett. **62**, 324 (1989)

[30] E. Müller-Hartmann, Z. Phys. B **76**, 211 (1989)

[31] U. Brandt and C. Mielsch, Z. Phys. B **75**, 365 (1989)

[32] A. Georges, G. Kotliar, W. Krauth, and M.J. Rozenberg, Rev. Mod. Phys. **68**, 13 (1996), for a review on the DMFT

[33] G. Kotliar and D. Vollhardt, Physics Today **57**, 53 (2204)

[34] K. Yamada, Prog. Theor. Phys. **54**, 316 (1975)

[35] C.D. Spataru, M.S. Hybertsen, S.G. Louie, and A.J. Millis,
Phys. Rev. B **79**, 155110 (2009)

[36] S. Schmitt and F.B. Anders, Phys. Rev. B **81**, 165106 (2010)

[37] N. Grewe, Z. Phys. B **52**, 193 (1983)

[38] Y. Kuramoto, Z. Phys. B **53**, 37 (1983)

[39] N.E. Bickers, Rev. Mod. Phys. **59**, 845 (1987)

[40] R. Peters, T. Pruschke, and F.B. Anders, Phys. Rev. B **74**, 245114 (2006)

[41] J.E. Hirsch and R.M. Fye, Phys. Rev. Lett. **56**, 2521 (1986)

[42] M. Jarrell and J.E. Gubernatis, Phys. Rep. **269**, 133 (1996),
for a review on the Maximum Entropy method

[43] E. Gull *et al.*, Rev. Mod. Phys. **83**, 349 (2011)

[44] F.B. Anders, N. Grewe, and A. Lorek, Z. Phys. B Condensed Matter **83**, 75 (1991)

[45] D. Goldhaber-Gordon *et al.*, Nature **391**, 156 (1998)

[46] M.A. Kastner, Rev. Mod. Phys. **64**, 849 (1992)

[47] K.A. Matveev, Zh. Eksp. Teor. Fiz. **99**, 1598 (1991)

[48] R.M. Potok *et al.*, Nature **446**, 167 (2007)

[49] Y. Meir and N.S. Wingreen, Phys. Rev. Lett. **68**, 2512 (1992)

[50] J. König and H. Schoeller, Phys. Rev. Lett. **81**, 3511 (1998)

[51] K.A. Matveev, Sov. Phys. JETP **72**, 892 (1991)

[52] E. Lebanon, A. Schiller, and F.B. Anders, Phys. Rev. B **68**, 041311(R) (2003)

12 The Numerical Renormalization Group

Ralf Bulla
Institut für Theoretische Physik
Universität zu Köln

Contents

E. Pavarini, E. Koch, F. Anders, and M. Jarrell
Correlated Electrons: From Models to Materials
Modeling and Simulation Vol. 2
Forschungszentrum Jülich, 2012, ISBN 978-3-89336-796-2
http://www.cond-mat.de/events/correl12

1 Introduction

In the preceding lecture notes by F. Anders you find an introduction to the Kondo effect and quantum impurity systems in general, along with the quantum mechanical models which are supposed to explain the phenomena observed in these systems. Some intuition is required to formulate these models, but the phenomena cannot be read off by just looking at the model Hamiltonian. To actually see the screening of the impurity magnetic moment below the Kondo temperature $T_{\rm K}$ we need (more or less) sophisticated techniques, and in the context of quantum impurity systems it is the Numerical Renormalization Group method (NRG, developed by K.G. Wilson in the early 1970's [1]) which helped a lot in understanding the Kondo and related effects.[1]

The NRG method is special compared to other methods (such as Quantum Monte Carlo) as it is designed exclusively for quantum impurity systems, with a small impurity – an object with a small number of degrees of freedom with arbitrary interactions – coupled to a non-interacting bath – usually a free conduction band, that is non-interacting fermions. Nevertheless, there is an enormous range of physical phenomena which can be realized in such systems, and to which the NRG has been applied. For an overview, see the review Ref. [4] and the hints for further reading in the final section.

In these lecture notes, we will purely focus on the single-impurity Anderson model, to be introduced in Sec. 2, for which all the technicalities of the NRG can be explained without the complications of multi-impurity or multi-channel systems. The single-impurity Anderson model has also been used as a prototype model in Sec. II of the NRG-review [4], and I will use basically the same notation here in the lecture notes.

Any introduction to the NRG method will go through the basic steps of logarithmic discretization, mapping onto a semi-infinite chain, iterative diagonalization and so on, and, of course, you will find precisely this structure in Sec. 2 (Figure 1 illustrates the initial steps of the NRG procedure). These technical steps can be understood with a background in quantum mechanics, in particular some experience in working with creation and annihilation operators for fermions ($c^\dagger_{i\sigma}/c_{i\sigma}$, see below), but even if each single step is clear, beginners in the field very often find it difficult to see the overall picture. I will try to convince the reader that there is indeed a general strategy behind the NRG approach, and that each individual step has its purpose.

There is one issue which very often leads to confusion: that is the role of geometry and the dimension of the bath in which the impurity is embedded. One frequently encounters correlated electron systems in which the dimension is crucial for the physical properties, but for quantum impurity systems you can find remarks in the literature saying that the impurity couples to a single channel only, so it is effectively a one-dimensional problem, possibly like the semi-infinite chain as depicted in Fig. 1c. So if the dimension does not play a role at all, you might want to define the model directly on a semi-infinite chain – I hope these lecture notes will help to clarify this issue.

[1] Of course, the NRG is not the only method which can be successfully applied to quantum impurity systems; for an overview see the lecture notes from last year's autumn school [2] and A.C. Hewson's book [3]

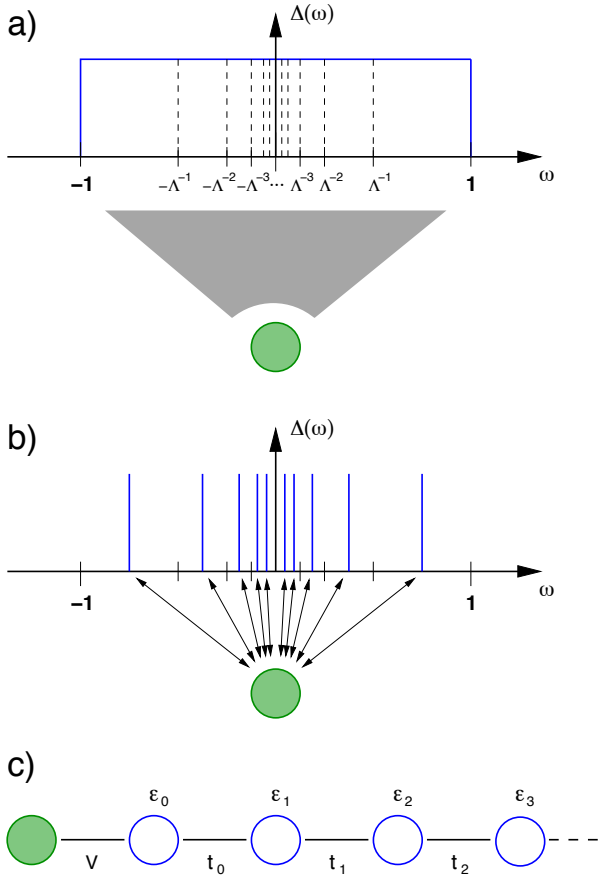

Fig. 1: *Initial steps of the NRG illustrated for the single-impurity Anderson model in which an impurity (filled circle) couples to a continuous conduction band via the hybridization function $\Delta(\omega)$; a) a logarithmic set of intervals is introduced through the NRG discretization parameter Λ; b) the continuous spectrum within each of these intervals is approximated by a single state; c) the resulting discretized model is mapped onto a semi-infinite chain where the impurity couples to the first conduction electron site via the hybridization V; the parameters of the tight-binding model (see Eq. (38)) are ε_n and t_n. Figure taken from Ref. [4].*

2 The single-impurity Anderson model

The Hamiltonian of a general quantum impurity model consists of three parts, the impurity $H_{\rm imp}$, the bath $H_{\rm bath}$, and the coupling between impurity and bath, $H_{\rm imp-bath}$:

$$H = H_{\rm imp} + H_{\rm bath} + H_{\rm imp-bath} \,. \tag{1}$$

In the single-impurity Anderson model (siAm, Ref. [5]), the impurity consists of a single level with energy $\varepsilon_{\rm f}$. The Coulomb repulsion between two electrons occupying this level (which then must have opposite spin, $\sigma = \uparrow$ and $\sigma = \downarrow$) is given by U. All the Hamiltonians appearing in these lecture notes are most conveniently written in second quantization, so we have

$$H_{\rm imp} = \sum_\sigma \varepsilon_{\rm f} f_\sigma^\dagger f_\sigma + U f_\uparrow^\dagger f_\uparrow f_\downarrow^\dagger f_\downarrow \,, \tag{2}$$

with $f_\sigma^{(\dagger)}$ annihilation (creation) operators for a fermion with spin σ on the impurity level.

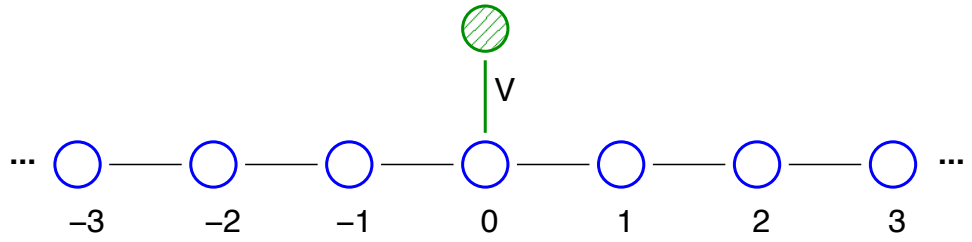

Fig. 2: *One possible realization of the single-impurity Anderson model in which the impurity couples to one site (site '0') of a one-dimensional tight-binding chain.*

Let us start with a specific geometry of the bath, that is a one-dimensional chain as shown in Fig. 2, with hopping between nearest neighbours (matrix element t_l) and on-site energies ε_l, so we have

$$H_{\rm bath} = \sum_\sigma \sum_{l=-\infty}^{\infty} \varepsilon_l \, c^\dagger_{l\sigma} c_{l\sigma} + \sum_\sigma \sum_{l=-\infty}^{\infty} t_l \left(c^\dagger_{l\sigma} c_{l+1\sigma} + c^\dagger_{l+1\sigma} c_{l\sigma} \right) \; . \tag{3}$$

The operators for the states at site l of the chain are denoted as $c^{(\dagger)}_{l\sigma}$. Note that there is no interaction term between the band states, which is first of all an assumption, but is actually necessary to perform the transformations to be described below.
As indicated in Fig. 2, the impurity only couples to the bath state at site $l = 0$, and in the siAm the form of this coupling is given by

$$H_{\rm imp-bath} = V \sum_\sigma \left(f^\dagger_\sigma c_{0\sigma} + c^\dagger_{0\sigma} f_\sigma \right) \; , \tag{4}$$

corresponding to a hybridization of the respective states, with V the hybridization strength.
One might want to set the parameters ε_l and t_l in Eq. (3) to a constant value, which simplifies the calculation, but in general, ε_l and t_l can be site-dependent and, for example, describe a one-dimensional disordered system.
Let us now generalize the model to an arbitrary non-interacting bath. The operators $H_{\rm imp}$ and $H_{\rm imp-bath}$ are still given by eqs. (2) and (4), respectively, and $H_{\rm bath}$ now has the form

$$H_{\rm bath} = \sum_\sigma \sum_l \varepsilon_l c^\dagger_{l\sigma} c_{l\sigma} + \sum_\sigma \sum_{ij} t_{ij} \left(c^\dagger_{i\sigma} c_{j\sigma} + c^\dagger_{j\sigma} c_{i\sigma} \right) \; . \tag{5}$$

For later use we write $H_{\rm bath}$ in the form

$$H_{\rm bath} = \sum_\sigma \vec{c^\dagger_\sigma} \, T \, \vec{c_\sigma} \; , \tag{6}$$

with

$$\vec{c^\dagger_\sigma} = \left(\ldots, c^\dagger_{-1\sigma}, c^\dagger_{0\sigma}, c^\dagger_{1\sigma}, \ldots \right) \; , \tag{7}$$

and the matrix elements of T built up by the ε_l and t_{ij} in Eq. (5).
The site index of the operators $c^{(\dagger)}_{l\sigma}$ now runs over all sites of an arbitrary geometry, for example, the two-dimensional lattice as shown in Fig. 3, and t_{ij} is the hopping between any pair (i, j) of

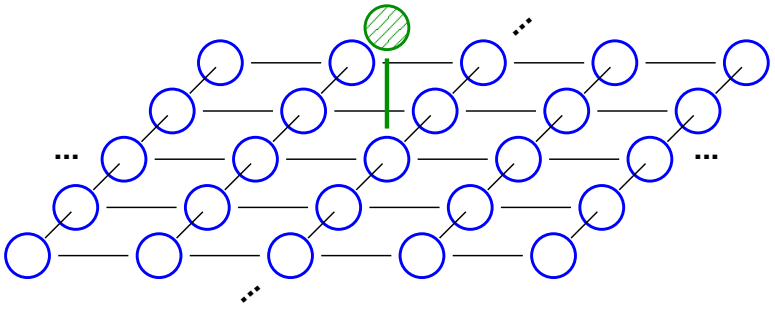

Fig. 3: *In this geometry, the impurity couples to one site of a two-dimensional lattice of conduction electrons.*

the bath states. The bath might have a complicated structure, but as it is non-interacting, it can always be written in a diagonal form:

$$H_{\rm bath} = \sum_{\sigma k} \varepsilon_k b^\dagger_{k\sigma} b_{k\sigma} \ , \tag{8}$$

with the operators $c^{(\dagger)}_{i\sigma}$ and $b^{(\dagger)}_{k\sigma}$ related via a unitary transformation

$$c_{i\sigma} = \sum_k a_{ik} b_{k\sigma} \ \ , \ \ c^\dagger_{i\sigma} = \sum_k a^*_{ik} b^\dagger_{k\sigma} \ . \tag{9}$$

The a_{ik} are the matrix elements of the unitary matrix A which diagonalizes the matrix T as defined above

$$\left(A^t T A\right)_{kq} = \varepsilon_k \delta_{kq} \ . \tag{10}$$

The actual diagonalization of the matrix T is, of course, limited by the size of the matrices which can be handled by the computer, but for now it is sufficient to assume that the diagonalization can de done in principle.

Inserting Eq. (9) for $i = 0$ into $H_{\rm imp-bath}$ from Eq. (4) gives the following form for the hybridization term

$$H_{\rm imp-bath} = \sum_{k\sigma} V_k \left(f^\dagger_\sigma b_{k\sigma} + b^\dagger_{k\sigma} f_\sigma \right) \ , \tag{11}$$

with $V_k = V a_{0k}$. Let us denote the Hamiltonian written with the operators $b^{(\dagger)}_{k\sigma}$, that is $H_{\rm imp}$ together with $H_{\rm bath}$ Eq. (8) and $H_{\rm imp-bath}$ Eq. (11), as the k-representation of the siAm, in contrast to the site-representation, eqs. (4,5).

We can now easily calculate the form of the hybridization function using equations of motion. This is described in detail in Ref. [6] and shall not be repeated here. The essential point is that the one-particle Green function $G_\sigma(z) = \langle\langle f_\sigma, f^\dagger_\sigma \rangle\rangle_z$ can be written in the form

$$G_\sigma(z) = \frac{1}{z - \varepsilon_f - \bar{\Delta}(z) - \Sigma^U(z)} \ \ , \ \ (z = \omega + i\delta) \ , \tag{12}$$

with $\Sigma^U(z)$ the correlation part of the one-particle self energy and the hybridization function

$$\bar{\Delta}(z) = \sum_k V_k^2 \frac{1}{z - \varepsilon_k} \ . \tag{13}$$

Usually it is the imaginary part of this quantity which is referred to as the hybridization function:

$$\Delta(\omega) = -\lim_{\delta\to 0} \mathrm{Im}\left[\bar{\Delta}(z=\omega+i\delta)\right] = \pi \sum_k V_k^2 \delta(\omega-\varepsilon_k) \;, \tag{14}$$

with the second equality following from Eq. (13). In any case, it is this single frequency dependent quantity in which all the details of the bath are encoded, or, in other words, all that the impurity sees from the bath is the hybridization function $\Delta(\omega)$. This can also be shown more formally by starting from the functional integral for the k-representation of the siAm, and by integrating out the conduction electron degrees of freedom (this can be done analytically, since the conduction electrons are non-interacting). The effective action for the impurity degree of freedom then contains the $\Delta(\omega)$ as the only remnant of the bath.

We are now able – at least in principle – to calculate the hybridization function for any given geometry, but can this be reversed? Is it possible to deduce the precise form of the siAm in the site representation, that is all the ε_l and t_{ij} in Eq. (5) purely from the form of $\Delta(\omega)$? This is, in fact, not the case, and to see this let us have a look at the siAm defined for a semi-infinite chain as shown in Fig. 4, with

$$H_{\mathrm{bath}} = \sum_\sigma \sum_{l=0}^{\infty} \varepsilon_l \, c^\dagger_{l\sigma} c_{l\sigma} + \sum_\sigma \sum_{l=0}^{\infty} t_l \left(c^\dagger_{l\sigma} c_{l+1\sigma} + c^\dagger_{l+1\sigma} c_{l\sigma} \right) \;, \tag{15}$$

and $H_{\mathrm{imp-bath}}$ given by Eq. (4).

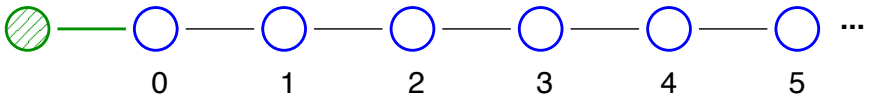

Fig. 4: *In this geometry, the impurity couples to the first site of a semi-infinite chain of conduction electrons.*

There is a straightforward procedure ('continued fraction expansion') to calculate, for a given $\Delta(\omega)$, the set of parameters $\{\varepsilon_l\}$ and $\{t_l\}$ of this semi-infinite chain. This means that we can start, for example, with a two-dimensional model as in Fig. 3, calculate the $\Delta(\omega)$ for this geometry, and then calculate the $\{\varepsilon_l\}$ and $\{t_l\}$ for the semi-infinite chain via a continued fraction expansion. The resulting model looks different, apparently, but for the impurity all that counts is the hybridization function and this is the same for both models. In this sense the siAm is said to be effectively a one-dimensional problem and we can view the chain in Fig. 4 as the single channel the impurity is coupling to.

A side remark: the calculation of $\Delta(\omega)$ for the siAm given in the form of a semi-infinite chain is rather simple, as it can be cast in the form of a continued fraction

$$\Delta(z) = \cfrac{V^2}{z-\varepsilon_0-\cfrac{t_0^2}{z-\varepsilon_1-\cfrac{t_1^2}{z-\varepsilon_2-\cfrac{t_2^2}{z-\varepsilon_3-\ldots}}}} \;. \tag{16}$$

In the site representation, we have so far considered a coupling of the impurity to a single site, as in Figs. 2 and 3. Let us now generalize this to

$$H_{\mathrm{imp-bath}} = \sum_{\sigma m} V_m \left(f_\sigma^\dagger c_{m\sigma} + c_{m\sigma}^\dagger f_\sigma \right) \ , \tag{17}$$

that is a coupling to the sites m with hybridization strength V_m. Figure 5 shows a possible realization.

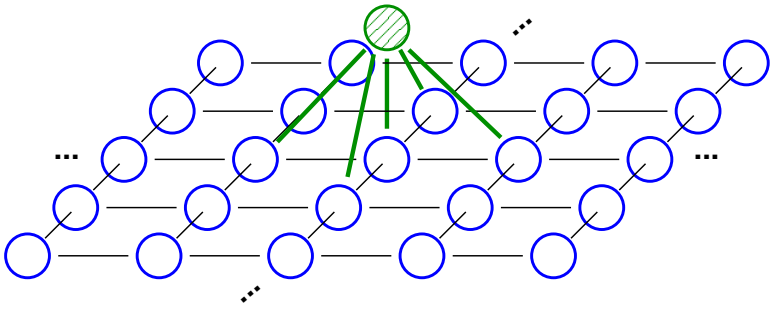

Fig. 5: *In this geometry, the impurity couples to one site plus the four nearest neighbours of this site of a two-dimensional lattice of conduction electrons.*

We can now insert Eq. (9) for $i = m$ into this expression and arrive at the same form of $H_{\mathrm{imp-bath}}$ Eq. (11) as above, with $V_k = \sum_m V_m a_{mk}$. The structure of the Hamiltonian in the k-representation is thus exactly the same as before.

Before we continue, let us summarize what we have learned so far. Whatever the geometry of the siAm, one can always write the model in the k-representation eqs. (8,11) (from which the form of $\Delta(\omega)$ follows directly) or as a semi-infinite chain. The actual calculation of $\Delta(\omega)$ can be done in various ways – in the simplest case H_{bath} is translationally invariant and the diagonalization of H_{bath} can be done via Fourier transformation, but in the general case one cannot avoid diagonalizing large matrices. Leaving aside these technical issues, we have obtained a quantity which completely characterizes the impurity-bath coupling, so the next question is, what $\Delta(\omega)$ can tell us about Kondo physics. The important feature here is the behaviour of $\Delta(\omega)$ for $\omega \to 0$. Standard Kondo physics requires $\Delta(\omega \to 0) \neq 0$, whereas the situation is more complex if $\Delta(\omega) \propto |\omega|^r$ for $\omega \to 0$, with an exponent $r > -1$ (see the discussion in Sec. IV.C.2 of Ref. [4]).

We have now seen various ways to write the siAm, but the actual starting point for the NRG procedure has not been introduced yet. This is the Hamiltonian in the 'integral representation'

$$\begin{aligned} H_{\mathrm{bath}} &= \sum_\sigma \int_{-1}^{1} \mathrm{d}\varepsilon \, g(\varepsilon) a_{\varepsilon\sigma}^\dagger a_{\varepsilon\sigma} \ , \\ H_{\mathrm{imp-bath}} &= \sum_\sigma \int_{-1}^{1} \mathrm{d}\varepsilon \, h(\varepsilon) \Big(f_\sigma^\dagger a_{\varepsilon\sigma} + a_{\varepsilon\sigma}^\dagger f_\sigma \Big). \end{aligned} \tag{18}$$

The conduction band is now assumed to be continuous, with the band operators satisfying the standard fermionic commutation relations: $\left[a_{\varepsilon\sigma}^\dagger, a_{\varepsilon'\sigma'} \right]_+ = \delta(\varepsilon - \varepsilon')\delta_{\sigma\sigma'}$. The dispersion of the

band is given by $g(\varepsilon)$, with the band cutoffs set to -1 and 1 (for simplicity). The hybridization between the impurity and the band states is given by $h(\varepsilon)$.
The calculation of the hybridization function for the model in this form works in the same way as for the k-representation, Eq. (14). The result is

$$\Delta(\omega) = \pi \int_{-1}^{1} \mathrm{d}\varepsilon \, h(\varepsilon)^2 \, \delta(\omega - g(\varepsilon)) = \pi h(g^{-1}(\omega))^2 \frac{\mathrm{d}}{\mathrm{d}\omega} g^{-1}(\omega) \; , \tag{19}$$

with $g^{-1}(\omega)$ the inverse function of $g(\varepsilon)$, that is $g^{-1}(g(\varepsilon)) = \varepsilon$. Now remember that the relevant quantity is the hybridization function $\Delta(\omega)$, given by the specific geometries as discussed above. For a given $\Delta(\omega)$, there are obviously many ways to divide the ω-dependence between $g^{-1}(\omega)$ and $h(g^{-1}(\omega))$, corresponding to different ways of dividing the ε-dependence between $g(\varepsilon)$ and $h(\varepsilon)$. This feature will be useful later.
With the siAm in the integral representation eqs. (18) we can now turn to the NRG treatment of the model.

3 The numerical renormalization group

3.1 Logarithmic discretization

The Hamiltonian in the integral representation Eq. (18) is a convenient starting point for the logarithmic discretization of the conduction band. As shown in Fig. 1a, the parameter $\Lambda > 1$ defines a set of intervals with discretization points

$$x_n = \pm \Lambda^{-n} \; , \quad n = 0, 1, 2, \ldots \; . \tag{20}$$

The width of the intervals is given by

$$d_n = \Lambda^{-n} (1 - \Lambda^{-1}) \; . \tag{21}$$

Within each interval we introduce a complete set of orthonormal functions

$$\psi^{\pm}_{np}(\varepsilon) = \begin{cases} \frac{1}{\sqrt{d_n}} e^{\pm i \omega_n p \varepsilon} & \text{for } x_{n+1} < \pm\varepsilon < x_n \\ 0 & \text{outside this interval .} \end{cases} \tag{22}$$

The index p takes all integer values between $-\infty$ and $+\infty$, and the fundamental frequencies for each interval are given by $\omega_n = 2\pi/d_n$. The next step is to expand the conduction electron operators $a_{\varepsilon\sigma}$ in this basis, i.e.

$$a_{\varepsilon\sigma} = \sum_{np} \left[a_{np\sigma} \psi^{+}_{np}(\varepsilon) + b_{np\sigma} \psi^{-}_{np}(\varepsilon) \right] \; , \tag{23}$$

which corresponds to a Fourier expansion in each of the intervals. The inverse transformation reads

$$\begin{aligned} a_{np\sigma} &= \int_{-1}^{1} \mathrm{d}\varepsilon \left[\psi^{+}_{np}(\varepsilon) \right]^* a_{\varepsilon\sigma} \; , \\ b_{np\sigma} &= \int_{-1}^{1} \mathrm{d}\varepsilon \left[\psi^{-}_{np}(\varepsilon) \right]^* a_{\varepsilon\sigma} \; . \end{aligned} \tag{24}$$

The operators $a^{(\dagger)}_{np\sigma}$ and $b^{(\dagger)}_{np\sigma}$ defined in this way fulfill the usual fermionic commutation relations. The Hamiltonian Eq. (18) is now expressed in terms of these discrete operators.
In particular, the transformed hybridization term (first part only) is

$$\int_{-1}^{1} \mathrm{d}\varepsilon\, h(\varepsilon) f^\dagger_\sigma a_{\varepsilon\sigma} = f^\dagger_\sigma \sum_{np} \left[a_{np\sigma} \int^{+,n} \mathrm{d}\varepsilon\, h(\varepsilon) \psi^+_{np}(\varepsilon) + b_{np\sigma} \int^{-,n} \mathrm{d}\varepsilon\, h(\varepsilon) \psi^-_{np}(\varepsilon) \right], \tag{25}$$

where we have defined

$$\int^{+,n} \mathrm{d}\varepsilon \equiv \int_{x_{n+1}}^{x_n} \mathrm{d}\varepsilon \ , \ \int^{-,n} \mathrm{d}\varepsilon \equiv \int_{-x_n}^{-x_{n+1}} \mathrm{d}\varepsilon \, . \tag{26}$$

For a constant $h(\varepsilon) = h$, the integrals in Eq. (25) filter out the $p = 0$ component only

$$\int^{\pm,n} \mathrm{d}\varepsilon\, h \psi^\pm_{np}(\varepsilon) = \sqrt{d_n} h\, \delta_{p,0} \, . \tag{27}$$

In other words, the impurity couples only to the $p = 0$ components of the conduction band states. It will become clear soon, that this point was essential in Wilson's original line of arguments, so we would like to maintain this feature ($h(\varepsilon)$ being constant in each interval of the logarithmic discretization) also for a general, non-constant $\Delta(\omega)$. Note that this restriction for the function $h(\varepsilon)$ does not lead to additional approximations for a non-constant $\Delta(\omega)$ as one can shift all the remaining ε-dependence to the dispersion $g(\varepsilon)$, see Eq. (19).
As discussed in [7] in the context of the soft-gap model, one can even set $h(\varepsilon) = h$ for all ε. Here we follow the proposal of [8], that is, we introduce a step function for $h(\varepsilon)$

$$h(\varepsilon) = h^\pm_n \ , \ \ x_{n+1} < \pm\varepsilon < x_n \, , \tag{28}$$

with $h^\pm_n$ given by the average of the hybridization function $\Delta(\omega)$ within the respective intervals,

$$h^{\pm 2}_n = \frac{1}{d_n} \int^{\pm,n} \mathrm{d}\varepsilon\, \frac{1}{\pi} \Delta(\varepsilon) \, . \tag{29}$$

This leads to the following form of the hybridization term

$$\int_{-1}^{1} \mathrm{d}\varepsilon\, h(\varepsilon) f^\dagger_\sigma a_{\varepsilon\sigma} = \frac{1}{\sqrt{\pi}} f^\dagger_\sigma \sum_n \left[\gamma^+_n a_{n0\sigma} + \gamma^-_n b_{n0\sigma} \right] \, , \tag{30}$$

with $\gamma^{\pm 2}_n = \int^{\pm,n} \mathrm{d}\varepsilon\, \Delta(\varepsilon)$.
Next, we turn to the conduction electron term, which transforms into

$$\begin{aligned} \int_{-1}^{1} \mathrm{d}\varepsilon\, g(\varepsilon) a^\dagger_{\varepsilon\sigma} a_{\varepsilon\sigma} &= \sum_{np} \left(\xi^+_n a^\dagger_{np\sigma} a_{np\sigma} + \xi^-_n b^\dagger_{np\sigma} b_{np\sigma} \right) \\ &+ \sum_{n, p \neq p'} \left(\alpha^+_n(p,p') a^\dagger_{np\sigma} a_{np'\sigma} - \alpha^-_n(p,p') b^\dagger_{np\sigma} b_{np'\sigma} \right) . \end{aligned} \tag{31}$$

The first term on the right hand side of Eq. (31) is diagonal in the index p. The discrete set of energies $\xi_n^\pm$ can be expressed as (see Ref. [8])

$$\xi_n^\pm = \frac{\int^{\pm,n} \mathrm{d}\varepsilon \Delta(\varepsilon)\varepsilon}{\int^{\pm,n} \mathrm{d}\varepsilon \Delta(\varepsilon)} \quad \left[= \pm\frac{1}{2}\Lambda^{-n}(1+\Lambda^{-1}) \right] , \tag{32}$$

where we give the result for a constant $\Delta(\varepsilon)$ in brackets. The coupling of the conduction band states with different p, p' (the second term) recovers the continuum (no approximation has been made so far, Eq. (31) is still exact). For the case of a linear dispersion, $g(\varepsilon) = \varepsilon$, the prefactors $\alpha_n^\pm(p,p')$ are the same for both sides of the discretization and take the following form

$$\alpha_n^\pm(p,p') = \frac{1-\Lambda^{-1}}{2\pi i} \frac{\Lambda^{-n}}{p'-p} \exp\left[\frac{2\pi i(p'-p)}{1-\Lambda^{-1}}\right] . \tag{33}$$

The actual discretization of the Hamiltonian is now achieved by dropping the terms with $p \neq 0$ in the expression for the conduction band Eq. (31). This is, of course, an approximation, the quality of which is not clear from the outset. To motivate this step we can argue that (i) the $p \neq 0$ states couple only indirectly to the impurity (via their coupling to the $p = 0$ states in Eq. (31)) and (ii) the coupling between the $p = 0$ and $p \neq 0$ states has a prefactor $(1 - \Lambda^{-1})$ which vanishes in the limit $\Lambda \to 1$. In this sense one can view the couplings to the states with $p \neq 0$ as small parameters and consider the restriction to $p = 0$ as zeroth order step in a perturbation expansion with respect to the coefficients $a_n^\pm(p,p')$ [1]. As it turns out, the accuracy of the results obtained from the $p = 0$ states only is surprisingly good even for values of Λ as large as $\Lambda = 2$, so that in all NRG calculations the $p \neq 0$ states have never been considered so far.
Finally, after dropping the $p \neq 0$ terms and relabeling the operators $a_{n0\sigma} \equiv a_{n\sigma}$, etc., we arrive at the discretized Hamiltonian as depicted by Fig. 1b:

$$\begin{aligned} H &= H_{\mathrm{imp}} + \sum_{n\sigma} \left[\xi_n^+ a_{n\sigma}^\dagger a_{n\sigma} + \xi_n^- b_{n\sigma}^\dagger b_{n\sigma} \right] \\ &+ \frac{1}{\sqrt{\pi}} \sum_\sigma f_\sigma^\dagger \left[\sum_n \left(\gamma_n^+ a_{n\sigma} + \gamma_n^- b_{n\sigma} \right) \right] + \frac{1}{\sqrt{\pi}} \sum_\sigma \left[\sum_n \left(\gamma_n^+ a_{n\sigma}^\dagger + \gamma_n^- b_{n\sigma}^\dagger \right) \right] f_\sigma \, . \end{aligned} \tag{34}$$

While the various steps leading to the discretized Hamiltonian, Eq. (34), are fairly straightforward from a mathematical point of view, the question may arise here, why are we performing such a specific discretization at all?
Quite generally, a numerical diagonalization of Hamiltonian matrices allows to take into account the various impurity-related terms in the Hamiltonian, such as a local Coulomb repulsion, non-perturbatively. Apparently, the actual implementation of such a numerical diagonalization scheme requires some sort of discretization of the original model, which has a continuum of bath states. There are, however, many ways to discretize such a system, so let me try to explain why the logarithmic discretization is the most suitable one here. As it turns out, quantum impurity models are very often characterized by energy scales orders of magnitudes smaller than the bare energy scales of the model Hamiltonian. If the ratio of these energy scales is, for example, of the order of 10^5, a linear discretization would require energy intervals of size at most 10^{-6} to

properly resolve the lowest scale in the system. Since for a finite system the splitting of energies is roughly inversely proportional to the system size, one would need of the order of 10^6 sites, which renders an exact diagonalization impossible.
Apparently, the logarithmic discretization reduces this problem in that the low-energy resolution now depends exponentially on the number of sites in the discretized model, so that energy scales of the order of 10^5 (in units of the bandwidth) can be reached by performing calculations for fairly small clusters, say with ≈ 20 sites.

3.2 Mapping on a semi-infinite chain

According to Fig. 1b and c, the next step is to transform the discretized Hamiltonian Eq. (34) into a semi-infinite chain form with the first site of the chain (filled circle in Fig. 1c) representing the impurity degrees of freedom. You will notice, of course, that we have introduced a representation of the siAm in the form of a semi-infinite chain already in Fig. 4, with the Hamiltonian given by Eq. (15). The structure of the Hamiltonian Eq. (15) and the one corresponding to Fig. 1c (see Eq. (38) below) is exactly the same, so why should we distinguish these Hamiltonians at all? The essential point here is that the semi-infinite chain introduced in Sec. 2 is an exact representation of the *original* model, that means it has the same hybridization function as the model in the original site representation, for example, the model for a single impurity coupled to a two-dimensional system as shown in Fig. 3.
In contrast, the semi-infinite chain to be introduced in this subsection corresponds to the discretized Hamiltonian Eq. (34), which is an approximation of the original, continuous model, so the model corresponding to Fig. 1c – for which the expression 'Wilson chain' is often used – is an approximation as well. As will be discussed in the following, the main feature of the Wilson chain is that the t_l are falling off exponentially with distance from the impurity.
In the Hamiltonian for the Wilson chain, the impurity directly couples only to one conduction electron degree of freedom with operators $c_{0\sigma}^{(\dagger)}$, the form of which can be directly read off from the second and third line in Eq. (34). With the definition

$$c_{0\sigma} = \frac{1}{\sqrt{\xi_0}} \sum_n \left[\gamma_n^+ a_{n\sigma} + \gamma_n^- b_{n\sigma} \right] , \tag{35}$$

in which the normalization constant is given by

$$\xi_0 = \sum_n \left((\gamma_n^+)^2 + (\gamma_n^-)^2 \right) = \int_{-1}^{1} \mathrm{d}\varepsilon \Delta(\varepsilon) , \tag{36}$$

the hybridization term can be written as

$$\frac{1}{\sqrt{\pi}} f_\sigma^\dagger \sum_n \left(\gamma_n^+ a_{n\sigma} + \gamma_n^- b_{n\sigma} \right) = \sqrt{\frac{\xi_0}{\pi}} f_\sigma^\dagger c_{0\sigma} , \tag{37}$$

(similarly for the Hermitian conjugate term). Note that for a coupling to a single site as in Eq. (4), the coupling in Eq. (37) reduces to $\sqrt{\xi_0/\pi} = V$.

The operators $c_{0\sigma}^{(\dagger)}$ are of course not orthogonal to the operators $a_{n\sigma}^{(\dagger)}$, $b_{n\sigma}^{(\dagger)}$. Constructing a new set of mutually orthogonal operators $c_{n\sigma}^{(\dagger)}$ from $c_{0\sigma}^{(\dagger)}$ and $a_{n\sigma}^{(\dagger)}$, $b_{n\sigma}^{(\dagger)}$ by a standard Gram-Schmidt procedure leads to the desired chain Hamiltonian, which takes the form

$$H = H_{\rm imp} + \sqrt{\frac{\xi_0}{\pi}} \sum_\sigma \left[f_\sigma^\dagger c_{0\sigma} + c_{0\sigma}^\dagger f_\sigma \right] + \sum_{\sigma,n=0}^{\infty} \left[\varepsilon_n c_{n\sigma}^\dagger c_{n\sigma} + t_n \left(c_{n\sigma}^\dagger c_{n+1\sigma} + c_{n+1\sigma}^\dagger c_{n\sigma} \right) \right] \ , \quad (38)$$

with the operators $c_{n\sigma}^{(\dagger)}$ corresponding to the n-th site of the conduction electron part of the chain. The parameters of the chain are the on-site energies ε_n and the hopping matrix elements t_n. The operators $c_{n\sigma}^{(\dagger)}$ in Eq. (38) and the operators $\{a_{n\sigma}^{(\dagger)}, b_{n\sigma}^{(\dagger)}\}$ in Eq. (34) are related via an orthogonal transformation

$$a_{n\sigma} = \sum_{m=0}^{\infty} u_{mn} c_{m\sigma} \ , \ \ b_{n\sigma} = \sum_{m=0}^{\infty} v_{mn} c_{m\sigma} \ ,$$
$$c_{n\sigma} = \sum_{m=0}^{\infty} \left[u_{nm} a_{m\sigma} + v_{nm} b_{m\sigma} \right] \ . \quad (39)$$

From the definition of $c_{0\sigma}$ in Eq. (35) we can read off the coefficients u_{0m} and v_{0m}

$$u_{0m} = \frac{\gamma_m^+}{\sqrt{\xi_0}} \ , \ \ v_{0m} = \frac{\gamma_m^-}{\sqrt{\xi_0}} \ . \quad (40)$$

For the remaining coefficients u_{nm}, v_{nm}, as well as for the parameters ε_n, t_n, one can derive recursion relations following the scheme described in detail in, for example, Appendix A of [9]. The starting point here is the equivalence of the free conduction electron parts

$$\sum_{n\sigma} \left[\xi_n^+ a_{n\sigma}^\dagger a_{n\sigma} + \xi_n^- b_{n\sigma}^\dagger b_{n\sigma} \right] = \sum_{\sigma,n=0}^{\infty} \left[\varepsilon_n c_{n\sigma}^\dagger c_{n\sigma} + t_n \left(c_{n\sigma}^\dagger c_{n+1\sigma} + c_{n+1\sigma}^\dagger c_{n\sigma} \right) \right] . \quad (41)$$

The recursion relations are initialized by the equations

$$\begin{aligned} \varepsilon_0 &= \frac{1}{\xi_0} \int_{-1}^{1} {\rm d}\varepsilon \Delta(\varepsilon) \varepsilon \ , \\ t_0^2 &= \frac{1}{\xi_0} \sum_m \left[(\xi_m^+ - \varepsilon_0)^2 (\gamma_m^+)^2 + (\xi_m^- - \varepsilon_0)^2 (\gamma_m^-)^2 \right] \ , \\ u_{1m} &= \frac{1}{t_0} (\xi_m^+ - \varepsilon_0) u_{0m} \ , \\ v_{1m} &= \frac{1}{t_0} (\xi_m^- - \varepsilon_0) v_{0m} \ . \end{aligned} \quad (42)$$

For $n \geq 1$, the recursion relations read

$$\begin{aligned} \varepsilon_n &= \sum_m \left(\xi_m^+ u_{nm}^2 + \xi_m^- v_{nm}^2 \right) \ , \\ t_n^2 &= \sum_m \left[(\xi_m^+)^2 u_{nm}^2 + (\xi_m^-)^2 v_{nm}^2 \right] - t_{n-1}^2 - \varepsilon_n^2 \ , \\ u_{n+1,m} &= \frac{1}{t_n} \left[(\xi_m^+ - \varepsilon_n) u_{nm} - t_{n-1} u_{n-1,m} \right] \ , \\ v_{n+1,m} &= \frac{1}{t_n} \left[(\xi_m^- - \varepsilon_n) v_{nm} - t_{n-1} v_{n-1,m} \right] \ . \end{aligned} \quad (43)$$

Note that for a particle-hole symmetric hybridization function, $\Delta(\omega) = \Delta(-\omega)$, the on-site energies ε_n are zero for all n.

For a general hybridization function, the recursion relations have to be solved numerically. Although these relations are fairly easy to implement, it turns out that the iterative solution breaks down typically after about 20-30 steps. The source of this instability is the wide range of values for the parameters entering the recursion relations (for instance for the discretized energies $\xi_m^{\pm}$). In most cases this problem can be overcome by using arbitrary precision routines for the numerical calculations. Furthermore, it is helpful to enforce the normalization of the vectors u_{nm} and v_{nm} after each step.

Analytical solutions for the recursion relations have so far been given only for few special cases. Wilson derived a formula for the t_n for a constant density of states of the conduction electrons in the Kondo version of the impurity model [1]; this corresponds to a constant hybridization function $\Delta(\omega)$ in the interval $[-1, 1]$. Here we have $\varepsilon_n = 0$ for all n and the expression for the t_n reads

$$t_n = \frac{(1+\Lambda^{-1})\,(1-\Lambda^{-n-1})}{2\sqrt{1-\Lambda^{-2n-1}}\sqrt{1-\Lambda^{-2n-3}}}\,\Lambda^{-n/2}\,. \tag{44}$$

Similar expressions have been given for the soft-gap model, see [8]. In the limit of large n this reduces to

$$t_n \longrightarrow \frac{1}{2}\left(1+\Lambda^{-1}\right)\,\Lambda^{-n/2}\,. \tag{45}$$

The fact that the t_n fall off exponentially with the distance from the impurity is essential for the following discussion, so let me briefly explain where this n-dependence comes from. Consider the discretized model Eq. (34) with a finite number $1 + M/2$ (M even) of conduction electron states for both positive and negative energies (the sum over n then goes from 0 to $M/2$). This corresponds to $2+M$ degrees of freedom which result in $2+M$ sites of the conduction electron part of the chain after the mapping to the Wilson chain. The lowest energies in the discretized model Eq. (34) are the energies $\xi_{M/2}^{\pm}$ which, for a constant hybridization function, are given by $\xi_{M/2}^{\pm} = \pm\frac{1}{2}\Lambda^{-M/2}(1+\Lambda^{-1})$, see Eq. (32). This energy shows up in the chain Hamiltonian as the last hopping matrix element t_M, so we have $t_M \sim \xi_{M/2}$ equivalent to Eq. (45).

Equation (38) is a specific one-dimensional representation of the siAm with the special feature that the hopping matrix elements t_n fall off exponentially. As mentioned above, this representation is not exact since in the course of its derivation, the $p \neq 0$ terms have been dropped. Nevertheless, the conduction electron sites of the chain do have a physical meaning in the original model as they can be viewed as a sequence of shells centered around the impurity. The first site of the conduction electron chain corresponds to the shell with the maximum of its wavefunction closest to the impurity [1,3]; this shell is coupled to a shell further away from the impurity and so on.

3.3 Iterative diagonalization

The transformations described so far are necessary to map the problem onto a form (the Wilson chain, Eq. (38)) for which an iterative renormalization group (RG) procedure can be defined.

This is the point at which, finally, the RG character of the approach enters.
The chain Hamiltonian Eq. (38) can be viewed as a series of Hamiltonians H_N ($N = 0, 1, 2, \ldots$) which approaches H in the limit $N \to \infty$.

$$H = \lim_{N\to\infty} \Lambda^{-(N-1)/2} H_N \;, \tag{46}$$

with

$$H_N = \Lambda^{(N-1)/2} \Bigg[H_{\rm imp} + \sqrt{\frac{\xi_0}{\pi}} \sum_\sigma \left(f_\sigma^\dagger c_{0\sigma} + c_{0\sigma}^\dagger f_\sigma \right) + \sum_{\sigma,n=0}^{N} \varepsilon_n c_{n\sigma}^\dagger c_{n\sigma} + \sum_{\sigma,n=0}^{N-1} t_n \left(c_{n\sigma}^\dagger c_{n+1\sigma} + c_{n+1\sigma}^\dagger c_{n\sigma} \right) \Bigg] \;. \tag{47}$$

The factor $\Lambda^{(N-1)/2}$ in Eq. (47) (and, consequently, the factor $\Lambda^{-(N-1)/2}$ in Eq. (46)) has been chosen to cancel the N-dependence of t_{N-1}, the hopping matrix element between the last two sites of H_N. Such a scaling is useful for the discussion of fixed points, as described below. For a different n-dependence of t_n, as for the spin-boson model [9], the scaling factor has to be changed accordingly. (The n-dependence of ε_n is, in most cases, irrelevant for the overall scaling of the many-particle spectra.)
Two successive Hamiltonians are related by

$$H_{N+1} = \sqrt{\Lambda} H_N + \Lambda^{N/2} \left[\sum_\sigma \varepsilon_{N+1} c_{N+1\sigma}^\dagger c_{N+1\sigma} + \sum_\sigma t_N \left(c_{N\sigma}^\dagger c_{N+1\sigma} + c_{N+1\sigma}^\dagger c_{N\sigma} \right) \right] \;, \tag{48}$$

and the starting point of the sequence of Hamiltonians is given by

$$H_0 = \Lambda^{-1/2} \left[H_{\rm imp} + \sum_\sigma \varepsilon_0 c_{0\sigma}^\dagger c_{0\sigma} + \sqrt{\frac{\xi_0}{\pi}} \sum_\sigma \left(f_\sigma^\dagger c_{0\sigma} + c_{0\sigma}^\dagger f_\sigma \right) \right] \;.$$

This Hamiltonian corresponds to a two-site cluster formed by the impurity and the first conduction electron site. Note that in the special case of the siAm, one can also choose $H_{-1} = \Lambda^{-1} H_{\rm imp}$ as the starting point (with a proper renaming of parameters and operators) since the hybridization term has the same structure as the hopping term between the conduction electron sites.
The recursion relation Eq. (48) can now be understood in terms of a renormalization group transformation R:

$$H_{N+1} = R\left(H_N\right) \;. \tag{49}$$

In a standard RG transformation, the Hamiltonians are specified by a set of parameters $\vec{K}$ and the mapping R transforms the Hamiltonian $H(\vec{K})$ into another Hamiltonian *of the same form*, $H(\vec{K'})$, with a new set of parameters $\vec{K}'$. Such a representation does not exist, in general, for the H_N which are obtained in the course of the iterative diagonalization to be described below. Instead, we characterize H_N, and thereby also the RG flow, directly by the many-particle energies $E_N(r)$

$$H_N |r\rangle_N = E_N(r) |r\rangle_N \;\;,\;\; r = 1, \ldots, N_{\rm s} \;, \tag{50}$$

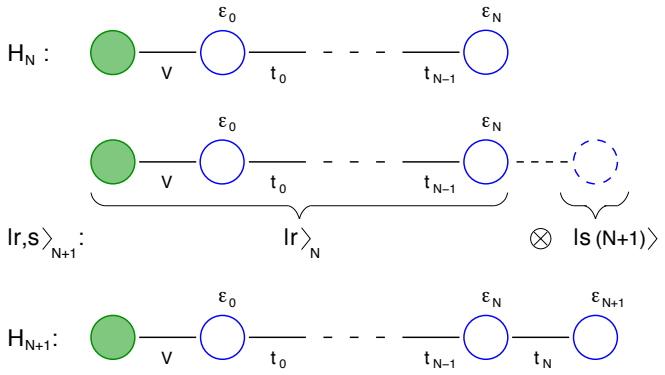

Fig. 6: *In each step of the iterative diagonalization scheme one site of the chain (with operators $c^{(\dagger)}_{N+1}$ and on-site energy ε_{N+1}) is added to the Hamiltonian H_N. A basis $|r;s\rangle_{N+1}$ for the resulting Hamiltonian, H_{N+1}, is formed by the eigenstates of H_N, $|r\rangle_N$, and a basis of the added site, $|s(N+1)\rangle$. Figure taken from Ref. [4].*

with the eigenstates $|r\rangle_N$ and N_s the dimension of H_N. This is particularly useful in the crossover regime between different fixed points, where a description in terms of an effective Hamiltonian with certain renormalized parameters is not possible. Only in the vicinity of the fixed points (except for certain quantum critical points) one can go back to an effective Hamiltonian description, as described below.

Our primary aim now is to set up an iterative scheme for the diagonalization of H_N, in order to discuss the flow of the many-particle energies $E_N(r)$. Let us assume that, for a given N, the Hamiltonian H_N has already been diagonalized, as in Eq. (50). We now construct a basis for H_{N+1}, as sketched in Fig. 6:

$$|r;s\rangle_{N+1} = |r\rangle_N \otimes |s(N+1)\rangle \; . \tag{51}$$

The states $|r;s\rangle_{N+1}$ are product states consisting of the eigenbasis of H_N and a suitable basis $|s(N+1)\rangle$ for the added site (the new degree of freedom). From the basis Eq. (51) we construct the Hamiltonian matrix for H_{N+1}:

$$H_{N+1}(rs,r's') = {}_{N+1}\langle r;s|H_{N+1}|r';s'\rangle_{N+1} \; . \tag{52}$$

For the calculation of these matrix elements it is useful to decompose H_{N+1} into three parts

$$H_{N+1} = \sqrt{\Lambda} H_N + \hat{X}_{N,N+1} + \hat{Y}_{N+1} \; , \tag{53}$$

(see, for example, Eq. (48)) where the operator $\hat{Y}_{N+1}$ only contains the degrees of freedom of the added site, while $\hat{X}_{N,N+1}$ mixes these with the ones contained in H_N. Apparently, the structure of the operators $\hat{X}$ and $\hat{Y}$, as well as the equations for the calculation of their matrix elements, depend on the model under consideration.

The following steps are illustrated in Fig. 7: In Fig. 7a we show the many-particle spectrum of H_N, that is the sequence of many-particle energies $E_N(r)$. Note that, for convenience, the ground-state energy has been set to zero. Figure 7b shows the overall scaling of the energies by the factor $\sqrt{\Lambda}$, see the first term in Eq. (48).

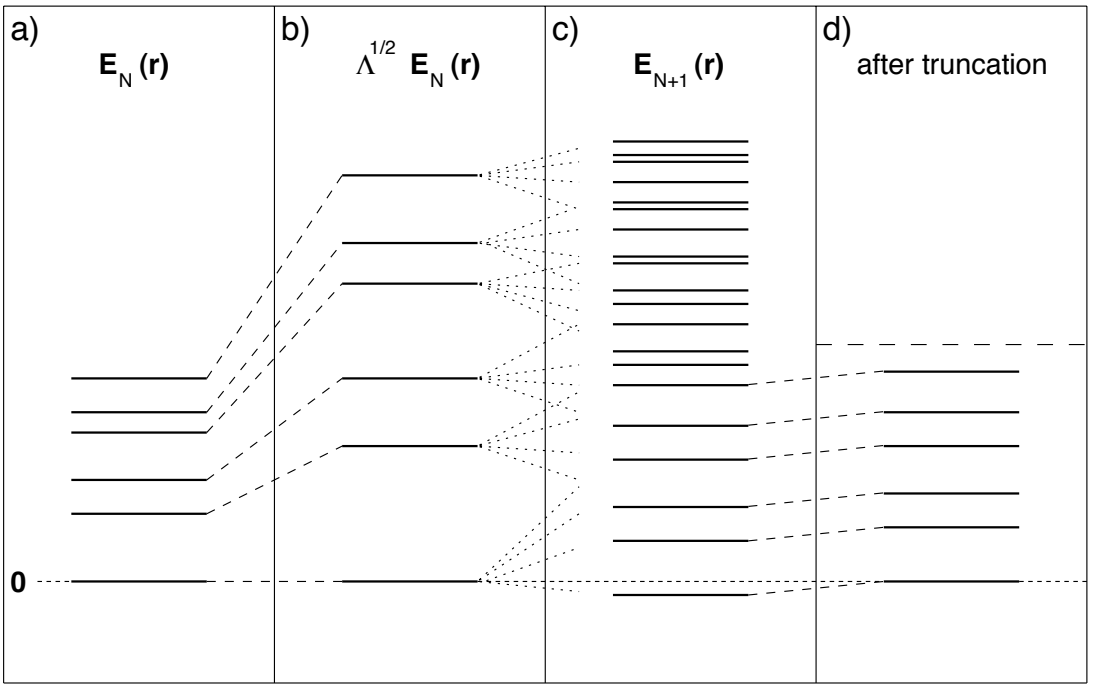

Fig. 7: *(a): Many-particle spectrum $E_N(r)$ of the Hamiltonian H_N with the ground-state energy set to zero. (b): The relation between successive Hamiltonians, Eq. (48), includes a scaling factor $\sqrt{\Lambda}$. (c) Many-particle spectrum $E_{N+1}(r)$ of H_{N+1}, calculated by diagonalizing the Hamiltonian matrix Eq. (52). (d) The same spectrum after truncation where only the N_s lowest-lying states are retained; the ground-state energy has again been set to zero. Figure taken from Ref. [4].*

Diagonalization of the matrix Eq. (52) gives the new eigenenergies $E_{N+1}(w)$ and eigenstates $|w\rangle_{N+1}$ which are related to the basis $|r;s\rangle_{N+1}$ via the unitary matrix U:

$$|w\rangle_{N+1} = \sum_{rs} U(w,rs)|r;s\rangle_{N+1} \; . \tag{54}$$

The set of eigenenergies $E_{N+1}(w)$ of H_{N+1} is displayed in Fig. 7c (the label w can now be replaced by r). Apparently, the number of states increases by adding the new degree of freedom (when no symmetries are taken into account, the factor is just the dimension of the basis $|s(N+1)\rangle$). The ground-state energy is negative, but will be set to zero in the following step.
The increasing number of states is, of course, a problem for the numerical diagonalization; the dimension of H_{N+1} grows exponentially with N, even when we consider symmetries of the model so that the full matrix takes a block-diagonal form with smaller submatrices. This problem can be solved by a very simple truncation scheme: after diagonalization of the various submatrices of H_{N+1} one only keeps the N_s eigenstates with the lowest many-particle energies. In this way, the dimension of the Hilbert space is fixed to N_s and the computation time increases linearly with the length of the chain. Suitable values for the parameter N_s depend on the model; for the siAm, N_s of the order of a few hundred is sufficient to get converged results for the many-particle spectra, but the accurate calculation of static and dynamic quantities usually requires larger values of N_s. The truncation of the high energy states is illustrated in Fig. 7d.

Such an ad-hoc truncation scheme needs further explanations. First of all, there is no guarantee that this scheme will work in practical applications and its quality should be checked for each individual application. Important here is the observation that the neglect of the high-energy states does not spoil the low-energy spectrum in subsequent iterations – this can be easily seen numerically by varying N_s. The influence of the high-energy on the low-energy states is small since the addition of a new site to the chain can be viewed as a perturbation of relative strength $\Lambda^{-1/2} < 1$. This perturbation is small for large values of Λ but for $\Lambda \to 1$ it is obvious that one has to keep more and more states to get reliable results. This also means that the accuracy of the NRG results is getting worse when N_s is kept fixed and Λ is reduced (vice versa, it is sometimes possible to improve the accuracy by *increasing* Λ for fixed N_s).

From this discussion we see that the success of the truncation scheme is intimately connected to the special structure of the chain Hamiltonian (that is $t_n \propto \Lambda^{-n/2}$) which in turn is due to the logarithmic discretization of the original model. A direct transformation of the siAm to a semi-infinite chain as in Eq. (15) results in $t_n \to \mathrm{const}$ [3], and the above truncation scheme fails.

Let us now be a bit more specific on how to construct the basis $|r;s\rangle_{N+1}$. For this we have to decide, first of all, which of the symmetries of the Hamiltonian should be used in the iterative diagonalization. In the original calculations of Ref. [1] and Refs. [10,11] the following quantum numbers were used: total charge Q (particle number with respect to half-filling), total spin S and z-component of the total spin S_z. It was certainly essential in the 1970's to reduce the size of the matrices and hence the computation time as much as possible by invoking as many symmetries as possible. This is no longer necessary to such an extent on modern computer systems, i.e. one can, at least for single-band models, drop the total spin S and classify the subspaces with the quantum numbers (Q, S_z) only. This simplifies the program considerably as one no longer has to worry about reduced matrix elements and the corresponding Clebsch-Gordan coefficients, see, for example [10]. The $|r;s\rangle_{N+1}$ are then constructed as:

$$\begin{aligned}
|Q,S_z,r;1\rangle_{N+1} &= |Q+1,S_z,r\rangle_N \ , \\
|Q,S_z,r;2\rangle_{N+1} &= c^\dagger_{N+1\uparrow}\,|Q,S_z-\tfrac{1}{2},r\rangle_N \ , \\
|Q,S_z,r;3\rangle_{N+1} &= c^\dagger_{N+1\downarrow}\,|Q,S_z+\tfrac{1}{2},r\rangle_N \ , \\
|Q,S_z,r;4\rangle_{N+1} &= c^\dagger_{N+1\uparrow}c^\dagger_{N+1\downarrow}\,|Q-1,S_z,r\rangle_N \ .
\end{aligned} \tag{55}$$

Note that the quantum numbers (Q, S_z) on each side of these equations refer to different systems: on the left-hand side they are for the system including the added site, and on the right-hand side without the added site. We do not go into the details of how to set up the Hamiltonian matrices Eq. (52), as this procedure is described in great detail in Appendix B of Ref. [10].

For fermionic baths, the discretization parameter Λ and the number of states N_s kept in each iteration are the only parameters which govern the quality of the results of the NRG procedure. For a bosonic bath, the infinite dimensional basis $|s(N+1)\rangle$ for the added bosonic site requires an additional parameter N_b, which determines the dimension of $|s(N+1)\rangle$.

3.4 Renormalization group flow

The result of the iterative diagonalization scheme are the many-particle energies $E_N(r)$ with $r = 1, \ldots, N_\mathrm{s}$ (apparently, the number of states is less than N_s for the very first steps before the truncation sets in). The index N goes from 0 to a maximum number of iterations, N_max, which usually has to be chosen such that the system has approached its low-temperature fixed point.

As illustrated in Fig. 7, the set of many-particle energies cover roughly the same energy range independent of N, due to the scaling factor $\Lambda^{(N-1)/2}$ in Eq. (47). The energy of the first excited state of H_N is of the order of $\Lambda^{(N-1)/2} t_{N-1}$, a constant according to Eq. (45). The energy of the highest excited state kept after truncation depends on N_s – for typical parameters this energy is approximately 5-10 times larger than the lowest energy.

Multiplied with the scaling factor $\Lambda^{-(N-1)/2}$, see Eq. (46), the energies $E_N(r)$ are an approximation to the many-particle spectrum of the Wilson chain Eq. (38) within an energy window decreasing exponentially with increasing N. Note, that the energies for higher lying excitations obtained for early iterations are not altered in later iteration steps due to the truncation procedure. Nevertheless one can view the resulting set of many-particle energies and states from all NRG iterations N as approximation to the spectrum of the full Hamiltonian and use them to calculate physical properties in the whole energy range.

Here we want to focus directly on the many-particle energies $E_N(r)$ and show how one can extract information about the physics of a given model by analyzing their flow, that is the dependence of $E_N(r)$ on N.

As a typical example for such an analysis, we show in Fig. 8 the flow of the many-particle energies for the symmetric siAm, with parameters $\varepsilon_f = -0.5 \cdot 10^{-3}$, $U = 10^{-3}$, $V = 0.004$, and $\Lambda = 2.5$ (the same parameters as used in Fig. 5 of Ref. [10]; note that we show here a slightly different selection of the lowest-lying states). The energies are plotted for odd N only, that is an odd total number of sites (which is $N+2$). This is necessary, because the many-particle spectra show the usual even-odd oscillations of a fermionic finite-size system (the patterns for even N look different but contain, of course, the same physics). The data points are connected by lines to visualize the flow. As in Ref. [10], the many-particle energies are labeled by total charge Q and total spin S.

What is the information one can extract from such a flow diagram? First of all we note the appearance of three different fixed points of the RG transformation for early iteration numbers $N < 10$, for intermediate values of N and for $N > 60$ (strictly speaking, because we look at N odd only, these are fixed points of R^2, not of R). The physics of these fixed points cannot be extracted by just looking at the pattern of the many-particle energies. This needs some further analysis, in particular the direct diagonalization of fixed point Hamiltonians (which usually have a simple structure) and the comparison of their spectrum with the numerical data. An excellent account of this procedure for the symmetric and asymmetric siAm has been given in Refs. [10, 11], and there is no need to repeat this discussion here. The analysis shows that for $N \approx 3 - 9$, the system is very close to the free-orbital fixed point, with the fixed point Hamiltonian given by Eq. (38) for $\varepsilon_\mathrm{f} = 0$, $U = 0$, and $V = 0$. This fixed point is unstable and

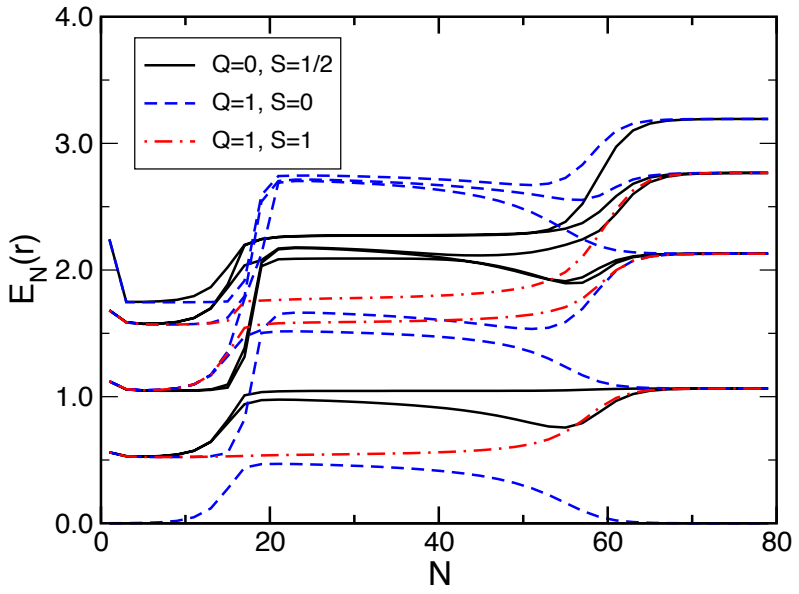

Fig. 8: *Flow of the lowest-lying many-particle energies of the single-impurity Anderson model for parameters $\varepsilon_f = -0.5 \cdot 10^{-3}$, $U = 10^{-3}$, $V = 0.004$, and $\Lambda = 2.5$. The states are labeled by the quantum numbers total charge Q and total spin S. See the text for a discussion of the fixed points visible in this plot. Figure taken from Ref. [4].*

for $N \approx 11 - 17$, we observe a rapid crossover to the local-moment fixed point. This fixed point is characterized by a free spin decoupled from the conduction band (here we have $\varepsilon_\mathrm{f} = -U/2$, $U \to \infty$, and $V = 0$). The local-moment fixed point is unstable as well and after a characteristic crossover (see the discussion below) the system approaches the stable strong-coupling fixed point of a screened spin (with $\varepsilon_\mathrm{f} = -U/2$ and $V^2/U \to \infty$). Note that the terminology 'strong-coupling' has been introduced originally because the fixed point Hamiltonian can be obtained from the limit $V \to \infty$, so 'coupling' here refers to the hybridization, not the Coulomb parameter U.

The NRG does not only allow to match the structure of the numerically calculated fixed points with those of certain fixed point Hamiltonians. One can in addition identify the deviations from the fixed points (and thereby part of the crossover) with appropriate perturbations of the fixed point Hamiltonians. Again, we refer the reader to Refs. [10, 11] for a detailed description of this analysis. The first step is to identify the leading perturbations around the fixed points. The leading operators can be determined by expressing them in terms of the operators which diagonalize the fixed point Hamiltonian; this tells us directly how these operators transform under the RG mapping R^2. One then proceeds with the usual classification into relevant, marginal, and irrelevant perturbations. The final results of this analysis perfectly agree with the flow diagram of Fig. 8: There is a relevant perturbation which drives the system away from the free-orbital fixed point, but for the local-moment fixed point there is only a marginally relevant perturbation, therefore the system only moves very slowly away from this fixed point. Note that this marginal perturbation – which is the exchange interaction between the local moment and the spin of the first conduction electron site – gives rise to the logarithms observed in various physical quan-

tities. Finally, there are only irrelevant operators which govern the flow to the strong-coupling fixed point. These are responsible for the Fermi-liquid properties at very low temperatures [3]. Flow diagrams as in Fig. 8 also give information about the relevant energy scales for the crossover between the fixed points. For example, an estimate of the Kondo temperature $T_{\rm K}$ (the temperature scale which characterizes the flow to the strong-coupling fixed point) is given by $T_{\rm K} \approx \omega_{\rm c} \Lambda^{-\bar{N}/2}$, with $\bar{N} \approx 55$ for the parameters in Fig. 8.

4 Final remarks

The main purpose of these lecture notes was to give a brief introduction to the basic steps of the NRG method, that is the logarithmic discretization (Sec. 3.1), the mapping onto a semi-infinite chain (Sec. 3.2), and the iterative diagonalization (Sec. 3.3). A number of improvements of these technical steps have been introduced since the development of the method by Wilson [1] and I just want to mention a few here.

The discreteness of the model Eq. (34) can be (in some cases) problematic for the calculation of physical quantities. As it is not possible in the actual calculations to recover the continuum by taking the limit $\Lambda \to 1$ (or by including the $p \neq 0$ terms), it has been suggested to average over various discretizations for fixed Λ [12–14]. The discretization points are then modified as

$$x_n = \begin{cases} 1 & : \quad n = 0 \\ \Lambda^{-(n+Z)} & : \quad n \geq 1 \,, \end{cases} \tag{56}$$

where Z covers the interval $[0, 1)$. This 'Z-averaging' indeed removes certain artificial oscillations.

Another shortcoming of the discretized model is that the hybridization function $\Delta(\omega)$ is systematically underestimated. It is therefore convenient to multiply $\Delta(\omega)$ with the correction factor

$$A_\Lambda = \frac{1}{2} \ln \Lambda \frac{\Lambda + 1}{\Lambda - 1} \,, \tag{57}$$

which accelerates the convergence to the continuum limit. For a recent derivation of this correction factor, see [15].

The equations for the recursive calculation of the parameters of the semi-infinite chain, the $\{\varepsilon_n\}$ and $\{t_n\}$ in Eq. (38), have been given in Sec. 3.2, but it is certainly not obvious how to arrive at analytical expressions as in Eq. (44) (for the special case of constant $\Delta(\omega)$). This issue has been discussed in more general terms in Ref. [16]. By using the theory of orthogonal polynomials, expressions for the parameters $\{\varepsilon_n\}$ and $\{t_n\}$ can now be given for more complex hybridization functions, like the ones appearing in the Ohmic and sub-Ohmic spin-boson model.

Another technical improvement to be mentioned here is about the truncation of basis states in the iterative diagonalization of the Wilson chain. It is not at all clear how many states one should keep here and the convergence is usually checked by repeating the calculation for various values of $N_{\rm s}$. A quantitative criterion to analyze the convergence, based on the discarded weight in the reduced density matrices, has been recently given in Ref. [17].

The physics of the siAm, in particular the Kondo effect, has been mentioned here only in the context of the renormalization group flow of the many-particle levels (Sec. 3.4). To actually see the screening of the local moment by the conduction electrons, one has to calculate an appropriate physical quantity, for example the magnetic susceptibility. Some extra care has to be taken to calculate such quantities, for more details, see Sec. III in Ref. [4]. As an example of the technical difficulties one has to solve to obtain reliable data for the specific heat, see the recent paper Ref. [18].
The starting point for the NRG is the integral representation Eq. (18), which is just one possible representation of the siAm. In Sec. 2 you have seen that there are many different ways to represent the model which are all equivalent provided they give the same hybridization function $\Delta(\omega)$. We have discussed that the siAm can always be viewed as a single-channel model. As a side remark, note that for multi-impurity Anderson models it is not at all trivial to count the number of screening channels. So far this has been done only for a few special cases.
There is a wide range of models and physical phenomena to which the NRG has been applied (for an overview, see Secs. 4 and 5 in Ref. [4]). To conclude, here is a list of a few very recent applications:

- Real-space charge densities and their connection to the Kondo-screening cloud [19].
- Real-time dynamics in quantum impurity systems [20].
- Steady-state currents through nanodevices [21].
- Transport through multi-level quantum dots [22].
- Multi-channel and multi-impurity physics [23].
- Zero-bias conductance in carbon nanotube quantum dots [24].

Acknowledgments

I would like to thank Theo Costi and Thomas Pruschke, the coauthors of the NRG-review [4] on which part of these lecture notes are based, for many helpful discussions, and Andrew Mitchell for carefully reading the manuscript. Funding from the Deutsche Forschungsgemeinschaft through SFB 608 and FOR 960 is gratefully acknowlegded.

References

[1] K.G. Wilson, Rev. Mod. Phys. **47**, 773 (1975)

[2] E. Pavarini, E. Koch, D. Vollhardt, and A. Lichtenstein (eds.):
The LDA+DMFT approach to strongly correlated materials,
Reihe Modeling and Simulation, Vol. 1 (Forschungszentrums Jülich, 2011)
`http://www.cond-mat.de/events/correl11`

[3] Alex C. Hewson: *The Kondo Problem to Heavy Fermions*,
(Cambridge University Press, Cambridge, England, 1993)

[4] R. Bulla, T.A. Costi, and Th. Pruschke, Rev. Mod. Phys. **80**, 395 (2008)

[5] P.W. Anderson, Phys. Rev. **124**, 41 (1961)

[6] R. Bulla, A.C. Hewson, and Th. Pruschke, J. Phys.: Condens. Matter **10**, 8365 (1998)

[7] K. Chen and C. Jayaprakash, J. Phys.: Condens. Matter **7**, L491 (1995)

[8] R. Bulla, Th. Pruschke, and A.C. Hewson, J. Phys.: Condens. Matter **9**, 10463 (1997)

[9] R. Bulla, H.-J. Lee, N.-H. Tong, and M. Vojta, Phys. Rev. B **71**, 045122 (2005)

[10] H.R. Krishna-murthy, J.W. Wilkins, and K.G. Wilson, Phys. Rev. B **21**, 1003 (1980)

[11] H.R. Krishna-murthy, J.W. Wilkins, and K.G. Wilson, Phys. Rev. B **21**, 1044 (1980)

[12] H.O. Frota and L.N. Oliveira, Phys. Rev. B **33**, 7871 (1986)

[13] M. Yoshida, M.A. Whitaker, and L.N. Oliveira, Phys. Rev. B **41**, 9403 (1990)

[14] W.C. Oliveira and L.N. Oliveira, Phys. Rev. B **49**, 11986 (1994)

[15] V.L. Campo Jr. and L.N. Oliveira, Phys. Rev. B **72**, 104432 (2005)

[16] A.W. Chin, Á. Rivas, S.F. Huelga, and M.B. Plenio, J. Math. Phys. **51**, 092109 (2010)

[17] A. Weichselbaum, Phys. Rev. B **84**, 125130 (2011)

[18] L. Merker and T.A. Costi, preprint arXiv:1206.3201 (2012)

[19] A.K. Mitchell, M. Becker, and R. Bulla, Phys. Rev. B **84**, 115120 (2011)

[20] F.B. Anders and A. Schiller, Phys. Rev. Lett. **95**, 196801 (2005)

[21] F.B. Anders, Phys. Rev. Lett. **101**, 066804 (2008)

[22] D.E. Logan, C.J. Wright, and M.R. Galpin, Phys. Rev. B **80**, 125117 (2009)

[23] E. Sela, A.K. Mitchell, and L. Fritz, Phys. Rev. Lett. **106**, 147202 (2011);
A.K. Mitchell, E. Sela, and D.E. Logan, Phys. Rev. Lett. **108**, 086405 (2012)

[24] F.B. Anders, D.E. Logan, M.R. Galpin, and G. Finkelstein,
Phys. Rev. Lett. **100**, 086809 (2008)

13 The Maximum Entropy Method: Analytic Continuation of QMC Data

Mark Jarrell
Department of Physics and Astronomy
Louisiana State University, Baton Rouge

Contents

E. Pavarini, E. Koch, F. Anders, and M. Jarrell
Correlated Electrons: From Models to Materials
Modeling and Simulation Vol. 2
Forschungszentrum Jülich, 2012, ISBN 978-3-89336-796-2
http://www.cond-mat.de/events/correl12

We present a pedagogical discussion of the maximum entropy method for the analytic continuation of Matsubara-time or -frequency quantum Monte Carlo data to real frequencies. Bayesian methods are employed to recast this daunting inverse problem into one of optimizing the posterior probability of a real-frequency spectral function. Bayesian methods are also used to optimize the inputs. We develop the formalism, present a detailed description of the data qualification, sketch an efficient algorithm to solve for the optimal spectra, give cautionary notes where appropriate, and present a detailed case study to demonstrate the method.

1 Introduction

Most quantum Monte Carlo (QMC) simulations produce Green's functions G of Matsubara imaginary time $\tau = it$ or frequency $i\omega_n$. However, real-frequency results are crucial since most experiments probe dynamical quantities, including transport, densities of states, nuclear magnetic resonance, inelastic scattering, etc. Thus, the inability to extract real-frequency or real-time results from Matsubara (imaginary) time QMC simulations presents a significant limitation to the usefulness of the method. The relation between $G(\tau)$ and $A(\omega) = -\frac{1}{\pi}\mathrm{Im}G(\omega)$ is linear and surprisingly simple

$$G(\tau) = \int d\omega A(\omega) K(\tau, \omega)\,, \tag{1}$$

or equivalently

$$G(i\omega_n) = \int d\omega A(\omega) K(i\omega_n, \omega)\,. \tag{2}$$

These two equations are related through a Fourier transform of the kernel and the Green function. For example, for a Fermionic single-particle Green's function G, $K(\tau,\omega) = e^{-\tau\omega}/(1 + e^{-\beta\omega})$ and $K(i\omega_n,\omega) = 1/(i\omega_n - \omega)$ [1]. These equations are equivalent since the Fourier transform is a unitary transformation. Despite this simplicity, inversion of these equations is complicated by the exponential nature of the kernel. For finite τ and large ω the kernel is exponentially small, so that $G(\tau)$ is insensitive to the high frequency features of $A(\omega)$. Equivalently, if we approximate both G and A by equal-length vectors and K by a square matrix, then we find that the determinant of K is exponentially small, so that K^{-1} is ill-defined. Apparently, there are an infinite number of A that yield the same G.

Previous attempts to address this problem include least-squares fits, Pade approximants and regularization. However, these techniques tend to produce spectra A with features which are overly smeared out by the regularization, or have parameters that are difficult to determine. In the least squares method, Schüttler and Scalapino [1] approximated the spectrum with a set of box functions. The location and weight of these functions was determined by minimizing the least-squares misfit between the spectrum and the QMC data. However, as the number of box functions is increased to better resolve features in the spectrum, the fit becomes unstable and noisy. In the Pade method [2], G (or rather its Fourier transform) is fit to a functional form, usually the ratio of two polynomials, which is then analytically continued formally by replacing

$i\omega_n \rightarrow \omega + i0^+$. This technique works when the data G is very precise, as when analytically continuing Eliashberg equations, or when the fitting function is known *a priori*. However, it is generally unreliable for the continuation of less-precise QMC data to real frequencies. A more useful approach is to introduce a regularization to the kernel, so that K^{-1} exists. This method was developed by G. Wahba [3], and employed by White et al. [4] and Jarrell and Biham [5]. They used similar methods to minimize $(G-KA)^2$ subject to constraint potentials which introduce correlations between adjacent points in A and impose positivity. The stochastic analytic continuation method of Sandvik and Beach [6, 7] treats the least squares measure of Schüttler as a thermodynamic potential and introduces a temperature to control the regularization.
In the Maximum Entropy Method (MEM) we employ a different philosophy. Using Bayesian statistics, we define the posterior probability of the spectra A given the data G, $P(A|G)$. We find the spectra which maximizes $P(A|G) \propto P(A)P(G|A)$ with the prior probability $P(A)$ defined so that A has only those correlations that are required to reproduce the data G. To define the likelihood function $P(G|A)$, we take advantage of the statistical sampling nature of the QMC process.
In this chapter, we will present a short pedagogical development of the MEM to analytically continue QMC data. A more detailed review has been presented previously [8], and to the extent possible, we will follow the notation used there. This chapter is organized as follows: In Sec. 2, we will present the MEM formalism. In Sec. 3, the Bryan MEM algorithm will be sketched, which has been optimized for this type of problem. In Sec. 4, we will illustrate these techniques with the spectra of the Periodic Anderson and Hubbard models, described below, and finally in Sec. 5, we will conclude.

2 Formalism

2.1 Green's functions

When a system is perturbed by an external field which couples to an operator B, the linear response to this field is described by the retarded Green's function

$$G(t) = -i\Theta(t) \left\langle \left[B(t), B^\dagger(0)\right]_\pm \right\rangle \tag{3}$$

where the negative (positive) sign is used for Boson (Fermion) operators B and $B^\dagger$, and makes reference to the Dirac (anti)commutator. The Fourier transform, $G(z)$, of $G(t)$ is analytic in the upper half plane, and its real and imaginary parts are related by

$$G(z) = \int d\omega \, \frac{\frac{-1}{\pi}\mathrm{Im}G(\omega)}{z-\omega} \, . \tag{4}$$

The Matsubara-frequency Green's function $G(i\omega_n)$ is obtained by letting $z \rightarrow i\omega_n$ in Eq. (4). This may be Fourier transformed to yield a relation between the Matsubara-time Green's function produced by the QMC procedure, and $\frac{-1}{\pi}\mathrm{Im}G(\omega)$

$$G(\tau) = \int d\omega \, \frac{\frac{-1}{\pi}\mathrm{Im}G(\omega)e^{-\tau\omega}}{1 \pm e^{-\beta\omega}} \, . \tag{5}$$

2.2 Bayesian statistics

We use our QMC algorithm to generate a set $\bar{G}_l^i$ of $i = 1, \ldots, N_d$ estimates for the Green's function at each time τ_l or frequency ω_l, $l = 1, \ldots, L$. Since many functions A correspond to the same data $\bar{G}$, we must employ a formalism to determine which $A(\omega)$ is the most probable, given the statistics of the data and any prior information that we have about A. To quantify the conditional probability of A given the data, and our prior knowledge, we use Bayesian statistics. If we have two events a and b, then according to Bayes theorem the joint probability of these two events is

$$P(a,b) = P(a|b)P(b) = P(b|a)P(a)\,, \tag{6}$$

where $P(a|b)$ is the conditional probability of a given b. The probabilities are normalized so that

$$P(a) = \int dbP(a,b) \quad \text{and } 1 = \int daP(a)\,. \tag{7}$$

In our problem, we search for the spectrum A which maximizes the conditional probability of A given the data $\bar{G}$,

$$P(A|\bar{G}) = P(\bar{G}|A)P(A)/P(\bar{G})\,. \tag{8}$$

Typically, we call $P(\bar{G}|A)$ the likelihood function, and $P(A)$ the prior probability of A (or the prior). Since we work with one set of QMC data at a time, $P(\bar{G})$ is a constant during this procedure, and may be ignored. The prior and the likelihood function require significantly more thought, and will be the subject of the next two subsections.

2.3 Prior probability

We can define a prior probability for positive-definite normalizable spectra. For Bosonic Green's functions, we may define positive definite spectra if we redefine the kernel, e.g.,

$$K(\tau,\omega) = \frac{\omega[e^{-\tau\omega} + e^{-(\beta-\tau)\omega}]}{1-e^{-\beta\omega}} \qquad \text{or} \qquad K(i\omega_n,\omega) = \frac{\omega^2}{\omega^2+\omega_n^2} \tag{9}$$

with $A(\omega) = \frac{-1}{\pi\omega}\mathrm{Im}G(\omega) \geq 0$ for Bosons. We modified the kernel to account for the symmetry of the Bosonic data $G(\tau) = G(\beta-\tau)$ or $G(i\omega_n) = G(-i\omega_n)$ and the spectrum $A(\omega) = A(-\omega)$. Note that the kernel is non-singular at $\omega = 0$ and the spectral density $A(\omega)$ is positive definite. For Fermionic Green's functions the spectra are already positive definite

$$K(\tau,\omega) = \frac{\exp(-\tau\omega)}{1+\exp(-\beta\omega)} \qquad \text{or} \qquad K(i\omega_n,\omega) = \frac{1}{i\omega_n-\omega} \tag{10}$$

with $A(\omega) = \frac{-1}{\pi}\mathrm{Im}G(\omega) \geq 0$ for Fermions. We may also define positive definite spectra for more exotic cases, such as for the Nambu off-diagonal Green function G_{12}. Since the corresponding spectrum $A_{12}(\omega) = \frac{-1}{\pi}\mathrm{Im}G_{12}(\omega)$ is not positive definite, we enforce positivity by adding a positive real constant b

$$G_{12}(\tau) + b\int d\omega K(\tau,\omega) = \int d\omega K(\tau,\omega)\left(A_{12}(\omega)+b\right)\,. \tag{11}$$

Here, we may incorporate the symmetry of the spectrum $A_{12}(\omega) = -A_{12}(-\omega)$ and the data $G_{12}(\tau) = -G_{12}(\beta - \tau)$ by modifying the kernel

$$K(\tau, \omega) = \frac{e^{-\tau\omega} - e^{-(\beta-\tau)\omega}}{1 + \exp(-\beta\omega)} \; . \tag{12}$$

With this kernel, the equation takes the canonical form Eq. (1), if we identify

$$A(\omega) = A_{12}(\omega) + b \text{ , and } \quad G(\tau) = G_{12}(\tau) + b \int d\omega K(\tau, \omega) \, . \tag{13}$$

The value of b is determined by optimizing its posterior probability as discussed below. In each of the Bosonic, Fermionic and Anomalous cases,

$$\int_{-\infty}^{\infty} d\omega A(\omega) < \infty \, . \tag{14}$$

Although not required, it is convenient to normalize each of the spectral functions to one. This is possible if we know the integral of the spectrum from other QMC measurements or if we know the high frequency limit analytically (see Sec. 4.6). These positive-definite normalized spectra A may be reinterpreted as probability densities.
Skilling [10] argues that the prior probability for such an unnormalized probability density is proportional to $\exp(\alpha S)$ where S is the entropy defined relative to some positive-definite function $m(\omega)$

$$S = \int d\omega \Big[A(\omega) - m(\omega) - A(\omega) \ln \left(A(\omega)/m(\omega) \right) \Big] \approx \sum_{i=1}^{N} A_i - m_i - A_i \ln \left(A_i/m_i \right) \; , \tag{15}$$

where $A_i = A(\omega_i) \, d\omega_i$, $i = 1, \ldots, N$. Thus, the prior is conditional on two as yet unknown quantities $m(\omega)$ and α

$$P(A|m, \alpha) = \exp \left(\alpha S \right) \; . \tag{16}$$

$m(\omega)$ is called the default model since, in the absence of data $\bar{G}$, $P(A|\bar{G}, m, \alpha) \propto P(A|m, \alpha)$, so the optimal A is equal to m. The choice of α will be discussed in Sec. 3.5.
Rather than trying to repeat Skilling's arguments here for the entropic form of $P(A|m, \alpha)$, we argue that this form yields the desired effects:

1. it enforces positivity of A,

2. it requires that A only have correlations which are required to reproduce the data $\bar{G}$, and

3. it allows us to introduce prior knowledge about the the spectra (e.g., exact results at high frequencies) in the default model.

The first effect follows from the form of $P(A|m, \alpha)$, assuming that m is positive definite. The third effect will be discussed in Sec. 4.5.

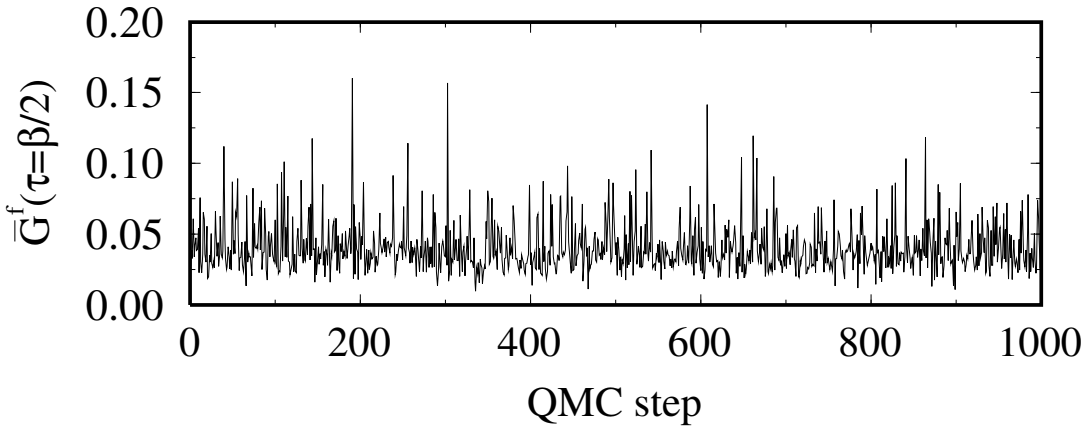

Fig. 1: *f-electron local Green's function $\bar{G}^f(\tau = \beta/2)$ plotted as a function of the QMC step for a symmetric periodic Anderson Model with $U = 2$, $V = 0.6$, and $\beta = 20$.*

2.4 Likelihood function

The form of the likelihood function is dictated by the central limit theorem, which for the purposes of this chapter may be illustrated with the following example. Suppose we use our QMC algorithm to generate N_d measurements of the Green's function $\bar{G}_l^i$ (where l is an integer from 1 to L, and i an integer from 1 to N_d). According to the central limit theorem, if each of these measurements is completely independent of the others, then, in the limit of large N_d, the distribution of $\bar{G}_l$ will approach a Gaussian, and the probability of a particular value G_l is given by

$$P(G_l) = \frac{1}{\sqrt{2\pi}\sigma} e^{-\chi^2/2}\,, \tag{17}$$

where

$$\chi^2 = \frac{1}{\sigma^2}\left(\frac{1}{N_d}\sum_{i=1}^{N_d}\bar{G}_l^i - G_l\right)^2 = \frac{1}{\sigma^2}\left(\langle\bar{G}_l\rangle - G_l\right)^2\,, \quad \sigma^2 = \frac{1}{N_d(N_d-1)}\sum_i\left(\langle\bar{G}_l\rangle - \bar{G}_l^i\right)^2\,,$$

and the angular brackets indicate an average over the bins of data

Of course, in the QMC process each of the measurements is not independent of the others. Correlations exist between adjacent measurements ($\bar{G}_l^i$ and $\bar{G}_l^{i+1}$) in the QMC process, and between the errors of the Green's function at adjacent time slices ($\bar{G}_l^i$ and $\bar{G}_{l+1}^i$) at the same QMC step. The removal of these correlations is the most critical step in the MEM analytic continuation procedure.

Correlations between adjacent measurements are illustrated in Fig 1 where measurements of $\bar{G}^f(\tau = \beta/2)$ are plotted as a function of the QMC step. Clearly, the data from adjacent QMC steps is correlated and the data are skewed since the Green's function is bounded from below ($\bar{G}_l^i > 0$). As a result the data are not Gaussianly distributed, as shown in Fig. 2(a). Here, a histogram of the data is compared to a Gaussian fit. The deviations from a Gaussian are quantified by the moments of the distribution. The most relevant ones in the present case are the skewness (third moment) and kurtosis (fourth moment) which measure the degree of

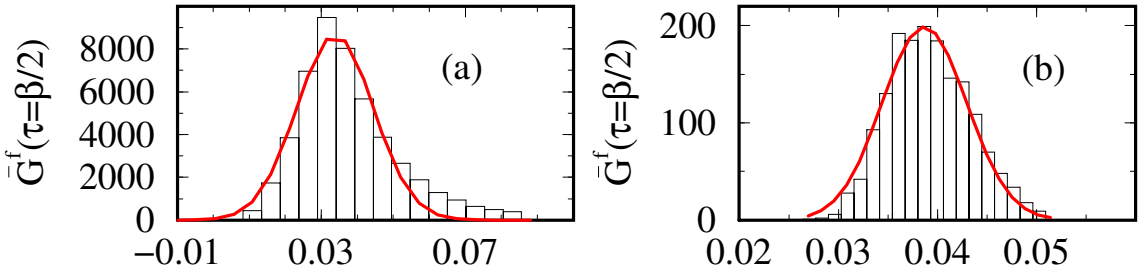

Fig. 2: *Distribution of the data shown in Fig. 1 (a) and after rebinning (b). The solid line is a Gaussian fit. In (b) the data was processed by packing it sequentially into bins of 30 measurements each.*

asymmetry around the mean and the pointedness (or flatness) of the distribution relative to the Gaussian [12]. The data are clearly not Gaussianly distributed, and display significant skew and kurtosis. To deal with this difficulty, we rebin the data. For example, we set $\bar{G}_l^1$ equal to the average of the first 30 measurements, $\bar{G}_l^2$ equal to the average of the next 30 measurements, etc. It is well approximated by a Gaussian fit (the solid line).

The bin size, here 30 measurements, must be chosen large enough so that the bin-averages are uncorrelated, but small enough so that sufficient bins remain to calculate the likelihood function. To determine the smallest bin size that yields uncorrelated data we quantify the deviation of the distribution from a Gaussian by measuring moments of the distribution. Of course, because the data are a finite set, each of these measured moments has some standard deviation (proportional to $1/\sqrt{N_{bins}}$). Thus, one way to determine if the skewness and kurtosis of a distribution are acceptably small is to measure these values relative to what is expected from a Gaussian distribution. We will use such relative values. As the bin size increases, the relative kurtosis and skewness decrease monotonically, indicating the convergence of the distribution to a Gaussian. This behavior is shown in Fig. 3a for the $G(\tau = \beta/2)$ data.

In addition, Fig. 3b shows that the error estimate also converges as the bin size increases. Here, the error estimate is given by

$$\sigma = \sqrt{\left(\langle \bar{G}^2 \rangle - \langle \bar{G} \rangle^2\right) / (N_{bins} - 1)} \tag{18}$$

where angular brackets indicate an average over the bins of data. Because correlations between successive Monte Carlo measurements always make this error-estimate smaller than the actual value, this error estimate should initially increase monotonically with bin size, as shown. This behavior is easily understood by considering a perfectly correlated sample where the data in each bin is identical. Clearly, for this perfectly correlated sample, the error estimate would be zero. As the bins become uncorrelated, the error estimate increases. With independent data and a large number of equally sized bins, eventually $\sigma^2 \sim 1/N_{bins}$. However, with a fixed amount of data, as is typical with a QMC simulation, increasing the bin size decreases N_{bins} proportionally, and the error estimate can saturate as illustrated in Fig. 3b. Thus, the saturation of the error estimate indicates that the correlations between Monte Carlo measurements, i.e., between bin averages, have been removed. The point at which saturation occurs in a plot like

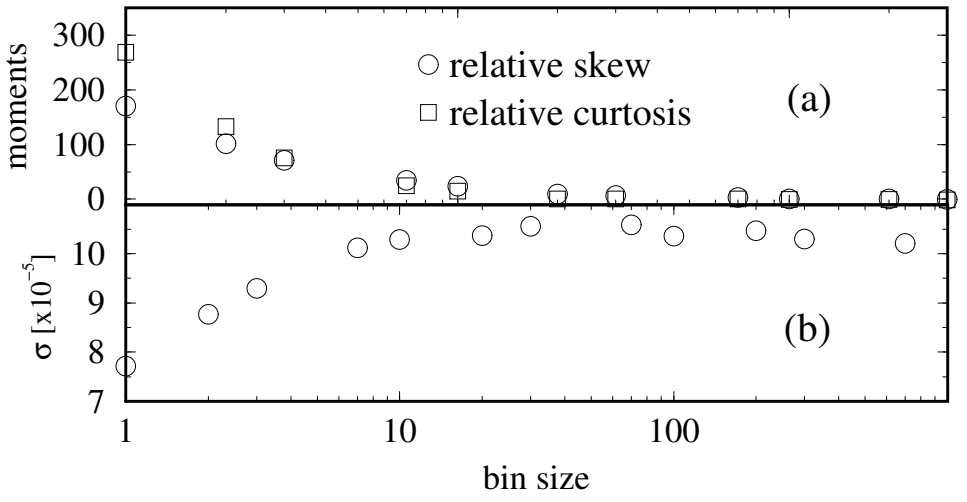

Fig. 3: *Relative kurtosis and skew (a) and error bar (b) of the data shown in Fig. 1 as a function of bin size. Here the total amount of data is fixed, so increasing the bin size decreases N_{bins} proportionately. As the bin size increases to about 30, the relative kurtosis and skew decrease to roughly zero and the error bar saturates, indicating that the bins are uncorrelated samples and that the data has become Gaussianly distributed.*

Fig. 3b provides a useful first estimate of the minimum bin size required to remove correlations between the bins. In general, one should perform this test for the Green's function at all times τ_l; however, we have found it is often sufficient to perform this test at only a few times. For the remainder of this section, we will assume that the bin size is sufficiently large so that both the error estimate and the moments of the distribution have converged to values which indicate that the data are both statistically independent and Gaussian-distributed.

Now, only the errors in the Green's function $\bar{G}$ at adjacent time slices remain correlated. This correlation may be seen by comparing the results from a single measurement with the essentially exact values obtained from averaging over many measurements. Such a comparison is shown in Fig. 4 where, if the result from a single measurement differs from the essentially exact result at a certain value of τ, then the results at adjacent values of τ also tend to deviate from the exact results in a similar way. These correlations of the error in Matsubara time are characterized by the covariance

$$C_{lk} = \frac{1}{N_{bins}(N_{bins}-1)} \sum_{j=1}^{N_{bins}} (\langle \bar{G}_l \rangle - \bar{G}_l^j)(\langle \bar{G}_k \rangle - \bar{G}_k^j)\,. \tag{19}$$

If C is diagonal, then according to the central limit theorem, the likelihood function is $P(\bar{G}|A) = \exp[-\chi^2/2]$ where

$$\chi^2 = \sum_{l=1}^{L} \left(\frac{\bar{G}_l - \sum_j K_{l,j} A_j}{\sigma_l} \right)^2 . \tag{20}$$

and σ_l^2 are the diagonal elements of C. However, in general, the covariance matrix C_{ij} is not diagonal because errors at different values of τ are correlated. To define a meaningful measure of how well A_i reproduces the data, we must find the transformation $\mathbf{U}$ which diagonalizes the

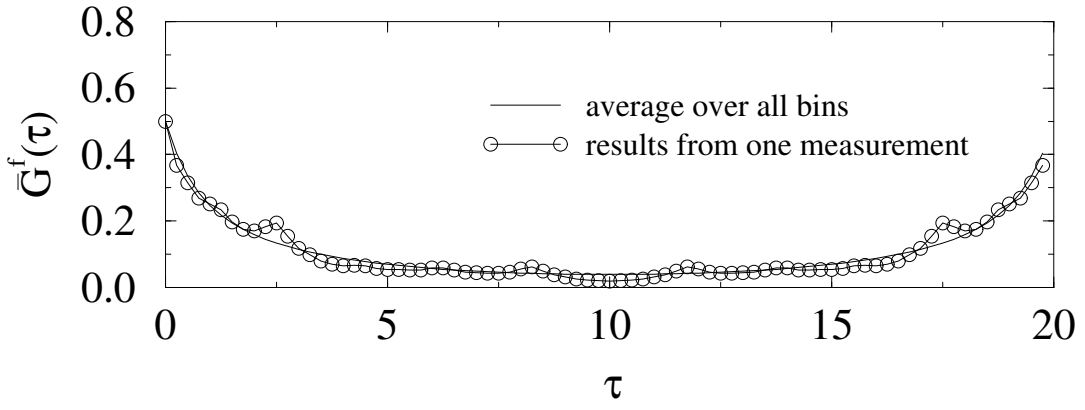

Fig. 4: *$\bar{G}^f(\tau)$ from one measurement compared to $\bar{G}^f(\tau)$ obtained from the average over 800 bins of data, each containing 1520 measurements. If the result from a single measurement at a certain point differs from the essentially exact result obtained by averaging over many bins, then the results at adjacent points also deviate from the exact results.*

covariance matrix

$$\mathbf{U}^{-1}\mathbf{C}\mathbf{U} = \sigma_i'^2 \delta_{ij} \,. \tag{21}$$

Both the data and kernel are now rotated into this diagonal representation

$$\mathbf{K}' = \mathbf{U}^{-1}\mathbf{K} \qquad \bar{\mathbf{G}}' = \mathbf{U}^{-1}\bar{\mathbf{G}} \,. \tag{22}$$

and each measurement $\bar{G}_i'$ is statistically independent. Therefore, we can use

$$\chi^2 = \sum_l \left(\frac{\bar{G}_l' - \sum_j K_{l,j}' A_j}{\sigma_l'} \right)^2 . \tag{23}$$

to measure the misfit between the spectrum and the data and to define the likelihood function.

Cautionary Notes. We find that the proper preparation of the data by removing correlations is the most critical step in the MEM procedure. If the data are uncorrelated or the covariance is calculated and diagonalized correctly, then the resulting spectra will be reliable (however, for weak data, it will show a significant bias towards the default model). If not, then the Gaussian form of the likelihood function is unjustified and the resulting spectra will generally have spurious features.

However, care must be taken when calculating and diagonalizing the covariance. First, Since the set of data is finite, it is necessary to balance the need of removing the correlations in imaginary-time with the need of removing the correlations between Monte Carlo steps. To remove the correlations in Monte Carlo steps the bin size must be large; however, to calculate the covariance accurately, many bins of data are required. If there are not enough bins of data, then the covariance and (as shown in Fig. 5) its eigenvalue spectrum can become pathological. The reason for this pathology is that when we diagonalize the covariance matrix, we are asking for L independent eigenvectors. We must have enough bins of data to determine these directions

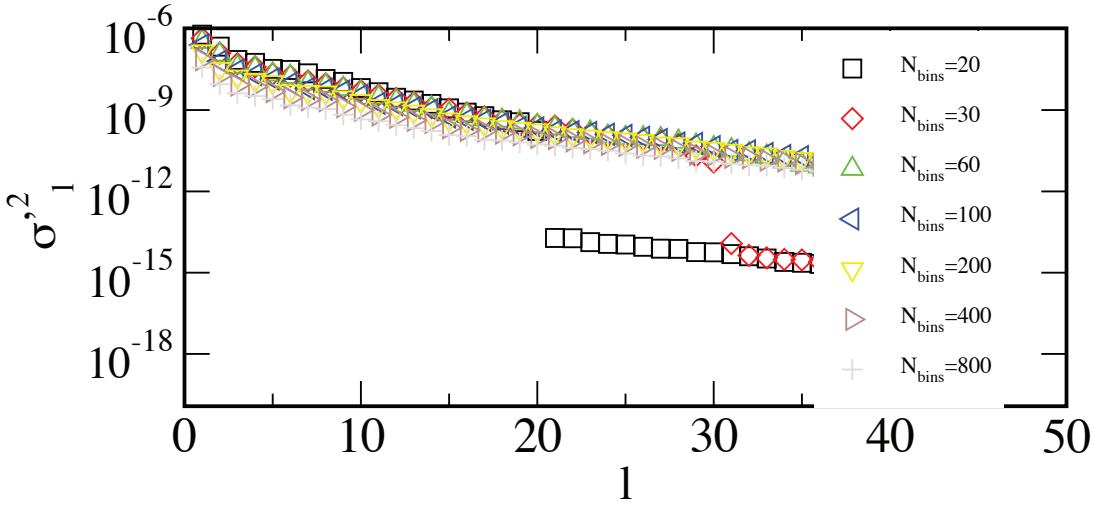

Fig. 5: *Eigenvalue spectra of the covariance of G^f for different numbers of bins of data. Each bin contains 100 measurements and $L = 41$. When $N_{bins} \lesssim 2L$, σ'^2_l develops a sharp break.*

so that N_{bins} must be greater than or equal to L. In fact, since the information contained in a given bin of data is not completely independent from the other bins, we must have $N_{bins} > L$. Otherwise, as shown in Fig. 5, where $L = 41$, the eigenvalue spectrum displays a sharp break when $N_{bins} < L$, indicating that only a finite number of directions, less than L, are resolved. The small eigenvalues after the break are essentially numerical noise and yield artifacts in the spectra. Simply throwing away the small eigenvalues and their associated eigenvectors does not cure the difficulty since the small eigenvalues and eigenvectors contain the most precise information about the solution. Thus, the only reasonable thing to do is to increase the number of bins. Empirically, we find that we need

$$N_{bins} \geq 2L \tag{24}$$

in order to completely remove the pathology of the sharp break in the eigenvalues [13]. Second, as illustrated in Fig. 4 adjacent data in time tend to be highly correlated. These correlations grow as the time step used in the QMC calculation is reduced, making the rows and columns of the covariance more correlated. Eventually, the covariance becomes ill conditioned and cannot be diagonalized. Such severe oversampling of the Green function data does not provide more information, but a small time step may be useful for other reasons (such as reducing Trotter errors). In this case we can fix the problem by eliminating some fraction of the data e.g., taking the data from every other time step.

2.5 Details of the MEM Formalism

We will now construct the formalism to locate the most likely spectrum $\hat{A}$ and set the value of α. The first step is to normalize the likelihood function $P(\bar{G}|A)$ and the prior $P(A|\alpha, m)$. Here it will be necessary to integrate over the space of all spectra A_i. This is done with Gaussian approximations to the integrals. Following Skilling and Bryan [14], we employ a measure

$d^N A/\prod_i \sqrt{A_i}$ which amounts to a change of variables to a space where the entropy S, Eq. (15), has no curvature [8]. For example, the normalized prior probability is

$$P(A|\alpha, m) = \frac{1}{Z_S} \exp\left\{\alpha\left(-\sum A_i \ln A_i/m_i - A_i + m_i\right)\right\} \tag{25}$$

where

$$Z_S = \int \frac{d^N A}{\prod_i \sqrt{A_i}} \exp\left\{\alpha\left(-\sum A_i \ln A_i/m_i - A_i + m_i\right)\right\} . \tag{26}$$

The integrand is maximized when $S = 0$, i.e., when $A = m$. We approximate the integral by expanding the argument of the exponent to second order around this maximum, $S \approx \frac{1}{2}\delta A^T \nabla\nabla S|_{A=m} \delta A = -\frac{1}{2}\delta A^T \{1/m\} \delta A$, where $\{1/m\}$ is the diagonal matrix with finite elements composed of $1/m_i$, and δA is the vector $A - m$.

$$Z_S \approx \int \frac{d^N A}{\prod_i \sqrt{A_i}} \exp\left\{\alpha\left(-\frac{1}{2}\delta A^T \{1/m\} \delta A\right)\right\} . \tag{27}$$

We define a change of variables, so that $dy_i = dA_i/\sqrt{A_i}$ and find

$$Z_S \approx \int d^N y \exp\left\{\alpha\left(-\frac{1}{2}\delta y^T \{m\}^{1/2} \{1/m\} \{m\}^{1/2} \delta y\right)\right\} = (2\pi/\alpha)^{N/2} \tag{28}$$

The likelihood function must also be normalized

$$P(\bar{G}|A) = e^{-\chi^2/2}/Z_L \tag{29}$$

where

$$\chi^2 = \sum_l \frac{\left(\bar{G}'_l - \sum_i K'_{li} A_i\right)^2}{\sigma'^2_l} \tag{30}$$

where K' and $\bar{G}'$ are the kernel and data rotated into the data space where the covariance is diagonal, and σ'^2_l are the eigenvalues of the covariance. If we let $G_l = \sum_i K'_{li} A_i$, then

$$Z_L = \int d^L G \exp\left\{\frac{1}{2}\sum_{l=1}^{L} \frac{\left(\bar{G}'_l - G_l\right)^2}{\sigma'^2_l}\right\} = (2\pi)^{L/2} \prod_l \sigma'_l \tag{31}$$

Using Bayes theorem, we find

$$\begin{aligned} P(A, G|m, \alpha) &= P(G|A, m, \alpha) P(A|m, \alpha) \\ &= P(A|G, m, \alpha) P(G|m, \alpha) \end{aligned} \tag{32}$$

or

$$P(A|G, m, \alpha) \propto P(G|A, m, \alpha) P(A|m, \alpha) = \frac{\exp(\alpha S - \chi^2/2)}{Z_S Z_L} \tag{33}$$

Since the normalization factors Z_S and Z_L are independent of the spectrum, for fixed α and data, the most probable spectrum $\hat{A}(\alpha)$ is the one which maximizes $Q = \alpha S - \chi^2/2$. An algorithm to find this spectrum is discussed in Sec. 3. However, the question of how to select α and the default model remains.

2.5.1 Selection of α

The selection of α strongly affects the choice of the optimal spectrum [15] since α controls the competition between S and χ^2. If α is large, the entropy term is emphasized and the data cannot move the spectrum far from the model. If α is small, then the least square misfit between the spectrum and the data is minimized so that $\chi^2 \ll L$. The numerical error in the QMC data then begins to dominate the solution and the spectra displays random oscillations and noise. Thus, it is important to find a sensible way of selecting α. Typically, α is selected in one of three ways described below.

Historic MEM [16,14] In the historic method, α is adjusted so that $\chi^2 = L$. The justification for this is that if the spectrum is known and the data was repeatedly measured, then the misfit between the data and the spectrum $\chi^2 = L$ on average. However, the data are only measured once and the spectrum is not known *a priori*. Also, setting $\chi^2 = L$ tends to under-fit the data since good data can cause structure in the spectrum which reduces χ^2 from L. Thus, there is little reason to believe that α can be chosen without input from the data itself.

Classic MEM [15] A more appropriate method of setting α is to choose the most probable value, defined by maximizing

$$P(\alpha|\bar{G},m) = \int \frac{d^N A}{\prod_i \sqrt{A_i}} P(A,\alpha|\bar{G},m)\,. \tag{34}$$

The integrand

$$P(A,\alpha|\bar{G},m) = P(A|\bar{G},m,\alpha)P(\alpha) \propto \frac{\exp(\alpha S - \chi^2/2)}{Z_S Z_L} P(\alpha) \tag{35}$$

involves the prior probability of α. Jeffreys [17] argues that since χ^2 and S have different units, α is a scale factor. He asserts that in lieu of prior knowledge, it should have the simplest scale invariant form $P(\alpha) = 1/\alpha$. Thus,

$$P(\alpha|\bar{G},m) = \int \frac{d^N A}{\prod_i \sqrt{A_i}} \frac{\exp(\alpha S - \chi^2/2)}{Z_S Z_L \alpha} = \frac{Z_Q}{Z_S Z_L \alpha} \tag{36}$$

Z_Q is calculated in a similar fashion as Z_S. We expand about the maximum of Q at $A = \hat{A}$ so that $\exp\{\alpha S - \chi^2/2\} \approx \exp\{Q(\hat{A}) + \frac{1}{2}\delta A^T \, \nabla\nabla Q|_{\hat{A}} \, \delta A\} = \exp\{Q(\hat{A}) + \frac{1}{2}\delta A^T \{\frac{1}{2} \, \nabla\nabla\chi^2|_{\hat{A}} - \{\alpha/\hat{A}\}\}\delta A\}$. We again make a Gaussian approximation to the integral, and if λ_i are the eigenvalues of $\frac{1}{2}\{A^{1/2}\} \, \nabla\nabla\chi^2|_{\hat{A}} \, \{A^{1/2}\}$, then

$$P(\alpha|\bar{G},m) = \frac{1}{W_\alpha} \prod_i \left(\frac{\alpha}{\alpha+\lambda_i}\right)^{1/2} \frac{e^{Q(\hat{A})}}{\alpha} \tag{37}$$

where

$$W_\alpha = \int \frac{d\alpha}{\alpha} \prod_i \left(\frac{\alpha}{\alpha+\lambda}\right)^{1/2} e^{Q(\hat{A})}\,. \tag{38}$$

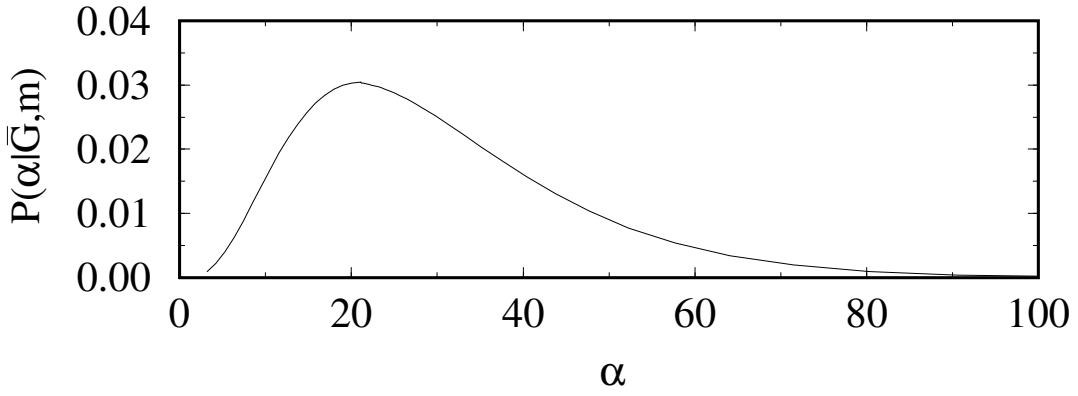

Fig. 6: *The posterior probability $P(\alpha|\bar{G}, m)$ as a function of α for the periodic Anderson model data presented in Fig. 1. Since $P(G|I)$ is unknown, the magnitude of the ordinate is also unknown. The distribution is wide, so many reasonable values of α exist. The distribution is also skewed, so the value of α at the peak is not representative of the mean.*

The optimal α, $\hat{\alpha}$, may be determined by the condition

$$\frac{\partial P(\alpha|\bar{G}, m)}{\partial \alpha} = 0\,. \tag{39}$$

For strong data, $P(\alpha|\bar{G}, m)$ is dominated by the product and $\exp Q(\hat{A})$ so that

$$-2\hat{\alpha}S \approx \sum_i \frac{\lambda_i}{\hat{\alpha} + \lambda_i}\,. \tag{40}$$

Each λ_i which is much greater than $\hat{\alpha}$ contributes one to the sum and hence one to the number of good observations in the data. If the number $N_{good} = -2\hat{\alpha}S$ is large, then $P(\alpha|\bar{G}, m)$ is very sharp and the spectra corresponding to $\alpha = \hat{\alpha}$ is a good approximation of the spectra which has been properly averaged over $P(\alpha|\bar{G}, m)$.

Bryan's Method [19] that $N_{good} \ll L$. Then $P(\alpha|\bar{G}, m)$ is a broad and highly skewed distribution. For example, $P(\alpha|\bar{G}, m)$ for the data shown in Fig. 1 is plotted in Fig. 6. The distribution is wide, so many reasonable values of α exist. The distribution is also skewed, so the value of α at the peak is not representative of the mean. To deal with this, Bryan [19] calculates the optimal spectrum $\hat{A}(\alpha)$ for each α. The solution is taken to be

$$\bar{A} = \int d\alpha \hat{A}(\alpha) P(\alpha|\bar{G}, m)\,. \tag{41}$$

These three MEM methods will produce essentially identical results if the data are uncorrelated and precise. However, when the data are less precise but still uncorrelated, the method suggested by Bryan, averaging $\hat{A}(\alpha)$ weighted by $P(\alpha|G, m)$, generally produces more acceptable results and converges to a good result faster than the classic method and much faster than the historic method as the data is improved. A further advantage of the averaging is that it allows an accurate relative assessment of the posterior probability ($\int_0^\infty d\alpha P(m|G, \alpha)$) of the default model. This information is invaluable in determining which default model yields the most likely A.

Cautionary Notes. Some care must be used when working with Classic MEM and Bryan's method. Both rely on the accuracy of Eq. (37) for $P(\alpha|\bar{G},m)$, which is calculated with a Gaussian approximation which is only accurate if Q is a sharply peaked function in the space of all images. This approximation clearly fails when $\alpha \to 0$. Here there is no regularization and infinitely many spectra will produce the same Q, so it is flat, not sharply peaked, in these directions. In this case, the algorithm can reach a run-away condition where it tends toward small values of α, the approximation for $P(\alpha|\bar{G},m)$ fails causing the calculation to tend towards ever smaller values of α. This condition is easily identified in the calculation, and it can be cured by increasing the quality of the data or by choosing a better default model (a Bryan or classic MEM calculation with a *perfect* default model will always tend toward a solution with large α), using the methods described below, or the annealing method described in the example Sec. 4.5.

2.6 Model selection

Bayesian statistics may also be employed to select the default model. I.e. if we must choose between different models, or set parameters used to define a default model function, then we choose these models or parameters based upon the posterior probability of the model

$$P(m|\bar{G}) = \int d\alpha P(\alpha|m,\bar{G})P(m)\,. \tag{42}$$

We see no *a priori* reason to favor one default model over another, so we typically set the prior probability of the model $P(m)$ =constant. Then the integrand in Eq. (42) is given by Eq. (37) so that

$$P(m|\bar{G}) \propto W_\alpha\,. \tag{43}$$

Since the prior probability of the model is unknown, $P(m|\bar{G})$ determines only the relative probability of two models and, by inference, the relative probability of their corresponding spectra.

Cautionary Notes. It can be tempting to try very informative models, such as the uncorrelated spectrum with sharp distinct features. Such default models will often have high posterior probabilities $P(m|\bar{G})$ but should nevertheless be avoided unless one can be sure, i.e., *certain*, that the sharp features are real. For example, a model with a delta function peak, has a huge amount of information, whereas the information from the QMC data is quite finite and may not be able to correct a wrong delta-function feature in the model. In this respect, again, the annealing technique described later is ideal.

2.7 Error propagation

To absolutely quantify the spectrum, we need to assign error bars to it. In the quadratic approximation, the probability of the spectral density is

$$P(A|\bar{G},m,\alpha) \propto e^{-\frac{1}{2}\delta A^T\cdot\nabla\nabla Q|_{\hat{A}}\cdot\delta A}\,, \tag{44}$$

thus the covariance of the spectral density is

$$\langle \delta A(\omega)\delta A(\omega')\rangle = -\left(\nabla\nabla Q|_{\hat{A}}\right)^{-1} . \tag{45}$$

It is not possible to assign error bars to each point in the spectral density since this matrix is generally not diagonal. Thus errors between different points are strongly correlated. Also, A_i represents the spectral probability within some region of finite width and hence lacks meaning at a specific value of ω. However, it is possible to assign error bars to integrated functions of the spectral density such as [18],

$$H = \int d\omega A(\omega)h(\omega) . \tag{46}$$

where $h(\omega)$ is an arbitrary function of ω. The error of H may be associated with the covariance of the spectral density $\langle \delta A(\omega)\delta A(\omega')\rangle$

$$\left\langle (\delta H)^2 \right\rangle = \int\int d\omega d\omega'\, h(\omega)h(\omega') \left\langle \delta A(\omega)\delta A(\omega')\right\rangle . \tag{47}$$

The matrix $\nabla\nabla Q|_{\hat{A}}$ is readily available because it is used as the Hessian of the Newton search algorithm typically used to find the optimal spectral density.

Cautionary Notes. Care should be taken in the interpretation of the error bars, especially if a highly informative default model is used. Suppose for example the data is weak, but a default model in essentially exact agreement with the data is used, then as discussed above, a large α solution will be found corresponding to a Q with small curvature in the space of images, and hence very small error bars. This does not necessarily mean that the resulting spectrum is accurate though, it just means that the default model is one of many which is consistent with the weak data. Unless the information in a default model is known to be accurate (such as the spectra from a higher temperature, or one which becomes exact at high frequencies), such highly informative default models should generally be avoided.

3 Bryan's method: a MEM algorithm

We will now sketch Bryan's numerical algorithm to find the optimal spectrum. For a more detailed description, we refer the reader to his paper [19]. We have found his algorithm to be very appropriate for the numerical analytic continuation problem for two reasons: First, due to the exponential nature of the kernel which relates A to the data $\bar{G}$, we typically have $L \gg N_{good}$. Thus, the problem is usually "oversampled." Bryan tailored his numerical algorithm [19] to this type of problem by working in a reduced space whose dimension is determined by singular-value-decomposition of the kernel K and is equal to the largest possible number of good, i.e. numerically significant, singular values which may parametrize the solution. The dimension of this space is usually much less than the number of A_i, and we found the computational advantage over methods that use the entire space determined by the number of A_i to be significant.

Second, for the analytic continuation problem, the approximation of setting α equal to its optimal value is questionable because of the wide range of reasonably acceptable values of α. Bryan deals with this by calculating a result which is averaged over $P(\alpha|G,m)$.

3.1 Typical algorithms

What distinguishes Bryan's numerical algorithm from its predecessors is the way in which the space of possible solutions is searched. Typical algorithms search for an optimal A by stepping through the entire space of A

$$A \rightarrow A + \delta A \tag{48}$$

with

$$\delta A = -(\nabla\nabla Q)^{-1}\nabla Q\,. \tag{49}$$

The Hessian $(\nabla\nabla Q)^{-1}$ is

$$(\nabla\nabla Q)^{-1} = (\alpha\nabla\nabla S - \nabla\nabla L)^{-1} = \left(\alpha\{A\}^{-1} - \nabla\nabla L\right)^{-1}\,. \tag{50}$$

where $\{A\}$ is a diagonal matrix with the elements of A along its diagonal. It may conceptually be expanded using the binomial theorem so that $(\nabla\nabla Q)^{-1}$ may be written as a power series in $\{A\}\nabla\nabla L$. Thus, δA may be written as a combination of $\{A\}\nabla Q = \{A\}\left(\alpha\nabla S - \nabla L\right)$, and powers of $\{A\}\nabla\nabla L$ acting on $\{A\}\nabla S$ and $\{A\}\nabla L$. Each of these vectors defines a direction in which the search can proceed. Typically, between three and ten directions are used; however, these directions are often inappropriate for the problem at hand, because as mentioned earlier, the space of all possible solutions is too large for such oversampled data.

3.2 Singular-space algorithm

To alleviate this problem, Bryan performs a singular-value decomposition (SVD) of the kernel K, i.e., $K = V\Sigma U^T$ where U and V are orthogonal matrices and Σ is a diagonal matrix, and works in the resulting singular space. To see that this space still contains the solution, we consider

$$\nabla L = \frac{\partial F}{\partial A}\frac{\partial L}{\partial F} = K^T\frac{\partial L}{\partial F} \tag{51}$$

where $F = KA$. We see that ∇L lies in the vector space defined by the columns of K^T. We next perform a SVD on K and assume the diagonal elements of Σ are ordered from largest to smallest. The smallest elements are essentially zero (to the numerical precision of the computer) since the kernel is effectively singular. However, s of the elements are assumed finite. Now the vector space spanned by the columns of K^T is the same as the space spanned by the columns of U associated with the non-singular values. Bryan calls this reduced space the *singular space*. Thus, to the precision that can be represented on the computer, $\{A\}\nabla L$ and all of the search directions formed by acting with $\{A\}\nabla\nabla L$ lie in the singular space spanned by the columns of $\{A\}U_s$, where U_s is the singular space projection of U. The only direction not in this space is $\{A\}\nabla S$. Thus, Bryan's algorithm works in *at most* an $s+1$-dimensional subspace of the N-dimensional space of A.

In this singular space, the condition for an extremum of Q, $\nabla Q = 0$, is

$$\alpha \nabla S - \nabla L = 0 \rightarrow -\alpha \ln (A_i/m_i) = \sum_j K_{ji} \frac{\partial L}{\partial F_j} \,. \tag{52}$$

Thus, the solution may be represented in terms of a vector u

$$\ln (A/m) = K^T u \,. \tag{53}$$

Unless K is of full rank, so that $s = N$, the components of u will not be independent. However, since K^T and U share the same vector space and since most of the relevant search directions lie in the singular space, Bryan proposes that the solution be represented in terms of U and u as

$$A_i = m_i \exp \sum_n U_{in} u_n \,. \tag{54}$$

Thus, to the precision to which it may be represented on the computer and determined by SVD, the space u must contain the solution defined by $\nabla Q = 0$, and the search can be limited to this s-dimensional space.

Bryan's algorithm proceeds by first reducing all the relevant matrices to the singular space. With the definitions $K = V \Sigma U^T$ and $\log(A/m) = Uu$, the condition for an extremum becomes

$$-\alpha U u = U \Sigma V^T \frac{\partial L}{\partial F} \,, \tag{55}$$

or

$$-\alpha u = \Sigma V^T \frac{\partial L}{\partial F} \equiv g \,, \tag{56}$$

where each of these matrices and vectors has been reduced to the singular space (u is now a vector of order s, Σ is an $s \times s$ diagonal matrix, etc.). Bryan then uses a standard Newton's search to find the solution in the singular space, starting from an arbitrary u. The increment at each iteration is given by

$$J \delta u = -\alpha u - g \,, \tag{57}$$

where $J = \alpha I + \partial g / \partial u$ is the Jacobian matrix, I the identity matrix, and

$$\frac{\partial g}{\partial u} = \Sigma V^T \frac{\partial^2 L}{\partial F^2} \frac{\partial F}{\partial A} \frac{\partial A}{\partial u} \,. \tag{58}$$

With the definition $W = \partial^2 L / \partial F^2$ (which is just the diagonal matrix with elements $1/\sigma_l'^2$), $M = \Sigma V^T W V \Sigma$, and $T = U^T A U$. M and T are symmetric $s \times s$ matrices, the Jacobian $J = \alpha I + MT$, and

$$(\alpha I + MT)\, \delta u = -\alpha u - g \tag{59}$$

At each iteration δu must be restricted in size so that the algorithm remains stable. Thus, another parameter μ (a Marquart-Levenberg parameter) is added

$$[(\alpha + \mu) I + MT]\, \delta u = -\alpha u - g \tag{60}$$

and adjusted to keep the step length $\delta u^T T \delta u$ below some the limit

$$\delta u^T T \delta u \leq \sum_i m_i \tag{61}$$

so the search is within the range of validity of a local quadratic expansion of Q.
This search can be made more efficient if Eq. (60) is diagonalized, so that of the order of s operations are required for each α μ pair. First, we diagonalize T

$$TP = P\Gamma \tag{62}$$

where P is an orthogonal matrix and Γ is diagonal with finite elements γ_i. Then we define

$$B = \{\gamma^{1/2}\} P^T M P \{\gamma^{1/2}\} \tag{63}$$

and solve the second eigenvalue equation

$$BR = R\Lambda \tag{64}$$

where R is orthogonal and Λ the diagonal matrix with finite elements λ_i. Finally, to diagonalize Eq. (60) we define

$$Y = P\{\gamma^{-1/2}\} R\,. \tag{65}$$

Then $Y^{-T} Y^{-1} = T$, and $Y^{-1} M Y^{-T} = \Lambda$, so that

$$Y^{-1}\left[(\alpha+\mu)I + MT\right]\delta u = \left[(\alpha+\mu)I + \Lambda\right] Y^{-1}\delta u = Y^{-1}\left[-\alpha u - g\right] \tag{66}$$

which yields s independent equations for $Y^{-1}\delta u$. Again, as these equations are iterated, μ must be adjusted to keep the step length

$$\delta u^T T \delta u = \left|Y^{-1}\delta u\right|^2 \leq \sum_i m_i\,. \tag{67}$$

3.3 Selection of α

The value α is adjusted so that the solution iterates to either a fixed value of χ^2 (for historic MEM) or to a maximum value of $P(\alpha|G,m)$ given by Eq. (37) (for classic MEM). Then, A is obtained from

$$A_i = m_i \exp\left(\sum_{n=1}^{s} U_{in} u_n\right)\,. \tag{68}$$

Alternatively, Bryan suggests that one may start the algorithm with a large α for which $P(\alpha|\bar{G},m)$ is negligibly small, and then iterate to $\alpha \approx 0$ so that the averaged spectrum may be approximated

$$\langle A\rangle = \int_0^\infty d\alpha P(\alpha|G,m)\hat{A}(\alpha) \tag{69}$$

where $\hat{A}(\alpha)$ is the optimal spectrum (that for which $\nabla Q = 0$) for the value of α specified in the argument. This latter step may be necessary when $P(\alpha|G,m)$ is not a sharply peaked distribution. In fact this is usually the case, as may be seen in Fig. 6.

3.4 Error propagation

As discussed in Sec. 3.7, it is possible to assign error bars to integrated functions of the spectrum $H = \int d\omega A(\omega)h(\omega)$

$$\left\langle (\delta H)^2 \right\rangle = \int\int d\omega d\omega' \, h(\omega)h(\omega') \left\langle \delta A(\omega)\delta A(\omega') \right\rangle \, , \tag{70}$$

where

$$\left\langle \delta A(\omega)\delta A(\omega') \right\rangle = - \left(\nabla\nabla Q|_{\hat{A}} \right)^{-1} \, . \tag{71}$$

This is the inverse of the Hessian of the algorithm discussed above and is easily calculated in terms of singular-space quantities

$$- \nabla\nabla Q|_{\hat{A}} = \{1/A\} U Y^{-T} \{\alpha I + \Lambda\} Y^{-1} U^T \{1/A\} \, . \tag{72}$$

Its inverse

$$- \left(\nabla\nabla Q|_{\hat{A}} \right)^{-1} = \{A\} U Y \left\{ \frac{1}{\alpha + \lambda} \right\} Y^T U^T \{A\} \tag{73}$$

may be used to calculate the error of H, $\sqrt{(\delta H)^2}$ for any α. In principle, one should average the error over $P(\alpha|m, \bar{G})$; however, we find that it is generally adequate to calculate the error of the spectrum at the optimal $\hat{\alpha}$.

We close this section with several practical comments: On a workstation, finding the optimal spectrum by searching in the singular space requires only a few minutes of computer time. This efficiency is in sharp contrast with the amount of computer we needed [20] even on a "supercomputer" for standard Newton algorithms [14] or simulated annealing methods that use the full space of A. We found it essential to use 64 bit arithmetic to obtain stable results. Also, we use LINPACK's [21] singular-value decomposition routine to do the SVD and also to compute any eigenvalues and eigenvectors. The SVD routine in Numerical Recipes [22] and the EISPACK [23] eigenvalue-eigenvector routine RS are not as stable.

4 Case study

In this section, we will demonstrate that it is possible to extract spectral densities from quantum Monte Carlo data that are essentially free from artifacts caused by over fitting to the data and have only small and controllable amounts of statistical error. We will use as an example the electronic spectral densities of the infinite-dimensional periodic Anderson model (PAM). We have already qualified the local Greens function data to remove correlations using the procedure discussed in Sec. 2.4, so we can begin to process the data to obtain the single-particle density of states spectral function.

For the majority of this section, we will consider particle-hole symmetric data $G(\tau) = G(\beta - \tau)$, and spectra $A(\omega) = A(-\omega)$. This prior information may be imposed on the solution by constructing a symmetric kernel and default models. We will use three symmetric default models:

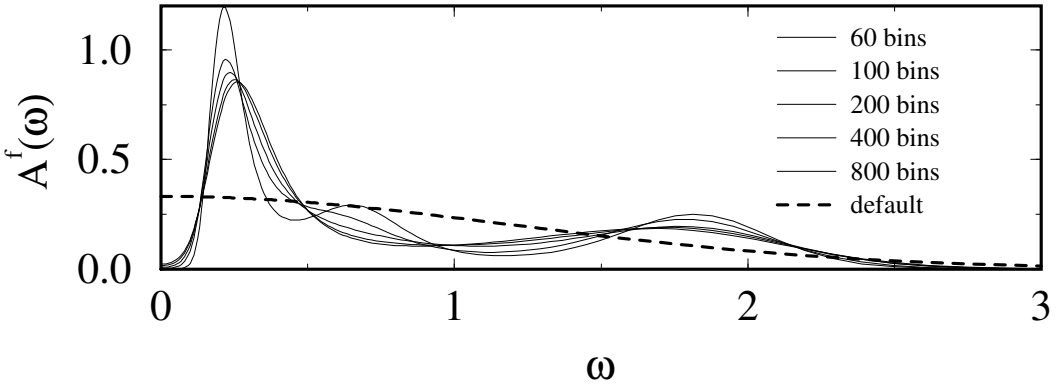

Fig. 7: *A sequence of spectral densities generated from increasingly accurate data with a Gaussian model (dashed line). Every time the number of bins of data is doubled, the error is reduced by* $1/\sqrt{2}$*. As* N_{bins} *increases beyond* $2L = 82$*, spurious structures are quickly suppressed.*

two non-informative models — the flat model $m(\omega) = \text{constant}$ and a simple Gaussian

$$m(\omega) = \frac{1}{\Gamma\sqrt{\pi}} \exp[-(\omega/\Gamma)^2] \tag{74}$$

and also a third one obtained from second-order perturbation theory in U [24, 25]. The kernel for symmetric Fermionic Green's functions may be modified to reflect the symmetry and the associated integral may be restricted to positive frequencies

$$G(\tau) = \int_0^\infty d\omega A(\omega) \frac{e^{-\tau\omega} + e^{-(\tau-\beta)\omega}}{1 + e^{-\beta\omega}} \,. \tag{75}$$

4.1 Convergence of spectra

To minimize the effects of statistical errors, the accuracy of the data needs to be increased until the spectral density has converged. This is demonstrated in Fig. 7, where the accuracy of the data are improved by increasing the number of bins of data. Here, a Gaussian default model is used whose width $\Gamma = 1.6$ (chosen by an optimization procedure to be discussed below). Each time the number of bins of data is doubled, the accuracy of the data increases by 41%. The spectral densities corresponding to the smallest number of bins of data have spurious features associated with over fitting. These features are associated with difficulties in calculating the covariance matrix, as discussed in Sec. 2.4. As N_{bins} increases beyond $2L = 82$, the spurious structure is quickly suppressed. By the time 800 bins of data have been used, the spectral density appears to be converged to within several line widths.

4.2 Default model selection

One may also test the dependence of the spectral density on the default model by changing its parameters or by using different models. The best model is the one with the largest posterior probability, calculated by assuming that the prior probability of the default model is flat, so

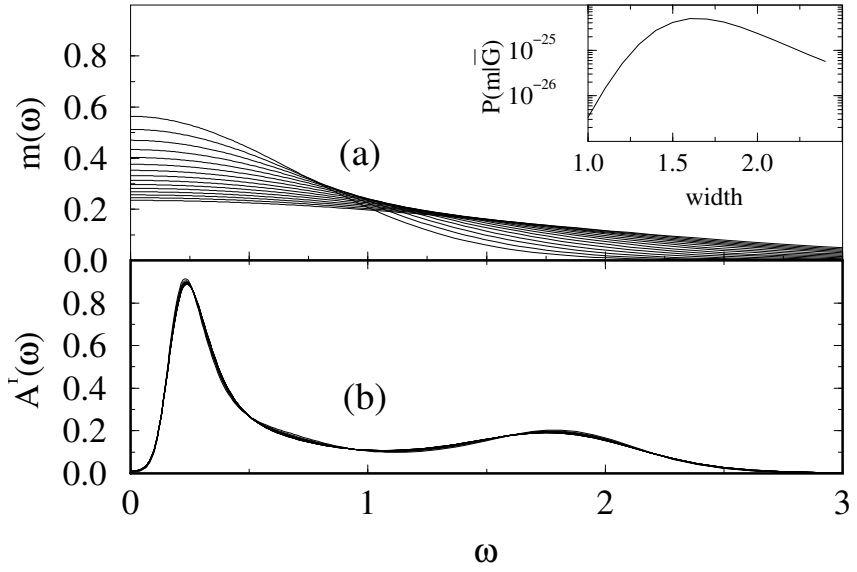

Fig. 8: *Dependence of the spectral density upon the default model. The width Γ of the Gaussian default model (a) is varied, producing a series of spectral densities (b). In the inset to (a) is the posterior probability of the default model $P(m|\bar{G})$, produced by integrating the joint probability $P(A, \alpha, m|\bar{G})$ over α and A, is plotted as a function of Γ. The normalization of $P(m|\bar{G})$ is unknown because it depends upon the probability of the data and the prior probability of the default model which are unknown.*

that $P(A, \alpha, m|\bar{G}) \propto P(A, \alpha|\bar{G}, m)$. Then $P(m|\bar{G})$ is obtained by integrating $P(A, \alpha, m|\bar{G})$ over A and α. The effects of varying the default model parameters are shown in Fig. 8a where the same data set is analytically continued with Gaussian default models whose widths satisfy $1.0 < \Gamma < 2.4$. The posterior probability $P(m|\bar{G})$ of these default models, shown in the inset, is peaked around $\Gamma \approx 1.6$ (We note that the normalization of $P(m|\bar{G})$ is unknown, since the prior probability of the default model and data are unknown). The resulting spectral densities are shown in Fig. 8b and are found to depend only weakly upon the default model. It is also possible to optimize the perturbation theory default model and hence to optimize the corresponding spectral densities. In the optimization of the default for the PAM spectra, the d-f-hybridization V may be treated as a variational parameter.

4.3 Error propagation

In Fig. 9, we compare the optimal spectral densities obtained with the optimal perturbation theory, Gaussian, and flat default models. (The flat default model, with no adjustable parameters, is not optimized.) The posterior probabilities for each result indicate that the perturbation theory default model produces by far the most probable spectral density. However, we note that the qualitative features of the spectral density change little with the default model even though a large variety of default models were used. This independence is one signature of good data!
As a final test of the quality of the spectral density, one can evaluate its error in different intervals of frequency. In Fig. 9, we chose to assign error bars to the integrated spectral density ($h(\omega) =$

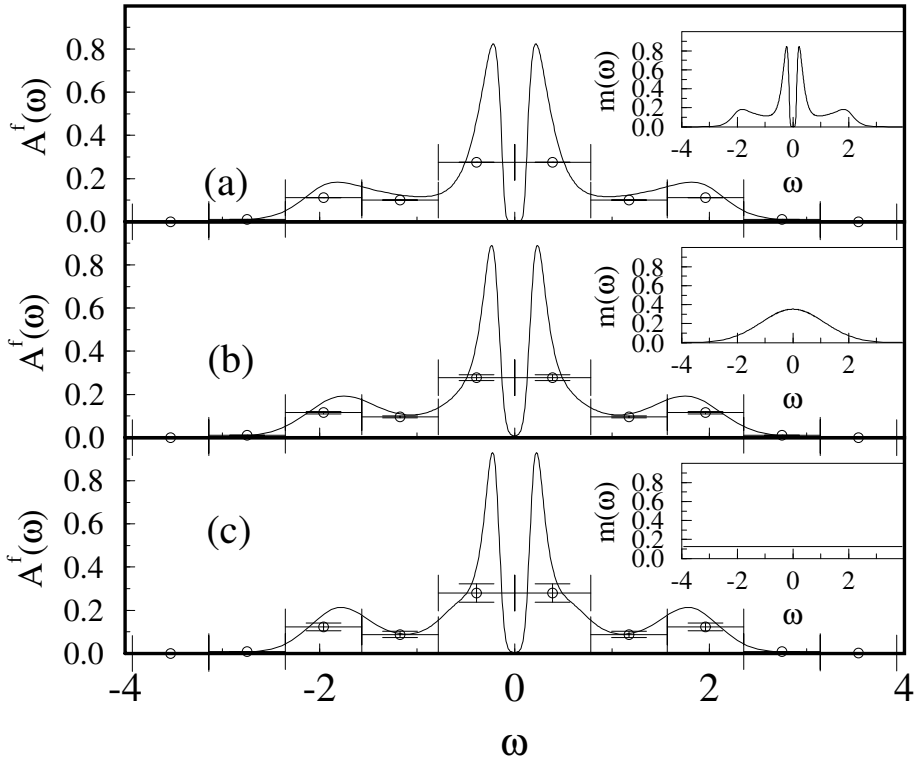

Fig. 9: *The f-electron density of states $A^f(\omega)$ generated using (a) a perturbation theory, (b) a Gaussian, and (c) a flat default model. These models are shown as insets to each graph. The data points indicate the integrated spectral weight within 10 non-overlapping regions of width indicated by the horizontal error bar. The vertical error bar indicates the uncertainty of the integrated weight within each region.*

1) over different non-overlapping regions. The width of the region centered at each error bar is indicated by the horizontal spread of the error bar, the spectral weight within this region is indicated by the value of the data point, while the estimate of the uncertainty is indicated by the vertical spread. The perturbation theory default model yields the most precise spectra at all frequencies, consistent with the posterior probabilities of the models.

4.4 Two-particle spectra

There are special difficulties associated with the calculation of spectral densities associated with two-particle Green's functions. These difficulties include noisier and more correlated data and the lack of a good default model. The latter problem stems from the traditional difficulties of performing perturbation theory for two-particle properties.

As an example, we will analytically continue the local f-electron dynamic spin susceptibility $\chi''(\omega)$ of the symmetric PAM. The Monte Carlo data $\chi(\tau) = 2\langle S^-(\tau)S^+(0)\rangle$ is related to $\chi''(\omega)$ by

$$\chi(\tau) = \int_0^\infty d\omega \frac{\omega[e^{-\tau\omega} + e^{-(\beta-\tau)\omega}](\chi''(\omega)/\omega)}{1 - e^{-\beta\omega}}\,. \tag{76}$$

To construct a model we will employ an alternative to perturbation theory, and construct a

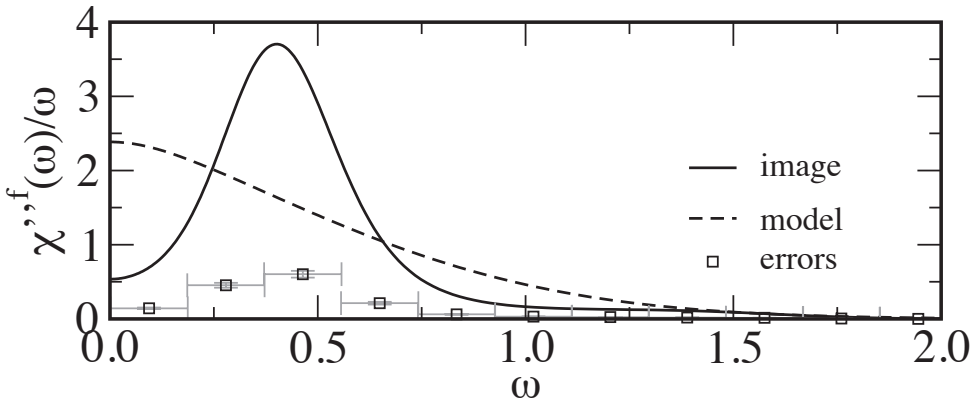

Fig. 10: $\chi''(\omega)/\omega$ *for* $V = 0.6$, $U = 2$ *and* $\beta = 20$ *for the PAM generated using a default model defined by two moments of the spectral density. The data points indicate the integrated spectral weight within 10 non-overlapping regions of width indicated by the horizontal error bar. The vertical error bar indicates the uncertainty of the integrated weight within each region.*

default model from different moments of the spectral function. They will be used as constraints to the principle of maximum entropy. The moments used to generate the default model are

$$\frac{1}{2}\chi(\omega = 0) = \int_0^\infty d\omega(\chi''(\omega)/\omega)\,. \tag{77}$$

$$\chi(\tau = 0) = \int_0^\infty d\omega\,(\chi''(\omega)/\omega)\,\omega\coth(\beta\omega/2)\,. \tag{78}$$

The (unnormalized) model is then generated by maximizing the entropy subject to these constraints imposed with Lagrange multipliers λ_0 and λ_1 and is easily found to be

$$m(\omega) = \exp[\lambda_0 + \lambda_1\omega\coth(\beta\omega/2)] \tag{79}$$

where λ_0 and λ_1 are determined by the constraint equations above.
Clearly this procedure may be generalized to utilize an arbitrary number of measured moments and often provides a better default model than perturbation theory. However, as shown in Fig. 10, the final spectral density can differ significantly from the default model when defined in this way. Nevertheless, the error bars indicate that the spectral density is trustworthy.

4.5 Annealing method

Occasionally we have reason to calculate a series of spectra for a variety of temperatures, e.g. for the calculation of transport coefficients. If this set is sufficiently dense, then starting from a perturbation theory default at high temperature, we may use the resulting spectra as a default model for the next lower temperature. As far as we know, this procedure has no Bayesian justification; however, it has significant physical motivation. At sufficiently high temperatures, perturbation theory often becomes exact. Thus, this annealing procedure may be initialized with an essentially exact result. Furthermore, as the temperature is lowered, we expect the high

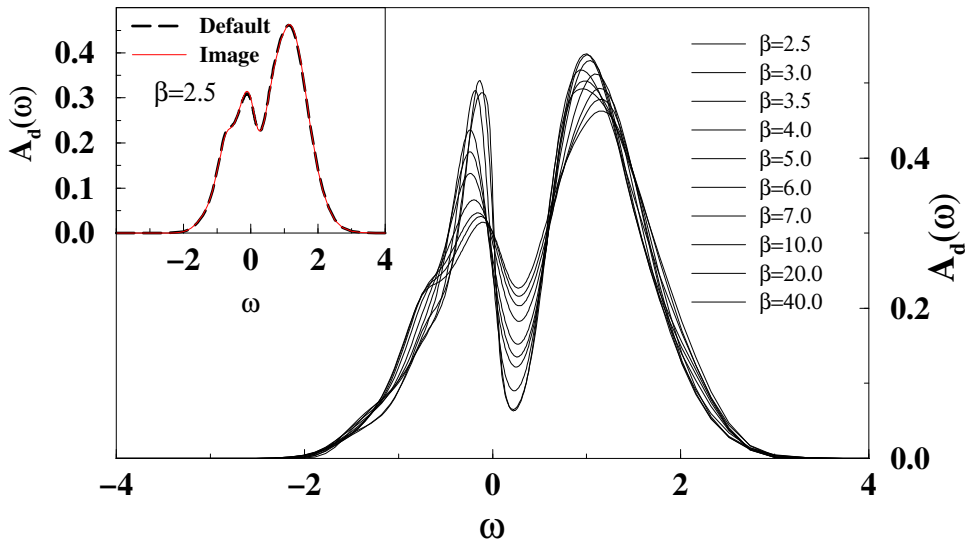

Fig. 11: *The evolution of the d-electron density of states of the asymmetric PAM when $U = 1.5$, $V = 0.6$ $n_d = 0.6$, and $n_f = 1.0$. At high temperatures, as shown in the inset, the spectra is in essentially exact agreement with second-order perturbation theory. In addition, the d-electron states far from the Fermi surface are weakly renormalized by the strong electronic correlation on the f-orbitals. Thus, as the temperature is lowered, the low-frequency spectra change continuously, whereas the high frequency features change very little.*

frequency features of many spectra to freeze out (this is an essential assumption behind the numerical renormalization group method). Thus, the QMC is only required to supply information about the low-frequency features. Since QMC is a discrete sampling procedure in Matsubara time, according to Nyquist's theorem QMC only provides information below the Nyquist frequency $\omega_N = \pi/\Delta\tau$. Thus, perturbation theory provides the high-frequency information, QMC the low-frequency information, and MEM provides a natural method for combining these information sources.

For example, the evolution of the d-electron density of states of the asymmetric PAM is shown in Fig. 11. At high temperatures, as shown in the inset, the spectra is in essentially exact agreement with second-order perturbation theory. In addition, the d-electron states far from the Fermi surface are weakly renormalized by the strong electronic correlation on the f-orbitals. Thus, as the temperature is lowered, the low-frequency spectra change continuously, whereas the high frequency features change very little.

4.6 Matsubara frequency self-energy

We obtain high-quality estimates of the self-energy $\Sigma(\mathbf{k}, \omega)$ by employing MEM directly to the Matsubara-frequency self-energies calculated from continuous-time quantum Monte Carlo (CTQMC) [26,27]. Since the self-energy lacks features due to the bare dispersion, its spectrum generally has less features than the single-particle spectral function. Therefore, higher quality results are obtained by directly analytically continuing the self energy and then constructing the Green function via the Dyson equation [2].

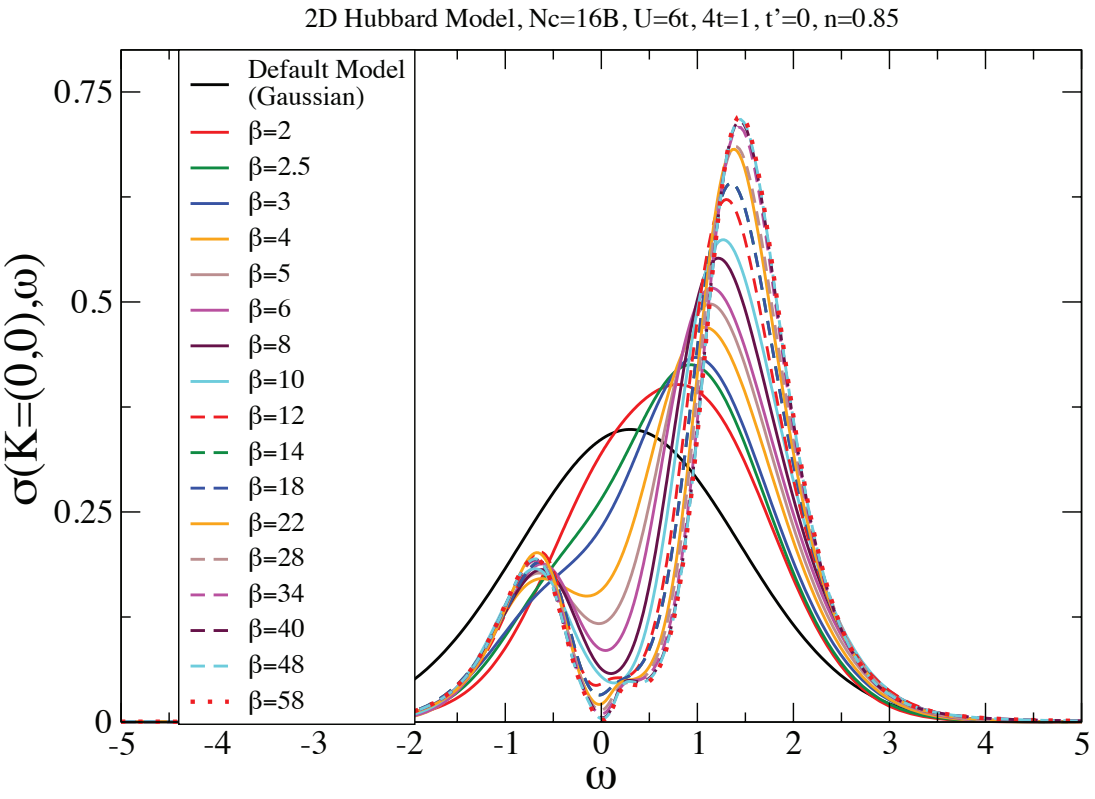

Fig. 12: *Self energy spectra* $\sigma(\mathbf{k},\omega) = -\frac{1}{\pi}\Sigma''(\mathbf{k},\omega)/U^2\chi_{\sigma,\sigma}$ *calculated by annealing for the Hubbard model calculated with the DCA with* $U = 6t$ *(*$4t = 1$*),* $t' = 0$*,* $\mathbf{k} = (0,0)$ *cluster size* $N_c = 16$ *and filling* $n = 0.85$ *with an optimized Gaussian default model.*

We illustrate this method with the self energy spectra of the 2D Hubbard model calculated with the Dynamical Cluster Approximation (DCA). Since the DCA is a self consistent method, we calculate the host Green's function from the penultimate iteration very precisely so that its error is negligible compared to the error measured in the last final iteration used to calculate the binned data. It is convenient to normalize the non-Hartree part of the $\Sigma(\mathbf{k}, i\omega_n)$ by $U^2\chi_{\sigma,\sigma}$, where $\chi_{\sigma,\sigma} = \langle n_\sigma n_\sigma\rangle - \langle n_\sigma\rangle^2 = n_\sigma(1-n_\sigma)$ and is the local polarization of a single spin species σ. The normalized spectrum of self-energy acts as a probability distribution:

$$\frac{\Sigma(\mathbf{k}, i\omega_n) - \Sigma_H}{U^2\chi_{\sigma,\sigma}} = \int d\omega \frac{\sigma(\mathbf{k},\omega)}{i\omega_n - \omega}, \tag{80}$$

where $\sigma(\mathbf{k},\omega) = -\frac{1}{\pi}\Sigma''(\mathbf{k},\omega)/U^2\chi_{\sigma,\sigma}$, $\int d\omega\sigma(\mathbf{k},\omega) = 1$, using $\chi_{\sigma,\sigma}$ obtained from the Monte Carlo process. Fig. 12 shows $\sigma(\mathbf{K} = (0,0),\omega)$ obtained by annealing, starting with a Gaussian default model with width and location optimized as discussed above.

We conclude this section by noting that while the systematic preparation of the data described in Sec. 2.4 and the qualification of the spectrum described in this section is time-consuming, we believe that it is as important to the quality of the final result, as is an accurate MEM code.

5 Conclusion

The Maximum Entropy Method is a precise and systematic way of analytically continuing Matsubara-time quantum Monte Carlo results to real frequencies. Due to the exponential nature of the kernel which relates the spectra and the data, there are many A which correspond to the same $\bar{G}$. With the MEM we employ Bayesian statistics to determine which of these is the most probable. Bayesian inference is also used to assign error bars to integrals over the spectrum and optimize the default model.

The posterior probability of the spectrum is given by the product of the prior probability and the likelihood function. The entropic nature of the prior ensures that the only correlated deviations from the default model which appear in the spectrum are those which are necessary to reproduce the data. The form of the likelihood function is determined by the central limit theorem, assuming that the data are statistically independent and Gaussianly distributed. Ensuring these preconditions is the most critical step in the MEM procedure, and requires that the data be systematically rebinned and that the data and the kernel be rotated into the space in which the covariance of the data is diagonal.

Once the data has been properly characterized, we calculate the optimal spectrum using Bryan's algorithm which searches for a solution in the reduced singular space of the kernel. Bryan's method is more efficient than conventional techniques which search the entire spectral space. For any search algorithm three different techniques can be employed to set the Lagrange parameter α which determines the relative weight of the entropy and misfit: the historic, classic or Bryan's averaging technique. With precise uncorrelated data, each returns essentially the same spectrum, but with less-precise uncorrelated data, Bryan's technique yields the best results. Also, as the QMC data are systematically improved, images produced with Bryan's technique appear to converge more quickly than those produced by the other techniques.

Together, the techniques discussed in this chapter provide a powerful, accurate, and systematic approach to the analytic continuation problem. In each case where we have employed these techniques we have been able to produce spectra that are precise at low frequencies, and free from spurious (unjustified) features at all ω.

5.1 Steps to ensure a robust MEM calculation

In this lecture we have summarized the proper implementation of MEM and given a number of cautionary notes. As a parting discussion, these will be summarized here along with a few other common sense rules of thumb.

1. Rebin your data to remove correlations in QMC time.
2. Generate sufficient bins of data so that $N_{bins} \gtrsim 2L$ where L is the number of Matsubara times or frequencies used.
3. If a self consistent method, such as DCA, is used to generate the data, be sure that the error in $\mathcal{G}$ from the previous iteration is negligible.

4. When possible, normalize your data so that the spectrum integrates to one.

5. Calculate the covariance of the (renormalized) data making sure that: (1) the eigenvalue spectrum is continuous (if not, increase N_{bins}), and (2) that the covariance matrix is well enough conditioned to allow it to be diagonalized (if not, the data is oversampled in Matsubara time).

6. Diagonalize the covariance and rotate the data and kernel into the diagonal frame.

7. Choose a good default model, hopefully you can use the annealing technique. Always use a non-informative default model unless you are *certain* that the information in the model is exact.

8. When possible, use Bryan's MEM for marginalizing over α.

9. Systematically improve your data until the calculated spectrum converges.

10. When the annealing method is used, if the temperature step appears large, i.e. the spectrum changes abruptly, you may want to introduce data at additional intermediate temperatures.

11. If the annealing method is not used, try different non-informative default models. A reliable result is independent of the model. You may also want to use the model with the highest posterior probability (calculated when Bryan's method is used).

Acknowledgment

We would like to acknowledge useful conversations and fruitful collaborations with J.E. Gubernatis, A. Macridin, R.N. Silver, D. Sivia, and A.N. Tahvildarzadeh. We thank H. Chen who performed the calculations of the self energy spectra in Sec. 4.6. This work was supported by the National Science Foundation LA-SiGMA EPSCoR grant EPS-1003897.

References

[1] H.-B. Schüttler and D.J. Scalapino, Phys. Rev. Lett. **55**, 1204 (1985) and Phys. Rev. B **34**, 4744 (1986)

[2] H.J. Vidberg and J.W. Serene, J. Low Temp. Phys. **29**, 179 (1977)

[3] G. Wahba, SIAM Journal on Numerical Analysis **14**, 651 (1977)

[4] S.R. White, D.J. Scalapino, R.L. Sugar, and N.E. Bickers, Phys. Rev. Lett. **63**, 1523 (1989)

[5] M. Jarrell and O. Biham, Phys. Rev. Lett. **63**, 2504 (1989)

[6] A.W. Sandvik, Phys. Rev. B 57, 1028710290 (1998)

[7] K.S.D. Beach, preprint, arXiv:cond-mat/0403055 (2004)

[8] M. Jarrell, and J.E. Gubernatis, Physics Reports **269**, 133-195, (1996)

[9] J.E. Hirsch and R.M. Fye, Phys. Rev. Lett. **56**, 2521 (1986)

[10] J. Skilling, in *Maximum Entropy and Bayesian Methods*, J. Skilling (ed.) (Kluwer Academic, Dordrecht, 1989), p. 45

[11] S.F. Gull and J. Skilling, IEE Proceedings **131**, 646 (1984)

[12] For a discussion of kurtosis and skewness, as well as a discussion of the probability that a distribution is Gaussian, see [22], chap. 14

[13] It is tempting to disregard (i.e., set to 0) the off-diagonal elements of the covariance matrix as an alternative method of alleviating this pathology. Then, the eigenvalues will simply be the well-defined variance of $\bar{G}(\tau)$. However, this procedure neglects the correlations in the error which are clearly visible in Fig. 4 and yeilds an incorrect likelihood function. We have found that this procedure produces unpredictable results, especially when the data quality is marginal.

[14] J. Skilling and R.K. Bryan, Mon. Not. R. astr. Soc. **211**, 111, (1984)

[15] S.F. Gull, in *Maximum Entropy and Bayesian Methods*, J. Skilling (ed.) (Kluwer Academic, Dordrecht, 1989), p. 53

[16] S.F. Gull and G.J. Daniels, Nature, **272**, 686 (1978)

[17] H. Jeffreys, **Theory of Probability**, (Oxford, Claredon Press, 1939); see also E. Jaynes, IEEE Trans. Sys. Sci. Cyb. Vol. SSC-4, (1993)

[18] J. Skilling, in *Maximum Entropy and Bayesian Methods*, J. Skilling (ed.) (Kluwer Academic, Dordrecht, 1989), p. 455

[19] R.K. Bryan, Eur. Biophys. J. **18**, 165 (1990)

[20] M. Jarrell, J.E. Gubernatis, and R.N. Silver. Phys. Rev. B, **44**, 5347 (1991)

[21] J.J. Dongarra, C.B. Moler, J.R. Bunch, and G.W. Stewart: *LINPACK User's Guide* (SIAM, Philadelphia, 1979)

[22] W.H. Press, S.A. Teukolsky, W.T. Vettering, and B.P. Flannery: *Numerical Recipes in Fortran, Second Edition* (Cambridge University Press, 1992)

[23] B.T. Smith, J.M. Boyle, Y. Ikebe, V.C. Klema, and C.B. Moler: *Matrix Eigensystems Routines – EISPACK Guide* (Springer-Verlag, New York, 1976)

[24] M. Jarrell, H. Akhlaghpour, and Th. Pruschke, Phys. Rev. Lett. **70**, 1670 (1993) and Phys. Rev. B. **51**, 7429-40 (15, March 1995)

[25] B. Horvatic, D. Sokcevic, and V. Zlatic, Phys. Rev. B **36**, 675 (1987)

[26] X. Wang, E. Gull, L. de' Medici, M. Capone, and A.J. Millis, Phys. Rev. B **80**, 045101 (2009)

[27] K.-S. Chen, S. Pathak, S.-X. Yang, S.-Q. Su, D. Galanakis, K. Mikelsons, M. Jarrell, and J. Moreno, Phys. Rev. B **84**, 245107 (2011)

14 Stochastic Optimization Method for Analytic Continuation

Andrey S. Mishchenko
RIKEN Advanced Science Institute (ASI)
Cross-Correlated Materials Research Group (CMRG),
Wako 351-0198, Japan

Contents

E. Pavarini, E. Koch, F. Anders, and M. Jarrell
Correlated Electrons: From Models to Materials
Modeling and Simulation Vol. 2
Forschungszentrum Jülich, 2012, ISBN 978-3-89336-796-2
http://www.cond-mat.de/events/correl12

Obtaining dynamical properties from quantum Monte Carlo (QMC) simulations is a notoriously difficult problem because QMC provides a limited number of values of a dynamical correlation function

$$\{G(m), m = 1, M\} \tag{1}$$

either at Matsubara frequencies $i\omega_m$ or at imaginary time points τ_m, whereas dynamical information is associated with a spectral function $A(\omega)$ depending on the continuous energy variable ω. The procedure of obtaining the dynamical correlation function $A(\omega)$ from the known set of values $G(m)$ is called *analytic continuation*. One of the most complete overview of this problem for the case when the set of values $\{G(m), m = 1, M\}$ is obtained from numeric calculations can be found in Ref. [1]. Generally, the procedure requires solving the Fredholm integral equation of the first kind [2]

$$G(m) = \int_{-\infty}^{\infty} d\omega \; \mathcal{K}(m, \omega) \; A(\omega) \; , \; m = 1, \ldots, M \; , \tag{2}$$

where $\mathcal{K}(m, \omega)$ is some known kernel which depends on what quantities are associated with $G(m)$ and $A(\omega)$.

One of numerous examples is when one wants to determine the Lehmann spectral function [3]. This function contains a lot of important information on quasiparticles. For example, the Lehmann function is proportional to the spectral response observed in experiments on angle resolved photoemission spectroscopy (ARPES) [4].

A typical quantity calculated in QMC is $G(m) = G(\tau_m)$ which is called imaginary time Green function (GF)

$$G(\tau_m) = \langle \; T_\tau c(\tau_m) c^\dagger(0) \; \rangle \; . \tag{3}$$

Here T_τ is the time ordering operator and c is the annihilation operator of a quasiparticle. The imaginary time GF satisfies the periodicity (anti-periodicity) relation

$$G(\tau + \beta) = \pm G(\tau) \tag{4}$$

with a period equal to the inverse temperature $\beta = 1/T$. Here upper (lower) sign is for boson (fermion) operators. Hence, there is an equivalent representation given by the values of the Fourier transform $G(m) = \mathcal{G}(i\omega_m)$ of the imaginary time GF

$$\mathcal{G}(i\omega_m) = \int_0^\beta d\tau \; e^{i\omega_m \tau} \; G(\tau) \tag{5}$$

at Matsubara frequencies $i\omega_m$ equal to $(2m+1)i\pi/\beta$ [$2im\pi/\beta$] for fermion [boson] operators [3]. The quantity $\mathcal{G}(i\omega_m)$ is the GF in the Mastubara representation. Indeed, there is the inverse Fourier transform from the Matsubara representation to the imaginary time GF

$$G(\tau) = \frac{1}{\beta} \sum_{\omega_m} \; e^{-i\omega_m \tau} \; \mathcal{G}(i\omega_m) \; . \tag{6}$$

It can be shown [3] that in the case when QMC data for the GF are obtained in the Matsubara representation (5), $G(m) = \mathcal{G}(i\omega_m)$, the kernel $\mathcal{K}(m,\omega) \equiv \mathcal{K}(i\omega_m,\omega)$ of the Eq. (2) is

$$\mathcal{K}(i\omega_m,\omega) = \pm\frac{1}{i\omega_m - \omega} \ , \tag{7}$$

where plus (minus) sign corresponds to boson (fermion) operators. On the other hand, if the QMC data are given in terms of the imaginary time GF, (3), the kernel $\mathcal{K}(m,\omega) \equiv \mathcal{K}(\tau_m,\omega)$ of the analytic continuation is

$$\mathcal{K}(\tau_m,\omega) = -\frac{\exp(-\tau_m\omega)}{\exp(-\beta\omega) \pm 1} \ , \tag{8}$$

where the positive (negative) sign is for fermion (boson) operators.
Another example is when the quantity of interest is the optical conductivity $\sigma(\omega)$ and the quantity supplied by QMC is the imaginary time current-current correlation function $G(m) = J(\tau_m)$. The kernel $\mathcal{K}(m,\omega) \equiv \mathcal{K}(\tau_m,\omega)$ in this case is

$$\mathcal{K}(\tau_m,\omega) = \frac{1}{\pi}\frac{\omega\exp(-\tau_m\omega)}{1-\exp(-\beta\omega)} \ . \tag{9}$$

Indeed, the problem of solving the Fredholm equation of the first kind is encountered in many areas which are far from the particular problem of analytic continuation. For example, one has to solve an equation of the same type to restore the thermodynamic properties of the quantum systems from QMC [5] or to recover the variety of impurity traps in organic materials from the ESR spectra [6, 7]. Moreover, a similar equation has to be solved for medical X-ray and impedance tomography, image deblurring, and many other practical applications [8]. Indeed, because of the notorious practical importance of the problem there is a long history of the vast amount of attempts to develop methods giving solutions for this class of equations. The main difficulty with the type of equations considered above is the following: they belong to the class of *ill-posed* problems. The main characteristic feature of this class is that there is no unique solution in the mathematical sense. Hence, to solve such an equation, one has to introduce some additional information specifying what kind of solution is expected. Therefore, it is impossible to single out the best method for solving this class of equations because each specific problem requires its own approach.
In the following we give a historical, although incomplete, overview of the approaches invented to solve the Fredholm equations of the first kind and follow the development of the methods up to recent times. In Sec. 1, we introduce the most simple minded approach, the least-squares fit, and show why it is not suitable for *ill-posed* problems. We describe various approaches to *ill-posed* problems in Sec. 2. In particular, we discuss there Tikhonov-Phillips regularization method, the maximum entropy method, and several variants of the stochastic sampling method. The stochastic optimization method (SOM), which is the main topic of this chapter, is compared with other stochastic sampling methods in Sec. 2.4. We give a detailed description of the SOM and some practical recipes in Secs. 3 and 4, respectively. Some tests of SOM are presented in Sec. 5.

1 Difficulties to solve ill-posed problems

To outline the difficulties encountered in the problem of solving the Fredholm equation of the first kind it is convenient to transform the equation into its discrete analog. The discrete analog is a matrix equation which seems to be easily solvable by least-squares fit. However, this naive approach immediately fails due to the *ill-posed* nature of the problem and the solution shows a *sawtooth noise* instability. We introduce the discrete analog of the Fredholm equation in Sec. 1.1. The least-squares fit approach, the nature of the *ill-posed* problems, and the features of the *sawtooth noise* instability are described in Sec. 1.2.

1.1 Discrete form of integral equation

Approximating the spectral function by its values on a finite spectral mesh of N points

$$A(\omega) = \sum_{n=1}^{N} A(\omega_n)\delta(\omega - \omega_n) \ , \tag{10}$$

the integral equation (2) can be rewritten in matrix form

$$G(m) = \sum_{n=1}^{N} \mathcal{K}(m, \omega_n)A(\omega_n) \ , \ m = 1, \ldots, M \ , \tag{11}$$

or equivalently presented as

$$\vec{G} = \widehat{\mathcal{K}}\vec{A} \, . \tag{12}$$

Here $\vec{G} \equiv (G(1), G(2), \ldots, G(M))$ [$\vec{A} \equiv (A(\omega_1), A(\omega_2), \ldots, A(\omega_N))$] is an M-dimensional [N-dimensional] vector and $\widehat{\mathcal{K}}(m, n) \equiv \mathcal{K}(m, \omega_n)$ is an $M \times N$ matrix ($M \geq N$). The matrix $\widehat{\mathcal{K}}(m, n)$ is known, depending on the kernel of the integral equation, $\vec{A}$ is the vector to be determined, and $\vec{G}$ is obtained by QMC with components known with some error-bars.

1.2 Sawtooth noise instability

In practice, the problem expressed by Eq. (12) is usually *ill-posed,* either because of non-existence or non-uniqueness of a solution $\vec{A}$ [9]: Noise, which is always present in a given vector $\vec{G}$, leads to the situation when there is no solution $\vec{A}$ that exactly satisfies Eq. (12). On the other hand, there is an infinite number of solutions which make the left hand side of Eq. (12) approximately equal to its right hand side. Therefore, one can not search for a unique vector $\vec{A}$ but has to find some solution which is the best in some sense, or find a set of solutions which are good according to some sensible criterion. The above features are the fingerprints of *ill-posed* problems.

The most simple minded approach in such a case is to search for the least-squares minimum-norm solution $\vec{A}$ which minimizes the *deviation measure* which is chosen in the form of the Euclidean residual norm

$$\| \widehat{\mathcal{K}}\vec{A} - \vec{G} \|^2 = \sum_{m=1}^{M} \left| \sum_{n=1}^{N} \mathcal{K}(m, \omega_n)A(\omega_n) - G(m) \right|^2 \ . \tag{13}$$

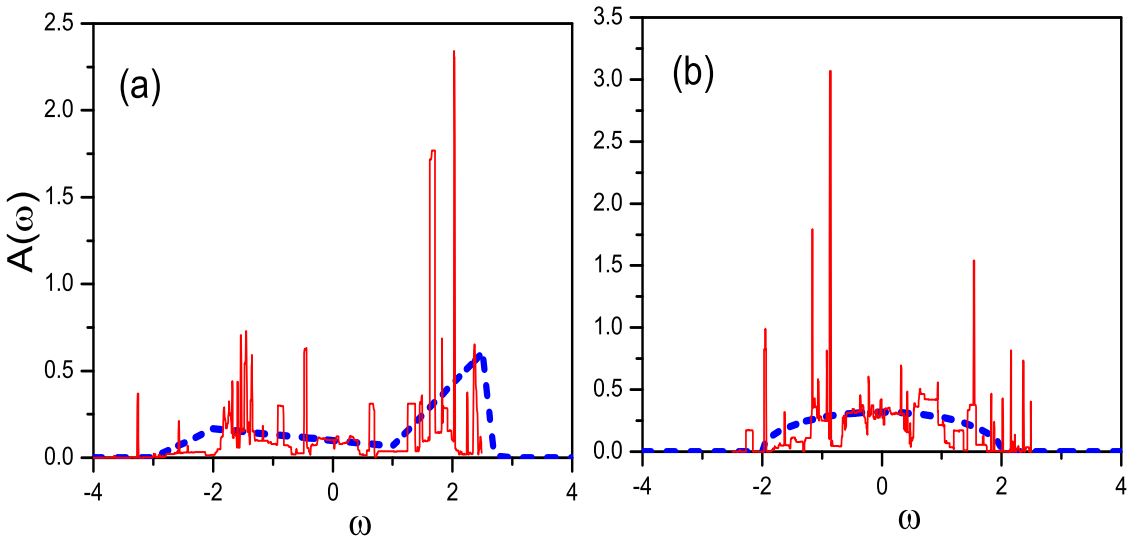

Fig. 1: *Examples of sawtooth noise in a least-squares fit with restricted positive spectral function. The spikes in non-regularized solutions (red solid line in panels (a) and (b)) are much larger than the actual value of the spectra (blue dashed lines in (a) and (b)).*

Indeed, one immediately surrenders to the *ill-posed* nature of the problem and tries to minimize, although the difference between the left- and right-hand sides of the Eq. (12) never reach zero. Choosing the Euclidean norm one admits the absence of a unique solution because the approximate equality in Eq. (12) can be defined in terms of an infinite number of another norms. For the Euclidean norm one can find the solution of the best least-squares fit in terms of the singular value decomposition of the matrix $\widehat{\mathcal{K}}$ into a weighted sum of separable matrices [10]

$$\widehat{\mathcal{K}} = \sum_{i=1}^{r} \sigma_i \, \vec{u}_i \otimes \vec{v}_i^{\dagger} \; , \tag{14}$$

where $\vec{u} \otimes \vec{v} \equiv \vec{u}(k)\vec{v}(l)$ is the matrix determined by the outer product of the left and right singular vectors of $\widehat{\mathcal{K}}$, $\vec{u}$ and $\vec{v}$, respectively. The real and nonnegative numbers $\sigma_1 \geq \sigma_2 \geq \ldots \sigma_r > 0$ are the singular values of $\widehat{\mathcal{K}}$. The least-squares solution $\vec{A}$ is given by the explicit expression

$$\vec{A} = \sum_{i=1}^{r} \frac{\vec{u}_i^{\dagger} \otimes \vec{v}_i}{\sigma_i} \vec{G} \; . \tag{15}$$

A problem arises from small singular values σ_i: Even very small statistical errors in $\vec{G}$ induce large perturbations to the solution $\vec{A}$. These perturbations, called *sawtooth noise*, are typical for *ill-posed* problems and look like fast oscillations with amplitude much larger than the actual solution $\vec{A}$. The origin of the *sawtooth noise* is that the solution $\vec{A}$ *over-fits* the statistical errors present in the input data $\vec{G}$. The *sawtooth noise* can even lead to large negative values of the otherwise positive actual solution $\vec{A}$. However, the least-squares fit under the condition of non-negativity of the spectral function $\vec{A}$ results in sawtooth noise too (see Fig. 1).

2 Methods to solve ill-posed problems

It was shown in the previous section that the least-squares fit approach to the matrix form (12) of the integral equation (2) leads to results with *sawtooth noise* which can be very far from the actual solution. The noise arises from the small singular values σ_i of the integral kernel $\widehat{\mathcal{K}}$.
There are many methods developed to fight this noise. The simplest and most obvious one is the truncated singular value decomposition (TSVD), where the terms in Eq. (15), that correspond to several of the smallest singular values σ_i, are neglected. However, the above trick is just a particular example of a broad general class of approaches. Most, if not all, methods to circumvent the problem of spurious noise in the solution of the integral equation (2) can be united under the title *regularization methods*. As a particular example, the simplest regularization method for the matrix representation (12) of the integral equation (2) is based on the following trick. A regularization functional $\mathcal{F}(\vec{A})$, suppressing the oscillations of the solution $\vec{A}$, is added to the Euclidean norm (13)

$$\| \widehat{\mathcal{K}}\vec{A} - \vec{G} \|^2 + \gamma\mathcal{F}(\vec{A}) \tag{16}$$

and the *deviation measure* (16) is minimized instead. So, in general words, the regularized solution is sought as a minimizer of the deviation measure which is a weighted combination of the residual norm $\| \widehat{\mathcal{K}}\vec{A} - \vec{G} \|^2$ and a constraint $\gamma\mathcal{F}(\vec{A})$. Indeed, to construct the functional $\mathcal{F}(\vec{A})$ one needs some prior knowledge about solution the $\vec{A}$.
The functional (16) is historically the very first approach, named Tikhonov-Phillips regularization, that was developed to fight the sawtooth noise instability. However, to introduce a generic classification of the regularization approaches, it is convenient to use Bayesian statistical inference. According to the Bayes' theorem [11]

$$P[A|G]\ P[G] = P[G|A]\ P[A]\ , \tag{17}$$

where $P[A|G]$ is the posterior or conditional probability that the spectral function is A, provided the correlation function is G. Neglecting the normalization factor $P[G]$, which is independent of A, one gets

$$P[A|G] \sim P[G|A]\ P[A]\ , \tag{18}$$

where the ill-posed problem to find the most probable A given G is converted into the much easier problem of finding G given A, i.e., of maximizing the *likelihood function*, $P[G|A]$ taking into account simultaneously the *prior knowledge* about the spectrum $P[A]$. Note that any attempt to neglect the prior knowledge, i.e., to set $P[A] \equiv$ const and reduce the problem to the maximizing just the likelihood function, leads to the sawtooth noise instability of the solution.
Notably, any method to regularize *ill-posed* problems can be presented in the form of a Bayesian approach and the distinctions between different approaches are restricted to the choice of the likelihood function $P[G|A]$ and the prior knowledge $P[A]$. Below, we introduce different possibilities of this choice. We describe the Tikhonov-Phillips regularization method in Sec 2.1, the maximum entropy method in Sec. 2.2, and several variants of the stochastic sampling method in Sec. 2.3. We finally consider the stochastic optimization method as an effective example of stochastic sampling methods in Sec. 2.4.

2.1 Tikhonov-Phillips regularization method

Historically, the approach called *Tikhonov-Phillips regularization method* (TPRM) has been invented independently in many different contexts and became the first approach to solve the above problems. The name comes from the first applications of the ideas to integral equations by A.N. Tikhonov [Tikhonoff] [12, 13] and D.L. Phillips [14] in the early 40ies of the last century. Independently, the regularization approache was applied in a different context to the discrete problem of matrix inversion [15–17] and is know in the statistical literature as ridge regression. However, leaving aside the differences in terminology and interpretations, the general idea is the following.

In the sense of Bayes' inference the TPRM is a choice where the likelihood function is

$$P[G|A] \sim \exp\{- \parallel \widehat{\mathcal{K}}\vec{A} - \vec{G} \parallel^2\} \tag{19}$$

and the prior knowledge is

$$P[A] \sim \exp\{-\lambda^2 \parallel \hat{\Gamma}\vec{A} \parallel^2\} \; . \tag{20}$$

Thus, the *deviation measure* to minimize is the sum $\parallel \widehat{\mathcal{K}}\vec{A} - \vec{G} \parallel^2 + \lambda^2 \parallel \hat{\Gamma}\vec{A} \parallel^2$. Here, the likelihood function requires the least-squares fit of $\vec{G}$ while the constraint, where the solution $\vec{A}$ is multiplied by a nonzero matrix $\hat{\Gamma}$, suppresses large absolute values of $A(\omega_k)$. Namely, the constraint removes spikes and, hence, large values of derivatives in the solution $[A(\omega_{k+1}) - A(\omega_k)]/[\omega_{k+1} - \omega_k]$.

The simplest modification of TPRM sets $\hat{\Gamma}$ as identity matrix $\hat{\Gamma} = \hat{I}$. In this case expression (15) for the solution $\vec{A}$ takes the form

$$\vec{A} = \sum_{i=1}^{r} \left\{ \frac{\sigma_i^2}{\sigma_i^2 + \lambda^2} \right\} \frac{\vec{u}_i^{\dagger} \otimes \vec{v}_i}{\sigma_i} \vec{G} \; . \tag{21}$$

It is clear that contributions, corresponding to small singular values $\sigma_i \ll \lambda$, are automatically filtered out by the factors in the curly brackets and large sawtooth spikes of the solution are suppressed. Thus *over-fitting* of the noise in the input data is avoided by restricting the possible solutions to the smooth ones. There are several approaches to find the optimal regularization parameter λ, L-curve [18, 19] and U-curve [20] methods in particular. These approaches consider relations between the Euclidean norm of the solution $\parallel \hat{\Gamma}\vec{A} \parallel^2$ and the residual $\parallel \widehat{\mathcal{K}}\vec{A} - \vec{G} \parallel^2$.

An interesting modification of the TPRM is given in [21, 22]. The method expresses the solution $\vec{A}$ in terms of an average over a correlation matrix $\langle \tilde{\vec{A}} \tilde{\vec{A}}^{\dagger} \rangle$ of possible solutions $\tilde{\vec{A}}$. The knowledge of this correlation matrix provides a prior knowledge about the solution.

There are other methods which are based on the suppression of the large derivatives of the solution. These methods are based on the form of the functional (16), where the constraint $\gamma\mathcal{F}(\vec{A})$ is explicitly taken in a form which suppresses large derivatives of the solution [23, 24]. Many similar functionals can be found in earlier studies, see [9] for details on the rigorous mathematical treatment of *ill-posed* problems.

2.2 Maximum entropy method

One can criticize the first historical method to solve ill-posed problems as relying on unconditional smoothening of the solution. The constraint of the TPRM suppresses solutions with large derivatives. This can be a problem when the spectral function has sharp edges or narrow peaks. One of the recent approaches, the *Maximum Entropy Method* (MEM) [1], provides an attractive strategy to circumvent some problems of the TPRM.

MEM searches for the most probable "true" solution $A(\omega)$ among many possible particular solutions $\widetilde{A}(\omega)$ assuming prior knowledge that the "true" solution $A(\omega)$ is close to a predefined function $D(\omega)$ called *default model*. The likelihood function of MEM is

$$P[G|\widetilde{A}] = \exp\{-\chi^2[\widetilde{A}]/2\} \,, \tag{22}$$

where

$$\chi^2[\widetilde{A}] = \sum_{m=1}^{M} \mathcal{E}^{-1}(m)[G(m) - \widetilde{G}(m)]^2 \,, \tag{23}$$

and $\tilde{G}(m)$ is related to a particular solution $\widetilde{A}(\omega)$ through $\widetilde{G}(m) = \int_{-\infty}^{\infty} d\omega \; \mathcal{K}(m,\omega) \; \widetilde{A}(\omega)$. The matrix $\mathcal{E}(m)$ is set by the noise in G and is related to the covariance matrix. The prior knowledge function is defined as

$$P[G|A] = \exp\{\alpha^{-1} S[\widetilde{A}]\} \,, \tag{24}$$

where the entropy

$$S[\widetilde{A}] = \int d\omega \; \widetilde{A}(\omega) \ln[\widetilde{A}(\omega)/D(\omega)] \tag{25}$$

characterizes the deviation of a particular solution $\widetilde{A}(\omega)$ from the default model $D(\omega)$, a function that serves as the maximum entropy configuration. The regularization parameter α controls how much weight is given to the minimization of the *deviation measure* $\chi^2[\widetilde{A}]$, i.e., to the resemblance of the solution $\widetilde{A}(\omega)$ to the default model $D(\omega)$.

The MEM is superior to TPRM in cases where a lot of explicit information is known about $A(\omega)$. Moreover, one can avoid smoothening of large derivatives, typical for TPRM, given the knowledge about sharp parts of the "true" solution $A(\omega)$. The nonphysical smoothening can be avoided if sharp parts of the solution can be explicitly included into the default model. However, the method highly relies on the default model which can be a serious drawback if the most interesting features of the spectra are very sensitive to the form of the chosen default model [25].

2.3 Stochastic sampling methods

Any *stochastic sampling method* (SSM) uses a minimal prior knowledge about the solution, does not require any default model, and does not introduce any apparent smoothening of the solution. The characteristic feature of this class of methods is a change of the likelihood function

$P[\widetilde{A}|G]$ into a likelihood functional (see, e.g., [26])

$$A = \int d\widetilde{A}\ \widetilde{A}\ P[\widetilde{A}|G]\,, \tag{26}$$

where the "true" solution A is obtained as an average of particular solutions $\widetilde{A}$, weighted by the likelihood function $P[\widetilde{A}|G]$. An optimal likelihood function has to prefer solutions $\widetilde{A}$ with small *deviation measure* $\chi^2[\widetilde{A}]$. Particular solutions $\widetilde{A}$ with too small $\chi^2[\widetilde{A}]$ over-fit the data G and suffer from sawtooth noise. However, although it has not been proven formally, it is known that in practice the sawtooth noise can be self-averaging in a sum over a large enough number of solutions. One has to keep $\chi^2[\widetilde{A}]$ not too restrictive because the sawtooth noise persists if most of the solutions in the functional (26) over-fit the input data. The requirement to take into account solutions $\widetilde{A}$ with large enough $\chi^2[\widetilde{A}]$ sets up an *implicit regularization procedure*.
Starting from the very first practical design of a SSM by Sandvik [27], most of SSMs suggest the likelihood function in the form of a Boltzmann distribution

$$\mathcal{P}[A|G] = \exp\{-\chi^2[\widetilde{A}]/\mathcal{T}\}, \tag{27}$$

where $\mathcal{T}$ is treated as a fictitious temperature and χ^2 is defined by Eq. (23) and can be considered as a fictitious energy. Then, because of the above interpretation, one can use the Metropolis algorithm [28] to sample possible functions $\widetilde{A}$. The prior knowledge function is usually defined by the condition that the spectral function $\widetilde{A}(\omega)$ is positively definite and that the first few known frequency moments are conserved.
In principle, although introducing many useful details, the approaches suggested in Refs. [25, 29] belong to the same class as that introduced by Sandvik [27]. All three approaches do not use any default model for defining the prior knowledge function and, thus, are convenient in the problems where there is not much knowledge about how the resulting spectral function $A(\omega)$ has to look like.
A somewhat different approach is suggested in the statistical MEM (SMEM) by Beach [30] and Jarrel [31]. The method defines a dimensionless field $n(x)$ which is related to the default model $D(\omega)$. Then, averaging is performed over the dimensionless field using the likelihood Boltzmann distribution Eq. (27). The useful feature of the method is that, depending on its parameters, it can interpolate between two limiting cases when the spectrum is completely governed by the deviation measure (27) and when it is defined solely by the default model.

2.4 Stochastic optimization method: relation to other stochastic sampling approaches

The stochastic optimization method (SOM) [32], which is the main topic of this lecture, is a particular example of SSMs. SOM also does not use any default model, does not impose any apparent smoothening on the solution, and restricts prior knowledge to normalization and positivity of the solution.
A particular feature of SOM, which singles it out among SSMs, is that the sampling of solutions, which optimizes the deviation measure, is made without the artificial interpretation of the

likelihood function as a Boltzmann distribution [32,33]. A similar idea was also suggested later in the "generic inversion via falsification of theories" strategy [34]. Indeed, averaging over particular solutions (26), weighted by some likelihood function, has no relation to any real partition function. On the contrary, one simply has to average over a set of particular solutions, each of which fits the input data well enough. Therefore, the interpretation of $\chi^2[\widetilde{A}]$ as an "energy" of some state in a system of a given temperature $\mathcal{T}$ is a superfluous feature of the traditional SSMs. There is no real Hamiltonian and real temperature in the averaging procedure (26) and the net goal is to accumulate a large enough number of solutions which fit, but not over-fit, the data set $G(m)$.

Hence, it does not matter how the set of averaged "good enough" solutions is found. This is why the strategy to find particular solutions in SOM is completely different from other SSMs. On every step SOM starts from an arbitrary chosen initial particular solution and minimizes its deviation measure until a "good enough" fit is found. In this way SOM finds a large-enough number of "good" particular solutions and calculates an average

$$A(\omega) = \sum_{j=1}^{L} \xi_j \widetilde{A}_j(\omega). \tag{28}$$

The simplest option is to set all coefficients equal to $\xi_j = 1/L$ for all L particular solutions whose deviation measure $\chi^2[\widetilde{A}]$ is smaller than some selected value. A detailed description of the SOM, i.e., how to organize the process and how to choose its optimal parameters, is given in Secs. 3 and 4.

3 Stochastic optimization method: general description

In comparison to other SSMs, the SOM uses a slightly different measure $\chi^2[\widetilde{A}]$, a considerably different way to parametrize a particular solution $\widetilde{A}_j(\omega)$, and a completely different way to accumulate the particular spectral functions $\widetilde{A}_j(\omega)$ for averaging. An important feature of SOM is that it treats the energy space continuously without imposing any finite ω-mesh. We describe the deviation measure and parametrization of the spectra in Secs. 3.1 and 3.2, respectively. Sections 3.3 and 3.4 discuss the way to obtain a particular solution and explain the general features of elementary updates which decrease the deviation measure of particular solutions. Global updates and the refinement of the solution are considered in Secs. 3.5, and 3.6, respectively. Finally, elementary updates of classes I and II are described in Secs. 3.7 and 3.8.

3.1 Deviation measure

The first step is to define the *deviation measure* determining which solution is a good approximation of the input data set G. The set G corresponds to some QMC data on imaginary times $G(m) = G(\tau_m)$ or at some Matsubara frequencies $G(m) = \mathcal{G}(i\omega_m)$, $m = 1, \ldots, M$. Then the

deviation measure of SOM is given by expression

$$D[\widetilde{A}] = \sum_{m=1}^{M} |\Delta(m)| \ . \tag{29}$$

Here $\Delta(m)$ is the *deviation function*

$$\Delta(m) = \frac{G(m) - \tilde{G}(m)}{\mathcal{S}(m)}, \tag{30}$$

which characterizes individual deviations of specific data points $G(m)$ from the values of the simulated function $\tilde{G}(m)$ defined by the particular spectral function $\widetilde{A}$ in terms of relation

$$\widetilde{G}(m) = \int_{-\infty}^{\infty} d\omega \ \mathcal{K}(m,\omega) \ \widetilde{A}(\omega) \ . \tag{31}$$

The factors $\mathcal{S}(m)$ can be chosen as error-bars of the QMC data $G(m)$, if they are known. However, there are plenty of sampling methods [32, 35–37], which can provide almost uniform, m-independent error-bars of the QMC data. These methods are usually used when $G(m)$ changes several orders of magnitude in the range $1 \leq m \leq M$. If the m-indepenent factor $\mathcal{S}(m) \equiv \mathcal{S}$ is put outside of the sum (29), the contribution of the data points with small $|G(m)|$ to the deviation measure $D[\widetilde{A}]$ is evidently underestimated. In this case a reasonable choice for $\mathcal{S}(m)$ is to take $\mathcal{S}(m) = |G(m)|^d$, where $0 \leq d \leq 1$. Then, the contributions from the points with small and large values of $|G(m)|$ are equally represented in the sum when $d \to 1$.

3.2 Parametrization of particular spectra

We parameterize the spectral function $\widetilde{A}$ as a sum

$$\widetilde{A}(\omega) = \sum_{t=1}^{K} \eta_{\{P_t\}}(\omega) \tag{32}$$

of rectangles $\{P_t\} = \{h_t, w_t, c_t\}$

$$\eta_{\{P_t\}}(\omega) = \begin{cases} h_t & , \quad \omega \in [c_t - w_t/2, c_t + w_t/2] \ , \\ 0 & , \quad \text{otherwise} \ , \end{cases} \tag{33}$$

determined by height $h_t > 0$, width $w_t > 0$, and center c_t.
A configuration

$$\mathcal{C} = \{\{P_t\}, \ t = 1, ..., K\} \tag{34}$$

with the normalization constraint

$$\sum_{t=1}^{K} h_t w_t = I, \tag{35}$$

defines, according to Eqs. (31), (32), and (33), the function $\tilde{G}(m)$ at any point m. Figure 2 shows how the intersection of rectangles is understood in SOM.

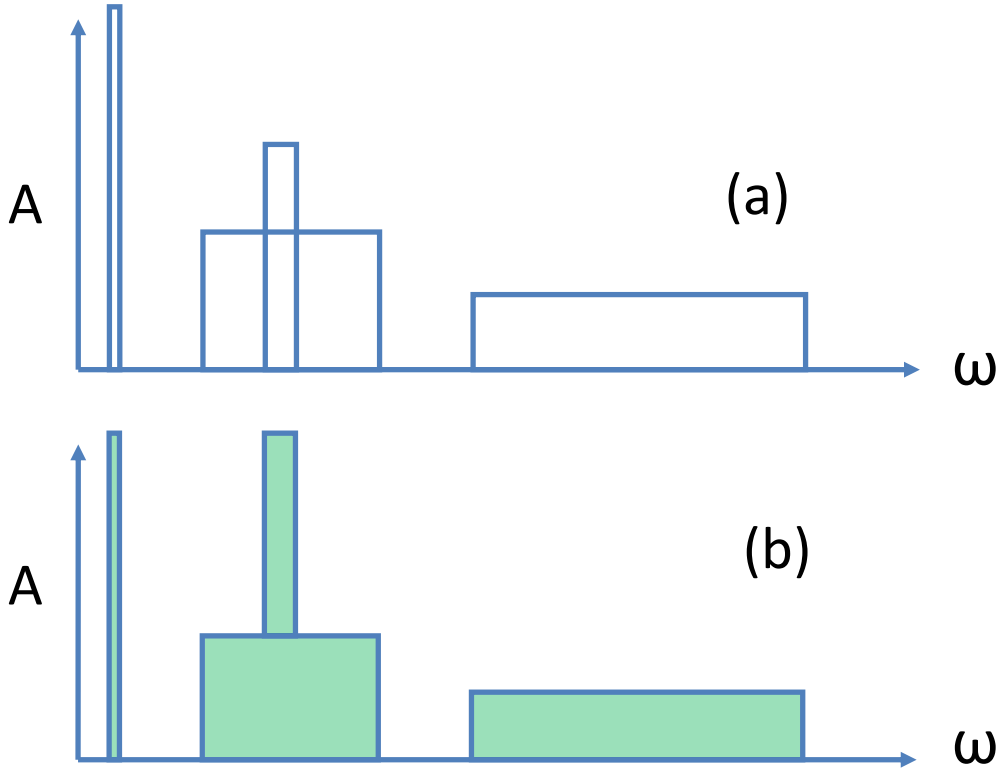

Fig. 2: *An example of a configuration with $K = 4$. Panel (b) shows how the intersection of rectangles in panel (a) is treated.*

Note that the specific type of the functions (33) is not crucial for the general features of the method although a simple form of the analytic expressions (31),(32), and (33) is of considerable importance for the performance of the method. If the analytic expression for $\tilde{G}(m)$ is not available for a given kernel $\mathcal{K}$, one tabulates the quantities

$$\Lambda(m, \Omega) = \int_{-\infty}^{\Omega} \mathcal{K}(m, x)\, dx \;, m = 1, \ldots, M \tag{36}$$

and finds the value of $\tilde{G}(m)$ using the following straightforward relation

$$\tilde{G}(m) = \sum_{t=1}^{K} h_t \left[\Lambda(m, c_t + w_t/2) - \Lambda(m, c_t - w_t/2)\right] \;. \tag{37}$$

In certain cases it is, however, straightforward to find analytic expressions. For example, let us consider the case when $G(m) = G(\tau_m)$ is a fermionic GF given by QMC at imaginary times (3) at zero temperature. In this case Eq. (8) reduces to $\mathcal{K}(\tau_\omega) = e^{-\tau_m \omega}$ and the spectral function is defined only at $\omega > 0$. It implies that in configuration (34) all $c_t - w_t/2 \geq 0$. Then, the explicit relation for the GF $\tilde{G}(\tau_m)$ in terms of the configuration $\mathcal{C}$ is

$$\tilde{G}_{\mathcal{C}}(\tau_m) = \begin{cases} I & , \quad \tau_m = 0 \;, \\ 2\tau_m^{-1} \sum\limits_{t=1}^{K} h_t e^{-c_t \tau_m} \sinh(w_t \tau_m/2) & , \quad \tau_m \neq 0 \;. \end{cases} \tag{38}$$

Another example of an analytic expression is when one has a Matsubara GF (5) given via the kernel (7). In this case the analytic expression for $\tilde{\mathcal{G}}(i\omega_m)$ is

$$\tilde{\mathcal{G}}_{\mathcal{C}}(i\omega_m) = \pm \sum_{t=1}^{K} h_t \ln \left[\frac{c_t - w_t/2 - i\omega_m}{c_t + w_t/2 - i\omega_m} \right] , \tag{39}$$

where the plus (minus) sign is for boson (fermion) operators.

3.3 General overview: obtaining particular solution and its sum

Here we survey the whole procedure while the following sections add the necessary details.
First, $L \geq 10$ attempts to find particular solutions are performed. An attempt to obtain each particular solution $\widetilde{A}_j$ consists of two stages. The first is a random generation of initial configurations of rectangles and the second is a fixed number F of *global updates* decreasing the deviation measure D.
At first stage of the attempt j, some initial configuration $\mathcal{C}_j^{\text{init}}$, (34), is randomly generated. This means that a number of rectangles K is randomly chosen, with K in some range $1 < K < K_{\text{max}}$. The parameters $\{P_t\}$ of all rectangles are randomly generated under the constraint of normalization (35). Indeed one can impose further constraints, if some additional information is available.
Then F global updates are performed. The *global update* consists of a randomly chosen sequence of *elementary updates* which are described in next sections. A global update, which modifies the configuration $\mathcal{C}_j(r) \to \mathcal{C}_j(r+1)$, is accepted when $D[\widetilde{A}_{r+1}] < D[\widetilde{A}_r]$. For the particular solution $\widetilde{A}_j$, obtained at each attempt after F global updates, one can control the quality of the fit of the input data using the deviation function $\Delta(m)$, (30). The number F of global updates is considered to be satisfactory, if the input data $G(m)$ are fit down to the noise level in a more than half of the L attempts. If not, the number of global updates F is increased and the procedure with $L \geq 10$ attempts is repeated.
Finally, when a satisfactory number of global updates F is found, an accumulation of $L \gg 10$ particular solutions $\widetilde{A}_j$ and their deviation measures $D[\widetilde{A}_j]$ is performed. After L attempts there is a minimal deviation measure $\text{MIN}\{D[\widetilde{A}_j]\}$, limited by the noise of the input data $G(m)$, and the rest of measures are larger. Tests show that to avoid over-fitting, i.e., to regularize the final solution, one has to include into the sum (28) all particular solutions whose deviation measures $D[\widetilde{A}_j]$ are smaller than the double of the minimal deviation measure

$$D[\widetilde{A}_j] \leq 2\,\text{MIN}\{D[\widetilde{A}_j]\} . \tag{40}$$

Such a choice of the regularization parameter is very similar to the strategy adopted in many other methods, e.g., SSM [29] or MEM [31]. Both in SOM and in many other methods the strategy is to keep differences between the fit $\tilde{G}(m)$ and data $G(m)$ of the order of the error-bars to avoid over-fitting. The inequality (40) is the way to introduce the regularization parameter in the most explicit manner.

3.4 General features of elementary updates

By elementary update we mean a random change of the configuration, which is either accepted or rejected in accordance with certain rules. There are two classes of elementary updates. The updates of class I do not alter the number of rectangles, K, changing only the values of the parameters from a randomly chosen set $\{P_t\}$. The updates of class II either add a new rectangle with randomly chosen parameters $\{h_{K+1}, w_{K+1}, c_{K+1}\}$, or remove a stochastically chosen rectangle t from the configuration. If a proposed change violates a constraint (38) (e.g., a change of w_t or h_t, or any update of the class II), then the necessary change of some other parameter set $\{P_{t'}\}$ is simultaneously proposed, to satisfy the requirement of the constraint.

The updates should keep the parameters of a new configuration within the domain of definition of the configuration $\mathcal{C}$. Formally, the domains of definition of a configuration (34) are $\Xi_{h_t} = [0, \infty]$, $\Xi_{c_t} = [-\infty, \infty]$, $\Xi_{w_t} = [0, \infty]$, and $\Xi_K \in [1, \infty]$. However, for the sake of faster convergence, one can reduce the domains of definition.

As there is no general *a priori* prescription for choosing reduced domains of definition, the rule of thumb is to start with maximal domains and then, after some rough solution is found, reduce the domains to reasonable values suggested by this solution. In particular, since the probability to propose a change of any parameter of a configuration is proportional to K^{-1}, it is natural to restrict the maximal number of rectangles $\Xi_K \in [1, K_{\max}]$ by some large number $K_{\max}$. To forbid rectangles with extremely small weight, which contribute to $\tilde{G}(\tau)$ less than the statistical errors of $G(\tau)$, one can impose the constraint $h_t w_t \in [S_{\min}, 1]$, with $S_{\min} \ll I K_{\max}^{-1}$. When there is some preliminary knowledge that an overwhelming majority of integral weight of the spectral function $\widetilde{A}(\omega)$ is in a range $[\omega_{\min}, \omega_{\max}]$, one can restrict the domain of definition of the parameter c_t by $\Xi_{c_t} = [\omega_{\min}, \omega_{\max}]$. Then, to reduce the phase space one can choose $\Xi_{h_t} = [h_{\min}, \infty]$ and $\Xi_{w_t} = [w_{\min}, \min\{2(c_t - \omega_{\min}), 2(\omega_{\max} - c_t)\}]$.

While the initial configuration, the update type, and the parameter to be altered are chosen stochastically, the variation of the value of the parameters relevant to the update is optimized to maximize the decrease of D. Each elementary update of our optimization procedure (even that of the class II) is organized as a proposal to change some continuous parameter ξ by a randomly generated $\delta\xi$ in a way that the new value belongs to Ξ_ξ. Although proposals with smaller values of $\delta\xi$ are accepted with higher probability it is important, for the sake of better convergence, to propose sometimes changes $\delta\xi$ that probe the whole domain of definition Ξ_ξ. To probe all scales of $\delta\xi \in [\delta\xi_{\min}, \delta\xi_{\max}]$ we generate $\delta\xi$ with the probability density function $\mathcal{P} \sim (\max(|\,\delta\xi_{\min}\,|, |\delta\xi_{\max}|)/|\delta\xi|)^\gamma$, where $\gamma \gg 1$.

Calculating the deviation measures $D(\xi)$, $D(\xi + \delta\xi)$, $D(\xi + \delta\xi/2)$, and searching for the minimum of the parabolic interpolation, we find an optimal value of the parameter change

$$\delta\xi_{\text{opt}} = -b/2a, \tag{41}$$

where

$$a = 2(D(\xi + \delta\xi) - 2D(\xi + \delta\xi/2) + D(\xi))(\delta\xi)^{-2}, \tag{42}$$

and

$$b = (4D(\xi + \delta\xi/2) - D(\xi + \delta\xi) - 3D(\xi))\delta\xi. \tag{43}$$

In the case $a > 0$ and $\xi_{\text{opt}} \in \Xi_\xi$ we adopt as the update proposal $\tilde{\delta\xi}$ the value $\delta\xi$, $\delta\xi/2$, or $\delta\xi_{\text{opt}}$ for which the deviation measure $D(\xi + \tilde{\delta\xi})$ is the smallest. Otherwise, if the parabola minimum is outside Ξ_ξ, one has to compare only deviations for $\delta\xi$ and $\delta\xi/2$.

3.5 Global updates

The updating strategy has to provide for the efficient minimization of the deviation measure. It is highly inefficient to accept only those proposals that lead to the decrease of the deviation, since there is an enormous number of local minima with values $D_{\text{loc}}[\mathcal{C}]$ much larger than that obtained as minimal deviation measure MIN$\{D[\widetilde{A}_j]\}$. As we observed in practice, these multiple minima drastically slow down (or even freeze) the process.

To optimize the escape from a local minimum, one has to provide a possibility of reaching a new local minimum with lower deviation measure through a sequence of less optimal configurations. It might seem that the most natural way of doing this would be to accept sometimes (with low enough probability) the updates leading to the increase of the deviation measure. However, this simple strategy turns out to be impractical. The reason is that the density of configurations per interval of deviation sharply increases with D. So that the acceptance probability for a deviation-increasing update should be fine-tuned to the value of D. Otherwise, the optimization process will be either non-convergent, or ineffective [if the acceptance probability is, correspondingly, either too large, or too small in some region of D].

A way out of the situation is to perform some sequence of T *temporary* elementary updates of a configuration $\mathcal{C}(0)$

$$\mathcal{C}(0) \to \mathcal{C}(1) \to ... \to \mathcal{C}(r) \to \mathcal{C}(r+1) \to ... \to \mathcal{C}(T)\ , \tag{44}$$

where the proposal to update the configuration $\mathcal{C}(r) \to \mathcal{C}(r+1)$ is (temporary) accepted with probability

$$\mathcal{P}_{r\to r+1} = \begin{cases} 1 & , \quad D[\mathcal{C}(r+1)] < D[\mathcal{C}(r)]\ , \\ Z\left(D[\mathcal{C}(r)]/D[\mathcal{C}(r+1)]\right) & , \quad D[\mathcal{C}(r+1)] > D[\mathcal{C}(r)]\ . \end{cases} \tag{45}$$

(Function Z satisfies the boundary conditions $Z(0) = 0$ and $Z(1) = 1$.) Then we choose out of the configurations $\{\mathcal{C}(r)\}$ (44) the one with minimal deviation measure and, if it is different from $\mathcal{C}(0)$, declare it to be the result of the global update, or, if this configuration turns out to be just $\mathcal{C}(0)$, reject the update.

We choose the function Z in the form

$$Z(x) = x^{1+d} \qquad (d > 0)\ , \tag{46}$$

which leads to comparatively high probabilities to accept small increases and hampers significant enlargements of the deviation measure. Empirically, we found out that the global update

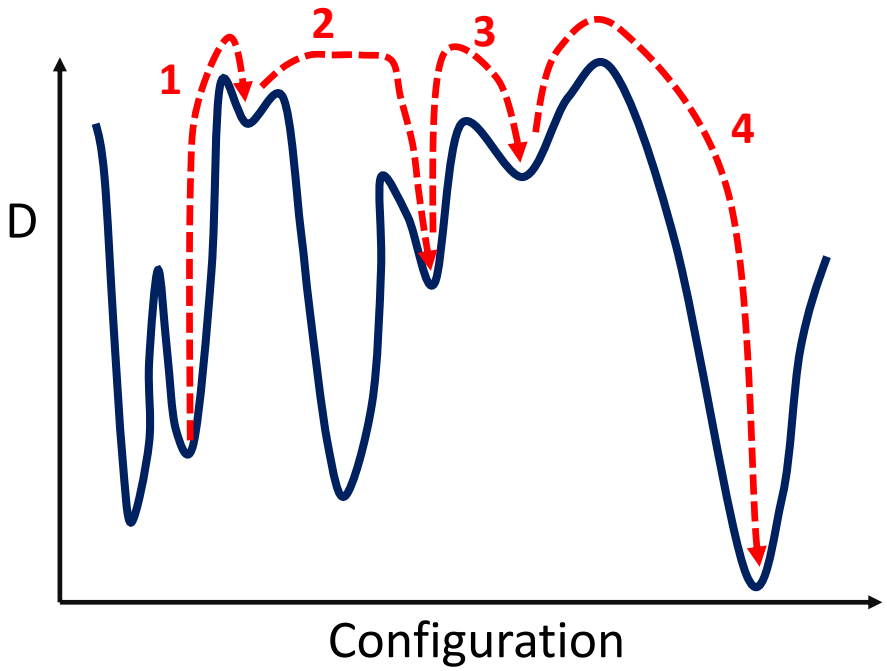

Fig. 3: *Example of a* global update *with 4 elementary updates. The process transfers initial configuration by 4* elementary updates *(dashed red arrows) from the initial minimum of the D-surface (solid blue line) to a lower minimum through the minima whose deviation measures are larger than that in the initial configuration.*

procedure is most effective if one keeps the parameter $d = d_1 \ll 1$ at the first T_1 steps of sequence (44) (to leave local minimum) and then changes it to a value $d = d_2 \gg 1$ for the last $T - T_1$ elementary updates (to decrease the deviation measure). In our algorithm the values $T \in [1, T_{\max}]$, $T_1 \in [1, T]$, $d_1 \in [0, 1]$, and $d_2 \in [1, d_{\max}]$ were stochastically chosen for each global update run.

The two-step procedure for the global update is a method to reach the same goal as the tempering and annealing procedures used in SSM methods [27, 25, 29]. A temporary rise and consequent drop of the fictitious temperature $\mathcal{T}$ is used in the standard SSMs. Similarly, temporary permission to grow up the deviation measure with the following directive to drop it down is introduced into SOM. An exchange between deep local minima of the deviation measures $D_{\text{loc}}[\mathcal{C}]$ has low probability. Therefore, the procedure which first rises and then drops the deviation measure arranges a path between some deep local minima through some shallow ones.

3.6 Final solution and refinement

After a set of L configurations

$$\left\{C_j^{\text{fin}}, j = 1, ..., L\right\} \tag{47}$$

that satisfy criterion (40) is produced, the solution (28) can be obtained by summing up the rectangles, (33) and (47).

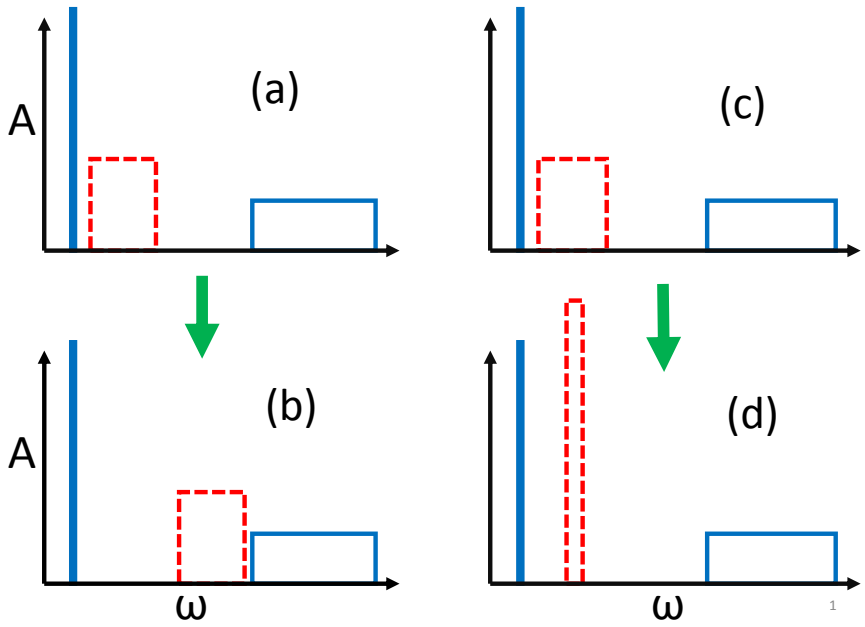

Fig. 4: *Some of the elementary updates of class I: (a)→(b) is the shift of a rectangle (dashed red line); (c)→(d) is the change of the height of a rectangle (dashed red line) without changing its weight $h_t w_t$ and center c_t.*

We employ, however, a more elaborated procedure, which we call refinement. Namely, we use the set (47) as a source of L_{ref} new independent starting configurations for further optimization. These starting configurations are generated as linear combinations of randomly chosen members of the set (47) with stochastic weight coefficients. Then, the refined final solution is represented as the average (28) of L_{ref} particular solutions resulting from the optimization procedure.
The main advantage of such a trick is that the initial configurations for the optimization procedure now satisfy the criterion (40) from the very beginning. Moreover, as any linear combination of a sufficiently large number R of randomly chosen parent configurations $\left\{C_\eta^{\text{fin}}, \eta = 1, ..., R\right\}$ smoothes the sawtooth noise, the deviation of a refined configuration $C_{\text{ref}}^{\text{fin}}$ is normally lower than that of each additive one.

3.7 Elementary updates of class I

(A) Shift of rectangle. Change the center c_t of a randomly chosen rectangle t (Fig. 4a and 4b). The continuous parameter for optimization (41-43) is $\xi = c_t$ which is restricted to the domain of definition $\Xi_{c_t} = [\omega_{\min} + w_t/2, \omega_{\max} - w_t/2]$.
(B) Change of width without change of weight. Alter the width w_t of a randomly chosen rectangle t without changing of the rectangle weight $h_t w_t = const$ and center c_t (Fig. 4c and 4d). The continuous parameter for optimization is $\xi = w_t$ which is restricted by $\Xi_{w_t} = [w_{\min}, \min\{2(c_t - \omega_{\min}), 2(\omega_{\max} - c_t)\}]$.
(C) Change of weight of two rectangles. Change the heights of two rectangles t and t' (where t is a randomly chosen and t' is either randomly chosen or closest to t rectangle) without change of widths of both rectangles. The continuous parameter for optimization is the variation of

the height $\xi = h_t$ of rectangle t. To restrict the weights of the chosen rectangles to $[S_{\min}, 1]$ and preserve the total normalization (35) this update suggests to change $h_t \to h_t + \delta\xi$ and $h_{t'} \to h_{t'} - \delta\xi w_{t'}/w_t$ with $\delta\xi$ confined to the interval

$$S_{\min}/w_t - h_t < \delta\xi < (h_{t'} - S_{\min}/w_{t'})w_t/w_{t'} \ . \tag{48}$$

3.8 Elementary updates of class II

(D) Adding a new rectangle. To add a new rectangle one has to generate some new set $\{P_{\text{new}}\} = \{h_{\text{new}}, w_{\text{new}}, c_{\text{new}}\}$ and reduce the weight of some other rectangle t (either randomly chosen or closest) in order to keep the normalization condition (35). The reduction of the rectangle weight t is obtained by decreasing its height h_t.
The center of the new rectangle is selected at random according to

$$c_{\text{new}} = (\omega_{\min} + w_{\min}/2) + (\omega_{\max} - \omega_{\min} - w_{\min})r \ . \tag{49}$$

As soon as the value c_{new} is generated, the maximal possible width of a new rectangle is given by

$$w_{\text{new}}^{\max} = 2\min(\omega_{\max} - c_{\text{new}}, c_{\text{new}} - \omega_{\min}) \ . \tag{50}$$

The continuous parameter for optimization $\delta\xi = h_{\text{new}}w_{\text{new}}$ is generated to keep the weights of both new rectangles and rectangle t larger than $S_{\min}$

$$\delta\xi = S_{\min} + r(h_t w_t - S_{\min}) \ . \tag{51}$$

Then, the value of the new rectangle height h_{new} for given $\delta\xi$ is generated to keep the width of new rectangles within the limits $[w_{\min}, w_{\text{new}}^{\max}]$

$$h_{\text{new}} = \delta\xi/w_{\text{new}}^{\max} + r(\delta\xi/w_{\min} - \delta\xi/w_{\text{new}}^{\max}) \ . \tag{52}$$

(E) Removing a rectangle. To remove some randomly chosen rectangle t, we enlarge the height $h_{t'}$ of some another (either randomly chosen or closest) rectangle t' according to the normalization condition (35). Since such a procedure does not involve a continuous parameter for optimization, we unite removing of rectangle t with the shift procedure *(A)* of the rectangle t'. Then, the proposal is the configuration with the smallest deviation measure.
(F) Splitting a rectangle. This update cuts some rectangle t into two rectangles with the same heights h_t and widths $w_{\text{new}_1} = w_{\min} + r(w_t - w_{\min})$ and $w_{\text{new}_2} = w_t - w_{\text{new}_1}$ (Fig. 5). Since removing a rectangle t and adding of two new glued rectangles does not change the spectral function we introduce the continuous parameter $\delta\xi$ which describes the shift of the center of the new rectangle with the smallest weight. The other rectangle is shifted in the opposite direction to keep the center of gravity of the two rectangles unaltered. The domain of definition Ξ_ξ obviously follows from the parameters of the new rectangles.
(G) Glueing rectangles. This update glues two (either randomly chosen or closest) rectangles t and t' into a single new rectangle with weight $h_{\text{new}}w_{\text{new}} = h_t w_t + w_{t'}h_{t'}$ and width $w_{\text{new}} = (w_t + w_{t'})/2$. The initial center of the new rectangle c_{new} corresponds to the center of gravity of rectangles t and t'. We introduce a continuous parameter by simultaneously shifting the new rectangle.

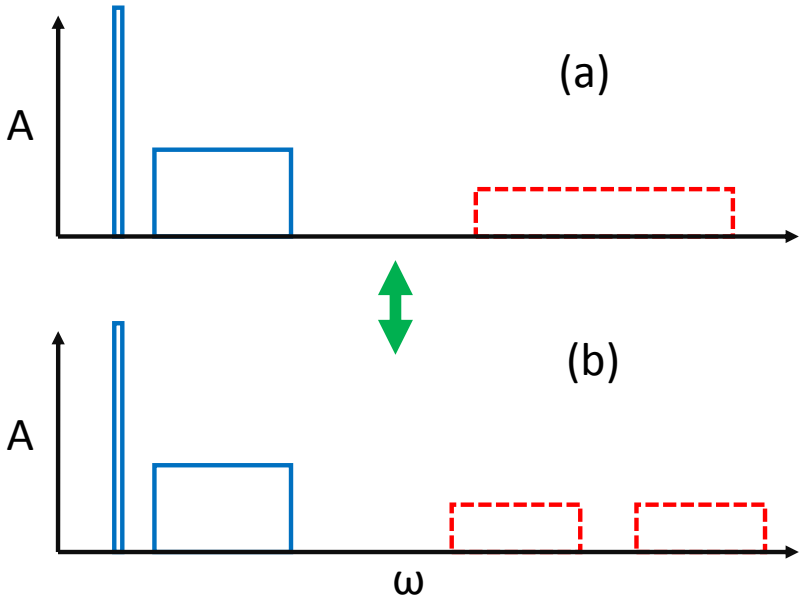

Fig. 5: *Elementary updates of class II: (a)→(b) splitting of rectangle (dashed red line) and (b)→(a) gluing of rectangles without changing its total weight $h_t w_t$ and center of gravity c_t.*

4 Practical aspects of the method

First, we summarize what is done by the SOM algorithm automatically and what are the numbers we need to determine in each particular case. The algorithm described in the previous section is able to search for as many particular solutions $\widetilde{A}_j$ as requested. For every attempt j to find a particular solution $\widetilde{A}$ it does the following steps:

(i) Generate an initial configuration $\mathcal{C}_j^{\text{init}}$ with $K < K_{\max}$ rectangles. Each initial configuration $\mathcal{C}_j^{\text{init}}$ is statistically independent from the previous one $\mathcal{C}_{j-1}^{\text{init}}$.

(ii) Search for a particular solution $\widetilde{A}_j$ performing F global updates.

(iii) Store the final configuration C_j^{fin} of solution $\widetilde{A}_j$ and its deviation measure $D[\widetilde{A}_j]$.

After L attempts one obtains the final regularized solution as the sum

$$A(\omega) = \frac{1}{L_{\text{good}}} \sum_{j=1}^{L} \theta\left\{2\text{MIN}\{D[\widetilde{A}_j]\} - D[\widetilde{A}_j]\right\} \widetilde{A}_j(\omega) \; . \tag{53}$$

Here $\theta(x)$ is the θ-function: $\theta(x \geq 0)$ equals to unity and zero otherwise. L_{good} is the number of "good" fits

$$L_{\text{good}} = \sum_{j=1}^{L} \theta\left\{2\text{MIN}\{D[\widetilde{A}_j]\} - D[\widetilde{A}_j]\right\} , \tag{54}$$

restricted by the regularization condition that the deviation measure is less than twice of the minimal deviation measure $\text{MIN}\{D[\widetilde{A}_j]\}$ found during L attempts.

To finalize the preparation of the method for solving different problems it is necessary to give recipes how to choose the numbers F (Sec. 4.1) and L (Sec. 4.2) in every particular case.

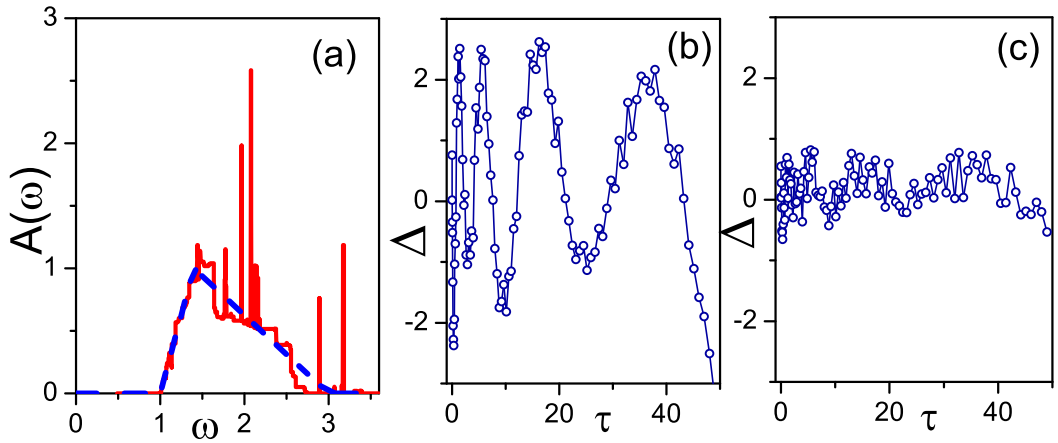

Fig. 6: *(a) Typical spectrum $\widetilde{A}_j(\omega)$ (red solid line), corresponding to a particular configuration $\mathcal{C}_j$, compared to the actual spectrum (blue dashed line). Typical dependence of the deviation function $\Delta(m)$ (30) on imaginary times τ_m corresponding to a spectrum $\widetilde{A}_j(\omega)$ which (b) under-fits and (c) over-fits the uncorrelated noise of imaginary time data.*

4.1 Choosing the number of global updates F

To check whether a particular number F is large enough to reproduce the given data set (1) it is enough to perform about $L \approx 10$ attempts to find particular solutions $\widetilde{A}_j$ and consider the deviation functions $\Delta(m)$, (30), which correspond to each particular solution.

Note that a particular solution itself does not bear any important information on the quality of the fit of the data. Indeed, every particular solution contains sawtooth noise and typically looks like the solid red line in Fig. 6(a). One can claim that the comparison with the exact answer (dashed blue line) can give some insight into the quality, but in practice the exact answer is not known.

On the contrary, the deviation function $\Delta(m)$ gives direct information on the quality of the fit. Such a test of the quality of the fit requires uncorrelated noise in the QMC data, i.e., when the deviation from the exact solution $\delta G(m)$ for any m-point is independent from that in the neighboring m-point. Indeed, we take the uncorrelated nature of the noise for granted because the analytic continuation from *correlated* QMC data is a way to a wrong answer from the onset.

For the sake of definiteness we consider here an example with imaginary time data. However, the case of the Matsubara representation is identical. Figure 6(b) shows an example when the input data are under-fitted by a particular solution. One can see that the typical period of oscillations of the deviation function $\Delta(m)$ around zero is much larger than the typical distance between the input data points τ_m. To the contrary, the fit shown in the Fig. 6(c) is noise-limited because the typical period of oscillations is comparable with a typical distance between data points. One can introduce a numeric criterion of the fit-quality

$$\kappa = \frac{1}{M-1} \sum_{m=2}^{M} \theta\left\{-\Delta(m)\Delta(m-1)\right\} \tag{55}$$

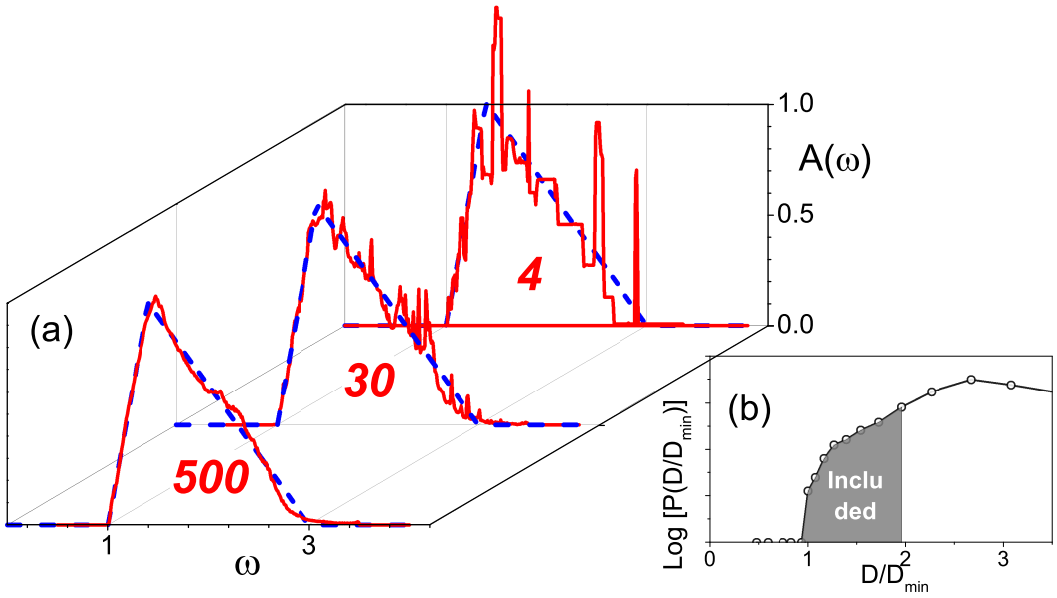

Fig. 7: *(a) Self-averaging of the sawtooth noise after summation of 4, 30, and 500 solutions. (b) Typical probability distribution $P(D/D_{min})$ of solutions with different deviation measures.*

which is the ratio of number of intersections of zero by the function $\Delta(m)$ and number of the intervals between M input data points. Ideally, one would like to have $\kappa \to 1/2$ though it happens very rarely that $\kappa > 1/3$. Practically, a solution with fit-quality $\kappa > 1/4$ can be considered a good one.

Then, after $L \approx 10$ attempts to find particular solutions $\widetilde{A}_j$, each by F global updates, the fit-qualities κ_j are considered. If $\kappa_j > 1/4$ for more than $L/2$ attempts, the number F is large enough. If not, it has to be increased.

4.2 Choosing the number of particular solutions L

SOM performs L attempts to find particular solutions $\tilde{A}_j$. The sum of particular solutions (28) becomes smoother as the number L of attempts increases. Figure 7(a) shows how the *sawtooth noise* self-averages when L increases. One can collect a distribution of the deviation measures and the typical picture is presented in Fig. 7(b). There is the minimal deviation measure $D_{\min}$ which corresponds to the best fit of the noisy data $G(m)$ and there is a probability distribution which increases when D is slightly larger than the minimal deviation measure $D_{\min}$. Indeed, the distribution has some maximum and decreases for larger deviation measures D because there is the most probable deviation measure which is reached after F global updates. The shaded area in Fig. 7(b) shows which part of the distribution is included in the final solution (53) in order to regularize the sawtooth noise. We can not formulate any rigorous criterion when one can stop the accumulation of particular solutions. However, it looks reasonable to stop when there is no significant difference between the final spectra with L_{good} and $(1-1/3)L_{\text{good}}$ particular spectra included. We found that the above criterion is similar to that when one compares the sum (53) with $\theta\left\{2\text{MIN}\{D[\widetilde{A}_j]\} - D[\widetilde{A}_j]\right\}$ and with $\theta\left\{2(1-1/3)\text{MIN}\{D[\widetilde{A}_j]\} - D[\widetilde{A}_j]\right\}$.

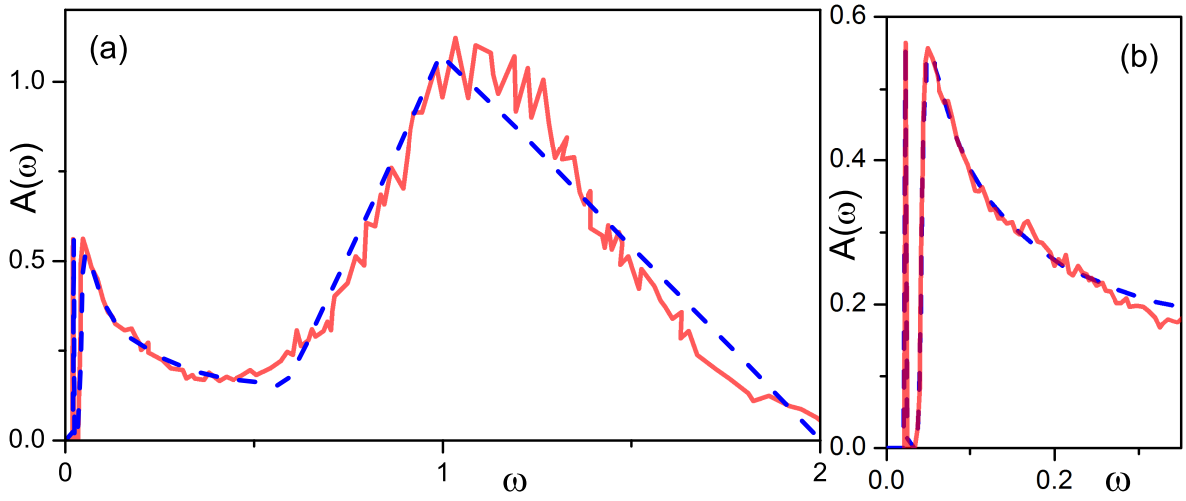

Fig. 8: *The test spectrum (dashed blue line) and the spectrum obtained by SOM (solid red line). Panels (a) and (b) show the whole spectrum and its low energy part, respectively.*

5 Tests of SOM

The procedure to check the SOM for different cases is the following. A spectral function $A(\omega)$, which is called *test spectrum*, is selected. Then, a set of input data with superimposed noise

$$\left\{ \tilde{G}(m) \left[1 + \frac{\mathcal{B}}{2} \mathcal{R} \right] \ , \ m = 1, M \right\} \tag{56}$$

is generated. Finally, the SOM procedure is performed to restore the test spectrum.
The generation procedure of $\tilde{G}(m)$ uses a particular kernel $\mathcal{K}$, relation (31), and the test spectrum. Statistical noise is added with amplitude $\mathcal{B}$ using a random number $\mathcal{R}$ in the range

$$\mathcal{R} \in [-1, 1] \ . \tag{57}$$

We present tests for the imaginary time representation in Sec. 5.1. In particular, we test the case of a zero temperature GF in Sec. 5.1.1, finite temperature GF for fermions in Sec. 5.1.2, and finite temperature optical conductivity in Sec. 5.1.3. The test for GF in the Matsubara representation is presented in Sec. 5.2.

5.1 Test of SOM for imaginary time representation

5.1.1 Zero temperature Green function for a quasiparticle

For zero temperature the GF the kernel (8) for fermions reduces to $\mathcal{K}(\tau_\omega) = e^{-\tau_m \omega}$ and the spectral function $A(\omega)$ is defined only at $\omega > 0$. To check the accuracy of SOM, we tested it for a spectral density distribution that spreads over a large range of frequencies and simultaneously possesses fine structure in the low-frequency region [32]. The test spectrum was modeled as the sum of a delta-function with the energy $\varepsilon_\delta = 0.03$ and the weight $Z_\delta = 0.07$, and a continuous

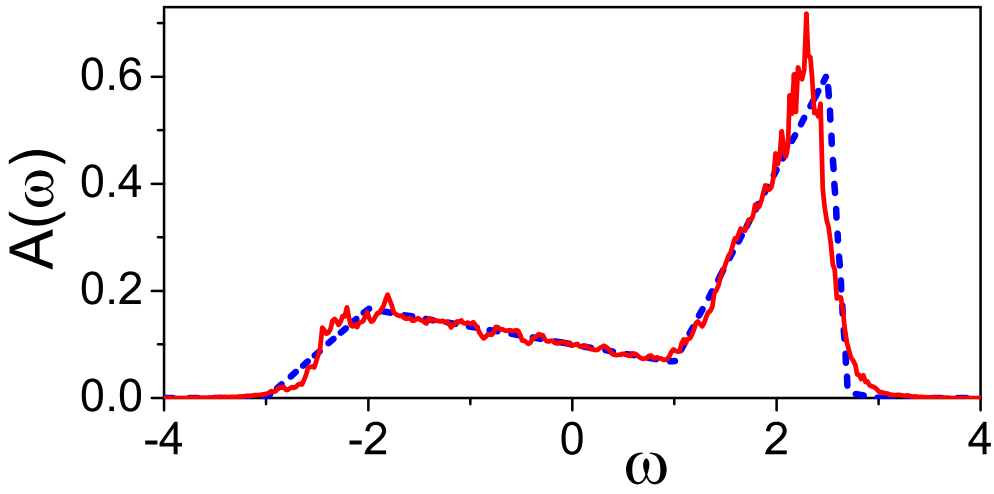

Fig. 9: *The test spectrum (dashed blue line) and the spectrum obtained by SOM (solid red line) for the Lehmann spectral function of fermions at finite temperature.*

high-frequency spectral density which starts at the threshold $\varepsilon_{\text{th}} = 0.04$. The continuous part of the spectral function A_{con} was modeled by the function

$$A_{\text{con}}(\omega) = \frac{Z_\delta \sqrt{\omega - \varepsilon_{\text{th}}}}{2\pi \sqrt{\varepsilon_{\text{gap}}}[(\omega - \varepsilon_{\text{th}}) + \varepsilon_{\text{gap}}]} \theta(\omega - \varepsilon_{\text{th}})\, \theta(0.566 - \omega) \tag{58}$$

(here $\varepsilon_{\text{gap}} = \varepsilon_{\text{th}} - \varepsilon_\delta$ is a microgap) in the range $\omega \in [\varepsilon_{\text{th}}, 0.566]$ and by a triangle at higher frequencies (see the blue dashed line in the Fig. 8).

The GF $G(\tau)$ was calculated from the test spectrum in the $M = 300$ points $\tau_m = \tau_{\text{max}} m^2/M^2$ in the time range from zero to $\tau_{\text{max}} = 1000$. The noise amplitude was chosen rather small $\mathcal{B} = 10^{-4}$. The restored spectral function reproduces both gross features of the high-frequency part (Fig. 8(a)) and the fine structure at small frequencies (Fig. 8(b)). The energy and the weight of the delta-function was restored with an accuracy of 10^{-4}. The final solution was obtained by averaging (53) $L_{\text{good}} = 1100$ particular solutions.

5.1.2 Finite temperature Green function for fermions

In this test the kernel is given by Eq. (8) for fermions and the spectral function $A(\omega)$ is defined in the whole range $-\infty < \omega < \infty$. The test spectrum was modeled by two triangles (blue dashed line in Fig. 9).

The GF $G(\tau)$ was calculated at finite temperature $\beta = 50$ on $M = 600$ uniformly spaced points in the range $[0, \beta]$. The noise amplitude was chosen rather small $\mathcal{B} = 10^{-4}$. The restored spectral function (red solid line in Fig. 9) reproduces the main features of the test spectrum. The final solution was obtained by averaging (53) $L_{\text{good}} = 150$ particular solutions.

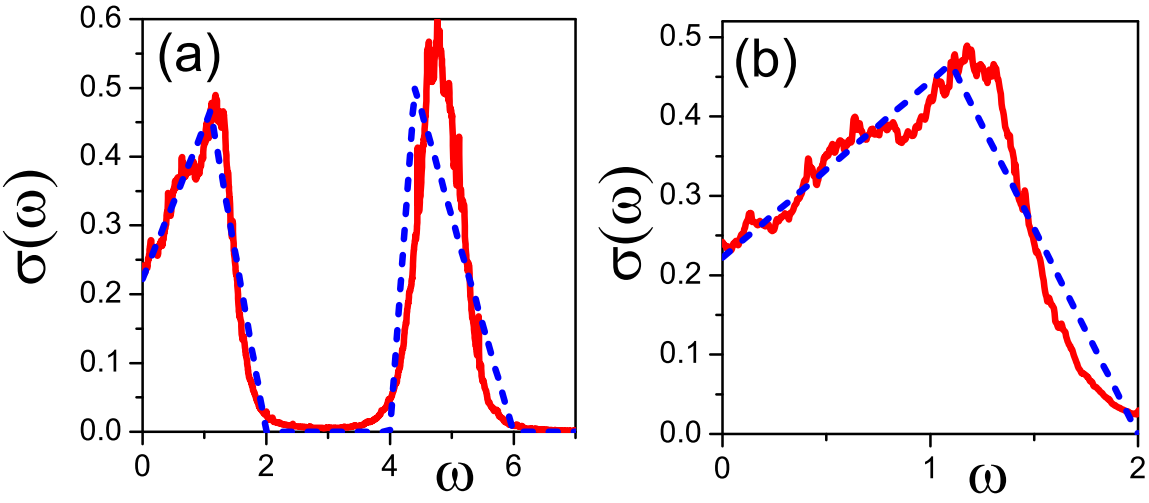

Fig. 10: *The test spectrum (dashed blue line) and the spectrum obtained by SOM (solid red line) for optical conductivity at finite temperature. Panels (a) and (b) show the whole range and low energy part, respectively.*

5.1.3 Finite temperature optical conductivity

In this test the kernel is given by Eq. (9) and the spectral function $\sigma(\omega)$ is symmetric $\sigma(\omega) = \sigma(-\omega)$. The test spectrum was modeled by two triangles (blue dashed line in Fig. 10). The current-current correlation function $J(\tau)$ was calculated at finite temperature $\beta = 20$ on $M = 200$ uniformly spaced points in the range $[0, \beta]$. The noise amplitude was chosen rather small $\mathcal{B} = 10^{-4}$. The restored optical conductivity (red solid line in Fig. 10) reproduces the main features of the test spectrum (Fig. 10(a)) and its low energy part (Fig. 10(b)). The final solution was obtained by averaging (53) $L_{\text{good}} = 200$ particular solutions.

5.2 Test of SOM for Matsubara representation

In this test the kernel is given by Eq. (7) and the spectral function $A(\omega)$ is defined in the whole ω-range. The test spectrum was modeled by two triangles (blue dashed line in Fig. 11(c)).
The GF $\mathcal{G}(i\omega_n)$ was calculated at finite temperature $\beta = 30$ for the first $M = 200$ positive Matsubara frequencies $i\omega_n$ and the analytic continuation was done directly from the set of GFs in Matsubara representation. The noise amplitude was $\mathcal{B} = 10^{-4}$. In Fig. 11 one can see rather good overall agreement between the test and the restored spectra. The final solution was obtained by averaging (53) $L_{\text{good}} = 200$ particular solutions.
The real and imaginary parts of the GF in Matsubara representation are shown in Fig. 11(a). the imaginary time GF, calculated from the test spectrum by Eq. (31), is shown in Fig. 11(b) by a solid black line. The imaginary time GF, calculated from the first 200 Matsubara components in the inverse Fourier transform (6), is shown in Fig. 11(b) by green circles. It is seen that the first 200 components of the GF in the Matsubara representation are not enough to describe the imaginary time GF at small values of τ. This discrepancy is a direct indication that the

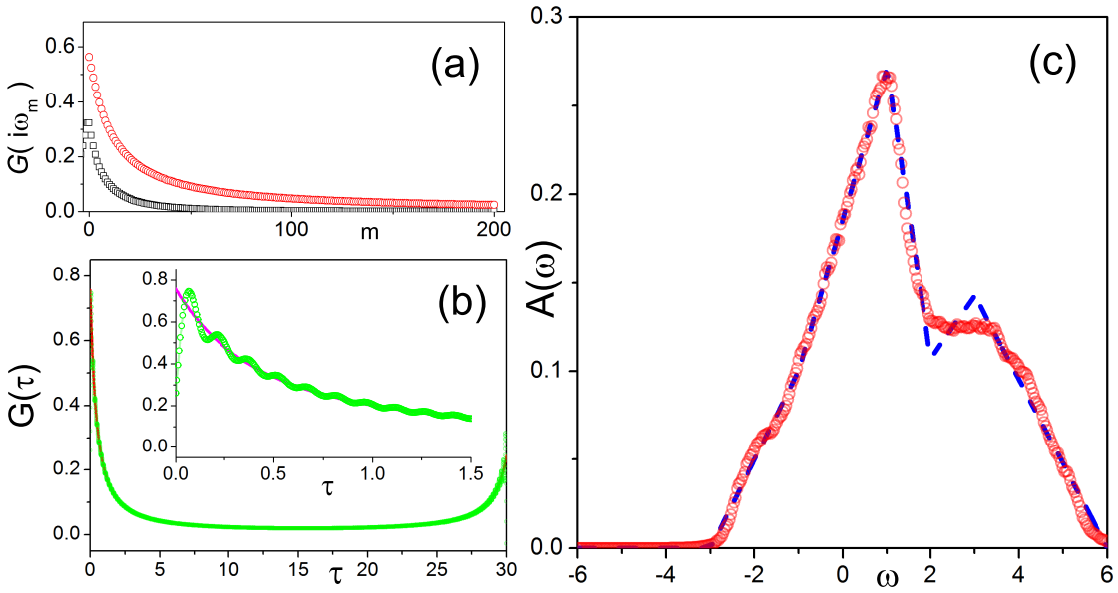

Fig. 11: *(a) First 200 Fourier components of the real (red circles) and imaginary (black squares) part of the GF in Matsubara representation obtained from the GF in imaginary time. (b) Imaginary time GF (solid line) and imaginary time GF obtained from first the $M = 200$ GFs in Matsubara representation. The inset shows low imaginary times. (c) Actual spectrum (dashed blue line) and that restored from 200 Matsubara components (red solid line).*

transformation of the QMC data from one representation into the other is a step which can lose information. Namely, it is dangerous to transform the Matsubara representation into the imaginary time representation because even a large number of Matsubara points still can lead to spurious oscillations of the imaginary time GF (Fig. 11(b)). Hence, it is preferable to make the analytic continuation from the same representation as that in which the QMC data are obtained.

Conclusion

We presented the stochastic optimization method for analytic continuation. The method was considered in relation with numerous other methods handling ill-posed problems. It was concluded that the method is the best for problems when one has to avoid any artificial smoothening of the spectral function and when there is no *a priory* knowledge about the expected solution. The method was successfully applied to many problems. The exponential kernel $\mathcal{K}(m,\omega) = \exp[-\tau_m\omega]$ for zero temperature was considered in Refs. [32, 38–57] and various kernels, ranging from Fermi distribution to the Matsubara frequency representation, are considered in Refs. [58–62]. The method was also used for Gaussian kernels in Refs. [6, 7]. Indeed, the broad area of the solved problems and the successful tests for problems which were not considered before give confidence that the method has considerable potential when application to problems where initial *a priori* knowledge is not available.

The author acknowledges support of RFBR 10-02-00047a and fruitful discussions with B.V. Svistunov and N.V. Prokof'ev.

References

[1] M. Jarrell and J.E. Gubernatis, Phys. Rep. **269**, 133 (1996)

[2] R. Kress, *Linear Integral Equations* (Springer, New York, 1999)

[3] G.D. Mahan, *Many Particle Physics* (Plenum Press, New York, 1990)

[4] A Damascelli, Z. Hussain, and Z.X. Shen, Rev. Mod. Phys. **75**, 473 (2003)

[5] C. Huscroft, R. Gass, and M. Jarrell, Phys. Rev. B **61**, 9300 (2000)

[6] H. Matsui, A.S. Mishchenko, and T. Hasegawa, Phys. Rev. Lett. **104**, 056602 (2010)

[7] A.S. Mishchenko, H. Matsui, and T. Hasegawa, Phys. Rev. B **85**, 085211 (2012)

[8] J. Kaipio and S. Erkki, *Statistical and Computational Inverse Problems*, (Applied Mathematical Sciences Vol. 160) (Springer, Berlin, 2005)

[9] A.N. Tikhonoff and V.Y. Arsenin, *Solutions of Ill-Posed Problems* (Winston & Sons, Washington, 1977)

[10] G.H. Golub and C. Reinsch, Numerische Mathematik **14**, 403 (1970)

[11] R.T. Cox, *The Algebra of Probable Inference* (Johns Hopkins University Press, 1961); A. Papoulis, *Probability and Statistics* (Prentice Hall, New York, 1990)

[12] A.N. Tikhonoff, Dokladyu Akademii Nauk SSSR **39**, 195 (1943)

[13] A.N. Tikhonoff, Dokladyu Akademii Nauk SSSR **151**, 501 (1963) (Soviet Mathematics **4**, 1035 (1963))

[14] D.L. Phillips, J. ACM **9**, 84 (1962)

[15] A.E. Hoerl, Chemical Engineering Progress **58**, 54 (1962)

[16] A.E. Hoerl and R.W. Kennard, Technometrics **12**, 55 (1970)

[17] M. Foster, J. Soc. Industr. Appl. Math. **9**, 387 (1961)

[18] P.C. Hansen, Soc. Industr. Appl. Math. Rev. **34**, 561 (1992)

[19] P.C. Hansen and D.P. O'Leary, Soc. Industr. Appl. Math. J. Sci. Comput. **14**, 487 (1993)

[20] D. Krawchuk-Stando and M. Rudnicki, Int. J. Appl. Math. Comput. Sci. **17**, 157 (2007)

[21] I.S. Krivenko and A.N. Rubtsov, arXiv:cond-mat/0612233

[22] I.S. Krivenko and A.N. Rubtsov, JETP Lett. **94**, 768 (2012)

[23] M. Jarrell and O. Biham, Phys. Rev. Lett. **63**, 2504 (1989)

[24] S.R. White, D.J. Scalapino, R.L. Sugar, and N.E. Bickers, Phys. Rev. Lett. **63**, 1523 (1989)

[25] K. Vafayi and O. Gunnarsson, Phys. Rev B **76**, 035115 (2007)

[26] J. Skilling, J. Microsc. **190**, 28 (1998)

[27] A.W. Sandvik, Phys. Rev B **57**, 10287 (1998)

[28] N. Metropolis, A.W. Rosenbluth, M.N. Rosenbluth, A.H. Teller, E. Teller, J. Chem. Phys. **21**, 1087 (1953)

[29] O.F. Syljuasen, Phys. Rev B **78**, 174429 (2008)

[30] K.S.D. Beach, arXiv:cond-mat/0403055

[31] S. Fuchs, T. Pruschke and M. Jarrell, Phys. Rev E **81**, 056701 (2010)

[32] A.S. Mishchenko, N.V. Prokofév, A. Sakamoto and B.V. Svistunov, Phys. Rev. B **62**, 6317 (2000)

[33] S.R. White, *Computer Simulation Studies of Condensed Matter Physics III* (Springer, Heidelberg, 1991), p. 145

[34] E. Vitali, M. Rossi, L. Reatto and D.E. Galli, Phys. Rev. B **82**, 174510 (2010)

[35] D.M. Ceperley, J. Comput. Phys. **51**, 404 (1983)

[36] D.M. Ceperley and B.J. Alder, J. Chem. Phys. **81**, 5833 (1984)

[37] N.V. Prokofév, B.V. Svistunov, and I.S. Tupitsyn, Phys. Rev. Lett. **82**, 5092 (1999)

[38] A.S. Mishchenko, N.V. Prokof'ev, and B.V. Svistunov, Phys. Rev. B **64**, 033101 (2001)

[39] A.S. Mishchenko, N.V. Prokof'ev, A. Sakamoto, and B.V. Svistunov, Int. J. Mod. Phys. B **15**, 3940 (2001)

[40] A.S. Mishchenko, N. Nagaosa, N.V. Prokof'ev, A. Sakamoto, and B.V. Svistunov, Phys. Rev. B **66**, 020301(R) (2002)

[41] A.S. Mishchenko, N. Nagaosa, N.V. Prokof'ev, A. Sakamoto, and B.V. Svistunov, Phys. Rev. Lett. **91**, 236401 (2003)

[42] A.S. Mishchenko and N. Nagaosa, Phys. Rev. Lett. **93**, 036402 (2004)

[43] A.S. Mishchenko and N. Nagaosa, Phys. Rev. B **73**, 092502 (2006)

[44] A.S. Mishchenko and N. Nagaosa, J. Phys. Chem. Solids **67**, 259 (2006)

[45] G. De Filippis, V. Cataudella, A.S. Mishchenko, C.A. Perroni, and J.T. Devreese, Phys. Rev. Lett. **96**, 136405 (2006)

[46] A.S. Mishchenko, Proceedings of the International School of Physics "Enrico Fermi", Course CLXI, 177-206 (2006)

[47] A.S. Mishchenko and N. Nagaosa, Polarons in Complex Matter, Springer Series in Material Science, Springer, ed. by A.S. Alexandrov, 503-544 (2007)

[48] V. Cataudella, G. De Filippis, A.S. Mishchenko, and N. Nagaosa, Phys. Rev. Lett. **99**, 226402 (2007)

[49] A.S. Mishchenko, in "Computational Many-Particle Physics", ed. by H. Fehske, R. Scheider and A. Weisse, Lect. Notes Phys. 739, pp. 367-395 (Springer, Berlin Heidelberg 2008)

[50] A.S. Mishchenko, N. Nagaosa, Z.-X. Shen, G. De Filippis, V. Cataudella, T.P. Devereaux, C. Bernhard, K.W. Kim, and J. Zaanen, Phys. Rev. Lett. **100**, 166401 (2008)

[51] V. Cataudella, G. De Filippis, A.S. Mishchenko, and N. Nagaosa, J. Supercond. Nov. Magn., **22**, 17 (2009)

[52] A.S. Mishchenko, N. Nagaosa, A. Alvermann, H. Fehske, G. De Filippis, V. Cataudella, and O.P. Sushkov, Phys. Rev. B, **79**, 180301(R) (2009)

[53] A.S. Mishchenko, Usp. Phys. Nauk **179**, 1259 (2009) [Phys. Usp. **52**, 1193 (2009)]

[54] A.S. Mishchenko, Advances in Condensed Matter Physics **2010**, 306106 (2010)

[55] G.L. Goodvin, A.S. Mishchenko, and M. Berciu, Phys. Rev. Lett. **107**, 076403 (2011)

[56] A.S. Mishchenko, N. Nagaosa, K.M. Shen, Z.-X. Shen, X.J. Zhou, T.P. Devereaux, Europhys. Lett. **95**, 57007 (2011)

[57] G. De Filippis, V. Cataudella, A.S. Mishchenko and N. Nagaosa, Phys. Rev. B, **85**, 094302 (2012)

[58] S.S. Aplesnin, Zh. Eksp. Teor. Fiz. **124** 1080 (2003) [JETR **97** 969 (2003)]

[59] H. Hafermann, S. Brener, A.N. Rubtsov, M.I. Katsnelson, and A.I. Lichtenstein, J. Phys.: Condens. Matter **21**, 064248 (2009)

[60] H. Hafermann, M.I. Katsnelson, and A.I. Lichtenstein, Europhys. Lett., **85**, 37006 (2009)

[61] E. Gorelov, M. Karolak, T.O. Wehling, F. Lechermann, A.I. Lichtenstein, and E. Pavarini, Phys. Rev. Lett. **104**, 226401 (2010)

[62] E. Gorelov, J. Kolorenč, T. Wehling, H. Hafermann, A.B. Shick, A.N. Rubtsov, A. Landa, A.K. McMahan, V.I. Anisimov, M.I. Katsnelson, and A.I. Lichtenstein, Phys. Rev. B **82**, 085117 (2010)

15 Introduction to Quantum Information

David P. DiVincenzo
Peter Grünberg Institut
Forschungszentrum Jülich GmbH

Contents

E. Pavarini, E. Koch, F. Anders, and M. Jarrell
Correlated Electrons: From Models to Materials
Modeling and Simulation Vol. 2
Forschungszentrum Jülich, 2012, ISBN 978-3-89336-796-2
http://www.cond-mat.de/events/correl12

1 Introduction

This lecture is, of course, not so closely connected with the other material of this School. Hopefully, it will give you some ideas that might come in handy when you think about the hard problems of strong correlations in electrons that you will be carefully studying in the other parts. *Quantum Information Theory* spends a lot of time thinking about the "trivial" aspects of quantum theory, the parts that you would call "kinematics" in more traditional treatments of quantum mechanics. Kinematics is the counterpart to dynamics; kinematics is the part of quantum theory where you set up your problem, get straight what basis states you will use, take care of selection rules and quantum numbers; dynamics is the part where you really solve for the behavior of your quantum system, including, as well as you can, the features of the real Hamiltonian that you want to study. I will try to convince you in this lecture that the "trivial", kinematic parts of quantum theory are really interesting in their own right, and are leading us to completely unanticipated applications of quantum theory. In fact, quantum information theory is anything but trivial, it has already generated proposed theorems that a lot of smart mathematicians worked on proving for many years (and, in one case, finally disproved). By the end of this chapter, I will at least be able to say what this particularly deep theorem was.

2 Teleportation and other quantum communication protocols

Much of quantum information theory is driven by thought experiments which explore the capabilities, in principle, for quantum systems to perform certain tasks. A few of these are very famous, like quantum cryptography, and have in fact been turned into real experiments. I will explore in detail another famous one called quantum teleportation; I will emphasize what resource question teleportation arises from, and I will show you how, by slightly changing the premise of the thought experiment, you come to another subject, which is called *remote state preparation*. Chances are you haven't heard of remote state preparation, but you will see that it is just as rich and interesting as teleportation (perhaps richer).

Quantum teleportation was first reported as a thought experiment in 1993 [1]. I have been told by two of the six authors (Bennett and Wootters) that this work arose from the question, "If Alice has a quantum state and wants to send it to Bob, how can she do it?" The presumption is that the quantum state is held in the internal state of a particle; we will often imagine that this is a *qubit* state, meaning that the Hilbert space containing the quantum state is just two dimensional. This could be because the state is that of the spin of a spin-1/2 particle, so that the two quantum basis states are "spin up" and "spin down". We will be more abstract and just give a binary labeling to these states (0/1).

The first answer to the Bennett/Wootters question is, "send the particle containing the state from Alice to Bob." So, since this was rather obvious, what Bennett and Wootters (and their co-authors Jozsa, Crépeau, Brassard, and Peres) really asked was, "what *other* method will do the same job?" In constructing their answer they were inspired by ideas in classical communication theory. Classically, there are other resources that can assist in communication tasks –

trusted third parties, authentication techniques, etc. At the basic level, many of these assistance techniques boil down to the idea that *shared classical information* between Alice and Bob, *even if it is completely random*, can greatly facilitate communication tasks. For example, it makes possible the sending of completely secret messages.

What was clear to Bennett and company was that no classical resource by itself was adequate for accomplishing the task of quantum state transmission; even an arbitrarily long classical message is inadequate for the task. The reason for this is that such classical information would have to come from somewhere, and since Alice is in possession of just one particle, the only thing she can do to make meaningful classical information is to measure this particle. But it was known since 1973 (it is called Holevo's theorem [8]) that Alice can get at most one bit of information from any measurement of a spin 1/2 particle. This is completely inadequate for Bob to reconstruct the state of the particle faithfully. A qubit quantum state in general takes two complex numbers (with a normalization constraint) to describe:

$$|\psi\rangle = \alpha|0\rangle + \beta|1\rangle. \tag{1}$$

But Bennett and company had another trick in mind, which concerned the other shared resource that is available in quantum physics: *entanglement [9]*. If two separated spins have never been correlated, then their joint quantum state can only be a tensor product:

$$\begin{aligned} |\psi_{AB}\rangle = |\psi_A\rangle \otimes |\psi_B\rangle &= (\alpha|0\rangle_A + \beta|1\rangle_A) \otimes (\gamma|0\rangle_B + \delta|1\rangle_B) &(2)\\ &= \alpha\gamma|00\rangle + \alpha\delta|01\rangle + \beta\gamma|10\rangle + \beta\delta|11\rangle) &(3)\end{aligned}$$

(I introduced a few different obvious conventions for representing this state.) This is the set of unentangled states; any pure state that cannot be written in a product form is entangled. (The situation is a little different for mixed quantum states, as I will touch on shortly.) Entanglement includes as a special case the notion of classical correlations; in fact this is represented by the mixed state

$$|\psi_{corr.}\rangle\langle\psi_{corr.}| = \frac{1}{2}\,|00\rangle\langle 00| + \frac{1}{2}\,|11\rangle\langle 11|. \tag{4}$$

In words: Alice and Bob have two particles whose state is certainly the same, but with a 50% probability to be in the 0 or the 1 state. But for the general case of Eq. (2), we have known since Bell that such quantum states have correlations that cannot be mimicked by any classical theory. Thus, Bennett *et al.* were motivated to explore this shared resource for the conveyance of an arbitrary quantum state. In particular, they used the "most entangled state":

$$|\beta_{00}\rangle = \frac{1}{\sqrt{2}}\,(|00\rangle + |11\rangle) \tag{5}$$

This is sometimes confusingly called an "Einstein-Podolsky-Rosen" state (it is a distant relative of the state that EPR wrote down, actually due to Bohm), and less confusingly called a "Bell state".

In fact, this state proves to be very useful for the problem of conveying the state of a particle from Alice to Bob. Let us go through the details, following pp. 26-28 of [10]. We suppose that

Alice has qubit state $|\psi_0\rangle$ to "teleport" to Bob, and that they have also previously shared the Bell pair in state $|\beta_{00}\rangle$. Of course the entanglement knows nothing about the message ψ_0. But with some simple unitary transformations, this total state can be brought to a useful form for performing the communication function.

The *quantum circuit* is a basic tool of quantum information theory, so let me spend some time discussing the rules of these circuits, before going into the particulars of quantum teleportation. Figure 1 is just one example of a huge variety of quantum circuits that are used to compactly express many of the primitive operations in quantum information or quantum computation. It is somewhat analogous to a Feynman diagram of scattering theory, in that each horizontal line indicates the presence of a single qubit (so Fig. 1 represents a three-qubit operation). Time goes from left to right. The first few symbols placed on these lines indicate the actions of *quantum logic gates*. These gates perform specific unitary transformations on the quantum state. In this way, quantum information is not only about kinematics, but, in this limited way, also about dynamics. That is to say, it is understood that this unitary transformation should come from some Hamiltonian acting on the qubits at the time indicated. But quantum information theory does not care about the details of what this Hamiltonian is, or where it comes from; it only requires that the indicated state transformation can be done.

The first symbol in the circuit diagram in Fig 1, involving the first two qubits, indicates the action of the *controlled NOT* gate, or CNOT. The transformation produced by this is "classical", in the sense that it can be defined by a truth table, *viz.*,

$$\begin{aligned} 00 &\longmapsto 00 \\ 01 &\longmapsto 01 \\ 10 &\longmapsto 11 \\ 11 &\longmapsto 10\,. \end{aligned} \tag{6}$$

But it is understood that, by the linearity of the Schrödinger equation, this truth table indicates the action on any arbitrary quantum state of these two qubits, which will involve a superposition of these two basis states. The idea of the gate is that it performs a NOT (i.e., inversion of 0 and 1) on the second qubit (the "target qubit"), if the first qubit (the "control qubit") is a 1; if the control qubit is a 0, nothing is done to the target qubit.

The second gate in the quantum circuit of Fig. 1, indicated as an "H" acting on the first qubit, is called a Hadamard gate. It performs the non-classical one-qubit rotation summarized by

$$\begin{aligned} |0\rangle &\longmapsto \frac{1}{\sqrt{2}}\left(|0\rangle + |1\rangle\right) \\ |1\rangle &\longmapsto \frac{1}{\sqrt{2}}\left(|0\rangle - |1\rangle\right)\,. \end{aligned} \tag{7}$$

The next symbol encountered in Fig. 1 is not a unitary operation, but indicates that *quantum measurement* is performed on qubits 1 and 2 separately. The symbol is meant to evoke the idea of an old-fashioned electrical measuring meter; but of course the measurement of a two-level quantum system gives only the two possible (classical) outcomes "0" or "1". M_1 and M_2 are

the classical variables representing these two binary outcomes; the double lines indicate that these classical values are communicated to the third qubit, controlling the action of two final one-qubit gates on this qubit. The measurement outcomes appear as an exponent in these gates; this simply means that, for example, if $M_1 = 0$, then nothing is done to the the third qubit (it has the "identity" operation performed on it), while if $M_1 = 1$, then the "X" gate is performed, which is just the NOT operation

$$\begin{aligned} 0 &\longmapsto 1 \\ 1 &\longmapsto 0\,. \end{aligned} \tag{8}$$

The action conditioned on M_2 is similar except that the "Z" gate (also known at the "π phase gate) is performed, specified by the quantum operation

$$\begin{aligned} |0\rangle &\longmapsto \quad |0\rangle \\ |1\rangle &\longmapsto -|1\rangle\,. \end{aligned} \tag{9}$$

Both X and Z, of course, act linearly on quantum superpositions. These simple examples give essentially all the rules that are needed to interpret quantum gate diagrams.
Now, we return to the details of quantum teleportation. First, given the starting state

$$|\psi_0\rangle = |\psi\rangle|\beta_{00}\rangle = \frac{1}{\sqrt{2}}\Big[\alpha|0\rangle(|00\rangle + |11\rangle) + \beta|1\rangle(|00\rangle + |11\rangle)\Big]\ , \tag{10}$$

local action by Alice (a "CNOT" operation between her two particles) brings this state to

$$|\psi_1\rangle = \frac{1}{\sqrt{2}}\Big[\alpha|0\rangle(|00\rangle + |11\rangle) + \beta|1\rangle(|10\rangle + |01\rangle)\Big]\ . \tag{11}$$

This and subsequent operations is schematized in Fig. 1. Alice then rotates her first qubit (the Hadamard rotation):

$$|\psi_2\rangle = \frac{1}{2}\Big[\alpha(|0\rangle + |1\rangle)(|00\rangle + |11\rangle) + \beta(|0\rangle - |1\rangle)(|10\rangle + |01\rangle)\Big]\ . \tag{12}$$

Here is a very simple but revealing way of simply rewriting this state, by regrouping of qubits:

$$\begin{aligned} |\psi_2\rangle \;=\; & \frac{1}{2}\Big[|00\rangle(\alpha|0\rangle + \beta|1\rangle) + |01\rangle(\alpha|1\rangle + \beta|0\rangle) \\ & +\ |10\rangle(\alpha|0\rangle - \beta|1\rangle) + |11\rangle(\alpha|1\rangle - \beta|0\rangle)\Big]\ . \end{aligned} \tag{13}$$

Recall that the first two qubits are in Alice's possession, and the third in Bob's. In this form it is easy to see what happens if Alice now measures her two qubits. If she gets "00", then the state "collapses" (by the projection postulate) to the first term. The job is then done: the state remaining with Bob is exactly the one with which Alice started. This occurs with probability 1/4. In the other 3/4 of the cases, Alice gets a different outcome, and Bob's state is something different from $|\psi\rangle$. This is summarized so:

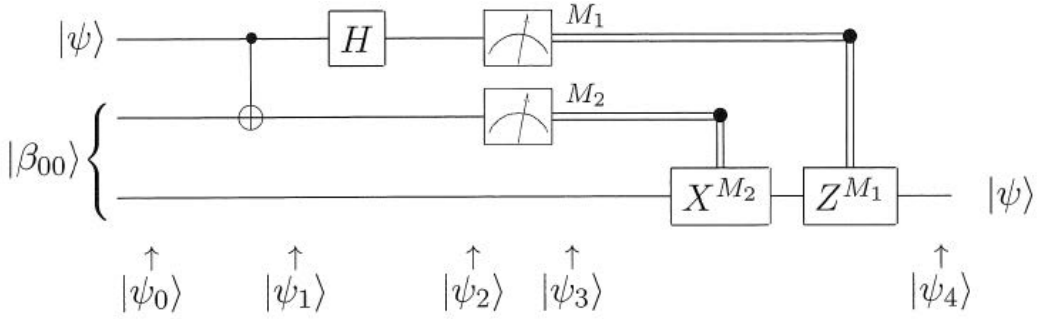

Fig. 1: *Quantum circuit summarizing the steps of quantum teleportation.*

$$00 \longmapsto |\psi_3(00)\rangle \equiv \Big[\alpha|0\rangle + \beta|1\rangle\Big] \tag{14}$$

$$01 \longmapsto |\psi_3(01)\rangle \equiv \Big[\alpha|1\rangle + \beta|0\rangle\Big] \tag{15}$$

$$10 \longmapsto |\psi_3(10)\rangle \equiv \Big[\alpha|0\rangle - \beta|1\rangle\Big] \tag{16}$$

$$11 \longmapsto |\psi_3(11)\rangle \equiv \Big[\alpha|1\rangle - \beta|0\rangle\Big] \ . \tag{17}$$

But for each of the three other outcomes, there is a simple local operation that Bob can perform which will rotate his state to $|\psi\rangle$. So, all that is required is the communication of the two measured bits from Alice to Bob, in order that he knows which rotation to perform.

To summarize the operational effect of quantum teleportation: By the prior sharing of one Bell pair, and the transmission of two classical bits, the same act of quantum communication is accomplished as the direct transmission of one arbitrary qubit state. The sharing of the Bell pair can be accomplished by the transmission of one qubit, which can be done ahead of time, as the state of this qubit is uncorrelated to the "message" qubit until the CNOT operation is performed. The classical two-bit message is also uncorrelated with the quantum message. No matter what the values of α and β, the four outcomes 00, 01, 10, and 11 occur at random with equal probability.

This is all well known and rather simple. But now, as promised, we change the premise of teleportation in an apparently trivial way. We imagine that the values of α and β are *known* to Alice. We might first wonder what "known" means; is it covered by the fact that Alice is in possession of the quantum particle with some state? The answer is "no", the particle, although it has some state, is to be unknown to Alice, supplied, say, by some third party; the particle's state may even be entangled with some other particle otherwise uninvolved in the transmission. So, in this new setting, we assume that Alice has *explicit* knowledge of α and β, by having them stored (to some high precision) in her computer memory.

This is the *remote state preparation* (RSP) setting. Alice and Bob can accomplish the task by the teleportation protocol, without making reference to the stored values α and β. But can any improvement be accomplished if Alice uses her extra knowledge?

The answer is not simple. We discovered [4] that in RSP it is necessary to discuss a resource

tradeoff between entangled pairs and communication of classical bits. In the teleportation setting (Alice having no knowledge of the state), no such tradeoff is available: it was shown that, if n states are to be teleported, it is necessary to use n entangled pairs, even if it is allowed to transmit more than $2n$ classical bits; and, it is necessary to transmit $2n$ classical bits, even if it is allowed to use more than n entangled pairs.

In RSP, both tradeoffs become remarkably nontrivial. We illustrate this with one protocol that we reported, which goes in the direction of less classical communication, at the cost of higher use of entanglement. It uses another feature of two-qubit entanglement, embodied in the following equation:

$$\frac{1}{\sqrt{2}}(|01\rangle - |10\rangle) = e^{i\phi}\frac{1}{\sqrt{2}}(|\psi\psi^{\perp}\rangle - |\psi^{\perp}\psi\rangle). \tag{18}$$

Here $|\psi\rangle$ is any state of a single qubit, $|\psi^{\perp}\rangle$ is orthogonal to $|\psi\rangle$, and ϕ is a $|\psi\rangle$-dependent but irrelevant phase (which can also be absorbed into the definition of $|\psi^{\perp}\rangle$). This amounts to the interesting spin-physics statement that in the two-particle spin singlet, the two spins are opposite in any basis.

The essence of the RSP protocol that we will describe is a projective measurement by Alice. With a knowledge of α and β, Alice constructs a quantum measurement in the basis $|\psi\rangle = \alpha|0\rangle + \beta|1\rangle$ and $|\psi^{\perp}\rangle = -\beta|0\rangle + \alpha|1\rangle$. Alice performs this measurement on her half of a singlet-entangled pair shared with Bob. With a probability of 50% she gets the outcome $\psi^{\perp}$, and in this case, because of Eq. (18), part of the job is done: At this point, Bob's state is ψ, as desired. Of course, he must be somehow informed of this fact, and something further must be done in the case of failure. Failure is not so straightforward to fix, as there is no rotation that Bob can perform to bring $\psi^{\perp}$ to ψ, given that he does not have any information about ψ. If we insist on near-certainty of success, it is not clear that any improvement can be achieved over regular teleportation.

But in fact a real improvement is possible, at least in the setting where some number of states specified by the constants $(\alpha^{(1)}, \beta^{(1)})$, $(\alpha^{(2)}, \beta^{(2)}), \ldots, (\alpha^{(n)}, \beta^{(n)})$ is given. The game will be to assume that a very large number of Alice-Bob singlets are available, and to try to successfully perform RSP on all n of these states, with the least amount of classical communication from Alice to Bob. Here is what we found [4]: Alice performs n projective measurements on her halves of the first n singlets. In all likelihood, about half of her outcomes will be $\psi^{(i)}$ and half will be $\psi^{\perp(i)}$. But if she takes many more blocks of n particles (all singlet-entangled with Bob), and repeats the same set of measurements, then eventually she will get all outcomes $\psi^{\perp(i)}$ for all n particles in that block. While this is very rare, it will happen almost certainly after she has done $2^{n+\log_2 n}$ tries. (This is the same as flipping n coins and asking if they are all "heads"; it does eventually happen.) Alice now just needs to report to Bob which of these tries was successful, and this takes $n + \log_2 n$ bits. Thus, in the limit of $n \to \infty$, the number of bits per state RSPed goes to 1. Thus, we have clearly improved on teleportation of unknown states, which cannot be done with fewer than 2 classical bits per teleportation.

This is perhaps unimpressive, given the gigantic (and diverging) amount of singlet resources that are consumed in this protocol. We found a significant improvement on this protocol, involving

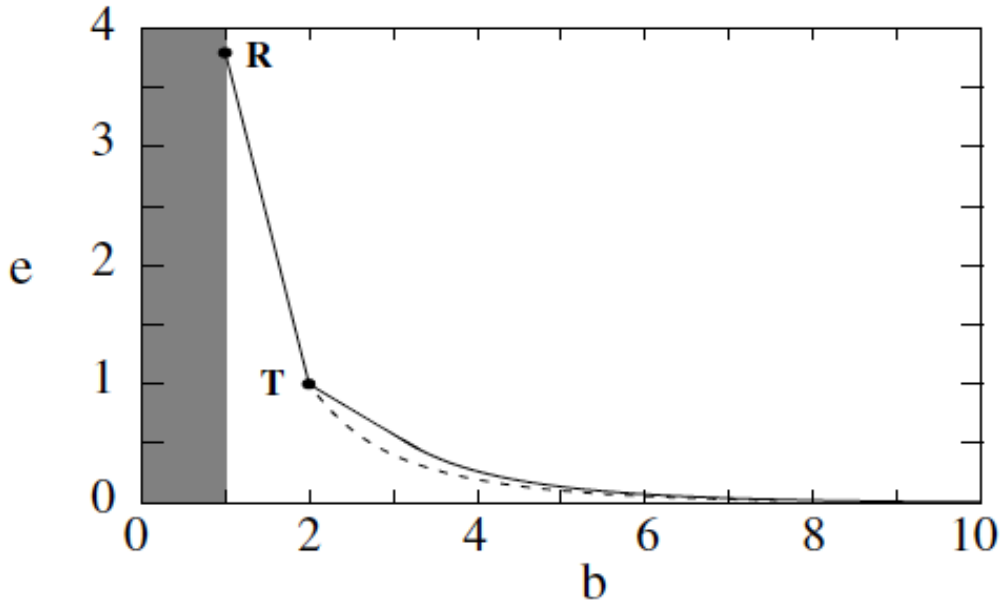

Fig. 2: *Quantum-classical tradeoff curve for Remote State Preparation, as reported in first discovery [4].*

something called entanglement recycling; I will not describe this here, but it decreases the consumption of entanglement from $2^{n+\log_2 n}$ singlets to $n(3+\frac{1}{2}\log_2 3) \approx 3.79\,n$ singlets. Fig. 2 shows that, unlike in teleportation, in RSP there is a continuous tradeoff between the number of singlets needed (called "ebits", or just "e" here) and the number of classical bits (b) that must be transmitted. Finally, within a few years the optimal tradeoff was found (Fig. 3, [5]); it was interesting that it was absolutely better than teleportation, in that it was possible to have protocols using both less entanglement (i.e., less than one singlet per RSP) and less classical communication (i.e., less than two classical bits per RSP).

It is worth noting that all of this work is "merely kinematical". It was not at all about understanding eigenstates, or about time evolution of quantum states. It all emerged from statements about the geometry of the quantum Hilbert space. But "kinematical" means anything but "trivial"; I believe that the reader of these lecture notes would find the final paper in this work, Ref. [5], a very challenging work to understand, invoking quite sophisticated statistical facts about randomly-chosen ensembles of unitary matrices.

3 More simple but deep questions about entanglement

Quantum teleportation posed more "elementary" questions about quantum entanglement that have led to extremely lengthy mathematical investigations. Bennett, Wootters, and company also wondered what would happen to teleportation if some lesser resource than perfect singlets were available. First they considered the case of states such as

$$|\psi(\alpha)\rangle = \alpha|01\rangle - \beta|10\rangle, \tag{19}$$

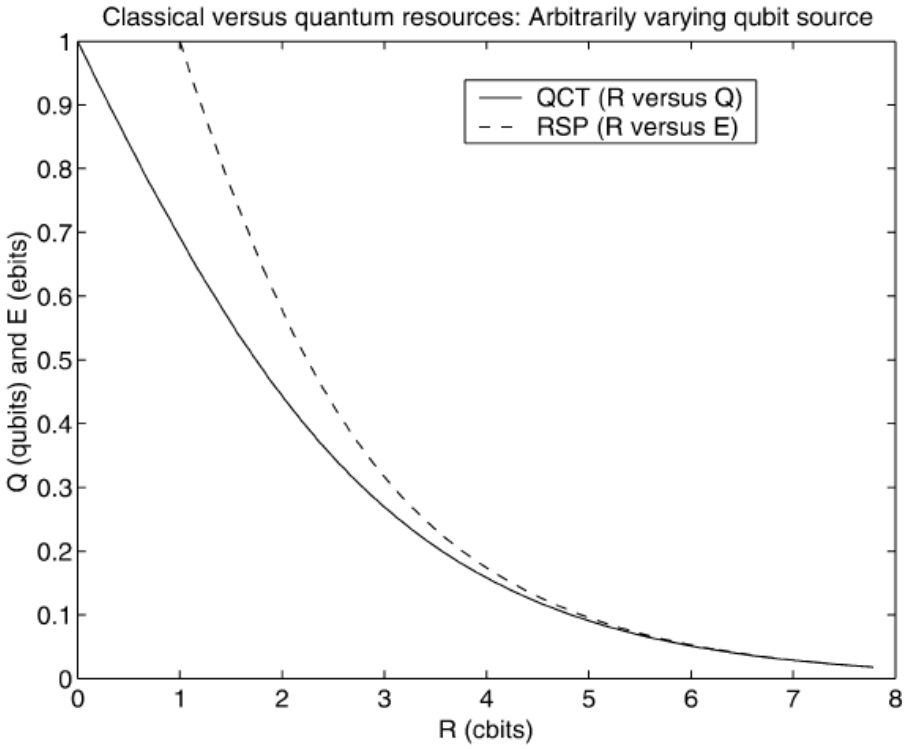

Fig. 3: *Final, optimal, quantum-classical tradeoff curve for Remote State Preparation, as calculated in [5].*

with $\alpha > 1/\sqrt{2}$, say (note the normalization condition $|\alpha|^2 + |\beta|^2 = 1$). That is, we consider states that are pure, but not maximally entangled. It was found [2] that the degree of entanglement of this state could be uniquely characterized by the entropy of the mixed state held by Alice (or Bob) alone, that is, of

$$\rho_A = \begin{pmatrix} |\alpha|^2 & 0 \\ 0 & 1-|\alpha|^2 \end{pmatrix}. \tag{20}$$

This von Neumann entropy function is just

$$H(\rho_A) = -|\alpha|^2 \log(|\alpha|^2) - (1-|\alpha|^2)\log(1-|\alpha|^2). \tag{21}$$

This function plays the following operational role: if Alice and Bob share N copies of $\psi(\alpha)$, they can, almost with certainly, *concentrate* this entanglement, obtaining $NH(\rho_A)$ copies of $\psi(1/\sqrt{2})$ (that is, of singlets). The entanglement concentration protocol is elementary, requiring only that Alice and Bob both measure the number of "0"s among their N states; no communication between them is required. It was also noted that this conversion is reversible in the limit of large N; that is, the conversion

$$N \text{ copies of } \psi(1/\sqrt{2}) \to N/H(\rho_A) \text{ copies of } \psi(\alpha) \tag{22}$$

can also be done by Alice and Bob. But the protocol (called *entanglement dilution*) is very different from that of concentration, and requires some communication (of order $\sqrt{N}$ bits) between Alice and Bob.

Returning to another operational question about teleportation, Bennett and coworkers next wondered of what use a collection of *impure* entangled states would be; by this we refer to Alice-Bob states that must be represented by density matrices – note that this is very different from the "impureness" of ρ_A above, that is just a consequence of the Alice-Bob entanglement. Said in another way, we now consider states for which the Alice and Bob parts are further entangled with a third subsystem – an "environment" – to which no one has any access. It was natural to ask whether pure entanglement could be extracted from these states, which we call ρ_{AB}. That is, we ask for a process

$$N \text{ copies of } \rho_{AB} \rightarrow D(\rho_{AB})N \text{ copies of } \psi(1/\sqrt{2}), \tag{23}$$

which may involve some classical communication between Alice and Bob, and we ask what conversion efficiency $D(\rho_{AB})$ is attainable. The process was given a new name, "distillation", because it was quickly observed that the strategies that Alice and Bob would need to employ were very different from those involved in concentration. $D(\rho_{AB})$ was referred to as the *distillable entanglement*, and it was seen to be related to various other quantities of interest in quantum communication theory. It proved, however, to be very difficult to calculate, as it remains to this day. This motivated the examination, again, of the reverse process: creating mixed states by a kind of dilution process, starting with pure entanglement. This process is defined by

$$N \text{ copies of } \psi(1/\sqrt{2}) \rightarrow N/E(\rho_{AB}) \text{ copies of } \rho_{AB}. \tag{24}$$

$E(\rho_{AB})$ is called the "entanglement cost" for forming state ρ_{AB}. It is an upper bound for the more operationally significant quantity $D(\rho_{AB})$, but there are definitely states for which they are not equal: the process of going back and forth between mixed and pure entanglement is not reversible, unlike for the pure-state case.

There is a straightforward approach to calculating $E(\rho_{AB})$, which has to do with the fact that every mixed state has an ensemble representation, that is, as mixtures of pure states:

$$\rho_{AB} = \sum_i p_i |\phi_i\rangle\langle\phi_i| \ . \tag{25}$$

Given such an ensemble $\mathcal{E}$, it is natural to define its entanglement as

$$E_{\mathcal{E}} = \sum_i p_i H(\phi_i). \tag{26}$$

This expression has a clear operational interpretation: starting with a supply of singlets, a supply of each bipartite state is created by dilution, then one of them is chosen (by the flip of a coin, so to speak). The randomness of the coin flipping creates the desired mixed state. Now, the ensemble $\mathcal{E}$ is not unique, but there is some ensemble for which the expenditure of entanglement is minimal. It is natural to conclude that

$$E(\rho_{AB}) = E_F(\rho_{AB}) = \min_{\mathcal{E}} E_{\mathcal{E}}(\rho_{AB}). \tag{27}$$

E_F, called the *entanglement of formation*, can be readily calculated for many mixed states of interest. Eq. (27) was considered so obvious in our original work that it was asserted without proof (and, in fact, with no notational distinction made between E and E_F). It became evident, however, that a proof was not obvious, and the conjecture, known as the "additivity of entanglement cost", became a central unproved proposition of quantum information theory. This conjecture received intensive scrutiny for more than 10 years. Several years ago, it was proved *false* [7]. No explicit violations of additivity have actually been exhibited, and the most explicit work on the matter shows that non-additivity will occur when the Hilbert space dimension of ρ_{AB} exceeds 3.9×10^4 (sic) [6].

4 Lessons

I hope that you have learned a few things from this lecture. First, quantum kinematics is not trivial! The structure of the quantum Hilbert space alone makes possible the posing of some very deep and complex questions, which profoundly affect how we can communicate and compute. Quantum information first identified itself as a discipline only about 20 years ago, but already there is a vast number of results, some with very profound implications for the further course of experimental physics, and some posing very deep questions for the mathematicians. We have gotten some glimpse, in our examples, of how quantum entanglement can be a unique resource for the accomplishment for a variety of concrete tasks. Theory is far, far ahead of experiment in quantum information science, but we can foresee that many of the capabilities that we theoretically envision will, someday, be a reality in the laboratory. This will give us theorists even more work to do!

References

[1] C.H. Bennett, G. Brassard, C. Crépeau, R. Jozsa, A. Peres, W.K. Wootters, "Teleporting an Unknown Quantum State via Dual Classical and Einstein-Podolsky-Rosen Channels", Phys. Rev. Lett. **70**, 1895-1899 (1993)

[2] C.H. Bennett, H.J. Bernstein, S. Popescu, and B. Schumacher, "Concentrating Partial Entanglement by Local Operations", Phys. Rev. A **53**, 2046-2052 (1996)

[3] C.H. Bennett, D.P. DiVincenzo, J.A. Smolin, W.K. Wootters, "Mixed State Entanglement and Quantum Error Correction", Phys. Rev. A **54**, 3824-3851 (1996); see also `http://en.wikipedia.org/wiki/Entanglement_distillation`

[4] C.H. Bennett, D.P. DiVincenzo, P.W. Shor, J.A. Smolin, B.M. Terhal, W.K. Wootters, "Remote State Preparation", Phys. Rev. Lett. **87**, 077902 (2001)

[5] C.H. Bennett, P. Hayden, D. W. Leung, P.W. Shor, A. Winter, "Remote preparation of quantum states", IEEE Trans. Inform. Theory, **51** (1), 56-74 (2005)

[6] M. Fukuda, C. King, and D. Moser, "Comments on Hastings' Additivity Counterexamples", `http://arxiv.org/abs/0905.3697`

[7] M.B. Hastings, "Superadditivity of communication capacity using entangled inputs", Nature Physics **5**, 255 - 257 (2009)

[8] A.S. Holevo, "Information-theoretic aspects of quantum measurement", [in Russian] Probl. Inform. Transm. **9**(2), 31-42 (1973)

[9] E. Schrödinger, "Die gegenwärtige Situation in der Quantenmechanik", Die Naturwissenschaften **23**, 807-812; 823-828; 844-849 (1935)

[10] M.A. Nielsen and I.L. Chuang, *Quantum Computation and Quantum Information* (Cambridge University Press, 2000)

16 Entanglement in correlated quantum systems: A quantum information perspective

Norbert Schuch
Institute for Quantum Information
RWTH Aachen, 52056 Aachen, Germany

Contents

E. Pavarini, E. Koch, F. Anders, and M. Jarrell
Correlated Electrons: From Models to Materials
Modeling and Simulation Vol. 2
Forschungszentrum Jülich, 2012, ISBN 978-3-89336-796-2
http://www.cond-mat.de/events/correl12

1 Introduction

Understanding the behavior of large interacting quantum systems is essential in quantum chemistry, in the study of exotic condensed matter phenomena such as high-Tc superconductivity or the fractional quantum Hall effect, and beyond. For sytems with only weak interactions, mean field approaches have been applied successfully. However, this approach breaks down when the interactions between parts of the system become sufficiently strong – interactions give rise to quantum correlations, i.e., entanglement, in the system, which is not captured by a mean field approach. The study of entanglement, on the other hand, is one of the core topics of Quantum Information Theory, where an extensive framework for the characterization, quantification, and manipulation of entanglement has been developed. This suggests to apply quantum information concepts, and in particular the theory of entanglement, to the description of quantum many-body systems. Indeed, an active field of research has grown during the last decade at the interface of quantum information theory and quantum many-body physics, and the aim of this lecture is to give an introduction to this area.

For clarity of the presentation, we will initially restrict to quantum spin systems on a lattice (such as a line or a square lattice in 2D), with a corresponding Hilbert space $(\mathbb{C}^d)^{\otimes N}$ (where each spin has d levels, and the lattice has N sites); generalizations to fermionic systems and beyond lattices will be discussed later. Also, we will for the moment focus on ground state problems, i.e., given some Hamiltonian H acting on our spin system, we will ask about properties of its ground state $|\Psi\rangle$. The approach we pursue will be variational – we will try to obtain a family of states which gives a good approximation of the ground state, for which quantities of interest can be evaluated efficiently, and where the best approximation to the ground state can be found efficiently. For instance, mean-field theory is a variational theory based on the class of product states (for spin systems) or Slater determinants (for electronic systems).

Of course, one could simply parametrize the ground state as

$$|\Psi\rangle = \sum_{i_1,\ldots,i_N} c_{i_1\ldots i_N} |i_1,\ldots,i_N\rangle \,, \tag{1}$$

and use the $c_{i_1\ldots i_N}$ as variational parameters. Unfortunately, the number of parameters $c_{i_1\ldots i_N}$ grows exponentially with N, making it impossible to have an efficient description of $|\Psi\rangle$ for growing system sizes. On the other hand, we know that efficient descriptions exist for physical Hamiltonians: Since $H = \sum_i h_i$ is a sum of few-body terms (even if we don't restrict to lattice systems), a polynomial number N^k of parameters (with k the bodiness of the interaction) allows to specify H, and thus its ground state. This is, while a general N-body quantum state can occupy an exponentially large Hilbert space, all physical states live in a very small "corner" of this space. The difficulty, of course, is to find an efficient parametrization which captures the states in this corner of Hilbert space, while at the same time allowing for efficient simulation methods.

2 Matrix product states (MPS)

2.1 The area law

In order to have a guideline for constructing an ansatz class, let us look at the entanglement properties of ground states of interacting quantum systems. To this end, we consider a ground state $|\Psi\rangle$ on a lattice and cut a contiguous region of length L (in one dimension) or an area A (in two dimensions), cf. Fig. 1. It is a well-known result from quantum information theory [1]

Fig. 1: *Area law: The entropy of the reduced states of a block A scales like the length of its boundary ∂A; in one dimension, this implies that the entropy is bounded by a constant.*

that the von Neumann entropy of the reduced density matrix ρ_A of region A,

$$S(\rho_A) = -\rho_A \log \rho_A \ ,$$

quantifies the entanglement between region A and the rest of the system. For a random quantum state, we expect this entanglement to be almost maximal, i.e., on the order of $|A| \log d$ (where $|A|$ is the number of spins in region A). Yet, if we study the behavior of $S(\rho_A)$ for ground states of local Hamiltonians, it is found that $S(\rho_A)$ essentially scales like the *boundary* of region A, $S(\rho_A) \propto |\partial A|$, with possible corrections for gapless Hamiltonians which are at most logarithmic in the volume, $S(\rho_A) \propto |\partial A| \log |A|$. This behavior is known as the *area law* for the entanglement entropy and has been observed throughout for ground states of local Hamiltonians (see, e.g., Ref. [2] for a review); for gapped Hamiltonians in one dimension, this result has been recently proven rigorously [3].

2.2 Matrix product states

Since the entropy $S(\rho_A)$ quantifies the entanglement between region A and its complement, the fact that $S(\rho_A)$ scales like the *boundary* of ρ_A suggests that the entanglement between region A and the rest is essentially located around the boundary between the two regions, as illustrated in Fig. 2. We will now construct an ansatz for many-body quantum systems, starting from the

Fig. 2: *The area law suggests that the entanglement between two regions is located around the boundary.*

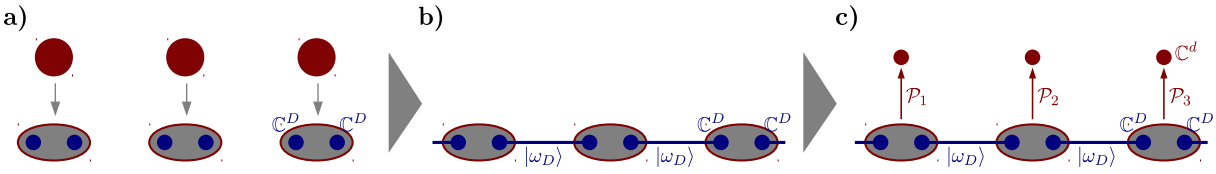

Fig. 3: *Construction of MPS:* ***a)*** *Each site is composed of two virtual subsystems.* ***b)*** *The virtual subsystems are placed in maximally entangled states.* ***c)*** *Linear maps $\mathcal{P}_s$ are applied which map the two virtual systems to the physical system.*

insight that the entanglement is concentrated around the boundary of regions; for the moment, we will focus on one-dimensional systems. Clearly, since we want to have this property for any partitioning of the lattice, we cannot just place entangled pairs as in Fig. 2, but we have to choose a more subtle strategy. To this end, we consider the system at each site as being composed of two "virtual" subsystems of dimension D each, as illustrated in Fig. 3a. Then, each of the two subsystems is placed in a maximally entangled state

$$|\omega_D\rangle = \sum_{i=1}^{D} |i,i\rangle$$

with the corresponding subsystems at the adjacent sites, as shown in Fig. 3b. The maximally entangled states are called "bonds", with D the "bond dimension". This construction already satisfies the area law: For any region we cut, there are exactly two maximally entangled states crossing the cuts, bounding the entanglement by $2\log D$. Finally, we apply at each site s linear maps $\mathcal{P}_s : \mathbb{C}^D \otimes \mathbb{C}^D \to \mathbb{C}^d$, which creates a description of a state on a chain of d-level systems, cf. Fig. 3c. (Note that the rank of the reduced density operator of any region cannot be increased by applying the linear maps $\mathcal{P}_s$.) The construction can be carried out either with periodic boundary conditions, or with open boundary conditions by omitting the outermost virtual subsystems at the end of the chain. The total state of the chain can be written as

$$|\Psi\rangle = (\mathcal{P}_1 \otimes \cdots \otimes \mathcal{P}_N)|\omega_D\rangle^{\otimes N} , \tag{2}$$

where the maps $\mathcal{P}_s$ act on the maximally entangled states as illustrated in Fig. 3c.
This class of states can be rewritten as follows: For each site s, define a three-index tensor $A^{[s]}_{i,\alpha\beta}$, $i = 1,\ldots,d$, $\alpha,\beta = 1,\ldots,D$, where the $A^{[s]}_i$ can be interpreted as $D \times D$ matrices, such that

$$\mathcal{P}_s = \sum_{i,\alpha,\beta} A^{[s]}_{i,\alpha\beta} |i\rangle\langle\alpha,\beta| . \tag{3}$$

Then, the state (2) can be rewritten as

$$|\Psi\rangle = \sum_{i_1,\ldots,i_N} \mathrm{tr}\left[A^{[1]}_{i_1} A^{[2]}_{i_2} \cdots A^{[N]}_{i_N}\right] |i_1,\ldots,i_N\rangle , \tag{4}$$

i.e., the coefficient $c_{i_1\ldots i_N}$ in (1) can be expressed as a product of matrices.[1] For this reason, these states are called *Matrix Product States* (MPS). For systems with open boundary conditions, the

[1] The equivalence of (2) and (4) can be proven straightforwardly by noting that for two maps $\mathcal{P}_1$ and $\mathcal{P}_2$, and

matrices $A^{[1]}_{i_1}$ and $A^{[N]}_{i_N}$ are $1 \times D$ and $D \times 1$ matrices, respectively, so that the trace can be omitted. More generally, D can be chosen differently across each link.

As it turns out, MPS are very well suited to describe ground states of one-dimensional quantum systems. On the one hand, we have seen that by construction, these states all satisfy the area law. On the other hand, it can be shown that all states which satisfy an area law, such as ground states of gapped Hamiltonians [3], as well as states for which the entanglement of a block grows slowly (such as for critical 1D systems), can be well approximated by an MPS [4, 3]: Given a state $|\Phi\rangle$ on a chain of length N for which the entropy of any block of length L is bounded by $S_{\max}$, $S(\rho_L) \leq S_{\max}$, there exists an MPS $|\Psi_D\rangle$ which approximates $|\Phi\rangle$ up to error[2]

$$\big|\,|\Phi\rangle - |\Psi_D\rangle\big| =: \epsilon \leq \text{const} \times \frac{N\ \ e^{cS_{\max}}}{D^c}\ . \tag{5}$$

Note that even if $S_{\max}$ grows logarithmically with N, the numerator is still a polynomial in N. This is, in order to achieve a given accuracy ϵ, we need to choose a bond dimension D which scales polynomially in N and $1/\epsilon$, and thus, the total number of parameters (and, as we will see later, also the computation time) scales polynomially as long as the desired accuracy is at most $1/\mathrm{poly}(N)$.

2.3 Tensor network notation

The defining equation (4) for Matrix Product States is a special case of a so-called *tensor network*. Generally, tensor networks are given by a number of tensors $A_{i_1,i_2,\ldots,i_K}$, $B_{i_1,i_2,\ldots,i_K}$, etc., where each tensor usually only depends on a few of the indices. Then, one takes the product of the tensors and sums over a subset of the indices,

$$c_{i_1\ldots i_k} = \sum_{i_{k+1},\ldots,i_K} A_{i_1,i_2,\ldots,i_K} B_{i_1,i_2,\ldots,i_K} \cdots\ .$$

For instance, in (4) the tensors are the $A^{[s]} \equiv A^{[s]}_{i,\alpha\beta}$, and we sum over the virtual indices $\alpha, \beta, \ldots$, yielding

$$c_{i_1\ldots i_N} = \mathrm{tr}\big[A^{[1]}_{i_1} A^{[2]}_{i_2} \cdots A^{[N]}_{i_N}\big]\ .$$

the bond $|\omega_D\rangle$ between them, it holds that

$$\mathcal{P}_1 \otimes \mathcal{P}_2 |\omega_D\rangle = \sum_{i_1,i_2,\alpha,\beta} (A^{[1]}_{i_1} A^{[2]}_{i_2})_{\alpha\beta} |i_1, i_2\rangle\langle\alpha,\beta|\ ,$$

and iterating this argument through the chain.

[2] Stricly speaking, this bound only follows from an area law for the *Rényi entropy*

$$S_\alpha = \frac{\log \mathrm{tr}[\rho^\alpha]}{1-\alpha}$$

for $\alpha < 1$, with c in (5) depending on α [4], which also holds for gapped Hamiltonians [3]. The proof uses the fact that a bound on the area law implies a fast decay of the Schmidt coefficients (i.e., the eigenvalues of the reduced density operator), and thus, one can construct an MPS by sequentially doing Schmidt decompositions of the state and discarding all but the largest D Schmidt coefficients [5, 4].

Tensor networks are most conveniently expressed in a graphical language. Each tensor is denoted by a box with "legs" attached to it, where each leg corresponds to an index – a three-index tensor $A^{[s]} \equiv A^{[s]}_{i,\alpha\beta}$ is then depicted as

$$A^{[s]}_{i,\alpha\beta} \equiv$$ 

Summing over a joint index is denoted by connecting the corresponding legs, e.g.,

$$\sum_\beta A_{i,\alpha\beta} B_{j,\beta\gamma} \equiv$$ 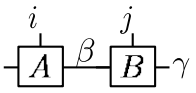

In this language, the expansion coefficient $c_{i_1 \ldots i_N}$ [Eq. (1)] of an MPS (which we will further on use interchangably with the state itself) is written as :

$$|\Psi\rangle \equiv$$ 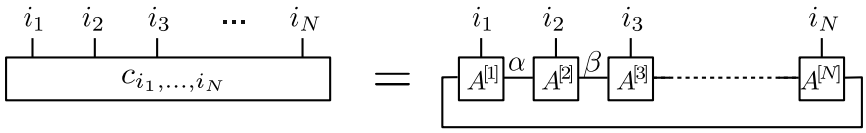

(6)

We will make heavy use of this graphical language for tensor networks in the following.

2.4 Evaluating expectation values for MPS

As we have discussed at the end of Section 2.2, MPS approximate ground states of local Hamiltonians efficiently, as the effort needed for a good approximation scales only polynomially in the length of the chain and the desired accuracy. Thus, it seems appealing to use the class of MPS as a variational ansatz to simulate the properties of quantum many-body systems. However, to this end it is not sufficient to have an efficient description of relevant states – after all, the Hamiltonian itself forms an efficient description of its ground state, but it is hard to extract information from it! Rather, a good variational class also requires that we can efficiently extract quantities of interest such as energies, correlation functions, and the like, and that there is an efficient way to *find* the ground state (i.e., minimize the energy within the variational class of states) in the first place.

Let us start by discussing how to compute the expectation value a local operator h (such as a term in the Hamiltonian) for an MPS. To this end, note that

$$\langle\Psi|h|\Psi\rangle = \sum_{\substack{i_1,\ldots,i_N \\ j_1,\ldots,j_N}} c^*_{i_1\ldots i_N} c_{j_1\ldots j_N} \delta_{i_1,j_1} \cdots \delta_{i_{k-1},j_{k-1}} h^{j_k j_{k+1}}_{i_k i_{k+1}} \delta_{i_{k+2},j_{k+2}} \cdots \delta_{i_N,j_N}$$

where

$$h = \sum_{\substack{i_k,i_{k+1} \\ j_k,j_{k+1}}} h^{j_k j_{k+1}}_{i_k i_{k+1}} |i_k, i_{k+1}\rangle\langle j_k, j_{k+1}|$$

acts on sites k and $k+1$. Using the graphical tensor network notation, this can be written as

$\langle\Psi|h|\Psi\rangle =$ 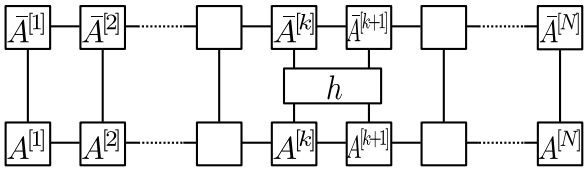

. (7)

In order to evaluate this quantity, we have to contract the whole diagram (7). In principle, contracting arbitrary tensor networks can become an extremely hard problem (strictly speaking, PP-hard [6]), as in some cases it essentially requires to determine exponentially big tensors (e.g., we might first have to compute $c_{i_1\ldots i_N}$ from the tensor network and from it determine the expectation value). Fortunately, it turns out that the tensor network of Eq. (7) can be contracted efficiently, i.e., with an effort polynomial in D and N. To this end, let us start from the very left of the tensor network in Eq. (7) and block the leftmost column (tensors $A^{[1]}$ and $\bar{A}^{[1]}$). Contracting the internal index, this gives a two-index tensor

$$\mathbb{L}^{\alpha\alpha'} = \sum_i A^{[1]}_{i\alpha}\bar{A}^{[1]}_{i\alpha'} ,$$

which we interpret as a (bra) *vector* with a "double index" $\alpha\alpha'$ of dimension D^2. Graphically, this can be denoted as

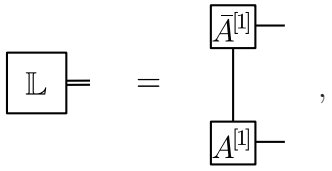

,

where we use a doubled line to denote the "doubled" index of dimension D^2. We can now continue this way, and define operators (called *transfer operators*)

$$(\mathbb{E}^{[s]})^{\beta\beta'}_{\alpha\alpha'} = \sum_i A^{[s]}_{i,\alpha\beta}\bar{A}^{[s]}_{i,\alpha'\beta'}$$

which we interpret as mapping the double index $\alpha\alpha'$ to $\beta\beta'$, and graphically write as

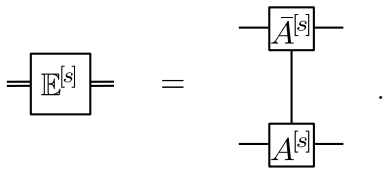

.

Similarly, we define operators

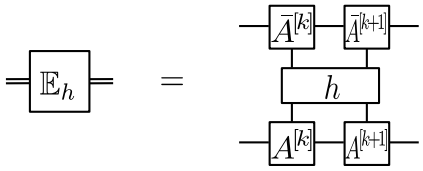

(8)

and

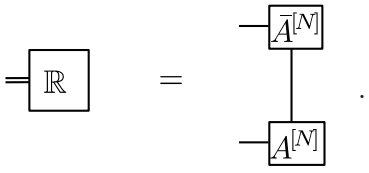

.

All of these operators can be computed efficiently (in the parameters D and N), as they are vectors/matrices of fixed dimension D^2, and can be obtained by contracting a constant number of indices.
Using the newly defined objects $\mathbb{L}$, $\mathbb{E}$, $\mathbb{E}_h$, and $\mathbb{R}$, the expectation value $\langle\Psi|h|\Psi\rangle$, Eq. (7), can be rewritten as

$$\langle\Psi|h|\Psi\rangle = \mathbb{L}\mathbb{E}^{[2]}\cdots\mathbb{E}^{[k-1]}\mathbb{E}_h\mathbb{E}^{[k+2]}\cdots\mathbb{R}$$

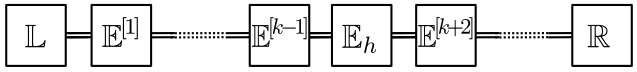

This is, $\langle\Psi|h|\Psi\rangle$ can be computed by multiplying a D^2-dimensional vector $O(N)$ times with $D^2 \times D^2$ matrices. Each of these multiplication takes $O(D^4)$ operations, and thus, $\langle\Psi|h|\Psi\rangle$ can be evaluated in $O(ND^4)$ operations. There are $O(N)$ terms in the Hamiltonian, and thus, the energy $\langle\Psi|\sum_i h_i|\Psi\rangle/\langle\Psi|\Psi\rangle$ can be evaluated in time $O(N^2D^4)$, and thus efficiently; in fact, this method can be easily improved to scale as $O(ND^3)$.[3] Similarly, one can see that e.g. correlation functions $\langle\Psi|P_i \otimes Q_j|\Psi\rangle$ or string order parameters $\langle\Psi|X \otimes X \otimes \cdots \otimes X|\Psi\rangle$ can be reduced to matrix multiplications and thus evaluated in $O(ND^3)$. Exactly the same way, evaluating expectation values for MPS with periodic boundary conditions can be reduced to computing the trace of a product of matrices $\mathbb{E}$ of size $D^2 \times D^2$. Each multiplication scales like $O(D^6)$, and using the same tricks as before, one can show that for systems with periodic boundary conditions, expectation values can be evaluated in time $O(ND^5)$.
In summary, we find that energies, correlations functions, etc. can be efficiently evaluated for MPS, with computation times scaling as $O(ND^3)$ and $O(ND^5)$ for open and periodic boundary conditions, respectively.

2.5 Variational optimization of MPS

As we have seen, we can efficiently compute the energy of an MPS with respect to a given local Hamiltonian $H = \sum_i h_i$. In order to use MPS for numerical simulations, we still need to figure out an efficient way to find the MPS which minimizes the energy for a given D. To this end, let us first pick a site k, and try to minimize the energy as a function of $A^{[k]}$, while keeping all other MPS tensors $A^{[s]}$, $s \neq k$, fixed. Now, since $|\Psi\rangle$ is a linear function of $A^{[k]}$, we have that

$$\frac{\langle\Psi|H|\Psi\rangle}{\langle\Psi|\Psi\rangle} = \frac{\vec{A}^{[k]\dagger} X \vec{A}^{[k]}}{\vec{A}^{[k]\dagger} Y \vec{A}^{[k]}}$$

is the ratio of two quadratic forms in $A^{[k]}$. Here, $\vec{A}^{[k]}$ denotes the vectorized version of $A^{[k]}_{i,\alpha\beta}$, where (i,α,β) is interpreted as a single index. The matrices X and Y can be obtained by contracting the full tensor network (7) except for the tensors $A^{[k]}$ and $\bar{A}^{[k]}$, which can be done

[3] Firstly, one uses that the products $\mathbb{L}\cdots\mathbb{E}^{[s]}$ and $\mathbb{E}^{[s]}\cdots\mathbb{R}$ need to be computed only once (this can be simplified even further by choosing the appropriate gauge [7, 8]), reducing the N-scaling to $O(N)$. Secondly, one slightly changes the contraction order: Starting from the left, one contracts $A^{[1]}$, $\bar{A}^{[1]}$, $A^{[2]}$, $\bar{A}^{[2]}$, $A^{[3]}$, etc.: This involves multiplications of $D \times D$ matrices with $D \times dD$ matrices, and $D \times Dd$ matrices with $Dd \times D$ matrices, yielding a $O(dD^3)$ scaling.

efficiently. The $\vec{A}^{[k]}$ which minimizes this energy can be found by solving the generalized eigenvalue equation

$$X\vec{A}^{[k]} = E\,Y\vec{A}^{[k]}$$

where E is the energy; again, this can be done efficiently in D. For MPS with open boundary conditions, we can choose a gauge[4] for the tensors such that $Y = \mathbb{1}$ [7, 8] – this reduces the problem to a usual eigenvalue problem, and avoids problems due to ill-conditioned Y.

This shows that we can efficiently minimize the energy as a function of the tensor $A^{[k]}$ at an individual site k. In order to minimize the overall energy, we start from a randomly chosen MPS, and then sweep through the sites, sequentially optimizing the tensor at each site. Itering this a few times over the system (usually sweeping back and forth) quickly converges to a state with low energy. Although in principle, such an optimization can get stuck [10, 11], in practice it works extremely well and generally converges to the optimal MPS (though some care might have to be put into choosing the initial conditions).

In summary, we find that we can use MPS to efficiently simulate ground state properties of one-dimensional quantum systems with both open and periodic boundary conditions. This simulation method can be understood as a reformulation of the Density Matrix Renormalization Group (DMRG) algorithm [12, 13], which is a renormalization algorithm based on keeping the states which are most relevant for the entanglement of the system, and which since its invention has been highly successful in simulating the physics of one-dimensional quantum systems (see Refs. [7, 14] for a review of the DMRG algorithm and its relation to MPS).

3 Projected entangled pair states (PEPS)

3.1 PEPS for two-dimensional systems

As we have seen, MPS are very well suited for simulating ground state properties of one-dimensional systems. But what if we want to go beyond one-dimensional systems, and, e.g., study interacting spin systems in two dimensions? Two-dimensional systems can exhibit a rich variety of phenomena, such as topologically ordered states [15, 16], which are states distinct from those in the trivial phase, yet which do not break any (local) symmetry. Moreover, two-dimensional spin systems can be highly frustrated due to the presence of large loops in the interaction graph, and even classical two-dimensional spin glasses can be hard to solve [17]. In the following, we will focus on the square lattice without loss of generality.

[4] MPS have a natural gauge degree of freedom, since for any X_s with a right inverse X_s^{-1}, we can always replace

$$A_i^{[s]} \leftrightarrow A_i^{[s]} X_s$$
$$A_i^{[s+1]} \leftrightarrow X_s^{-1} A_i^{[s+1]}$$

without changing the state; this gauge degree of freedom can be used to obtain standard forms for MPS with particularly nice properties [9, 8].

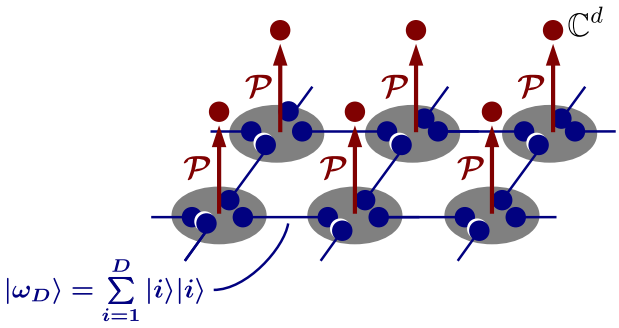

Fig. 4: *PEPS construction for a 2D square lattice, where we have omitted the site-dependence $\mathcal{P} \equiv \mathcal{P}_s$ of the maps $\mathcal{P}_s$.*

A first idea to simulate two-dimensional systems would be to simply use an MPS, by choosing a one-dimensional ordering of the spins in the two-dimensional lattice. While this approach has been applied successfully (see, e.g., Ref. [18]), it cannot reproduce the entanglement features of typical ground states in two dimensions as one increases the system size: As we have discussed in Section 2.1, two-dimensional systems also satisfy an area law, i.e., in the ground state we expect the entanglement of a region A with its complement to scale like its boundary, $S(\rho_A) \sim |\partial A|$. To obtain an ansatz with such an entanglement scaling, we follow the same route as in the construction of MPS: We consider each site as being composed of *four* D-dimensional virtual subsystems, place each of them in a maximally entangled state $|\omega_D\rangle$ with the corresponding subsystem of each of the adjacent sites, and finally apply a linear map

$$\mathcal{P}_s : \mathbb{C}^D \otimes \mathbb{C}^D \otimes \mathbb{C}^D \otimes \rightarrow \mathbb{C}^d$$

at each site s to obtain a description of the physical state on a 2D lattice of d-level sytems. The construction is illustrated in Fig. 4. Due to the way they are constructed, these states are called *Projected Entangled Pair States* (PEPS). Again, we can define five-index tensors $A^{[s]} = A^{[s]}_{i,\alpha\beta\gamma\delta}$, where now

$$\mathcal{P}_s = \sum_{i\alpha\beta\gamma\delta} A^{[s]}_{i,\alpha\beta\gamma\delta} |i\rangle\langle\alpha,\beta,\gamma,\delta| \,,$$

and express the PEPS in Fig. 4 graphically as a tensor network

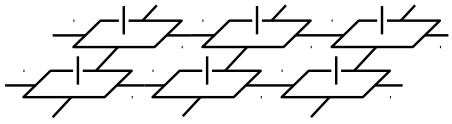

(where we have omitted the tensor labels). Similar to the result in one dimension, one can show that PEPS approximate ground states of local Hamiltonians well as long as the density of states grows at most polynomially with the energy [19, 20], and thereby provide a good variational ansatz for two-dimensional systems. (Note, however, that it is not known whether all 2D states which obey an area law are approximated well by PEPS.)

3.2 Contraction of PEPS

Let us next consider what happens if we try to compute expectation values of local observables for PEPS. For simplicity, we first discuss the evaluation of the normalization $\langle\Psi|\Psi\rangle$, which is obtained by sandwiching the ket and bra tensor network of $|\Psi\rangle$,

$\langle\Psi|\Psi\rangle$ =

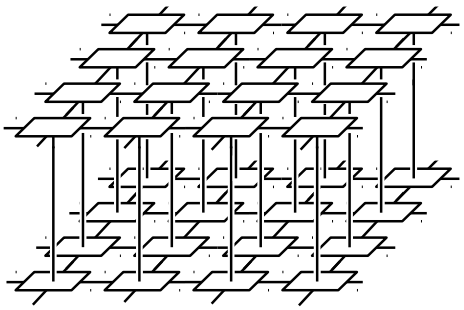

. (9)

This can again be expressed using transfer operators

(the $\mathbb{E}$ should be thought of as being "viewed from the top"), leaving us with the task of contracting the network

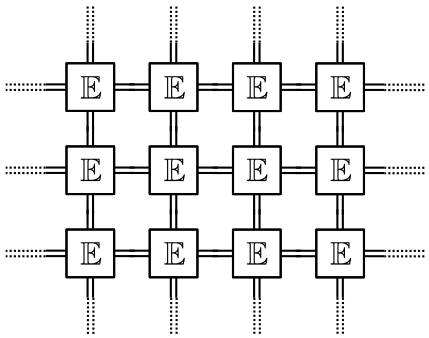

.

[This easily generalizes to the computation of expectation values, where some of the $\mathbb{E}$ have to be modified similarly to Eq. (8)]. Different from the case of MPS, there is no one-dimensional structure which we can use to reduce this problem to matrix multiplication. In fact, it is easy to see that independent of the contraction order we choose, the cluster of tensors we get (such as a rectangle) will at some point have a boundary of a length comparable to the linear system size. This is, we need to store an object with a number of indices proportional to $\sqrt{N}$ – and thus an *exponential* number of parameters – at some point during the contraction, making it impossible to contract such a network efficiently. (Indeed, it can be proven that such a contraction is a computationally hard problem [6].)

This means that if we want to use PEPS for variational calculations in two dimensions, we have to make use of some approximate contraction scheme, which of course should have a small and ideally controlled error. To this end, we proceed as follows [21]: Consider the contraction of a

two-dimensional PEPS with open boundary conditions,

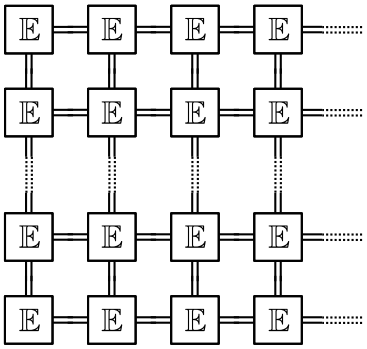

. (10)

Now consider the first two columns, and block the two tensors in each column into a new tensor $\mathbb{F}$ (with vertical bond dimension D^4):

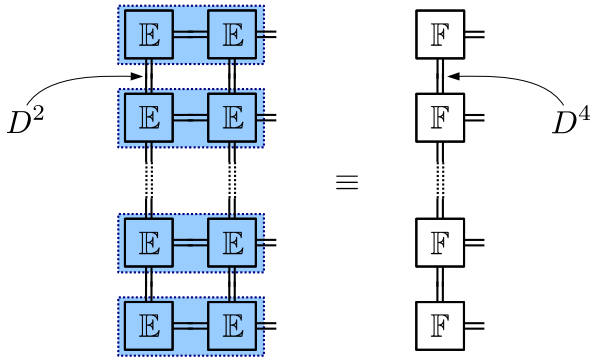

. (11)

This way, we have reduced the number of columns in (10) by one. Of course, this came at the cost of squaring the bond dimension of the first column, so this doesn't help us yet. However, what we do now is to approximate the right hand side of (11) by an MPS with a (fixed) bond dimension αD^2 for some α. We can then iterate this procedure column by column, thereby contracting the whole PEPS, and at any point, the size of our tensors stays bounded. It remains to be shown that the elementary step of approximating an MPS $|\Phi\rangle$ [such as the r.h.s. of (11)] by an MPS $|\Psi\rangle$ with smaller bond dimension can be done efficiently: To this end, it is sufficient to note that the overlap $\langle\Phi|\Psi\rangle$ is linear in each tensor $A^{[s]}$ of $|\Psi\rangle$, and thus, maximizing the overlap

$$\frac{\big|\langle\Phi|\Psi\rangle\big|^2}{\langle\Psi|\Psi\rangle}$$

can again be reduced to solving a generalized eigenvalue problem, just as the energy minimization for MPS in the one-dimensional variational method. Differently speaking, the approximate contraction scheme succeeds by reducing the two-dimensional contraction problem to a sequence of one-dimensional contractions, i.e., it is based on a dimensional reduction of the problem.

This shows that PEPS can be contracted approximately in an efficient way. The scaling in D is naturally much less favorable than in one dimension, and for the most simple approach one finds a scaling of D^{12} for open boundaries, which using several tricks can be improved down to D^8. Yet, the method is limited to much smaller D as compared to the MPS ansatz. It should be

noted that the approximate contraction method we just described has a controlled error, as we know the error made in in each approximation step. Indeed, the approximation is very accurate as long as the system is short-range correlated, and the accuracy of the method is rather limited by the D needed to obtain a good enough approximation of the ground state. Just as in one dimension, we can use this approximate contraction method to build a variational method for two-dimensional systems by successively optimizing over individual tensors [21].

3.3 Extensions of PEPS

The PEPS construction is not limited to square lattices, but can be adapted to other lattices, higher dimensions, and even arbitrary interaction graphs. Clearly, the approximate contraction scheme we just presented works for any two-dimensional lattice, and in fact for any planar graph. In order to approximately contract systems in more than two dimensions, note that the approximate contraction scheme is essentially a scheme for reducing the dimension of the problem by one; thus, in order to contract e.g. three-dimensional systems we can nest two layers of the scheme. In cases with a highly connected PEPS graph (e.g., when considering systems with highly connected interaction graphs such as orbitals in a molecule), one can of course still try to find a sequential contraction scheme, though other contraction methods might be more promising.

The contraction method described in Section 3.2 is not the only contraction scheme for PEPS. One alternative method is based on renormalization ideas [22–24]: There, one takes blocks of e.g. 2×2 tensors and tries to approximate them by a tensor with lower bond dimension by the appropriate truncation,

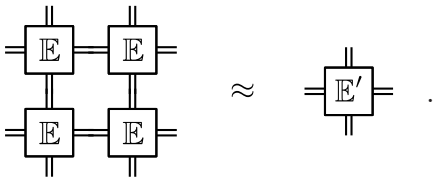

Finding the best truncation scheme requires exact knowledge of the environment, i.e., the contraction of the remaining tensor network. Since this is as hard as the original problem, heuristic methods to approximate the environment (such as to only contract a small number of surrounding tensors exactly, and imposing some boundary condition beyond that) have been introduced. While these approximations are in principle less accurate and the error is less controlled, their more favorable scaling allows for larger D and thus potentially better approximations of the ground state.

Another approach to speed up PEPS contraction is using Monte Carlo sampling [25–27]: We can always write

$$\frac{\langle\Psi|O|\Psi\rangle}{\langle\Psi|\Psi\rangle} = \sum_i p(i) \frac{\langle i|O|\Psi\rangle}{\langle i|\Psi\rangle} \,, \tag{12}$$

where the sum runs over an orthonormal basis $|i\rangle$, and $p(i) = |\langle i|\Psi\rangle|^2/\langle\Psi|\Psi\rangle$; in particular, we want to consider the local spin basis $i = (i_1, \ldots, i_N)$. If we can compute $\langle i|\Psi\rangle$ and $\langle i|O|\Psi\rangle$ (where the latter reduces to the former if O is a local operator), then we can use Monte Carlo

sampling to approximate the expectation value $\langle\Psi|O|\Psi\rangle$. In particular, for PEPS $\langle i|\Psi\rangle$ can again be evaluated by contracting a two-dimension tensor network; however, this network now has bond dimension D rather than D^2. Thus, we can apply any of the approximate contraction schemes described before, but we can go to much larger D with the same computational resources; it should be noted, however, that the number of operations needs to be multiplied with the number M of sample points taken, and that the accuracy of Monte Carlo sampling improves as $1/\sqrt{M}$.

4 Simulating time evolution and thermal states

Up to now, our discussion has been focused on ground states of many-body systems. However, the techniques described here can also be adapted to simulate thermal states as well as time evolution of systems governed by local Hamiltonians. In the following, we will discuss the implementation for one-dimensional systems; the generalization to to 2D and beyond is straightforward.

Let us start by discussing how to simulate time evolutions. (This will also form the basis for the simulation of thermal states.) We want to study how an initial MPS $|\Psi\rangle$ changes under the evolution with e^{iHt}; w.l.o.g., we consider H to be nearest neighbor. To this end, we perform a Trotter decomposition

$$e^{iHt} \approx \left(e^{iH_{\text{even}}t/M} e^{iH_{\text{odd}}t/M}\right)^M$$

where we split $H = H_{\text{even}} + H_{\text{odd}}$ into even and odd terms (acting between sites 12, 34, …, and 23, 45, …, respectively), such that both H_{even} and H_{odd} are sums of non-overlapping terms. For large M, the Trotter expansion becomes exact, with the error scaling like $O(1/M)$. We can now write

$$e^{iH_{\text{even}}\tau} = \bigotimes_{i=1,3,5,\ldots} e^{ih_{i,i+1}\tau} = \boxed{e^{ih_{12}\tau}}\ \boxed{e^{ih_{34}\tau}}\ \cdots$$

(with $\tau = t/M$), and similarly for $e^{iH_{\text{odd}}\tau}$. Thus, after one time step τ the initial MPS is transformed into

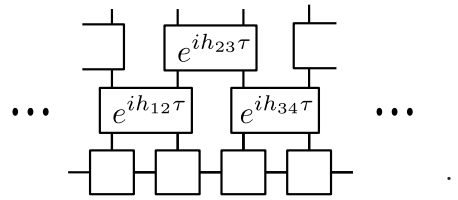

Here, the lowest line is the initial MPS, and the next two lines the evolution by H_{even} and H_{odd} for a time τ, respectively. We can proceed this way and find that the state after a time t is described as the boundary of a two-dimensional tensor network. We can then use the same procedure as for the approximate contraction of PEPS (proceeding row by row) to obtain an MPS description of the state at time t [5]. A caveat of this method is that this only works well as long as the state has low entanglement at all times, since only then, a good MPS approximation of the state exists [4, 28]. While this holds for low-lying excited states with a small number of quasiparticles, this is not true after a quench, i.e., a sudden change of the overall

Hamiltonian of the system [29, 30]. However, this does not necessarily rule out the possibility to simulate time evolution using tensor networks, since in order to compute an expectation value $\langle\Psi|e^{-iHt}Oe^{iHt}|\Psi\rangle$, one only needs to contract a two-dimensional tensor network with no boundary, which can not only be done along the time direction (row-wise) but also along the space direction (column-wise), where such bounds on the correlations do not necessarily hold; indeed, much longer simulations times have be obtained this way [31].
In the same way as real time evolution, we can also implement imaginary time evolution; and since $e^{-\beta H}$ acting on a random initial state approximates the ground state for $\beta \to \infty$, this can be used as an alternative algorithm for obtaining MPS approximations of ground states.
In order to simulate thermal states, we use Matrix Product Density Operators (MPDOs) [32]

$$\rho = \sum_{\substack{i_1,\ldots,i_N \\ j_1,\ldots,j_N}} \mathrm{tr}[A^{[1]}_{i1,j1}\cdots A^{[N]}_{i_N,j_N}]|i_1,\ldots,i_N\rangle\langle j_1,\ldots,j_N|$$

$=$ 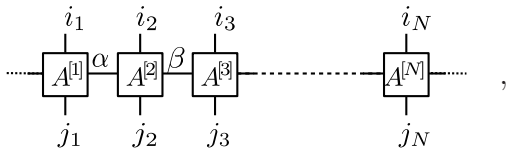

,

where each tensor $A^{[s]}$ now has two physical indices, one for the ket and one for the bra layer. We can then write the thermal state as

$$e^{-\beta H} = e^{-\beta H/2}\,\mathbb{1}\,e^{-\beta H/2}$$

and use imaginary time evolution (starting from the maximally mixed state $\mathbb{1}$ which has a trivial tensor network description) and the Trotter decomposition to obtain a tensor network for $e^{-\beta H}$, which can again be transformed into an MPDO with bounded bond dimension using approximate contraction [32].

5 Other tensor network ansatzes

There is a number of other entanglement based ansatzes beyond MPS and PEPS for interacting quantum systems, some of which we will briefly sketch in the following.
Firstly, there is the Multiscale Entanglement Renormalization Ansatz (MERA) [33], which is an ansatz for scale invariant systems (these are systems at a critical point where the Hamiltonian is gapless, and which have algebraically decaying correlation functions), and which incorporates the scale-invariance in the ansatz. A first step towards a scale-invariant ansatz would be to choose a tree-like tensor network. However, such an ansatz will not have sufficient entanglement between different blocks. Thus, one adds additional *disentanglers* which serve to remove the entanglement between different blocks, which gives rise to the tensor network shown in Fig. 5. In order to obtain an efficiently contractible tensor network, one chooses the tensors to be unitaries/isometries in vertical direction, such that each tensor cancels with its adjoint. It is easy to see that this way for any local O, in the tensor network for $\langle\Psi|O|\Psi\rangle$ most tensors cancel, and one only has to evaluate a tensor network of the size of the *depth* of the MERA, which is

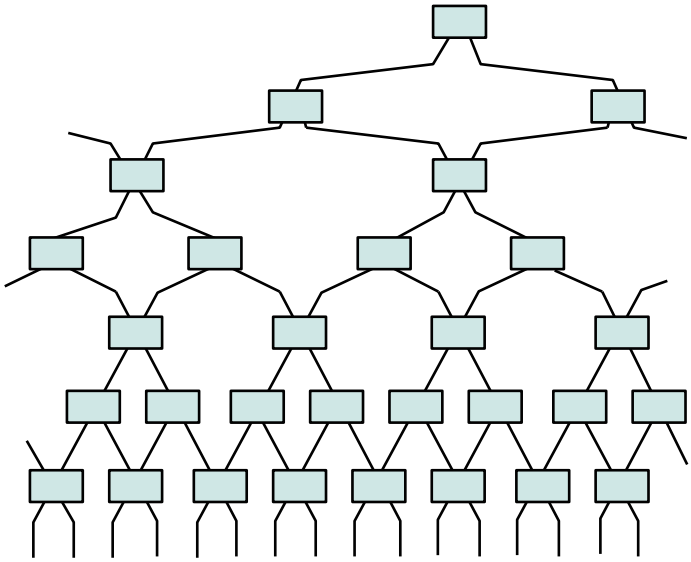

Fig. 5: *The Multi-Scale Entanglement Renormalization Ansatz (MERA) in 1D. (The left and right boundary are connected.)*

logarithmic in its length [33]. The MERA ansatz is not restricted to one dimension and can also be used to simulate critical system in 2D and beyond [34].

A different variational class is obtained by studying states for which expectation values can be computed efficiently using Monte Carlo sampling. Following Eq. (12), this requires (for local quantities O) that we can compute $\langle i|\Psi\rangle$ efficiently for all $i = (i_1, \ldots, i_N)$. One class of states for which this holds is formed by MPS, which implies that we can evaluate expectation values for MPS using Monte Carlo sampling [26, 25] (note that the scaling in D is more favorable since $\langle i|\Psi\rangle$ can be computed in time $\propto ND^2$). This can be extended to the case where $\langle i|\Psi\rangle$ is a product of efficiently computable objects, such as products of MPS coefficients defined on subsets of spins: We can arrange overlapping one-dimensional strings in a 2D geometry and associate to each of them an MPS, yielding a class known as string-bond states [25, 35], which combines a flexible geometry with the favorable scaling of MPS-based methods. We can also consider $\langle i|\Psi\rangle$ to be a product of coefficients each of which only depends on the spins i_k supported on a small plaquette, and where the lattice is covered with overlapping plaquettes, yielding a family of states known as Entangled Plaquette States (EPS) [36] or Correlator Product States (CPS) [37], which again yields an efficient algorithm with flexible geometries. In all of these ansatzes, the energy is minimized by using a gradient method, which is considerably facilitated by the fact that the gradient can be sampled directly without the need to first compute the energy landscape.

In order to simulate infinite lattices, it is possible to extend MPS and PEPS to work for infinite systems: iMPS and iPEPS. The underlying idea is to describe the system by an infinite MPS and PEPS with a periodic pattern of tensors such as ABABAB... (which allows the system to break translational symmetry and makes the optimization more well-behaved). Then, one fixes all tensors except for one and minimizes the energy as a function of that tensor until convergence is reached. For the optimization, one needs to determine the dependence of the energy on the

selected tensor, which can be accomplished in various ways, such as using the fixed point of the transfer operator, renormalization methods (cf. Section 3.3), or the corner transfer matrix approach. For more information, see, e.g., [38–40].

6 Simulation of fermionic sytems

Up to now, we have considered the simulation of spin systems using tensor networks. On the other hand, in many cases of interest, such as for the Hubbard model or the simulation of molecules, the underlying systems are fermionic in nature. In the following, we will discuss how tensor network methods such as MPS, PEPS, or MERA can be extended to the simulation of fermionic systems.

In order to obtain a natural description of fermionic systems, the idea is to replace each object (i.e., tensor) in the construction of MPS, PEPS, or MERA by fermionic operators [41–43]. This is, in the construction of MPS and PEPS, Fig. 3 and Fig. 4, both the maximally entangled bonds and the $\mathcal{P}_s$ are now built from fermionic operators and need to preserve parity; equally, in the MERA construction, Fig. 5, all unitaries and isometries are fermionic in nature. The resulting states are called fermionic PEPS (fPEPS) and fermionic MERA (fMERA).

Let us now have a closer look at a fermionic tensor network, and discuss how to compute expectation values for those states. E.g., the fPEPS construction yields a state

$$(\mathcal{P}_1 \otimes \mathcal{P}_2 \otimes \cdots)(\omega_1 \otimes \omega_2 \otimes \cdots)|\Omega\rangle \ ,$$

where $|\Omega\rangle$ is the vacuum state, the ω_i create entangled fermionic states between the corresponding auxiliary modes, and the $\mathcal{P}_s$ map the auxiliary fermionic modes to the physical fermionic modes at site s (leaving the auxiliary modes in the vacuum). While the product of the ω_i contains only auxiliary mode operators in a given order, the product of the $\mathcal{P}_s$ contains the physical and auxiliary operators for each site grouped together. To compute expectation values, on the other hand, we need to move all the physical operators to the left and the virtual operators to the right in the product of the $\mathcal{P}_s$; additionally, the virtual operators have to be arranged such that they cancel with the ones arising from the product of the ω_i. Due to the fermionic anti-commutation relations, this reordering of fermionic operators results in an additional complication which was not present for spin systems. Fortunately, it turns out that there are various ways how to take care of the ordering of fermionic operators at no extra computational cost: One can use a Jordan-Wigner transformation to transform the fermionic system to a spin system [41, 43]; one can map the fPEPS to a normal PEPS with one additional bond which takes care of the fermionic anticommutation relations [42]; or one can replace the fermionic tensor network by a planar spin tensor network with parity preserving tensors, where each crossing of lines [note that a planar embedding of a network such as the 2D expectation value in Eq. (9) gives rise to crossings of lines, which corresponds to the reordering of fermionic operators] is replaced by a tensor which takes care of the anticommutation rules [44, 45].

7 Summary

In this lecture, we have given an overview over entanglement-based ansatzes for the description and simulation of quantum many-body systems. We started by discussing the area law for the entanglement entropy which is obeyed by ground states of local interactions, and used this to derive the Matrix Product State (MPS) ansatz which is well suited to describe the physics of such systems. We showed that the one-dimensional structure of MPS allows for the efficient evaluation of expectation values, and that this can be used to build a variational algorithm for the simulation of one-dimensional systems. We have then discussed Projected Entangled Pair States (PEPS), which naturally generalize MPS and are well suited for the description of two-dimensional systems, and we have shown how approximation methods can be used to implement efficient PEPS based simulation. We have also demonstrated that MPS and PEPS can be used to simulate the time evolution and thermal states of systems governed by local Hamiltonians. Finally, we have discussed other tensor network based approaches, such as MERA for scale-invariant systems or iMPS and iPEPS for infinite sytems, and concluded with a discussion on how to apply tensor network methods to fermionic systems.

At the end, let us note that while we have focused on Tensor Networks in the context of numerical simulations, these ansatzes also serve as powerful analytical tools. To name just a few, MPS and PEPS can be used to build exactly solvable models (most prominently, the AKLT model [46]), where a given MPS or PEPS arises as the exact ground state of a local Hamiltonian [9, 47, 48], and they serve as a framework to understand entanglement properties of quantum states and thus to classify quantum phases, such as topological phases [49] and symmetry protected phases [50–53], thereby going beyond the framework of Landau theory which can be understood using product states, i.e., MPS with $D = 1$.

References

[1] C.H. Bennett, H.J. Bernstein, S. Popescu, and B. Schumacher, Phys. Rev. A **53**, 2046 (1996), quant-ph/9511030

[2] J. Eisert, M. Cramer, and M. Plenio, Rev. Mod. Phys. **82**, 277 (2010), arXiv:0808.3773

[3] M. Hastings, J. Stat. Mech. , P08024 (2007), arXiv:0705.2024

[4] F. Verstraete and J.I. Cirac, Phys. Rev. B **73**, 094423 (2006), cond-mat/0505140

[5] G. Vidal, Phys. Rev. Lett. **93**, 040502 (2004), quant-ph/0310089

[6] N. Schuch, M. M. Wolf, F. Verstraete, and J.I. Cirac, Phys. Rev. Lett. **98**, 140506 (2007), quant-ph/0611050

[7] U. Schollwöck, Rev. Mod. Phys. **77**, 259 (2005), cond-mat/0409292

[8] D. Perez-Garcia, F. Verstraete, M.M. Wolf, and J.I. Cirac, Quant. Inf. Comput. **7**, 401 (2007), quant-ph/0608197

[9] M. Fannes, B. Nachtergaele, and R.F. Werner, Commun. Math. Phys. **144**, 443 (1992)

[10] J. Eisert, Phys. Rev. Lett. **97**, 260501 (2006), quant-ph/0609051

[11] N. Schuch, I. Cirac, and F. Verstraete, Phys. Rev. Lett. **100**, 250501 (2008), arXiv:0802.3351

[12] S.R. White, Phys. Rev. Lett. **69**, 2863 (1992)

[13] F. Verstraete, D. Porras, and J.I. Cirac, Phys. Rev. Lett. **93**, 227205 (2004), cond-mat/0404706

[14] U. Schollwöck, Ann. Phys. **326**, 96 (2011), arXiv:1008.3477

[15] X.-G. Wen, *Quantum Field Theory of Many Body Systems* (Oxford University Press, 2004)

[16] A. Kitaev, Ann. Phys. **303**, 2 (2003), quant-ph/9707021

[17] F. Barahona, J. Phys. A **15**, 3241 (1982)

[18] S. Yan, D.A. Huse, and S.R. White, Science **332**, 1173 (2011), arXiv:1011.6114

[19] M.B. Hastings, Phys. Rev. B **73**, 085115 (2006), cond-mat/0508554

[20] M.B. Hastings, Phys. Rev. B **76**, 035114 (2007), cond-mat/0701055

[21] F. Verstraete and J.I. Cirac, (2004), cond-mat/0407066

[22] H.C. Jiang, Z.Y. Weng, and T. Xiang, Phys. Rev. Lett. **101**, 090603 (2008), arXiv:0806.3719

[23] Z.-C. Gu, M. Levin, and X.-G. Wen, Phys. Rev. B **78**, 205116 (2008), arXiv:0806.3509

[24] Z.Y. Xie, H.C. Jiang, Q.N. Chen, Z.Y. Weng, and T. Xiang, Phys. Rev. Lett. **103**, 160601 (2009), arXiv:0809.0182

[25] N. Schuch, M.M. Wolf, F. Verstraete, and J.I. Cirac, Phys. Rev. Lett. **100**, 40501 (2008), arXiv:0708.1567

[26] A.W. Sandvik and G. Vidal, Phys. Rev. Lett. **99**, 220602 (2007), arXiv:0708.2232

[27] L. Wang, I. Pizorn, and F. Verstraete, Phys. Rev. B **83**, 134421 (2011), arXiv:1010.5450

[28] N. Schuch, M.M. Wolf, F. Verstraete, and J.I. Cirac, Phys. Rev. Lett. **100**, 30504 (2008), arXiv:0705.0292

[29] P. Calabrese and J. Cardy, J. Stat. Mech. P04010 (2005), cond-mat/0503393

[30] N. Schuch, M.M. Wolf, K.G.H. Vollbrecht, and J.I. Cirac, New J. Phys. **10**, 33032 (2008), arXiv:0801.2078

[31] M.C. Bañuls, M.B. Hastings, F. Verstraete, and J.I. Cirac, Phys. Rev. Lett. **102**, 240603 (2009), arXiv:0904.1926

[32] F. Verstraete, J.J. Garcia-Ripoll, and J.I. Cirac, Phys. Rev. Lett. **93**, 207204 (2004), cond-mat/0406426

[33] G. Vidal, Phys. Rev. Lett. **101**, 110501 (2008), quant-ph/0610099

[34] G. Evenbly and G. Vidal, Phys. Rev. Lett. **102**, 180406 (2009), arXiv:0811.0879

[35] A. Sfondrini, J. Cerrillo, N. Schuch, and J.I. Cirac, Phys. Rev. B **81**, 214426 (2010), arXiv:0908.4036

[36] F. Mezzacapo, N. Schuch, M. Boninsegni, and J.I. Cirac, New J. Phys. **11**, 083026 (2009), arXiv:0905.3898

[37] H.J. Changlani, J. M. Kinder, C.J. Umrigar, and G.K.-L. Chan, arXiv:0907.4646

[38] G. Vidal, Phys. Rev. Lett. **98**, 070201 (2007), cond-mat/0605597

[39] J. Jordan, R. Orus, G. Vidal, F. Verstraete, and J.I. Cirac, Phys. Rev. Lett. **101**, 250602 (2008), cond-mat/0703788

[40] R. Orus and G. Vidal, Phys. Rev. B **80**, 094403 (2009), arXiv:0905.3225

[41] P. Corboz, G. Evenbly, F. Verstraete, and G. Vidal, Phys. Rev. A **81**, 010303(R) (2010), arXiv:0904.4151

[42] C.V. Kraus, N. Schuch, F. Verstraete, and J.I. Cirac, Phys. Rev. A **81**, 052338 (2010), arXiv:0904.4667

[43] C. Pineda, T. Barthel, and J. Eisert, Phys. Rev. A **81**, 050303(R) (2010), arXiv:0905.0669

[44] P. Corboz and G. Vidal, Phys. Rev. B **80**, 165129 (2009), arXiv:0907.3184

[45] P. Corboz, R. Orus, B. Bauer, and G. Vidal, Phys. Rev. B **81**, 165104 (2010), arXiv:0912.0646

[46] A. Affleck, T. Kennedy, E.H. Lieb, and H. Tasaki, Commun. Math. Phys. **115**, 477 (1988)

[47] B. Nachtergaele, Commun. Math. Phys. **175**, 565 (1996)

[48] D. Perez-Garcia, F. Verstraete, J.I. Cirac, and M.M. Wolf, Quantum Inf. Comput. **8**, 0650 (2008), arXiv:0707.2260

[49] N. Schuch, I. Cirac, and D. Pérez-García, Ann. Phys. **325**, 2153 (2010), arXiv:1001.3807

[50] F. Pollmann, A.M. Turner, E. Berg, and M. Oshikawa, Phys. Rev. B **81**, 064439 (2010), arXiv:0910.1811

[51] X. Chen, Z. Gu, and X. Wen, Phys. Rev. B **83**, 035107 (2011), arXiv:1008.3745

[52] N. Schuch, D. Perez-Garcia, and J.I. Cirac, Phys. Rev. B **84**, 165139 (2011), arXiv:1010.3732

[53] X. Chen, Z.-X. Liu, and X.-G. Wen, Phys. Rev. B **84**, 235141 (2011), arXiv:1106.4752

Index

X

1. **The LDA+DMFT approach to strongly correlated materials**
   Lecture Notes of the Autumn School 2011 Hands-on LDA+DMFT
   edited by E. Pavarini, E. Koch, D. Vollhardt, A. Lichtenstein (2011), 420 pages
   ISBN: 978-3-89336-734-4

2. **Correlated Electrons: From Models to Materials**
   Lecture Notes of the Autumn School on Correlated Electrons 2012
   edited by E. Pavarini, E. Koch, F. Anders, M. Jarrell (2012), 450 pages
   ISBN: 978-3-89336-796-2